Exploiting multiple hit-identification strategies to identify novel inhibitors of the anti-infective target DXPS

Dissertation

Zur Erlangung des Grades der Doktorin der Naturwissenschaften

der Naturwissenschaftlich-Technischen Fakultät

der Universität des Saarlandes

vorgelegt von

M. Sc. Sandra Johannsen

Saarbrücken

2022

Tag des Kolloquiums:	22. September 2022
Dekan:	Prof. Dr. Jörn Eric Walter
Berichterstatter:	Prof. Dr. Anna K. H. Hirsch
	Prof. Dr. Christian Ducho
Akad. Mitglied:	Dr. Josef Zapp
Vorsitz:	Prof. Dr. Claus-Michael Lehr

Die vorliegende Arbeit wurde von April 2018 bis April 2022 unter Anleitung von Frau Prof. Dr. Anna K. H. Hirsch in der Fachrichtung Pharmazeutische und Medizinische Chemie der Naturwissenschaftlich-Technischen Fakultät der Universität des Saarlandes, sowie am Helmholtz-Institut für Pharmazeutische Forschung Saarland (HIPS) in der Abteilung Drug Design and Optimization (DDOP) angefertigt.

To my parents

Acknowledgements

First and foremost, I want to express my gratitude towards Prof. Dr. Anna K. H. Hirsch for her supervision and guidance during this thesis. I would also like to thank my thesis committee and co-examiners Prof. Dr. Christian Ducho and Dr. Josef Zapp for our productive and inspiring meetings and discussions.

Working on a project together makes successes a reason to celebrate and disappointments less painful. Many thanks to the amazing members of the DXPS team: Dr. Ravindra P. Jumde, Robin M. Gierse, Zhoor Hamid, Alaa Alhayek, Antoine Lacour, Dr. Sebastian Adam and Zhu Di. I want to give a special thank you to Ravi who has not only been great company and support in the lab, but has also corrected most of this thesis together with Dr. Mostafa Hamed.

There have been six amazing students whom I had the pleasure to supervise in the last years and to whom I am very grateful: Vittoria Nanna, Anna Fontana, Lea Eschweiler, Aleksandra Olshanova, Ellie Smerznak and Zahra Adeli.

I would like to thank Dr. Josef Zapp for his help with establishing the STD-NMR at HIPS and with NMR issues in general. Many thanks to Dr. Andreas Kany for helping me with the HPLC-MS/MS-based assay and for his corrections of that chapter. Tabea-Catharina Wittmann has helped me a lot in the last months of the thesis by performing the DXPS-IspC-coupled and the HPLC-MS/MS-based assays for me. Thank you to Dr. Walid A. M. Elgaher for working with me on the SPR and to Dr. Jörg Haupenthal, Selina Wolter, Jeannine Jung, Simone Amann and Dennis-Thomas Jener for organizing and performing assays, and assistance in the biology lab. Many thanks to Samira Speicher for saving all of us in the chemistry lab. While scientific support is important, this would not have been possible without the administrative, technical and IT support of Bahareh Kadkhodazadeh, Lisa Marie Andre, Julia Mohr, Annette Herkströter, Christian Zeuner, Frank Jakob, Mark Caspari and Michael Roth.

Since writing a thesis is impossible to do without good colleagues and friends, I first and foremost want to thank Christina Kosch, who has literally been with me from day one, for our talks, and breaks and all the fun outside of work. I had great office mates over the years and I would like to thank Serena Della Volpe and Henni-Karoliina Ropponen for the great times we spent together. Cansu Kaya has been my best conference buddy and I am very sad that Corona prevented us from seeing more of

the world together. In addition, I want to thank, in no particular order, all the other people who have made the time at HIPS truly special: Jelena Konstantinović, Christian Schütz, Alexander Kiefer, Federica Mancini, Eva Záhorská, Marta Czekańska, Joscha Meiers, Spyros Bousis, Aketza Romaniega Bilbao, Mostafa Hamed, Eleonora Diamanti, Uladzislau Hapko and Sanguen Lee. A special thanks goes to Yingwen Wu and Dominik Kolling for their entertaining distractions during the hard hours of writing.

Thank you, Eike Siebs for always being by my side.

Curriculum Vitae

Sandra Johannsen
born on 7th December 1991 in Pirmasens, Germany

Education

2018–2022	PhD in the group of Prof. Anna K. H. Hirsch Helmholtz Institute for Pharmaceutical Research Saarland (HIPS)
2015–2018	M.Sc. Medicinal and Natural Product Chemistry Leibniz University of Hanover
2012–2015	B.Sc. Chemistry Leibniz University of Hanover
2011	Abitur Gymnasium Neustadt am Rübenberge

Research Experience

2018	Master's thesis in the group of Prof. Oliver Plettenburg Leibniz University of Hanover Thesis: Synthese neuartiger Aureothin-Derivate
2016–2017:	Research internship in the group of Prof. Steven Ley University of Cambridge
2015	Bachelor's thesis in the group of Prof. Russell Cox Leibniz University of Hanover Thesis: Synthesis of Substrates for the SQTKS Dehydratase

Publications

D. Zhu,‡ S. Johannsen,‡ T. Masini,‡ C. Simonin,‡ J. Haupenthal, B. Illarionov, A. Andreas, M. Awale, R. M. Gierse, T. van der Laan, R. van der Vlag, R. Nasti, M. Poizat, E. Buhler, N. Reiling, R. Müller, M. Fischer, J.-L. Reymond, A. K. H. Hirsch, *Discovery of novel drug-like antitubercular hits targeting the MEP pathway enzyme DXPS by strategic application of ligand-based virtual screening*, *Chem. Sci.* **2022**, *13*, 10686–10698.

Contribution: see Chapter 6.1.1.

S. Johannsen,‡ R. M. Gierse,‡ A. Krüger, R. L. Edwards, V. Nanna, A. Fontana, D. Zhu, T. Masini, L. Pessanha de Carvalho, M. Poizat, B. Kieftenbelt, D. M. Hodge, S. Alvarez, D. Bunt, K. A. Meissner, E. Elisa de Souza, M. Dröge, B. van Vliet, J. den Hartog, M. C. Hutter, J. Held, A. R. Odom John, C. Wrenger, A. K. H. Hirsch, *Identification of three new inhibitor classes against Plasmodium falciparum*, uploaded to ChemRxiv (doi: 10.26434/chemrxiv-2022-npslc) and submitted to *European Journal of Medicinal Chemistry* on 15th September 2022.

Contribution: see Chapter 3.5.1.

R. P. Jumde, M. Guardigni, R. M. Gierse, A. Alhayek, D. Zhu, Z. Hamid, S. Johannsen, W. A. M. Elgaher, P. J. Neusens, C. Nehls, J. Haupenthal, N. Reiling, A. K. H. Hirsch, *Hit-optimization using target-directed dynamic combinatorial chemistry: development of inhibitors of the anti-infective target 1-deoxy-D-xylulose-5-phosphate synthase*, *Chem. Sci.* **2021**,*12*, 7775–7785.

Contribution: Surface plasmon resonance experiments against Δ*Mt*DXPS.

H.-K. Ropponen,‡ E. Diamanti,‡ S. Johannsen, L. Lucaroni, B. Illarionov, M. Fischer, J. Haupenthal, A. K. H. Hirsch, *Novel Class Inhibitors of Escherichia coli IspE Originating from a Virtual Screening*, manuscript in preparation.

Contribution: STD-NMR experiments of hit compounds. Writing of the manuscript.

‡ These authors have contributed equally.

Zusammenfassung

Die Corona Pandemie hat dafür gesorgt, dass Infektionskrankheiten und damit auch der Kampf gegen antibiotikaresistente Keime ins Bewusstsein der Öffentlichkeit gerückt sind. Ein neues Target in diesem Kampf ist die 1-Deoxy-D-xylulose-5-phosphat Synthase (DXPS). Das Enzym ist bereits seit einigen Jahrzehnten bekannt, aber bisher wurden nur wenige Inhibitoren gefunden. In dieser Arbeit wurden verschiedene Hit-Identifikationsstrategien genutzt, um neue Inhibitoren gegen *Mycobacterium tuberculosis* und *Plasmodium falciparum* DXPS zu finden.

Dafür wurde eine fokussierte Fragmentbibliothek gegen DXPS in verschiedenen biophysikalischen Assays untersucht, ein HPLC-MS/MS-basierter DXPS Assay wurde etabliert, in Kooperation mit der Firma Atomwise wurde ein virtuelles Screening an DXPS durchgeführt und drei bereits bekannte Hit-Klassen wurden im Rahmen dieser Arbeit in phänotypischen Assays gegen *P. falciparum* getestet und synthetisch optimiert.

Zusammengefasst hat diese Arbeit zur Identifikation mehrerer Binder und Inhibitoren beigetragen, die vielversprechende Eigenschaften aufweisen und weiter zu Lead-Verbindungen optimiert und somit für die Medikamentenentwicklung genutzt werden können.

Summary

The coronavirus pandemic has raised awareness for infectious diseases, which also put a spotlight on the fight against anti-microbial resistance. A promising new target in this fight is 1-deoxy-D-xylulose-5-phosphate synthase (DXPS). Although it has been known for the past few decades, only a few promising inhibitors have been identified so far. For this thesis, multiple hit-identification strategies were pursued with a special focus on *Mycobacterium tuberculosis* and *Plasmodium falciparum* DXPS to find new inhibitors.

For this thesis a focused fragment library was screened against DXPS in different biophysical assay, in collaboration with the company Atomwise, a virtual screening was performed and three previously identified hit classes were investigated in phenotypic assays against *P. falciparum* and synthetically optimized.

In summary, this thesis has contributed to the identification of several new binders and inhibitors that have promising properties to continue their optimization into leads for drug development.

Abbreviations

%inhi.	percent inhibition
ACTs	artemisinin-based combination therapies
ADP	adenosine diphosphate
AMR	antimicrobial resistance
Atc	anhydrotetracycline
ATP	adenosine triphosphate
b.	binding
b.p.	broad peaks
BAP	butyl-acetylphosphonate
BME	β-mercaptoethanol
Boc	*tert*-butyloxycarbonyl
CAS	Chemical Abstract Service
CDP-ME	4-diphosphocytidyl-2-*C*-methylerythritol
CDP-MEP	4-diphosphocytidyl-2-*C*-methylerythritol phosphate
CI	confidence intervall
Cl	*Chlamymodomas*
clogP	partition coefficient
CMP	cytidine monophosphate
Cpd.	compound
Cmpd.	compound
CRISPRi	clustered regularly interspaced short palindromic repeats interference
CTP	cytidine triphosphate
Da	Dalton
DIPEA	*N*,*N*-diisopropylethylamine
DMADP	dimethylallyl diphosphate
DMB	1,2-diamino-4,5-methylenedioxybenzene
DMB-py	7-methyl-[1,3]dioxolo[4,5-g]quinoxalin-6(5H)-one
DMF	dimethylformamide
DMSO	dimethyl sulfoxide
DOXP	1-deoxy-D-xylulose 5-phosphate
Dr	*Deinococcus radiodurans, D. radiodurans*
DXPS	1-deoxy-D-xylulose-5-phosphate synthase
e.g.	*exempli gratia*
E1-PDH	pyruvate dehydrogenase
Ec	*Escherichia coli, E. coli*
EC_{50}	half maximal effective concentration
EDC	1-ethyl-3-(3-dimethylaminopropyl)-carbodiimide
E-LThDP	DXPS complex with ThDP and covalently bound pyruvate
ERAD	endoplasmic reticulum assisted degradation
et al.	*et alii*
EtOAc	ethyl acetate
FabI	enoyl-[acyl-carrier-protein] reductase
FAS	fatty acid biosynthesis pathway

FBDD	fragment-based drug design
FSM	fosmidomycin
GAP	glyceraldehyde 3-phosphate
HEFL	halogen-enriched fragment library
HEPES	2-[4-(2-hydroxyethyl)piperazin-1-yl]ethane-1-sulfonic acid
Hi	*Haemophilus influenza, H. influenza*
HIPS	Helmholtz Institute for Pharmaceutical Research Saarland
HMBC	heteronuclear multiple bond correlation
HMBDP	(*E*)-4-hydroxy-3-methyl-but-2-enyl diphosphate
HOBt	1-hydroxybenzotriazole
HPLC	high-performance liquid chromatography
HR-ESI	high-resolution electron spray ionization
HRP2	histidine-rich protein 2
HSQC	heteronuclear single-quantum correlation spectroscopy
HTS	high-throughput screening
Huh7	human hepatoma cells
Hz	Hertz
IC_{50}	half maximal inhibitory concentration
IDP	isopentenyl diphosphate
irr.	irradiation
IspC	1-deoxy-D-xylulose-5-phosphate reductoisomerase
IspD	2-*C*-methyl-D-erythritol 4-phosphate cytidylyltransferase
IspE	4-diphosphocytidyl-2-*C*-methyl-D-erythritol kinase
IspF	2-*C*-methyl-D-erythritol 2,4-cyclodiphosphate synthase
IspG	4-hydroxy-3-methylbut-2-en-1-yl diphosphate synthase
IspH	4-hydroxy-3-methylbut-2-enyl diphosphate reductase
ITC	isothermal titration calorimetry
KasA	β-ketoacyl ACP synthase
K_D	dissociation constant
K_i	inhibition constant
K_i*	Morrison inhibition constant
K_M	Michaelis constant
LBVS	ligand-based virtual screening
MDR	multi-drug resistant
MEcDP	2-*C*-methyl-D-erythritol 2,4-cyclodiphosphate
MEP	2-*C*-methyl-D-erythritol 4-phosphate
MIC	minimum inhibitory concentration
MOI	mode of inhbition
MS	mass spectrometry
MST	microscale thermophoresis
Mt	*Mycobacterium tuberculosis, M. tuberculosis*
n.b.	no binding
n.f.	no fit
NADPH	nicotinamide adenine dinucleotide phosphate
NaHMDS	sodium bis(trimethylsilyl)amide

NDM-1	New Dehli metallo-β-lactamase-1
NHS	*N*-hydroxysuccinimide
NMM	*N*-methylmorpholine
NMR	nuclear magnetic resonance
NOESY	nuclear overhauser and exchange spectroscopy
o2s	over two steps
OD	optical density
ORF	open reading frame
Pa	*Pseudomonas aeruginosa, P. aeruginosa*
PBMN	polymyxin B nonapeptide
PBS	phosphate-buffered saline
PDB	protein data bank
Pf	*Plasmodium falciparum, P. falciparum*
pH	potential of hydrogen
PPB	PolyPharmacology Browser
ppm	parts per million
Pv	*Plasmodium vivax, P. vivax*
r.t.	room temperature
RIU	refractive index unit
rpm	revolutions per minute
RU	response unit
SAR	structure-activity relationship
SBVS	structure-based virtual screening
Se	*Salmonella enterica, S. enterica*
spp.	*species pluralis*
SPR	surface plasmon resonance
STD	saturation-transfer difference
TBAF	*tetra*-butylammonium fluoride
TBDMS	*tert*-butyldimethylsilyl chloride
TBME	*tert*-butyl methyl ether
TCA	tricarboxylic acid
tdDCC	target-directed dynamic combinatorial chemistry
ThDP	thiamine diphosphate
THF	tetrahydrofuran
TIS	TurboIonSpray
TLC	thin-layer chromatography
TPK	thiamine pyrophosphokinase
Tris	tris(hydroxymethyl)-aminomethane
TSA	thermal shift assay
UNT	untreated
UV	ultraviolet
VCP	Valosin-containing protein
VS	virtual screening
WHO	World Health Organization
YP	*Yersinia pestis, Y. pestis*

Table of contents

1 Introduction

Antimicrobial resistance (AMR) has dramatically increased in the past decades due to over- and misuse of antibiotics, antivirals, antifungals and antiparasitics.[1] In contrast to the Covid-19 pandemic, the progression of the so called silent AMR pandemic is less visible, but might now be further accelerated by the increased use of disinfectants and antibiotics during the last two years.[2] To raise awareness and streamline research efforts, the World Health Organization (WHO) has published a list of pathogens for which new antimicrobials are urgently needed (**Table 1**).[3] Not only have these organisms acquired multi-drug resistance, but also the development of new antimicrobials has slowed down in recent decades, which makes efficient treatment of infections difficult.[1] In addition, the WHO has prioritized *Mycobacterium tuberculosis* that is often multi-drug resistant (MDR) and responsible for 10 million infections and 1.2 million deaths per year worldwide.[4] The current standard of care for the drug sensitive pathogen is a six-month treatment with a combination of isoniazid, rifampin, pyrazinamide and ethambutol. If adhered to, this regimen is effective, but compliance is a major problem and accelerates the development of MDR strains.[5] In 2019, 485,000 cases of MDR tuberculosis infections have been reported.[4]

Another important target for drug development is the parasite *Plasmodium falciparum* that is responsible for most malaria infections in humans. In 2019, 229 million cases and 409,000 deaths have been reported.[6] Although, the parasite is not mentioned specifically in the WHO priority list to develop new antimicrobials, the emerging resistance to current drugs is becoming a problem. Artemisinin-based combination therapies (ACTs) are recommended for uncomplicated malaria, but delayed parasite clearance is observed especially if the parasite is resistant to the partner drug of artemisinin.[7] In addition, artemisinin resistance is spreading throughout Southeast Asia that also results in slow parasite clearance.[8]

Pathogenic organisms are either already resistant to certain antimicrobials (intrinsic and induced resistance) or they have different mechanisms to acquire AMR. While some mechanisms are not target-related (*e.g.* decreasing the uptake or increasing the efflux of the antimicrobial), others can reduce for example the binding affinity of the antimicrobial by either changing the drug (antimicrobial-modifying enzymes) or the target structure (mutations in the active site). This can happen by small mutations in the genome.[9] Since bacteria have a high mutation and division rates, these mutations

can occur relatively fast, especially if the antibiotic treatment is not followed properly and the dose of antibiotic in the body is not high enough to ensure killing the bacteria as fast as possible.[10] To address these problems, combination therapies of more than one drug are often administered, so that two or more mutations have to occur at the same time to create resistance. Preventing the development of new resistances is the focus on the administrative side of patient care by improving diagnostics, prescription practices and infection prevention.[11] On the research side, known drugs are modified in a way that circumvents the resistance mechanism, but the success is usually only short-term, because the structural differences are not big enough. The same is true for new structures that address the same targets. Therefore, the identification of new targets and the development of new antimicrobials with a novel mode of action are important research areas.

1.1 The MEP pathway

One promising pool of new targets is the 2-*C*-methyl-D-erythritol 4-phosphate (MEP) pathway. It is utilized by a variety of organisms to synthesize the universal isoprenoid precursors isopentenyl diphosphate (IDP) and dimethylallyl diphosphate (DMADP).[12]

Table 1: Utilization of the 2-*C*-methyl-D-erythritol 4-phosphate (MEP) or mevalonate pathways of a selection of pathogens for which new antibiotics are needed.

Pathogen (Gram +/-)	WHO priority	MEP	Mevalonate	Ref.
M. tuberculosis	*	+	-	13
Acinetobacter baumannii (-)	Critical	+	-	14
Pseudomonas aeruginosa (-)	Critical	+	-	15
Klebsiella pneumoniae (-)	Critical	+	-	16
Escherichia coli (-)	Critical	+	-	17
Enterococcus faecium (+)	High	-	+	18
Staphylococcus aureus (+)	High	-	+	19
Helicobacter pylori (-)	High	+	-	20
Campylobacter spp. (-)	High	+	-	21
Salmonella spp. (-)	High	+	-	21
Neisseria gonorrhoeae (-)	High	+	-	21
Streptococcus pneumoniae (+)	Medium	-	+	22
Haemophilus influenzae (-)	Medium	+	-	23
Shigella spp. (-)	Medium	+	-	21

Pathogen (Gram +/-)	WHO priority	MEP	Mevalonate	Ref.
P. falciparum	*	+	-	24

*Not included in the list. spp. = *species pluralis*.

It has been proven by genetic analyses and knockout studies of several organisms that the MEP pathway is essential for the organism's survival since isoprenoids are involved in vital biological functions.[25–29] While many bacteria use the MEP pathway, their human hosts synthesize the same precursors *via* the mevalonate pathway, making the MEP pathway enzymes excellent targets for new antimicrobials. When taking a closer look at the WHO's list of prioritized pathogens, all Gram-negative bacteria utilize the MEP pathway including *M. tuberculosis* and *P. falciparum*, while the Gram-positive ones use the mevalonate pathway (**Table 1**).[3]

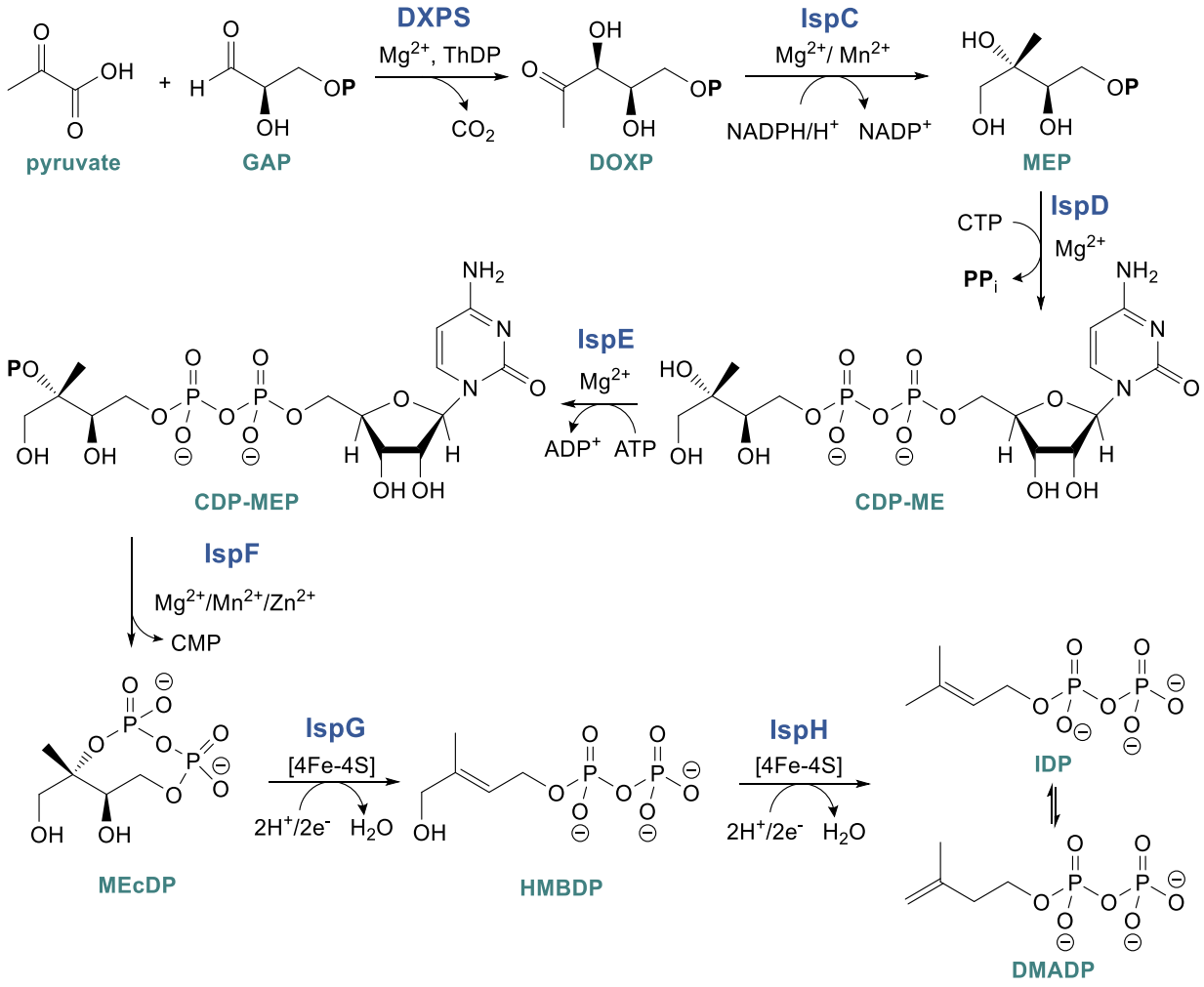

Scheme 1: Schematic overview of the 2-*C*-methyl-D-erythritol 4-phosphate (MEP) pathway. **P** = PO_3^{2-}, GAP = glyceraldehyde 3-phosphate, DXPS = 1-deoxy-D-xylulose-5-phosphate synthase, ThDP = thiamine diphosphate, DOXP = 1-deoxy-D-xylulose-5-phosphate, IspC = 1-deoxy-D-xylulose-5-phosphate reductoisomerase, NADPH = nicotinamide adenine dinucleotide phosphate, IspD = 2-*C*-methyl-D-erythritol 4-

phosphate cytidylyltransferase, CTP = cytidine triphosphate, **PP**i = $P_2O_7^{4-}$, CDP-ME = 4-diphosphocytidyl-2-*C*-methylerythritol, IspE = 4-diphosphocytidyl-2-*C*-methyl-D-erythritol kinase, ATP = adenosine triphosphate, ADP = adenosine diphosphate, CDP-MEP = 4-diphosphocytidyl-2-*C*-methylerythritol, CMP = cytidine monophosphate, IspF = 2-*C*-methyl-D-erythritol 2,4-cyclodiphosphate synthase, MEcDP = 2-*C*-methyl-D-erythritol 2,4-cyclodiphosphate, IspG = 4-hydroxy-3-methylbut-2-en-1-yl diphosphate synthase, HMBDP = (*E*)-4-hydroxy-3-methyl-but-2-enyl diphosphate, IspH = 4-hydroxy-3-methylbut-2-enyl diphosphate reductase, IDP = isopentenyl diphosphate, DMADP = dimethylallyl diphosphate.

The MEP pathway comprises seven enzymes (**Scheme 1**).[30] At the beginning, 1-deoxy-D-xylulose-5-phosphate synthase (DXPS) catalyzes the first rate-limiting decarboxylative condensation step between pyruvate and glyceraldehyde 3-phosphate (D-GAP) to 1-deoxy-D-xylulose-5-phosphate (DOXP). The reaction from DOXP to 2-*C*-methyl-D-erythritol 4-phosphate (MEP) is catalyzed by 1-deoxy-D-xylulose-5-phosphate reductoisomerase (IspC) with nicotinamide adenine dinucleotide phosphate (NADPH) as a reducing agent. After that, 2-*C*-methyl-D-erythritol 4-phosphate cytidylyltransferase (IspD) glycosylates MEP to 4-diphosphocytidyl-2-*C*-methylerythritol (CDP-ME) and 4-diphosphocytidyl-2-*C*-methyl-D-erythritol kinase (IspE) utilizes adenosine triphosphate (ATP) to phosphorylate one of the hydroxyl groups of CDP-ME to form 4-diphosphocytidyl-2-*C*-methylerythritol (CDP-MEP). In the next step, 4-diphosphocytidyl-2-*C*-methyl-D-erythritol kinase (IspF) cyclizes the compound under the release of cytidine monophosphate (CMP) to 2-*C*-methyl-D-erythritol 2,4-cyclodiphosphate (MEcDP). The last two enzymes, 4-hydroxy-3-methylbut-2-en-1-yl diphosphate synthase (IspG) and 4-hydroxy-3-methylbut-2-enyl diphosphate reductase (IspH), in the MEP pathway use [4Fe-4S] clusters to dehydrate MEcDP twice to form IDP and its isomer DMADP. While all of these enzymes are potential drug targets, special focus should be placed on the first and rate-determining one, DXPS.[31] Its product, DOXP, is not exclusively used in the MEP pathway, but is also fed into the biosynthesis of the vitamins thiamine (B_1) and pyridoxine (B_6).[32,33] Therefore, inhibiting DXPS can be more effective than just inhibiting one biosynthetic pathway. DXPS also has the highest flux-control coefficient which means its activity influences the production of IDP and DMADP the most of all MEP enzymes and hence, its inhibition will lower isoprenoid production most effectively.[34,35]

1.2 DXPS as a (drug) target

On the previous pages, the importance to target the MEP pathway and especially DXPS was described. As a ThDP-dependent enzyme, the question is, if it is possible

to address it selectively over human ThDP-dependent enzymes such as pyruvate dehydrogenase (E1-PDH). Crystallization studies of *E. coli* (*Ec*)DXPS and *Deinococcus radiodurans* (*Dr*)DXPS revealed a different domain arrangement that distinguishes DXPS from its close homologues. The active site of DXPS is located in each monomer of a dimer between domains I and II, while in E1-PDH the active sites are at the dimer interface.[36] It was also shown that the active site of DXPS is two-fold larger than that of E1-DPH, which allows the design of sterically demanding inhibitors to achieve selectivity.[37]

1.2.1 Unique reaction mechanism

As described above, DXPS catalyzes the reaction of pyruvate and D-GAP to form DOXP. The group of Caren L. Freel Meyers has started working on elucidating the mechanism of this reaction over a decade ago. Since then, they confirmed DXPS follows a unique random sequential mechanism that further validates it as an interesting target for antimicrobial drug-discovery. They use *Dr*DXPS and *Ec*DXPS as model enzymes in most of their studies and similar results were also found for other homologues.[38,39]

Initially, they could show that DXPS does not follow the typical ping-pong mechanism of other ThDP-dependent enzymes.[40] Normally, pyruvate binds to the enzyme, decarboxylates, and then D-GAP binds and reacts to DOXP in a sequential manner. In contrast, the DXPS complex with ThDP and covalently bound pyruvate (E-LThDP) is stable when there is no decarboxylation trigger present (**Scheme 2**).[41,42] Such a trigger is either D-GAP or oxygen that can also accept two electrons and form peracetate.[43] Before activation, the E-LThDP complex is stable in a closed conformation that opens into a ternary complex when D-GAP is bound, facilitated by the large active site of DXPS.[41,44] Subsequent decarboxylation forms an enamine, which reacts with D-GAP to DOXP. The conformation of the enzyme with DOXP is unknown, but when DOXP is cleaved, the enzyme adopts an open form, and upon release of DOXP, it equilibrates between open and closed form until another pyruvate is bound.[45,46]

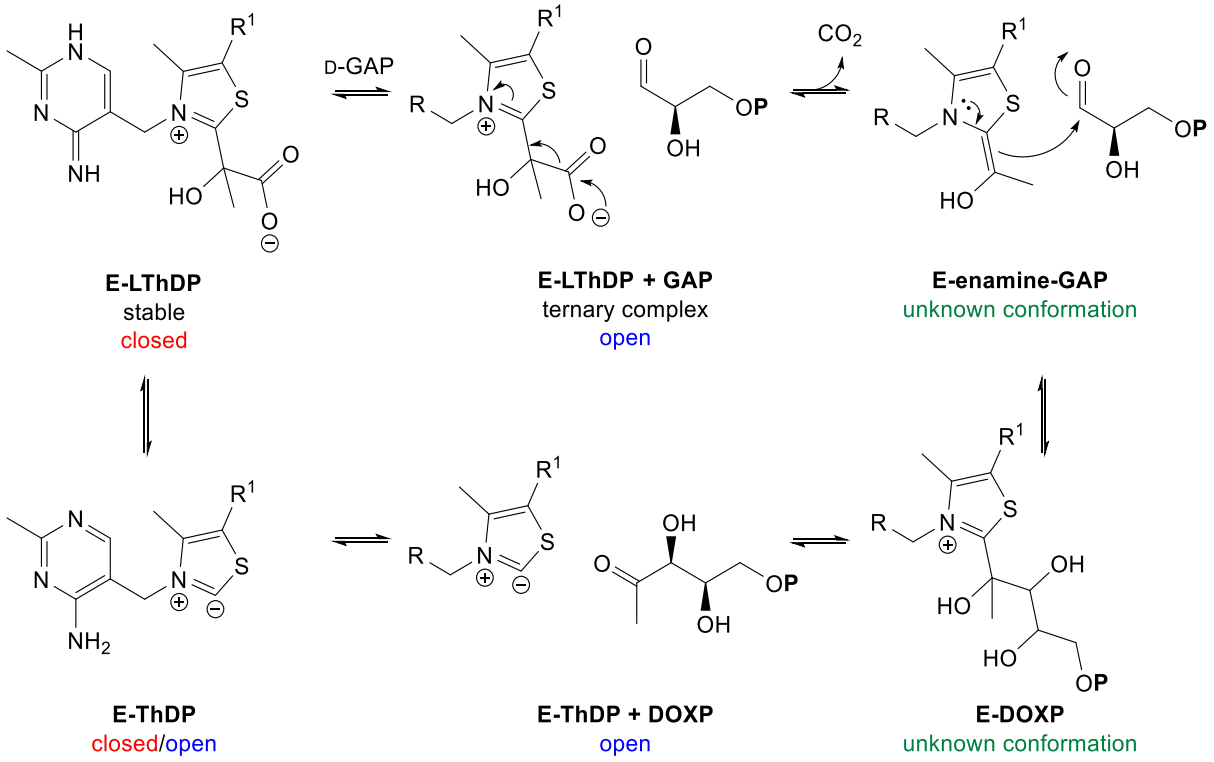

Scheme 2: Mechanism of DXPS-catalyzed 1-deoxy-D-xylulose-5-phosphate (DOXP) formation adapted from Chen *et al*.[47] E = DXPS, R = 4′-amino-2-methyl-5-pyrimidyl, R^1 = β-hydroxyethyldiphosphate; **P** = PO_3^{2-}.

1.2.2 Druggability of the active site of different DXPS homologues

Masini *et al*. further validated DXPS as a drug target by analyzing a published crystal structure of *Dr*DXPS (protein data bank (PDB) ID: 2O1X) with the web-based program DoGSiteScorer.[48] The program evaluates the druggability of a pocket by analyzing its size, solvent exposure and hydrophilicity, since druggable pockets are bigger and deeper, less solvent-exposed and more hydrophobic than undruggable pockets.[49] For DXPS they found five druggable pockets, one of which is the active site. It has a low lipophilic character due to the polar amino acid residues in the diphosphate pocket. Replacing the co-factor ThDP from that part of the pocket will be very challenging to predict accurately with structure-based docking calculations. For the other four identified pockets, favorable scores were calculated, which can be explored as allosteric pockets in the future. Only the inhibitor ketoclomazone (**2**) (see below) has been reported as being uncompetitive to pyruvate and non-competitive to GAP, which indicates binding in an allosteric pocket.[50] However, its exact binding site has not been located yet.

When aligning the DXPS sequences of *E. coli*, *Arabidopsis thaliana*, *M. tuberculosis, P. falciparum* with *Dr*DXPS, a high degree of sequence similarity (45%, 40%, 40% and

33%, respectively) can be seen.[51] The experimental inhibition data for *Dr*DXPS and *M. tuberculosis* (*Mt*)DXPS were used to validate a homology model of *Mt*DXPS that helped to explain differences in inhibition.[52]

A small number of published crystal structures also confirms the conservation of the active site.[36,51] Crystallization of DXPS enzymes is notoriously difficult, because of their flexibility, but anoxic conditions can facilitate crystal formation.[47] In addition, Gierse *et al*. obtained a truncated version of *Dr*DXPS (indicated as Δ*Dr*DXPS) by cutting out a flexible loop from the structure.[53] It crystallizes readily under aerobic conditions and the truncation does not influence the activity of the enzyme. Using the truncation strategy, we were able to obtain different homologues of DXPS, which will be mentioned throughout this thesis: Δ*Mt*DXPS, *P. aeruginosa* Δ(*Pa*)DXPS and *K. pneumoniae* Δ(*Kp*)DXPS.[54,55]

1.2.3 Known DXPS inhibitors

In the past decades, several inhibitors of different DXPS homologues have been identified. They were organized by structural similarity (**Table 2**) and described below.

Table 2: Summary of selected known DXPS inhibitors. *Pa = P. aeruginosa*, *Ec = E. coli*, *Pf = P. falciparum*, *Pv = Plasmodium vivax*, *Cl = Chlamymodomas*, *Hi = Haemophilus influenza*, *Dr = Deinococcus radiodurans*, *Yp = Yersinia pestis*, *Se = Salmonella enterica*, MIC = minimum inhibitory concentration, IC_{50} = half maximal inhibitory concentration.

Structure	IC_{50} or K_i of DXPS homologues or MIC
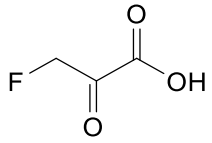 **1**	IC_{50} (*Pa*DXPS) = 400 µM[56] IC_{50} (*Ec*DXPS) = 80 µM[56] K_i (*Pf*DXPS) = 43 ± 1.7 µM[38] K_i (*Pv*DXPS) = 35 ± 1.7 µM[38]
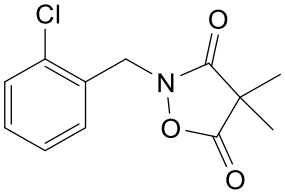 **2**	IC_{50} (*Cl*DXPS) = 100 µM[57] K_i (*Hi*DXPS) = 28 µM[50] K_i (*Ec*DXPS) = 75 µM[50]
MAIPTRGKMPQY (8x)	IC_{50} (*Dr*DXPS) = 461 ± 25 µM[58]

Structure	IC_{50} or K_i of DXPS homologues or MIC
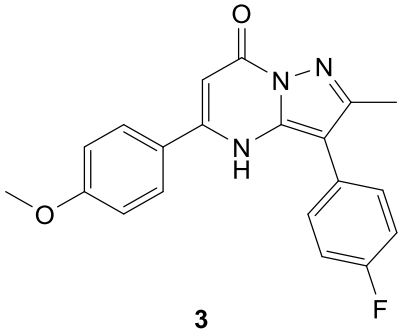 **3**	IC_{50} (*Mt*DXPS) = 10.6 ± 3.1 µM[59] MIC (H37Rv) = 7.7 µM[59]
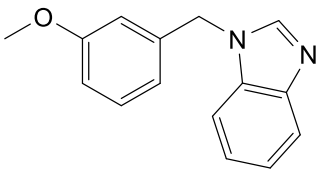 **4**	IC_{50} (*Dr*DXPS) = 595 ± 81 µM[60]
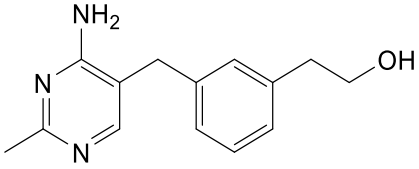 **5**	IC_{50} (*Dr*DXPS) = 109 ± 16 µM[52] IC_{50} (*Mt*DXPS) >2000 µM[52]
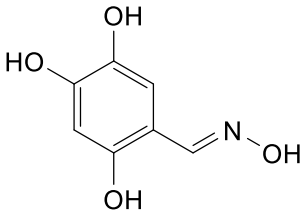 **6**	K_i (*Ec*DXPS) = 2.6 ± 0.6 µM[61]
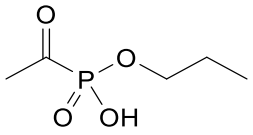 **7**	K_i (*Ec*DXPS) = 5.6 ± 0.6 µM[62] K_i (*Yp*DXPS) = 51 ± 6 µM[63] K_i (*Mt*DXPS) = 81 ± 3 µM[63] K_i (*Se*DXPS) = 76 ± 19 µM[63]
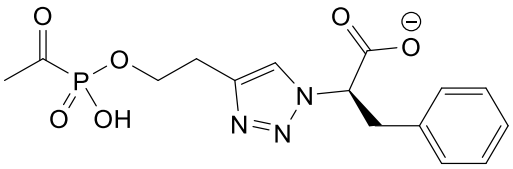 **8**	K_i (*Ec*DXPS) = 0.09 ± 0.01 µM[64]

Structure	IC_{50} or K_i of DXPS homologues or MIC
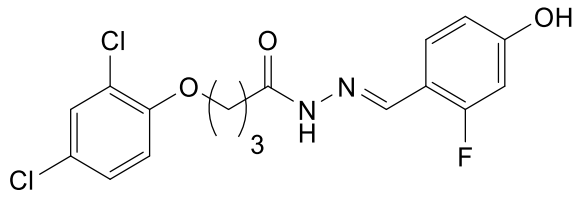 **9**	IC_{50} (*Dr*DXPS) = 34 ± 4 µM[65]

1.2.3.1 Fluoropyruvate (**1**) for studying the reaction mechanism of DXPS

The first compound found that inhibits *Pa*DXPS and *Ec*DXPS was fluoropyruvate (**1**) with a half maximal inhibitory concentration (IC_{50}) of 400 µM and 80 µM, respectively.[56] Later, it was tested against *P. falciparum* (*Pf*) and *P. vivax* (*Pv*) DXPS and shows inhibition constants (K_i) of 43 µM (*Pf*DXPS) and 35 µM (*Pv*DXPS).[38] It covalently binds to ThDP like pyruvate, but the elimination of fluorine leads to an acetyl-ThDP that cannot react again. Fluoropyruvate (**1**) was used for studying the mechanism of DXPS, but it is not a candidate for drug development, since it binds to ThDP and inhibits ThDP-dependent pyruvate carboxylases indiscriminately.[39,66]

1.2.3.2 The herbicide (keto)clomazone (**2**)

The herbicide clomazone was found to be converted to ketoclomazone (**2**), which inhibits different plant and algae DXPS enzymes.[57,67] It is also active against *Haemophilus influenza* DXPS (*Hi*DXPS) with a K_i of 28 µM and *Ec*DXPS with an K_i of 75 µM.[50]

1.2.3.3 Peptidic inhibitor by phage display

Our group has used phage display to identify the only known peptidic inhibitor to date. It inhibits *Dr*DXPS with an IC_{50} of 461 µM.[58]

1.2.3.4 Pyrimidinones against *M. tuberculosis*

Finding inhibitors against *M. tuberculosis* DXPS is one of the focuses of DXPS research. One early example is a class of pyrimidinones that not only inhibit *Mt*DXPS in the low micromolar range but also have a minimum inhibitory concentration (MIC) value in the same range against *M. tuberculosis* H37Rv.[59] This class was further developed as *M. tuberculosis* inhibitors, but a small change in the structure led to a completely different mode of action and loss of activity against DXPS.[68]

1.2.3.5 Fragment-based design led to ThDP competitive inhibitors

While exploring a combination of different nuclear magnetic resonance (NMR) techniques for hit identification, Masini *et al*. from our group identified a fragment inhibitor **4** of *Dr*DXPS. They confirmed the binding of **4** in the ThDP binding pocket.[60] Building on those results, they found other ThDP-competitive inhibitors, which are close analogues of ThDP. Compound **5** inhibits *Dr*DXPS with an IC_{50} of 109 µM and is selective for this homologue over *Mt*DXPS, which they could explain using their *Mt*DXPS homology model presented in the same paper.[52]

1.2.3.6 The first GAP-competitive inhibitors: Hydroxybenzaldoximes

This compound class was found, when Bartee *et al*. tried to find inhibitors that occupy the pyruvate and GAP binding site simultaneously.[61] But instead of finding compounds with the desired properties, they identified a group of hydroxybenzaldoxime derivatives that inhibited *Ec*DXPS with a K_i of 2 µM (compound **6**) that turned out to be the first GAP-competitive inhibitors. All other inhibitors presented in this chapter are (when determined) competitive to pyruvate, while the hydroxybenzaldoximes are uncompetitive or noncompetitive to pyruvate.

1.2.3.7 Acetylphosphonates

Methylacetylphosphonate has been used as a pre-decarboxylation reaction intermediate analogue to study the decarboxylation reaction of pyruvate in DXPS.[69] The group of Caren L. Freel Meyers used this as a starting point to further study the reaction mechanism of DXPS, but also to develop potent inhibitors. Their first report analyzes the differences between methyl-, ethyl- and butyl- acetylphosphonate (BAP). BAP (**7**) not only inhibits *Ec*DXPS with a K_i of 5.6 µM, but is also selective towards DXPS over other ThDP-dependent enzymes.[62] They improved the selectivity further by replacing the butyl group of **7** with a benzyl group forming BnAP. This compound's activity was comparable to **7**, but it was even more selective toward DXPS over other ThDP-dependent enzymes.[37] Later, BAP was also tested against several DXPS homologues from *Y. pestis*, *M. tuberculosis* and *S. enterica* with smaller K_i values for all of them, but with the same mode of action.[63] In the same study, DXPS was confirmed as the target in *E. coli* MG1655 by rescuing growth with feeding 1-deoxy-D-xylulose. However, the compound shows a weak cellular activity (MIC = 1 mg/mL), which might be due to low cell uptake.

The next improvement was achieved when they grew the acetylphosphonates in the direction of the GAP binding site. They installed groups that are negatively charged at physiological pH and can interact at the same cationic binding site as GAP. The best inhibitor **8** has a K_i of 90 nM and is the most potent inhibitor of DXPS to date.[64] Using a prodrug approach, Bartee *et al*. also tried to improve its activity against *E. coli*, but for this compound, the prodrug did not improve the MIC value. However, the parent alkyne compound before the click reaction, is highly active with a MIC of 20 nM.[70] These compounds are a good foundation to continue their development into antibacterial drugs.

1.2.3.8 Acylhydrazones

The newest class of inhibitors was developed by our group using target-directed dynamic combinatorial chemistry (tdDCC).[65] In this method, the protein of interest selects its binders from a library of acylhydrazones that are in equilibrium with each other. The formation of the best binder(s) is amplified. After several rounds of tdDCC to improve the binding affinity, we found compound **9** with an IC_{50} of 34 µM against *Dr*DXPS. Some of the amplified acylhydrazones were active against *E. coli* ΔTolC and *M. tuberculosis*.

1.3 Hit-identification strategies

Identifying a hit is the first step in any drug-discovery program. When screening a compound library in a cellular or animal disease model, a change of phenotype indicates a promising compound (phenotypic drug-discovery).[71] In this approach, the protein target is unknown but can be identified later. Alternatively, the compound library can be tested against the target of interest directly (target-based drug-discovery), but for this, a particular target has to be identified and validated for the disease of interest first and the hits have to be optimized later for cellular activity.[72] Which of these methods is used is usually dependent on the availability of a druggable target. We found inhibitors of *P. falciparum* using a phenotypic assay (for more details see Chapter 3.5), but as has been established in the previous section, DXPS is a promising drug target, so target-based hit identification will be employed throughout most of this thesis.

First, a functional assay is needed to evaluate tested compounds based on the assay read-out. For DXPS, this is an activity assay observing its catalytic reaction either on its own or coupled with IspC. Part of this work was the establishment of a high-

performance liquid chromatography-mass spectrometry (HPLC-MS)/MS-based assay in our lab (see Chapter 3.3). The functional assay is then used to screen large compound libraries, determine the hits with the highest inhibition value and then optimize the structure found further. Since this involves a lot of work, there are strategies to reduce the number of tested compounds. Depending on the availability of a crystal structure of the protein of interest, different computer-assisted methods are utilized.

1.3.1 Ligand- and structure-based virtual screening

In case there is no crystal structure available, ligand-based virtual screening (LBVS) can be utilized to identify new inhibitors as it relies only on the structural and/ or physicochemical information of inhibitors and non-inhibitors.[73] The compounds' features are represented by descriptors that can describe 1D or 2D properties. From this information, predictions about the inhibitory potential of other compounds can be made and thereby the number of compounds to test is reduced. We used LBVS to identify inhibitors against *Mt*DXPS and *M. tuberculosis* (see Chapter 6.1). Structure-based virtual screening (SBVS) aids the identification of compounds just as LBVS does, but is based on the protein structure. Within the protein, a binding site is defined around a co-crystallized inhibitor a bound cofactor or substrate. Compounds are virtually fit (docked) into this binding side and evaluated (scored) according to their predicted interactions with the protein.[73] In Chapter 3.4, we have performed a SBVS campaign against Δ*Mt*DXPS.

1.3.2 Fragment-based drug design (FBDD)

Instead of performing a high-throughput screening (HTS) with a large number of compounds, smaller libraries can be designed with properties that are more specific. One design strategy is to use small compounds, so-called fragments, as starting points for hit development.[74] At the time of writing this thesis, six approved drugs on the market originate from FBDD campaigns, which demonstrates the effectiveness of this approach (Erdafitinib[75], Pexidartinib[76], Vemurafenib[77], Venetoclax[78], Sotorasib[79], Asciminib[80]). However, none of them is an antibiotic and only a few fragment-derived antimicrobials are in clinical trials.[81] Using a fragment library has several advantages. For example, it covers a wider chemical space within a smaller number of compounds than a HTS library.[74] The chances of finding a hit increase and the modification possibilities with small compounds increase as well. Fragments are usually more

soluble, which improves their handling in biophysical assays that are employed for library screenings. While advancing a hit fragment into a drug, its pharmacokinetic profile can be monitored and adjusted along the way which makes the compound more drug-like and orally available with fewer side-effects.[82]

1.3.3 Biophysical screening techniques for FBDD and beyond

Choosing the right method for fragment screening is important for optimal outcome. It is recommended to utilize at least two orthogonal methods to validate fragment hits since each has advantages and disadvantages (**Table 3**).[74] Method selection is dependent on the properties of the target protein (*e.g.* stability in solution, size or amino acids on the surface).

Table 3: Selection of biophysical methods used in fragment-based screenings, and their advantages and disadvantages.[83–85] NMR = nuclear magnetic resonance, STD = saturation-transfer difference, HSQC = heteronuclear single-quantum correlation spectroscopy, SPR = surface plasmon resonance, MST = microscale thermophoresis, ITC = isothermal titration calorimetry, TSA = thermal shift assay.

Method	Advantages	Disadvantages
Ligand-observed NMR (*e.g.* STD-NMR)	+ fast + fragment mixtures for medium throughput + low protein concentrations	– poor performance with small proteins – no binding site information
Target-observed NMR (*e.g.* ^{15}N-HSQC)	+ binding site and mode can be identified + small proteins	– isotopically labeled protein – time consuming – high protein concentrations needed
SPR	+ binding kinetics + low protein amount + sensitive	– finding immobilization conditions – protein not in solution – stable protein needed
MST	+ in solution	– labeling necessary – low throughput
ITC	+ thermodynamic parameters	– enthalpic binding needed – high protein consumption – compounds have to be soluble
TSA	+ fast + high throughput + low protein amount	– fluorescent dye – artefacts from dye and aggregation

X-ray	+	binding site and mode can be identified	–	protein has to crystallize and diffract well

NMR based techniques are very popular since they enable observation of the protein in solution. Target-based methods use isotopically labeled proteins, and while it is time-consuming and more difficult to analyze the data, they give detailed information about the binding site and the binding mode of the compound.[86] For small proteins (<40 kDa), these experiments work well, but a lot of protein is needed. Ligand-observed techniques are a good alternative, if no labeled protein is available or if the protein is bigger than 40 kDa. Mixtures of fragments can easily be analyzed in one experiment and even with low protein concentrations, good results can be achieved. Saturation-transfer difference (STD)-NMR is the most popular of the ligand-based NMR methods. Here, the protein is selectively saturated by irradiating at a region of the spectrum that only contains protein resonances (–2 ppm to 1 ppm).[86] The saturation is transferred to any bound, small molecule by spin diffusion, through the nuclear Overhauser effect. The difference of the spectrum, where the solution was irradiated at a region without protein signals (off-resonance, no saturation of the protein), to the spectrum, where the protein got saturated (on-resonance), results in the STD spectrum, in which only the proton signals of a binding compound remain.[85] If a selection of compounds is used with no signal overlap, they can be measured in the same solution and only the signals from the binding compounds remain. In addition, this technique can give a first indication of the binding mode. Protons that are closer to the protein receive more saturation and have a bigger signal in the STD spectrum.[87] This so called epitope mapping can help guide synthesis efforts for further development.

For surface plasmon resonance (SPR), the protein of interest is immobilized on a chip and compounds are run over the surface.[88] Polarized light induces a plasmon wave on the chip, whose refractive index changes upon binding of a compound. The change of the reflection angle is measured in real time as response units and gives information about the kinetics, such as off- and on-rate as well as the dissociation constant (K_D), of the binding event. This method works well for proteins that can be immobilized on the chip and stay stable over the time of the measurement. Finding the correct immobilization conditions can be difficult and careful preparation before the experiment is necessary. The method is very sensitive and therefore, popular in fragment screening.

Another sensitive method is microscale thermophoresis (MST).[89] Thermophoresis, the movement of molecules in temperature gradients, is measured. Since a protein with a bound compound moves differently than a free protein, the binding event can be followed. Not all proteins are suitable for this approach, because a fluorescent label is necessary. In many cases, SPR is more applicable and reliable than MST.

To get the most information about a binding event, isothermal titration calorimetry (ITC) is the method of choice.[84] By measuring the generation or consumption of heat when titrating a protein and a compound together, stoichiometry, K_D, and changes in enthalpy and entropy can be determined. However, for fragments with a low binding affinity, a lot of protein is needed and the compounds have to be readily soluble.

Thermal shift assay (TSA) is a fast and cheap method that measures the shift in melting temperature of the protein upon binding of a compound.[84] A fluorescent dye is needed, that binds to the hydrophobic surface of an unfolding protein, which makes the method prone to artefacts from aggregation.

X-ray crystallography can be used as a screening tool for targets that crystallize well and if access to a synchrotron is readily available. To confirm the binding mode of fragment hits from other techniques, a co-crystal structure can guide the synthetic efforts to progress a fragment project further.[83]

All of these techniques can also be used for bigger compounds to validate target binding and can give additional information about the binding event. In SPR, MST, ITC and TSA more detailed information about the binding kinetics can be gained, but for that, the compounds have to be either potent binders or soluble enough to give reliable results.

2 Aims of the thesis

The identification of hit compounds against novel targets is an important first step in drug discovery. Several inhibitors of DXPS have been published, but most of them could not be developed further. There are different options to find and validate new hits. In this thesis, we used a variety of methods to find new structures and develop them into hit compounds. We were especially interested in inhibitors against *M. tuberculosis* DXPS and *P. falciparum*. The purification and stability of the native *M. tuberculosis* enzyme (*Mt*DXPS) so far is unreliable, but truncated Δ*Mt*DXPS is easier to handle and was therefore used throughout this thesis instead. We also took advantage of the model enzyme *Dr*DXPS for assays where a higher amount of protein was needed as Δ*Mt*DXPS is usually reacting slowly. Since there was no *Pf*DXPS available for this thesis, inhibitory activity was tested in blood-stage *P. falciparum.*

First, we used STD-NMR and SPR to screen a halogen-enriched fragment library to find and validate the binding of fragments to Δ*Mt*DXPS. A selection of structurally related fragments of the most promising hits was purchased and tested. Using STD-NMR, we also determined the binding epitope to identify potential growth vectors. From there, suggestions for optimized, more complex compounds were made that will be synthesized in the future.

Measuring enzyme inhibition reliably is crucial for successful medicinal chemistry projects. We implemented and validated a HPLC-MS/MS-based assay that is independent of IspC as an auxiliary enzyme to identify new inhibitors against a variety of DXPS enzymes.

The HPLC-MS/MS-based assay was then used together with SPR to validate hits from a virtual screening performed by Atomwise. After applying for the AIMS award, Δ*Mt*DXPS was selected for a virtual screening of the Enamine library using Atomwise's in-house program Atomnet. As a result, 94 compounds were delivered to us for testing. The most promising hit was derivatized and a follow-up VS delivered another 86 compounds for testing. In parallel, compounds were tested against *E. coli* K12 and ΔTolC as a Gram-negative model organisms that also utilizes DXPS.

We also focused on three inhibitor classes that have previously been identified by LBVS against *M. tuberculosis* (manuscript see Appendix 6.1) and show activity against

P. falciparum. Therefore, new derivatives were synthesized and tested to improve activity and for target validation. The results were summarized in a manuscript.

It was shown how important it is to pursue multiple hit-identification routes to increase the pool of hit classes that can be further developed into lead compounds.

3 Results and discussion

3.1 General comments

All projects are presented in the following four chapters. At the beginning of each sub-chapter, a contribution overview is presented to indicate who has been involved in the different parts of the thesis. At the end of each sub-chapter, a short conclusion and an outlook are given. Abbreviations are introduced again at the beginning of each chapter. Numbering of compounds starts at the beginning of each chapter to keep it more concise. Numbering in the supplementary materials follows the numbering of the respective chapters. Supplementary materials for Chapters 3.2, 3.3 and 3.4 are combined at the end of this thesis and the chemical syntheses are combined in Chapter 5.5. Supplementary materials for Chapter 3.5 are included in the manuscript, while supplementary figures can be found in Chapter 5.4. NMR and MS spectra can be found online at ChemRxiv (doi: 10.26434/chemrxiv-2022-npslc). All supplementary information for Chapter 6.1 is also available online (doi: 10.1039/D2SC02371G). All references are collectively presented at the end of the thesis except for the ones from Chapter 6.1, which can be found included in the manuscript (pages 276–278).

3.2 Fragment screening by STD-NMR spectroscopy as a tool for hit-identification against the anti-infective target DXPS

S. Johannsen, R. M. Gierse, A. Alhayek, R. P. Jumde, D. Willocx, A. K. H. Hirsch.

This part of the thesis will be prepared for publication after additional experiments described in Chapter 3.2.8 are finished.

3.2.1 Contributions

Sandra Johannsen planned and performed all experiments and syntheses in this chapter. She wrote the main text and supplementary information. Robin M. Gierse and Alaa Alhayek expressed and purified the proteins and Dr. Ravindra P. Jumde helped with immobilization and data analysis for the SPR experiments. In addition, Dr. Josef Zapp gave valuable input for the implementation of the STD-NMR procedure at HIPS and Dr. Walid A. M. Elgaher helped with the SPR setup. Daan Willocx will perform the synthesis of new derivatives of the hit fragment and perform follow-up SPR experiments that are not part of this thesis, but will be part of the publication that will be summarizing this work. Zhoor Hamid and Sebastian Adam have performed co-crystallization experiments with fragment **10** that are still ongoing. Anna K. H. Hirsch was responsible for supervision, conceptualization and project administration.

3.2.2 Advantages of a HEFL

Fragment-based drug discovery (FBDD) can be a powerful tool to identify new hit structures as discussed in the introduction. For this project, we screened a halogen-enriched fragment library (HEFL) of 146 compounds against Δ*Mt*DXPS by saturation-transfer difference nuclear magnetic resonance (STD-NMR) and validated the hits by SPR.[90]

Halogens, especially fluorine and chlorine, are present in many commercial drugs. Often they are introduced to tune physiochemical properties, but they can also interact with the carbonyl groups of the protein backbone or amino acid side chains and form halogen–protein bonds that contribute to the binding affinity.[91] Halogen bonds are formed *via* the σ-hole at the end of the R-X (X = halogen) bond, where anisotropy of electron density results in a positive charge. The strength of the halogen bond cannot compete with that of a hydrogen bond, but it was shown that replacing R-H with R-I could increase affinity up to two orders of magnitude.[91]

Halogen-containing fragments can be an optimal starting point to exploit halogen–protein interactions from the beginning of the drug-discovery process. The strength of the halogen bond in the binding site is highly dependent on the angle and the distance between an amino acid residue functioning as the electron-donor and the σ-hole of the halogen.[92] Since fragments are small, they have a higher probability to bind in the optimal position. In general, it is possible to cover a wide range of chemical space with a well-designed fragment library, which increases the likelihood to find high-quality interactions with the protein of interest. Focusing on halogen-bond interactions can help to produce hits with a novel mode of action and to explore innovative chemical space for known targets. In case a hit fragment does not bind *via* its halogen, it also gives a good starting point for synthetic modifications using cross-coupling reactions such as SUZUKI–MIYAURA or BUCHWALD–HARTWIG.[93]

The library we used was designed and provided by the group of F. M. Böckler.[90] They mainly followed the “rule of three” for fragment libraries (molecular weight ≤300, number of hydrogen bond donors and acceptors ≤3, clogP = 3).[82] Instead of selecting compounds with a molecular weight of ≤300, they used 22 heavy atoms as their upper limit and the compound had to contain a halide. Based on these criteria, they chose commercially available, soluble and unreactive fragments.

3.2.3 STD-NMR screening

In total, the HEFL comprises 146 fragments of which we excluded two that did not contain any protons and two that precipitated from the dimethyl sulfoxide (DMSO) stock solution. First, a ^{1}H NMR spectrum of each individual compound was recorded to determine its chemical shifts in water. Mixtures 1–14 of up to ten fragments were created based on differences >0.04 ppm between signals to be able to clearly distinguish individual compounds. Then, a ^{1}H NMR spectrum of the fragment mixtures without protein was taken to confirm the desired difference in chemical shifts and to identify compounds with unwanted behavior in the mixture like line broadening due to aggregation. After removing all molecules that aggregated or had solubility issues (18 fragments) under the assay conditions from the library, we analyzed a total of 124 fragments (**1**–**124**, **Table S 1**).

STD spectra of the mixtures without protein were taken to determine the correct irradiation conditions avoiding direct saturation of the compounds. Only if no signals were visible (blank STD spectra), the same mixtures were tested in the presence of protein. The difference in intensity due to saturation transfer was quantified using $STD_{effect} = (I_0 – I_{sat})/I_0$ as an indication of binding.[85] I_{sat} is the intensity of a signal in the on-resonance NMR spectrum, and I_0 is the intensity of the signal in the off-resonance or reference NMR spectrum.

The screening against Δ*Mt*DXPS resulted in 42 hits (STD_{effect} >50% see Chapter 5.1.6 mixtures 1–14), which were carefully analyzed to find the strongest binders and the most promising structural motifs. A selected number of binding fragments (mixture 15) was then tested against *Mt*DXPS that is difficult to purify and has therefore to be used considerately. The results were the same for both DXPS enzymes (**Spectrum 1**), which confirmed that they can be used interchangeably.

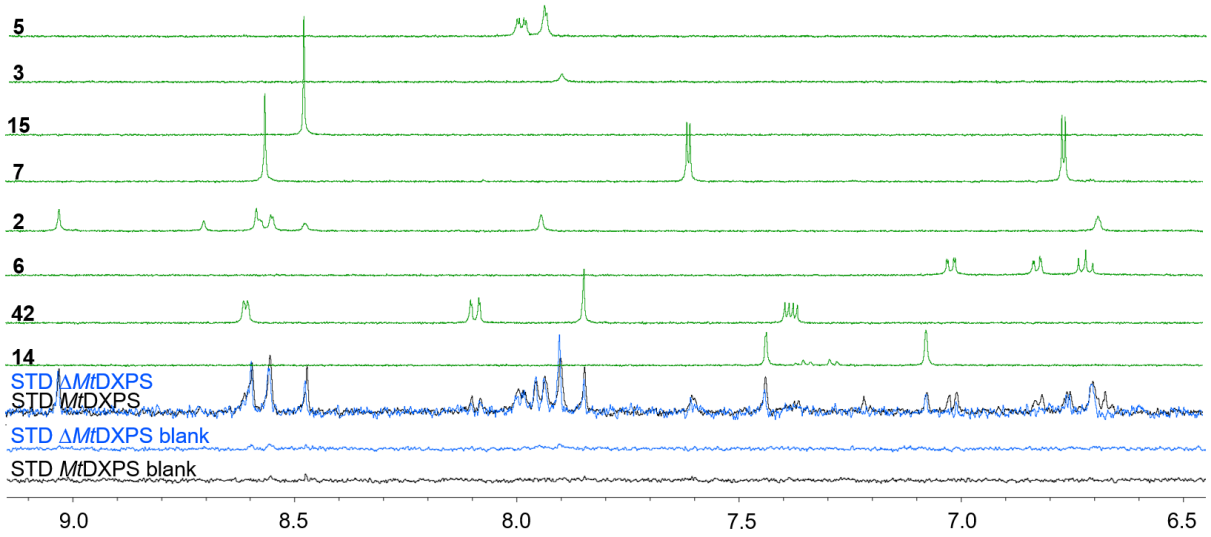

Spectrum 1: STD-NMR experiment of eight selected, binding fragments (mixture 15) against *Mt*DXPS (black) and Δ*Mt*DXPS (blue) to confirm that both enzymes can be used interchangeably in STD-NMR binding studies. Spectra shown between 6.5–9.0 ppm for better visibility.

3.2.4 Hit selection

The 42 hit compounds were clustered based on structural similarity, which resulted in eleven groups (**Figure 1**). To reduce the number of molecules to investigate further, compounds with the highest STD_{effect} were prioritized (**1**–**6**). However, aminopyridine **5** was excluded because of results from other projects regarding its instability in solution. Compound **6** precipitated out of dimethyl sulfoxide (DMSO) and aqueous solution over time (see **Figure S 1**) and was subsequently excluded, too. Because of this pre-selection, four compound classes were prioritized (pyrrolopyrimidines, pyrazines, 2-aminopyridines and pyrimidines). The class of morpholines/ piperazines was also prioritized to find highly soluble hits.

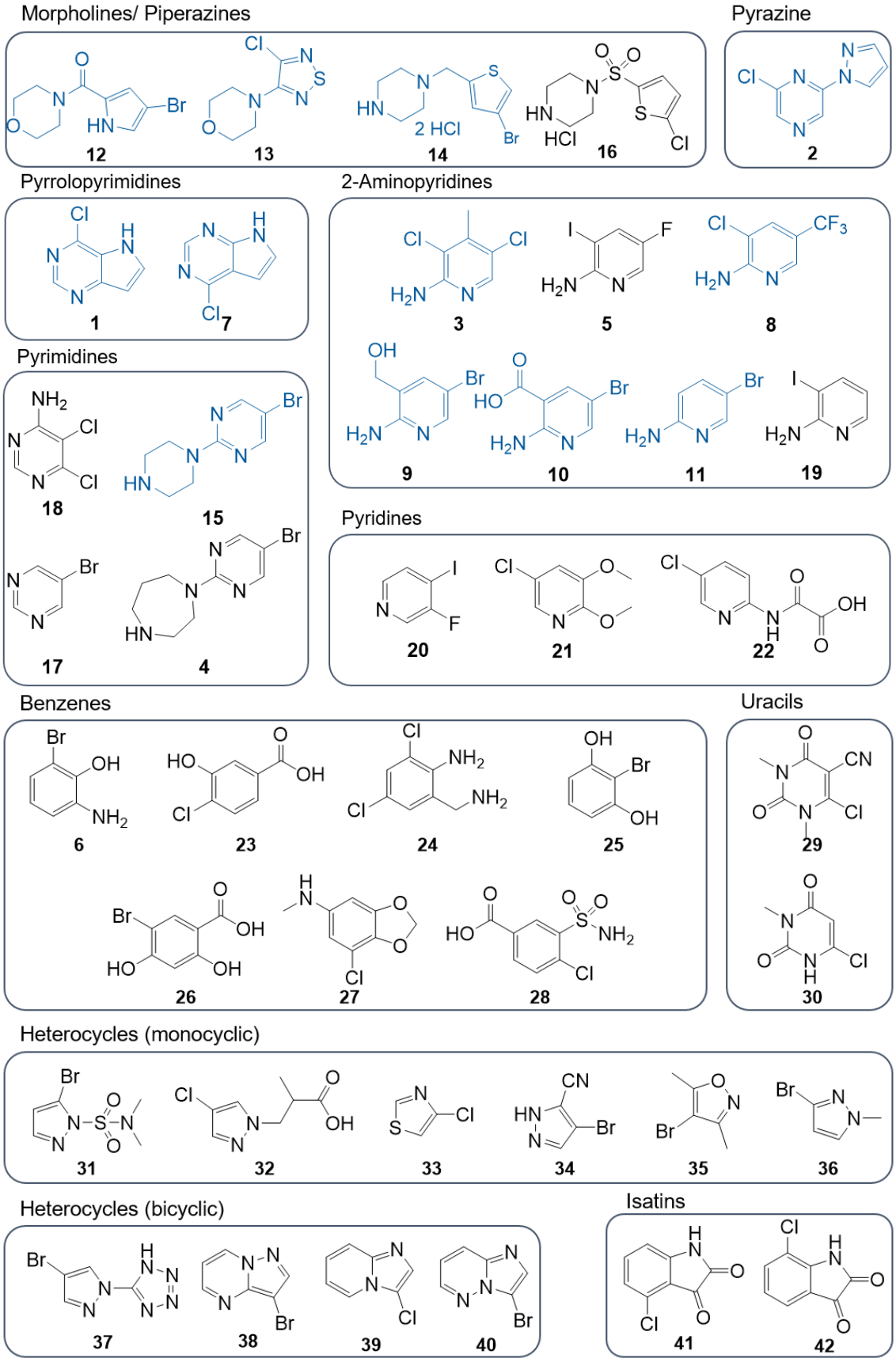

Figure 1: Hit compounds from STD-NMR screening summarized in structural groups. Blue compounds: Purchased hits for further analysis.

The following fragments from these classes were purchased: For the pyrrolopyrimidines **1** and **7**, for the pyrazine **2**, for the 2-aminopyrimidines **3**, **8**, **9**, **10** and **11**, for the morpholines **12** and **13**, for the piperazines **14** and for the pyrimidines **15**. Piperazine **16** and pyrimidine **4** were not purchased due to their high prize and **17** and **18** because of their much weaker binding in comparison to **15**. 2-Aminopyridine **19** was not purchased due to its structural similarity to **5** and therefore, possible instability. Instead, two more fragments were purchased that are similar to 2-aminopyridine **3**, which was the strongest binder overall. Compounds **125** and **126** (**Figure 2**) have more protons, which could give valuable insights into the growth possibilities of this compound class. All other compound classes were excluded. The uracils and the mono- and bicyclic heterocycles were excluded because of limited positions for modifications and due to some of their prizes. The isatins were excluded because of their relatively weak STD_{effect}. The pyridines were interesting, but we excluded them because of their much weaker STD_{effect} compared to the 2-aminopyridines. In the benzene class, too many different compounds with no clear common feature, except for the benzene ring, were present and potential solubility issues were an additional concern later on. All compounds that were excluded could be reconsidered if the other classes displayed no significant improvement with promising on-target activities.

3.2.5 Epitope mapping of selected fragments by STD-NMR

The 14 selected compounds were purchased as solids to make fresh stock solutions and measured separately in single STD-NMR experiments to get better information about their binding behavior (see Chapter 5.1.7).[87] Re-examining the mixtures could have given the same results, but may lead to misinterpreting possible competition effects between fragments. **Figure 2** displays a color-coded overview of the binding epitopes of these compounds based on their STD_{effect}. Protons that are closest to the protein should have the highest amplification factor, because the most magnetization is transferred to them during the experiment (green).[87] Protons that are further away and therefore interesting positions for chemical modifications, are marked yellow and red. By comparing structurally similar compounds, several interesting observations can be made. Fragments **1** and **7** are structural isomers and H^2 in both compounds binds closest to the protein. However, H^1 behaves differently binding equally well as H^2 in **1** and being further away in **7**.

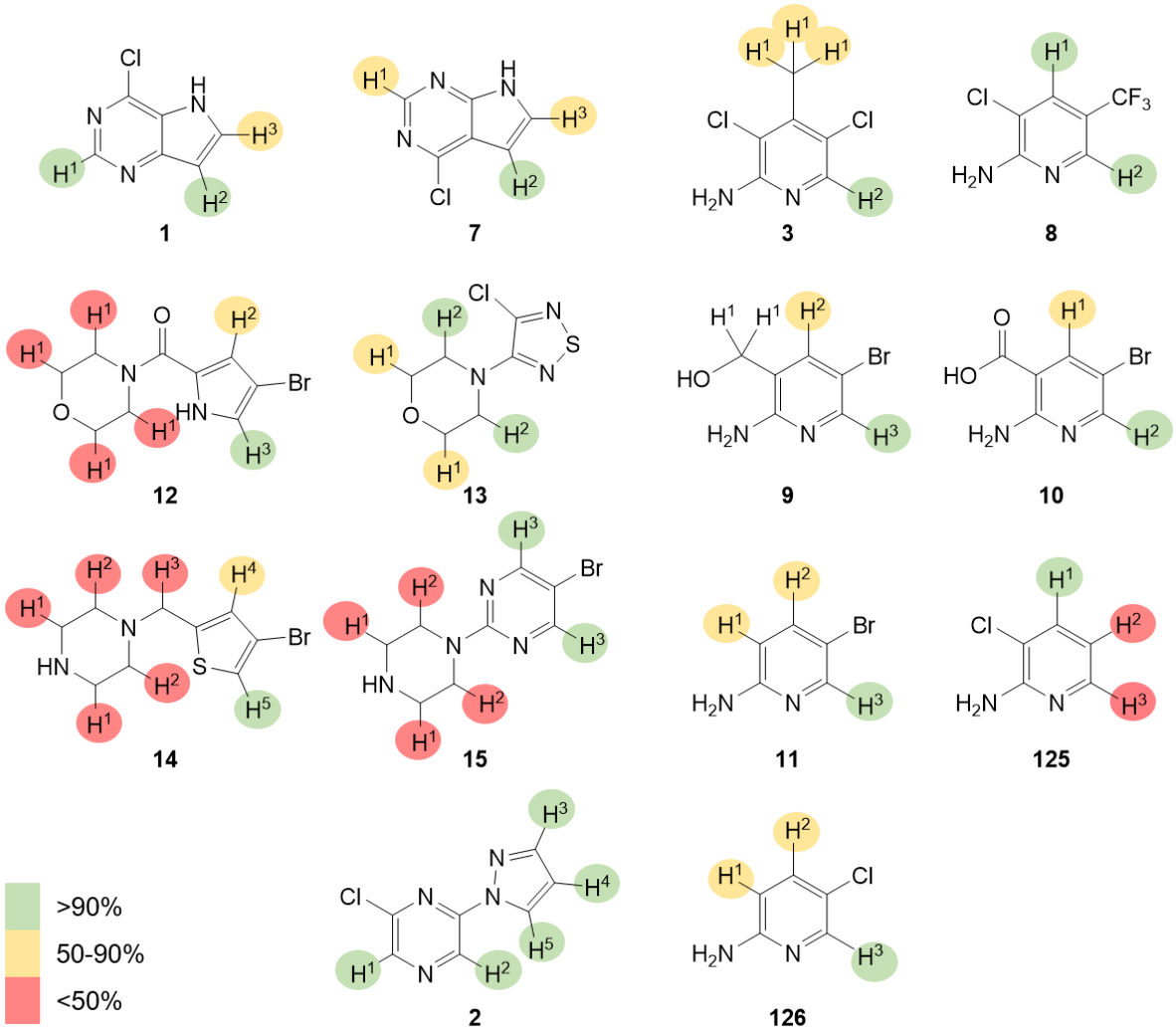

Figure 2: Binding epitope of selected hit compounds against Δ*Mt*DXPS determined by single STD-NMR experiments.

Most 2-aminopyridines have a similar binding pattern. Fragments **3**, **9**, **10**, **11** and **126** all show tightest binding with the proton directly next to the pyridine nitrogen. On the top part of the compound, space for growth seems to be available. However, two 2-aminopyridines behave differently. In **8**, all protons bind well, which can be a sign for unspecific binding. In fragment **125**, protons H^2 and H^3 seem to be binding very weakly, which could be the result of a different binding mode.

All fragments with a solubility enhancing group show weak interaction of those groups, but good binding from the aromatic parts of the molecules. Especially interesting are compound **12** and **14**. Replacing the ketone in **12** with a CH_2-group in **14** results in weak binding in this position. Those very soluble compounds could be grown in that direction. The only fragment that shows no binding epitope is compound **2**, which could indicate unspecific binding.

3.2.6 Binding validation and K_D determination by SPR

To confirm binding, the 14 compounds were tested by SPR against Δ*Mt*DXPS and *Mt*DXPS. Since no SPR experiment had been performed before on any DXPS enzyme, the immobilization conditions had to be established. This turned out to be straight-forward as DXPS has lysines on its surface and could be immobilized at the first attempt on a medium density carboxymethyl dextran hydrogel CMD500M chip (conditions see 5.1.8).

For both enzymes, binding results are comparable (**Table 4**). The K_D values were estimated with Scrubber from the binding sensorgrams.[94] For none of the compounds a full curve with two plateaus was reached, on the contrary when using concentrations higher than 1 mM we observed unspecific binding. Therefore, all measurements were started at 625 µM. The estimated K_D has to be interpreted with caution, but a clear trend to good binding for most of the 2-aminopyridines was detected.

Table 4: Estimated dissociation constants (K_D) of hit fragments by SPR on Δ*Mt*DXPS and *Mt*DXPS.

Fragment	K_D Δ*Mt*DXPS (µM)	K_D *Mt*DXPS (µM)
1	480 ± 20	1410 ± 700
2	14000 ± 3000	n.f.
3	610 ± 40	1400 ± 100
7	1330 ± 60	n.f.
8	920 ± 40	530 ± 20
9	4400 ± 300	n.f.
10	270 ± 10	143 ± 8
11	450 ± 20	375 ± 9
12	950 ± 40	18000 ± 6000
13	144 ± 4	510 ± 60
14	1590 ± 80	19000 ± 6000
15	2000 ± 200	880 ± 40
125	2600 ± 300	n.f.
126	880 ± 30	480 ± 20

n.f. = no fit.

The two most promising fragments are **10** (K_D Δ*Mt*DXPS = 270 µM and K_D *Mt*DXPS = 143 µM) and **11** (K_D Δ*Mt*DXPS = 450 µM and K_D *Mt*DXPS = 375 µM) with a close

overlap in K_D values for both DXPS homologous, but better binding to *Mt*DXPS. All 2-aminopyridines with one or two chlorine substituents (**3**, **8**, **125**, **126**) show a poor overlap between the results and had higher K_D values than **10** and **11**. Fragment **3** that shows the strongest STD_{effect} has a K_D of 610 µM against Δ*Mt*DXPS and of 1400 µM against *Mt*DXPS. Its two close analogues, **125** and **126**, show different binding behavior. If the chlorine in 3-position is retained (compound **125**), the data cannot be fitted for *Mt*DXPS and the K_D for Δ*Mt*DXPS is in the millimolar range. However, if the chlorine in 5-position is retained (compound **126**), both K_D values can be determined (K_D Δ*Mt*DXPS = 880 µM and K_D *Mt*DXPS = 480 µM), but are higher than for the close analogue **11** where chlorine and bromine are exchanged. This suggests, that bromine is the more suitable substituent for the 5-position. While in STD-NMR fragment **8** seems to be binding unspecifically, in SPR this was not the case. The molecule is binding well to both homologues (K_D Δ*Mt*DXPS = 920 µM and K_D *Mt*DXPS = 530 µM). Compound **9**, in which the carboxylic acid moiety of **10** is replaced by a hydroxyl methyl group, binds Δ*Mt*DXPS much weaker than **10** and for *Mt*DXPS no fit could be calculated. The pyrrolopyrimidines, **1** and **7**, looked promising in the STD-NMR and showed different binding behavior despite their structural similarities. The same could be observed in SPR, where **1** is binding to Δ*Mt*DXPS with a K_D of 480 µM, but to *Mt*DXPS only with a K_D of 1410 µM. No fit was possible for molecule **7** against *Mt*DXPS, but it binds weakly to Δ*Mt*DXPS with a K_D of 1330 µM. Fragments **12** and **14** are both binding weakly to Δ*Mt*DXPS and even more weakly to *Mt*DXPS, however, morpholine **12** has the stronger binding interaction of the two. This suggests a favorable interaction of either the carboxyl oxygen or the morpholine oxygen of **12** with the protein. Since the binding remains weaker than for most 2-aminopyridines, this compound class is not considered as a hit. Compounds **13** and **15** are binding to both homologues and their K_D values are in a similar range as the other compounds, but should not be considered as hits since the data quality is not as good as for the other compounds. The same is true for compound **2** that was binding unspecifically in STD-NMR and only shows weak binding and poor data quality for both homologues.

3.2.7 Fragment optimization guided by SPR

We bought, synthesized (**127**, **128**) or chose from the original HEFL a selection of closely related compounds to **10** and **11** and tested them against Δ*Mt*DXPS. Here, only results of acceptable data quality are presented to be able to make more accurate predictions about potential growth vectors. Data for which no fit of the sensorgrams

with Scrubber was possible, were excluded from this analysis (see **Figure S 60** for a list of tested compounds that were not included into the analysis). First, compounds **10** and **11** were tested again (**Table 5**). The results differ between this and the previous measurement, but considering the difference in amount of protein immobilized and that two different instruments were used, these results were encouraging enough to continue testing all selected derivatives.

The selected compounds do not cover enough structural variation to establish a full structure-activity relationship (SAR), but they still give insights into the binding behavior that will help to determine the most promising growth vector. The only structural difference between **10** and **11** is the carboxylic acid substituent. When looking at the results of 3-, 4- and 6-bromo-2-aminopyridine (**129**, **130**, **131**), only the 6-bromo-substituent in **131** is tolerated, but the K_D is two-fold lower than for **11**. The bromo-substituent is essential in either position five or six, because 2-aminopyridine (**132**) does not bind. Two derivatives, **133** and **144**, with a methyl ester and a CF_3 group in 4-position do not bind. Since also the bromine substituent is missing, this does not exclude position four for substitution. The four-fold increase in K_D for compound **135** in comparison to **10** demonstrates that the bromine is important, but that the carboxylic acid group also plays a role in binding. The bromine in position five can be replaced by a carboxylic acid (compound **136**) under loss of some binding affinity. Exchanging the bromine and carboxylic acid substituent (compound **66**) or having the carboxylic acid in 6-position (compound **119**) leads to weak or no binding. The bromine in **10** can be directly replaced by iodine, although the K_D is higher. This can be an indication for a halogen–protein bond; especially since replacing the halogen with a methyl substituent (compound **138**) leads to loss of binding. Taking a closer look at the carboxylic acid moiety, some variability seems to be accepted. A methyl ester (compound **127**) or an aldehyde (compound **139**) in 3-position result in higher K_D values, but the compounds are still binding. However, the amino group cannot be replaced easily. If only the amino group is methylated (compound **128**), the K_D is increased eight-fold, but if the amino and the carboxylic acid group are methylated at the same time (compound **140**) the increase is only two-fold. This is difficult to understand without further information on the binding mode of these two compounds. It might be that the binding mode changes completely with different methylation patterns. What is not tolerated is the removal or move of the amino group. In both cases the binding is completely lost (compounds **61**,

82, **141**–**143**). Compound **61** is binding in SPR, but shows broad peaks in the STD-NMR suggesting aggregation.

Table 5: Estimated dissociation constants (K_D) for second round of surface plasmon resonance (SPR) against Δ*Mt*DXPS including non-binders from saturation-transfer difference nuclear magnetic resonance and SPR for fragment-optimization analysis. Non-binding compounds either had no dose response or a dose-response curve that could not be evaluated by the program because the spacing between different concentrations was wrong.

Structure	K_D (µM)	STD_{effect}	Structure	K_D (µM)	STD_{effect}
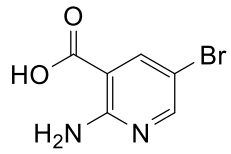 **10**	172 ± 6	>50%	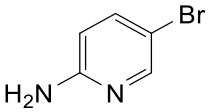 **11**	245 ± 6	>50%
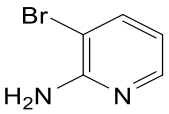 **129**	n.b.	-	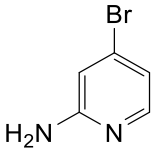 **130**	n.b.	-
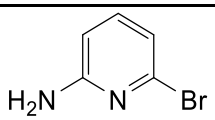 **131**	480 ± 20	-	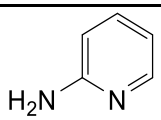 **132**	n.b.	-
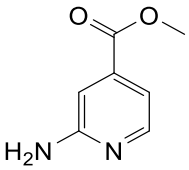 **133**	n.b.	-	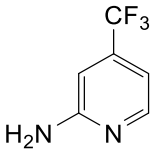 **134**	n.b.	-
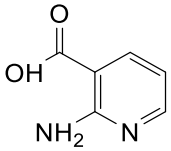 **135**	850 ± 40	-	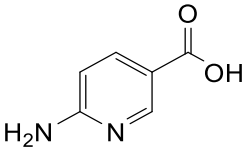 **136**	780 ± 80	-
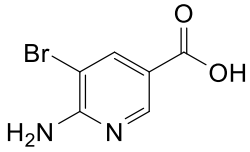 **66**	3200 ± 300	n.b.	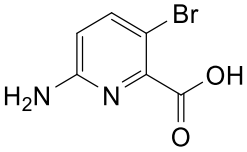 **119**	solubility issues	n.b.

Structure	K_D (µM)	STD$_{effect}$	Structure	K_D (µM)	STD$_{effect}$
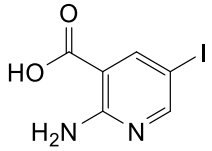 **137**	350 ± 10	-	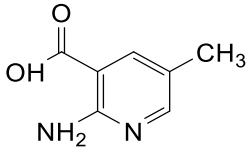 **138**	n.b.	-
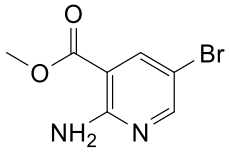 **127**	590 ± 10	-	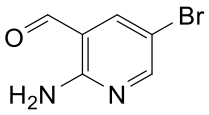 **139**	660 ± 70	-
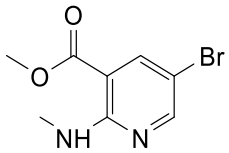 **140**	340 ± 160	-	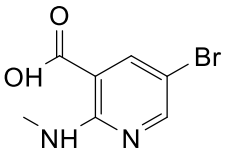 **128**	1380 ± 50	-
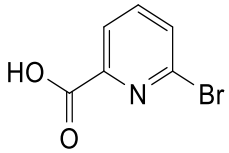 **141**	n.b.	-	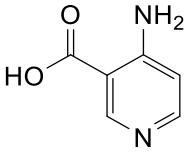 **142**	n.b.	-
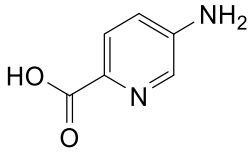 **143**	n.b.	-	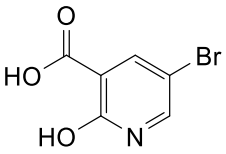 **61**	370 ± 10	b.p.
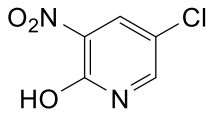 **82**	n.b.	n.b.			

n.b. = no binding, b.p. = broad peaks.

3.2.8 Conclusions and outlook

At this point, it would be interesting to know if these compounds bind in the active site of the enzyme. Unfortunately, none of the inhibitors available during this thesis are soluble enough to result in a good quality SPR curve. Several compounds were tested, but none reached full occupation of the binding site for an accurate K_D determination. This is why no competition experiments with the fragments were performed. This could change in the future if we find more soluble or stronger binders. Alternatively,

crystallization of the fragments together with the protein could have confirmed the binding mode, but several co-crystallization attempts by Zhoor Hamid with Δ*Pa*DXPS and by Sebastian Adam with Δ*Kp*DXPS have been unsuccessful until the submission of this thesis.

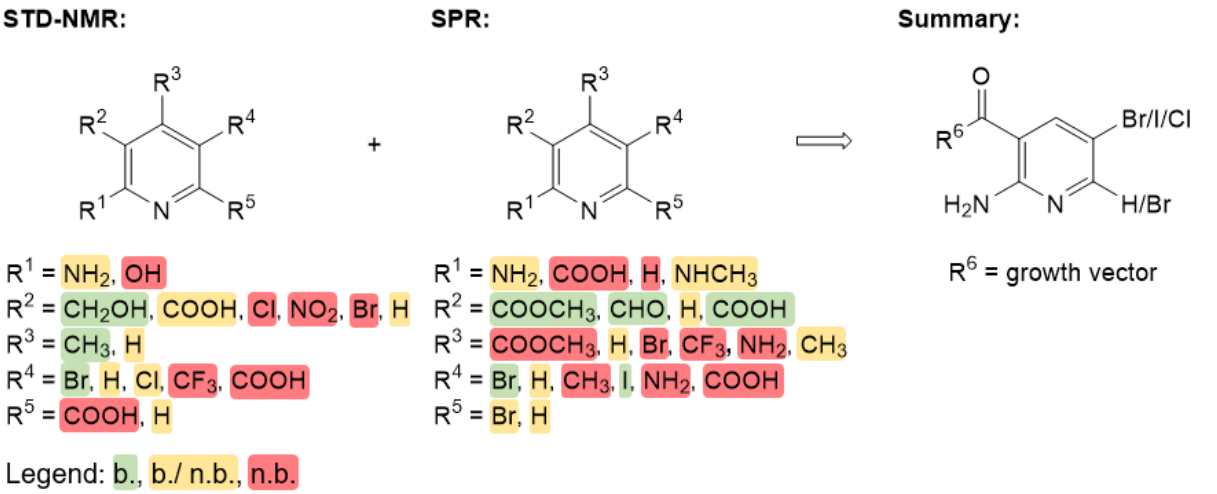

Figure 3: Results from STD-NMR and SPR to make suggestions for synthetic modifications. Color coding for substituents that are present in binding compounds (green), in some binding and some non-binding compounds (yellow) and in non-binding compounds (red). b. = binding, n.b. = no binding.

In summary, this focused list of derivatives does not give the full picture of possible synthetic modifications, but taking together the results from STD-NMR and SPR a trend is visible. **Figure 3** combines the results from both assays to make suggestions for further synthetic modifications. Since there are gaps in the SAR, the color code is just a rough guideline. Green substituents result in binding, yellow substituents can be found in binding and non-binding fragments and red substituents result in no binding. In position R^1, the amino group is the only accepted substituent, although in some cases no binding can be observed. Methylations of the amine is accepted in molecule **140**, but not in others. Substituent R^4 should be a halogen atom, although in some cases a proton is accepted as well. However, bromine results in the lowest K_D overall. R^5 can be a bromine or a proton, but this position has to be explored further, especially with a halogen as R^4. The same goes for R^3, because it looks like this position should be a proton or a methyl group, but all derivatives with different substituent here are missing essential other substituents such as the bromine and the amino group. In addition, R^3 was identified in STD-NMR as a potential growth vector. The most promising position for modifications is R^2 since a carboxyl group seems to be beneficial and an ester is accepted in this position. A variety of esters or amides (R^6) can be

synthesized easily to confirm this hypothesis. For all modifications, solubility should be kept in mind.

The progression of this project has been slow due to a lack of reference compounds and the difficulties with co-crystallization. In the next chapter, we identified an inhibitor with a promising IC_{50} value and good solubility, but it has not been tested by SPR yet. This could be an excellent starting point for competitive SPR experiments with the identified fragments. After confirming that one or more of the fragments bind in the active site, synthetic modifications can be planned.

Another option is the synthesis of derivatives to close the knowledge gaps in the SAR. In **Figure 4**, a few suggestions are made on how to further modify fragment **10**.

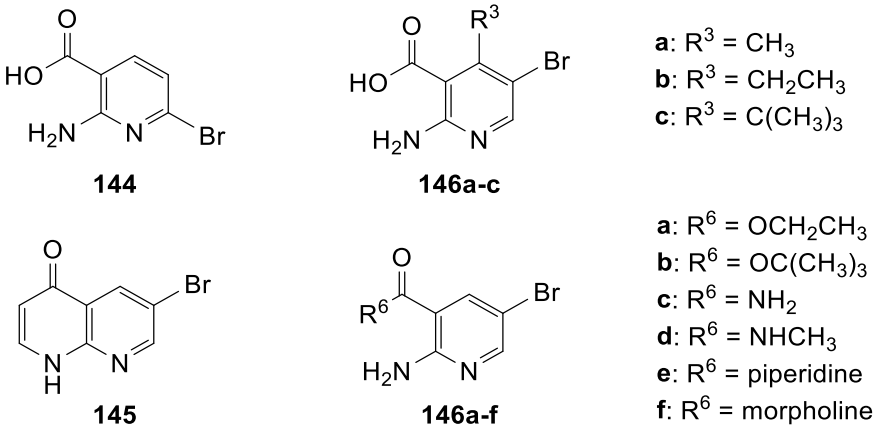

Figure 4: Possible derivatives of fragment **10** to gain further insights into the structure-activity relationship.

One easy modification is to move the bromine (**144**) to see whether its position is flexible. Since it was possible to replace the carboxylic acid and methylation of the amine was tolerated in some cases, compound **145** should be synthesized to change the scaffold while keeping the main substituents intact. It is then possible to determine possible growth vectors again by STD-NMR. Positions R^3 and R^6 should be explored further by using substituents of different sizes and chemical properties (compounds **146a**–**c, 147a**–**f**). This will help to confirm that they are growth vectors and might increase the affinity enough to determine inhibition.

3.3 Implementation and validation of a HPLC-MS/MS-based DXPS activity assay

S. Johannsen, A. Kany, Z. Adeli, Z. Hamid, T. Wittmann, A. K. H. Hirsch.

This is a summary on how we implemented a previously published HPLC-MS/MS-based DXPS activity assay is our laboratory and used it for the first time to measure the inhibitory activity of compounds.

3.3.1 Contributions

Sandra Johannsen performed all experiments to optimize and validate the assay conditions as well as the concentration determination for *Dr*DXPS. She wrote the main text and experimental section. Andreas Kany supervised the adaptation of the assay to our HPLC-MS/MS system. Zahra Adeli performed the concentration determinations for Δ*Kp*DXPS, Δ*Pa*DXPS, Δ*Mt*DXPS and Δ*Dr*DXPS, and continued to work with the assay during her Master's thesis. She and Zhoor Hamid expressed and purified *Dr*DXPS that has been used for the assay. Tabea-Catharina Wittmann performed the K_M determination assays for all homologues. Anna K. H. Hirsch was responsible for supervision, conceptualization and project administration.

3.3.2 Introduction

Successful hit identification relies on an activity assay with which inhibitors can be analyzed. Several assays to determine DXPS activity are published.[95] For example, some methods are using ^{14}C-pyruvate as a tracer and although ^{14}C is a safe radio isotope, the experimental setup and separation of labeled pyruvate and 1-deoxy-D-xylulose-5-phosphate (DOXP) is cumbersome. There is also a fluorometric end-point assay based on the reaction of DOXP with 3,5-diaminobenzoic acid, but D-glyceraldehyde 3-phosphate (D-GAP) is interfering.

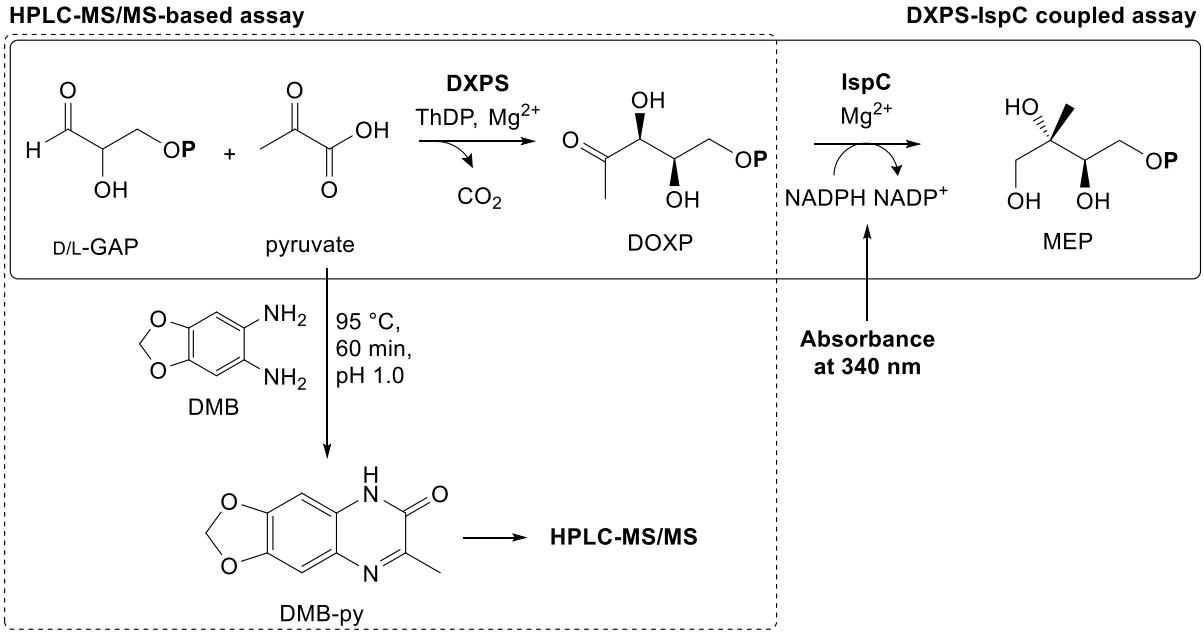

Scheme 3: Reactions involved in the DXPS-IspC-coupled assay in comparison to the DXPS high-performance liquid chromatography-tandem mass spectrometry (HPLC-MS/MS)-based assay. **P** = phosphate. GAP = glyceraldehyde 3-phosphate, DXPS = 1-deoxy-D-xylulose-5-phosphate synthase, DOXP = 1-deoxy-D-xylulose-5-phosphate, IspC = 1-deoxy-D-xylulose-5-phosphate reductoisomerase, NADPH = nicotinamide adenine dinucleotide phosphate, MEP = 2-*C*-methyl-d-erythritol 4-phosphate, DMB = 1,2-diamino-4,5-methylenedioxybenzene, DMB-py = 7-methyl-[1,3]dioxolo[4,5-g]quinoxalin-6(5*H*)-one.

Furthermore, several high-performance liquid chromatography-tandem mass spectrometry (HPLC-MS/MS)-based assays have been established, but they usually directly quantify DXP, which needs special HPLC-columns. The most popular assay is the DXPS-1-deoxy-D-xylulose-5-phosphate reductoisomerase (IspC)-coupled assay in which the activity of DXPS is observed by monitoring the absorbance of nicotinamide adenine dinucleotide phosphate (NADPH) that is consumed by IspC (**Scheme 3**).[56] DXPS is used as the rate-limiting enzyme in this setup so that the turnover of NADPH correlates to the reaction velocity of DXPS. However, compounds can potentially

inhibited both enzymes (making an additional IspC-assay necessary to exclude IspC-inhibitors) and since we were only interested in DXPS inhibitors, we implemented a HPLC-MS/MS-based activity assay that only involves DXPS. Liang *et al.* published the procedure depicted in **Scheme 3**.[95] After 30 minutes, the DXPS reaction is thermally terminated and remaining pyruvate is converted with 1,2-diamino-4,5-methylenedioxybenzene (DMB) to DMB-py, which is highly ultraviolet (UV)-active and ionizes well. As a result, the signal-to-noise ratio is better in their experiments than in the DXPS-IspC-coupled assay. Since we often observed significant differences between measurements in the coupled assay, we wanted to obtain data that are better reproducible. In addition, UV-active compounds often caused problems due to interference with the monitoring of the NADPH absorption, which we hoped to prevent by determining the amount of DMB-py from the MS peak area. So far, this method has not been used to screen or characterize DXPS inhibitors.

3.3.3 Assay optimization

For the HPLC-MS/MS method, we synthesized DMB-py (see Chapter 5.5.1) to have the compound available for method establishment.[96] We selected a column and a method (see Chapter 5.2) enabling detection of the mass of DMB-py after 1.9 minutes.

To confirm that 60 min of reaction time between pyruvate and DMB are optimal as previously published, both reagents were mixed and samples were taken after 30 min, 60 min and 150 min. As can be seen in **Figure 5A**, after 30 min only half of the reaction is complete while there is no difference between 60 min and 150 min.

Then, we determined calibration curves from the synthesized DMB-py (**Figure 5B** red balls) and the *in situ* reaction with pyruvate and DMB (**Figure 5B** gray squares), but the absolute values of the peak area were different. The reason could be that the synthesized compound was not dry enough or was still contaminated by DMB, since it was not purified after filtration. After this result, the calibration curve was determined *in situ*.

Next, different enzyme concentrations were tested to find the optimal conditions to have a sufficient difference between the blank and the uninhibited control. Since absence of inhibition results in low DMB-py levels, values for the uninhibited control should not be too low. Otherwise the reaction could be complete and we could not observe it while it is still in the linear area of substrate consumption.[97,98] Furthermore, DMB-py levels in the control should still be above the detection limit. When performing

the assay with 100 µM pyruvate (K_M^{py} = 94 ± 17 µM, **Table S 6**), the difference between the blank and the control is sufficient to determine the effects and in comparison to the original publication, corresponds to a twenty-fold reduction in pyruvate levels so that less of the expensive DMB is needed. Later, a pyruvate concentration of 200 µM was used to increase the difference between blank and control pyruvate levels to improve the signal-to-noise ratio when analyzing inhibitors.

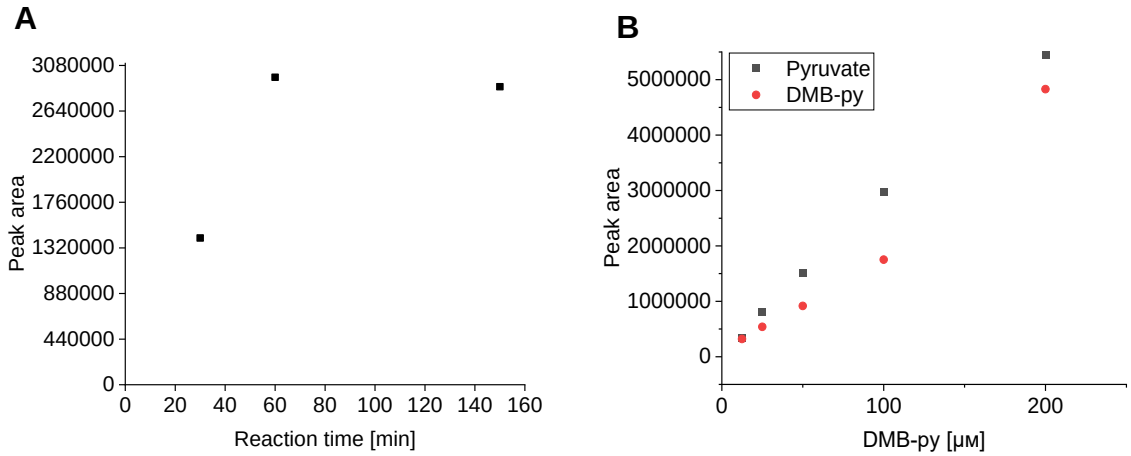

Figure 5: (**A**) Reaction of pyruvate with 1,2-diamino-4,5-methylenedioxybenzene (DMB) after 30, 60 and 150 min. (**B**) Comparison of DMB-py calibration (red balls, dilution of DMB-py stock solution) with *in situ* calibration (black squares, pyruvate + DMB).

In **Table 6**, the absolute peak area was used to calculate the percentage of pyruvate left after 30 minutes (area sample/ area blank*100, **Table S 7**). It was decided that 500 nM of *Dr*DXPS with 20% residual pyruvate will be used for further experiments. The optimal enzyme concentration has to be determined with every new enzyme and the results for Δ*Mt*DXPS, Δ*Kp*DXPS, Δ*Pa*DXPS and Δ*Dr*DXPS are shown in **Table 6**.[54,55,99] The differences in activity are clearly visible between the different homologues, with Δ*Mt*DXPS being the least, and Δ*Pa*DXPS being the most active, requiring a concentration of 10 µM and 100 nM, respectively.

Table 6: Overview over residual pyruvate after 30 minutes of incubation with different DXPS concentrations and comparison of five DXPS homologues (*Dr*DXPS, Δ*Kp*DXPS, Δ*Pa*DXPS, Δ*Mt*DXPS, Δ*Dr*DXPS). Concentration for final assay highlighted in bold.

DXPS [µM]	**Residual pyruvate**				
	***Dr*DXPS**	**Δ*Kp*DXPS***	**Δ*Pa*DXPS***	**Δ*Mt*DXPS***	**Δ*Dr*DXPS***
0.05	n.d.	n.d.	54%	n.d.	n.d.
0.625	n.d.	n.d.	n.d.	n.d.	38%
0.1	n.d.	n.d.	**24%**	n.d.	**n.d.**
0.125	n.d.	50%	n.d.	n.d.	12%
0.25	n.d.	**16%**	n.d.	n.d.	6%
0.5	**20%**	4%	n.d.	n.d.	6%
0.75	6%	n.d.	n.d.	n.d.	n.d.
1.0	3%	2%	n.d.	n.d.	5%
1.25	4%	n.d.	n.d.	87%	n.d.
2.5	n.d.	n.d.	n.d.	65%	n.d.
5.0	n.d.	n.d.	n.d.	46%	n.d.
10.0	n.d.	n.d.	n.d.	**22%**	n.d.

n.d. = not determined; *experiments performed by Zahra Adeli.[99]

To streamline the work-flow for inhibitor testing, the procedure was optimized by using four 96-well plates. In the first plate, the DMSO stock solutions of the compounds were prepared. On the second plate, buffer A containing the enzyme, ThDP and MgCl was prepared, then the DMSO stocks were transferred from the first plate and incubated for ten minutes. Buffer B with the substrates was added and the plate was incubated at 37 °C for 30 minutes. On a third plate, 50 µL of a 1.0 mM DMB solution were put in every well and 50 µL from the assay plate were added. This plate was then incubated for one hour at 95 °C. After this time, 2 µL from every well of that plate were added to 198 µL of acetonitrile, which was directly used for the HPLC-MS/MS measurement. With this setup, 64 compounds can be tested per plate with 16 blanks (no enzyme, no inhibitor) and 16 controls (enzyme, no inhibitor), which allows for relatively high throughput. Since there is some variation in the blanks and controls, 16 samples each are necessary to identify outliers. For IC_{50} determination, eight compounds can be tested per plate at eight concentrations.

3.3.4 Assay validation

Next, we tested a diverse set of inhibitors against *Dr*DXPS to validate the assay. The calculation of the residual pyruvate concentration *via* the calibration curve was very inconsistent, so we performed analyses from the absolute peak areas. Percent inhibition (%inhi.) was calculated using the blank peak area as the upper limit (no pyruvate consumption corresponding to full inhibition) and the control peak area as the lower limit (no inhibition and maximum pyruvate consumption).

$$\%\text{inhi.} = \frac{\text{area (sample} - \text{control)}}{\text{area (blank} - \text{control)}} * 100$$

Most of the tested compounds did not inhibit the reaction of *Dr*DXPS fully (data not shown), but the previously identified IspE inhibitor **1** turned out to also be an excellent DXPS inhibitor with an IC_{50} value of 33 ± 2 µM. Here, only the data for *Dr*DXPS are shown, but it also inhibits all other homologues (43–74 µM).[99] The IC_{50} calculations were performed in OriginPro using nonlinear sigmoidal fitting.[100] The upper limit of 100% inhibition was fixed and a curve was fitted through the data points.

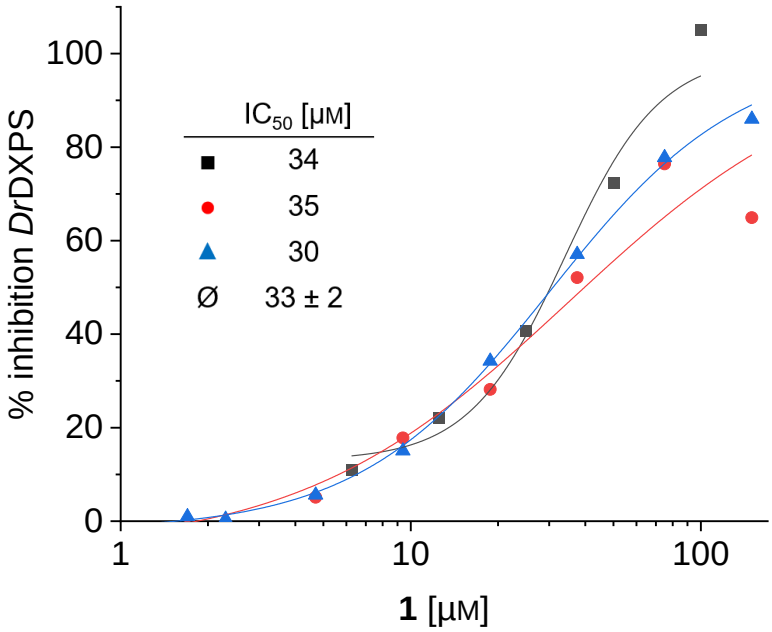

Figure 6: Results of three independent IC_{50} experiments with compound **1** against *Dr*DXPS in the HPLC-MS/MS assay. Graph created in OriginPro 2020.[100]

3.3.5 Conclusions and outlook

In summary, we implemented and validated the HPLC-MS/MS-based assay for the identification of DXPS inhibitors, affording reproducible results from a set of different inhibitors. Based on the experience gained from these experiments, performing single-

point measurements at least three times independently and using inhibitor **1** as a positive control in all assays is recommended. In case, not all data are of high quality (*e.g.* low inhibition of compound **1**, small difference between blank and uninhibited control or big differences among blanks and controls), the single-point measurements have to be repeated before IC_{50} determination to exclude false positive or false negative hits. The assay has been used by Zahra Adeli in her Master's thesis to identify compounds for crystallization studies with Δ*Dr*DXPS, Δ*Pa*DXPS and Δ*Kp*DXPS.[99] In addition, we used it to test the inhibition of *Dr*DXPS with compounds identified by virtual screening (see Chapter 3.4).

When comparing the DXPS-IspC-coupled assay that we have used previously with the HPLC-MS/MS-based assay both have a similar throughput when using 96-well plates. However, the HPLC-MS/MS-based assay should be run with two control and two blank wells per row, which reduces the number of compounds that can be tested from 80 to 64 compounds per plate. Preparation and measurement time is higher for the HPLC-MS/MS-based assay, which means only two plates can be measured per day instead of up to six for the coupled assay unless a second HPLC-MS/MS instrument is used in parallel. As long as no large compound libraries are tested this is not a disadvantage. No additional control experiments with IspC are needed for the HPLC-MS/MS-based assay which reduces the overall protein use. Although the expensive DMB (1060 € for 100 mg) is needed, it is possible to synthesize it which reduces the cost (approximately 220 € for 2 g) and can be done within four days.

Overall, these results demonstrate that the HPLC-MS/MS-based assay can be used to identify and validate inhibitors against a variety of different DXPS homologues and is a valuable alternative to the DXPS-IspC coupled assay.

3.4 Hit identification utilizing deep convolutional neural networks against Δ*Mt*DXPS

S. Johannsen, R. M. Gierse, A. Olshanova, E. Smerznak, L. Eschweiler, Z. Adeli, C. Laggner, Z. Hamid, A. Alhayek, N. Reiling, T. Wittmann, S. Eisa, J. Haupenthal, A. K. H. Hirsch.

This part of the thesis has been performed in collaboration with Atomwise Inc. and will be prepared for publication after additional experiments have been performed.

3.4.1 Contributions

Sandra Johannsen synthesized compounds **22a**–**i**, **38c** and their precursors, and performed the testing of all compounds unless indicated otherwise. She wrote the main text and the experimental section. Robin M. Gierse was responsible for initiating the collaboration with Atomwise Inc. and organizing the first round of virtual screening. Christian Laggner has performed the virtual screening with AtomNet at Atomwise Inc. Lea Eschweiler performed the re-synthesis of hit **1** and of derivative **36**. Aleksandra Olshanova and Ellie Smerznak synthesized all Western ring derivatives (A. O.: **29a**, **29d**–**f**; E. S.: **29b**, **29c**, **29g**), most of the linker derivatives (E. S.: **38a**, **38b**, **38d**, **38e**), three Eastern ring derivatives (A. O.: **22h**, **22i**; E. S.: **22j**) and the respective precursors. Robin M. Gierse and Alaa Alhayek expressed and purified both *Mt*DXPS homologues, while Zhoor Hamid did the same for *Dr*DXPS. Norbert Reiling tested **1**, **7**, **8** and **12** against *M. tuberculosis* HR37v. Tabea-Catharina Wittmann helped with testing compounds **4**, **22j**, **29c**, **29g**, **38b**, **38d** and **38e** in the HPLC-MS/MS-based assay and performed the DXPS-IspC-coupled assay as well as the IspC assay. Jörg Haupenthal and Jeannine Jung were responsible for the *E. coli* and HepG2 testing of compounds. Selina Wolter tested the solubility of the compounds. Sidra Eisa purified the new batch of compound **4**. Anna K. H. Hirsch was responsible for supervision, conceptualization and project administration.

3.4.2 Deep convolutional neural networks in drug discovery

Atomwise Inc. developed the first deep convolutional neural network for molecular binding affinity predication. Their program AtomNet is also the first system that uses structural information of the target protein to make predictions.[101] The model takes millions of experimentally determined bioactivity values and thousands of protein structures from different families into account. Based on this information, it is even possible to use AtomNet on targets for which no binding partners are known. Since 2017, Atomwise Inc. offers partnerships with academic groups (AIMS award) to find new chemical structures for biological targets. The only prerequisites are a crystal structure or good homology model, a defined binding site for the chemical compound and a functional assay to determine bioactivity data. Virtually screening millions of commercially available compounds against the target of interest enables the filtration to a manageable number of compounds that could be advanced for further biological validation. A functional assay is then used to identify a set of promising compounds. In a follow-up virtual screening (VS) the results from the functional assay are taken into account to generate another set of promising compounds. In the last years, three stories of successful partnerships with Atomwise have been published.[102–104] *N*-Acetyltransferase is involved in the rare Canavan disease, no crystal structure is available and only a small number of inhibitors is known. Despite these challenges, it was possible to identify five novel and diverse inhibitor scaffolds within a selection of 60 compounds.[104] It was also possible to identify inhibitors targeting the Miro1 enzyme involved in Parkinson's disease and against the protein–protein interaction between the porcine reproductive and respiratory syndrome virus and a membrane receptor in pig macrophages.[102,103] In all cases, the application of AtomNet has helped to find new structures quickly and based on little prior knowledge.

After Gierse *et al.* solved the crystal structure of truncated *M. tuberculosis* 1-deoxy-D-xylulose-5-phosphate synthase (Δ*Mt*DXPS) (protein data bank (PDB) ID: 7A9H), Christian Laggner at Atomwise performed a virtual screening with AtomNet using the Enamine library of several million compounds.[55] We have previously performed a ligand-based virtual screening (LBVS) using thiamine diphosphate (ThDP) analogues (Chapter 6.1) and therefore, focused now on the D-glyceraldehyde 3-phosphate (D-GAP) binding site for the AtomNet screening (gray mesh **Figure 7**). Below the substrate pocket, ThDP is bound to the protein (yellow and red sticks) and coordinates magnesium (green ball). As described in Chapter 1.2.1, pyruvate binds first to ThDP

and they form a stable enamine intermediate that can be crystallized in the absence of D-GAP. Finding inhibitors for the D-GAP binding site has the benefit of not interfering with the stable and tightly binding enamine, but preventing D-GAP from binding. In addition, this is the pocket that differs most from other ThDP-dependent enzymes, so the development of a DXPS-selective inhibitor should be possible. In total, 94 compounds were identified and purchased from Enamine for testing.

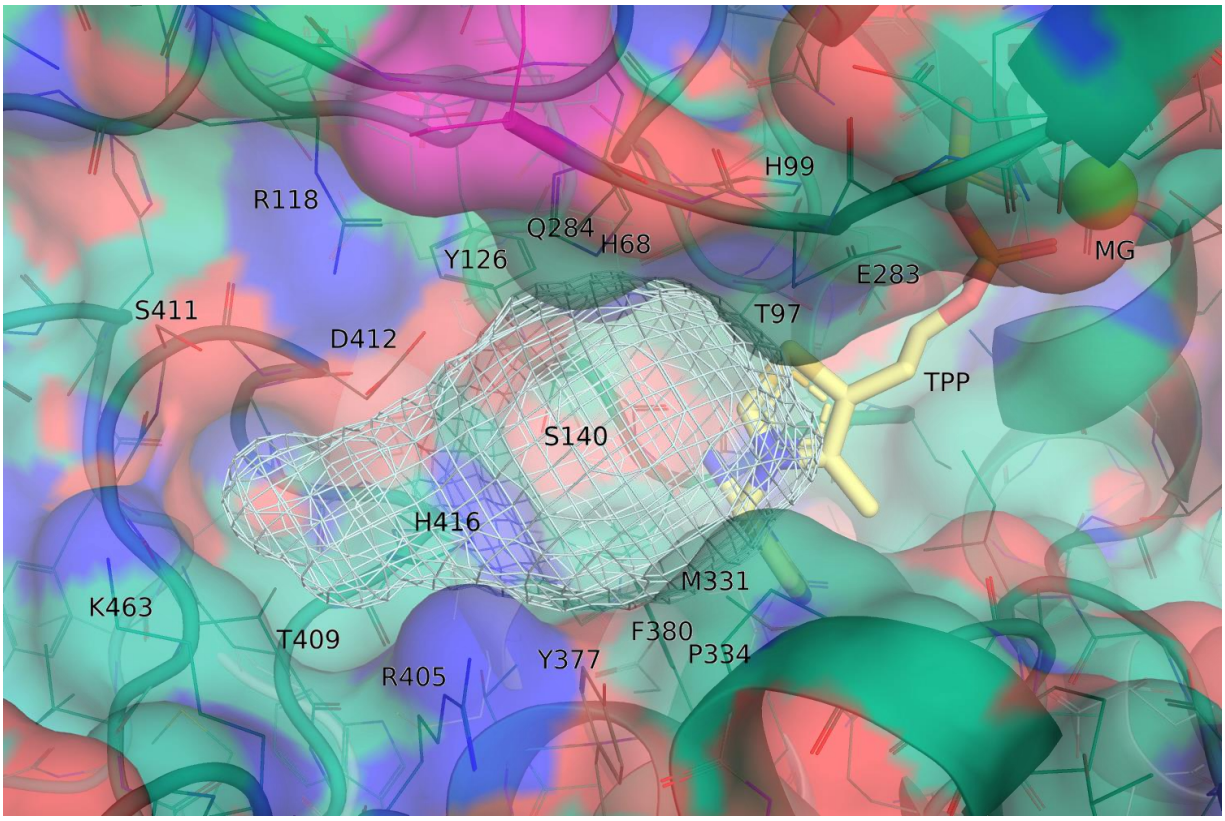

Figure 7: Binding site of D-glyceraldehyde 3-phosphate (gray mesh) with bound thiamine diphosphate (yellow and red structure) and Mg^{2+} (green structure) next to it. The acronyms present the amino acid residues surrounding the pocket in Δ*Mt*DXPS (protein data bank ID: 7A9H). Figure created by Robin M. Gierse.

3.4.3 Hit-identification and validation

We wanted to verify that the truncation of *Mt*DXPS not only provides a more stable and easier to crystallize protein, but that both homologues can be used interchangeably in binding studies. Both proteins were immobilized on the surface of a surface plasmon resonance (SPR) chip (Chapter 5.3.2). In both cases, the proteins were giving a steady response signal (Δ*Mt*DXPS: **Figure S 47**, *Mt*DXPS: **Figure S 31**) over a period of four weeks. All 94 compounds and two dimethyl sulfoxide (DMSO) blanks were blindly tested at 100 µM (**Figure 8**, **Table S 9**), and for each protein the four compounds with the highest response unit (RU) were defined as hits (**1**, **2**, **3**, **4** and **1**, **3**, **5**, **6**). There is

an overlap of two compounds (**1** and **3**), and a third compound (**4**) is also binding well to both although it is not among the best four against *Mt*DXPS. Dissociation constant (K_D) determinations are not possible as none of the compounds is soluble enough to reach saturation of the binding site.

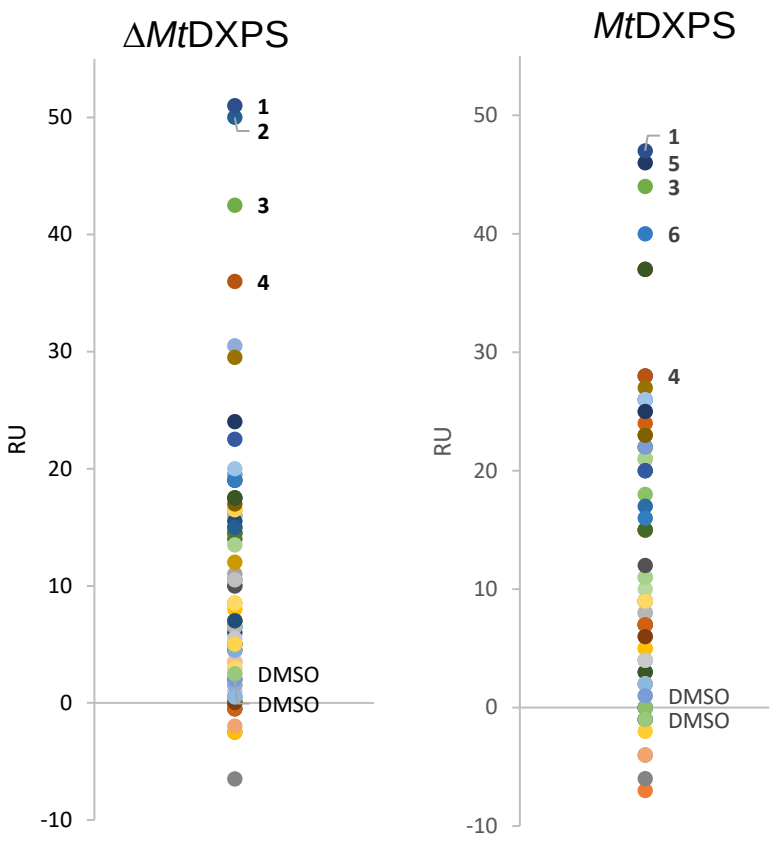

Figure 8: Surface plasmon resonance response of 94 compounds and two dimethyl sulfoxide (DMSO) samples from the first round of virtual screening against truncated and native *Mt*DXPS. All compounds were measured at 100 µM. Response unit (RU) values for Δ*Mt*DXPS are shown as the mean of duplicates. RU values for *Mt*DXPS are single measurements.

After validating the binding of all 94 compounds, their inhibitory activity against *Deinococcus radiodurans* (*Dr*)DXPS,[(1)] a closely related *Mt*DXPS homologue, was measured in the DXPS-1-deoxy-D-xylulose 5-phosphate reductoisomerase (IspC)-coupled assay. None of the six SPR hits show inhibition of over 50% at 100 µM (**Table 7**). The best inhibitor **1** with 39% inhibition of *Dr*DXPS is also the best binder in SPR while the other SPR hits **2**–**6** inhibit below 20%. Overall, the activity data of the 94 compounds is not very encouraging. The best compound is **1** and five others inhibit *Dr*DXPS by more than 28% (**7**–**12**). Since the activity assay was based on the

(1) Δ*Mt*DXPS was not active enough to be used in the activity assay.

D. radiodurans homologue and the SPR was based on the *M. tuberculosis* homologue of DXPS, the results should not be compared directly, but should be interpreted with care although the binding sites are similar.

Table 7: Activity of selected compounds against *Dr*DXPS. Activity was measured at 100 µM in the DXPS-IspC-coupled assay and is reported as %inhibition.

SPR hits	%inhi.	Assay hits	%inhi.
1*	39 ± 16	**7***	28 ± 25
2	8 ± 10	**8***	29 ± 18
3	13 ± 2	**9***	36 ± 9
4	13 ± 8	**10**	31 ± 12
5	8 ± 10	**11**	35 ± 16
6	7 ± 2	**12***	23 ± 19

%inhi. = percent inhibition (the mean value of three independent measurements), * = compounds selected for follow-up VS.

After two single point experiments at 100 µM, the most active hits (**1**, **7**, **8**, **9** and **12**) were selected as a starting point for a follow-up virtual screening (**Figure 9**). When later a third measurement was performed for validation, the results changed, so that also **10** and **11** show acceptable inhibition, while **12** lost most of its activity. However, the second VS was already ongoing at this point.

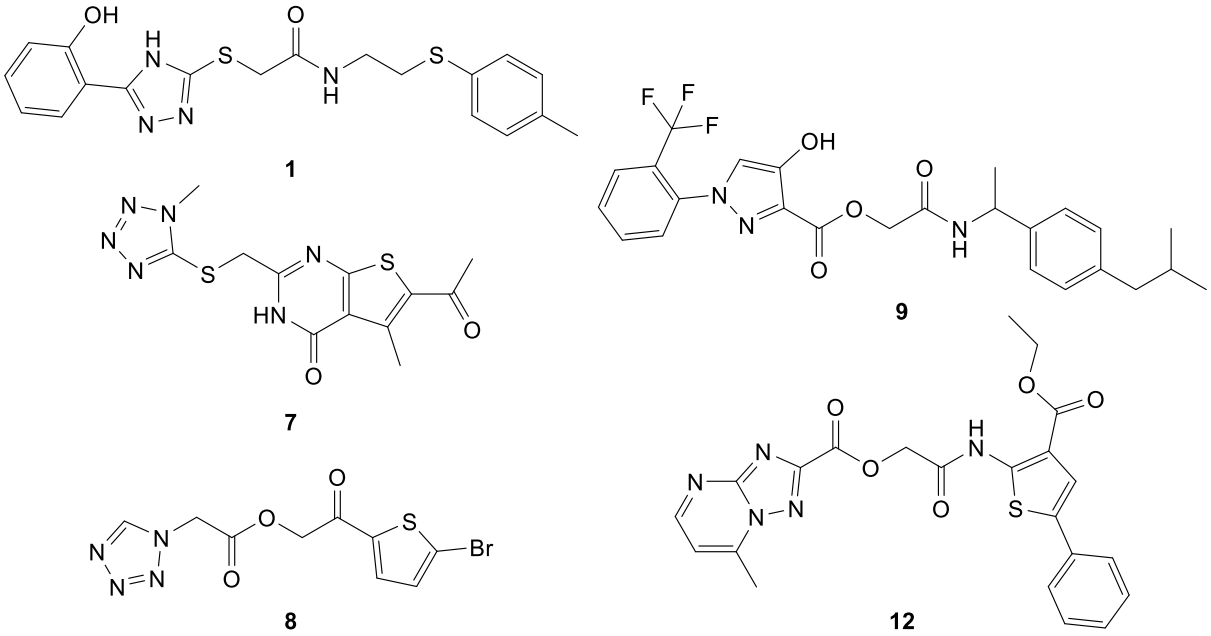

Figure 9: Hit compounds identified by virtual screening (VS) and validated by surface plasmon resonance or enzyme-inhibition assay. The second round of VS was based on this selection.

Nonetheless, all hits listed in **Table 7** were tested against *E. coli* as a model organism for Gram-negative activity. The results will be further discussed in Chapter 3.4.8, but compound **1** has the best activity with a good minimum inhibitory concentration (MIC) value of 28 µM. Then, **1** was also tested against *M. tuberculosis* H37Rv by Norbert Reiling (Forschungszentrum Borstel), but no inhibition was seen at 64 µM (data not shown). Based on these data, it was decided to make a compound library with closely related derivatives of **1** to advance this most promising hit, while the follow-up VS was ongoing.

3.4.4 Hit re-synthesis and validation

First, a synthetic pathway was developed that allowed easy derivatization on both sides of the molecule (**Scheme 4**). The synthesis started from hydrazide **13** which upon reaction with NH_4SCN and HCl (37%) in ethanol afforded the thioamide **14**.[105] To make derivatives of the Western ring of the compound, a variety of hydrazides can be used that are either commercially available or can be synthesized from the corresponding esters. Ring closure of thioamide **14** was achieved by refluxing in NaOH (10%). Ethyl-2-bromo acetate was introduced to form ester **16** followed by saponification using NaOH in tetrahydrofuran (THF).[106,107] Amine **20** was synthesized from 2-oxazolidone (**18**) and 1-phenylethanethiol (**19**) under decarboxylation.[108] A variety of derivatives can be synthesized by using different thiols or coupling different amines to acid **17**. The amide coupling between **17** and **20** proceeded smoothly with 1-ethyl-3-(3-dimethylaminopropyl)-carbodiimide hydrochloride (EDC*HCl) and 1-hydroxybenzotriazole (HOBt) as coupling reagents in dimethylformamide (DMF).[109]

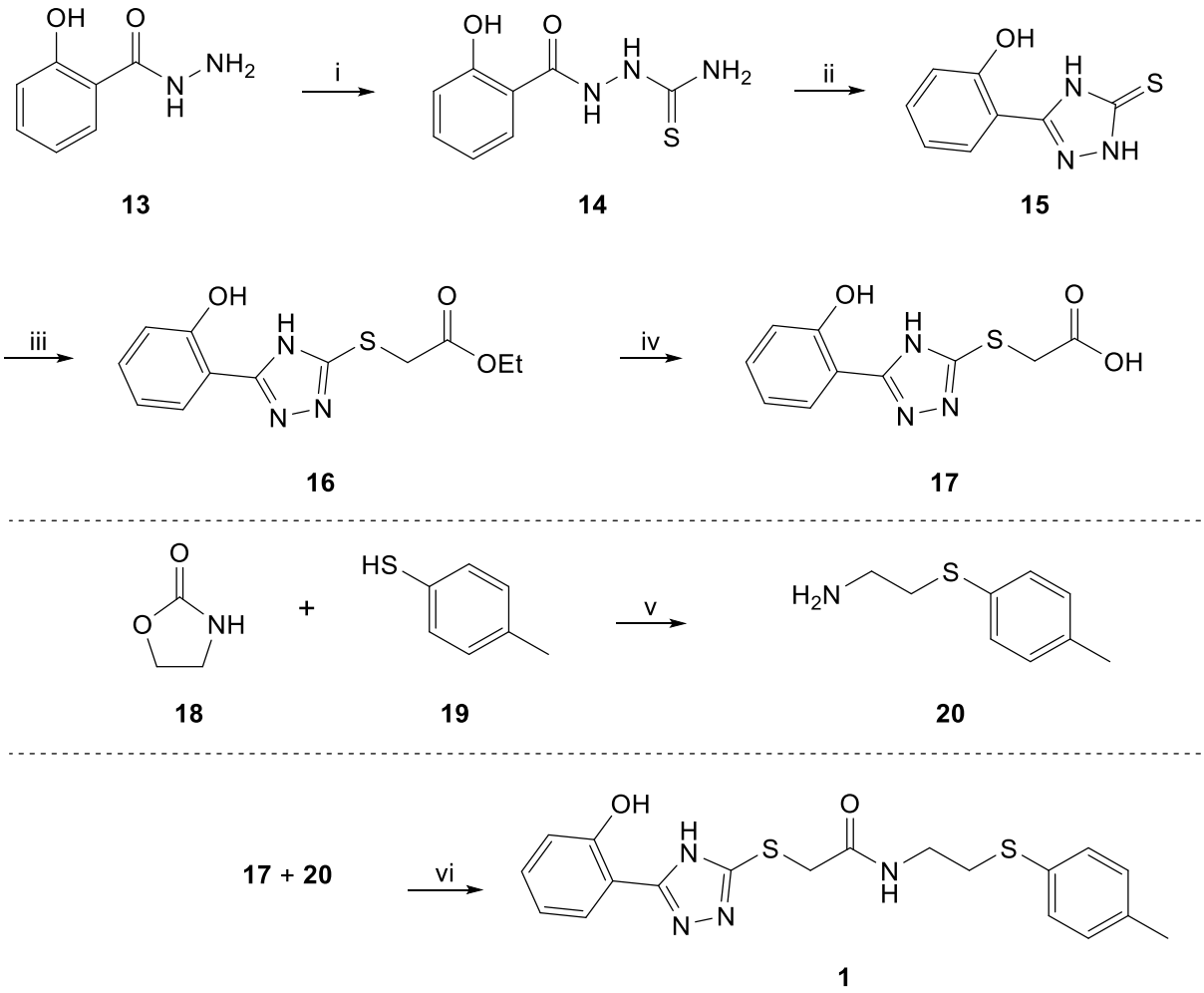

Scheme 4: Re-synthesis of hit **1**. i) NH_4SCN (1.0 equiv.), HCl (37%), EtOH, 90 °C, 48 h; ii) NaOH 10%, 105 °C, 2 h, 68% over two steps (o2s); iii) ethyl-2-bromo acetate (1.2 equiv.), $NaHCO_3$ (1.0 equiv.), EtOH, 25 °C, 74%; iv) NaOH (4.0 equiv.), THF, 25 °C, 16 h, 100%; v), NaOEt (2.0 equiv.), EtOH, 85 °C, 24 h, 89%; vi) EDC*HCl (1.1 equiv.), HOBt (1.0 equiv.), *N*-methylmorpholine (NMM) (2.0 equiv.), DMF, 25 °C, 24 h, 83%.

The successfully synthesized compound **1** was tested again in the DXPS-IspC coupled assay and an estimated IC_{50} of 100 µM (**Figure S 62**) was determined as the solubility limit of this compound is around 100 µM (**Table S 10**).

3.4.5 Synthesis of derivatives

3.4.5.1 Modifications on the Eastern ring

The synthesis of twelve derivatives with different substituents on the Eastern ring was performed by using a variety of different thiols (**Scheme 5**).

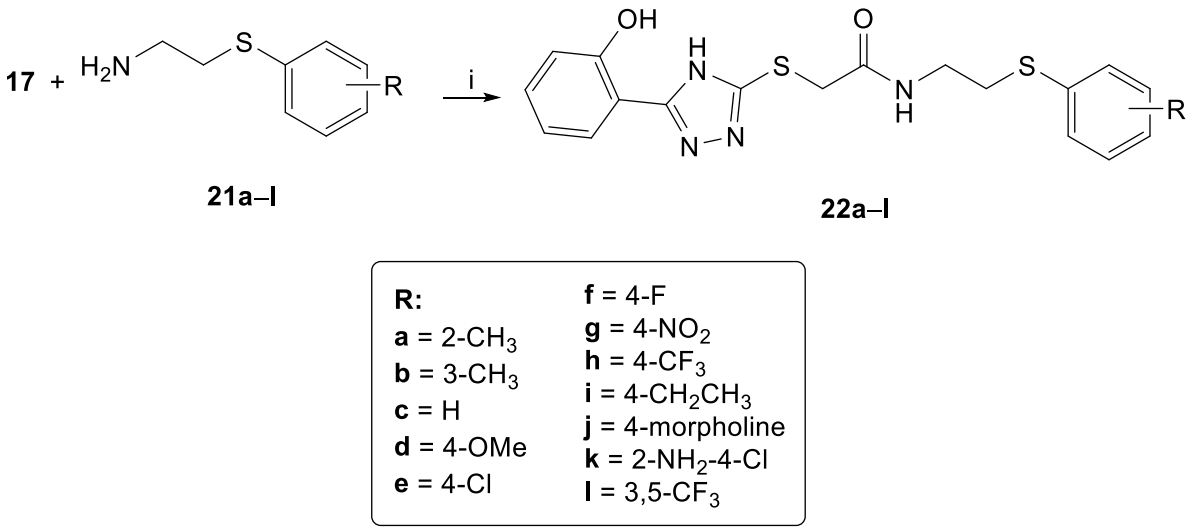

Scheme 5: Synthesis of Eastern ring derivatives. i) EDC*HCl (1.1 equiv.), HOBt (1.0 equiv.), NMM (2.0 equiv.), DMF, 25 °C, 24–72 h, 15%–88%.

The amines **21a** and **21b** were synthesized as described for **20**. However, it was previously shown that the reaction between 2-oxazolidone (**18**) and aromatic thiols converts faster and with higher yields when isopropanol is used instead of ethanol, so **21c**–**i** and **21k**–**l** were synthesized in isopropanol.[108] Amine **21j** was synthesized by protecting the amino group of **21e** with a *tert*-butyloxycarbonyl (Boc)-group (**Scheme 6**). Using a palladium catalyzed BUCHWALD–HARTWIG reaction, chlorine was replaced with morpholine. Subsequent de-protection, resulted in the amine **21j**. With all amines, the amide coupling was performed as for the hit **1**. Depending on the amines and the purification procedure, the final compounds were afforded with yields of 15%–88%.

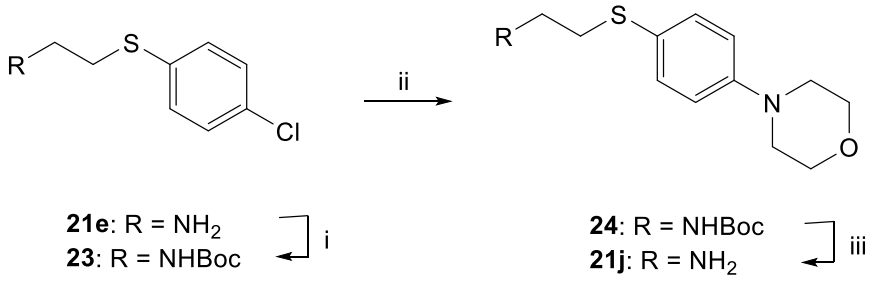

Scheme 6: Synthesis of amine **21j**. i) Di-*tert*-butyl dicarbonate (1.0 equiv.), $CHCl_3$, 0 °C, 16 h, 67%; ii) morpholine (1.0 equiv.), NaO^tBu (1.5 equiv.), *t*BuXPhos (0.1 equiv.), dioxane, 80 °C, 24 h, 6%; iii) HCl in dioxane (4 M), 25 °C, 6 h.

The selection of derivatives was based on the premise of making only small changes to get a clear picture of the SAR. Therefore, the methyl group was moved to position two and three of the ring (**22a**, **22b**) or removed completely (**22c**). A variety of

substituents in 4-position (**22d**–**j**) was chosen to explore this position further before looking into substituents in *ortho* or *meta* position. We also tested the effect of having two substituents on the Eastern ring (**22k** and **22l**).

3.4.5.2 Modifications on the Western ring

The synthesis of the Western part was done following the same procedure as for hit **1** with slight modifications (**Scheme 7**).

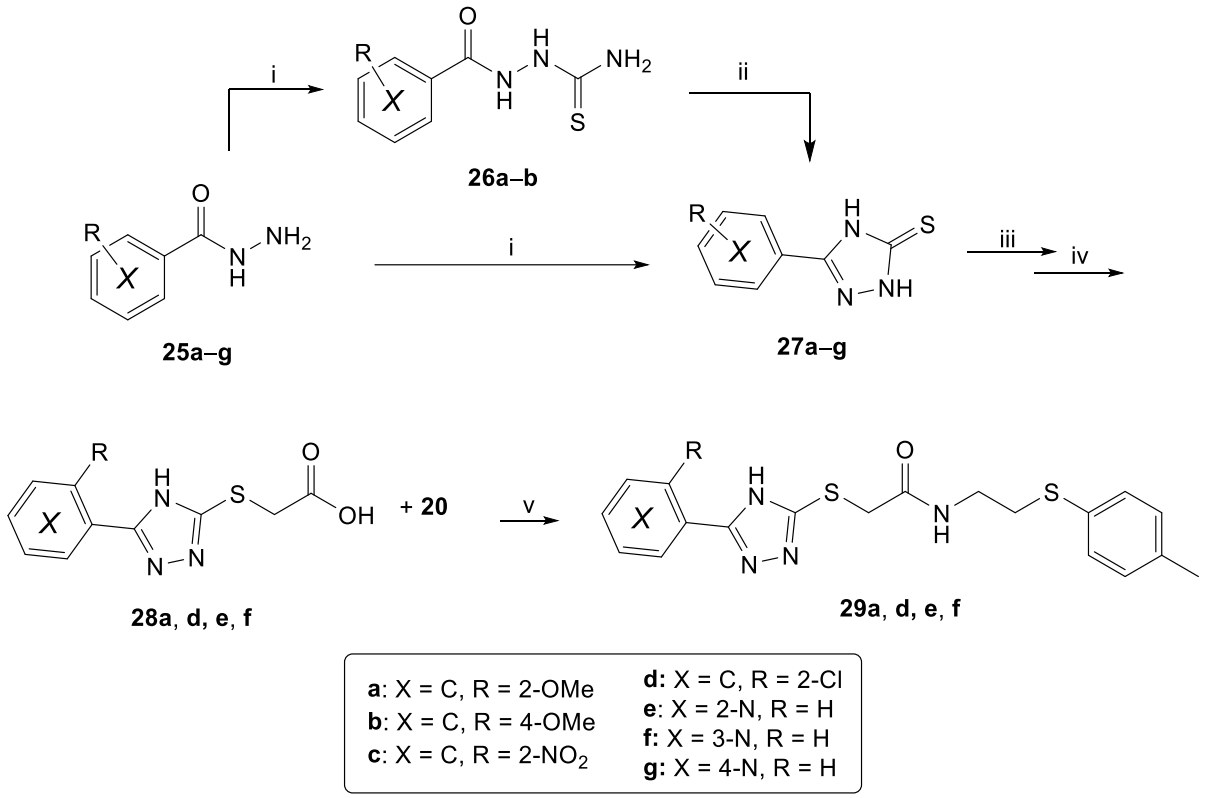

Scheme 7: Synthesis of Western ring derivatives. i) HCl (1 M), reflux, 48 h, 74%; ii) NaOH (10%), reflux, 48 h, 34%–100%; iii) ethyl-2-bromoacetate (1.2 equiv.), $NaHCO_3$ (1.0 equiv.), EtOH, 25 °C, 63%–90%; iv) NaOH (2.0 equiv.), H_2O, 25 °C, 24 h, 80%–100%; v) EDC*HCl (1.1 equiv.), HOBt (1.0 equiv.), NMM (2.0 equiv.), DMF, 25 °C, 24 h, 40%–57%.

Hydrazides (**25a**–**g**) decomposed in concentrated hydrochloric acid and a 1 M aqueous solution had to be used instead. In addition, the thioamide precursors **26a** and **26b** were only found for trizoles **27a** and **27b** while all other reactions led to the cyclized compounds **27c**–**g** directly. This was unexpected in acidic solution and has not been reported before. If the thiadiazole is the intended isomer, the thioamide is normally treated with concentrated sulfuric acid, while the triazole is formed under basic conditions.[105] To confirm that the correct cycle was formed and not the thiadiazole isomer **30**, the ^{1}H-NMR and ^{13}C-NMR chemical shift of compounds **27g** and **30**

(commercially available) were compared (**Table 8**). The differences especially of the proton chemical shifts confirmed that the correct isomer was formed.

Table 8: Comparison of ^{1}H- and ^{13}C-NMR chemical shifts of thiadiazole **30** and triazole **27g**.

	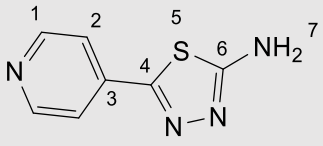 **30**		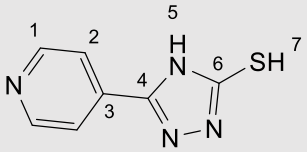 **27g**	
Proton	^{1}H-NMR	^{13}C-NMR	^{1}H-NMR	^{13}C-NMR
1	8.65 ppm (2H)	150.50 ppm	8.74 ppm (2H)	150.67 ppm
2	7.71 ppm (2H)	120.20 ppm	7.85 ppm (2H)	119.46 ppm
3	-	137.79 ppm	-	132.51 ppm
4	-	153.96 ppm	-	148.35 ppm
5	-	-	14.12 ppm (1H)	-
6	-	169.82 ppm	-	167.69 ppm
7	7.69 ppm (2H)	-	13.94 ppm (1H)	-

Next, ethyl-2-bromoacetate was used to install the desired ester and subsequent saponification resulted in the free acids (**28a**, **d**–**f**). The amide coupling to the final product was performed as described previously (**29a**, **d**–**f**).

We also planned to synthesize the 2-hydroxy and the 3-hydroxy Western ring derivatives, but their synthesis failed after several different approaches. Using the unprotected hydroxyl hydrazides directly resulted in decomposition of the starting material in the first step in hydrochloric acid. Therefore, two different protection groups, a methoxy and a benzyl group, were used. Benzyl-protected 4-hydroxybenzhydrazide did not cyclize in concentrated or 1 M hydrochloric acid, but benzyl-protected 3-hydroxybenzhydrazide did (1 M HCl). However, saponification of the ester two steps later failed, and an unidentifiable compound was formed for which several proton and carbon signals in the NMR were missing. 3-Methoxybenzhydrazide did not react in diluted hydrochloric acid while 4-methoxybenzhydrazide did react and the reaction stopped at the thioamide form **26b** (**Scheme 7**). The cyclization in sodium hydroxide worked as expected, but the subsequent reaction with ethyl-2-bromoacetate failed.

As an alternative strategy it was tried to first perform the amide coupling between **20** and 2-chloroacetic acid to form chloride **31** and then add different triazoles directly (**Scheme 8**). As a model reaction, **27g** was chosen and the reaction worked well with a yield of 53% for **29g**. The same was true for **27c**, which reacts with ethyl-2-bromoacetate but in a low yield and the ester intermediate is difficult to purify. For the 4-methoxy derivative **27b**, the reaction also resulted in the desired final compound **29b**. In summary, the alternative route made it possible to circumvent saponification and more challenging purification steps, and resulted in a higher overall yield in fewer steps. Then, compound **29b** was mixed with BBr_3 to deprotect the hydroxyl group, but the compound decomposed.

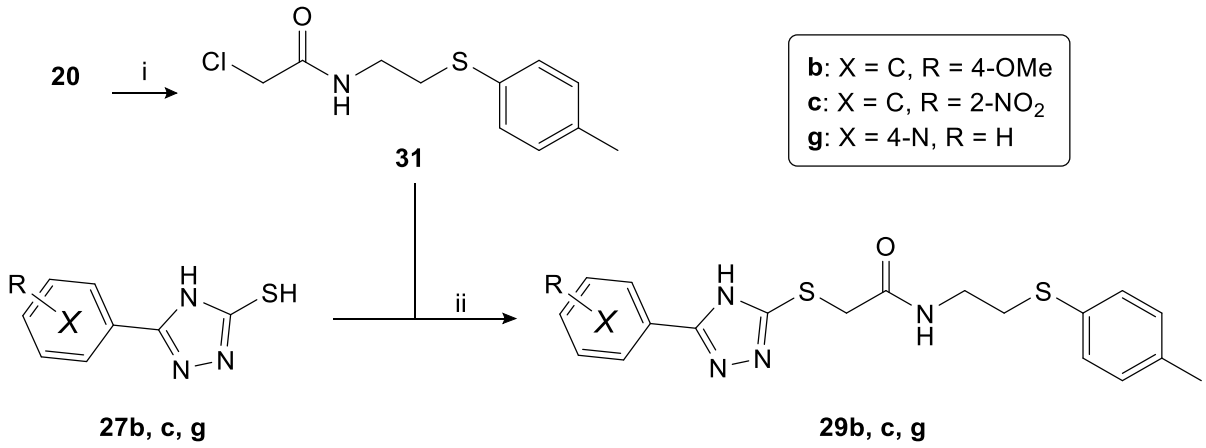

Scheme 8: Alternative synthesis to circumvent difficult saponifications. i) 2-chloroacetic acid (1.0 equiv.), EDC*HCl (1.1 equiv.), HOBt (1.0 equiv.), NMM (2.0 equiv.), DMF, 25 °C, 24 h, 29%. ii) $NaHCO_3$ (1.0 equiv.) or $NaHCO_3$ (aq)/ethanol 1:1, ethanol, 25 °C, 24 h, 24%–53%.

There are a few things that can be tried to make the syntheses work. The 3-methoxybenzhydrazide should be dissolved in concentrated instead of in diluted hydrochloric acid, especially because there was no reaction progress seen for this reaction in diluted acid. The concentration of BBr_3 and the reaction time should be reduced to see if this helps with the deprotection. Alternatively, the reaction can be performed at lower temperature.

3.4.5.3 Modifications of the triazole ring

One modification that would also allow for easy derivatization, is the replacement of the 1,2,4-triazole with a 1,2,3-triazole ring (**Scheme 9**). The 1,2,3-triazole **35** can be synthesized by click-chemistry between an alkyne and an azide functional group, which reduces the number of steps from five to three. In the synthesis of **1**, most reactions need stirring over night, while the synthesis of **36** comprises two quick steps.

The azide **33** is formed from **32** within two hours and the click reaction with **34** is also quick if 1.0 equivalent of copper sulfate is added from the beginning. Only the amide coupling needs up to 72 hours.

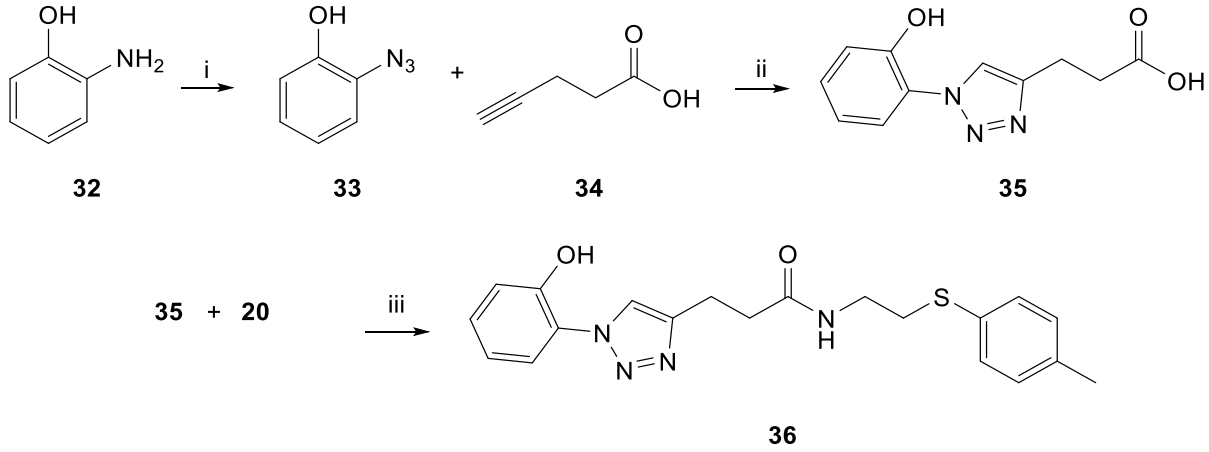

Scheme 9: Synthesis of 1,2,3-triazole **36** *via* click-chemistry. i) $NaNO_2$ (3.0 equiv.), H_2O, HCl (6 N), 0 °C, 30 min, then NaN_3 (3.0 equiv.), 0 °C, 2 h; ii) sodium ascorbate (4.0 equiv.), $CuSO_4 \cdot 5H_2O$ (1.0 equiv.), MeCN, 25 °C, 72 h; iii) EDC*HCl (1.1 equiv.), HOBt (1.0 equiv.), NMM (2.0 equiv.), DMF, 25 °C, 72 h, 34%.

3.4.5.4 Linker modifications

Two compounds with different linkers between the amide and the Eastern ring system were synthesized and three derivatives lacking the Eastern ring following the same amide coupling reaction as before (**Scheme 10**).

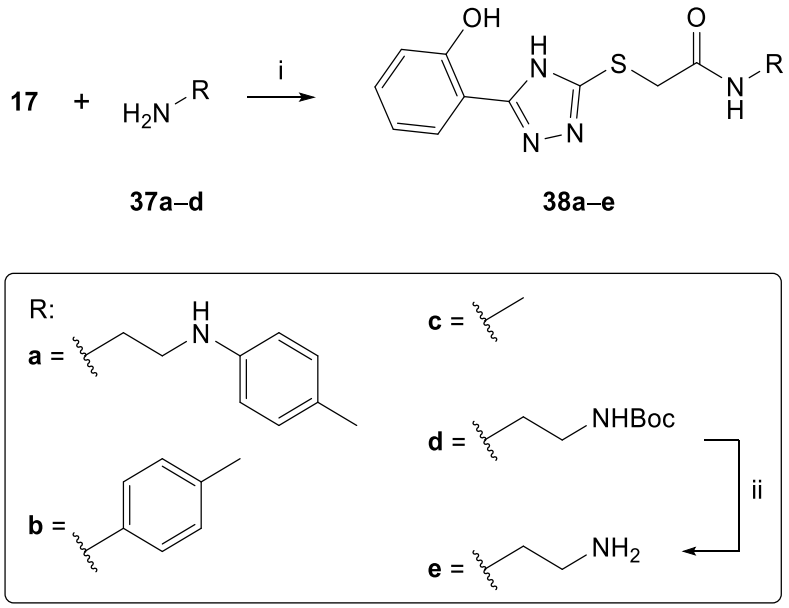

Scheme 10: Synthesis for linker derivatives. i) EDC*HCl (1.1 equiv.), HOBt (1.0 equiv.), NMM (2.0 equiv.), DMF, 25 °C, 72 h, 10%–31%. ii) HCl in dioxane (4 M), 0 °C to 25 °C, 16 h, 69%.

First, the sulfur atom was replaced with a nitrogen atom (compound **38a**). To do so, amine **37a** was synthesized following a literature procedure.[110] Removing the aliphatic linker led to derivative **38b** with the aromatic ring directly linked to the amide. The whole Eastern part of the molecule was replaced by just a methyl group (compound **38c**). In an attempt to improve the Gram-negative activity (results see Chapter 3.4.8), a primary amine was introduced by amide coupling between **17** and *N*-Boc-ethylenediamine (compound **38d**) and subsequent deprotection (compound **38e**).

3.4.6 Activity of derivatives against *Dr*DXPS and *Ec*IspC

After the synthesis was completed, all compounds were tested in the newly implemented high-performance liquid chromatography-tandem mass spectrometry (HPLC-MS/MS)-based assay described in Chapter 3.3. In order to see if the acid precursors are also active, they were included in all testings. First, the solubility limit for all compounds was determined (**Table S 10**) and based on the results, the assay was performed at 200 µM, 100 µM or 50 µM (**Table 9**). However, none of the derivatives were active (more than 50% inhibition) at the respective highest soluble concentrations. Amides **22d**, **22j** and **38b** and acid **17** are the only compounds that show an inhibition higher than 30% at a concentration of 200 µM. The standard deviations for these measurements are high and the data difficult to rely on and to interpret. As these results were not expected, the activity of a selection of compounds was also tested in the DXPS-IspC coupled assay. Again, no inhibition can be detected and also hit **1** is not active anymore. One explanation for these results could be that the compounds are selective IspC inhibitors, but when running the assay without DXPS, none of the compounds are active (**Table 9**). There was also no correlation between the two DXPS assays. The four compounds that seemed to be performing the best in the HPLC-MS/MS-based assay show no or lower activity in the DXPS-IspC-coupled assay, which we cannot explain. A compound that inhibits DXPS should inhibit in both assays, while an IspC inhibitor should only show inhibition in the coupled assay.

Table 9: Activity data of derivatives in functional assays against *Dr*DXPS and *Ec*IspC.

Cpd.	%inhi. DXPS	%inhi. DXPS-IspC	%inhi. IspC
1[b]	11 ± 20	27 ± 12	21 ± 14
17[a]	**37 ± 16**	9 ± 9	4 ± 3
22a[b]	18 ± 44	13 ± 4	–13 ± 24
22b[a]	14 ± 8	16 ± 3	14 ± 3

Cpd.	%inhi. DXPS	%inhi. DXPS-IspC	%inhi. IspC
22c[a]	14 ± 9	22 ± 3	–6 ± 0
22d[a]	**36 ± 19**	23 ± 2	3 ± 0
22e[c]	6 ± 9	17 ± 4	–2 ± 0
22f[a]	28 ± 18	21 ± 4	15 ± 3
22g[b]	13 ± 17	12 ± 1	7 ± 0
22h[c]	15 ± 18	–6 ± 0	14 ± 5
22i[c]	14 ± 6	13 ± 4	14 ± 1
22j[a]	**34 ± 3**	n.d.	n.d.
22k[b]	22 ± 27	12 ± 4	7 ± 1
22l[c]	18 ± 12	12 ± 15	–2 ± 3
28a[a]	7 ± 10	3 ± 0	19 ± 21
28d[a]	–3 ± 9	1 ± 0	3 ± 3
28e[a]	–6 ± 16	–1 ± 1	–12 ± 19
28f[a]	7 ± 12	2 ± 1	13 ± 1
29a[c]	–2 ± 8	10 ± 0	13 ± 5
29b[c]	n.d.	n.d.	n.d.
29c[b]	18 ± 15	n.d.	n.d.
29d[c]	2 ± 12	9 ± 2	n.d.
29e[a]	1 ± 4	n.d.	5 ± 0
29f[a]	0 ± 11	6 ± 0	7 ± 0
29g[b]	25 ± 21	n.d.	n.d.
36[b]	–1 ± 14	8 ± 2	0
38a[a]	11 ± 10	9 ± 2	5 ± 1
38b[a]	**34 ± 15**	n.d.	n.d.
38c[a]	1 ± 20	5 ± 4	5 ± 0
38d[a]	27 ± 16	n.d.	n.d.
38e[a]	11 ± 10	n.d.	n.d.

Activity measured at compound concentrations of [a] 200 µM, [b] 100 µM, [c] 50 µM. n.d. = not determined, %inhi. = percent inhibiton.

Overall, these results suggest that the compounds are neither DXPS nor IspC inhibitors and the original data are false positive. This could be explained by the low solubility of hit **1** and that therefore, the estimated IC_{50} value of 100 µM should not have been relied upon.

Since the SPR was performed against *Mt*DXPS, it is possible that hit **1** is not binding or inhibiting *Dr*DXPS, but is only binding and inhibiting Δ*Mt*DXPS. In Chapter 3.3, the optimal concentration of Δ*Mt*DXPS for the HPLC-MS/MS-based assay was determined. However, a large amount of the enzyme was needed for inhibitor testing, which was not available to confirm this hypothesis.

3.4.7 Activity of VS hits in the HPLC-MS/MS-based assay

The inconclusive data from the coupled assay in comparison to the HPLC-MS/MS-based assay, led us to testing all VS hits in the DXPS-only assay and see if there are compounds that have been eliminated previously as hits (**Table S 11**). Again, the same behavior was observed, namely that compounds that are not active in the coupled assay, show good inhibition in the DXPS-only assay. Four VS hits with more than 50% inhibition of *Dr*DXPS at 95 µM were found (**Table 10**). Compounds **39**, **40** and **41** do not show inhibition in the coupled assay and show no binding in SPR. Molecule **4** is one of the best binders against both *Mt*DXPS homologues in SPR and is active against *Dr*DXPS in the HPLC-MS/MS-based assay with an IC_{50} of 25 µM (**Figure S 63**). The solubility of this compound is 107 µM at 5% DMSO, but at this concentration the inhibition is 90%, so an IC_{50} can be determined reliably. The solubility of **40** and **41** is higher, but in the IC_{50} determination no dose-response could be observed. Compound **39** also shows a good IC_{50} value of 61 µM, but the data quality between measurements was not as consistent as for **4**, so the results have to be taken with caution (**Figure S 64**).

Table 10: Most active virtual screening hits in the HPLC-MS/MS-based assay against *Dr*DXPS.

Cpd.	%inhi. DXPS at 95 µM	IC_{50} [µM]
4	89 ± 20	25 ± 2
39	77 ± 8	61 ± 15
40	56 ± 9	n.d.r.
41	49 ± 13	n.d.r.

%inhi. = percent inhibiton, n.d.r. = no dose-response.

One explanation for the different assay results can be the concentration of the substrates. In the HPLC-MS/MS assay, we have reduced the substrate concentration from 1 mM to 200 µM (pyruvate) and 400 µM (D-GAP). If compound **4** is substrate competitive this can be the reason why it shows no inhibition in the coupled assay. To

verify this hypothesis, the IC_{50} value was determined while D-GAP was titrated from 1 mM to 31.3 µM. Pyruvate was not titrated as it is used for the assay read-out. The experiment was performed with a new batch of compound that was ordered after the initial stock ran out. The compound was purified by preparative HPLC to remove impurities. IC_{50} value determination was much more difficult than with the original stock. After four repetitions and removal of outliers an IC_{50} value of 47 µM was determined (**Figure S 65**). Although this value seems to be comparable to the original one, the data quality is not as good as before and the result has to be treated with caution. A shift in this IC_{50} value with different D-GAP concentrations would confirm that the compound is indeed D-GAP-competitive. However, the assay was repeated five times and it was not possible to determine an IC_{50} value for any of the different concentrations.

In **Figure 10**, observations from the mode of inhibition (MOI) assay are summarized visually. The absolute values of the peak areas change with different D-GAP concentrations. While the blank peak-area (gray squares) is approximately 3 million for all D-GAP concentrations, the control peak-area increases with lower D-GAP concentrations from 200,000 to 1.6 million. At 500 and 1000 µM D-GAP, the reaction velocity is equal leaving a comparable amount of pyruvate (peak area 140,000 and 200,000, respectively). This is expected as the K_M value of D-GAP for *Dr*DXPS is 204 µM. Above this concentration the reaction reached the steady-state and the substrate concentration has no influence on velocity. Below that concentration, the reaction velocity is substrate-dependent. One problem could be the detection limit if the pyruvate concentration drops too low. To investigate this further, higher D-GAP concentrations should be analyzed while using higher pyruvate concentrations as well. During the assay development, a low pyruvate concentration was used to reduce the amount of needed DMB (compare Chapter 3.3.3). Since we are now able to synthesize the expensive DMB in higher quantities, it is not a limiting factor anymore. Although no IC_{50} values could be determined for compound **4**, it is encouraging to see the influence of lower D-GAP concentrations on the inhibition at 100 µM **4** (blue stars). The highest inhibition is 28% at 31.3 µM D-GAP, which is much lower than expected, but at 1000 µM D-GAP the inhibition is only 9%. As mentioned before, the purified batch of compound **4** was less active than the original one and the measurements had a bigger error than the measurements with the original stock solution. It could be that an impurity in the original solution was responsible for the activity.

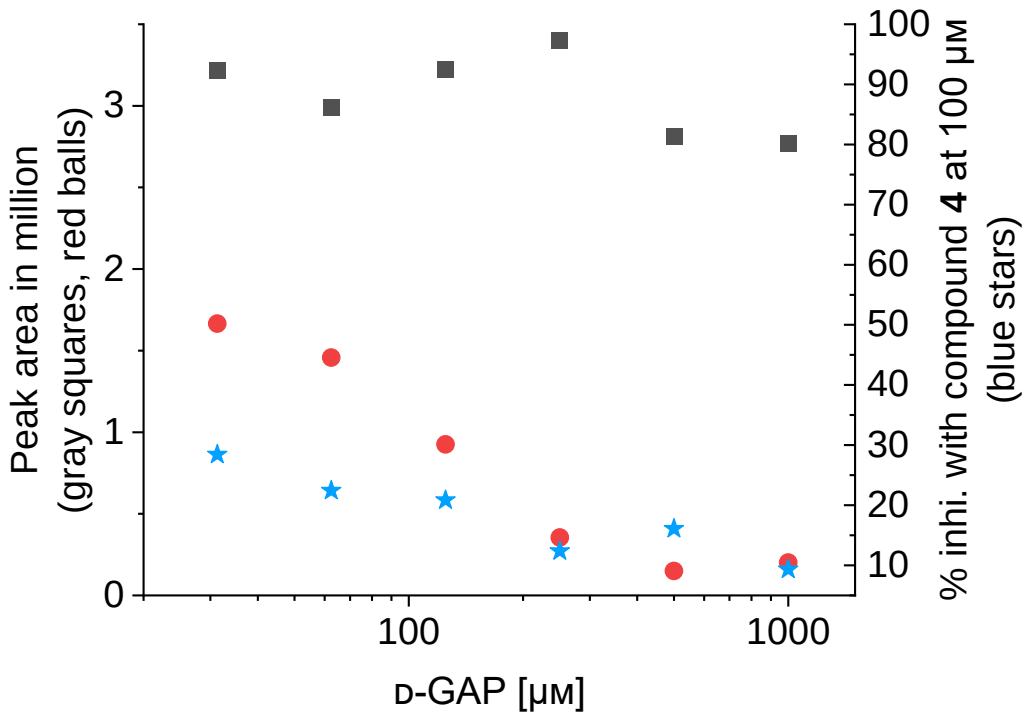

Figure 10: Influence of D-GAP on activity and inhibition of *Dr*DXPS with **4**. Differences in peak area between blank (gray squares) and control (red balls) at different D-GAP concentrations. Percent inhibition of compound **4** at 100 µM (blue stars) at different D-GAP concentrations.

All these factors should be investigated in more detail before synthesizing any derivatives. The MOI assay should be performed and validated with the reference compound presented in Chapter 3.3. In addition, the original stock of **4** should be analyzed for impurities.

3.4.8 Biological data

AMR is especially problematic in Gram-negative bacteria (**Table 1**). Therefore, we wanted to check in parallel if our VS hits are active in *E. coli* as a Gram-negative model organism that utilizes the MEP pathway. The 12 initial hits that performed best in the SPR and *Dr*DXPS activity assay were also tested against *E. coli* K12 and *E. coli* ΔTolC. The latter is a mutant of the former in which the efflux channel TolC is removed.[111] This mutant lacks the ability to efficiently pump the molecules outside the bacterial cells. Therefore, a compound that inhibits the growth of *E. coli* ΔTolC but not the wild-type strain K12 is probably eliminated by the efflux TolC system. With this knowledge good inhibitors are not excluded by accident but can be optimized to also inhibit *E. coli* K12.

From the 12 hit compounds, compound **1** has a MIC value against *E. coli* ΔTolC of 28 µM, and shows a 11% growth inhibition at 50 µM of *E. coli* K12 (**Table 11**). It was

not possible to determine a MIC value for any of the other hit compounds, although five show activity against *E. coli* ΔTolC. Compound **4** is not active on *E. coli* K12, but inhibits the growth of *E. coli* ΔTolC by 43% at 50 μM, which can be an interesting starting point for optimization. The *E. coli* activity should be monitored when derivatives are made in the future.

All derivatives of **1** were tested against both *E. coli* strains and only three have a MIC value lower than 28 μM in *E. coli* ΔTolC. They are all Eastern-ring derivatives and are substituted in the 4-position (**22e**: 4-Cl, **22h**: 4-CF_3, **22i**: 4-CH_2CH_3). In general, the Eastern-ring derivatives are active against *E. coli*. Most have a MIC value of 20–100 μM and only the morpholine derivative **22j** and the 4-NO_2-derivative **22g** show inhibition below 90% at 100 μM. Compounds **22i** and **22j** are the only two derivatives that do not inhibit *E. coli* K12, which indicates that aliphatic substitution in the 4-position affects efflux. In contrast, all Western-ring derivatives are inactive against *E. coli* K12 and do not inhibit the growth of *E. coli* ΔTolC more than 82% at 100 μM. The only exception is compound **29c** with a NO_2-group in 2-position, which shows that the 2-hydroxy moiety can be replaced with a reduction, but not a complete loss of activity.

Table 11: Activity against *E. coli* K12 and *E. coli* ΔTolC of virtual screening hits and derivatives of compound **1**. Activity is reported as MIC or %inhi. at 100 μM.

Cpd.	*E. coli* K12	*E. coli* ΔTolC	Cpd.	*E. coli* K12	*E. coli* ΔTolC
SPR and DXPS-IspC-based assay hits					
1	**11 ± 2%[a]**	**28 ± 0 μM**	**7**	n.i.	n.i.
2	n.i	63 ± 0%	**8**	n.i.	26 ± 3%
3	n.i. [b]	53 ± 13%[b]	**9**	n.i.[b]	n.i. [b]
4	n.i. [a]	43 ± 14%[a]	**10**	n.i.[b]	n.i. [b]
5	15 ± 0%	46 ± 1%	**11**	n.i.[b]	19 ± 1%
6	n.i.	34 ± 7%	**12**	n.i.	n.i.
Eastern-ring derivatives					
22a	16 ± 13%	49 ± 1 μM	**22g**	19 ± 0%	82 ± 3%
22b	21 ± 3%	49 ± 0 μM	**22h**	22 ± 6%[a]	**18 ± 3 μM**
22c	14 ± 1%	93 ± 2 μM	**22i**	n.i.	**19 ± 3 μM**
22d	6 ± 1%	96 ± 4 μM	**22j**	n.i.	63 ± 1%
22e	**30 ± 7%**	**25 ± 3 μM**	**22k**	23 ± 14%	48 ± 1 μM
22f	16 ± 2%	96 ± 1 μM	**22l**	11 ± 3%[b]	75 ± 5%[b]

Cpd.	*E. coli* K12	*E. coli* ΔTolC	Cpd.	*E. coli* K12	*E. coli* ΔTolC
Western-ring derivatives					
29a	n.i.	n.i.	**29e**	n.i.	82 ± 3%
29b	n.i. at 50 µM	48 ± 1%[a]	**29f**	n.i.	44 ± 6%
29c	20 ± 0%	99 ± 1 µM	**29g**	n. i. [a]	38 ± 15%[a]
29d	n.i.	50 ± 11%	**36**	1 ± 3%	8 ± 0%
Linker derivatives					
38a	n.i.	47 ± 2%[a]	**38d**	n.i.	28 ± 10%
38b	**51 ± 10%**	58 ± 6 µM	**38e**	n.i.	n.i.
38c	n.i.	n.i.			
Acid derivatives					
17	n.i.	n.i.	**28e**	13 ± 4%	17 ± 3%
28a	n.i.	n.i.	**28f**	n.i.	n.i.
28d	n.i.	n.i.			
HPLC-MS/MS-based assay hits					
39	n.i.	n.i.	**41**	n.i.[b]	24 ± 7%[b]
40	n.i.	16 ± 3%			

%inhi. = percent inhibition, n.i. = no inhibition, measured at [a] 50 µM, [b] 25 µM.

The linker derivatives are more diverse, but it can be seen that the sulfur atom is essential as compound **38a** (nitrogen instead of sulfur) loses activity against both strains in comparison to parent compound **1**. Removing the Eastern aromatic ring leads to complete loss of activity (**38c**–**e**). This was unexpected because we specifically installed a primary amine to improve Gram-negative activity. In 2017, Richter *et al.* coined the term eNTRy rules after analyzing the ability of over 180 diverse compounds to accumulate in *E. coli*.[112] They found that an ionizable, sterically non-hindered primary amine, a globularity (three-dimensionality) below 0.25 and less than five rotatable bonds help with accumulation in Gram-negative bacteria. Compound **38e** was designed to fulfill these criteria (primary amine, globularity = 0.063) except for the number of rotatable bonds, which is six. However, from the analysis of the activities of the other compounds, the primary amine should have been installed at a different position as the removal of the Eastern rings system led to a loss of activity. Even if compound **38e** is now accumulating in the cell it is not active anymore. This has to be taken into consideration when making more derivatives.

Surprisingly, compound **38b** with the aromatic ring directly attached to the amide has the best inhibition against *E. coli* K12 and a moderate MIC value of 58 µM against *E. coli* ΔTolC. Similar compounds have been reported to be New Dehli metallo-β-lactamase-1 (NDM-1) inhibitors (**Figure 11**).[113] NDM-1 is present in several bacteria such as *E. coli* and *K. pneumoniae*, and makes them resistant to β-lactam antibiotics. The only structural difference between the reported compound **42** and compound **38b** is the position of the methyl-group on the Eastern ring. The compounds in that study have only been tested on NDM-1 directly and their intrinsic inhibitory activity against bacteria has not been investigated yet. However, another very similar compound class (representative **43** closest structural analogue to **38b**) has been tested against a variety of clinically relevant strains and its activity was promising in *E. coli*, although the target has not been determined.[114]

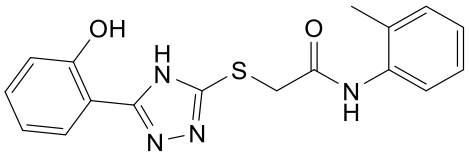

42

IC_{50} (NDM-1) = 0.16 ± 0.005 µM

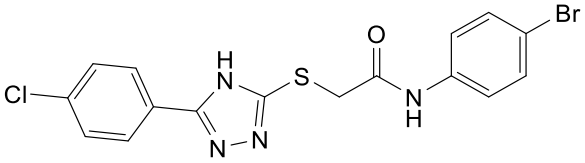

43

MIC (*E. coli*) = 40 µg/mL

Figure 11: Two examples of derivatives of compound **38b** and their biological activities that have been reported before.

This could lead to the development of a dual inhibitor that can be used in combination with a β-lactam antibiotic. On the one hand, it can prevent the resistance against the antibiotic and on the other hand, it kills the bacteria through a different mechanism. It might be interesting to investigate this class of compounds further by installing a primary amine at the methyl-substituent of the aromatic ring to see if accumulation can be improved.

Finally, the acid precursors and the new hits from the HPLC-MS/MS-based assay have been tested but they have no interesting inhibitory activities.

Compound **1** was also tested against human Hep G2 cells to determine its liver toxicity. It is not inhibiting cell growth at 25 µM, but at 100 µM, 49 ± 1% inhibition was measured. This value is acceptable as its MIC in *E. coli* ΔTolC is 28 µM. It can be assumed that the toxicity is comparable in all derivatives of the class but this has to be confirmed if more diverse compounds are synthesized.

In summary, the Western part of the molecule is essential for its activity in *E. coli*, if the Eastern part contains a sulfur atom and a phenyl ring, preferably with a 4-CF_3 substituent. The 1,3,4-triazole cannot be replaced by a 1,2,3-triazole and the 2-hydroxy-substituent on the Western ring can only be replaced with a NO_2-group albeith with loss of some activity. Derivatives of compound **38b** should be investigated further as potential dual inhibitors.

3.4.9 Activity of hits from the second VS round

Five compounds were selected for a second round of VS as described in Chapter 3.4.3. The selection was based on the results from the DXPS-IspC-coupled assay (data presented again in **Table 12**). Later, all compounds from the first VS round were tested again in the HPLC-MS/MS-based assay and the initial activity could not be confirmed. The activity of all hits that originally inhibited up to 39% in the coupled assay is below 17% in the DXPS-only assay except for compound **7** at 27%. However, the second round of VS was already being performed at that point.

Table 12: Overview of second round of virtual screening. Original activities of hits are presented in comparison to their activities in the second round. Number of derivatives from each compound is shown and number of hits (%inhi. >50%, mean of three measurements) from the second round is presented. Measured at 95 µM.

Cpd.	%inhi.			No. of derivatives 2nd VS	No. of hits
	DXPS-IspC	DXPS 1st VS	DXPS 2nd VS		
1	39 ± 16	14 ± 10	17 ± 6	20	-
7	28 ± 25	27 ± 4	2 ± 4	14	3
8	29 ± 18	17 ± 3	12 ± 11	15	-
9	36 ± 9	5 ± 6	0 ± 7	18	-
12	23 ± 19	5 ± 16	32 ± 10	14	-

%inhi. = percent inhibition, no. = number.

In total, 86 hits were identified in the VS and they were tested together with the five parent compounds in the DXPS-only assay. The activities were close to the results from the first round, especially when taking the error into account. This group of compounds is a good representation of the variation that we observed in the DXPS-only assay. The results can vary up to 50% between days and we should only consider compounds that inhibit between 50–100% at a certain concentration and whose IC_{50} value can be reproduced reliably. From the second round of VS, only three compounds show an inhibition of more than 50% and they are all derived from compound **7** that

itself is not active anymore in the second VS round (1st: 27%, 2nd: 2%). The stock solution of **7** has to be checked for the correct compound mass to determine wheather decomposition is responsible for the loss in activity.

Overall, the data quality is not promising. The inhibition of the three hits varied greatly between measurements (**Table 13**). As the second VS round was based on single-point data that could have been dismissed as misleading if IC_{50} values had been determined, this time the three hits were further analyzed before drawing any conclusions. For compound **44** an IC_{50} value of 90 µM was determined. However, when looking at the IC_{50} curve, the error is not only very high with 36 µM for the calculated IC_{50} value, but it is also high between the individual measurements especially at higher concentrations (**Figure S 66**). It was also possible to calculate an IC_{50} value for compound **45**, but the relationship between concentration and increase of inhibition is too linear to be reliable (**Figure S 67**). The third compound with interesting single-point activity (**46**) showed no dose-response at all (**Figure S 68**).

Table 13: Hit compounds after second round of VS with a single-point inhibition higher than 50% at 95 µM. Mean of two measurements.

Cpd.	%inhi. at 95 µM	IC_{50} [µM]
44	56 ± 38	90 ± 36
45	52 ± 24	l.d.r.
46	86 ± 45	n.d.r.

n.d.r.= no dose-response, l.d.r. = linear dose-response.

When looking at the structures, it is interesting to note that they are all very similar. The core of compound **7** is the same and only the tetrazole ring is either changed to a triazole (**44**) or carries a different substituent (**45**, **46**). However, very similar compounds (**47**, **48**, **49**; see **Table S 12**) that have other modifications on the same ring are not active. This could be an indication for a structure–activity relationship, but this should be confirmed by testing the compounds again.

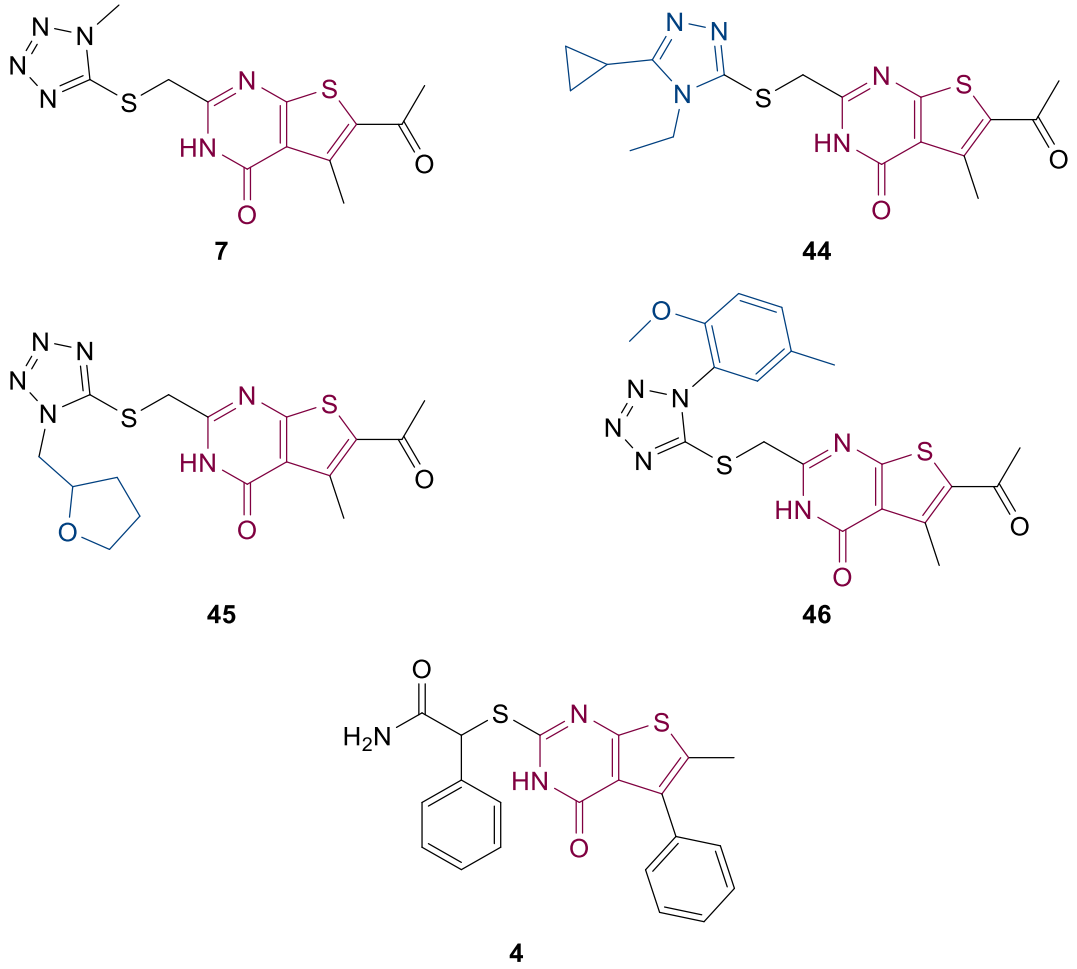

Figure 12: Structures of first-round hit **7** and second-round derivatives **44**–**46** in comparison to hit **4**. Blue = Differences in structures in comparison to parent compound **7**. Magenta = identical core structure.

Another promising aspect of this compound class is that it has the same core structure as compound **4**. Compound **7** is in contrast to **4** more soluble (>250 µM at 5% DMSO) and combining different structural aspects of the two compounds could be interesting. However, the activity of all compounds has to be verified first as described above.

3.4.10 Conclusions and outlook

The WHO has defined *M. tuberculosis* as one of the important organisms against which new antibiotics are urgently needed. As *M. tuberculosis* utilizes the MEP pathway and the structure of the first enzyme of this pathway, DXPS, has been recently solved, we performed a VS using the deep convolutional network program Atomnet. From several million compounds that were screened, we identified 94 hits that were purchased and tested by SPR against *Mt*DXPS and Δ*Mt*DXPS. Afterwards they were also tested against *Dr*DXPS in two activity assays. Initially, hit **1** was chosen for derivatization and further investigation against *E. coli*. A synthetic route was chosen that enabled easy

derivatization on the Eastern-ring system. While investigating the Western-ring derivatization it was possible to reduce the number of steps needed by performing the amide coupling separately and not as the last step. This also helped to circumvent difficult purification steps. However, compound **1** was not as active as originally thought and no improvement could be achieved regarding the on-target activity. A small SAR study against *E. coli* was performed but only a small improvement in activity could be achieved against *E. coli* ΔTolC. Introduction of a primary amine had no positive effect on activity, probably because the amine was not introduced at the optimal position (compound **38e**). Compound **38b** was the most active against *E. coli* K12 and similar compounds were found in literature. This class could be further investigated as dual inhibitors that inhibit β-lactamase activity and an unknown, additional target.

The main issue that we encountered was a discrepancy between the results from the DXPS-IspC-coupled assay and the HPLC-MS/MS-based DXPS-only assay. To find out what was going on, all compounds were analyzed in both assays and the results were compared. There is a number of compounds that is only active in the DXPS-only assay so we used the most active one with an IC_{50} value of 25 µM **4** to investigate the differences. When checking competition with D-GAP we had problems reproducing the original IC_{50} value with a new batch of the compound. This has to be further investigated before continuing with this compound class. Also, the MOI experiment has to be carried out with other inhibitors, although the initial results with **4** were interesting and suggest a change in inhibition with different D-GAP concentrations.

Before looking into the differences of the two DXPS-activity assays, a second round of VS was started on the hits identified from the first VS after testing them in the IspC-DXPS-coupled assay. Based on **1**, **12**, **9**, **7** and **8** a total of 86 compounds were purchased and tested. Only three of these compounds showed interesting activity after single point measurement. They are all derived from compound **7**. When determining their IC_{50} values, no clear dose-response was seen expect for compound **44**. These results have to be confirmed first, because the data quality was not satisfactory after two measurements. Also, the original hit **7** was not active anymore in the second round of testing which can be due to a contaminated stock solution in the first assay or can indicate an issue with the measurement of the second-round compound selection. The class is interesting as it has the same core structure as **4**.

Overall, the assay data are not reliable enough at this point to continue working on any of these compound classes before having a closer look at the assay again. The assay itself and the MOI experiment should be carefully analyzed with the inhibitor identified in Chapter 3.3. Another point that has to be investigated further is, that the VS was performed on Δ*Mt*DXPS while all activity data were generated using *Dr*DXPS. Since the crystal structure of Δ*Mt*DXPS revealed different conformations of key amino acids in the active site in comparison to *Dr*DXPS, it was suggested that this leads to different enzyme reactivity and different conformations of the active site during the enzymatic reaction between the two homologues.[55] The newly discovered hits should be tested in an activity assay with more active Δ*Mt*DXPS or by SPR to confirm this hypothesis. In addition, it has to be kept in mind that the VS was performed on a truncated structure *in silico* with a relatively wide, open substrate pocket, and the compounds might be too bulky to fit into the pocket *in vitro.* The activity against *E. coli* of compound **1** demonstrated that the hit class can still have interesting properties that potentially lead to promising inhibitors against other targets or other Gram-negative pathogens.

3.5 Three novel inhibitor classes against *Plasmodium falciparum*

Sandra Johannsen[1,2,†], Robin M. Gierse[1,2,3,†], Arne Krüger[4], Rachel L. Edwards[5,a], Vittoria Nanna[1], Anna Fontana[1], Di Zhu[1,3], Tiziana Masini[3], Lais Pessanha de Carvalho[6], Mael Poizat[7], Bart Kieftenbelt[7], Dana M. Hodge[8], Sophie Alvarez[9], Daan Bunt[3], Kamila Anna Meissner[4], Edmarcia Elisa de Souza[4], Melloney Dröge[7], Bernard van Vliet[7], Jack den Hartog[7], Michael C. Hutter[10], Jana Held[6], Audrey R. Odom John[8], Carsten Wrenger[4], Anna K. H. Hirsch[1,2,3]

1 Helmholtz Institute for Pharmaceutical Research Saarland (HIPS) – Helmholtz Centre for Infection Research (HZI), Campus Building E8.1, 66123 Saarbrücken, Germany

2 Department of Pharmacy, Saarland University, Campus Building E8.1, 66123 Saarbrücken, Germany

3 Stratingh Institute for Chemistry, University of Groningen, Nijenborgh 7, 9747 AG Groningen, The Netherlands

4 Unit for Drug Discovery, Department of Parasitology, Institute of Biomedical Sciences, University of São Paulo, Av. Prof. Lineu Prestes 1374, 05508-000 São Paulo-SP, Brazil

5 Department of Pediatrics, Washington University School of Medicine, Saint Louis, Missouri 63110, United States

6 Institute of Tropical Medicine, University of Tübingen, Wilhelmstraße 27, 72074 Tübingen, Germany

7 Symeres, Kadijk 3, 9747 AT Groningen, The Netherlands

8 Department of Pediatrics, Children's Hospital of Philadelphia, Perelman School of Medicine, University of Pennsylvania, Philadelphia PA 19104, United States

9 Proteomics & Metabolomics Facility, Center for Biotechnology, Department of Agronomy and Horticulture, University of Nebraska-Lincoln, Lincoln , Nebraska 68588, United States

10 Center for Bioinformatics, Saarland University, Campus Building E2.1, 66123 Saarbrücken, Germany.

†These authors contributed equally.

This part of the thesis has been uploaded to ChemRxiv (doi: 10.26434/chemrxiv-2022-npslc) and submitted to the *European Journal of Medicinal Chemistry*.

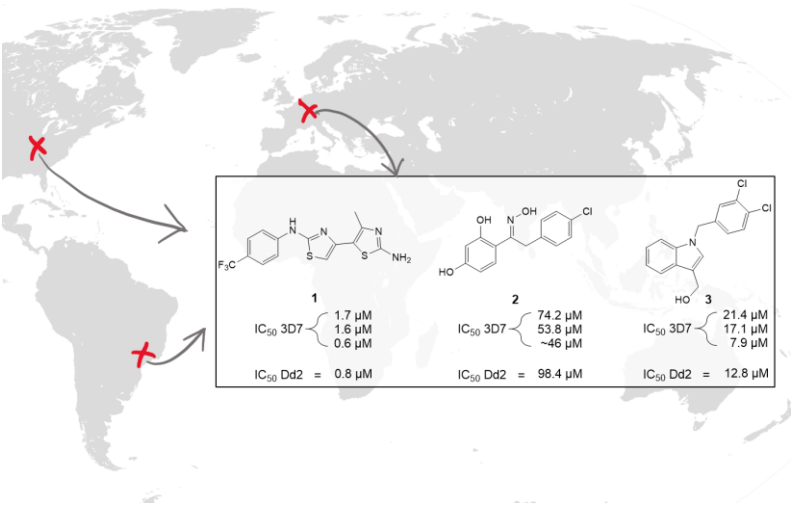

In this study, we identified three novel compound classes with potent activity against *Plasmodium falciparum*, the most dangerous human malarial parasite. Resistance of this pathogen to known drugs is increasing and compounds with different modes of actions are urgently needed. One promising drug target is the enzyme 1-deoxy-D-xylulose-5-phosphate synthase (DXPS) of the methylerythritol 4-phosphate (MEP) pathway for which we have previously identified three active compound classes against *Mycobacterium tuberculosis*. The close structural similarities in the active sites of the DXPS enzymes of *P. falciparum* and *M. tuberculosis* prompted investigation of its antiparasitic action, displaying good cell-based activity for all classes. Through structure-activity relationship studies we increased their antimalarial potency, and two classes also showed good metabolic stability and low toxicity against human liver cells. The most active compound **1** inhibits the growth of blood-stage *P. falciparum* with an IC_{50} of 600 nM. The results from three different methods for target validation of compound **1** suggest intracellular polypharmacy. Similarity-based searches revealed two other possible target enzymes for this compound, which were further analyzed by docking calculations. All inhibitor classes are active against chloroquine resistant strains, confirming a new mode of action.

3.5.1 Contributions

For the “Three novel inhibitor classes against *Plasmodium falciparum*” manuscript, Sandra Johannsen coordinated the writing process and organized the structure and the content. She examined all previous experiments and synthesized a selection of compounds (**4**, **5**, **22**, **25**, **26**, **42**, **49**–**52** and **64**) to fill gaps in the SAR. Two students, Vittoria Nanna and Anna Fontana synthesized **6**–**8*Z***, **37**, **40**, **41**, **45**, **53**–**55** and **65**. Mael Poizat, Bart Kieftenbelt, , Daan Bunt, Melloney Dröge, Bernard van Vliet and Jack den Hartog synthesized **1**–**3**, **13**–**24**, **27**–**36**, **38**, **39**, **43**, **44**, **46**–**48** and **56**–**62**. Sandra Johannsen wrote the introduction, the SAR analysis and target validation discussion as well as the abstract and the main part of the conclusion. She has measured and analyzed all synthesized compounds by NMR and HRMS and wrote the corresponding supplemental information, including the experimental procedures, analyses and spectra. For all experiments that were performed by collaborators, she collected, sorted, and checked the experimental procedures and combined them. Robin M. Gierse performed the *in silico* search of the PolyPharmacology Browser and wrote that part of the manuscript. He was also involved in the structure and content of the manuscript. Arne Krüger, with the help of Kamila A. Meissner and Edmarcia E. de Souza, was responsible for creating the overexpression cell lines and testing the hit compounds on them. Rachel L. Edwards, Dana M. Hodge and Sophie Alvarez performed and analyzed the results of the rescue assay and the target-validation assay by LC-MS. Zhu Di and Tiziana Masini were involved in the early stages of the project and coordinated the initial testing of the compounds. Lais Pessanha de Carvalho and Jana Held tested all compounds against *P. falciparum* 3D7 and Dd2 for the SAR study. Michael C. Hutter created the homology model of *Pf*DXPS. Audrey R. Odom John, Carsten Wrenger and Anna K. H. Hirsch were responsible for supervision, conceptualization and project administration.

3.5.2 Introduction

Malaria remains one of the major diseases with a high impact on health and welfare worldwide, especially in sub-tropical regions. In 2020, the World Health Organization (WHO) reported an estimated number of 627,000 deaths worldwide.[115] Among the six known human malaria parasites, *Plasmodium falciparum* is responsible for the majority of deaths. To treat uncomplicated *P. falciparum* malaria, artemisinin-based combination therapies (ACTs) are recommended, but the potent artemisinin derivatives must be partnered with a second drug due to their short half-life. Currently, six different ACTs are in use, but decreasing potency of artemisinin derivatives displayed by a delayed clearance phenotype is wide-spread in South-East Asia, together with resistances to the partner drugs in this combinations are threatening the efficacy of these treatments.[116] Therefore, finding new compounds with novel modes of action is of great importance.

A promising pool of targets is the methylerythritol 4-phosphate (MEP) pathway that is utilized by many human pathogens, such as *P. falciparum* and *Mycobacterium tuberculosis* (**Scheme 11**). The final products of the MEP pathway are isopentenyl diphosphate (IDP) and dimethylallyl diphosphate (DMADP), two precursors for the biosynthesis of isoprenoids. In malaria parasites, the MEP pathway is located in the apicoplast, a plastid-like organelle of prokaryotic origin. Removing this organelle showed its crucial role for cell survival, but also that addition of IDP or DMADP rescues the parasites. This result demonstrated the significance of the MEP pathway in *P. falciparum* and its validity as a drug target.[117] Further, since humans utilize a completely different pathway for isoprenoid biosynthesis, the parasite enzymes can be targeted without causing side effects on the host.[118–120]

The identification of fosmidomycin as a potent inhibitor of the enzyme 1-deoxy-D-xylulose 5-phosphate reductoisomerase (DXR), which is investigated in several clinical trials, nicely demonstrates the effectiveness of MEP pathway inhibitors (**Scheme 11**).[121] Fosmidomycin mimics the substrate of DXR, 1-deoxy-D-xylulose 5-phosphate (DOXP) and it was shown that the hydroxamate group and the phosphonate group are essential for binding.[122] However, the high polarity of fosmidomycin greatly limits its application and leaves little room for modifications to the original structure. Its promising inhibition profile validates the effectiveness of targeting the MEP pathway and more research is urgently needed to expand the pool of potent inhibitors.

Particularly, 1-deoxy-D-xylulose-5-phosphate synthase (DXPS) attracted our attention. The rate-limiting, first enzyme in the pathway catalyzes the condensation of pyruvate and glyceraldehyde 3-phosphate (D-GAP) and concomitant decarboxylation with thiamine diphosphate (ThDP) as a cofactor. A unique advantage over the other MEP enzymes is that by targeting DXPS both the production of isoprenoid precursors and the biosynthesis of the vitamins B_1 and B_6 are inhibited effectively.[123–125]

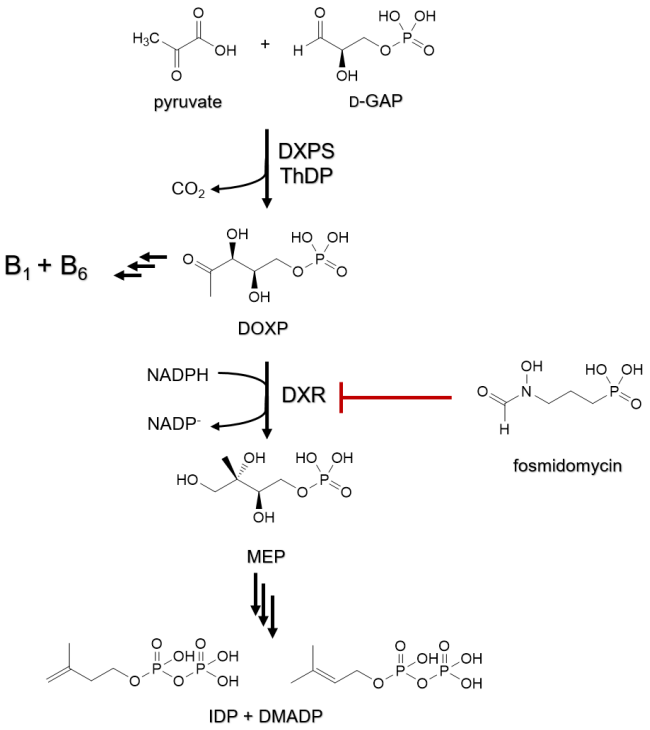

Scheme 11: Schematic illustration of the MEP pathway, highlighting the important branch point enzyme DXPS. D-GAP = glyceraldehyde 3-phosphate, DXPS = 1-deoxy-D-xylulose-5-phosphate synthase, B_1 = thiamine, B_6 = pyridoxine, DOXP = 1-deoxy-D-xylulose 5-phosphate, DXR = 1-deoxy-D-xylulose 5-phosphate reductoisomerase, MEP = 2-*C*-methylerythritol 4-phosphate, IDP = isopentenyl diphosphate, DMADP = dimethylallyl diphosphate.

In our previous efforts to identify inhibitors of *M. tuberculosis* (*Mt*)DXPS we found three promising compound classes.[126] Superposition of the crystal structure of *Mt*DXPS (protein data bank (PDB): 7A9H) and a homology model of *P. falciparum* (*Pf*)DXPS showed a similar structure with several loops in *Pf*DXPS that are not present in *Mt*DXPS (**Figure S 69**). However, a closer look at the active site revealed high conservation of the essential amino acids between *Mt*DXPS and *Pf*DXPS (**Figure S 70**), which suggested that active compounds against *Mt*DXPS may be effective against *Pf*DXPS.[127,128]

3.5.3 Results and Discussion

3.5.3.1 Structure-activity relationship (SAR) of hit compounds

In our previous work, we used ligand-based virtual screening (LBVS) as a powerful tool to identify new inhibitors based on known reference compounds for the target of interest.[126] LBVS relies solely on the use of descriptors of molecular structures and properties to compare various molecules and does not require crystallographic data.[129] As there were no suitable known inhibitors that could directly initialize the LBVS campaign against *Mt*DXPS, we used pseudo-inhibitors as initial ligands, with validation of key pharmacophores on the homologue *Deinococcus radiodurans* (*Dr*)DXPS, a model enzyme for *Mt*DXPS. We selected three compounds from a previous project, one ThDP analogue and two inhibitors from a *de novo* fragment design campaign.[130] Their 3D shape was generated and compared to all commercially available compounds from the Princeton database.[131] After each round of LBVS, all compounds were tested on *Dr*DXPS, as well as *Mt*DXPS. We identified three promising, structurally diverse hit classes. The most active compound in each class inhibited *Mt*DXPS in a slow-, tight-binding pattern, with submicromolar Morrison inhibition constants (K_i*) between 0.2–1.3 µM and showed promising minimum inhibitory concentrations (MICs) of 5–10 µM against *M. tuberculosis* (**Figure 13**).

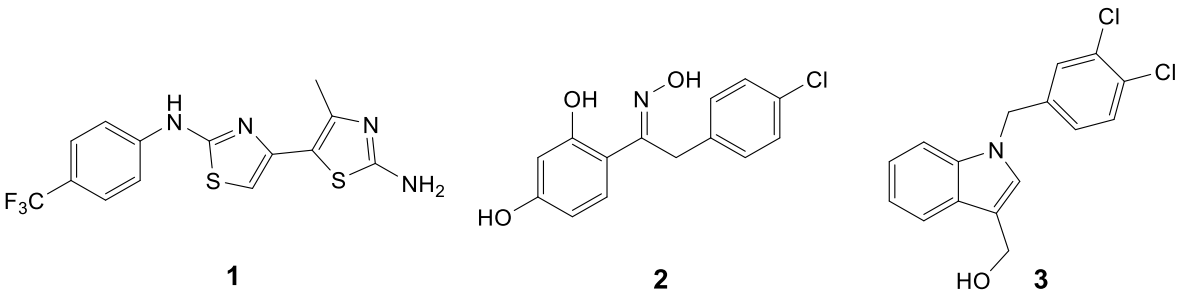

1

K_i* *Mt*DXPS = 0.21 ± 0.03 µM
MIC = 5–10 µM

2

K_i* *Mt*DXPS = 0.27 ± 0.02 µM
MIC = 10 µM

3

K_i* *Mt*DXPS = 1.29 ± 0.20 µM
MIC = 10 µM

Figure 13: Ligand-based virtual screening hits (**1, 2**, **3**) were tested against *M. tuberculosis* DXPS. Minimum inhibitory concentrations (MICs) were determined against the *M. tuberculosis* H37Rv strain.

Despite ongoing efforts, we have no *Pf*DXPS enzyme for on-target testing available and therefore, the antimalarial activity was evaluated *ex vivo* against cultured blood-stage *P. falciparum* 3D7. Several compounds were tested in three different laboratories on three continents under varying experimental conditions, but in all cases the data were similar (Methods I–III). Compound **1** shows the most notable variation

with a half-maximal inhibitory concentration (IC_{50}) between 0.6 µM and 1.7 µM (**Figure 14**). Compounds **2** and **3** vary between 44–74 µM and 8–21 µM, respectively, which gives us great confidence in our results. All compounds were additionally tested on NF54 (Method II), a chloroquine-sensitive strain and on Dd2 (Method III), a chloroquine-resistant strain (**Table S 16**). The differences in inhibition were small, indicating a different mode of action than chloroquine for all three compound classes, suitable for treatment of chloroquine-resistant strains. To the best of our knowledge, compounds **1**–**3** represent promising hits as novel antimalarials.

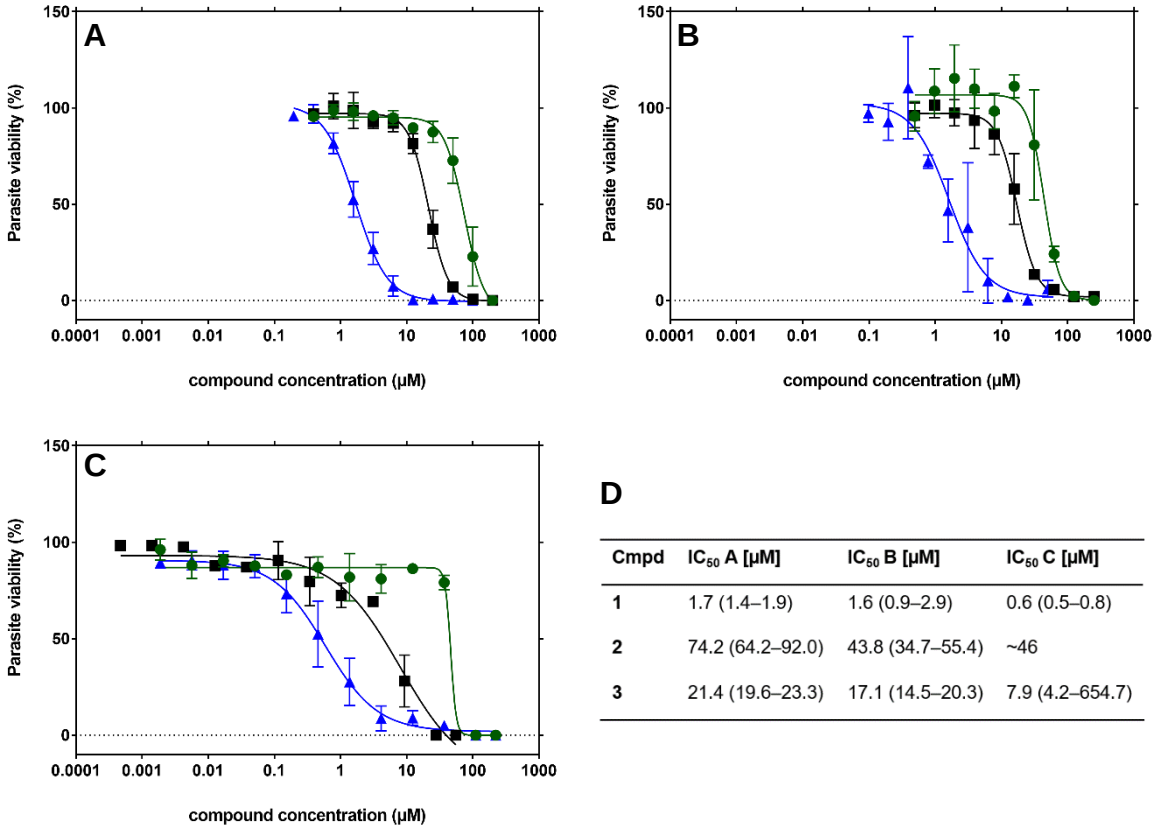

D

Cmpd	IC_{50} A [µM]	IC_{50} B [µM]	IC_{50} C [µM]
1	1.7 (1.4–1.9)	1.6 (0.9–2.9)	0.6 (0.5–0.8)
2	74.2 (64.2–92.0)	43.8 (34.7–55.4)	~46
3	21.4 (19.6–23.3)	17.1 (14.5–20.3)	7.9 (4.2–654.7)

Figure 14: *Ex vivo* antiplasmodial activity of DXPS compounds against *P. falciparum* 3D7 from three different laboratories and assays; following (**A**) Method I, (**B**) Method II and (**C**) Method III. IC_{50} curves of **1** (blue triangles), **2** (green circles) and **3** (black squares). All data was averaged from two to four independent experiments conducted in duplicate or triplicate and is shown including SD (error bars). (**D**) For IC_{50} determination, data were analyzed using nonlinear regression of the log-dose-response curves and interpolated from the sigmoidal curve. 95% CI is displayed as error measure.

We synthesized several derivatives of all three classes to see if we could improve potency and achieve favorable cytotoxicity and metabolic stability properties. Here, we only discuss the measurements on 3D7 that were performed with all compounds in more detail (using Method III).

3.5.3.2 Oximes

In derivatives for compound **2**, we maintained the two aromatic rings, connected by a two-carbon linker, but changed the substituents on the rings as well as the oxime functionality (**Table 14**). To improve solubility, we replaced the chlorine with an amino group (compounds **4**, **5** and **6**). While these modifications improve solubility two-fold to ~200 µM (**Table S 13**) for compounds **4** and **5,** the activity for all three compounds is lost. Replacing the Western aromatic ring with a pyridine neither improves the activity for the *E*- nor the *Z*-isomer (compounds **7E**, **7Z**, **8E** and **8Z**). Methylation of one of the hydroxyl-groups (compound **9**) increases the activity two-fold (46.8 µM). Compound **10**, where in comparison to **2** a NH_2- is replacing a hydroxyl-group, is the most active oxime against *P. falciparum* with an IC_{50} value of 38.2 ± 2.2 µM. Although, we increased the activity two-fold with compound **10**, replacing the oxime moiety with an imine (**11**) or a hydrazone (**12**) improves activity. Replacing the oxime with an alcohol group (**13**) leads to a ten-fold increase (IC_{50} = 9.9 ± 1.7 µM) in comparison to the parent compound **2**. In our investigations into the mode of action of the oxime class on *Mt*DXPS we identified a hydrogen bond between the hydroxyl-group of the oxime and a histidine in the active site as the critical functionality for activity. The change to the hydroxyl-group seems to improve this interaction due to the shorter chain lacking the nitrogen atom.

Table 14: Inhibition data for all oxime derivatives. IC_{50} measured against *P. falciparum* 3D7 (see supplementary information Method III). Original hit is compound **2** and best derivative **13** (in bold).

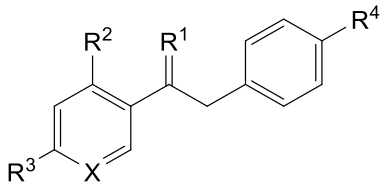

ID	R^1	R^2	R^3	R^4	X	IC_{50} [µM]
4	NOH	OMe	OH	NH_2	C	>111
5	NOH	OH	OH	NH_2	C	>111
6	NOH	OMe	OMe	NH_2	C	>111
7Z	NOH	-	OMe	Cl	N	>111
8E	NOH	-	OH	Cl	N	>111
8Z	NOH	-	OH	Cl	N	>28
2	**NOH**	**OH**	**OH**	**Cl**	**C**	**93.8 ± 8.0**
9	NOH	OH	OMe	Cl	C	46.8 ± 15.0
7E	NOH	-	OMe	Cl	N	43.6 ± 9.5
10	NOH	OH	NH_2	Cl	C	38.2 ± 11.2
11	NOMe	OH	OH	Cl	C	28.0 ± 8.8

12	NNH_2	OH	OH	Cl	C	16.0 ± 0.2
13	**OH**	**OH**	**OH**	**Cl**	**C**	**9.9 ± 1.7**

3.5.3.3 Indoles

Giving the promising activity of indole **3**, we additionally explored different substitution patterns to gain insight into the SARs. The most prominent difference is observed after removal of one methylene group. Replacing the C7-carbon in the indole with a nitrogen (**14**) leads to a loss of activity. The same can be observed when attaching the phenyl ring directly to the nitrogen of the indole (compound **15**). Also, a methoxy substituent in this position is not tolerated (**16**) and a nitrile substituent in position six (**17**) results in a two-fold decrease in comparison to the original hit **3**. Replacing the core indole with an indazole (**18**) or inserting a methylene group in the R^1-residue (**19**) does not result in significant changes. Removing one of the chloro-substituents gives a first interesting difference. If only the 3-chloro substituent is removed (**20**), the activity stays the same, but removal of the 4-chloro substituent (**24**) leads to a two-fold increase in activity. Interestingly, the complete removal or only removal of the hydroxyl group of the R^1-substituent leads to IC_{50} values of ~8 µM (**29**) and ~10 µM (**27**), respectively. We have shown previously that this group is essential for binding to *Mt*DXPS, which suggests a different mode of inhibition in *P. falciparum*.[126] Mostly, substituents on the indole core are tolerated. While a 7-methoxy substituent is not tolerated as mentioned before, the electron-withdrawing 7-chloro group increases the activity to 13 µM (**23**). A methoxy substituent in position four is favorable (**32**), but moving it to position five (**21**) or removing one chlorine of the R^2-group (**22**) reduces the activity again. A 5-nitro-substituent (**30**) or 5-bromo- (**31**) results in IC_{50} values below 10 µM, as do a 6-fluoro (**28**) and 5-fluoro (**33**) substituent; only a fluorine in the four-position affords an activity close to the nanomolar range (**34**). Fine-tuning the compound by removing one (**25**) or two (**26**) of the R^2-chlorines does not improve the activity but lowers it to ~12 µM. Since many compounds show an activity between 2 and 20 µM, these subtle changes do not have a substantial impact. To make a more significant change, we tested a bulky substituent in the R^1-position (which is essential for binding to *Mt*DXPS but not for the *P. falciparum* activity as shown earlier) and determined an IC_{50} value of 800 ± 200 nM for compound **35**.

Table 15: Inhibition data for all indole derivatives. IC_{50} values measured against *P. falciparum* 3D7 (see supplementary information Method III). Original hit is compound **3** and best derivative **35** (in bold).

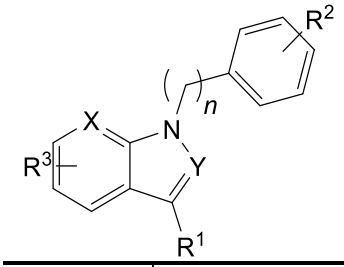

ID	R^1	R^2	R^3	*n* X Y	IC_{50} [µM]
14	-CH_2OH	3,4-di-Cl	-	*n* = 1 X = N Y = C	> 111
15	-CH_2OH	3,4-di-Cl	-	*n* = 0 X, Y = C	> 55.5
16	-CH_2OH	3,4-di-Cl	7-OMe	*n* = 1 X, Y = C	> 55.5
17	-CH_2OH	3,4-di-Cl	6-CN	*n* = 1 X, Y = C	43.8 ± 19.2
18	-CH_2OH	3,4-di-Cl	-	*n* = 1 X = C Y = N	33.9 ± 0.2
19	-CH_2CH_2OH	3,4-di-Cl	-	*n* = 1 X, Y = C	28.9 ± 1.2
20	-CH_2OH	4-Cl	-	*n* = 1 X, Y = C	27.7 ± 13.6
3	**-CH_2OH**	**3,4-di-Cl**	**-**	***n* = 1 X, Y = C**	**23.6 ± 6.4**
21	-CH_2OH	3,4-di-Cl	5-OMe	*n* = 1 X, Y = C	18.5 ± 1.1
22	-CH_2OH	3-Cl	4-OMe	*n* = 1 X, Y = C	15.6 ± 3.3
23	-CH_2OH	3,4-di-Cl	7-Cl	*n* = 1 X, Y = C	13.8 ± 0.9
24	-CH_2OH	3-Cl	-	*n* = 1 X, Y = C	12.2 ± 2.8
25	-CH_2OH	3-Cl	4-F	*n* = 1 X, Y = C	12.0 ± 1.0
26	-CH_2OH	-	4-F	*n* = 1 X, Y = C	11.9 ± 1.5
27	-CH_3	3,4-di-Cl	-	*n* = 1 X, Y = C	10.2 ± 3.4
28	-CH_2OH	3,4-di-Cl	6-F	*n* = 1 X, Y = C	8.9 ± 2.4
29	-	3,4-di-Cl	-	*n* = 1 X, Y = C	8.1 ± 0.1

30	-CH_2OH	3,4-di-Cl	5-NO_2	*n* = 1 X, Y = C	7.2 ± 0.1
31	-CH_2OH	-	5-Br	*n* = 1 X, Y = C	6.1 ± 1.3
32	-CH_2OH	3,4-di-Cl	4-OMe	*n* = 1 X, Y = C	5.5 ± 1.5
33	-CH_2OH	3,4-di-Cl	5-F	*n* = 1 X, Y = C	5.3 ± 1.3
34	-CH_2OH	3,4-di-Cl	4-F	*n* = 1 X, Y = C	2.4 ± 0.2
35	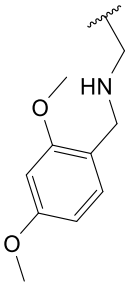	**3,4-di-Cl**	**-**	***n* = 1** **X, Y = C**	**0.8 ± 0.2**

3.5.3.4 Aminothiazoles

For the most promising class, the aminothiazoles, we investigated many derivatives with substantial changes on both ends of the molecule, while keeping the middle aminothiazole motif intact. We did not observe a severe reduction in activity, which indicates that the central core is essential. Changing the position of the CF_3-group on the left side of the original molecule **1** results in a lower activity for 3-CF_3-aminothiazole **46** (2.5 µM) and 2-CF_3-aminothiazole **36** (43.0 µM)**.** Modification of the right part of the molecule to a 2-pyridyl ring, affords single-digit micromolar activities when the left part of the molecule is either a phenyl ring with 2,5-dimethyl- (**44**), a 3,4-dimethyl- (**47**) or a 3-chloro-2-methyl- substitution (**45**). A 4-pyridyl ring does not show the same trend and the activity drops to 34 µM (**37**). A 2,4-dihydroxyphenyl ring (**38**, **39**) on the right side of the molecules is not tolerated. Utilizing a 3,4-dihydroxyphenyl on the right side and a 3,4-dimethylphenyl on the left side, however, results in an IC_{50} value of 4.4 µM (**43**). When keeping the second aminothiazole ring on the right side, modifications on the left ring with 3-methoxy- (**40**) or 3-chloro-2-methyl-substituents (**41**) do not improve the activity. Simply replacing the NH_2-group on the right side with a methyl-group the activity drops ten-fold to ~10 µM (**42**), which shows the importance of this group. Another promising compound, **48** with a 4-chloro-pyridine on the right side of the molecule, has a similar potency as **1** (IC_{50} = 1.0 µM). Overall, the original hit compound **1** was the most active with an IC_{50} of 600 nM.

Table 16: Inhibition data for all aminothiazole derivatives. IC_{50} values measured against *P. falciparum* 3D7 (see supplementary information Method III). Original hit is compound **1** (in bold).

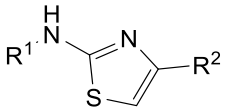

ID	R^1	R^2	IC_{50} [µM]
36	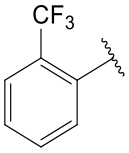	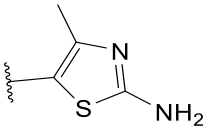	43.0 ± 2.4
37	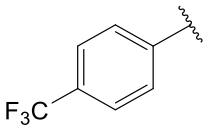	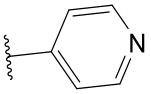	34.2 ± 1.8
38	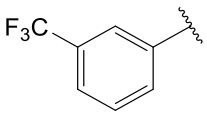	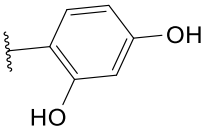	23.0 ± 0.7
39	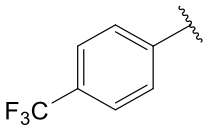	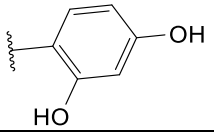	22.1 ± 5.6
40	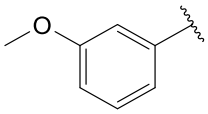	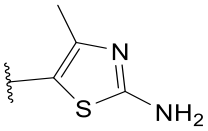	17.9 ± 0.4
41	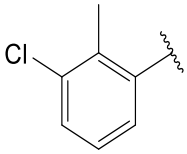	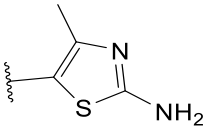	15.9 ± 1.8
42	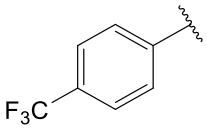	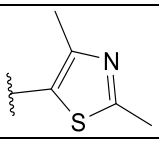	9.5 ± 1.1
43	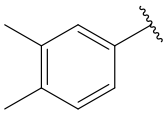	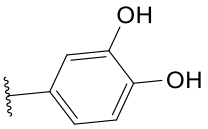	4.4 ± 1.0
44	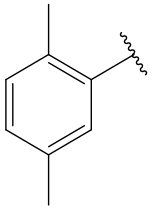	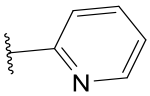	3.7 ± 1.6
45	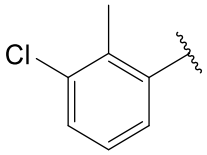	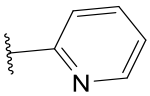	2.8 ± 0.1

46	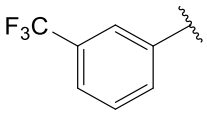	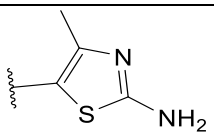	2.5 ± 0.1
47	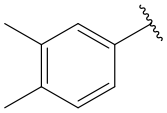	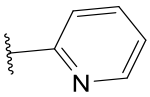	1.5 ± 0.8
48	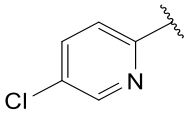	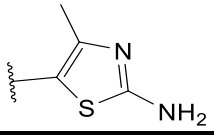	1.0 ± 0.1
1	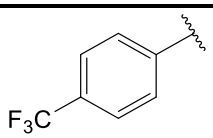	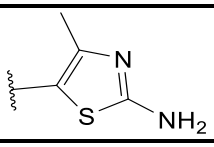	**0.6 ± 0.2**

3.5.3.5 Cytotoxicity and metabolic stability of selected compounds

The promising *ex vivo* results motivated us to thoroughly investigate the properties of all three hit classes further. We tested them for their respective cytotoxicity and metabolic stability (**Table 17**). Indole **3** exhibits an IC_{50} at 23.6 ± 6.4 µM against 3D7. Evaluating its cytotoxicity against human hepatocytes (Hep G2) results in a lower IC_{50} value of 0.8 ± 0.2 µM, suggesting the compound lacks specificity against asexual parasites. The two most active indole derivatives on *P. falciparum*, **34** and **35**, are equally as potent against Hep G2 cells (0.79 ± 0.37 µM and 90% inhibition at 10 µM, respectively). When investigating the metabolic stability, we found that indole **3** has a half-life of only 10 min in human liver S9 fractions. More synthetic work is needed to balance these properties. While oxime **2** is active against *P. falciparum* (IC_{50} = 93.8 ± 8.0 µM), it is similarly potent against Hep G2 (>50 µM). The best oxime hit **10** is two-fold more active against *P. falciparum* but equally inhibits Hep G2 cells. After removing the oxime functionality and replacing it with a hydroxyl-group, we found that compound **13** is not only the most active oxime derivative (IC_{50} = 9.9 ± 1.7 µM) but it also does not inhibit the growth of Hep G2 cells at 100 µM. With the synthetic modifications we improved the metabolic stability from 28 min for compound **2** to 98 min for alcohol **13**. We therefore excluded the indole and oxime class from further investigations, but compound **13** emerged as a new potent inhibitor class for *P. falciparum* with an improved cytotoxicity and metabolic stability profile.

Table 17: Summary of *P. falciparum* activity, cytotoxicity (activity against Hep G2 in µM or %inhibition) and metabolic stability in human liver S9 fraction (half-life in min) of selected compounds from all three hit classes. n.d. = not determined.

Compound	IC_{50} *P. falciparum* 3D7 (µM)	IC_{50} Hep G2	$t_{1/2}$ (min)
1	0.6 ± 0.2	>50 µM	>240
2	93.8 ± 8.0	>50 µM	28.5 ± 0.7
10	38.2 ± 11.2	50–100 µM	55.8 ± 0.4
13	9.9 ± 1.7	> 100 µM	97.8 ± 9.9
3	23.6 ± 6.4	0.8 ± 0.2 µM	10.0 ± 0.4
34	2.4 ± 0.2	0.79 ± 0.37 µM	n.d.
35	0.8 ± 0.2	at 10 µM 90 ± 2% inhibition	n.d.

Compound **1** exhibits a promising IC_{50} value (IC_{50} = 0.6 ± 0.2 µM) in addition to a weaker inhibition of Hep G2 with 54.0 ± 2.4 µM. It is also the most stable compound in human liver S9 fraction (>240 min) that we tested. As such, aminothiazole **1** is a potent hit and inhibitor of *P. falciparum* growth *ex vivo*. It will be further optimized against *P. falciparum* and *M. tuberculosis* in parallel.

3.5.3.6 Target validation

We have strong reason to believe that DXPS is the main target of all hit compounds in *M. tuberculosis*.[126] To confirm *Pf*DXPS as a target in *P. falciparum*, we chose to further investigate compound **1**, since it showed the most promising activity. One well established method is a rescue assay with IDP, the product of the MEP pathway. It has been shown that the addition of IDP to blood-stage *Plasmodium* spp. rescued parasite survival after treatment with fosmidomycin (FSM), which inhibits the second enzyme in the MEP pathway, as well as survival of apicoplast-minus *Plasmodium* spp.[117] We determined the growth inhibition of blood-stage *P. falciparum* with selected compounds, including the most active compound **1**, in the presence and absence of 125 µM IDP. This assay has never been performed with a DXPS inhibitor, but we expected a rescue effect if DXPS was the main target of compound **1**.

While, as expected, the antiparasitic activity of FSM was rescued by IDP addition, compound **1** still inhibited *P. falciparum* growth under IDP supplementation. Similar results were observed for two other active aminothiazole derivatives, **47** and **48** and the indole derivative **34** (**Figure S 71**, **Figure S 72** and **Table S 14**). Together, these data suggest that our compounds inhibit additional pathways within *P. falciparum* apart from the MEP pathway.

In order to elucidate whether **1** interacts with DXPS, we profiled the cellular concentration of MEP pathway intermediates by LC-MS. In this experiment, we analyzed the concentration changes of MEP pathway metabolites in the presence and absence of **1** in *P. falciparum* and *E. coli*. If a compound inhibits the MEP pathway, a reduced concentration of all metabolites downstream of the inhibited enzyme is expected. In *E. coli*, however, all downstream metabolites of DXPS are increased upon inhibitor treatment, while the pyruvate concentration drops (**Figure S 73**). This behavior has not previously been reported, but it suggests an influence on the pathway that requires further investigation. In *P. falciparum*, we observe no difference in the metabolite concentrations, but a reduction in pyruvate levels (**Figure S 74**, **Table S 15**). This decrease is consistent with a reduction in tricarboxylic acid (TCA) cycle metabolites (**Figure S 75**, **Table S 15**), but since pyruvate is tied to many other metabolic pathways, we could not determine the reason for the decrease. Although these results did not confirm our hypothesis, they indicated that a different mode of action in *P. falciparum* and *E. coli* is responsible for the anti-infective activities of **1** *ex vivo*.

To address the ambiguous result from the previous assays, we screened the three original LBVS hits against transgenic parasites overexpressing thiamine pyrophosphokinase (*Pf*TPK) and *Pf*DXPS (DOXP cell line) and compared the results to the MOCK cell line that contained only the transfected vector backbone. All three hit compounds are ThDP-competitive inhibitors as we have shown previously.[126] Therefore, it is possible that the compounds indiscriminately bind to *Pf*TPK as well as *Pf*DXPS. In case of inhibition, we would expect a higher IC_{50} value for the overexpressing cell lines than for the MOCK cell line, but a statistical difference (**Table S 16**) was not detected for either *Pf*DXPS (**Figure S 76**) or *Pf*TPK (**Figure S 77**). While these results leave the compound's main target unclear, we can exclude *Pf*TPK as an off-target.

3.5.3.7 PolyPharmacology Browser (PPB) analysis to identify alternative targets

Despite extensive efforts to experimentally verify DXPS as the molecular target, the results were not conclusive. To extend our knowledge of other possible targets and off-target proteins, we turned to an *in silico* approach using the PPB to search for other potential target enzymes. The PPB search engine employs a similarity-based approach following the idea that similar compounds should target the same proteins.[132,133] Several methods are used in parallel to calculate molecular fingerprints

of a query compound, which are then used to search the open-access bioactivity database ChEMBL.[134] The search output contains compounds similar to the query molecule, associated with their biological activity. We manually analyzed the results, looking for alternative targets of our compounds.

3.5.3.8 Oximes

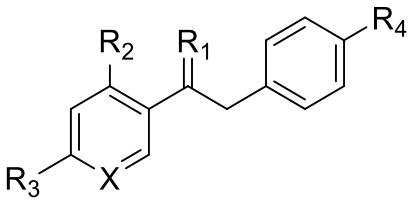

Oxime core structure

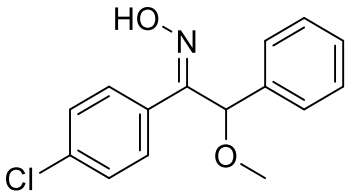

CHEMBL581471

Figure 15: The oxime scaffold and the related compound **CHEMBL581471**. For elucidation of X and the R_1-R_4 groups, please see **Table 14**.

Similar to our core structure, we found the related oxime **CHEMBL581471** (**Figure 15**). This compound was identified in 2008 by Novartis in a high-throughput screening (HTS) and showed activity against *P. falciparum* in a liver-stage assay. The oxime was a hit in the initial HTS, but could not be confirmed and was therefore not evaluated further. The reported EC_{50} values are >0.912 µM in 3D7 and >1.607 µM in W2. The compound also showed good cytotoxicity behavior with >10 µM Huh7 (human hepatoma cells) inhibition, about 10 fold higher than the EC_{50}.[135]

Although no molecular target is assigned to compound **CHEMBL581471**, the finding gives us additional insights for the design of further derivatives. It seems that the CH_2 of the linker might be a possible growth vector. Together with the replacement of the oxime functionality with an amino or hydroxyl-group, as suggested by our SAR study, the initial oxime hit offers the potential to be developed into a different class in the future.

3.5.3.9 Indoles

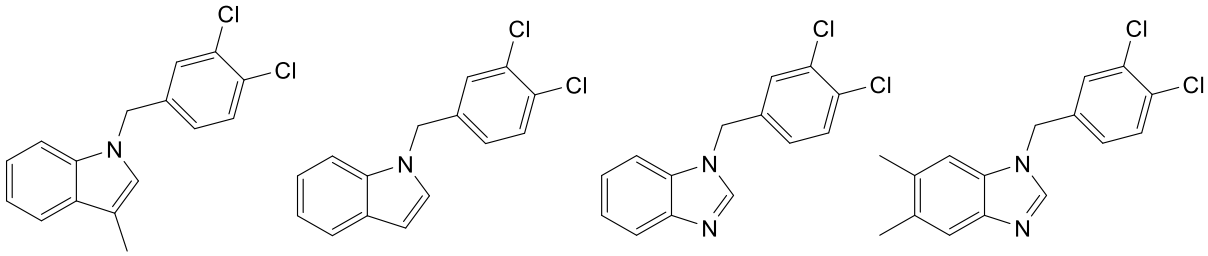

27 IC_{50} *P.f.* = 10.2 µM

29 IC_{50} *P.f.* = 8.1 µM

CHEMBL570782 IC_{50} FabI = 4.7 µM

CHEMBL1945694 IC_{50} FabI = 0.3 µM

Figure 16: Compounds **29** and **31** (IC_{50} cell-based using *P. falciparum* 3D7, Method III) shown with the related compounds inhibiting the Enoyl-[acyl-carrier-protein] reductase (FabI) (IC_{50} based on enzymatic assay).

Our search for compounds **27** and **29** yielded the similar compounds **CHEMBL1945694** and **CHEMBL570782** (**Figure 16**), which are reported to inhibit the Enoyl-[acyl-carrier-protein] reductase (ENR or FabI) from *Francisella tularensis*.[136] The two compounds we found belong to a larger class of benzimidazoles, first identified to inhibit *F. tularensis* FabI in 2012 using a LBVS approach by Johnson and coworkers.[137] In follow-up studies, they reported derivatives with improved activity against the FabI enzyme of up to 14 nM and determined the crystal structure of FabI from *F. tularensis* in complex with **CHEMBL1945694**. [138,139]

To compare our indole-class with the benzimidazoles, we docked all compounds into the reported *F. tularensis* structure with the PDB-code 3uic and, as several protein structures of FabI from *P. falciparum* are available, also to this homologue. The *P. falciparum* structure is mainly solved in complex with triclosan and its analogues and some induced fit of the binding site is known.[140] Because of the induced fit, we selected the structure with the PDB-code 2op1, hosting a larger ligand of similar size as the benzimidazoles.

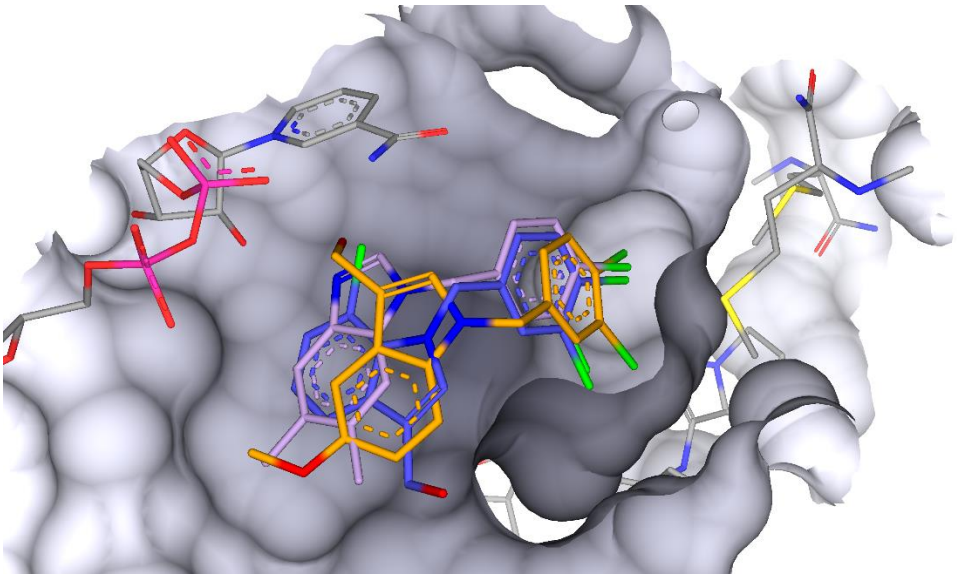

Figure 17: Docking poses of our compounds into *Pf*FabI (PDB: 3uic) in complex with the co-crystallized inhibitor. The co-crystallized ligand is shown for comparison and colored purple, compound **23** in blue and compound **22** in orange. The conserved interaction of the N3 atom from the benzimidazole ring system with Tyr156 is either compensated by a hydroxyl substituent at the 3-position or substituted by flipping of the indole moiety and interaction with a Cl-substituent in 7-position.

The compounds of our indole class dock to the *F. tularensis* structure in a pose similar to the co-crystallized **CHEMBL1945694** benzimidazole and are calculated to have a very high affinity in the pico- to nanomolar range (**Table S 18)**. A superposition of the best pose is shown in **Figure 17**. Docking to the FabI enzyme from *P. falciparum* also predicted nanomolar binding affinities. For both homologues, the calculated binding affinity of the best indoles presented in this study is similar to **CHEMBL1945694**, with **18** binding even slightly better (**Table S 19**).

Our aminothiazole class showed binding affinities in the nano- to micromolar range, while binding of the oximes was calculated to be in the micromolar range (**Table S 20** to **Table S 23**).

The FabI enzyme is part of the fatty acid biosynthesis pathway-II (FAS-II) found in a variety of microorganisms, including *P. falciparum.* The mammalian counterpart FAS-I consists of one protein complex with low homology to the FAS-II enzymes.[141–143] The FabI enzyme catalyzes the final reduction step, suppling fatty acids for cell-wall biosynthesis. Enzymes of the pathway are used for the development of new antimicrobial agents.[144–147] It was, however, shown that the blood stage of *P. falciparum* does not require the FAS-II pathway for proliferation.[148–150] Therefore, inhibition of FabI cannot explain the activity we observed in the blood stage assays.

However, it could be beneficial for a new anti-malarial drug to inhibit FabI as a second target, as FabI is essential for liver stage proliferation and therefore transmission.[150]

Taken together, the structural similarity of the compounds (**Figure 16**) hints to FabI being an additional target of our hit classes. In particular, the indole-class is very likely to bind to FabI, as there are co-crystal structures of related compounds. Inhibition of FabI does not explain the observed *ex vivo* effects in our assays, as this pathway is only important during the liver stage of *P. falciparum* growth.[142]

3.5.3.10 Aminothiazoles

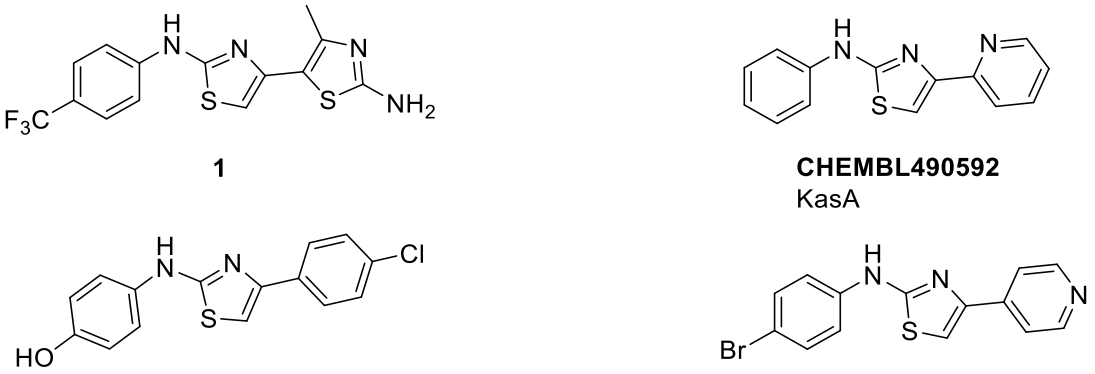

Figure 18: Aminothiazole hit compound **1** and similar compounds we found during the PPB search, with their reported target. KasA = β-ketoacyl ACP synthase; VCP = Valosin-containing protein.

For all 15 queried aminothiazole molecules we could find related compounds that are reported to target *P. falciparum*. However, the majority of the reported activities are based on cell-based assays without an assigned molecular target. Only the compounds with a known target are further analyzed below.

With the aminothiazole **CHEMBL490592** (**Figure 18**, **Figure 17**) we found a compound similar to our herein described aminothiazole class. It is part of a different group of aminothiazole-based inhibitors with activity against *M. tuberculosis*.[151,126] In a previous study, we could also observe anti-tubercular activity for our group of aminothiazoles. In 2014, P. Makam and T. Kannan reported that a possible target of 2-aminothiazoles in *M. tuberculosis* is the enzyme β-ketoacyl ACP synthase (KasA).[152] The KasA protein is part of the FAS-II pathway, and involved in the biosynthesis of mycolic acid, an essential cell wall component. It is also present and active in *P. falciparum*, but similar to FabI it has been found to be dispensable for the blood stage of *P. falciparum* (please see section Indoles).[148,153,154] Since the protein structure of *P. falciparum* KasA has not

been determined, we docked our inhibitors to the KasA homologue from *M. tuberculosis* (PDB: 2wgd), which was used to develop the aminothiazole **CHEMBL3344230**.[152] This enables us to directly compare our compounds with the previously published compound **CHEMBL3344230**.[152] A superposition of the docked compounds is shown in **Figure 19**. The calculated binding poses and affinities of our hits are in the nano- to micromolar range, similar to the reported compound (**Table S 23**), suggesting that KasA may be a target of our aminothiazole hit class.

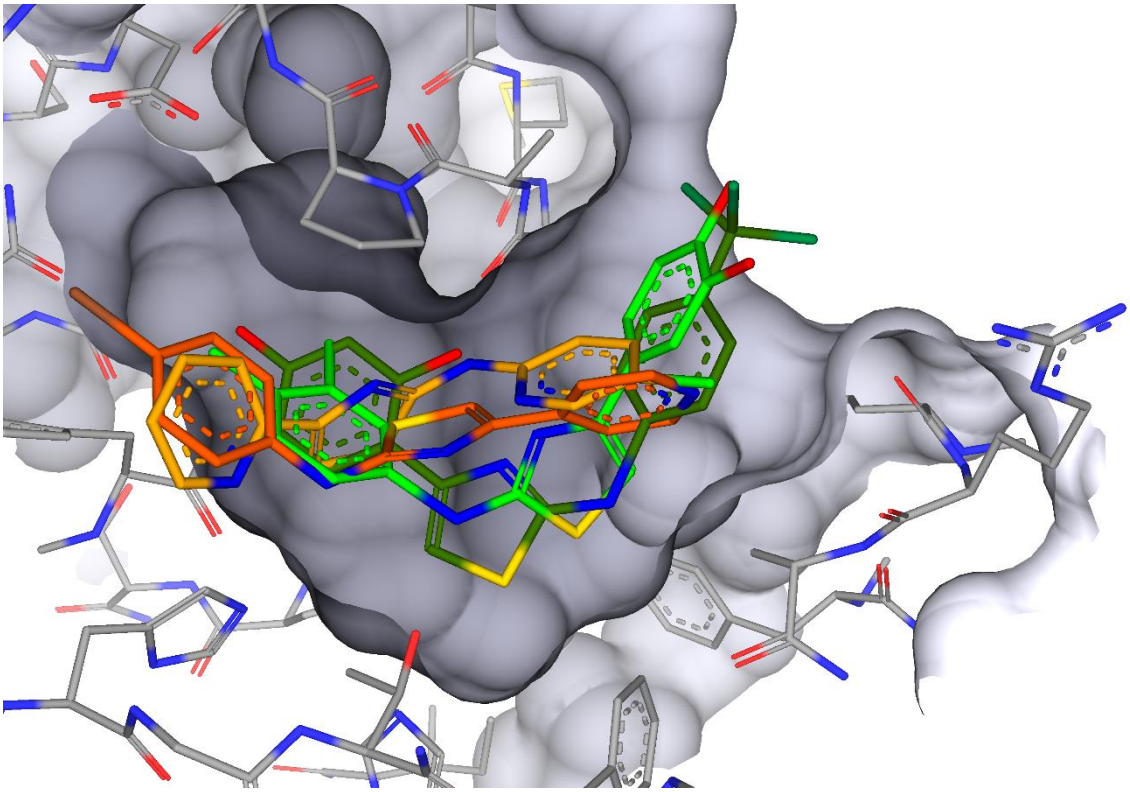

Figure 19: Superposition of compounds **39 (dark green), 43 (green), CHEMBL3344230 (red)** and **CHEMBL546826 (orange)** docked to the KasA enzyme from *M. tuberculosis* (PDB: 2wge). Although not exactly in the same pose, they all dock well into the pocket.

In addition, a series of aminothiazoles have been developed as antileishmanial agents, a protozoan parasite, despite no identified target protein.[155] Based on the structural similarity and docking of their reported best hit **CHEMBL546826**, it seems likely that KasA may be the target, which is also present in *Leishmania* spp. **(Figure 19**, **Table S 24).**

We identified compound **CHEMBL1076555** (**Figure 18**), which was included in a series of cancer inhibitors targeting the Valosin-containing protein (VCP).[156] Furthermore, the endoplasmic reticulum assisted degradation (ERAD) is also gaining

attention as a target against protozoan pathogens, as they have only a very small network for their protein quality control system.[157] One of these members is VCP, which might be targeted by the reported aminothiazoles.[158] As a consequence of this pared down network of protein degradation, *P. falciparum* is highly susceptible to ERAD inhibitors, a VCP-knockout strain is not viable. Although VCP is also present in mammals (often termed p97), it was shown that selectivity towards VCP from *P. falciparum* can be achieved.[157,159] Docking into VCP was not performed, as the structure of the large hexameric protein is only solved for mammals and no co-crystal structure is available to identify the binding site. Testing our hits as well as the previously reported VCP inhibitors against *P. falciparum* might reveal VCP as an additional target, which could explain the inhibitory activity we observed in the blood-stage assays.[156]

3.5.3.11 Human off-targets

During the search for antimicrobial targets, we found mammalian enzymes that are affected by compounds similar to our hits, including enzymes of the eicosanoid metabolism, the membrane protein KDR kinase and RNA polymerase II (**Table S 25**).[160–162] These early data are beneficial, as we now have the possibility to develop and test our hits for selectivity for the bacterial over the human targets. Further, if we can confirm activity against human enzymes, it is possible that some derivatives could be re-purposed. For example, we report three compounds (**3**, **15**, **20**) that are identical to derivatives of the Oncrasin-1 inhibitor of the RNA polymerase II, which is discussed as a new class of anti-cancer drugs.[162]

3.5.4 Conclusions

We showed that our previously identified small-molecule inhibitors against *M. tuberculosis* DXPS from a LBVS campaign are also active against several *P. falciparum* strains. We successfully improved the activity of two of our three initial hit classes. The oxime **2** was improved 2.5-fold from 93.8 µM to 38.2 µM by replacing one hydroxyl-group with an amino-group (compound **10**). By removing the oxime we also identified several new compounds that require further investigation. Imine **11**, hydrazone **12** or alcohol **13** are promising alternative functionalities to the oxime **2** with low cytotoxicity and improved metabolic stability in the case of compound **13**. The best hit of the indole class, compound **3** with an IC_{50} value of 23.6 µM was improved 30-fold to 0.8 µM by adding a bulky substituent to the hydroxyl-group (**35**). We discontinued

this class due to the toxicity issues. Overall, we identified the aminothiazole **1** as a promising compound against *P. falciparum* with good activity, selectivity and excellent metabolic stability.

Using compound **1**, we investigated *Pf*DXPS as a potential target. Several lines of evidence suggest compound **1** has on- and off-target effects. First, IDP failed to rescue growth after treatment. LC-MS analysis of metabolites downstream of DXPS following inhibition in both *P. falciparum* and *E. coli* was ambiguous. In *P. falciparum* we observe a reduction in pyruvate levels that is consistent with the downregulation of TCA-cycle metabolites indicating complex effects on parasite metabolism. To further investigate potential interaction with *Pf*DXPS as well as *Pf*TPK we used genetically modified parasites overexpressing the respective enzymes. Here, we cannot observe any significant difference between the MOCK and the overexpressing cell lines, which means DXPS is most likely not the main target of compound **1**. However, we can exclude *Pf*TPK as an off-target, which suggests the compound shows no specific inhibition of thiamine-dependent proteins.

The validation of molecular targets is notoriously difficult. Using the PPB search engine, we identified three possible additional targets for our hit classes, the enzymes FabI, KasA and VCP. The independent occurrence of two enzymes from the FAS-II pathway is remarkable and offers a potential dual role of our hit compounds as drug targeting DXPS and chemoprophylaxis agent, inhibiting the FAS-II pathway and thereby the onset of parasite infection by targeting *P. falciparum* liver stage development. However, as FAS-II inhibition is not essential for proliferation in the *P. falciparum* blood stage, it cannot explain the observed asexual growth inhibition. The VCP protein could be the alternative target explaining our biological activity, but it could not be assessed further because of the lack of a protein structures from *Plasmodium* spp. Whether our hits are dual inhibitors of DXPS and enzymes of the FAS-II pathway, will need to be determined experimentally in future studies. Antimalarial drugs on the market such as artemisinin and chloroquine also have multiple targets, which makes them highly potent, but emerging resistance increases the need for alternative treatments.[163,164] We showed that the discussed compounds effectively kill the chloroquine resistant *P. falciparum* strain Dd2, which makes them suitable candidates for further investigation as alternative drugs or combination partners with existing therapeutic agents.

3.5.5 Experimental section

General procedures. NMR experiments were run on a Bruker Avance Neo 500 MHz (^{1}H at 500.0 MHz; ^{13}C at 126.0 MHz; ^{19}F NMR at 470 MHz), equipped with a Prodigy Cryo-probe. Spectra were acquired at 298 K, using deuterated dimethylsulfoxide ($(CD_3)_2SO$, ^{1}H: 2.50 ppm, ^{13}C: 39.52 ppm), deuterated methanol (CD_3OD, ^{1}H: 3.31 ppm, ^{13}C: 49.00 ppm) or deuterated chloroform ($CDCl_3$, ^{1}H: 7.26 ppm, ^{13}C: 77.16 ppm) as solvent. Chemical shifts for ^{1}H and ^{13}C spectra were recorded in parts per million (ppm) using the residual non-deuterated solvent as the internal standard. Coupling constants (*J*) are given in Hertz (Hz). Data are reported as follows: Chemical shift, multiplicity (s = singlet, d = doublet, t = triplet, q = quartet, m = multiplet, br = broad and combinations of these) coupling constants and integration. Mass spectrometry was performed on a SpectraSystems-MSQ LCMS system (Thermo Fisher, Dreieich, Germany). Purification of the final products was performed using preparative HPLC (Dionex UltiMate 3000 UHPLC+ focused, Thermo Scientific) on a reversed-phase column (C18 column, 5 µM, Macherey-Nagel, Germany) or flash chromatography was performed using the automated flash chromatography system CombiFlash Rf+ (Teledyne Isco, Lincoln, NE, USA) equipped with RediSepRf silica columns (Axel Semrau, Sprockhövel Germany). High-resolution mass (HRMS) of final products was determined by LCMS/MS using Thermo Scientific Q Exactive Focus Orbitrap LC-MS/MS system. The purity of the final compounds was determined using Dionex Ultimate 3000 HPLC system (Thermo Fisher Scientific). Chromatographic separation was performed on an EC 150/2 Nucleodur C18 Pyramid (3 µm particle size) analytical column (Macherey-Nagel). The mobile phase consisted of solvent A (water containing 0.1% formic acid) and solvent B (acetonitrile containing 0.1% formic acid) with a flow rate of 0.25 mL/min. All final compounds had a purity >95%. Yields refer to analytically pure compounds and have not been optimized. All chemicals were purchased at SigmaAldrich or comparable commercial suppliers and used without further purification.

General remarks about the analysis: Full characterization is provided for final compounds that have not been published before or have been published in different NMR-solvents. The identity of intermediates was determined by ^{1}H-NMR, ^{13}C-NMR and ^{19}F-NMR if applicable. The ^{13}C-NMR signals are doublets in the case of six carbons in the F-substituted aromatic ring in **28**, seven carbons including –**C**CH_2OH for **25**, eight carbons including -**CC**H_2OH for **34** and **26**. Many indole HR-ESI-MS

measurements give [M-18], due to fragmentation during ionization. The identity of *E*/*Z* isomers was determined by 1D-NOESY NMR for compounds **7*E*** and **7*Z***. All other compounds with isomers were assigned based on carbon shifts. *E*-Oxime C7-shift (ppm) > *Z*-oxime C7-shift (ppm). All compounds are >95% pure by HPLC analysis.

Synthesis and characterization of oximes. The synthesis and characterization of **2**, **9**, **10**, and **12** were described previously by us.[126] 2-(4-((*tert*-Butoxycarbonyl)amino)phenyl)acetic acid (**49**) was synthesized following a literature procedure and all data were consistent with the reported values.[165]

Condensation (procedure O-A). Synthesis of the protected ketone intermediate followed a previously reported procedure.[166] To a Schlenk flask, methyl benzoate and phenylacetic acid (1.0 equiv.) were added and dissolved in dry dimethylformamide (DMF) under nitrogen. The yellow solution was cooled to –10 °C, and then sodium *bis*(trimethylsilyl)amide (2 M in tetrahydrofuran (THF), 4.0 equiv.) was added dropwise under stirring. After full conversion of the starting material (3–72 h) monitored by thin layer chromatography (TLC) or LC-MS, the reaction was terminated by adding saturated aqueous NH_4Cl solution and concentrated *in vacuo* to remove DMF. Subsequently, the residue was extracted with ethyl acetate (3 x), and the combined organic layers were washed with saturated aqueous NaCl solution. The organic layer was dried over Na_2SO_4, filtered and concentrated *in vacuo*.

Deprotection (procedure O-B). The deprotection reaction followed a previously reported procedure.[167] To a solution of the condensation product from procedure **O-A** in dry dichloromethane (9 mL) under nitrogen, boron tribromide was added (1 M in dichloromethane, 12.0 equiv.) under stirring at 25 °C. After 5 h, a saturated aqueous Na_2CO_3 solution was added to the solution, which was extracted with dichloromethane. The organic layer was washed with water (2 x), then dried over Na_2SO_4, filtered and concentrated *in vacuo*.

Oxime formation (procedure O-C). Oximation followed a previously reported procedure.[168] To a solution of the deprotected product in methanol, potassium acetate (3.0 equiv.) and hydroxylamine hydrochloride (1.5 equiv.) were subsequently added under stirring. The light-yellow suspension was refluxed for 2 h. Subsequently, water was added to the mixture. The organic layer was washed with saturated aqueous NaCl solution, dried over Na_2SO_4, filtered and concentrated *in vacuo*.

***tert*-Butyl (4-(2-(2,4-dimethoxyphenyl)-2-oxoethyl)phenyl)carbamate (50).** Compound **50** was synthesized following procedure **O-A**, using **49** (650 mg, 2.59 mmol, 1.0 equiv.), methyl-2,4-dimethoxybenzoate (508 mg, 2.59 mmol, 1.0 equiv.) and sodium *bis*(trimethylsilyl)amide (10.4 mL, 10.4 mmol, 3.0 equiv.) in dry DMF (20 mL). After 72 h, no full conversion was achieved, so it was decided to terminate the reaction. Flash column chromatography (petroleum benzine/ethyl acetate 2:1 + 1% acetic acid) afforded a mixture of the product and starting material **49**. To remove the acid, the mixture was dissolved in ethyl acetate and washed with saturated aqueous $NaHCO_3$ solution (6 x). The product (106 mg, 11% yield) was obtained as a white solid. ^{1}H-NMR (500 MHz, CD_3OD): δ (ppm) = 7.69 (d, *J* = 8.57 Hz, 1H), 7.29 (d, *J* = 8.37 Hz, 2H), 7.08 (d, *J* = 8.57 Hz, 2H), 6.56 (m, 2H), 4.19 (s, 2H), 3.91 (s, 3H), 3.85 (s, 3H), 1.50 (s, 9H). ^{13}C-NMR (126 MHz, CD_3OD): δ (ppm) = 200.8, 166.6, 162.4, 155.4, 139.0, 133.8, 131.2, 130.9, 121.5, 119.8, 106.9, 99.2, 56.1, 56.0, 50.1, 28.70. HR-ESI-MS: calculated for $C_{21}H_{26}NO_5$ $[M+H]^+$ 372.1805, found 372.1806.

2-(4-Aminophenyl)-1-(4-hydroxy-2-methoxyphenyl)ethan-1-one (51). Following procedure **O-B** using **50** (90 mg, 0.24 mmol, 1.0 equiv.) and boron tribromide (1.2 mL, 1.2 mmol, 5.0 equiv.) in dry dichloromethane (2 mL), compound **51** (28 mg, 45% yield) was obtained as a white solid after flash column chromatography (CH_2Cl_2/CH_3OH 19:1). Compound **52** was purified as a side product (4 mg, 7% yield). ^{1}H-NMR (500 MHz, CD_3OD): δ (ppm) = 7.90 (d, *J* = 8.99 Hz, 1H), 7.03 (d, *J* = 8.50 Hz, 2H), 6.68 (d, *J* = 8.50 Hz, 2H), 6.47 (dd, *J* = 2.50, 8.99 Hz, 1H), 6.41 (d, *J* = 2.50 Hz, 1H), 4.09 (s, 2H), 3.82 (s, 3H). ^{13}C-NMR (126 MHz, CD_3OD): δ (ppm) = 204.9, 167.7, 166.8, 147.5, 134.1, 131.0, 125.7, 116.9, 114.2, 108.3, 101.9, 56.1, 45.1. HR-ESI-MS: calculated for $C_{15}H_{16}NO_2$ $[M+H]^+$ 258.1125, found 258.1123.

2-(4-Aminophenyl)-1-(2,4-dihydroxyphenyl)ethan-1-one (52). To achieve full deprotection in one step, compound **50** (22 mg, 0.06 mmol, 1.0 equiv.) was heated to 110 °C in the microwave (5 min, 15 W) with pyridine hydrochloride (1 mL). The reaction was diluted with saturated aqueous Na_2SO_4 solution and this aqueous solution was extracted with ethyl acetate (3 x 5 mL). The combined organic layers were dried over Na_2SO_4, filtered and concentrated *in vacuo*. The residue was co-evaporated with toluene (3 x 10 mL) to remove residual pyridine. The product (6 mg, 40% yield) was obtained as a white solid. ^{1}H-NMR (500 MHz, $(CD_3)_2SO$): δ (ppm) = 12.67 (s, 1H), 10.60 (s, 1H), 7.90 (d, *J* = 8.89 Hz, 1H), 6.92 (m, 2H), 6.49 (m, 2H), 6.36 (dd, *J* = 2.31, 8.89 Hz, 1H), 6.23 (d, *J* = 2.31 Hz, 1H), 4.95 (s, 2H), 4.02 (s, 2H). ^{13}C-NMR (126 MHz,

$(CD_3)_2SO$): δ (ppm) = 43.4, 102.5, 108.2, 111.9, 114.0, 121.8, 129.7, 133.7, 147.3, 164.8, 164.9, 203.1. HR-ESI-MS: calculated for $C_{14}H_{14}NO_3$ $[M+H]^+$ 244.0968, found 244.0969.

(*E*)-2-(4-Aminophenyl)-1-(4-hydroxy-2-methoxyphenyl)ethan-1-one oxime (4). Following procedure **O-C**, using compound **51** (20 mg, 0.07 mmol, 1.0 equiv.), potassium acetate (7 mg, 0.21 mmol, 3.0 equiv.) and hydroxylamine hydrochloride (7 mg, 0.1 mmol, 1.5 equiv.), the oxime (20 mg, 100% yield) was afforded as a white solid and not purified further. ^{1}H-NMR (500 MHz, $(CD_3)_2SO$): δ (ppm) = 11.96 (s, 1H), 11.44 (s, 1H), 7.39 (d, *J* = 9.43 Hz, 1H), 6.90 (d, *J* = 8.41 Hz, 2H), 6.45 (m, 2H), 6.40 (m, 2H), 4.88 (s, 2H), 3.99 (s, 2H), 3.71 (s, 3H). ^{13}C-NMR (126 MHz, $(CD_3)_2SO$): δ (ppm) = 160.7, 159.7, 159.4, 146.9, 129.4, 128.9, 123.4, 114.1, 111.3, 105.4, 101.5, 55.1, 28.9. HR-ESI-MS: calculated for $C_{15}H_{17}N_2O_3$ $[M+H]^+$ 273.1234, found 273.1232.

(*E*)-2-(4-Aminophenyl)-1-(2,4-dihydroxyphenyl)ethan-1-one oxime (5). Following procedure **O-C** using compound **52** (6 mg, 0.03 mmol, 1.0 equiv.), potassium acetate (7 mg, 0.07 mmol, 3.0 equiv.) and hydroxylamine hydrochloride (3 mg, 0.04 mmol, 3.0 equiv.), the oxime (5 mg, 77% yield) was afforded as a white solid after purification by flash column chromatography (CH_2Cl_2/CH_3OH, 3% CH_3OH). ^{1}H-NMR (500 MHz, $(CD_3)_2SO$): δ (ppm) = 11.85 (s, 1H), 11.31 (s, 1H), 9.68 (s, 1H), 7.28 (d, *J* = 8.65 Hz, 1H), 6.90 (d, *J* = 8.40 Hz, 2H), 6.44 (m, 2H), 6.23 (dd, *J* = 2.43, 8.65 Hz, 1H), 6.21 (d, *J* = 2.43 Hz, 1H), 4.87 (s, 2H), 3.95 (s, 2H). ^{13}C-NMR (126 MHz, $(CD_3)_2SO$): δ (ppm) = 159.9, 159.4, 159.2, 146.9, 129.4, 128.9, 123.5, 114.0, 110.0, 106.8, 102.9, 54.9. HR-ESI-MS: calculated for $C_{14}H_{15}N_2O_3$ $[M+H]^+$ 259.1077, found 259.1075.

1-(2,4-Dimethoxyphenyl)-2-(4-nitrophenyl)ethan-1-one (53). Following a published procedure, 2-(4-aminophenyl)acetic acid (420 mg, 3.0 mmol) was dissolved with 1,3-dimethoxybenzene (450 mg, 3.0 mmol, 1.0 equiv.) in dichloroethane (6 mL).[169] Polyphosphoric acid (7 g) was added, and the reaction stirred for 3 h at 85 °C. After full conversion, the mixture was cooled to 0 °C and carefully basified with ammonia. The resulting solution was extracted with ethyl acetate (3 x 50 mL – the pH has to be over 7) and the combined organic layers were dried over Na_2SO_4, filtered and concentrated *in vacuo*. Purification by flash column chromatography (CH_2Cl_2/ethyl acetate + 1% NH_3, gradient from 0% to 40% ethyl acetate) afforded the product (200 mg, 15%) as a yellow solid. ^{1}H-NMR (500 MHz, CD_3OD): δ (ppm) = 7.66 (d, *J* = 8.67 Hz, 1H), 6.92 (d, *J* = 2.83 Hz, 2H), 6.64 (d, *J* = 2.83 Hz, 2H), 6.57 (d,

J = 2.28 Hz, 1H), 6.54 (dd, *J* = 2.28, 8.67 Hz, 1H), 4.11 (s, 2H), 3.90 (s, 3H), 3.84 (s, 3H). ^{13}C-NMR (126 MHz, CD_3OD): δ = 201.6, 166.4, 162.3, 147.0, 133.8, 131.2, 126.5, 121.7, 116.7, 106.8, 99.2, 56.1, 56.0, 50.0. HR-ESI-MS: calculated for $C_{16}H_{18}NO_3$ $[M+H]^+$ 272.1281, found 272.1281.

(*E*)-2-(4-Aminophenyl)-1-(2,4-dimethoxyphenyl)ethan-1-one oxime (6). Following procedure **O-C**, compound **53** (125 mg, 0.5 mmol, 1.0 equiv.), potassium acetate (136 mg, 1.5 mmol, 3.0 equiv.) and hydroxylamine hydrochloride (48 mg, 0.7 mmol, 1.5 equiv.) were dissolved in methanol (10 mL) and the oxime was formed. Purification by preparative HPLC (H_2O/CH_3CN + 0.1% formic acid, gradient 5% to 100% CH_3CN) afforded product **6** (35 mg, 27%) as a white solid. ^{1}H-NMR (500 MHz, $(CD_3)_2SO$): δ (ppm) = 3.72 (s, 3H), 3.76 (s, 3H), 3.81 (s, 2H), 4.78 (s, 2H), 6.35 (d, *J* = 8.40 Hz, 2H), 6.39 (dd, *J* = 2.35, 8.36 Hz, 1H), 6.51 (d, *J* = 2.30 Hz, 1H), 6.67 (d, *J* = 8.35 Hz, 2H), 6.88 (d, *J* = 8.30 Hz, 1H), 10.90 (s, 1H). ^{13}C-NMR (126 MHz, $(CD_3)_2SO$): δ (ppm) = 160.7, 158.1, 157.0, 146.5, 131.0, 129.3, 124.1, 118.8, 113.8, 104.5, 98.4, 55.4, 55.2, 32.6. HR-ESI-MS: calculated for $C_{16}H_{19}N_2O_3$ $[M+H]^+$ 287.1390, found 287.1384.

2-(4-Chlorophenyl)-1-(6-methoxypyridin-3-yl)ethan-1-one (54). Following procedure **O-A**, using commercially available methyl 6-methoxynicotinate (1.0 g, 5.9 mmol, 1.0 equiv.) and 4-chlorophenylacetic acid (1.0 g, 5.9 mmol, 1.0 equiv.), the pure product (1.1 g, 72%) was obtained after flash column chromatography (petroleum benzine/ethyl acetate, gradient from 0% to 100% ethyl acetate) as a white solid. ^{1}H-NMR (500 MHz, $CDCl_3$): δ (ppm) = 8.76 (s, 1H), 8.08 (d, *J* = 8.80 Hz, 2H), 7.23 (m, 2H), 7.12 (m, 2H), 6.72 (d, *J* = 8.80 Hz, 1H), 4.12 (s, 2H), 3.93 (s, 3H). ^{13}C-NMR (126 MHz, $CDCl_3$): δ (ppm) = 195.0, 167.0, 149.7, 138.7, 133.2, 132.7, 130.9, 129.1, 126.2, 111.6, 54.3, 44.8. HR-ESI-MS: calculated for $C_{14}H_{13}ClNO_2$ $[M+H]^+$ 262.0629 (^{35}Cl), 264.0600 (^{37}Cl), found 262.0609 (100%), 264.0577 (30%).

2-(4-Chlorophenyl)-1-(6-methoxypyridin-3-yl)ethan-1-one oxime (7*E* and 7*Z*). Starting from compound **54** (500 mg, 1.9 mmol, 1.0 equiv.) following procedure **O-C**, using potassium acetate (563 mg, 5.8 mmol, 3.0 equiv.) and hydroxylamine hydrochloride (200 mg, 2.7 mmol, 1.5 equiv.) in methanol (33 mL), the products (**7*E*:** 370 mg, 70%, **7*Z*:** 45 mg, 9%) were obtained after flash column chromatography (cyclohexane/ethyl acetate, gradient 0% to 30% ethyl acetate) as white solids. Note: 1D-NOESY experiments were performed on both compounds, irradiating the oxime-hydroxy proton. The isomers could be identified unambiguously. **7*E***: ^{1}H-NMR

(500 MHz, CD_3OD): δ (ppm) = 8.30 (dd, *J* = 0.51, 2.49 Hz, 1H), 7.96 (dd, *J* = 2.49, 8.79 Hz, 1H), 7.23 (s, 4H), 6.74 (dd, *J* = 0.51, 8.79 Hz, 1H), 4.16 (s, 2H), 3.88 (s, 3H). ^{13}C-NMR (126 MHz, CD_3OD): δ (ppm) = 165.8, 154.4, 145.9, 138.2, 137.2, 133.1, 131.3, 129.6, 126.7, 111.5, 54.2, 31.2. 1D-NOESY (500 MHz, $(CD_3)_2SO$): δ (ppm) = 11.56 (irradiation point), 8.40, 7.99, 7.31, 7.24, 6.80, 4.14. HR-ESI-MS: calculated for $C_{14}H_{14}ClN_2O_2$ $[M+H]^+$ 277.0738 (^{35}Cl), 279.0709 (^{37}Cl), found 277.0738 (100%), 279.0705 (30%). **7*Z***: ^{1}H-NMR (500 MHz, $(CD_3)_2SO$): δ (ppm) = 11.09 (s, 1H), 8.36 (d, *J* = 2.32 Hz, 1H), 7.90 (dd, *J* = 2.32, 8.71 Hz, 1H), 7.30 (d, *J* = 8.40 Hz, 2H), 7.20 (d, *J* = 8.40 Hz, 2H), 6.78 (d, *J* = 8.71 Hz, 1H), 3.89 (s, 2H), 3.82 (s, 3H). ^{13}C-NMR (126 MHz, $(CD_3)_2SO$): δ (ppm) = 162.9, 151.0, 147.1, 139.6, 136.7, 131.0, 130.6, 128.4, 122.1, 109.7, 53.2, 40.0. 1D-NOESY (500 MHz, $(CD_3)_2SO$): δ (ppm) = 11.09 (irradiation point), 8.36, 7.90, 7.20, 6.78, 3.89. HR-ESI-MS: calculated for $C_{14}H_{14}ClN_2O_2$ $[M+H]^+$ 277.0738 (^{35}Cl), 279.0709 (^{37}Cl), found 277.0740 (100%), 279.0709 (30%).

2-(4-Chlorophenyl)-1-(6-hydroxypyridin-3-yl)ethan-1-one (55). Compound **54** (0.2 g, 0.38 mmol), LiCl (0.16 g, 1.9 mmol, 5.0 equiv.) and *p*-toluenesulfonic acid (0.33 g, 1.9 mmol, 5.0 equiv.) were dissolved in dry DMF (15 mL) and heated to 150 °C for 24 h. The reaction was diluted with H_2O (40 mL), and the mixture was extracted with ethyl acetate (3 x 30 mL). The combined organic layers were washed with saturated aqueous NaCl solution (30 mL), dried over $MgSO_4$, filtered and concentrated *in vacuo*. Purification by flash column chromatography (petroleum benzine/ethyl acetate + 1% acetic acid, gradient from 0% or 100% ethyl acetate) afforded the product (54 mg, 29%) as a yellow solid. Note: The deprotection as described in procedure **O-B** does not yield any of the desired product. ^{1}H-NMR (500 MHz, $(CD_3)_2SO$): δ (ppm) = 12.25 (s, 1H), 8.38 (d, *J* = 2.56 Hz, 1H), 7.88 (dd, *J* = 2.74, 9.70 Hz, 1H), 7.37 (d, *J* = 2.80 Hz, 2H), 7.25 (d, *J* = 8.39 Hz, 2H), 6.38 (d, *J* = 9.67 Hz, 1H), 4.21 (s, 2H). ^{13}C-NMR (126 MHz, $(CD_3)_2SO$): δ (ppm) = 193.1, 162.5, 141.6, 138.5, 134.4, 131.7, 131.3, 128.2, 119.8, 116.0, 42.7. HR-ESI-MS: calculated for $C_{13}H_{11}ClNO_2$ $[M+H]^+$ 248.0473 (^{35}Cl), 250.0443 (^{37}Cl), found 248.0472 (100%), 250.0440 (30%).

2-(4-Chlorophenyl)-1-(6-hydroxypyridin-3-yl)ethan-1-one oxime (8*E* and 8*Z*). Starting from compound **55** (40 mg, 0.2 mmol, 1.0 equiv.) following procedure **O-C**, using potassium acetate (48 mg, 0.5 mmol, 3.0 equiv.) and hydroxylamine hydrochloride (16 mg, 0.2 mmol, 1.5 equiv.), the products (**8*E*:** 10 mg, 24%, **8*Z*:** 3 mg, 8%) were afforded after preparative HPLC (H_2O/CH_3CN + 1% formic acid, gradient

from 5% to 100% CH_3CN) as white solids. **8*E***: ^{1}H-NMR (500 MHz, $(CD_3)_2SO$): δ (ppm) = 11.71 (s, 1H), 11.36 (s, 1H), 7.83 (dd, *J* = 2.55, 9.75 Hz, 1H), 7.53 (d, *J* = 2.55 Hz, 1H), 7.33 (d, *J* = 8.42 Hz, 2H), 7.22 (d, *J* = 8.42 Hz, 2H), 6.33 (d, *J* = 9.75 Hz, 1H), 4.01 (s, 2H). ^{13}C-NMR (126 MHz, $(CD_3)_2SO$): δ (ppm) = 162.1, 151.4, 137.9, 136.3, 133.6, 130.8, 130.2, 128.5, 120.4, 113.8, 28.7. HR-ESI-MS: calculated for $C_{13}H_{12}ClN_2O_2$ [*M*+H]$^+$ 263.0582 (^{35}Cl), 265.0552 (^{37}Cl), found 263.0581 (100%), 265.0549 (30%). **8*Z***: ^{1}H-NMR (500 MHz, $(CD_3)_2SO$): δ (ppm) = 11.78 (s, 1H), 11.17 (s, 1H), 7.93 (d, *J* = 2.52 Hz, 1H), 7.70 (dd, *J* = 2.52, 9.68 Hz, 1H), 7.33 (d, *J* = 8.42 Hz, 2H), 7.21 (d, *J* = 8.42 Hz, 2H), 6.25 (d, *J* = 9.68 Hz, 1H), 3.81 (s, 2H). ^{13}C-NMR (126 MHz, $(CD_3)_2SO$): δ (ppm) = 161.7, 149.7, 141.8, 138.1, 137.5, 131.4, 130.9, 128.9, 119.3, 110.8, 38.8. HR-ESI-MS: calculated for $C_{13}H_{12}ClN_2O_2$ [*M*+H]$^+$ 263.0582 (^{35}Cl), 265.0552 (^{37}Cl), found 263.0581 (100%), 265.0549 (30%).

(*E*)-2-(4-Chlorophenyl)-1-(2,4-dihydroxyphenyl)ethan-1-one *O*-methyl oxime (11). 2-(4-Chlorophenyl)-1-(2,4-dihydroxyphenyl)ethan-1-one (100 mg, 0.38 mmol, 1.0 equiv) and *O*-methylhydroxylamine•HCl (64 mg, 0.76 mmol, 2.0 equiv) were dissolved in methanol/pyridine (10:1, 4 mL) and added to a flask under N_2 atmosphere in solution.[126] Sodium sulfate (135 mg, 0.95 mmol, 2.5 equiv) was added and the reaction mixture was heated to 95 °C under reflux. The reaction mixture was refluxed for 18 h and then allowed to cool to room temperature. H_2O (15 mL) was added followed by ethyl acetate (15 mL). The layers were mixed and separated and the aqueous layer was extracted with ethyl acetate (2x, 10 mL). The combined organic layers were washed with brine, dried over Na_2SO_4, filtered and concentrated to give a pale yellow sticky solid which was purified by flash column chromatography (heptane:ethyl acetate, gradient from 0% to 100% ethyl acetate) to give the product (80 mg, 72%) as a white solid. ^{1}H-NMR (500 MHz, CD_3OD): δ = 7.25 (m, 5H), 6.31 (d, *J* = 2.40 Hz, 1H), 6.28 (q, *J* = 3.71 Hz, 1H), 4.17 (s, 2H), 3.98 (s, 3H). ^{13}C-NMR (126 MHz, CD_3OD): δ = 161.3, 161.1, 161.0, 136.8, 133.2, 131.0, 130.7, 129.6, 110.9, 108.3, 104.3, 62.7, 31.3. HR-ESI-MS: calculated for $C_{15}H_{15}ClNO_3$ [*M*+H]$^+$ 292.0735 (^{35}Cl), 294.0705 (^{37}Cl), found 292.0706 (100%), 294.0674 (30%).

4-(2-(4-Chlorophenyl)-1-hydroxyethyl)benzene-1,3-diol (13). 2-(4-Chlorophenyl)-1-(2,4-dihydroxyphenyl)ethan-1-one (100 mg, 0.38 mmol, 1.0 equiv.) was dissolved in methanol and added to a solution of sodium borohydride (22 mg, 0.58 mmol, 1.5 equiv.) in methanol (5 mL).[126] $NaBH_4$ was added two more times (16 mg, 0.42 mmol, 1.1 equiv. and 40 mg, 1.1 mmol, 2.8 equiv.), and the reaction was stirred

for 1 h after each addition. After full conversion, the solvent was removed under reduced pressure and the solids were dissolved in a mixture of dichloromethane (20 mL), saturated aqueous NaCl solution (5 mL), and water (5 mL). The mixture was acidified to pH 5, and the organic layer was separated. The aqueous layer was further extracted with dichloromethane (2 x 35 mL), dried over Na_2SO_4, filtered and concentrated. The product was purified by reverse-phase flash column chromatography (H_2O/CH_3OH gradient from 5% to 100% CH_3OH) to give the product as a white solid (21 mg, 21%). ^{1}H-NMR (500 MHz, CD_3OD): δ (ppm) = 7.20 (d, *J* = 2.81 Hz, 2H), 7.12 (d, *J* = 2.81 Hz, 2H), 6.94 (d, *J* = 7.99 Hz, 1H), 6.23 (m, 1H), 5.04 (d, *J* = 5.36, 7.70 Hz, 1H), 2.95 (ddd, *J* = 5.36, 7.70, 13.56, 54.73 Hz, 2H). ^{13}C-NMR (126 MHz, CD_3OD): δ (ppm) = 158.5, 156.6, 139.4, 132.7, 132.2, 128.9, 128.5, 122.5, 107.3, 103.4, 72.0, 44.6. HR-ESI-MS: calculated for $C_{14}H_{12}ClO_3$ $[M+H]^-$ 263.0480 (^{35}Cl), 265.0451 (^{37}Cl), found 263.0457 (100%), 265.0426 (30%).

Synthesis and characterization of indoles. The synthesis and characterization of **3**, **16**, **17**, **20**, **24**, **33** were described previously.[126,162]

Aldehyde formation (procedure I-A). When the indole-carbaldehydes were not commercially available they were synthesized following a literature procedure.[170] $POCl_3$ (1.3 equiv.) was stirred in DMF for 15 minutes. A solution of 1-(4-chlorophenyl)-1*H*-indole (1.0 equiv.), 1-(4-chlorophenyl)-1*H*-indole (1.0 equiv.) or 1*H*-indole (1.0 equiv.) in DMF was added, and the reaction mixture was stirred at 80 °C for 15 min. Then aqueous NaOH solution (2 M) was added and stirred at 110 °C for 45 min. The reaction mixture was diluted with *tert*-butyl methyl ether (TBME) and H_2O. The organic layer was separated, and the aqueous layer was extracted with TBME (2 x). The combined organic layers were dried over Na_2SO_4, filtered and concentrated *in vacuo* to obtain the crude product that was used without further purification unless stated otherwise.

S_N2 substitution (procedure I-B). The 1-substituted-1*H*-indole-3-carbaldehyde products were synthesized by following a previously reported procedure.[171] Sodium hydride (1.8 equiv.) was suspended in DMF, and the suspension was cooled to 0 °C under nitrogen atmosphere. 1*H*-Indole-3-carbaldehyde (1.0 equiv.) was added. The mixture was stirred at 25 °C for 30 min, after which 3,4-dichlorobenzylbromide (1.2 equiv.) was added. The resulting mixture was stirred for 16 h. Water and ethyl acetate were added, and the layers were separated. The aqueous layer was extracted

with ethyl acetate (2 x). The combined organic layers were washed with water (3 x) and saturated aqueous NaCl solution, dried over Na_2SO_4, filtered and concentrated *in vacuo*. The crude product was directly used without further purification for the next reaction unless stated otherwise.

Reduction (procedure I-C). The (1-substituted-1*H*-indol-3-yl)methanol products were synthesized by following a previously reported procedure.[172] To a solution of 1-substituted-1*H*-indole-3-carbaldehyde (1.0 equiv.) in methanol, sodium borohydride (3.2 equiv.) was added portion-wise, and the reaction mixture was stirred for 1 h at 25 °C. Water was added with care to the reaction, and the mixture was extracted with dichloromethane (2 x). The combined organic layers were dried over Na_2SO_4, filtered and concentrated *in vacuo*.

(1-(3,4-Dichlorobenzyl)-1*H*-pyrrolo[2,3-b]pyridin-3-yl)methanol (14). 1*H*-Pyrrolo[2,3-b]pyridine-3-carbaldehyde (500 mg, 3.4 mmol, 1.0 equiv.) and 3,4-dichlorobenzyl-bromide (1.2 g, 4.9 mmol, 1.2 equiv.) were added as described in procedure **I-B** to a solution of NaH (150 mg, 60% dispersion in mineral oil, 3.8 mmol, 1.1 equiv.) in DMF (14 mL), and the alkylation product (600 mg, 58%) was purified by flash column chromatography (CH_2Cl/CH_3OH 99.5:0.5). Following procedure **I-C** the alkylation product (600 mg, 1.97 mmol, 1.0 equiv.) was reduced to the alcohol with $NaBH_4$ (240 mg, 6.3 mmol, 3.2 equiv.) in methanol (250 mL), and pure product **14** (507 mg, 84% yield) was obtained without further purification as a white solid. ^{1}H-NMR (500 MHz, $CDCl_3$): δ (ppm) = 8.35 (dd, *J* = 1.54, 4.77 Hz, 1H), 8.06 (dd, *J* = 1.54, 7.89Hz, 1H), 7.36 (d, *J* = 8.27 Hz, 1H), 7.31 (d, *J* = 2.05 Hz, 1H), 7.16 (s, 1H), 7.13 (dd, *J* = 4.77, 7.89 Hz, 1H), 7.05 (dd, *J* = 2.05, 8.27 Hz, 1H), 5.41 (s, 2H), 4.85 (s, 2H). ^{13}C-NMR (126 MHz, $CDCl_3$): δ (ppm) = 147.9, 143.7, 138.0, 132.9, 131.9, 130.8, 129.5, 128.1, 126.9, 125.9, 119.5, 116.3, 114.7, 57.3, 46.8. HR-ESI-MS: calculated for $C_{15}H_{13}Cl_2N_2O$ $[M+H]^+$ 307.0399 (^{35}Cl), 309.0370 (^{37}Cl), found 307.0394 (100%), 309.0361 (60%).

(1-(3,4-Dichlorophenyl)-1*H*-indol-3-yl)methanol (15). In contrast to procedure **I-B**, the suspension of indole-3-carbaldehyde (500 mg, 3.5 mmol, 1.0 equiv.) in DMF (10 mL), 3,4-dichlorofluorobenzene (0.5 mL, 4.2 mmol, 1.2 equiv.) and NaH (350 mg, 8.6 mmol, 2.4 equiv.) was stirred for 24 h at 190 °C.[173] After full conversion, the reaction mixture was diluted with TBME (10 mL) and washed with saturated aqueous NaCl solution (3 x 10 mL). The organic layer was dried over Na_2SO_4, filtered and

concentrated *in vacuo* to obtain product **56** (960 mg, 3.3 mmol) that was used without further purification. Compound **15** was synthesized following procedure **I-C**, using **56** (960 mg, 3.3 mmol, 1.0 equiv.) and $NaBH_4$ (430 mg, 11.34 mmol, 3.4 equiv.) in methanol (200 mL). The reaction mixture was concentrated, the residue was dissolved in TBME (50 mL) and washed with saturated aqueous NaCl solution (100 mL) and water (100 mL). The organic layer was dried over Na_2SO_4, filtered and concentrated *in vacuo*. Purification by reversed phase column chromatography (H_2O/CH_3CN, gradient 20% to 100% CH_3CN) afforded **15** (20% over two steps) as a yellow sticky solid. ^{1}H-NMR (500 MHz, $(CD_3)_2SO$): δ (ppm) = 7.72 (d, *J* = 7.74 Hz, 1H), 7.58 (m, 4H), 7.22 (t, *J* = 6.91 Hz, 1H), 7.15 (t, *J* = 6.91 Hz, 1H), 4.98 (t, *J* = 5.33 Hz, 1H), 4.70 (d, *J* = 5.33 Hz, 2H). ^{13}C-NMR (126 MHz, $(CD_3)_2SO$): δ (ppm) = 138.0, 135.4, 131.4, 129.8, 129.7, 128.2, 126.1, 125.1, 125.1, 122.8, 120.2, 119.9, 118.8, 110.32 55.2. HR-ESI-MS: calculated for $C_{15}H_{10}Cl_2N^{\cdot}$ [*M*-OH]$^{\cdot}$ 274.0190 (^{35}Cl), 276.0161 (^{37}Cl), found 274.0184 (100%), 276.0153 (70%).

(1-(3,4-Dichlorobenzyl)-1*H*-indazol-3-yl)methanol (18). Following procedure **I-B**, 3-iodo-1*H*-indazole (1.5 g, 6.1 mmol, 1.0 equiv.) was dissolved in a suspension of NaH (270 mg, 6.7 mmol, 1.1 equiv.) in DMF (40 mL). 3,4-Dichlorobenzylbromide (1 mL, 7.36 mmol, 1.2 equiv.) was added. The crude material was purified by column chromatography (heptane/ethyl acetate 97:3) affording 1-(3,4-dichlorobenzyl)-3-iodo-1*H*-indazole (**57**) as a white solid (2.1 g, 85% yield). A round-bottomed flask was charged with *i*-PrMgCl (2 M in THF, 3.0 mL, 6.0 mmol, 1.5 equiv.) and dry THF (5 mL) and was cooled to 0 °C.[174] A solution of compound **57** (1.6 g, 4.0 mmol) in dry THF (20 mL) was added dropwise, and the resulting mixture was stirred at 0 °C for 1 h. DMF (1.2 mL, 16.0 mmol, 4.0 equiv.) was added, and the mixture was stirred for 5 h. After full conversion, aqueous HCl solution (1 M 10 mL) and toluene (10 mL) were added to the reaction mixture. The layers were separated, and the organic layer was washed with saturated aqueous $NaHCO_3$ solution (5 mL) and concentrated *in vacuo*. The crude material was purified using column chromatography (heptane/ethyl acetate 95:5) affording 1-(3,4-dichlorobenzyl)-1*H*-indazole-3-carbaldehyde (**58**) as a white solid (73 mg, 6% yield). Indole **18** was synthesized following procedure **I-C**, using **58** (70 mg, 0.23 mmol, 1.0 equiv.) and $NaBH_4$ (9 mg, 0.23 mmol, 1.0 equiv.) in ethanol (10 mL). The crude product was purified using flash column chromatography (heptane/ethyl acetate 8:2) to provide **18** as a white solid (35 mg, 50%). ^{1}H-NMR (500 MHz, $(CD_3)_2SO$): δ (ppm) = 7.86 (d, *J* = 8.09 Hz, 1H), 7.70 (d, *J* = 8.49 Hz, 1H), 7.58 (d, *J* =

8.30 Hz, 1H), 7.52 (d, *J* = 1.96 Hz, 1H), 7.39 (m, 1H), 7.15 (m, 2H), 5.62 (s, 2H), 5.32 (t, *J* = 5.81 Hz, 1H), 4.77 (d, *J* = 5.81 Hz, 2H). ^{13}C-NMR (126 MHz, $(CD_3)_2SO$): δ (ppm) = 145.8, 140.4, 138.9, 131.1, 130.9, 130.2, 129.4, 127.8, 126.6, 122.3, 121.1, 120.3, 109.6, 56.6, 50.2. HR-ESI-MS: calculated for $C_{15}H_{13}Cl_2N_2O$ $[M+H]^+$ 307.0399 (^{35}Cl), 309.0370 (^{37}Cl), found 307.0400 (100%), 309.0368 (70%), 289.0293 (20%).

2-(1-(3,4-Dichlorobenzyl)-1*H*-indol-3-yl)ethan-1-ol (19). Tryptophol (0.59 g, 3.7 mmol), *tert*-butyldimethylsilyl (TBDMS) chloride (0.86 g, 5.7 mmol, 1.5 equiv.), and imidazole (0.38 g, 5.6 mmol, 1.5 equiv.) were dissolved in CH_2Cl_2 (50 mL).[175] The reaction mixture was stirred at 25 °C for 24 h. Then it was diluted with CH_2Cl_2 (50 mL), washed with saturated aqueous NaCl solution (100 mL), and water (100 mL). The organic layer was dried over Na_2SO_4, filtered and concentrated *in vacuo* to obtain crude 3-(2-((*tert*-butyldimethylsilyl)oxy)ethyl)-1*H*-indole (**59**) (1.03 g, 3.75 mmol) as a thick red oil, which was used without further purification in the next step. Compound **59** (1.03 g, 3.75 mmol, 1.0 equiv.) and 3,4-dichlorobenzyl bromide (1.08 g, 4.5 mmol, 1.2 equiv.) were mixed as described in procedure **I-B** in DMF (10 mL) with NaH (355 mg, 8.9 mmol, 2.4 equiv.). After workup, crude 3-(2-((*tert*-butyldimethylsilyl)oxy)ethyl)-1-(3,4-dichlorobenzyl)-1*H*-indole (**60**) was obtained as a yellow-green oil. Purification by normal phase column chromatography (heptane/EtOAc, gradient 0% to 10% EtOAc) afforded compound **60** (0.86 g, 205 mmol). To a solution of compound **60** (0.86 g, 2.05 mmol, 1.0 equiv.) in THF (50 mL), *tetra*-butylammonium fluoride (TBAF) in THF (1 M, 4.1 mL, 4.1 mmol, 2.0 equiv.) was added. The reaction mixture was stirred at 90 °C for 24 h. The reaction mixture was concentrated and purified by reverse phase column chromatography (H_2O/CH_3CN + 0.1% formic acid, gradient 20% to 100% CH_3CN), affording compound **19** (0.32 g, 0.99 mmol, 26% over three steps) as a yellowish sticky oil. ^{1}H-NMR (500 MHz, $(CD_3)_2SO$): δ (ppm) = 7.56 (d, *J* = 8.31 Hz, 1H), 7.54 (d, *J* = 7.89 Hz, 1H), 7.48 (d, *J* = 1.96 Hz, 1H), 7.40 (d, *J* = 8.19 Hz, 1H), 7.32 (s, 1H), 7.10 (m, 2H), 7.01 (m, 1H), 5.37 (s, 2H), 4.67 (t, *J* = 5.32 Hz, 1H), 3.65 (m, 2H), 2.84 (t, *J* = 7.21 Hz, 2H). ^{13}C-NMR (126 MHz, $(CD_3)_2SO$): δ (ppm) = 139.8, 135.8, 131.1, 130.8, 129.9, 129.1, 128.1, 127.4, 126.6, 121.4, 118.9, 118.7, 112.1, 109.9, 61.6, 47.6, 28.7. HR-ESI-MS: calculated for $C_{17}H_{16}Cl_2NO$ $[M+H]^+$ 320.0603 (^{35}Cl), 322.0574 (^{37}Cl), found 320.0605 (100%), 322.0573 (70%).

(1-(3,4-Dichlorobenzyl)-5-methoxy-1*H*-indol-3-yl)methanol (21). 5-Methoxy-1*H*-indole-3-carbaldehyde (500 mg, 2.9 mmol, 1.0 equiv.) and 3,4-dichlorobenzylbromide

(823 mg, 3.4 mmol, 1.2 equiv.) were mixed as described in procedure **I-B** in a suspension of NaH (125 mg, 60% dispersion in mineral oil, 3.1 mmol, 1.1 equiv.) in DMF (14 mL). The alkylation product (950 mg, 99%) was used without further purification. Following procedure **I-C**, the aldehyde (358 mg, 1.07 mmol, 1.0 equiv.) was reduced to the alcohol with $NaBH_4$ (130 mg, 3.42 mmol, 3.2 equiv.) in methanol (100 mL) and the pure product **21** (300 mg, 83%) was obtained without further purification as a yellowish solid. ^{1}H-NMR (500 MHz, $(CD_3)_2SO$): δ (ppm) = 7.56 (d, *J* = 8.30 Hz, 1H), 7.47 (d, *J* = 1.95 Hz, 1H), 7.38 (s, 1H), 7.31 (d, *J* = 8.90 Hz, 1H), 7.12 (m, 2H), 6.75 (dd, *J* = 2.50, 8.90 Hz, 1H), 5.34 (s, 2H), 4.83 (t, *J* = 5.45 Hz, 1H), 4.61 (d, *J* = 5.45 Hz, 2H), 3.75 (s, 3H). ^{13}C-NMR (126 MHz, $(CD_3)_2SO$): δ (ppm) = 153.4, 139.8, 131.3, 131.1, 130.7, 129.9, 129.0, 127.7, 127.5, 127.4, 115.9, 111.6, 110.7, 101.2, 55.3, 55.3, 47.8. HR-ESI-MS: calculated for $C_{17}H_{14}Cl_2NO^{\cdot}$ [*M*-OH]$^{\cdot}$ 318.0452 (^{35}Cl), 320.0423 (^{37}Cl), found 318.0415 (100%), 320.0383 (60%).

(1-(3-Chlorobenzyl)-4-methoxy-1*H*-indol-3-yl)methanol (22). 4-Methoxy-1*H*-indole-3-carbaldehyde (200 mg, 1.14 mmol, 1.0 equiv.) was synthesized following procedure **I-A**, using 4-methoxy-1*H*-indole (1.0 g, 6.8 mmol, 1.0 equiv.) as the starting material with $POCl_3$ (1.3 g, 8.2 mmol, 1.2 equiv.) and DMF (2.5 g, 34 mmol, 5.0 equiv.) in NaOH (2 M, 40 mL). 3-Chlorobenzylbromide (282 mg, 1.37 mmol, 1.1 equiv.) was added as described in procedure **I-B** with NaH (82 mg, 60% in mineral oil, 2.05 mmol, 1.8 equiv.) in DMF (10 mL). Product **22** was synthesized by reduction of 1-(3-chlorobenzyl)-4-methoxy-1*H*-indole-3-carbaldehyde (380 mg, 1.27 mmol, 1.0 equiv.) following procedure **I-C**, using $NaBH_4$ (154 mg, 4.06 mmol, 3.2 equiv.). The product (195 mg, 57% yield over three steps) was obtained after flash column chromatography (petroleum benzine/ethyl acetate, gradient from 0% to 100% ethyl acetate) as a sticky yellow solid. ^{1}H-NMR (500 MHz, $(CD_3)_2SO$): δ (ppm) = 7.32 (m, 2H), 7.24 (m, 1H), 7.22 (m, 1H), 7.12 (m, 1H), 7.00 (d, *J* = 0.99 Hz, 1H), 6.99 (s, 1H), 6.49 (m, 1H), 5.35 (s, 2H), 4.75 (d, *J* = 2.87 Hz, 2H), 4.65 (t, *J* = 5.54 Hz, 1H), 3.82 (s, 3H). ^{13}C-NMR (126 MHz, $(CD_3)_2SO$): δ (ppm) = 154.1, 141.1, 137.7, 133.1, 130.5, 127.3, 126.8, 125.8, 125.2, 122.4, 116.7, 116.3, 103.4, 99.5, 56.9, 55.2, 48.4. HR-ESI-MS: calculated for $C_{17}H_{15}ClNO^{\cdot}$ [*M*-OH]$^{\cdot}$ 284.0842 (^{35}Cl), 286.0813 (^{37}Cl), found 284.0831 (100%), 286.0800 (70%).

(7-Chloro-1-(3,4-dichlorobenzyl)-1*H*-indol-3-yl)methanol (23). 7-Chloro-1*H*-indole-3-carbaldehyde (500 mg, 2.8 mmol, 1.0 equiv.) and 3,4-dichlorobenzylbromide (804 mg, 3.4 mmol, 1.2 equiv.) were added as described in procedure **I-B** to a

suspension of NaH (123 mg, 60% dispersion in mineral oil, 3.1 mmol, 1.1 equiv.) in DMF (14 mL). The alkylation product (577 mg, 61%) was purified by flash column chromatography (dichloromethane/heptane 3:1). Following procedure **I-C** the aldehyde (387 mg, 1.14 mmol, 1.0 equiv.) was reduced to the alcohol with $NaBH_4$ (140 mg, 3.68 mmol, 3.2 equiv.) in methanol (100 mL), and pure product **23** (360 mg, 93%) was obtained without purification as a white solid. ^{1}H-NMR (500 MHz, $(CD_3)_2SO$): δ (ppm) = 7.62 (dd, *J* = 0.91, 7.85 Hz, 1H), 7.56 (d, *J* = 8.34 Hz, 1H), 7.49 (s, 1H), 7.29 (d, *J* = 2.01 Hz, 1H), 7.13 (dd, *J* = 0.91, 7.50 Hz, 1H), 7.03 (t, *J* = 7.72 Hz, 1H), 6.90 (dd, *J* = 2.01, 8.34 Hz, 1H), 5.73 (s, 2H), 4.98 (t, *J* = 5.38 Hz, 1H), 4.65 (d, *J* = 5.38 Hz, 2H). ^{13}C-NMR (126 MHz, $(CD_3)_2SO$): δ (ppm) = 141.1, 131.2, 130.9, 130.9, 130.6, 130.2, 129.7, 127.9, 126.2, 123.2, 120.3, 118.8, 117.1, 115.4, 55.0, 49.7. HR-ESI-MS: calculated for $C_{16}H_{11}Cl_3N^{\cdot}$ [*M*-OH]$^{\cdot}$ 321.9957(^{35}Cl), 323.9928 (^{37}Cl), found 321.9953 (100%), 323.9921 (95%), 325.9889 (30%).

(1-(3-Chlorobenzyl)-4-fluoro-1*H*-indol-3-yl)methanol (25). 4-Fluoro-1*H*-indole-3-carbaldehyde (200 mg, 1.23 mmol, 1.0 equiv.) was synthesized following procedure **I-A** using 4-fluoro-1*H*-indole (1.0 g, 7.4 mmol, 1.0 equiv.) as starting material with $POCl_3$ (1.4 g, 8.9 mmol, 1.2 equiv.) and DMF (2.7 g, 37 mmol, 5.0 equiv.) in NaOH (2 M, 40 mL). From there, 3-chlorobenzylbromide (302 mg, 1.47 mmol, 1.2 equiv.) was added as described in procedure **I-B** with NaH (88 mg, 60% mineral oil, 2.21 mmol, 1.8 equiv.) in DMF (10 mL). The final indole **25** was synthesized by reduction of 1-benzyl-4-fluoro-1*H*-indole-3-carbaldehyde (420 mg, 1.46 mmol, 1.0 equiv.) following procedure **I-C**, using $NaBH_4$ (175 mg, 4.67 mmol, 3.2 equiv.) in methanol (10 mL). The product **25** (144 mg, 41% over three steps) was obtained after flash column chromatography (petroleum benzine/ethyl acetate, gradient from 0% to 100% ethyl acetate) as a sticky orange oil. ^{1}H-NMR (500 MHz, $(CD_3)_2SO$): δ (ppm) = 7.45 (s, 1H), 7.33 (m, 2H), 7.29 (m, 2H), 7.16 (m, 1H), 7.07 (td, *J* = 5.13, 7.79 Hz, 1H), 6.77 (dd, *J* = 7.82, 11.17 Hz, 1H), 5.41 (s, 2H), 4.93 (t, *J* = 5.25 Hz, 1H), 4.69 (d, *J* = 5.25 Hz, 2H). ^{13}C-NMR (126 MHz, $(CD_3)_2SO$): δ (ppm) = 156.4 (d, *J* = 245.28 Hz), 140.6, 139.0 (d, *J* = 12.18 Hz), 133.2, 130.6, 127.6, 127.5, 127.0, 125.9, 122.1 (d, *J* = 7.74 Hz), 115.2 (d, *J* = 21.04 Hz), 114.7 (d, *J* = 3.39 Hz), 106.7 (d, *J* = 3.00 Hz), 104.2 (d, *J* = 19.07 Hz), 56.0, 48.5. ^{19}F-NMR (470 MHz, $(CD_3)_2SO$): δ (ppm) = -122.62 (q, *J* = 5.27 Hz). HR-ESI-MS: calculated for $C_{16}H_{12}ClFN^{\cdot}$ [*M*-OH]$^{\cdot}$ 272.0642 (^{35}Cl), 274.0613 (^{37}Cl), found 272.0630 (100%), 274.0600 (30%).

(1-Benzyl-4-fluoro-1*H*-indol-3-yl)methanol (26). 4-Fluoro-1*H*-indole-3-carbaldehyde (200 mg, 1.23 mmol, 1.0 equiv.) was synthesized following procedure **I-A**, using 4-fluoro-1*H*-indole (1.0 g, 7.4 mmol, 1.0 equiv.) as starting material with $POCl_3$ (1.4 g, 8.9 mmol, 1.2 equiv.) and DMF (2.7 g, 37 mmol, 5.0 equiv.) in NaOH (2 M, 40 mL). From there, benzylbromide (252 mg, 1.5 mmol, 1.2 equiv.) was added as described in procedure **I-B**, using NaH (88 mg, 2.21 mmol, 1.8 equiv.) in DMF (10 mL). The final indole **26** was synthesized by reduction of the aldehyde (330 mg, 1.3 mmol, 1.0 equiv.) following procedure **I-C** using $NaBH_4$ (158 mg, 4.16 mmol, 3.2 equiv.) in methanol (10 mL). The product (203 mg, 67% over three steps) was obtained after flash column chromatography (petroleum benzine/ethyl acetate, gradient 0% to 100% ethyl acetate) as a sticky orange oil. ^{1}H-NMR (500 MHz, $(CD_3)_2SO$): δ (ppm) = 7.42 (s, 1H), 7.28 (m, 4H), 7.21 (d, *J* = 7.12 Hz, 2H), 7.05 (td, *J* = 5.33, 8.06 Hz, 1H), 6.75 (dd, *J* = 7.82, 11.32 Hz, 1H), 5.39 (s, 2H), 4.90 (t, *J* = 5.21 Hz, 1H), 4.69 (d, *J* = 5.21 Hz, 2H). ^{13}C-NMR (126 MHz, $(CD_3)_2SO$): δ (ppm) = 156.4 (d, *J* = 245.10 Hz), 139.0 (d, *J* = 12.12 Hz), 138.0, 128.6, 127.7, 127.5, 127.2, 121.9 (d, *J* = 7.76 Hz), 115.2 (d, *J* = 21.04 Hz), 114.4 (d, *J* = 3.37 Hz), 106.8 (d, *J* = 3.12 Hz), 104.0 (d, *J* = 19.11 Hz), 56.0 (d, *J* = 1.18 Hz), 49.2. ^{19}F-NMR (470 MHz, $(CD_3)_2SO$): δ (ppm) = -122.76 (q, *J* = 5.42 Hz). HR-ESI-MS: calculated for $C_{16}H_{13}FN^{\cdot}$ [*M*-OH]$^{\cdot}$ 238.1032, found 238.1021.

1-(3,4-Dichlorobenzyl)-3-methyl-1*H*-indole (27). 3-Methyl-1*H*-indole (498 mg, 3.8 mmol, 1.0 equiv.) and 3,4-dichlorobenzylbromide (1.0 g, 4.2 mmol, 1.1 equiv.) were added as described in procedure **I-B** to a suspension of NaH (339 mg, 8.5 mmol, 2.2 equiv.) in DMF (10 mL), and pure product **27** (210 mg, 19%) was obtained after purification by flash column chromatography (heptane/ethyl acetate, gradient 0% to 100% ethyl acetate) followed by reversed-phase flash column chromatography (H_2O/CH_3CN, gradient 20% to 100% CH_3CN) as an off-white solid. ^{1}H-NMR (500 MHz, $(CD_3)_2SO$): δ (ppm) = 7.55 (d, *J* = 8.30 Hz, 1H), 7.50 (d, *J* = 7.82 Hz, 1H), 7.47 (d, *J* = 1.99 Hz, 1H), 7.41 (d, *J* = 8.20 Hz, 1H), 7.27 (d, *J* = 0.87 Hz, 1H), 7.10 (m, 2H), 7.01 (td, *J* = 0.87, 7.46 Hz, 1H), 5.36 (s, 2H), 2.26 (d, *J* = 0.94 Hz, 3H). ^{13}C-NMR (126 MHz, $(CD_3)_2SO$): δ (ppm) = 139.8, 135.9, 131.1, 130.8, 129.9, 129.0, 128.6, 127.4, 126.5, 121.4, 118.8, 118.7, 109.8, 109.8, 47.6, 9.5. HR-ESI-MS: calculated for $C_{16}H_{14}Cl_2N$ [*M*+H]$^+$ 290.0498 (^{35}Cl), 292.0468 (^{37}Cl), found 290.0497 (100%), 292.0466 (70%).

(1-(3,4-Dichlorobenzyl)-6-fluoro-1*H*-indol-3-yl)methanol (28). 6-Fluoro-1*H*-indole-3-carbaldehyde (500 mg, 3.1 mmol, 1.0 equiv.) and 3,4-dichlorobenzylbromide (883 mg, 3.7 mmol, 1.2 equiv.) were added as described in procedure **I-B** in a suspension of NaH (135 mg, 60% dispersion in mineral oil, 3.4 mmol, 1.1 equiv.) in DMF (14 mL). The alkylation product (1.0 g, 98%) was used without further purification. Following procedure **I-C**, the aldehyde (1.0 g, 3.0 mmol, 1.0 equiv.) was reduced to the alcohol with $NaBH_4$ (385 mg, 10.2 mmol, 3.4 equiv.) in methanol (130 mL), and product **28** (473 mg, 48% yield over two steps) was obtained after purification by flash column chromatography (dichloromethane) as a white solid. ^{1}H-NMR (500 MHz, $(CD_3)_2SO$): δ (ppm) = 7.59 (m, 2H), 7.55 (d, *J* = 1.95 Hz, 1H), 7.43 (s, 1H), 7.38 (dd, *J* = 2.29, 10.49 Hz, 1H), 7.18 (dd, *J* = 1.95, 8.33 Hz, 1H), 6.89 (m, 1H), 5.36 (s, 2H), 4.90 (t, *J* = 5.40 Hz, 1H), 4.61 (d, *J* = 5.40 Hz, 2H). ^{13}C-NMR (126 MHz, $(CD_3)_2SO$): δ (ppm) = 159.2 (d, *J* = 235.08 Hz), 139.3, 136.2 (d, *J* = 12.27 Hz), 131.1, 130.9, 130.1, 129.3, 127.6, 127.3 (d, *J* = 3.45 Hz), 123.9, 120.6 (d, *J* = 10.28 Hz), 116.7, 107.4 (d, *J* = 24.49 Hz), 96.5 (d, *J* = 26.48 Hz), 55.2, 47.7. ^{19}F-NMR (470 MHz, $(CD_3)_2SO$): δ (ppm) = -120.84 (m). HR-ESI-MS: calculated for $C_{16}H_{11}Cl_2FN^{\bullet}$ [*M*-OH]$^{\bullet}$ 306.0253 (^{35}Cl), 308.0223 (^{37}Cl), found 306.0248 (100%), 308.0215 (70%).

1-(3,4-Dichlorobenzyl)-1*H*-indole (29). Indole (509 mg, 4.35 mmol, 1.0 equiv.) and 3,4-dichlorobenzylbromide (0.87 mL, 5.12 mmol, 1.2 equiv.) were added as described in procedure **I-B** to a suspension of NaH (381 mg, 9.5 mmol, 2.2 equiv.) in DMF (20 mL). The obtained crude material was purified by flash column chromatography (heptane/ethyl acetate, gradient 0% to 20% ethyl acetate) followed by reversed-phase column chromatography (H_2O:CH_3CN + 0.1% formic acid, gradient 20% to 100% CH_3CN), affording compound **29** (63 mg, 5% yield) as a pale yellow sticky oil. ^{1}H-NMR (500 MHz, $(CD_3)_2SO$): δ (ppm) = 7.57 (d, *J* = 8.26 Hz, 1H), 7.56 (d, *J* = 7.83 Hz, 1H), 7.54 (d, *J* = 3.16 Hz, 1H), 7.48 (dd, *J* = 0.68, 8.26 Hz, 1H), 7.45 (q, *J* = 2.98 Hz, 1H), 7.11 (m, 2H), 7.02 (td, *J* = 0.94, 7.47 Hz, 1H), 6.50 (dd, *J* = 0.78, 3.16 Hz, 1H), 5.44 (s, 2H). ^{13}C-NMR (126 MHz, $(CD_3)_2SO$): δ (ppm) = 139.62, 135.6, 131.1, 130.8, 130.0, 129.1, 129.0, 128.3, 127.4, 121.4, 120.6, 119.4, 110.1, 101.4, 47.8. HR-ESI-MS: calculated for $C_{15}H_{12}Cl_2N$ [*M*+H]$^{+}$ 276.0341 (^{35}Cl), 278.0312 (^{37}Cl), found 276.0339 (100%), 278.0309 (70%).

(1-(3,4-Dichlorobenzyl)-5-nitro-1*H*-indol-3-yl)methanol (30). 5-Nitro-1*H*-indole-3-carbaldehyde (1.0 g, 5.3 mmol, 1.0 equiv.) and 3,4-dichlorobenzylbromide (1.5 g, 6.3 mmol, 1.2 equiv.) were added as described in procedure **I-B** to a suspension of

NaH (231 mg, 60% dispersion in mineral oil, 5.8 mmol, 1.1 equiv.) in DMF (40 mL). The alkylation product (1.5 g, 98%) was obtained without further purification. Following procedure **I-C**, the aldehyde (2.0 g, 5.7 mmol, 1.0 equiv.) was reduced to the alcohol with $NaBH_4$ (693 mg, 18.3 mmol, 3.2 equiv.) in methanol (600 mL), and pure product **30** (800 mg, 40% over two steps) was obtained after purification by flash column chromatography (dichloromethane/ethyl acetate 95:5) as dark yellow crystals. ^{1}H-NMR (500 MHz, $(CD_3)_2SO$): δ (ppm) = 8.63 (d, *J* = 2.28 Hz, 1H), 8.03 (dd, *J* = 2.28, 9.16 Hz, 1H), 7.71 (d, *J* = 9.16 Hz, 2H), 7.59 (m, 2H), 7.18 (dd, *J* = 2.11, 8.30 Hz, 1H), 5.50 (s, 2H), 5.14 (t, *J* = 5.46 Hz, 1H), 4.70 (d, *J* = 5.46 Hz, 2H). ^{13}C-NMR (126 MHz, $(CD_3)_2SO$): δ (ppm) = 140.7, 139.1, 138.7, 131.3, 131.0, 130.4 130.4, 129.4, 127.6, 126.5, 119.3, 117.0, 116.7, 110.7, 54.9, 48.0. HR-ESI-MS: calculated for $C_{16}H_{11}Cl_2N_2O_2^{\bullet}$ [*M*-OH]$^{\bullet}$ 333.0198 (^{35}Cl), 335.0168 (^{37}Cl), found 333.0193 (100%), 335.0161 (60%).

(1-Benzyl-5-bromo-1*H*-indol-3-yl)methanol (31). 1-Benzyl-5-bromo-1*H*-indole (100 mg, 0.35 mmol, 1.0 equiv.) was added to a solution of $POCl_3$ (40 µL, 0.43 mmol, 1.2 equiv.) in DMF (3 mL) as described in procedure **I-A**. Crude 1-benzyl-5-bromo-1*H*-indole-3-carbaldehyde (**61**) was used without further purification in the next step. Compound **61** was reduced to the alcohol **31** following procedure **I-C**, using an excess of $NaBH_4$ in methanol (50 mL). The pure product (65 mg, 60% over two steps) was obtained without further purification as a white solid. ^{1}H-NMR (500 MHz, $(CD_3)_2SO$): δ (ppm) = 7.79 (d, *J* = 1.89 Hz, 1H), 7.46 (s, 1H), 7.42 (d, *J* = 8.71 Hz, 1H), 7.30 (m, 2H), 7.22 (m, 4H), 5.38 (s, 2H), 4.91 (t, *J* = 5.48 Hz, 1H), 4.60 (d, *J* = 5.48 Hz, 2H). ^{13}C-NMR (126 MHz, $(CD_3)_2SO$): δ (ppm) = 138.1, 135.0, 129.0, 128.6, 128.5, 127.5, 127.1, 123.7, 121.7, 115.8, 112.3, 111.5, 55.1, 49.1. HR-ESI-MS: calculated for $C_{16}H_{13}BrN^{\bullet}$ [*M*-OH]$^{\bullet}$ 298.0232 (^{35}Cl), 300.0211 (^{37}Cl), found 298.0226 (100%), 300.0202 (95%).

(1-(3,4-Dichlorobenzyl)-4-methoxy-1*H*-indol-3-yl)methanol (32). 4-Methoxy-1*H*-indole-3-carbaldehyde (500 mg, 2.9 mmol, 1.0 equiv.) and 3,4-dichlorobenzylbromide (820 mg, 3.4 mmol, 1.2 equiv.) were added as described in procedure **I-B** to a suspension of NaH (123 mg, 60% dispersion in mineral oil, 3.1 mmol, 1.1 equiv.) in DMF (14 mL). The alkylation product (200 mg, 21%) was purified by flash column chromatography (dichloromethane). Following procedure **I-C**, the aldehyde (200 mg, 0.6 mmol, 1.0 equiv.) was reduced to the alcohol using $NaBH_4$ (113 mg, 3.0 mmol, 5.0 equiv.) in methanol (100 mL), and pure product **32** (150 mg, 74% over two steps)

was obtained without further purification as a pinkish solid. ^{1}H-NMR (500 MHz, $(CD_3)_2SO$): δ (ppm) = 7.57 (d, *J* = 8.30 Hz, 1H), 7.45 (d, *J* = 1.94 Hz, 1H), 7.25 (s, 1H), 7.10 (dd, *J* = 1.94, 8.30 Hz, 1H), 7.00 (m, 2H), 6.49 (dd, *J* = 2.94, 5.54 Hz, 1H), 5.35 (s, 2H), 4.75 (d, *J* = 5.33 Hz, 2H), 4.66 (t, *J* = 5.54 Hz, 1H), 3.82 (s, 3H). ^{13}C-NMR (126 MHz, $(CD_3)_2SO$): δ (ppm) = 154.1, 139.7, 137.6, 131.1, 130.8, 129.9, 129.0, 127.4, 125.1, 122.5, 116.8, 116.4, 103.4, 99.6, 56.9, 55.2, 47.8. HR-ESI-MS: calculated for $C_{17}H_{14}Cl_2NO^{\cdot}$ [*M*-OH]$^{\cdot}$ 318.0452 (^{35}Cl), 320.0423 (^{37}Cl), found 318.0448 (100%), 320.0416 (70%).

(1-(3,4-Dichlorobenzyl)-4-fluoro-1*H*-indol-3-yl)methanol (34). The aldehyde **62** (900 mg, 91%) was synthesized as a white solid, following procedure **I-B** using 4-fluoro-1H-indole-3-carbaldehyde (500 mg, 3.1 mmol, 1.0 equiv.) and 3,4-dichlorobenzylbromide (0.55 mL, 3.7 mmol, 1.2 equiv.) in a suspension of NaH (134 mg, 3.4 mmol, 1.1 equiv.) in DMF (40 mL) and purified by flash column chromatography (dichloromethane). Indole **34** was synthesized following procedure **I-C**, using **62** (100 mg, 0.3 mmol, 1.0 equiv.) and $NaBH_4$ (12 mg, 0.3 mmol, 1.0 equiv.) in THF (25 mL). The crude product was purified using flash column chromatography (heptane/ethyl acetate 8:2) to provide **34** (25 mg, 26%). ^{1}H-NMR (500 MHz, $(CD_3)_2SO$): δ (ppm) = 7.64 (d, *J* = 8.30 Hz, 1H), 7.59 (d, *J* = 2.02 Hz, 1H), 7.52 (s, 1H), 7.35 (d, *J* = 8.25 Hz, 1H), 7.21 (dd, *J* = 2.02, 8.30 Hz, 1H), 7.13 (td, *J* = 5.25, 8.01 Hz, 1H), 6.83 (dd, *J* = 6.27 Hz, 1H), 5.47 (s, 2H), 4.98 (t, *J* = 5.27 Hz, 1H), 4.75 (d, *J* = 5.20 Hz, 2H). ^{13}C-NMR (126 MHz, $(CD_3)_2SO$): δ (ppm) = 156.8 (d, *J* = 245.14 Hz), 139.7, 139.4 (d, *J* = 12.06 Hz), 131.6, 131.3, 130.54, 129.6, 128.0 (d, *J* = 3.17 Hz), 122.7 (d, *J* = 7.59 Hz), 115.7, 115.5, 115.3 (d, *J* = 3.46 Hz), 107.1 (d, *J* = 3.30 Hz), 104.7 (d, *J* = 18.98 Hz), 56.4 (d, *J* = 1.38 Hz), 48.4. ^{19}F-NMR (470 MHz, $(CD_3)_2SO$): δ (ppm) = -122.57 (dd, *J* = 5.33 Hz). HR-ESI-MS: calculated for $C_{16}H_{11}Cl_2FN^{\cdot}$ [*M*-OH]$^{\cdot}$ 306.0253 (^{35}Cl), 308.0223 (^{37}Cl), found 306.0248 (100%), 308.0215 (70%).

1-(1-(3,4-Dichlorobenzyl)-1*H*-indol-3-yl)-*N*-(2,4-dimethoxybenzyl)methanamine (35). 1-(3,4-Dichlorobenzyl)-1*H*-indole-3-carbaldehyde was prepared according to procedure **I-B**. To a solution of 1-(3,4-dichlorobenzyl)-1*H*-indole-3-carbaldehyde (0.5 g, 1.6 mmol, 1.0 equiv.) in dichloroethane (33 mL) sodium triacetoxyborohydride (1.05 g, 4.9 mmol, 3.0 equiv.), 2,4-dimethoxy benzylamine (0.74 mL, 4.9 mmol, 3.0 equiv.) and acetic acid (0.09 mL, 1.6 mmol, 1.0 equiv.) were added. The reaction mixture was stirred for 23 h and terminated by the addition of water and a saturated aqueous $NaHCO_3$-solution (10 mL). The organic layer was dried over Na_2SO_4, filtered

and concentrated *in vacuo*. The crude material was purified by non-pressurized flash column chromatography (CH_2Cl_2:CH_3OH 96:4). The product was a yellow oil (17 mg, 2%). Note: Several attempts with different pressurized column chromatography methods did not provide the clean compound. ^{1}H-NMR (500 MHz, CD_3OD): δ (ppm) = 7.56 (d, *J* = 7.90 Hz, 1H), 7.39 (d, *J* = 8.30 Hz, 1H), 7.31 (t, *J* = 5.77 Hz, 2H), 7.24 (d, *J* = 1.95 Hz, 1H), 7.14 (m, 3H), 7.03 (dd, *J* = 3.40, 8.33 Hz, 1H), 6.54 (d, *J* = 2.30 Hz, 1H), 6.48 (dd, *J* = 3.53, 8.34 Hz, 1H), 5.35 (s, 2H), 4.05 (s, 2H), 3.85 (s, 2H), 3.78 (s, 3H), 3.71 (s, 3H). ^{13}C-NMR (126 MHz, CD_3OD): δ (ppm) = 162.7, 160.3, 140.4, 137.9, 133.5, 132.5, 132.3, 131.8, 129.8, 129.4, 129.1, 127.8, 123.4, 120.9, 119.6, 118.0, 111.8, 111.1, 105.4, 99.4, 55.8, 55.8, 49.5, 48.3, 43.4. HR-ESI-MS: calculated for $C_{25}H_{25}Cl_2N_2O_2$ $[M+H]^+$ 455.1288 (^{35}Cl), 457.1258 (^{37}Cl), found 455.1290 (100%), 457.1257 (60%).

Synthesis and characterization of aminothiazoles. We previously reported the synthesis and characterization of compounds **1**, **36**, **38**, **46**, and **48**.[126] 1-(2-Amino-4-methylthiazol-5-yl)-2-bromoethan-1-one (**63**), 2-bromo-1-(2,4-dimethylthiazol-5-yl)ethan-1-one (**64**), and 2-bromo-1-(pyridin-2-yl)ethan-1-one (**65**) were synthesized following literature procedures and all data were consistent with the reported values.[176,58]

Aminothiazole formation (procedure A-A). Synthesis of aminothiazoles followed a previously reported procedure.[176] The impure mixture of α-bromoketones (1.0 equiv.) and substituted thiourea (0.95 equiv.) were dissolved in absolute ethanol. Then, *N*,*N*-diisopropylethylamine (DIPEA) (1.1 equiv.) was added, and the mixture stirred for up to three days. TLC analysis showed that the product spot turned red after irradiation with UV-light. After completion of the reaction, the solvent was evaporated, the residue diluted with ethyl acetate and filtered through Celite. The filtrate was washed with water (3 x) and saturated aqueous NaCl solution (2 x), dried over $MgSO_4$, filtered and concentrated *in vacuo*.

5-(Pyridin-4-yl)-*N*-(4-(trifluoromethyl)phenyl)thiazol-2-amine (37). Compounds 2-bromo-1-(pyridin-4-yl)ethan-1-one hydrochloride (150 mg, 0.5 mmol, 1.0 equiv.) and 1-(4-(trifluoromethyl)phenyl) thiourea (117 mg, 0.5 mmol, 1.0 equiv.) were mixed as described in procedure **A-A** in ethanol (15 mL). The pure product (172 mg, 100%) was afforded as a yellow solid without further purification. ^{1}H-NMR (500 MHz, CD_3OD): δ (ppm) = 8.80 (d, *J* = 6.90 Hz, 2H), 8.56 (d, *J* = 6.90 Hz, 2H), 8.18 (s, 1H), 7.95 (d, *J* =

8.65 Hz, 2H), 7.66 (d, *J* = 8.65 Hz, 2H). ^{13}C-NMR (126 MHz, $(CD_3)_2SO$): δ (ppm) = 163.4, 148.5, 145.5, 143.9, 142.5, 126.5 (d, *J* = 3.66 Hz), 124.6 (q, *J* = 270.96 Hz), 122.4, 121.6 (q, *J* = 31.99 Hz), 117.0, 116.6. ^{19}F-NMR (470 MHz, $(CD_3)_2SO$): δ (ppm) = -59.96. HR-ESI-MS: calculated for $C_{15}H_{11}F_3N_3S$ $[M+H]^+$ 322.0620, found 322.0613.

4-(2-((4-(Trifluoromethyl)phenyl)amino)thiazol-5-yl)benzene-1,3-diol (39). This compound was ordered from Princeton Biomolecular Research and analyzed by NMR and MS prior to IC_{50} determination. ^{1}H-NMR (500 MHz, $(CD_3)_2SO$): δ (ppm) = 10.63 (s, 1H), 10.46 (s, 1H), 9.50 (s, 1H), 8.18 (s, 1H), 7.76 (m, 2H), 7.58 (t, *J* = 8.03 Hz, 1H), 7.30 (d, *J* = 7.44 Hz, 1H), 7.25 (s, 1H), 6.37 (m, 1H), 6.31 (d, *J* = 8.46 Hz, 1H). ^{13}C-NMR (126 MHz, $(CD_3)_2SO$): δ (ppm) = 161.5, 158.1, 156.3, 147.4, 141.6, 130.3, 129.8 (q, *J* = 31.54 Hz), 128.9, 124.2 (q, *J* = 272.27 Hz), 120.4, 117.4 (q, *J* = 3.52 Hz), 112.8 (q, *J* = 4.03 Hz), 111.9, 107.0, 102.9, 102.3. ^{19}F-NMR (470 MHz, $(CD_3)_2SO$): δ (ppm) = -61.41. HR-ESI-MS: calculated for $C_{16}H_{12}F_3N_2O_2S$ $[M+H]^+$ 353.0566, found 353.0559.

***N*^{2}-(3-Methoxyphenyl)-4'-methyl-[5,5'-bithiazole]-2,2'-diamine (40).** Compounds **63** (401 mg, 1.7 mmol, 1.0 equiv.) and 1-(3-methoxyphenyl)thiourea (310 mg, 1.7 mmol, 1.0 equiv.) were mixed as described in procedure **A-A** in ethanol (15 mL). Purification by preparative HPLC (H_2O:CH_3OH + 0.05% formic acid, gradient 5% to 100% CH_3OH) afforded the product (27 mg, 7%) as a light-pink solid. ^{1}H-NMR (500 MHz, $(CD_3)_2SO$): δ (ppm) = 10.23 (s, 1H), 8.13 (s, 1H, formic acid), 7.54 (t, *J* = 2.21 Hz, 1H), 7.19 (t, *J* = 8.12 Hz, 1H), 7.01 (dd, *J* = 1.57, 8.12 Hz, 1H), 6.96 (s, 2H), 6.60 (s, 1H), 6.52 (dd, *J* = 2.21, 8.25 Hz, 1H), 3.76 (s, 3H), 2.32 (s, 3H). ^{13}C-NMR (126 MHz, $(CD_3)_2SO$): δ (ppm) = 165.8, 163.1 (formic acid), 162.1, 159.9, 144.2, 143.6, 142.3, 129.6, 114.3, 109.2, 106.8, 102.5, 99.8, 55.0, 17.1. HR-ESI-MS: calculated for $C_{14}H_{15}N_4OS_2$ $[M+H]^+$ 319.0682, found 319.0674.

***N*^{2}-(3-Chloro-2-methylphenyl)-4'-methyl-[5,5'-bithiazole]-2,2'-diamine (41).** Compounds **63** (752 mg, 3.1 mmol, 1.0 equiv.) and 1-(3-chloro-2-methylphenyl)thiourea (619 mg, 3.1 mmol, 1.0 equiv.) were mixed as described in procedure **A-A** in ethanol (31 mL). Purification by preparative HPLC (H_2O/CH_3OH + 0.05% formic acid, gradient from 5% to 100% CH_3OH) afforded the product (240 mg, 23%) as a pink solid. ^{1}H-NMR (500 MHz, $(CD_3)_2SO$): δ (ppm) = 9.51 (s, 1H), 8.13 (s, 1H, formic acid), 7.87 (q, *J* = 3.10 Hz, 1H), 7.18 (q, *J* = 5.32 Hz, 2H), 6.93 (s, 2H), 6.58 (s, 1H), 2.31 (s, 3H), 2.27 (s, 3H). ^{13}C-NMR (126 MHz, CD_3OD): δ (ppm) = 165.8,

164.3, 163.3 (formic acid), 144.3, 143.5, 141.0, 134.0, 127.2, 127.1, 124.1, 120.1, 114.2, 100.5, 17.0, 15.0. HR-ESI-MS: calculated for $C_{14}H_{14}ClN_4S_2$ [*M*+H]$^+$ 337.0343 (^{35}Cl), 339.0313 (^{37}Cl), found 337.0334 (100%), 339.0302 (30%).

2',4'-Dimethyl-*N*-(4-(trifluoromethyl)phenyl)-[5,5'-bithiazol]-2-amine (42). Compounds **64** (100 mg, 0.4 mmol, 1.0 equiv.) and 1-(4-(trifluoromethyl)phenyl)thiourea (79 mg, 0.4 mmol, 1.0 equiv.) were mixed as described in procedure **A-A** in ethanol (4 mL). Purification by flash column chromatography (petroleum benzine/ethyl acetate, gradient 0% to 100% ethyl acetate) afforded the product (112 mg, 73%) as a yellow solid. ^{1}H-NMR (500 MHz, $(CD_3)_2SO$): δ (ppm) = 10.76 (s, 1H), 7.85 (d, *J* = 8.50 Hz, 2H), 7.69 (d, *J* = 8.50 Hz, 2H), 7.09 (s, 1H), 2.61 (s, 3H), 2.54 (s, 3H). ^{13}C-NMR (126 MHz, $(CD_3)_2SO$): δ (ppm) = 162.4, 162.1, 147.3, 144.2, 142.3, 126.4 (q, *J* = 3.59 Hz), 126.4, 124.7 (q, *J* = 270.86 Hz), 121.2 (q, *J* = 31.94 Hz), 116.6, 104.8, 18.7, 17.0. ^{19}F-NMR (470 MHz, $(CD_3)_2SO$): δ (ppm) = -59.88. HR-ESI-MS: calculated for $C_{15}H_{13}F_3N_3S_2$ [*M*+H]$^+$ 356.0497, found 356.0491.

4-(2-((3,4-Dimethylphenyl)amino)thiazol-4-yl)benzene-1,2-diol (43). This compound was ordered from Princeton Biomolecular Research and analyzed by NMR and MS prior to IC_{50} determination. ^{1}H-NMR (500 MHz, $(CD_3)_2SO$): δ (ppm) = 9.97 (s, 1H), 9.08 (s, 1H), 9.04 (s, 1H), 7.46 (dd, *J* = 2.13, 8.28 Hz, 1H), 7.39 (d, *J* = 2.13 Hz, 1H), 7.30 (d, *J* = 2.05 Hz, 1H), 7.17 (dd, *J* = 2.05, 8.28 Hz, 1H), 7.07 (d, *J* = 8.20 Hz, 1H), 6.91 (s, 1H), 6.76 (d, *J* = 8.20 Hz, 1H), 2.22 (s, 3H), 2.16 (s, 3H). ^{13}C-NMR (126 MHz, $(CD_3)_2SO$): δ (ppm) = 163.2, 150.7, 145.5, 145.3, 139.4, 136.8, 130.1, 129.1, 126.7, 118.5, 117.3, 115.8, 114.6, 113.6, 99.6, 20.0, 18.9. HR-ESI-MS: calculated for $C_{17}H_{17}N_2O_2S$ [M+H]$^+$ 313.1005, found 313.0992.

***N*-Phenyl-5-(pyridin-2-yl)thiazol-2-amine (44).** Compounds **65** (156 mg, 0.6 mmol, 1.0 equiv.) and 1-(2,5-dimethylphenyl)thiourea (100 mg, 0.6 mmol, 1.0 equiv.) were mixed as described in procedure **A-A** in ethanol (5 mL). The pure product (157 mg, 95%) was obtained after workup as an orange-brown solid. ^{1}H-NMR (500 MHz, $(CD_3)_2SO$): δ (ppm) = 9.37 (s, 1H), 8.57 (dt, *J* = 1.27, 4.78 Hz, 1H), 7.87 (m, 2H), 7.78 (m, 1H), 7.47 (s, 1H), 7.30 (ddd, J = 2.24, 5.57, 6.63 Hz, 1H), 7.11 (d, *J* = 7.55 Hz, 1H), 6.85 (dd, *J* = 1.27, 7.55 Hz, 1H), 2.30 (s, 3H), 2.23 (s, 3H). ^{13}C-NMR (126 MHz, $(CD_3)_2SO$): δ (ppm) = 165.9, 152.2, 150.1, 149.4, 139.2, 137.4, 135.6, 130.6, 126.1, 124.4, 122.6, 122.0, 120.2, 106.7, 21.0, 17.7. HR-ESI-MS: calculated for $C_{16}H_{16}N_3S$ [*M*+H]$^+$ 282.1059, found 282.1054.

***N*-(3-Chloro-2-methylphenyl)-5-(pyridin-2-yl)thiazol-2-amine (45).** Compounds **65** (20 mg, 0.1 mmol, 1.0 equiv.) and 1-(3-chloro-2-methylphenyl)thiourea (20 mg, 0.1 mmol, 1.0 equiv.) were mixed as described in procedure **A-A** in ethanol (5 mL). The pure product (20 mg, 66%) was obtained after workup as an orange solid. ^{1}H-NMR (500 MHz, $(CD_3)_2SO$): δ (ppm) = 9.60 (s, 1H), 8.57 (d, *J* = 4.65 Hz, 1H), 8.01 (d, *J* = 8.02 Hz, 1H), 7.86 (m, 2H), 7.53 (s, 1H), 7.29 (ddd, *J* = 1.72, 5.80, 6.99 Hz, 1H), 7.25 (d, *J* = 8.02 Hz, 1H), 7.20 (d, *J* = 7.44 Hz, 1H), 2.34 (s, 3H). ^{13}C-NMR (126 MHz, $(CD_3)_2SO$): δ (ppm) = 165.2, 152.1, 150.1, 149.4, 140.9, 137.3, 134.0, 127.4, 126.9, 124.0, 122.6, 120.3, 120.0, 107.5, 15.0. HR-ESI-MS: calculated for $C_{15}H_{13}ClN_3S$ $[M+H]^+$ 302.0513 (^{35}Cl), 304.0484 (^{37}Cl), found 302.0490 (100%), 304.0456 (30%).

***N*-(3,4-Dimethylphenyl)-4-(pyridin-2-yl)thiazol-2-amine (47).** Compounds **65** (390 mg, 1.39 mmol, 1.0 equiv.) and 1-(3,4-dimethylphenyl)thiourea (250 mg, 1.39 mmol, 1.0 equiv.) were mixed as described in procedure **A-A** in ethanol (10 mL). The pure product (388 mg, 95%) was obtained after workup as a yellow-brown solid. ^{1}H-NMR (500 MHz, $(CD_3)_2SO$): δ = 10.13 (s, 1H), 8.55 (m, 1H), 7.97 (d, *J* = 7.85 Hz, 1H), 7.90 (td, *J* = 1.89, 7.57 Hz, 1H), 7.48 (m, 2H), 7.42 (d, *J* = 1.89 Hz, 1H), 7.31 (ddd, *J* = 1.07, 4.80, 7.46 Hz, 1H), 7.10 (d, *J* = 8.24 Hz, 1H), 2.23 (s, 3H), 2.18 (s, 3H). ^{13}C-NMR (126 MHz, $(CD_3)_2SO$): δ = 163.8, 152.2, 150.3, 149.4, 139.0, 137.5, 136.7, 130.0, 129.2, 122.7, 120.4, 118.5, 114.7, 106.5, 19.9, 18.8. HR-ESI-MS: calculated for $C_{16}H_{16}N_3S$ $[M+H]^+$ 282.1059, found 282.1047.

Method I: Cell culture and growth-inhibition assay of *P. falciparum*. *P. falciparum* 3D7 parasites (Wellcome Trust Dundee) and all derived transgenic cell lines (see below) were maintained in continuous culture at 37 °C and an atmosphere consisting of 90% N_2, 5% O_2, and 5% CO_2 as described previously[177] with modifications.[178] Parasites were maintained in 25 mM 4-(2-hydroxyethyl)-1-piperazineethanesulfonic acid (HEPES) and 11.9 mM sodium bicarbonate buffered RPMI 1640 medium supplemented with D-glucose (11 mM), hypoxanthine, Albumax-II (0.5% w/v), and 10 µg/mL gentamicin. Fresh 0+ blood was provided by the Brazilian blood bank ProSangue (Brazil) and in agreement with the ethics committee at ICB-USP. The antiplasmodial effect of the *de novo* synthesized compounds was validated against *P. falciparum* 3D7 strain conducting SYBR Green I (Invitrogen) drug assays as reported.[179,180] Briefly, two-fold serial dilutions of compounds were prepared in 96-well plates in a range of 200 µM to 0.4 µM in triplicate and incubated for 96 h under normal growth conditions using an initial parasitemia of 0.5% and a hematocrit of 2% in a

volume of 100 µL per well. Parasite proliferation was determined by measuring DNA load via fluorescence in the wells through addition of 100 µL lysis buffer supplemented with SYBR Green I (0.02% v/v) and incubation for 1 h at room temperature in the dark. Fluorescence was quantified using a CLARIOstar plate reader (BMG Labtech, Germany) at excitation and emission wavelength bands of 485 (± 9) and 530 (± 12) nm, respectively. Focal and gain adjustment was performed using the non-treated controls (highest expected fluorescence signal). Data was acquired via the CLARIOstar (V5.20) and MARS software, manually normalized, and plotted using the nonlinear regression curve fit implemented in GraphPad Prism as described below in more detail (version 7.00 for Windows, GraphPad Software, La Jolla California USA, www.graphpad.com). Non-treated parasites, highest solvent concentration on parasites, and highest drug concentration in medium were used as controls for maximal growth, solvent control, and native drug fluorescence, respectively.

Method II: Cell culture and growth-inhibition assay of *P. falciparum*. *P. falciparum* strain 3D7 was obtained through the MR4 as part of the BEI Resources Repository, NIAID, NIH (www.mr4.org) and strain NF54 was generously supplied by D.A. Fidock (Columbia University). Parasites were cultured in a 2% suspension of human erythrocytes and RPMI 1640 (Sigma) medium supplemented with 27 mM sodium bicarbonate, 11 mM glucose, 5 mM HEPES, 1 mM sodium pyruvate, 0.37 mM hypoxanthine, 0.01 mM thymidine, 10 µg/mL gentamicin, and 0.5% Albumax (Gibco) at 37°C, 5% O_2/5% CO_2/90% N_2 atmosphere as previously described.[181,182] Asynchronous cultures of *P. falciparum* 3D7 and NF54 were diluted to 1% parasitemia and treated with DXPS inhibitors at concentrations ranging from 97.7 nM–250 µM. Assays were performed in opaque 96-well plates in 100 µL culture volume. After three days, parasite growth was quantified by measuring DNA content using PicoGreen (Life Technologies) as described.[183] Fluorescence was measured on a FLUOstar Omega microplate reader (BMG Labtech) at 485 nm excitation and 528 nm emission.

Method III: Cell culture and growth inhibition assay of *P. falciparum*. Two laboratory strains *of P. falciparum*, the chloroquine-sensitive 3D7 and the multi-resistant Dd2 (obtained from MR4) were kept in complete culture medium (RPMI 1640, 25 mM HEPES, 2 mM L-glutamine, 50 µg/mL gentamicin and 0.5% w/v AlbuMAX) at 37 °C, 5% CO_2 and 5% oxygen at 2.5% hematocrit with daily change of medium.[181] All compounds were dissolved in DMSO at stock solutions between 25 and 100 mM; the reference drug chloroquine diphosphate (MW: 515.86 g/mol) was diluted in distilled

water. Further dilutions were prepared in complete culture medium so that final concentrations of solvent did not interfere with parasite growth. Antiplasmodial activity of the different compounds was tested in a drug-sensitivity assay against the two laboratory strains using the histidine-rich protein 2 (HRP2) assay as described previously.[184,185] In brief: 96-well plates were pre-coated with the different compounds in a threefold dilution before ring-stage parasites were added in complete culture medium at a hematocrit of 1.5% and a parasitemia of 0.05% in a total volume of 225 µL per well. After three days of incubation, plates were frozen until analyzed by HRP2-ELISA. All compounds were evaluated in duplicate in at least two independent experiments. Statistics: The 50% IC_{50} was determined by analyzing the nonlinear regression of log concentration–response curves using the drc-package v0.9.0 of R v2.6.1.[186]

HepG2 cell culture and viability assay as counter screens. HepG2, A549 or HEK293 cells (2 x 105 cells per well) were seeded in 24-well, flat-bottomed plates. Culturing of cells, incubations and OD measurements were performed as described previously with small modifications.[187] 24 h after seeding the cells, the incubation was started by the addition of compounds in a final DMSO concentration of 1%. The metabolic activity of the living cell mass was determined after 48 h. At least three independent measurements were performed for each compound. The IC_{50} values were determined during logarithmic growth using GraphPad Prism software. All experiments were performed at least in triplicate and data reported represent the mean ± SD.

Metabolic Stability Tests in Human Liver S9 Fraction. For the evaluation of combined phase I and phase II metabolic stability, the compound (1 µM) was incubated with 1 mg/mL pooled liver S9 fraction (Xenotech), 2 mM NADPH, 1 mM UDPGA, 10 mM $MgCl_2$, 5 mM GSH and 0.1 mM PAPS at 37 °C for 0, 5, 15, 30 and 60 min. The metabolic stability of testosterone (1 µM), verapamil (1 µM) and propranolol (1 µM) were determined in parallel to confirm the enzymatic activity of the S9 fraction. The incubation was stopped by precipitation of S9 enzymes with two volumes of cold acetonitrile containing internal standard (150 nM diphenhydramine). Samples were stored on ice for 10 min, and precipitated protein was removed by centrifugation (15 min, 4 °C, 4,000 rpm). Concentration of the remaining test compound at the different time points was analyzed by LC-MS/MS (TSQ Quantum Access MAX, Thermo Fisher, Dreieich, Germany) and used to determine half-life ($t_{1/2}$).

Kinetic solubility determination. The desired compounds were sequentially diluted in DMSO in a 96-well plate. 3 µL of each well were transferred into another 96-well plate and mixed with 147 µL of PBS. Plates were shaken for 5 min at 600 rpm at room temperature (r.t.), and the absorbance at 620 nm was measured. Absorbance values were normalized by blank subtraction and plotted using GraphPad Prism 8.4.2 (GraphPad Software, San Diego, CA, USA). Solubility (S) was determined based on the First X value of AUC function using a threshold of 0.005.

IDP rescue assay in P. falciparum. *P. falciparum* cultures were treated as described in **Method II**. For IDP (Isoprenoids.com) rescue experiments, 125 µM IDP was added to the appropriate wells for the duration of the experiment. The well-described DXR inhibitor FSM was used as a positive control. IC_{50} values were calculated by nonlinear regression analysis using GraphPad Prism software. All experiments were performed at least in triplicate and data reported represent the mean ± SD.

***P. falciparum* sample preparation for mass spectrometry analysis.** *P. falciparum* strain 3D7 was cultured at 37 °C in 30 mL volumes in 100 mm tissue culture dishes (Techno Plastic Products) at 4% hematocrit until >6.5% parasitemia. Cultures were synchronized until >75% of parasites were in ring stage growth, and then treated for 12 h with or without compound **1** at 7.65 µM (5 x the 3D7 IC_{50}) in triplicate. Cultures were lysed with 5% saponin, the parasite pellets washed with 1x phosphate-buffered saline (PBS; Gibco), and the pellets stored at –80 °C.

***E. coli* sample preparation for mass spectrometry analysis.** Overnight cultures of *E. coli* ΔTolC were diluted 1:1000 in LB media and grown at 37 °C until reaching mid-logarithmic phase (OD_{600} = 0.67–7.2). Cultures were then treated with or without compound **1** at 48 µM (10 x the IC_{50}) in triplicate for 2 h while shaking at 37 °C. For normalization, the OD_{600} was determined after 2 h of treatment with the inhibitor. Cells were pelleted by centrifugation for 5 min at 3000 x g at 4 °C. The supernatants were removed, and cells were washed twice with 1x PBS. The supernatants were removed, and the pellets stored at –80°C until analysis.

LC-MS/MS analysis. Metabolites were extracted via the addition of glass beads (212–300 u) and 600 µL chilled H_2O: chloroform: methanol (3:5:12 v/v) spiked with PIPES (piperazine-N,N′-bis(2-ethanesulfonic acid) as internal standard. The cells were disrupted with the TissueLyser II instrument (Qiagen) using a microcentrifuge tubes adaptor set pre-chilled for 2 min at 20 Hz. The samples were then centrifuged at 16,000

g at 4 ºC, the supernatants collected, and pellet extraction repeated once more. The supernatants were pooled and 300 µL chloroform and 450 µL of chilled water were added to the supernatants. The tubes were vortexed and centrifuged. For *E. coli* samples, the upper layer was transferred to a new tube and dried using a speed-vac. For *P. falciparum* samples, the upper layer was transferred to a 2-mL tube PVDF filter (ThermoFisher, F2520-5) and centrifuged for 5 min at 4,000 x g at 4 ºC. The samples were then transferred to new tubes and dried using a speed-vac. Both *E. coli and P. falciparum* pellets were re-dissolved in 100 µL of 50% acetonitrile.

For pyruvate analysis from the *E. coli* samples, the LC separation was done on the Shimadzu Nexera II using the Poroshell 120 (Agilent, 2.7 µm, 150 X 2.1 mm) flowing at 0.5 mL/min. The gradient of the mobile phases A (20 mM ammonium acetate, pH 9.8, 5% ACN) and B (100% acetonitrile) was as follow: 85% B for 1 min, to 40% B in 9 min, hold at 40% B for 2 min, then back to 85% B in 0.5 min. For the TCA/glycolysis/pentose phosphate pathway metabolites from the *P. falciparum* samples, the same mobile phases were used on a Luna-NH2 column (3 µm, 150 x 2 mm, Phenomenex) at a flow rate of 1 mL/min. The gradient was as follow: 80% B for 1 min, to 30% B in 6 min, hold at 30% B for 5 min, then back to 80% B in 0.5 min. Finally, for the MEP metabolites, same column and mobile phases were used as the latter, except the gradient was as follow: 60% B for 1 min, to 6% B in 3 min, hold at 6% B for 5 min, then back to 60% B in 0.5 min. The LC system was interfaced with a Sciex QTRAP 6500+ mass spectrometer equipped with a TurboIonSpray (TIS) electrospray ion source. Analyst software (version 1.6.3) was used to control sample acquisition and data analysis. The QTRAP 6500+ mass spectrometer was tuned and calibrated according to the manufacturer's recommendations. Metabolites were detected using MRM transitions that were previously optimized using standards. The instrument was set-up to acquire in negative mode. For quantification, an external standard curve was prepared using a series of standard samples containing different concentrations of metabolites and fixed concentration of the internal standard. The limit of detection for deoxyxylulose 5-phosphate (DOXP), methylerythritol phosphate (MEP), cytidine diphosphate methylerythritol (CDP-ME), and methylerythritol cyclodiphosphate (MEcPP) was 0.0064 µM for a 10 µL injection volume. The limits of detection for a 5 µL injection volume for the TCA cycle, glycolytic and pentose phosphate metabolites were as follows: aconitate, malate, succinate = 0.31 µM; glucose-6-phosphate and glycerol-3-phosphate = 0.78 µM; citrate, glucose-1-phosphate and fructose-6-phosphate = 1.56

μM; ribose-5-phosphate and ribulose-5-phosphate = 2.34 μM; 2-phospho gylceric acid, 3-phospho glyceric acid and lactate = 3.12 μM; fumarate, pyruvate, phosphoenolpyruvate and sedoheptulose-7-phosphate = 6.25 μM. T-tests were used to test for significance between untreated (UNT) and drug-treated bacteria (Prism).

Generation of transgenic parasite lines. The open reading frame (ORF) encoding 1-deoxy-D-xylulose-5-phosphate synthase (*Pf*DXPS; PF3D7_1337200) was amplified from genomic DNA isolated from unsynchronized *P. falciparum* 3D7 cultures using the Platinum PCR SuperMix High Fidelity (Invitrogen). Forward and reverse primers contained restriction sites for *Kpn*I and *Avr*II in sense and antisense orientation, respectively (Oligonucleotides *pf*DXPS-Kpn1-S: GAGAGGTACCATGATTTTTAATTATGTGTTTTTTAAGAAC; *pf*DXPSmyc-Avr2-AS: GAGACCTAGGTTACAGGTCCTCCTCTGAGATCAGCTTCTGCTCGCCTGTAGGAT TATTTTTAAGATAATTTTTAATTCTATTGAC). PCR products and the transfection vector pARL1a-hDHFR P*f*ARG-GFP were digested with *Kpn*I and *Avr*II, purified (Gel extraction Kit and PCR purification kit; QIAGEN), and cloned into the transfection vector yielding the construct for overexpression pARL-DXS-strep. XL 10-Gold *E. coli* ultra-competent cells (Agilent Technologies) were transformed with the generated construct to amplify the plasmid and colonies checked using restriction analysis and sequencing of the plasmid. Bacterial clones carrying the overexpression construct and the empty pARL1a vector (MOCK plasmid) were amplified in over-night cultures, isolated (Plasmid Maxi Kit; QIAGEN) and subsequently used to transfect *P. falciparum* 3D7 ring-stage parasites, as already described.[188] Briefly, 120 μg plasmid DNA was centrifuged, air dried, the pellet resuspended in TE-buffer and cytomix reagent and mixed with the *P. falciparum* culture. Parasites were transfected using electroporation and selected with WR 99210. The generation and characterization of the *Pf*TPK overexpression cell line has been reported before.[189]

Quantification of DXPS overexpression in *P. falciparum* 3D7 transgenic cell lines. Total RNA was isolated from *P. falciparum* using TRIzol Reagent (Invitrogen). First-strand cDNA synthesis was prepared using a RevertAid™H Minus First Strand cDNA Synthesis Kit (Thermo Fisher Scientific) from a total of 1 μg of RNA. Real-time PCR was performed with 1 μL of cDNA, 7.5 μL SYBR green fast master mix (Applied Biosystems), 0.45 μL (10 μM) each of the forward and reverse primers and 5.6 μL DEPC-treated water, on an Applied Biosystems® QuantStudio® 3 Real-Time PCR System (Thermo Fisher Scientific). After cycling, melting curve analysis was

performed. The relative transcription levels of MOCK (control) and the DXS (DXS-pARL) were determined by the ΔΔCT method.[190] Target transcription levels were normalized to the housekeeping gene, *Pf*Aldolase, as endogenous control reference as reported before.[189] Sequences of primers were as follows: *Pf*Aldolase forward: tgtaccaccagccttaccag; reverse: ttccttgccatgtgttcaat; DXS-pARL forward: tcagtggagagggtgaaggt; reverse: gttggccatggaacaggtag. Three technical replicates from three biological replicates were performed for each experiment. Expression was found to be six times higher in comparison to the MOCK control cell line.

Growth-inhibition assay of transgenic *P. falciparum* cell lines. *P. falciparum* cultures were treated as described in **Method I**. For target specification towards *Pf*TPK and *Pf*DXPS, compounds were tested in comparison against overexpressing cell lines and the respective MOCK line containing only the transfected vector backbone. Parasite viability/proliferation was determined Analysis of the IC_{50} values and interpretation of the curves was performed as described in **Growth inhibition and IDP rescue assays of *E. coli***.

Nonlinear regression fit and analysis of dose-response drug assays of compound 1, 2 and 3. Nonlinear regression as implemented in GraphPad Prism 7.00 (log(inhibitor) vs. response – Variable slope (four parameters)) was used to fit the measured data to interpolate the IC_{50} value from the curve. No specific model was applied. Data was pre-processed by normalizing according to the following formula

$$y_{normalized} = \frac{y - y_{minimum}}{y_{maximum} - y_{minimum}}$$

Where y is the fluorescence signal in each well, $y_{minimum}$ the background fluorescence, and $y_{maximum}$ the highest measured fluorescence signal in the untreated wells. Drug concentrations (in µM) were transformed to the log(10)of the values. Means of each independent experiment were plotted as individual values, and the SD of the mean from the means shown as error bars. The 95% CI is indicated as measure of error for the calculated IC_{50}s. In case of transgenic cell lines, the built-in comparison Akaike's Information Criteria (AICc) method was applied to the Log IC_{50}s of the different cell lines. The test calculates a percentage probability of the simpler model "Log IC_{50} is the same for datasets" being correct. The test for *homoscedasticity* was performed to confirm if no weighting of values was appropriate.

Computational Methods, homology model of *Pf*DXPS. As template for the homology model of *Pf*DXPS the crystal structure of DXPS from *D. radiodurans* (2o1x, chain B) was used because the corresponding region in the active center of the likewise related DXPS from *E. coli* (2o1s) strongly deviates in comparison to the DXPS from *M. tuberculosis*. Subsequently, the actual homology model was generated by the SWISS-MODEL web service, yielding a QMEAN4 value of −6.43.[191,192] The magnesium atom was added manually using the coordinates from the template.

3.5.6 Acknowledgments

We thank Selina Wolter, Jeannine Jung, Dennis Jener, Andreas M. Kany, and Jörg Haupenthal at the HIPS for performing the cytotoxicity, solubility, and metabolic stability assays and Ravindra P. Jumde for proofreading of the manuscript.

Notes:

The authors declare no competing financial interest.

This work has been supported by The Netherlands Organisation for Scientific Research (LIFT grant: 731.015.414, A. K. H. H. and R. M. G.) and the Helmholtz Association's Initiative and Networking fund. D. Z. acknowledges support from the CSC Fellowship. A.O.J. is supported by NIH/NIAID R01-AI103280, R21-AI123808, and R21-AI130584, and A.O.J. is an Investigator in the Pathogenesis of Infectious Diseases (PATH) of the Burroughs Wellcome Fund. Further, the authors acknowledge the financial support provided by Fundação de Amparo à Pesquisa do Estado de São Paulo (FAPESP) via the grants 2015/26722-8, 2016/24790-9, 2017/03966-4, 2018/08820-0, 2020/12277-0.

3.5.7 Conclusions and outlook

To summarize, we found three new hit classes that inhibited the growth of *P. falciparum*. The indole class is toxic to human HepG2 cells in low micromolar concentrations and improvements in activity on *P. falciparum* goes hand in hand with increasing toxicity. Work on this class should therefore not be continued. The oxime class has a better ADMET profile but more synthetic effort is needed to improve activity. Replacement of the oxime with a hydroxyl group resulted in the best derivative and this class is a potential new starting point for further development. Closely related structures have been patented as urease inhibitors but otherwise have not been investigated.[193] The most promising aminothiazole class could not be improved by

synthesis so far. To guide optimization efforts, identification of the target is necessary. Therefore, additional work on synthesizing a probe was performed that can be found in appendix Chapter 6.2. Our on-going efforts to validate the target of the aminothiazole class in *M. tuberculosis* is also presented in the Appendix.

4 Conclusions and outlook

Finding solutions against AMR is becoming more urgent as pharmaceutical companies drop out of the research due to high costs and low returns. At the beginning of each successful drug candidate stands a hit-identification process. Here, it is important to carefully evaluate the potential of each compound, but also to use a variety of methods to confirm activity before moving the hit forward into lead development. For this thesis, a variety of hit-identification strategies were employed to identify compounds with good properties for further development.

The MEP pathway is a promising target for the development of new drugs. DXPS is its first enzyme and there are several advantages to focus on this branch-point in the pathway. However, it has several challenging features and only a few good inhibitors are known so far.

To find new inhibitors for *M. tuberculosis* DXPS, a focused fragment library was tested by STD-NMR and the hits were validated by SPR. The class of 2-aminopyridines had the best properties (good binding, high solubility) and a selection of closely related commercially available or synthesized derivatives was further analyzed. Several compounds have estimated K_D value below 500 µM, but their binding site is unknown. Two potential growth vectors were identified by determining the binding epitope in STD-NMR and analyzing the differences in binding behavior in SPR that will be used to explore this compound class further. Attempts at obtaining crystal structures were so far unsuccessful, so a selection of derivatives will be synthesized to improve binding and achieve inhibition of enzyme activity.

For this work, an alternative DXPS activity assay was implemented in our laboratory. In contrast to the DXSP-IspC-coupled assay, this HPLC/MS-based assay only uses DXPS and therefore, no IspC inhibitors can interfere with the assay results. The optimal HPLC-MS/MS method was determined and the assay conditions were optimized to identify inhibitors. A reference compound was successfully identified that validated the assay setup and that showed an excellent IC_{50} of 33 µM. This compound can now be used as a control in the assay and can be further investigated synthetically. It should be possible to perform MOI studies with this assay as is routinely done with the DXPS-IspC-coupled assay. For that the concentration of the substrates have to be varied while determining the IC_{50} value of compounds. A shift in IC_{50} values with changing

substrate concentrations will indicate (un)competitive inhibition. If this gives reliable results has to be tested further, preferably in comparison to the coupled assay. Initial experiments were promising, but the conditions have to be optimized.

In cooperation with Atomwise, a VS campaign was performed against Δ*Mt*DXPS. Two compounds were investigated more closely. The first was the best binder in SPR experiments against *Mt*DXPS and it showed some inhibition against *Dr*DXPS in the DXPS-IspC-coupled assay (Chapter 3.4, compound **1**). Its solubility limit is 100 µM and all experiments indicated that its IC_{50} value was in the same range. Later, it turned out that the assay results are very unreliable when insoluble compounds are investigated. At that point 30 compounds had been synthesized to determine the SAR, but all are inhibiting *Dr*DXPS below 50% at 50–200 µM. However, they are active against *E. coli* ΔTolC. One Eastern-ring derivative was more active than the original hit (MIC = 28 µM) with a MIC of 18 µM. Derivatization on other parts of the molecule led to a loss of activity. Removing the linker to the Eastern ring of the molecule, resulted in the best activity against *E. coli* K12. Similar compounds are known in literature as β-lactamase inhibitors, which opens an interesting starting point for the development of dual inhibitors. The second investigated compound was identified after testing all VS hits again in the HPLC-MS/MS-based assay (Chapter 3.4, compound **4**). The compound showed good inhibition of 25 µM. It was ordered as a solid and purified but inhibition could not be confirmed. Some measurements were good enough and suggested an IC_{50} value of 47 µM, but determination of the MOI was not possible as the inhibition in those experiments was below 30% at 100 µM. A second round of VS was performed and initial data suggest that there are hits with a similar core structure to the previously identified hit (Chapter 3.4, compound **4**). Overall, this project showed that the HPLC-MS/MS-based assay has to be investigated further and steps have to be taken to improve its reproducibility. However, a robust synthetic route was established for making derivatives of the first investigated hit that could be relevant for other targets in the future. The Gram-negative activity of the reduced-linker compound is promising and should be further analyzed in combination with its activity against β-lactamase.

In previous studies, LBVS had resulted in three small-molecule hit classes against *M. tuberculosis*. During this thesis, a selection of derivatives of these three hit classes was synthesized and their SAR was explored against blodd-stage *P. falciparum*. We improved the activity of the oxime and the indole class 2.5-fold and 30-fold,

respectively. In addition, we found a structurally different compound derived from the oxime class that has good pharmacokinetic properties and should be investigated further. The aminothiazole hit turned out to be the most potent against *P. falciparum* and no improvement of its activity could be made. Although the hits were inhibiting *Mt*DXPS as we have shown previously, the DXPS homologue in *P. falciparum* could not be confirmed as the target despite using a variety of methods. However, the discussed compounds effectively kill the chloroquine resistant *P. falciparum* strain Dd2, which indicates a different target and makes the compounds good candidates for further development. We analyzed the hits in the PolyPharmacology Browser and found three alternative targets FabI, KasA and VCP. Additional experiments are needed to verify these targets. The results have been summarized and have been submitted to *European Journal of Medicinal Chemistry*.

In conclusion, DXPS is not an easy target to address. The common activity assays can be unreliable when working with insoluble compounds and results are varying greatly between measurements unless the compounds are fully inhibiting at a soluble concentration. These issues should be taken into consideration when working with DXPS. However, following different routes for hit identification can help to have a broad spectrum of starting points for further development. In this thesis, it was shown how important it is to start from different angles, to change methods and go back to previously eliminated compounds and re-evaluate them if necessary. If an enzyme-based assay does not yield the desired results it might also be necessary to switch to a binding affinity assay or to a phenotypic approach worrying about the target later. To successfully fight AMR, it is important to find compounds with good activities and promising physicochemical properties and base the development of lead compounds on reliable and reproducible data.

5 Experimental section

5.1 Supplementary information Chapter 3.2

Numbering of compounds in this chapter follows the numbering in Chapter 3.2.

5.1.1 Gene expression and protein purification of Δ*Mt*DXPS

Gene expression and protein purification of native and truncated *M. tuberculosis* DXPS followed previously reported protocols.[55]

5.1.2 SMILES codes of HEFL compounds

Table S 1: List with SMILES codes of all tested library compounds.

Cpd.	SMILES	Cpd.	SMILES
1	Clc1ncnc2c1[nH]cc2	**63**	Clc1c(ccc(c1)C#N)O
2	Clc1nc(cnc1)[n]2nccc2	**64**	Ic1c([n](nc1)C)C(=O)NN
3	Clc1c(ncc(c1C)Cl)N	**65**	Clc1nc2nc[nH]c2c(n1)N
4	Brc1cnc(nc1)N2CCNCCC2	**66**	Brc1c(ncc(c1)C(=O)O)N
5	Ic1c(ncc(c1)F)N	**67**	Brc1cnccc1C(=O)O
6	Brc1c(c(ccc1)N)O	**68**	Clc1nc(cnc1)C(=O)O
7	Clc1ncnc2[nH]ccc21	**69**	Clc1nc(ccc1N)C
8	FC(F)(F)c1cnc(c(c1)Cl)N	**70**	Clc1[o]c(cc1)C(=O)O
9	Brc1cnc(c(c1)CO)N	**71**	Ic1c([nH]nc1C)C
10	Brc1cnc(c(c1)C(=O)O)N	**72**	[s]1c(ncc1Br)N.Br
11	Brc1cnc(cc1)N	**73**	Clc1c(ncnc1C(=O)O)N
12	Brc1c[nH]c(c1)C(=O)N2CCOCC2	**74**	Clc1c(cc(cc1)N)C(=O)O
13	[s]1nc(c(n1)N2CCOCC2)Cl	**75**	Clc1nccc(c1)C(=O)O
14	[s]1c(cc(c1)Br)CN2CCNCC2.Cl.Cl	**76**	Brc1c(nccc1)C
15	Brc1cnc(nc1)N2CCNCC2	**77**	Clc1nnc(cc1C(=O)O)Cl
16	[S](=O)(=O)(N2CCNCC2)c1[s]c(cc1)Cl.Cl	**78**	Clc1cnc(c(c1)C(=O)O)OC
17	Brc1cncnc1	**79**	Clc1[nH]c2c(n1)N(C(=O)N(C2=O)C)C
18	Clc1ncnc(c1Cl)N	**80**	Clc1c([n](nc1C(=O)O)C)C
19	Ic1c(nccc1)N	**81**	Clc1ncc(cc1)CO
20	Ic1c(cncc1)F	**82**	Clc1cnc(c(c1)[N+](=O)[O-])O
21	Clc1cnc(c(c1)OC)OC	**83**	Clc1c(ncc(c1)Cl)C(=O)O
22	Clc1cnc(cc1)NC(=O)C(=O)O	**84**	Clc1c(ccc(c1)N)C(=O)O
23	Clc1c(cc(cc1)C(=O)O)O	**85**	Brc1c(ncnc1O)O
24	Clc1c(c(cc(c1)Cl)CN)N	**86**	Brc1c(nccc1)C(=O)O
25	Brc1c(cccc1O)O	**87**	Clc1c(nc(cc1)NC(=O)C)C(=O)O
26	Brc1c(cc(c(c1)C(=O)O)O)O	**88**	Brc1c[n](nc1N)C
27	Clc1c2c(cc(c1)NC)OCO2.Cl	**89**	Clc1nc(ccc1C(=O)O)C
28	[S](=O)(=O)(N)c1c(ccc(c1)C(=O)O)Cl	**90**	Brc1c[nH]c(c1)C(=O)O
29	ClC1=C(C(=O)N(C(=O)N1C)C)C#N	**91**	Brc1[n]2c(nc1)C=NC=C2
30	ClC1=CC(=O)N(C(=O)N1)C	**92**	[s]1c(c(cc1)Cl)C(=O)O
31	[S](=O)(=O)([n]1nccc1Br)N(C)C	**93**	Brc1cnc(c(c1)C(=O)O)OC

Cpd.	SMILES	Cpd.	SMILES
32	Clc1c[n](nc1)CC(C)C(=O)O	**94**	Clc1nc(ccc1C(=O)N)C
33	[s]1cnc(c1)Cl	**95**	Clc1ncc(cc1)CC(=O)O
34	Brc1c([nH]nc1)C#N	**96**	[S](=O)(=O)(C)c1nc(c(cn1)Cl)C(=O)O
35	Brc1c(n[o]c1C)C	**97**	[s]1c(ccc1CN2CCNCC2)Cl
36	Brc1n[n](cc1)C	**98**	Clc1ncnc(c1)N2CCC(CC2)O
37	Brc1c[n](nc1)c2[nH]nnn2	**99**	Ic1c(nc(nc1C)O)O
38	Brc1c2[n](nc1)C=CC=N2	**100**	Clc1ccncc1.Cl
39	Clc1[n]2c(nc1)C=CC=C2	**101**	[S](=O)(=O)(C)c1c(ccc(c1)[S](=O)(=O)C)Cl
40	Brc1[n]2c(nc1)C=CC=N2	**102**	Clc1cncc(c1)C(=O)O
41	Clc1c2c(ccc1)NC(=O)C2=O	**102**	Clc1nc(cnc1C)C
42	Clc1c2c(ccc1)C(=O)C(=O)N2	**104**	Clc1ccc(cc1)C(=O)N2CCOCC2
43	Clc1nc(c[o]1)C(=O)OCC	**105**	Clc1ncccn1
44	ClC1=CC(=O)N(C(=O)N1C)C	**106**	Clc1ncc(cn1)Cl
45	Clc1ncc(cc1)CN2CCNCC2.Cl.Cl	**107**	Ic1c(nccc1)F
48	[S](=O)(=O)(N)c1c([n](nc1C)C)Cl	**108**	Clc1c(cccc1)[C@@H](O)C(=O)O
46	Clc1c[n](nc1)CCCN.Cl	**109**	Clc1nc(cc(n1)OC)OC
47	Brc1c[n](nc1)C(C)C(=O)O	**110**	Brc1cnc(cc1)C(=O)O
49	Clc1nc(ccc1)C(=O)O	**111**	Clc1ccc(cc1)C(N)CC
51	Clc1ccc(cc1)O	**112**	Brc1cnc(cc1)N2CCN(CC2)C
50	Clc1c(cccc1)C(N2CCN(CC2)C)CN	**113**	Clc1cnc(nc1)O.Cl
52	Brc1n[o]c(c1)CN.Cl	**114**	Clc1cncc(c1C(=O)O)Cl
53	Brc1n[nH]c(n1)CCC(=O)O	**115**	Clc1nccc(c1)C#N
54	Brc1n[n](c(n1)NN)C	**116**	Clc1nccnc1
56	Brc1c(cncc1)N	**117**	Clc1cc2c(cc1CO)OCO2
55	Fc1c(c(ccc1C)Cl)CN	**118**	ClC1=CC=Cc2[n]1nnn2
57	Clc1c(ccc(c1)OC)CN	**119**	Brc1c(nc(cc1)N)C(=O)O
58	Clc1c([n](nc1[N+](=O)[O-])CC(=O)O)C	**120**	Clc1cc[n+](cc1)[O-]
59	Brc1c([n](nc1)C)C(=O)O	**121**	Clc1cnc(cc1O)O
60	Ic1c(c(ncc1)F)C(=O)O	**122**	Brc1c2c(ccc1)CNC2.Cl
61	Brc1cnc(c(c1)C(=O)O)O	**123**	Clc1ncccc1C(=O)O
62	Brc1c(nc(nc1)O)O	**124**	Clc1ncc(nc1)C(=O)O

5.1.3 Kinetic-solubility determination

The desired compounds were sequentially diluted in DMSO in a 96-well plate. 3 µL of each well were transferred into another 96-well plate and mixed with 147 µL of 2-[4-(2-hydroxyethyl)piperazin-1-yl]ethane-1-sulfonic acid (HEPES) buffer (see below). Plates were shaken at room temperature (r.t.) for 5 min at 600 revolutions per minute (rpm), and the absorbance at 620 nm was measured after 72 h. Absorbance values were normalized by blank subtraction and plotted using GraphPad Prism 8.4.2 (GraphPad Software, San Diego, CA, USA).

5.1.4 Solubility of initial 14 fragment hits

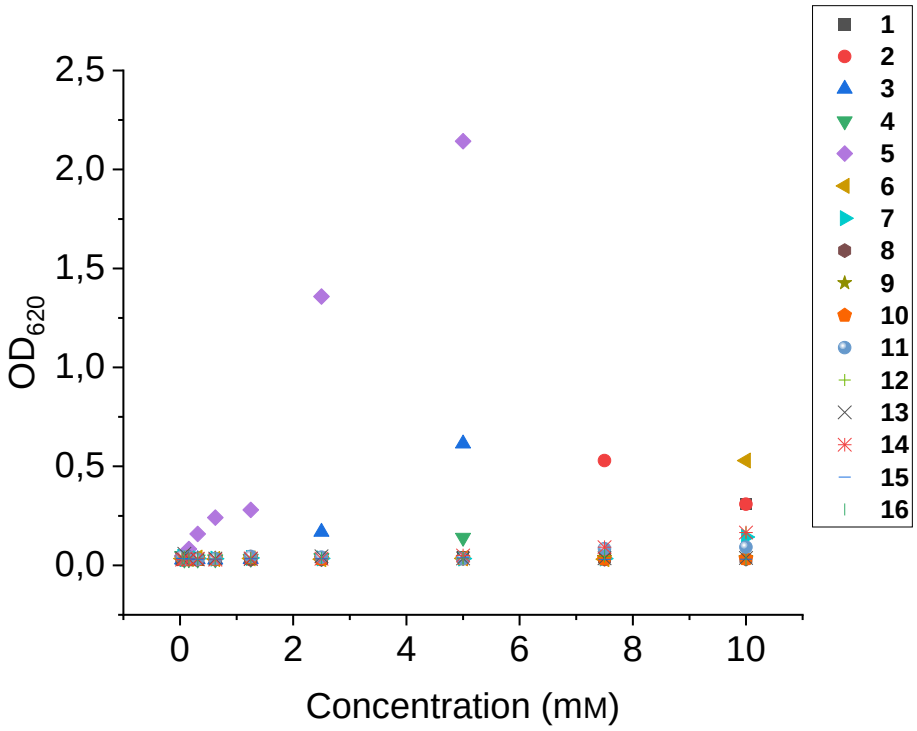

Figure S 1: Solubility of hit fragments in SPR buffer after three days (50 mM HEPES, 150 mM NaCl, 1 mM $MgCl_2$, 0.05% Tween20, 5% DMSO, pH = 8.0).

5.1.5 STD-NMR procedure

The STD experiments were recorded at 298 K on a Bruker Fourier spectrometer (500 MHz). The samples contained a 100-fold excess of compound (250 µM screening, 500 µM single compound) relative to Δ*Mt*DXPS (2.5 µM screening, 5.0 µM single compound). The STD-NMR buffer differed slightly between the screening and the single-compound measurements. Screening buffer: 25 mM Tris(hydroxymethyl)-aminomethan (Tris), 150 mM NaCl, 0.5 mM $MgCl_2$, pD = 8.0. Single compound buffer: 25 mM Tris, 100 mM NaCl, 1 mM $MgCl_2$, pD = 8.0. The compounds were dissolved in $(CD_3)_2SO$ and added to the buffer to reach a final concentration of 5% $(CD_3)_2SO$. Screening mixtures were chosen based on assumed chemical shift. In all cases, this assumption led to a difference in chemical shift of more than 0.4 ppm or (in case of mixture 9) compounds with very similar chemical shifts were both not binding.

All experiments were performed using the *stddiffesgp.3* pulse program by Bruker. Blank spectra were recorded for all mixtures and single compounds to establish the parameters at which no residual compound peaks were visible. The screening experiments were all recorded with a carrier set at 0 ppm for the on-resonance and

−40 ppm for the off-resonance irradiation. Selective protein saturation was carried out at 2 s (D20 parameter in TopSpin) by using a train of 50 ms Gauss-shaped pulses, each separated by a 1 s delay (D1 parameter in TopSpin). The conditions for the single compound measurements are listed below (**Table S 2**). The difference in intensity due to saturation transfer was quantified using $STD_{effect} = (I_0 - I_{sat})/I_0$ and constitutes an indication of binding.[85] I_{sat} is the intensity of a signal in the on-resonance NMR spectrum, and I_0 is the intensity of one signal in the off-resonance or reference NMR spectrum. The STD_{effect} was used to define binding (STD_{effect} > 50%) and to determine the binding epitopes for the single compounds.

5.1.6 Spectra of STD-NMR screening

Compounds were measured only in buffer without water suppression. Peak between 3.5 and 4 ppm is Tris. Green = binder. Red = non-binder. Gray = off-resonance. Black = STD spectra. “Best” (highest integration value) binder in each mixture was used as reference and set to 1. All compounds with an amplification factor less than 50% were defined as non-binders. When artefacts of aliphatic proton peaks were visible in the blank spectra, only the aromatic peaks were used.

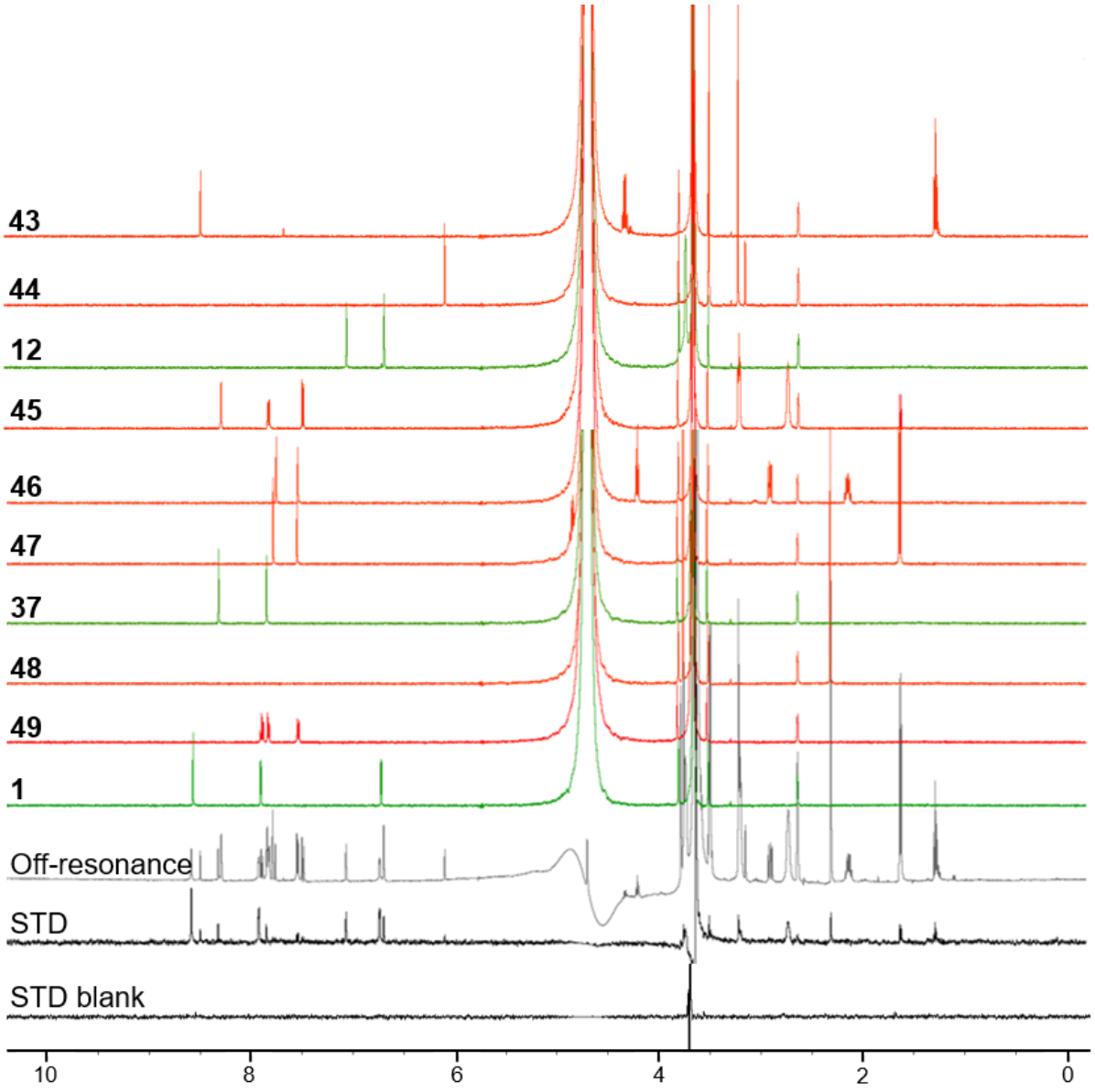

Figure S 2: ^{1}H NMR and STD-NMR spectra of mixture 1.

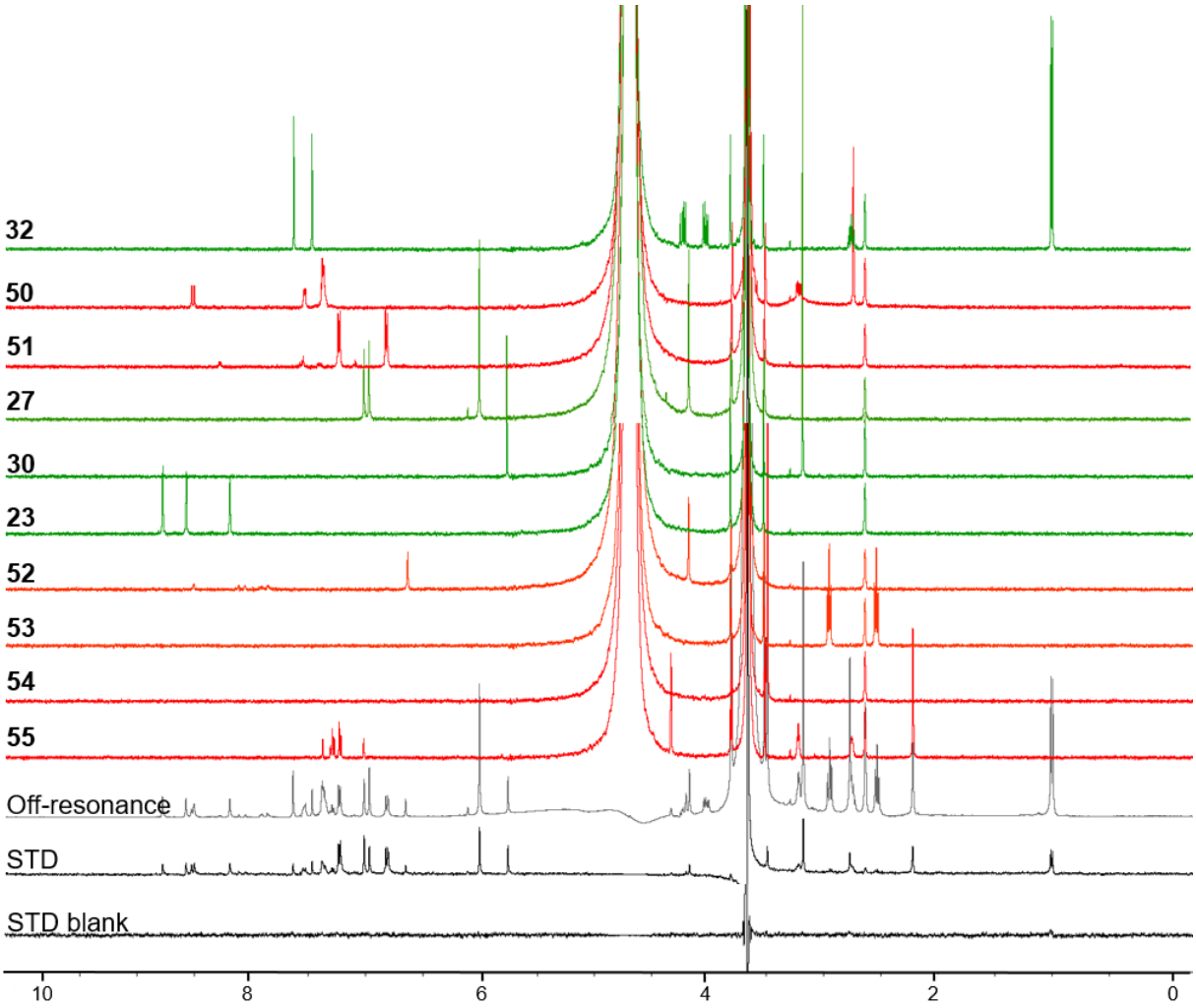

Figure S 3: ^{1}H NMR and STD-NMR spectra of mixture 2. Impurities in **51** and **52** were not taken into account.

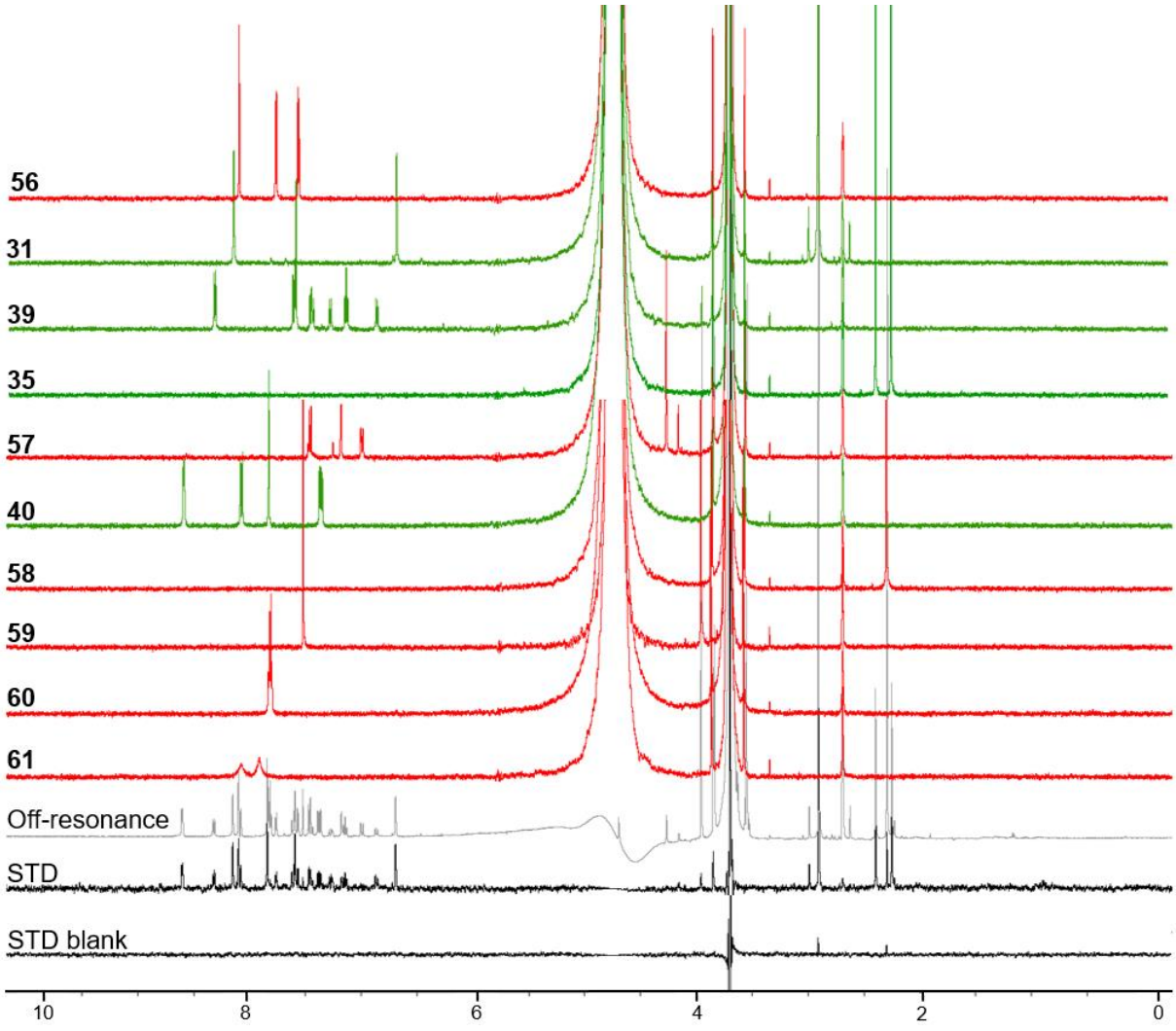

Figure S 4: ^{1}H NMR and STD-NMR spectra of mixture 3.

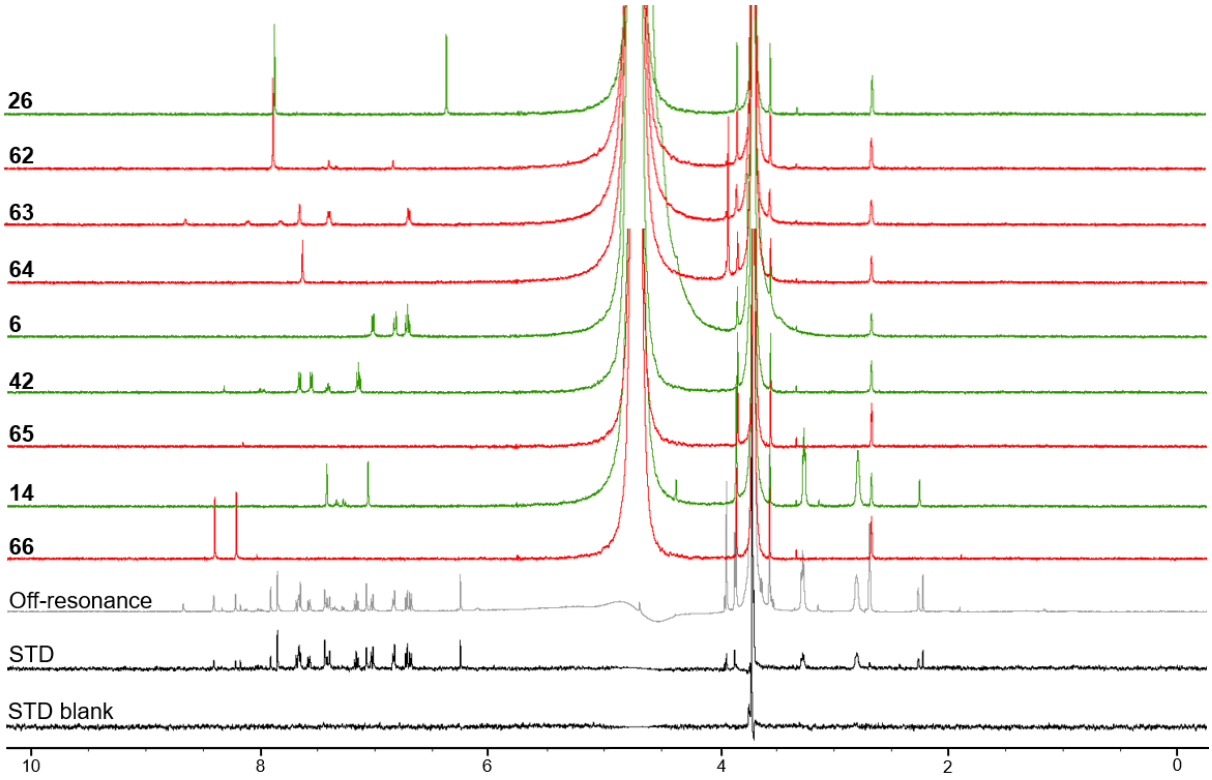

Figure S 5: ^{1}H NMR and STD-NMR spectra of mixture 4. Impurities in **14**, **42**, **62** and **63** were not taken into account.

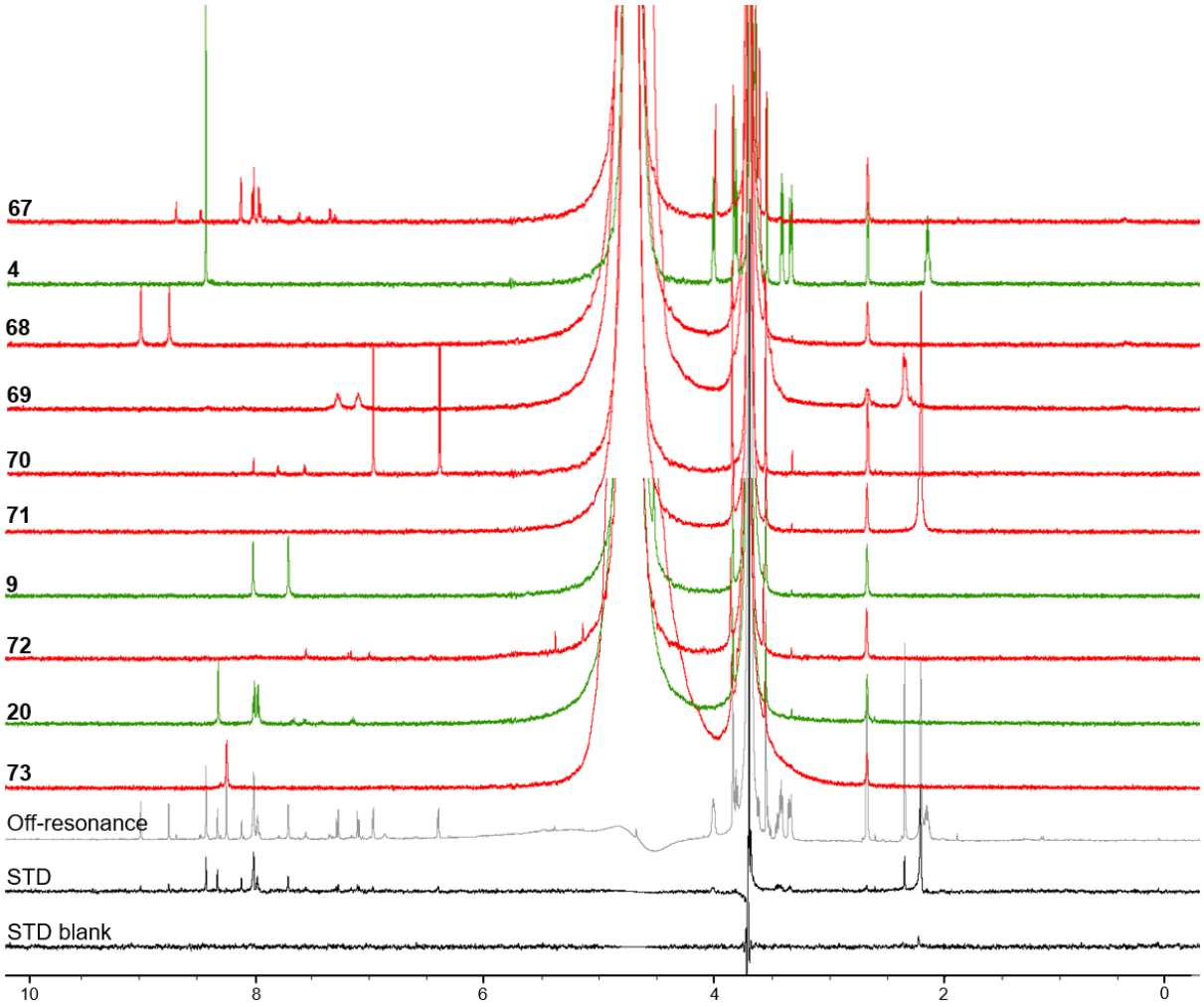

Figure S 6: ^{1}H NMR and STD-NMR spectra of mixture 5. Impurities in **20**, **67** and **70** were not taken into account.

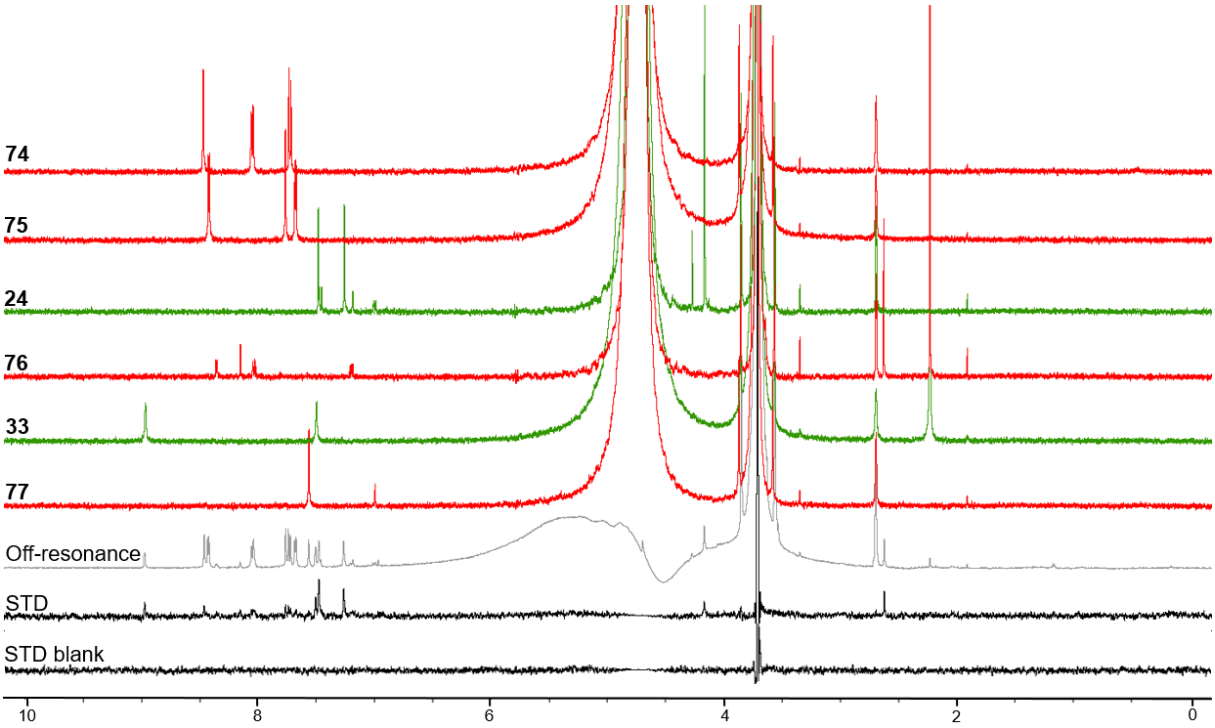

Figure S 7: ^{1}H NMR and STD-NMR spectra of mixture 6. Impurities in **24** were not taken into account.

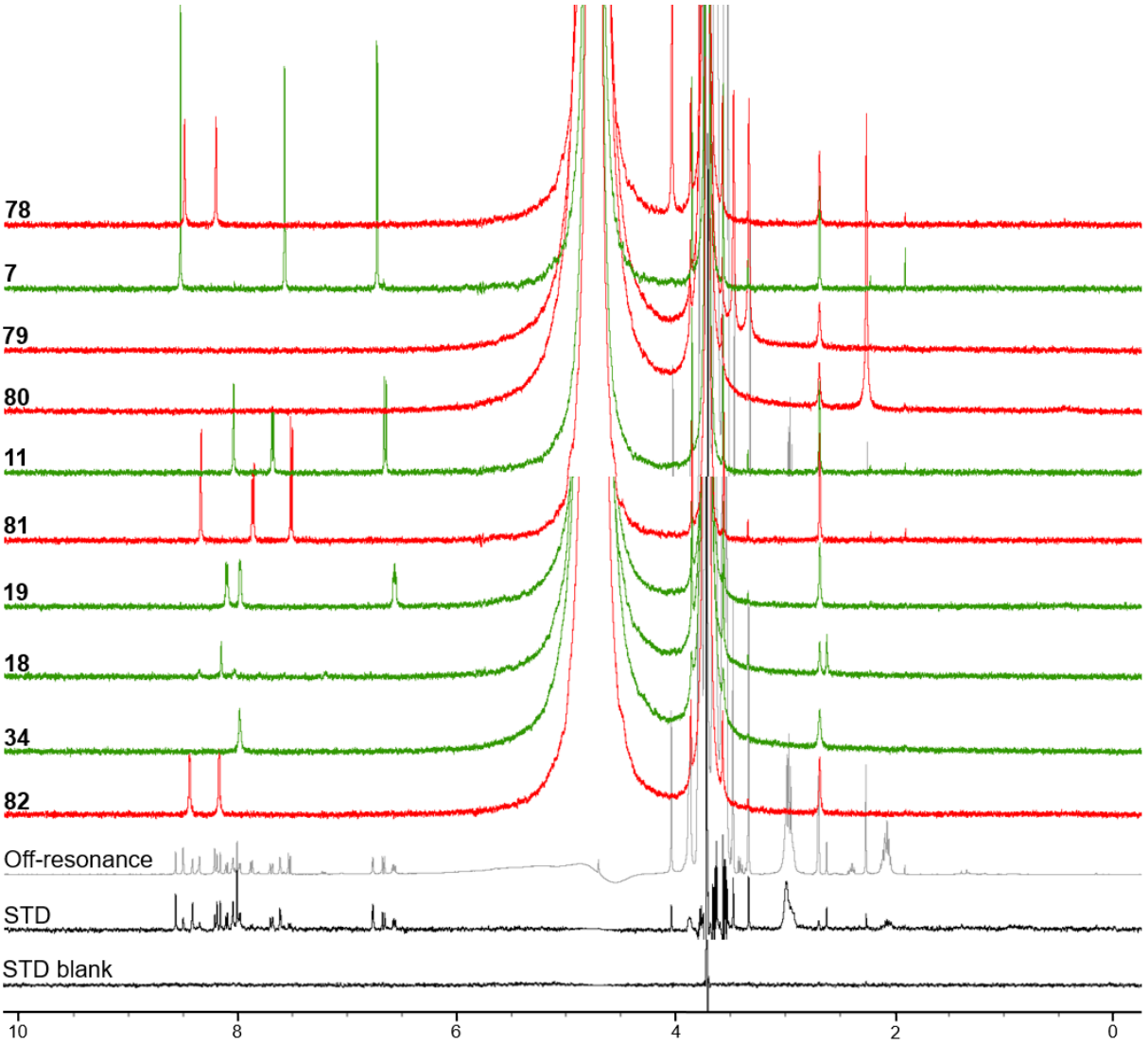

Figure S 8: ^{1}H NMR and STD-NMR spectra of mixture 7.

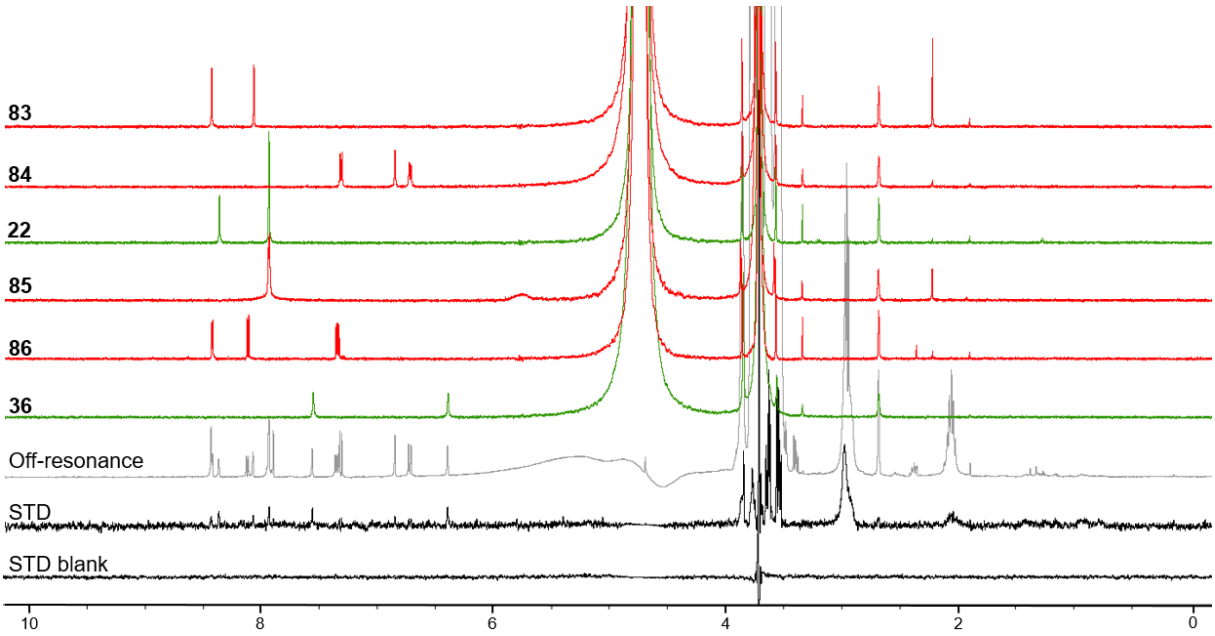

Figure S 9: ^{1}H NMR and STD-NMR spectra of mixture 8.

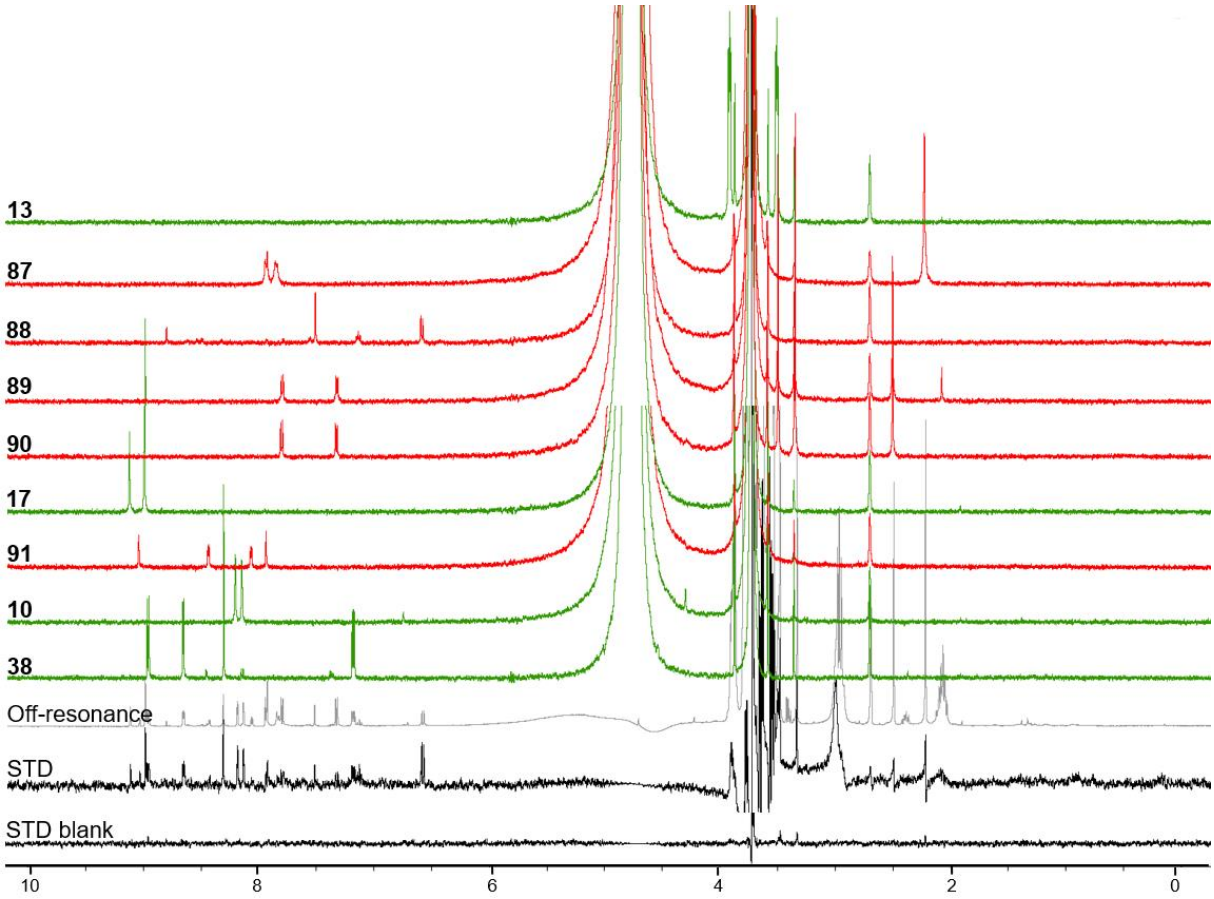

Figure S 10: ^{1}H NMR and STD-NMR spectra of mixture 9.

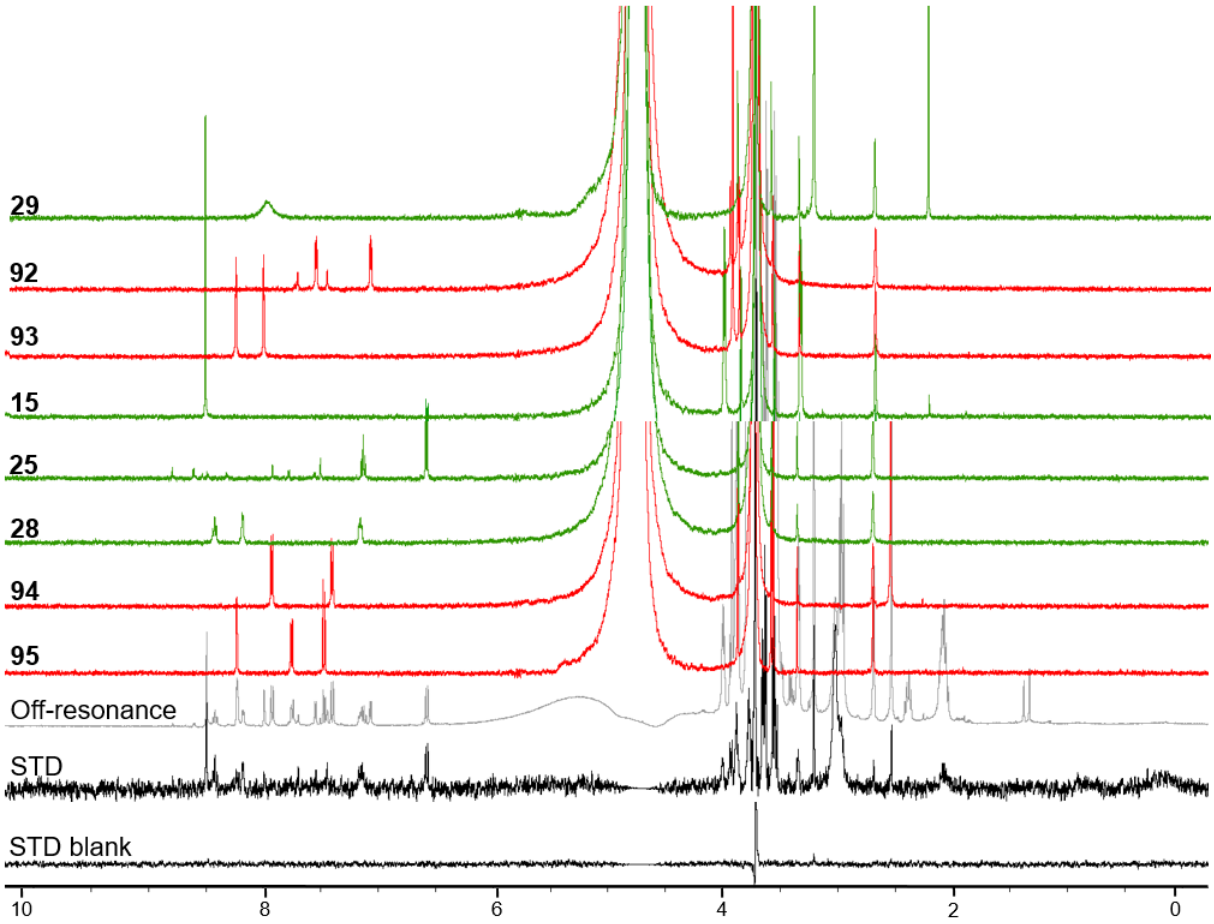

Figure S 11: ^{1}H NMR and STD-NMR spectra of mixture 10.

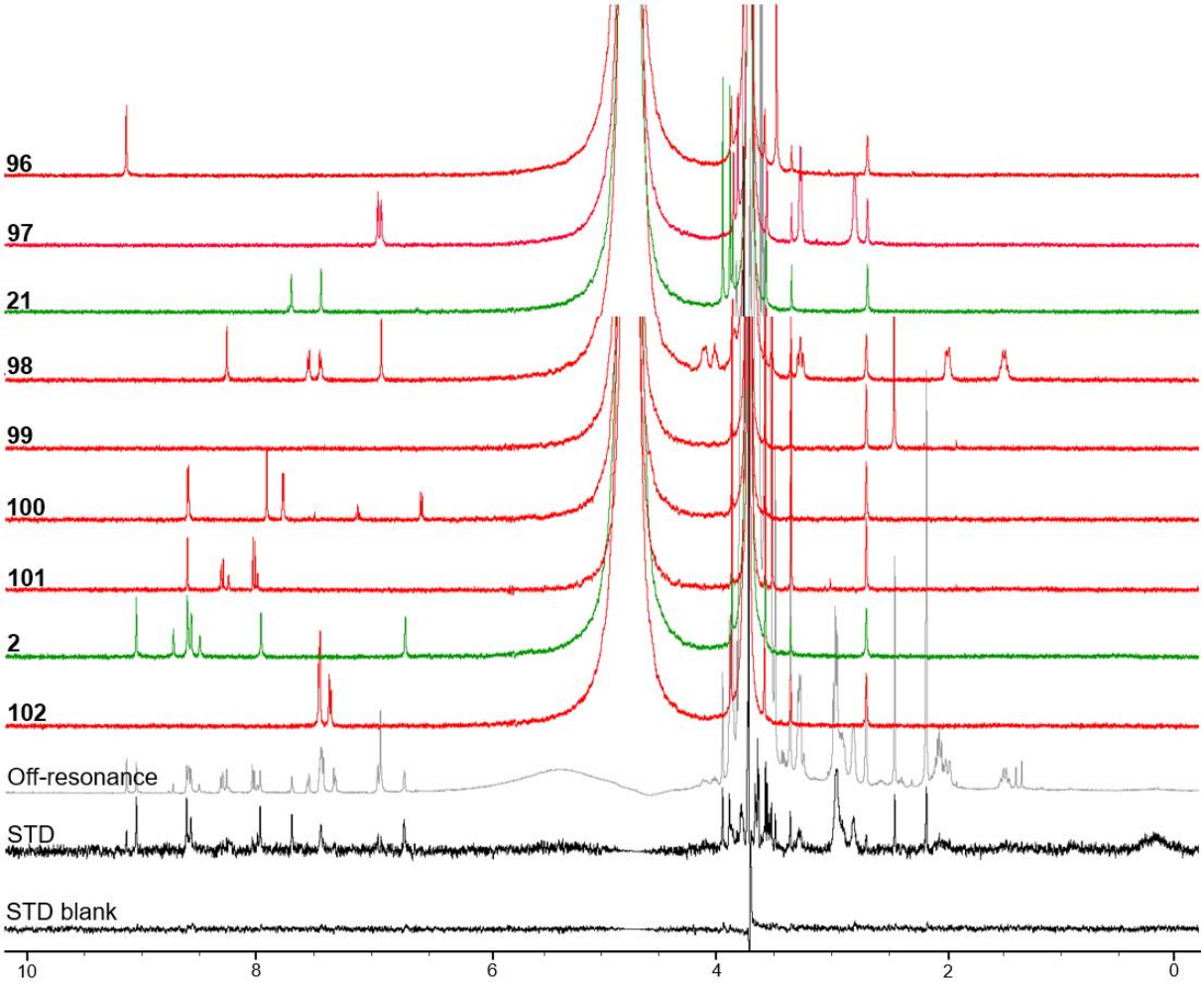

Figure S 12: ^{1}H NMR and STD-NMR spectra of mixture 11.

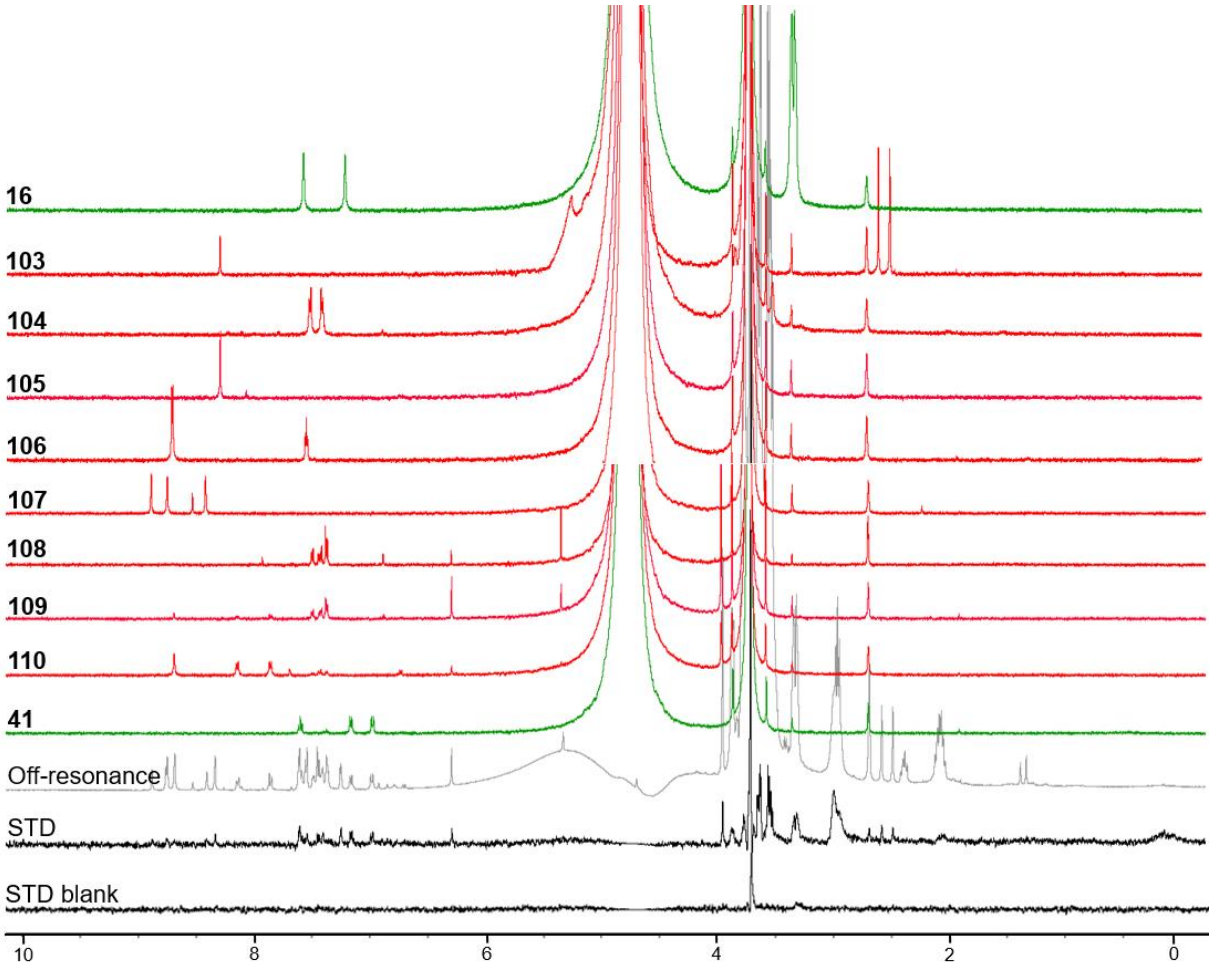

Figure S 13: ^{1}H NMR and STD-NMR spectra of mixture 12. Impurities in **108**, **109**, **110** were not taken into account.

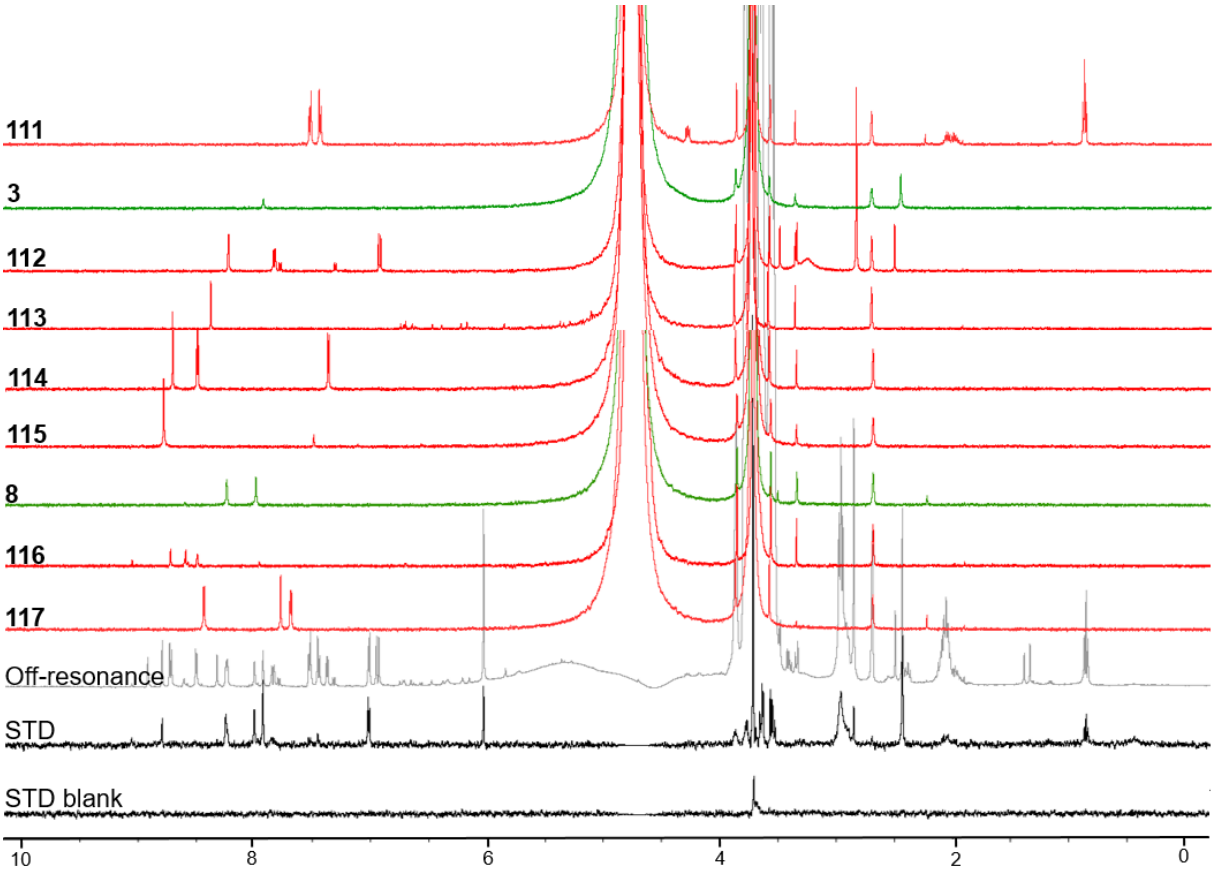

Figure S 14: ^{1}H NMR and STD-NMR spectra of mixture 13.

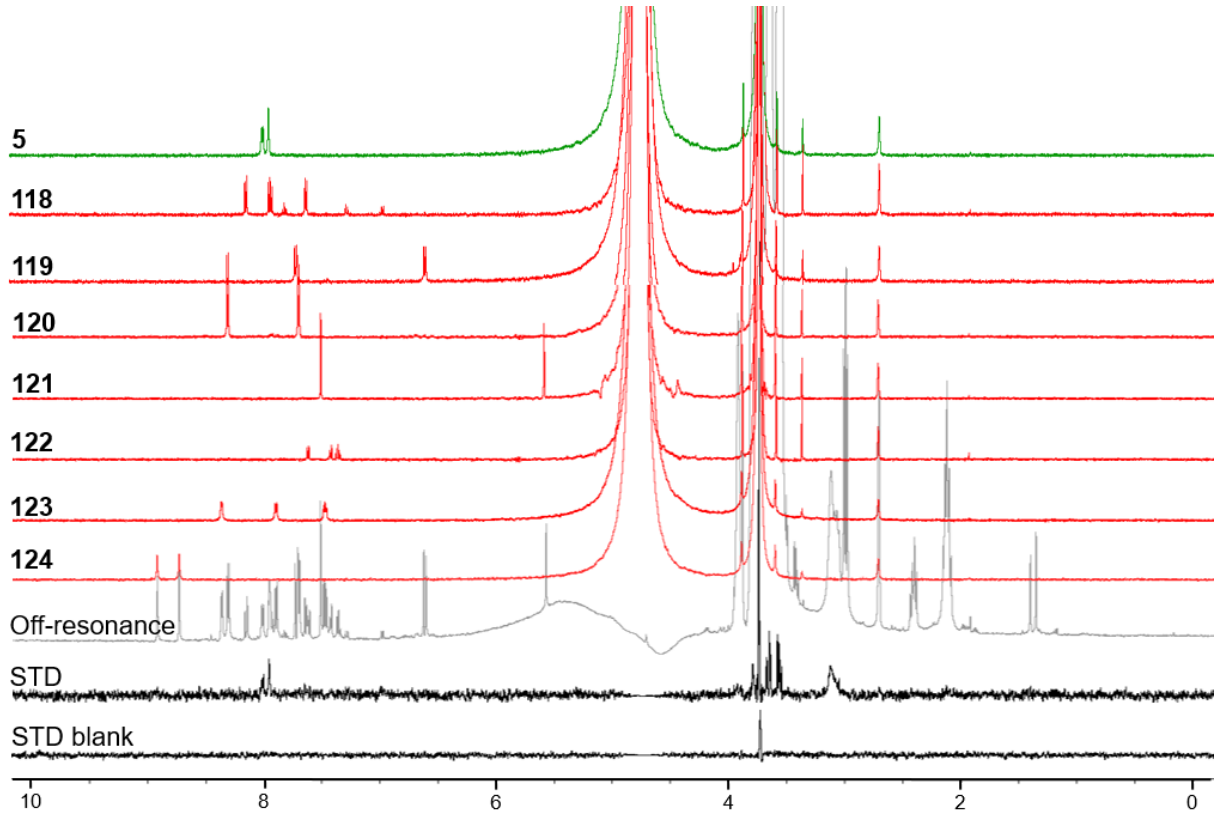

Figure S 15: ^{1}H NMR and STD-NMR spectra of mixture 14.

5.1.7 STD-NMR experiments of single compounds

Table S 2: STD-NMR conditions for single measurements of hit fragments. Buffer in D_2O: 25 mM tris(hydroxymethyl)-aminomethan (Tris), 100 mM NaCl, 1 mM $MgCl_2$, pD = 8.0. Concentration of the ligand was 500 µM, number of scans was 128 in all cases. Measurements with protein were done with 256 scans.

	Fragment	On/Off irr. (ppm)	D1 (s)	D20 (s)	Binding
1	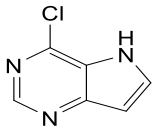	0/–40	2	2	**Figure S 16**
2	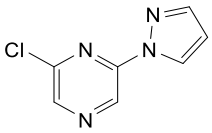	0/–40	2	2	**Figure S 17**
3	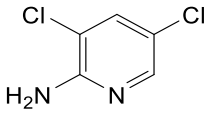	0/–40	2	2	**Figure S 18**
7	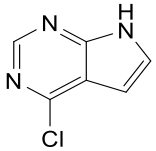	–2/–40	2	0.5	**Figure S 19**
8	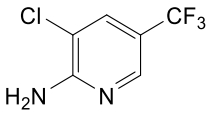	0/–40	2	2	**Figure S 20**
9	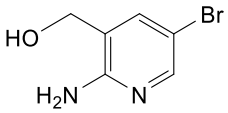	–2/–40	2	2	**Figure S 21**
10	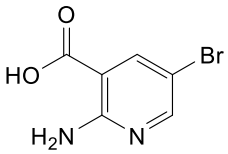	0/–40	2	2	**Figure S 22**
11	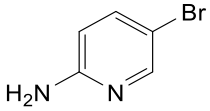	0/–40	2	2	**Figure S 23**
12	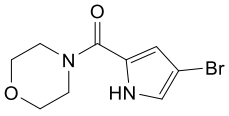	–2/–40	2	2	**Figure S 24**

	Fragment	On/Off irr. (ppm)	D1 (s)	D20 (s)	Binding
13	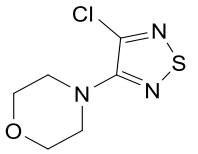	–2/–40	2	2	**Figure S 25**
14	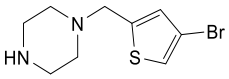	–2/–40	2	0.5	**Figure S 26**
15	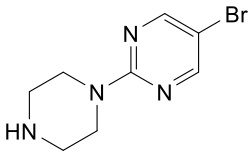	0/–40	2	2	**Figure S 27**
125	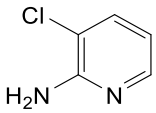	0/–40	2	2	**Figure S 28**
126	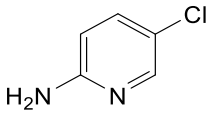	–1/–40	2	1	**Figure S 29**

Irr.: irradiation, D1 = delay, D20 = saturation time.

Hit compounds were measured in $D_2O/(CD_3)_2SO$ to assign protons. The STD_{effect} was calculated by using the water-suppressed proton spectra since they looked better after processing than the off-resonance spectra. To make sure that this method gives the same results, the calculations were also performed with the off-resonance spectra and no difference could be seen.

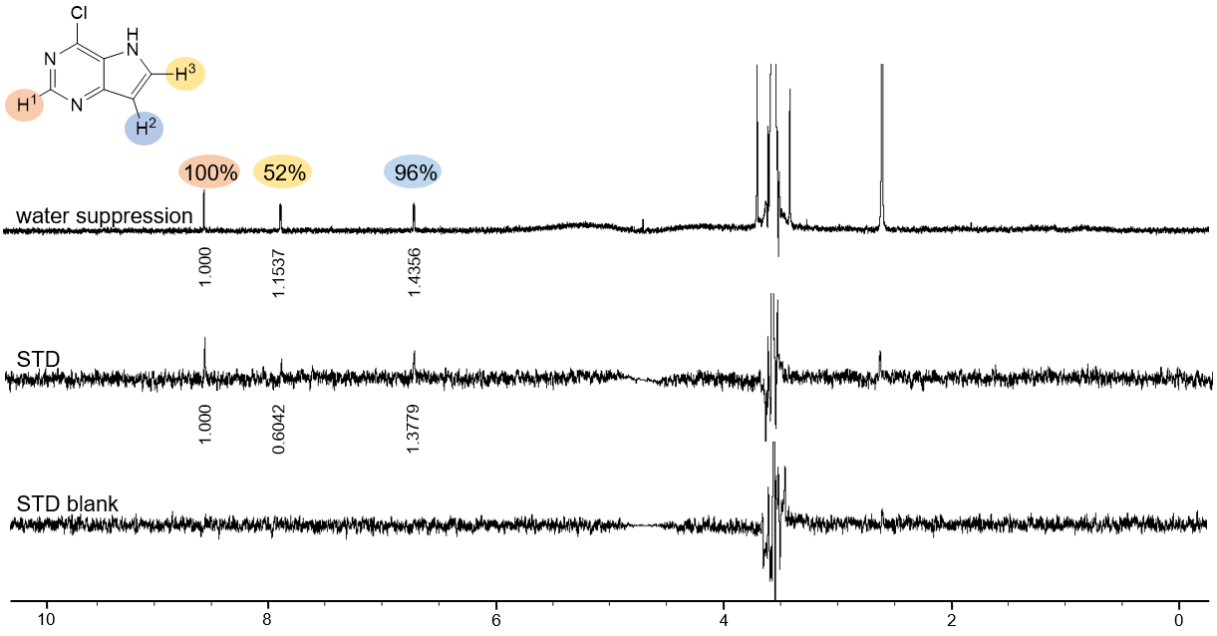

Figure S 16: ^{1}H NMR and STD-NMR spectra of compound **1** to determine binding epitope.

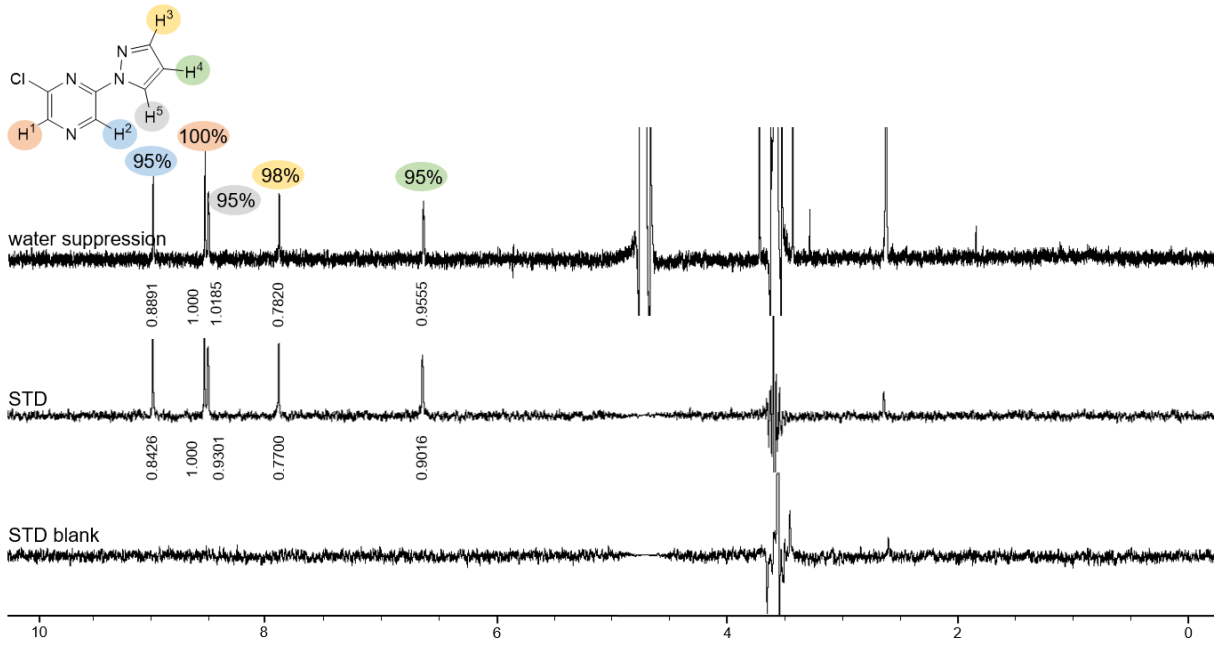

Figure S 17: ^{1}H NMR and STD-NMR spectra of compound **2** to determine binding epitope.

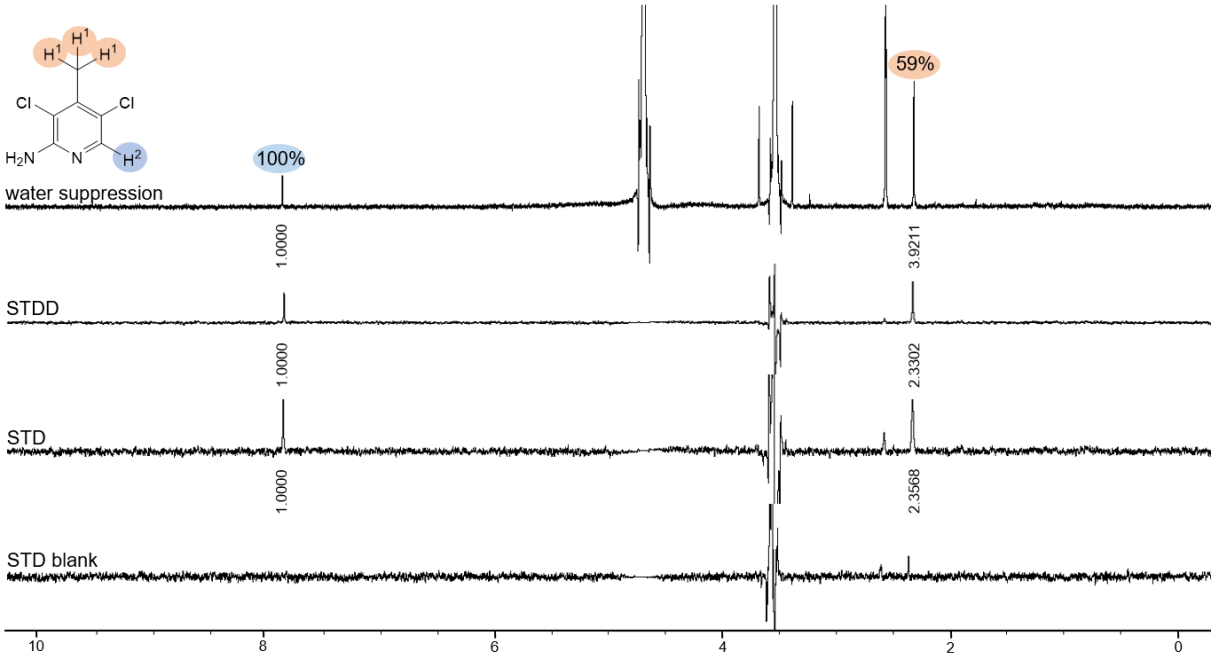

Figure S 18: ^{1}H NMR and STD-NMR spectra of compound **3** to determine binding epitope. Here, a STDD (double difference) spectrum was used to take the small artefact in the blank spectrum into account.

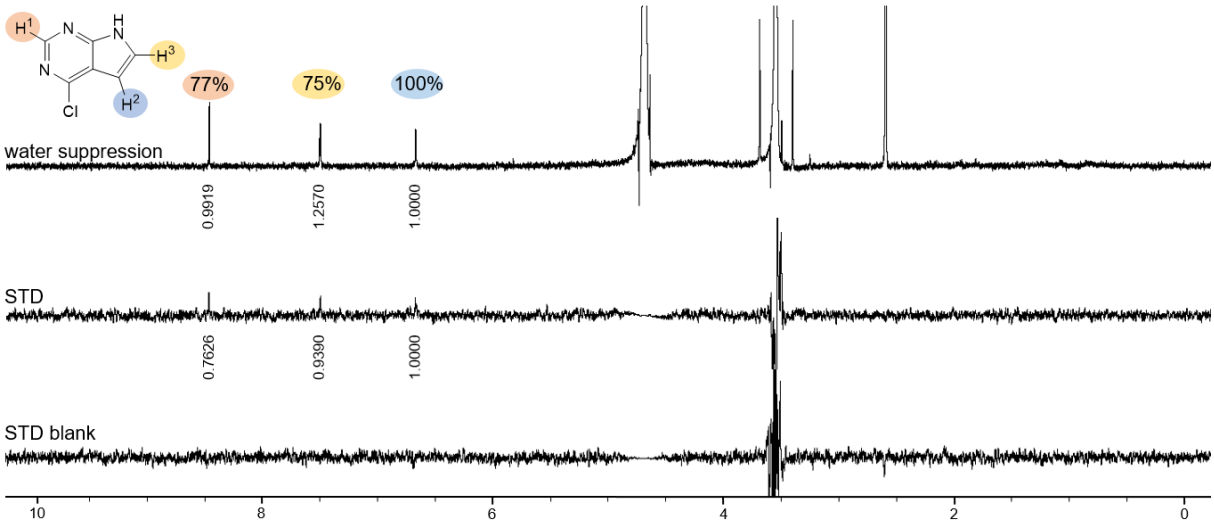

Figure S 19: ^{1}H NMR and STD-NMR spectra of compound **7** to determine binding epitope.

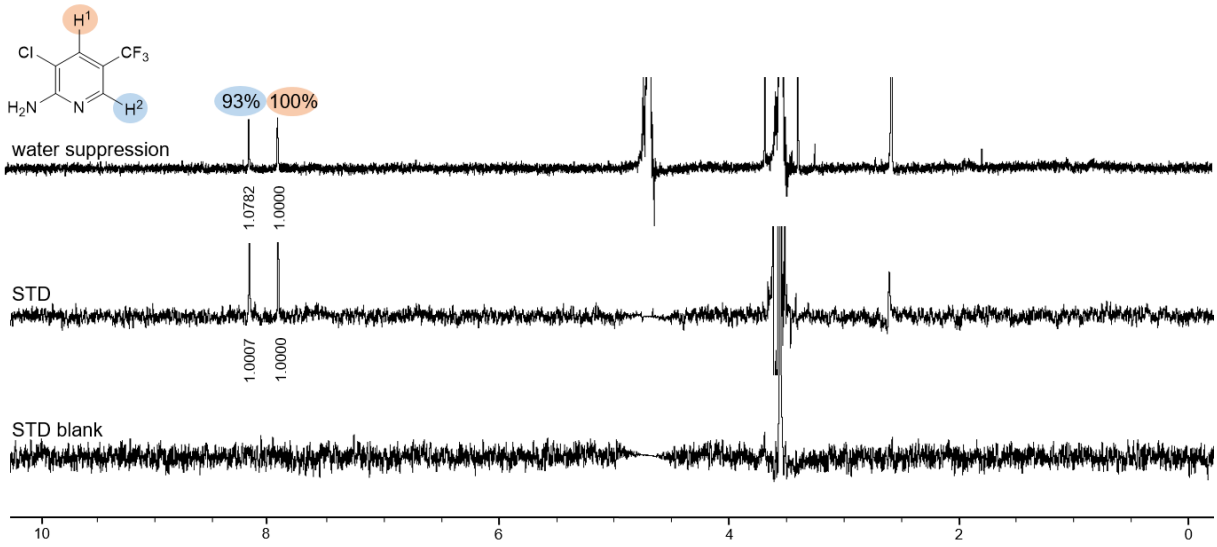

Figure S 20: ^{1}H NMR and STD-NMR spectra of compound **8** to determine binding epitope.

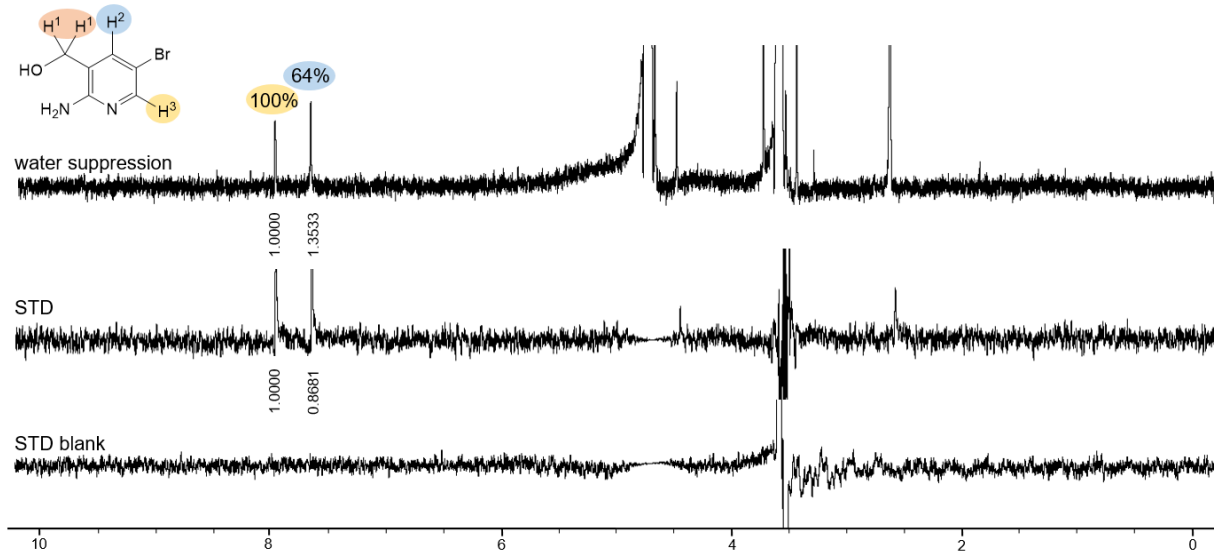

Figure S 21: ^{1}H NMR and STD-NMR spectra of compound **9** to determine binding epitope. H^{1} is too close to the suppressed water peak to be used.

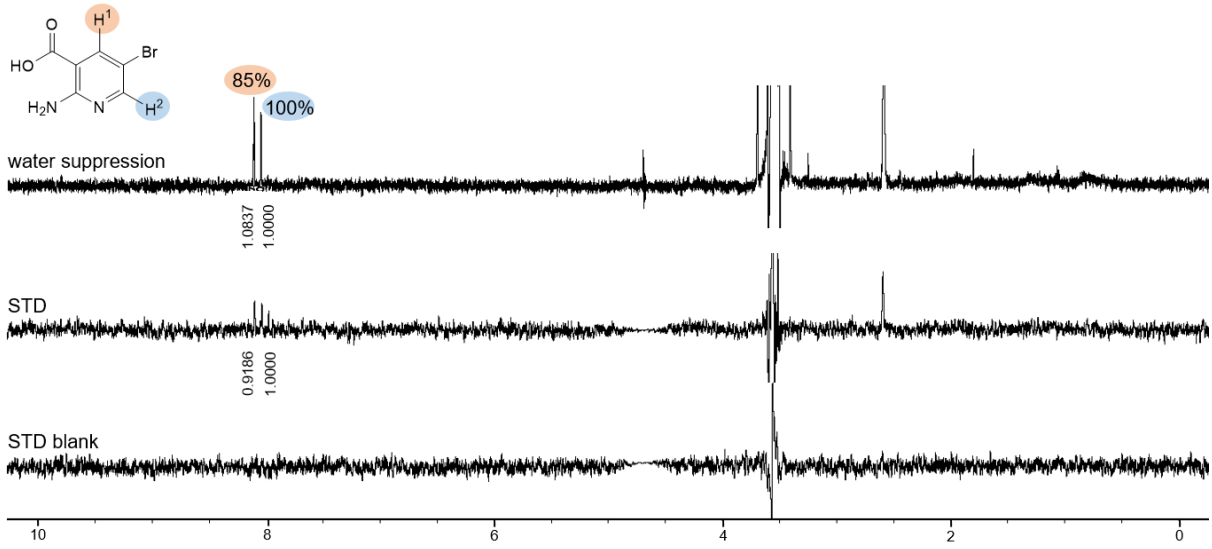

Figure S 22: ^{1}H NMR and STD-NMR spectra of compound **10** to determine binding epitope.

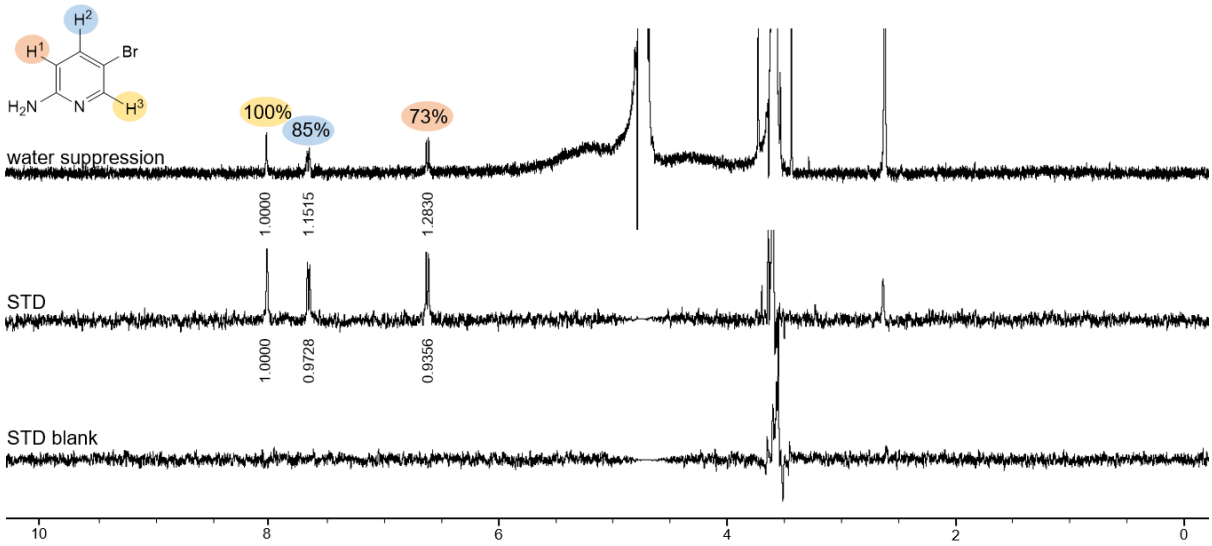

Figure S 23: ^{1}H NMR and STD-NMR spectra of compound **11** to determine binding epitope.

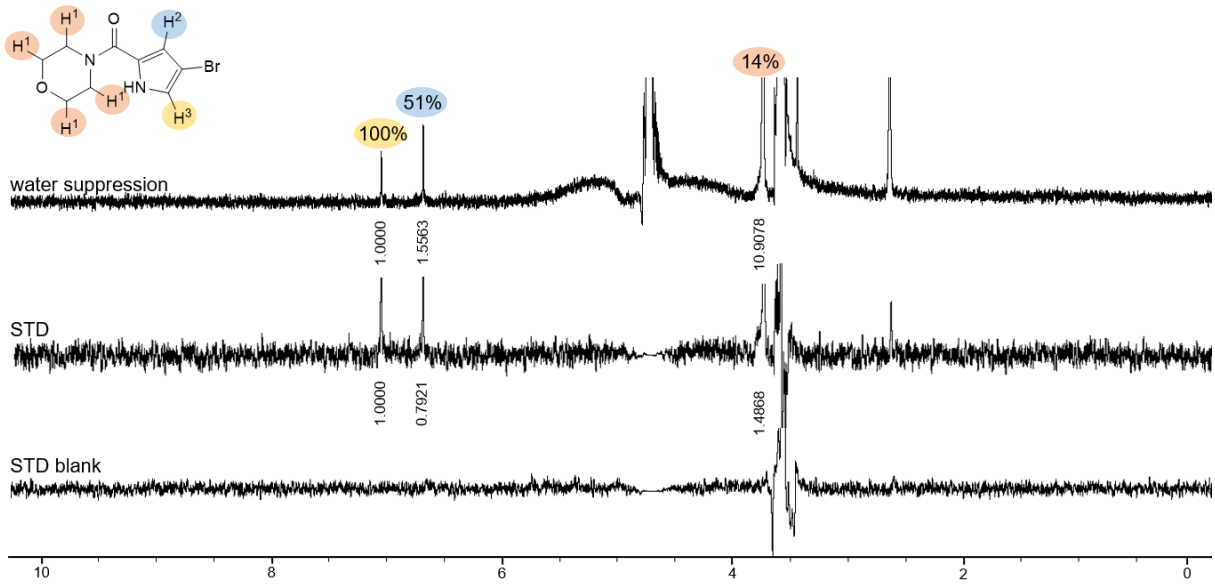

Figure S 24: ^{1}H NMR and STD-NMR spectra of compound **12** to determine binding epitope.

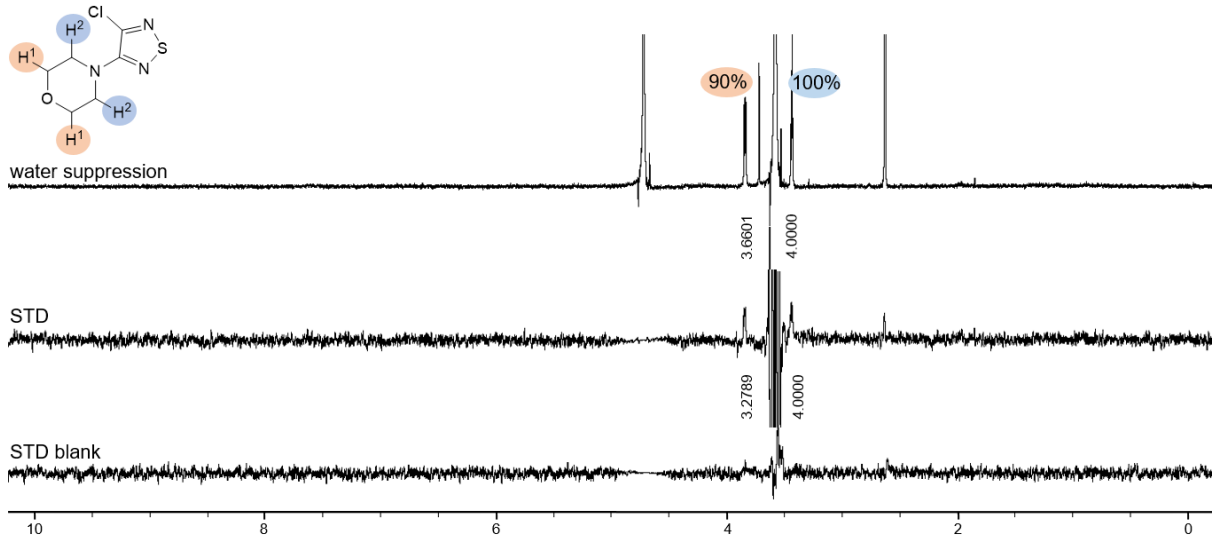

Figure S 25: ^{1}H NMR and STD-NMR spectra of compound **13** to determine binding epitope.

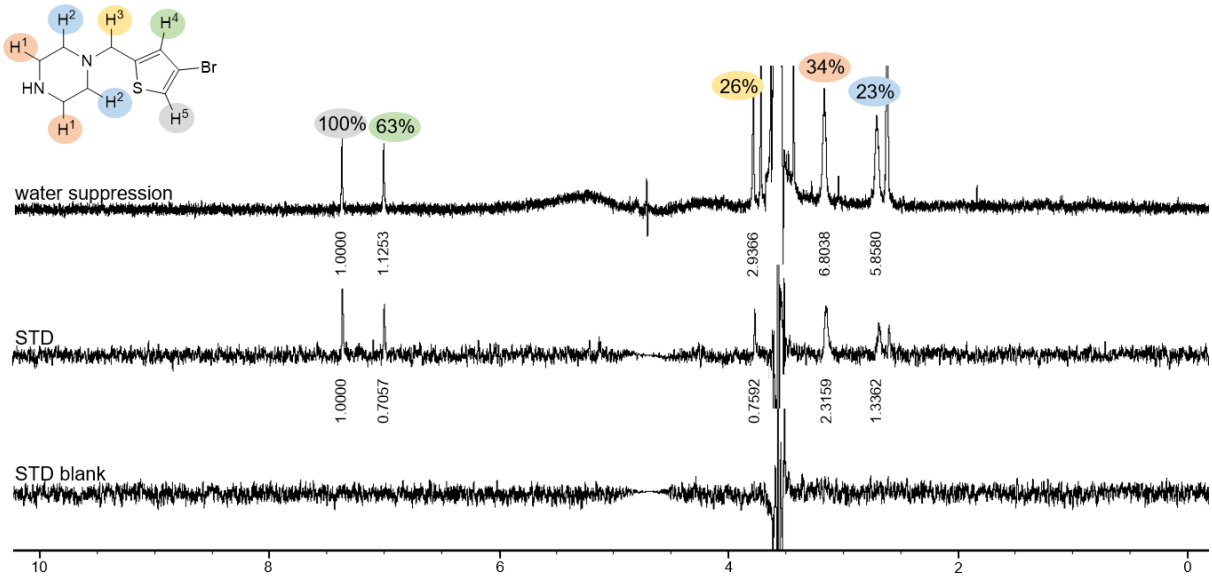

Figure S 26: ^{1}H NMR and STD-NMR spectra of compound **14** to determine binding epitope.

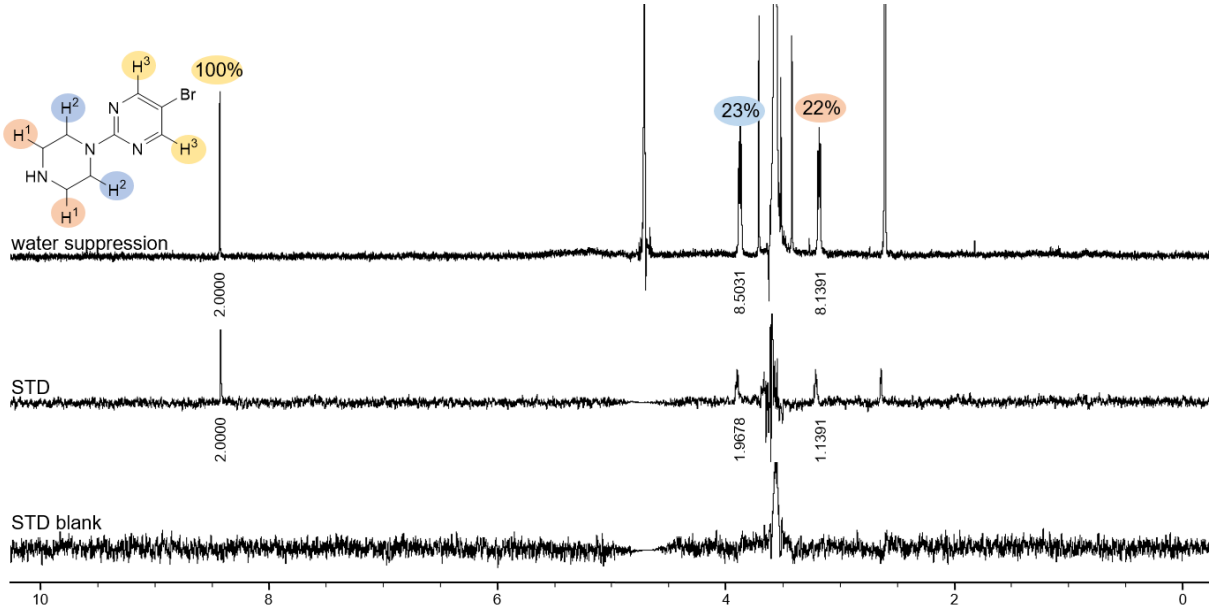

Figure S 27: ^{1}H NMR and STD-NMR spectra of compound **15** to determine binding epitope.

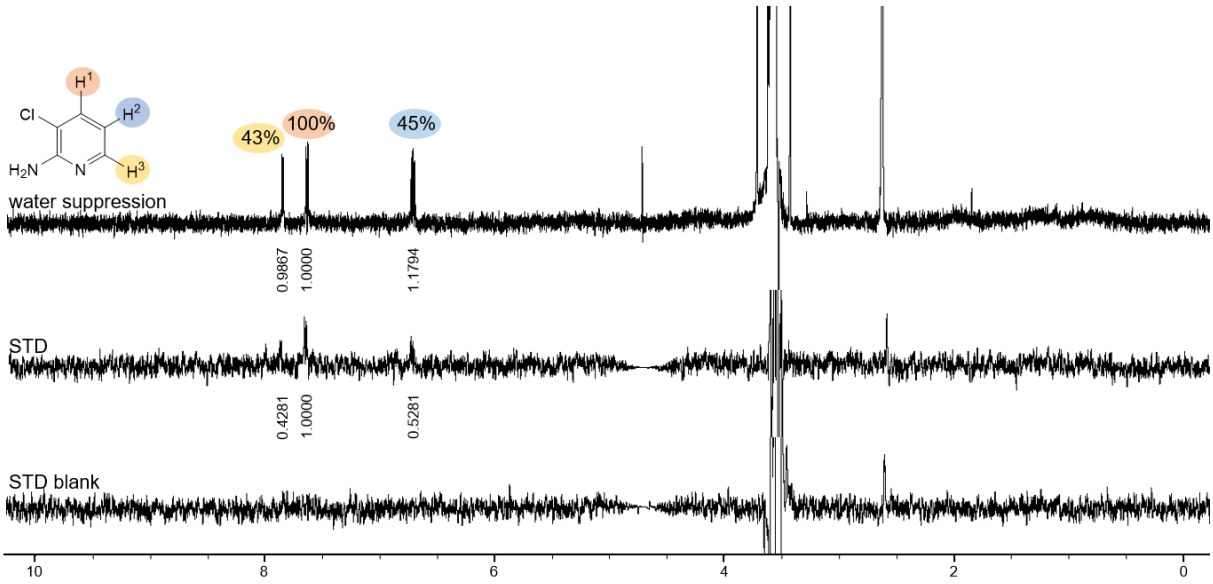

Figure S 28: ^{1}H NMR and STD-NMR spectra of compound **125** to determine binding epitope.

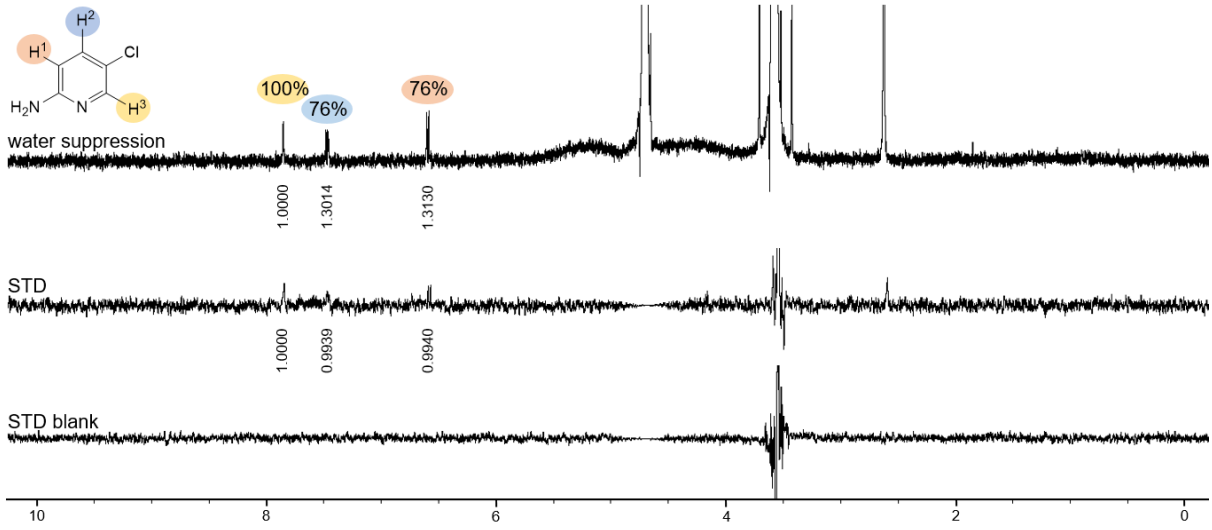

Figure S 29: ^{1}H NMR and STD-NMR spectra of compound **126** to determine binding epitope.

5.1.8 Binding affinity (K_D) determinations by SPR

The SPR binding studies were performed using a Reichert SR7500DC surface plasmon resonance spectrometer (Reichert Technologies, Depew, NY, USA), and medium density carboxymethyl dextran hydrogel CMD500M sensor chips (XanTec Bioanalytics, Düsseldorf, Germany). Milli-Q water was used as the running buffer for immobilization. Truncated *M. tuberculosis* DXPS (Δ*Mt*DXPS, 66.61 kDa) and native *Mt*DXPS (67.88 kDa) were immobilized in one of the two flow cells according to reported amine-coupling protocols.[194] The other flow cell was left blank to serve as a reference. The system was initially primed with borate buffer 100 mM (pH 9.0), then

the carboxymethyldextran matrix was activated by a 1:1 mixture of EDC*HCl 100 mM and *N*-hydroxysuccinimide (NHS) 100 mM at a flow rate of 10 µL min^{-1} for 7 min. The Δ*Mt*DXPS or *Mt*DXPS was diluted to a final concentration of 1.1 µM and 1.4 µM, respectively, in 10 mM sodium acetate buffer (pH 4.5) and was injected at a flow rate of 5 µL min^{-1} for 10 min. Non-reacted surface was quenched with 1 M ethanolamine hydrochloride (pH 8.5) at a flow rate of 25 µL min^{-1} for 3 min. A series of 10 buffer injections was run initially on both reference and active surfaces to equilibrate the system resulting in a stable immobilization level of approximately 8,000 (9,000 for *Mt*DXPS) µ refractive index unit (µRIU) (**Figure S 30**, **Figure S 31**), respectively. HEPES buffer (50 mM HEPES, 150 mM NaCl, 0.05% v/v Tween 20, 1 mM $MgCl_2$, pH 8.0) containing 5% v/v DMSO was used as the running buffer for binding studies. The running buffer was filtered and degassed prior to use. Binding experiments were performed at 20 °C. Compounds dissolved in DMSO were diluted with the running buffer (final DMSO concentration of 5% v/v) and were injected at a flow rate of 30 µL min^{-1}. Single-cycle kinetics were applied for K_D determination. The association time was set to 60 s, and the dissociation phase was recorded for 120 s. Ethylene glycol 80% in the running buffer was used for regeneration of the gold-chip surface. Differences in the bulk refractive index due to DMSO were corrected by a calibration curve (nine concentrations: 3–7% v/v DMSO in the running buffer). Data processing and analysis were performed by Scrubber software (Version 2.0c, 2008, BioLogic Software). Sensorgrams were calculated by sequential subtractions of the corresponding curves obtained from the reference flow cell and the running buffer (blank). SPR responses are expressed in RU. The K_D values were calculated by global fitting of the kinetic curves as well as fitting of the steady state binding responses to a 1:1 LANGMUIR interaction model.

5.1.9 SPR Sensorgrams of initial 14 hit fragments

General remarks about data analysis: The response of each fragment was normalized by dividing it by their respective molecular weight and multiplying the result by 100.

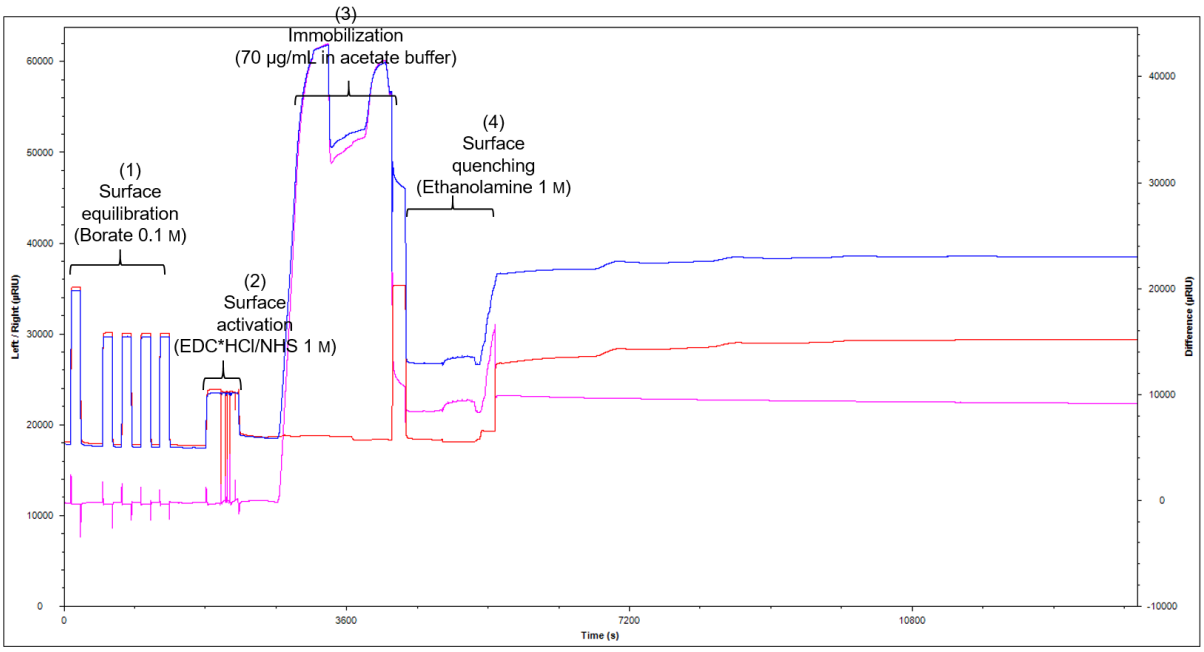

Figure S 30: Sensorgram of the immobilization procedure for Δ*Mt*DXPS on CMD500M sensor chip: (1) Five injections of cleaning solution, (2) activation solution, (3) Δ*Mt*DXPS, and (4) quenching solution. The blue, red, and magenta curves represent the left (active) channel, right (reference) channel, and the difference, respectively.

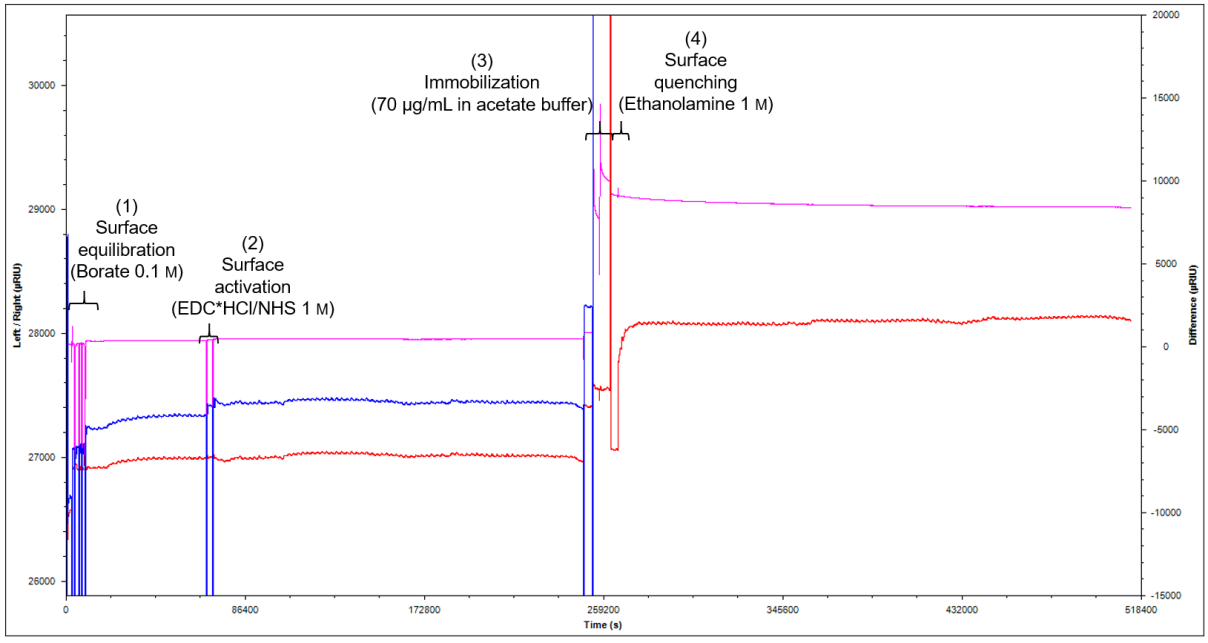

Figure S 31: Sensorgram of the immobilization procedure for *Mt*DXPS on CMD500M sensor chip: (1) Four injections of cleaning solution, (2) activation solution, (3) *Mt*DXPS, and (4) quenching solution. The blue, red, and magenta curves represent the left (active) channel, right (reference) channel, and the difference, respectively.

Table S 3: Kinetics and binding affinities of all fragments against Δ*Mt*DXPS by SPR. RU after immobilization = 7,970.

Fragment	R_{max} (RU)[a]	k_{on} ($M^{-1}s^{-1}$)[b]	k_{off} (s^{-1})[c]	K_D (μM)[d]	RU at 625 μM
1	37.1 ± 0.8	114 ± 4	0.0548 ± 0.0009	480 ± 20	24
2	170 ± 30	50 ± 10	0.78 ± 0.03	14000 ± 3000	8
3	36 ± 2	2300 ± 200	1.4 ± 0.1	610 ± 40	24
7	34 ± 1	350 ± 20	0.47 ± 0.1	1330 ± 60	12
8	19.3 ± 0.6	700 ± 40	0.64 ± 0.03	920 ± 40	8
9	43 ± 2	270 ± 20	1.19 ± 0.05	4400 ± 300	5
10	17.9 ± 0.5	33 ± 1	0.0090 ± 0.0002	270 ± 10	11
11	15.2 ± 0.3	800 ± 40	0.36 ± 0.01	450 ± 20	10
12	20.5 ± 0.6	4700 ± 200	0.45 ± 0.02	950 ± 40	8
13	5.86 ± 0.07	3200 ± 100	0.46 ± 0.02	144 ± 4	8
14	51 ± 2	3300 ± 200	0.53 ± 0.02	1590 ± 80	15
15	38 ± 3	1000 ± 100	2.2 ± 0.2	2000 ± 200	9
125	28 ± 3	130 ± 10	0.33 ± 0.01	2600 ± 300	6
126	16.3 ± 0.4	420 ± 20	0.37 ± 0.1	880 ± 30	7

[a] maximum analyte binding capacity; [b] association constant rate; [c] dissociation constant rate; [d] equilibrium dissociation constant.

Table S 4: Kinetics and binding affinities of all fragments against *Mt*DXPS by SPR. RU after immobilization = 8394.

Cpd.	R_{max} (RU)[a]	k_{on} ($M^{-1}s^{-1}$)[b]	k_{off} (s^{-1})[c]	K_D (μM)[d]	RU at 625 μM
1	61 ± 3	28 ± 1	0.0396 ± 0.0004	1410 ± 700	18
2	n.f.	n.f.	n.f.	n.f.	8
3	67 ± 4	80 ± 5	0.112 ± 0.001	1400 ± 100	22
7	n.f.	n.f.	n.f.	n.f.	14
8	10.0 ± 0.3	198 ± 9	0.104 ± 0.003	530 ± 20	6
9	n.f.	n.f.	n.f.	n.f.	6
10	18.2 ± 0.5	24.9 ± 0.9	0.0036 ± 0.0001	143 ± 8	10
11	9.1 ± 0.1	430 ± 10	0.163 ± 0.003	375 ± 9	6
12	170 ± 60	7 ± 2	0.177 ± 0.001	18000 ± 6000	6
13	10.7 ± 0.8	350 ± 40	0.18 ± 0.01	510 ± 60	6
14	300 ± 100	7 ± 2	0.133 ± 0.001	19000 ± 6000	11
15	23.8 ± 0.7	105 ± 4	0.093 ± 0.002	880 ± 40	11
125	n.f.	n.f.	n.f.	n.f.	5
126	12.3 ± 0.3	143 ± 5	0.068 ± 0.001	480 ± 20	7

[a] maximum analyte binding capacity; [b] association constant rate; [c] dissociation constant rate; [d] equilibrium dissociation constant. n.f. = no fit possible.

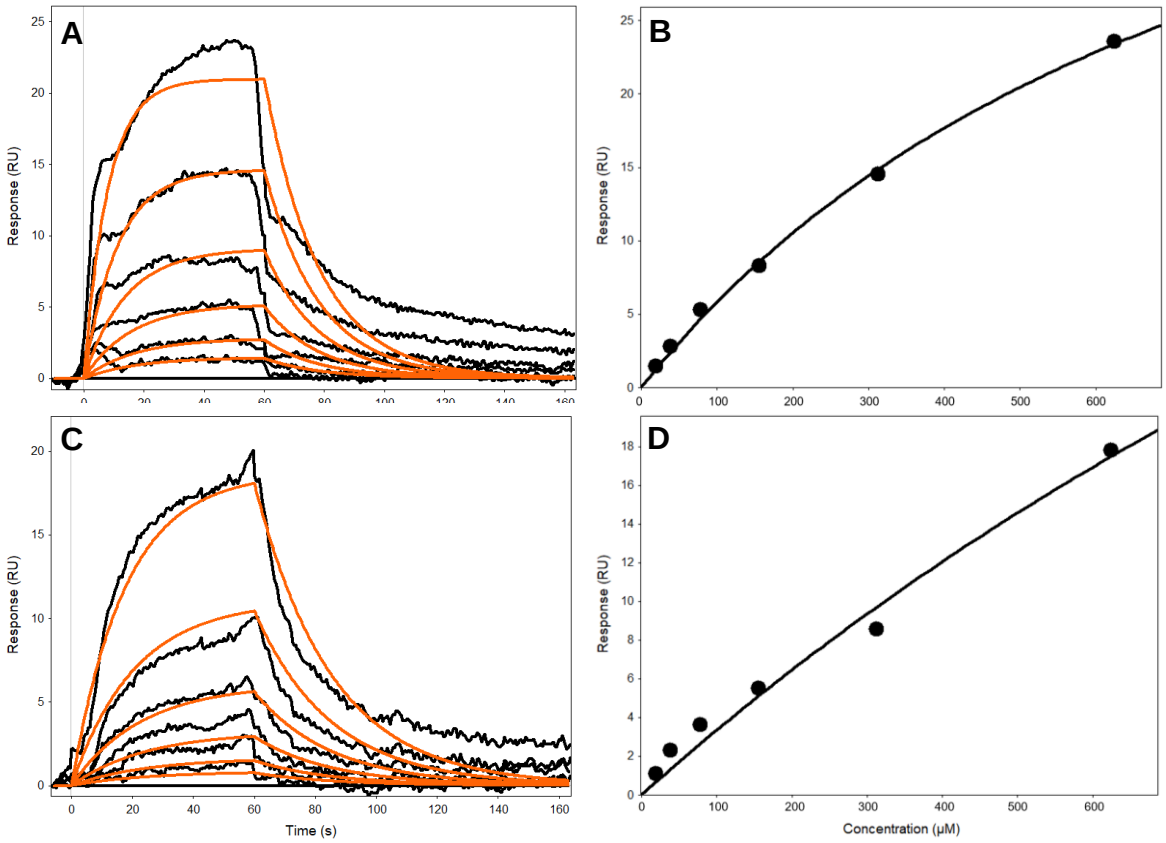

Figure S 32: Overlay of sensorgrams of fragment **1** injected at concentrations of 19.6−625.0 µM over immobilized **A**) Δ*Mt*DXPS and **C**) *Mt*DXPS. Fitting of responses at equilibrium according to 1:1 LANGMUIR binding model (orange lines). RU at equilibrium from 46−50 s plotted against fragment concentration in µM **B**) Δ*Mt*DXPS and **D**) *Mt*DXPS.

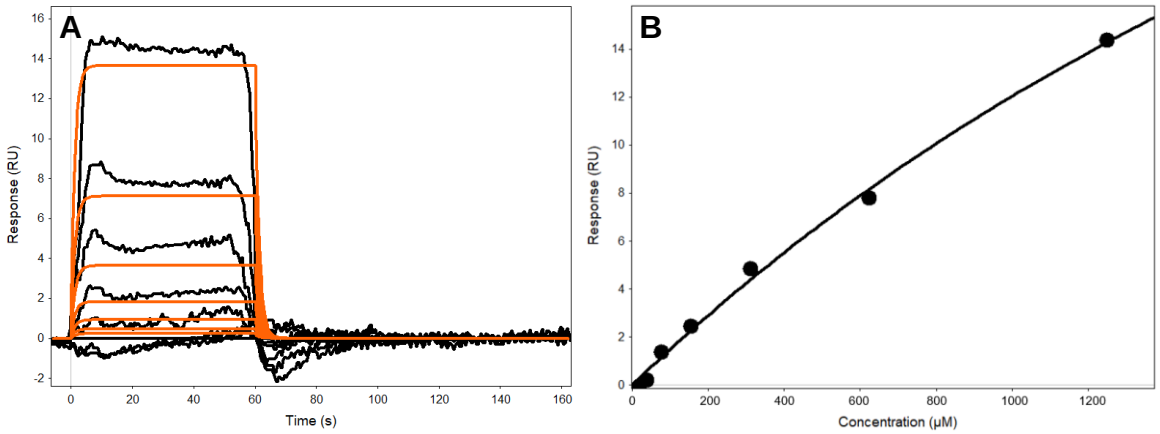

Figure S 33: Overlay of sensorgrams of fragment **2** injected at concentrations of 19.6−1250.0 µM over immobilized **A**) Δ*Mt*DXPS. Fitting of responses at equilibrium according to 1:1 LANGMUIR binding model (orange lines). RU at equilibrium from 46−50 s plotted against fragment concentration in µM **B**) Δ*Mt*DXPS.

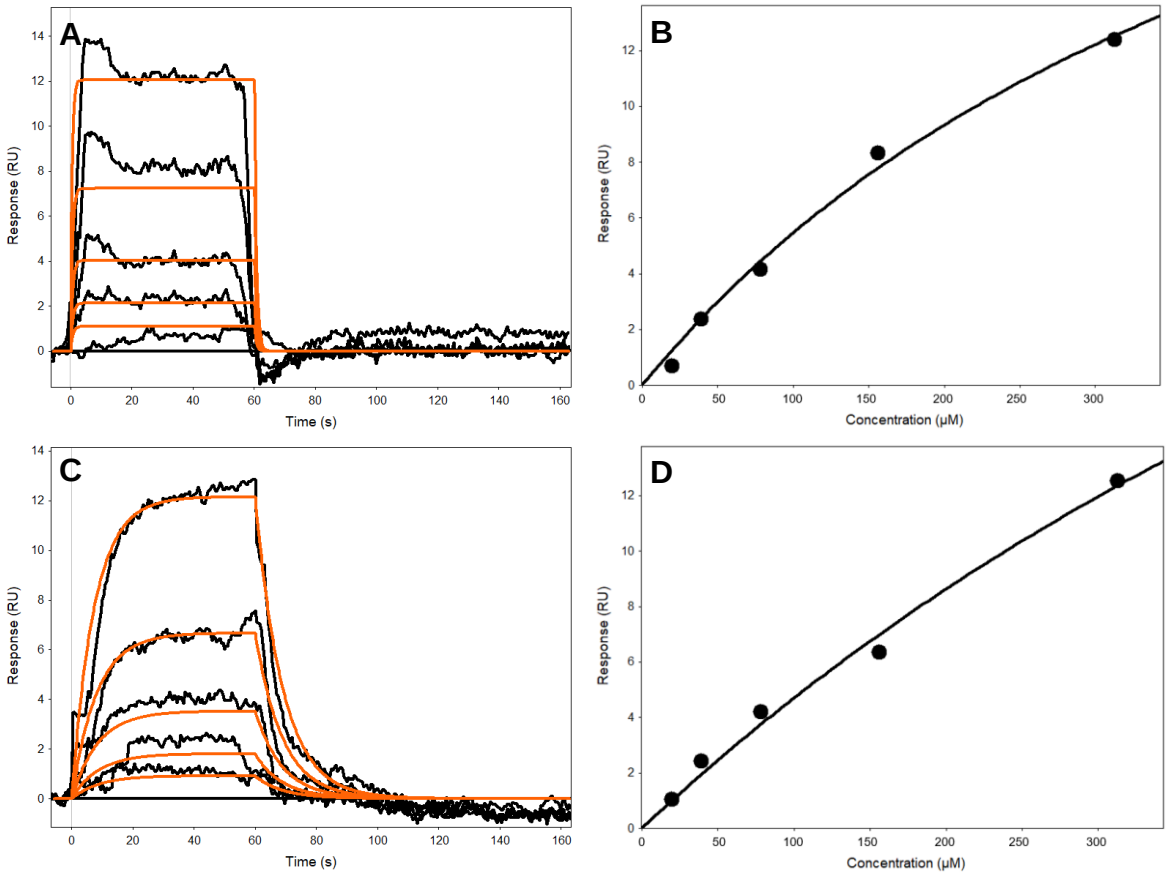

Figure S 34: Overlay of sensorgrams of fragment **3** injected at concentrations of 19.6−313.0 µM over immobilized **A**) Δ*Mt*DXPS and **C**) *Mt*DXPS. Fitting of responses at equilibrium according to 1:1 LANGMUIR binding model (orange lines). RU at equilibrium from 46−50 s plotted against fragment concentration in µM **B**) Δ*Mt*DXPS and **D**) *Mt*DXPS.

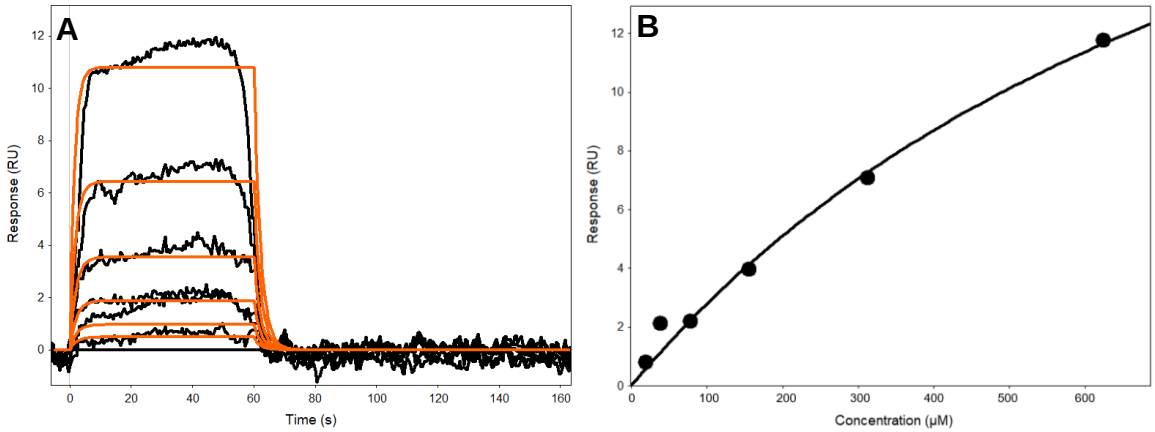

Figure S 35: Overlay of sensorgrams of fragment **7** injected at concentrations of 19.6−625.0 µM over immobilized **A**) Δ*Mt*DXPS. Fitting of responses at equilibrium according to 1:1 LANGMUIR binding model (orange lines). RU at equilibrium from 46−50 s plotted against fragment concentration in µM **B**) Δ*Mt*DXPS.

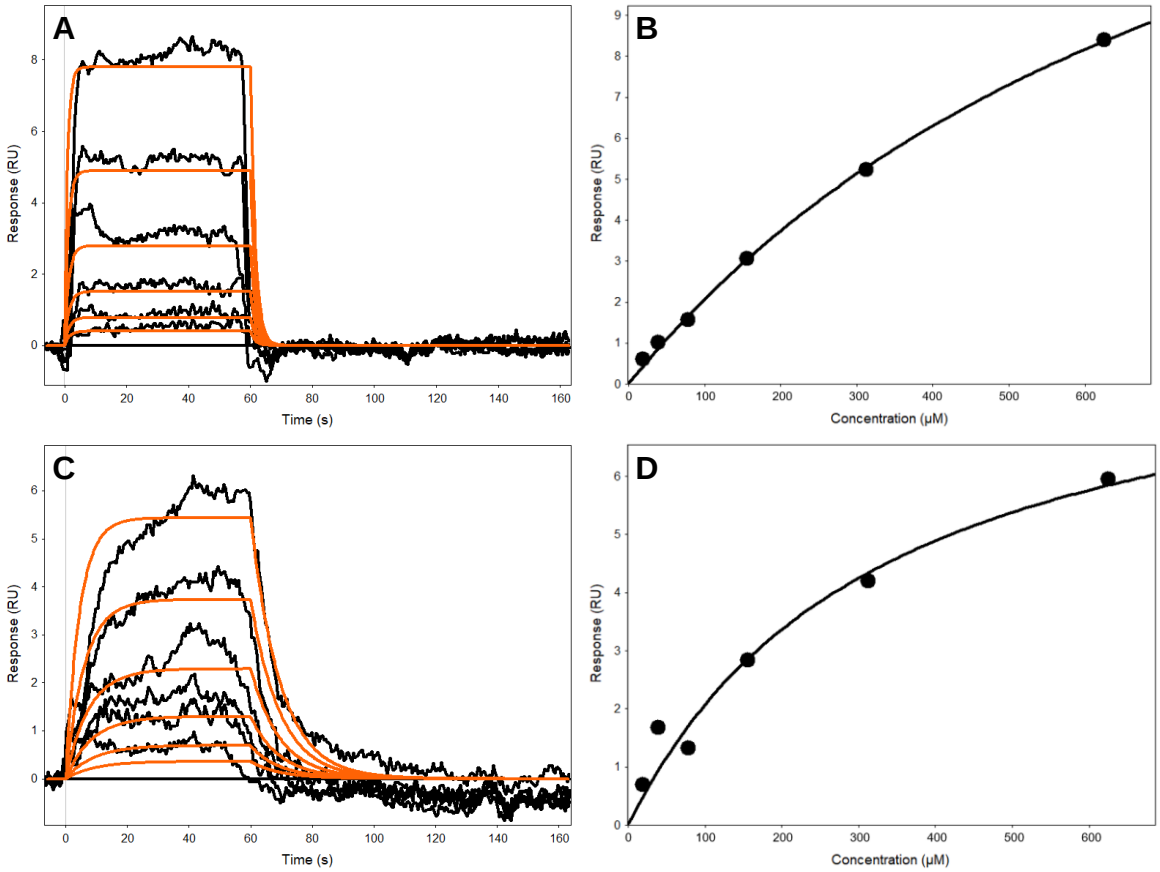

Figure S 36: Overlay of sensorgrams of fragment **8** injected at concentrations of 19.6−625.0 µM over immobilized **A**) Δ*Mt*DXPS and **C**) *Mt*DXPS. Fitting of responses at equilibrium according to 1:1 LANGMUIR binding model (orange lines). RU at equilibrium from 46−50 s plotted against fragment concentration in µM **B**) Δ*Mt*DXPS and **D**) *Mt*DXPS.

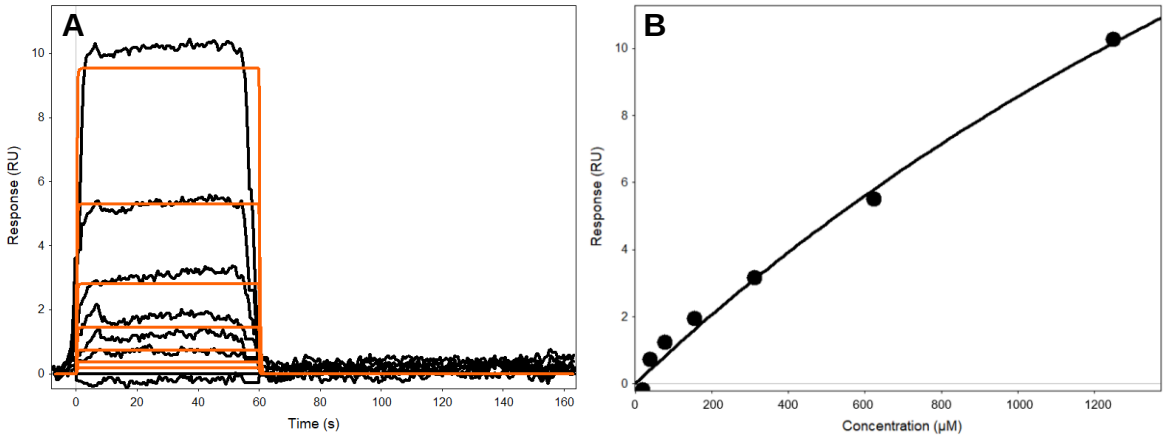

Figure S 37: Overlay of sensorgrams of fragment **9** injected at concentrations of 19.6−1250.0 µM over immobilized **A**) Δ*Mt*DXPS. Fitting of responses at equilibrium according to 1:1 LANGMUIR binding model (orange lines). RU at equilibrium from 46−50 s plotted against fragment concentration in µM **B**) Δ*Mt*DXPS.

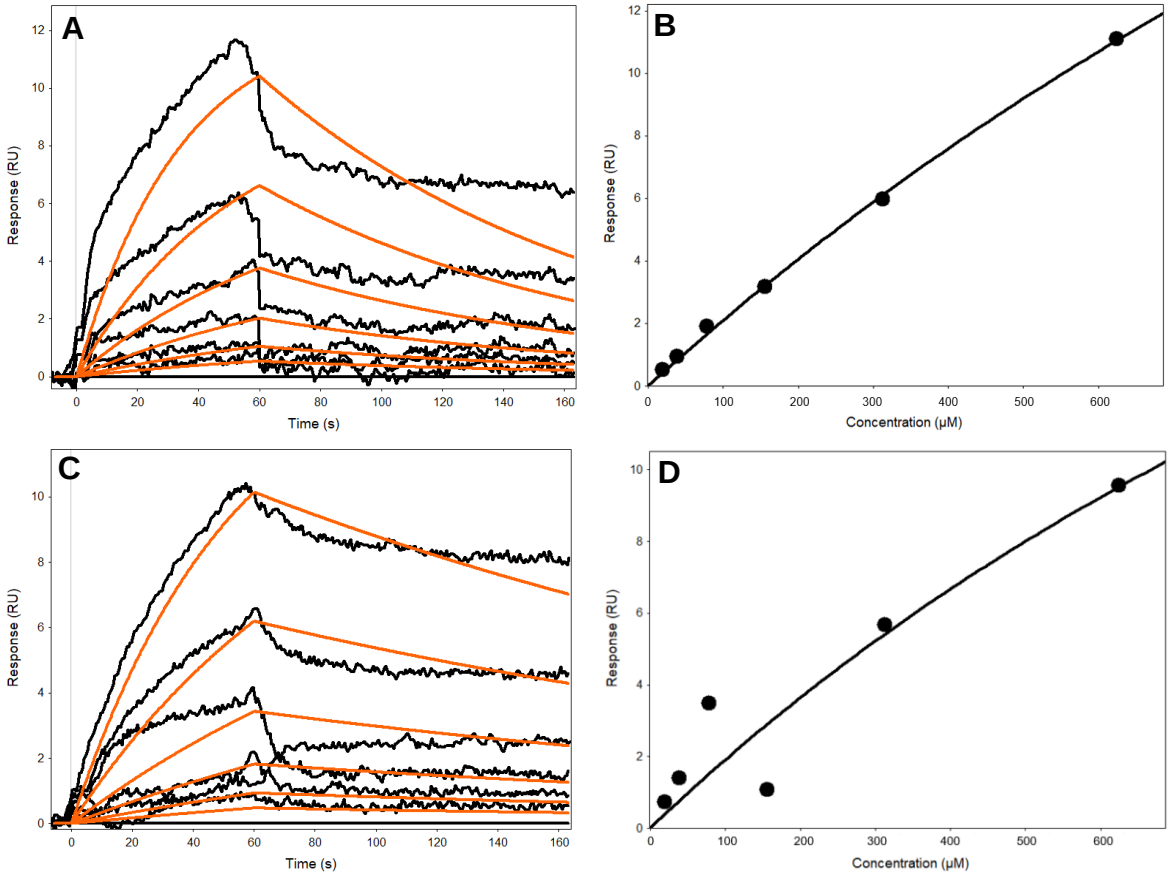

Figure S 38: Overlay of sensorgrams of fragment **10** injected at concentrations of 19.6−625.0 µM over immobilized **A**) Δ*Mt*DXPS and **C**) *Mt*DXPS. Fitting of responses at equilibrium according to 1:1 LANGMUIR binding model (orange lines). RU at equilibrium from 46−50 s plotted against fragment concentration in µM **B**) Δ*Mt*DXPS and **D**) *Mt*DXPS.

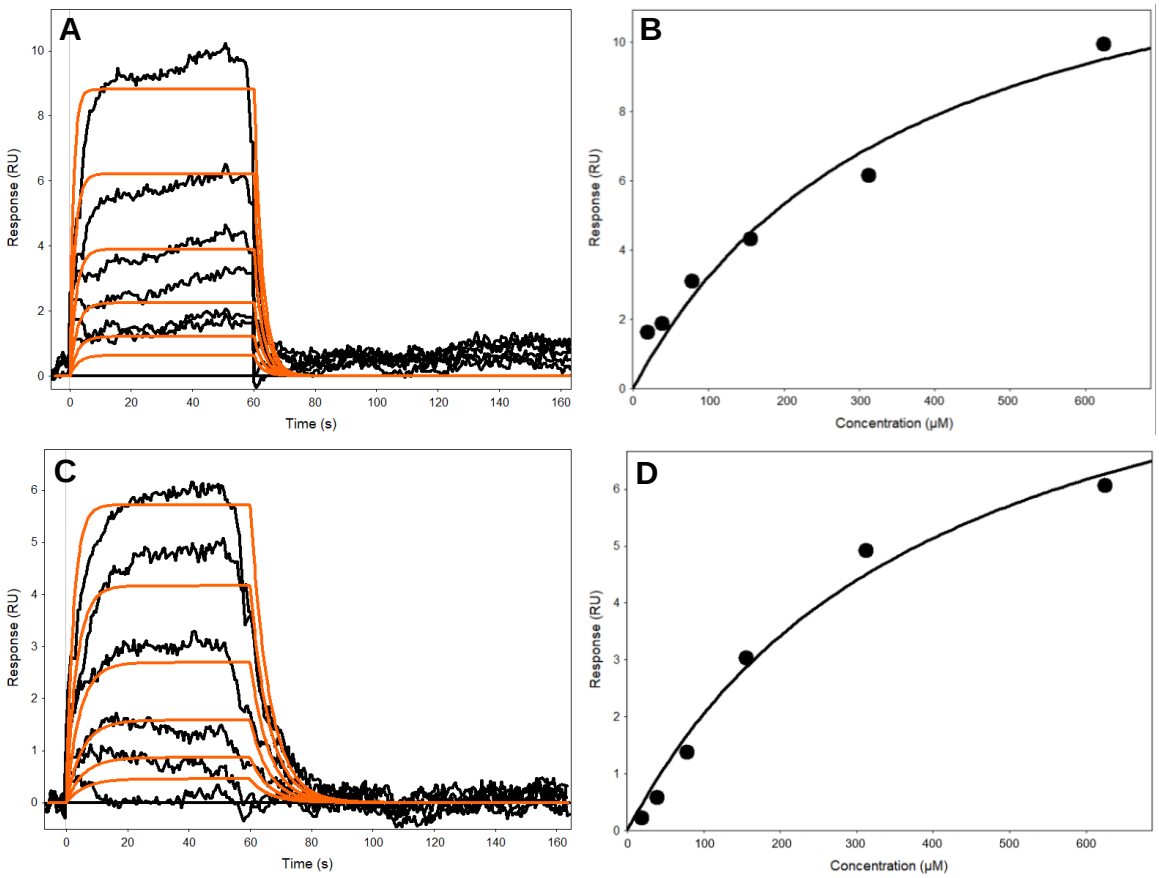

Figure S 39: Overlay of sensorgrams of fragment **11** injected at concentrations of 19.6−625.0 µM over immobilized **A**) Δ*Mt*DXPS and **C**) *Mt*DXPS. Fitting of responses at equilibrium according to 1:1 LANGMUIR binding model (orange lines). RU at equilibrium from 46−50 s plotted against fragment concentration in µM **B**) Δ*Mt*DXPS and **D**) *Mt*DXPS.

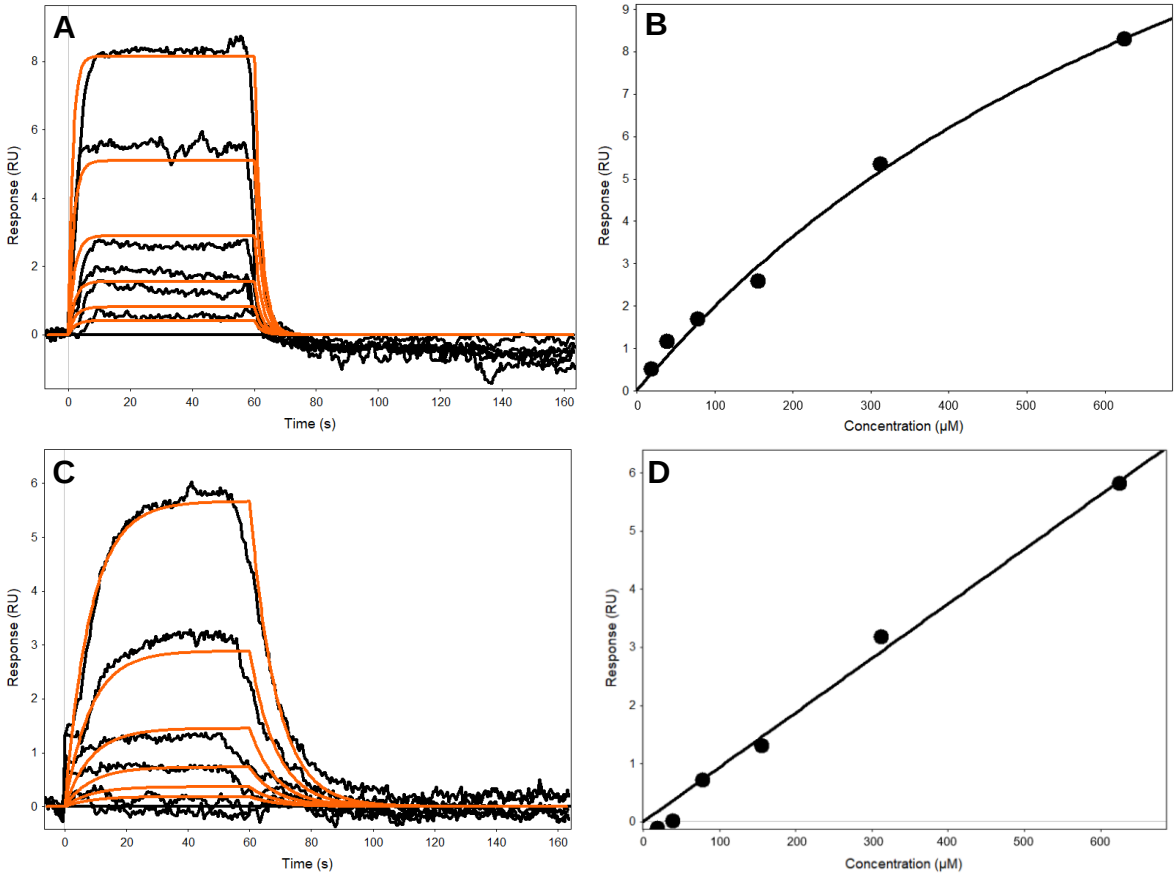

Figure S 40: Overlay of sensorgrams of fragment **12** injected at concentrations of 19.6−625.0 µM over immobilized **A**) Δ*Mt*DXPS and **C**) *Mt*DXPS. Fitting of responses at equilibrium according to 1:1 LANGMUIR binding model (orange lines). RU at equilibrium from 46−50 s plotted against fragment concentration in µM **B**) Δ*Mt*DXPS and **D**) *Mt*DXPS.

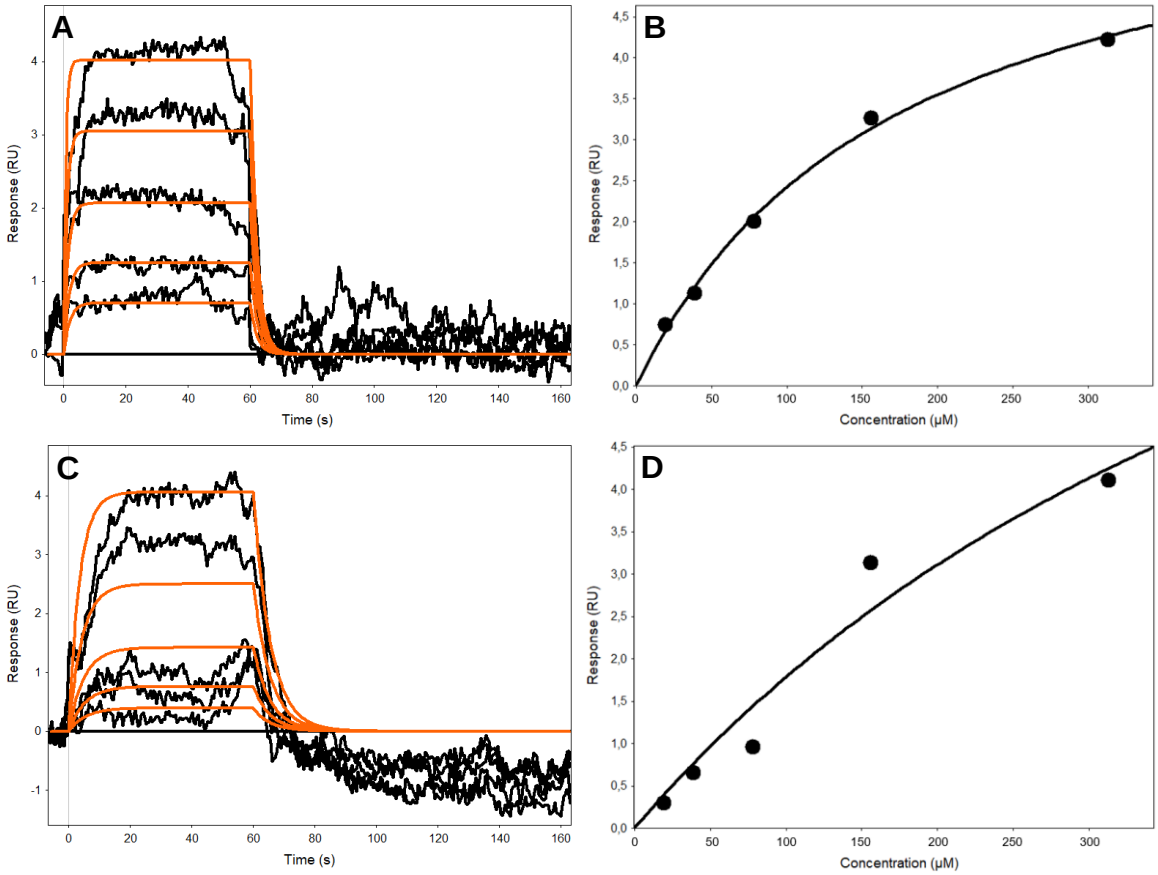

Figure S 41: Overlay of sensorgrams of fragment **13** injected at concentrations of 19.6−313.0 µM over immobilized **A**) Δ*Mt*DXPS and **C**) *Mt*DXPS. Fitting of responses at equilibrium according to 1:1 LANGMUIR binding model (orange lines). RU at equilibrium from 46−50 s plotted against fragment concentration in µM **B**) Δ*Mt*DXPS and **D**) *Mt*DXPS.

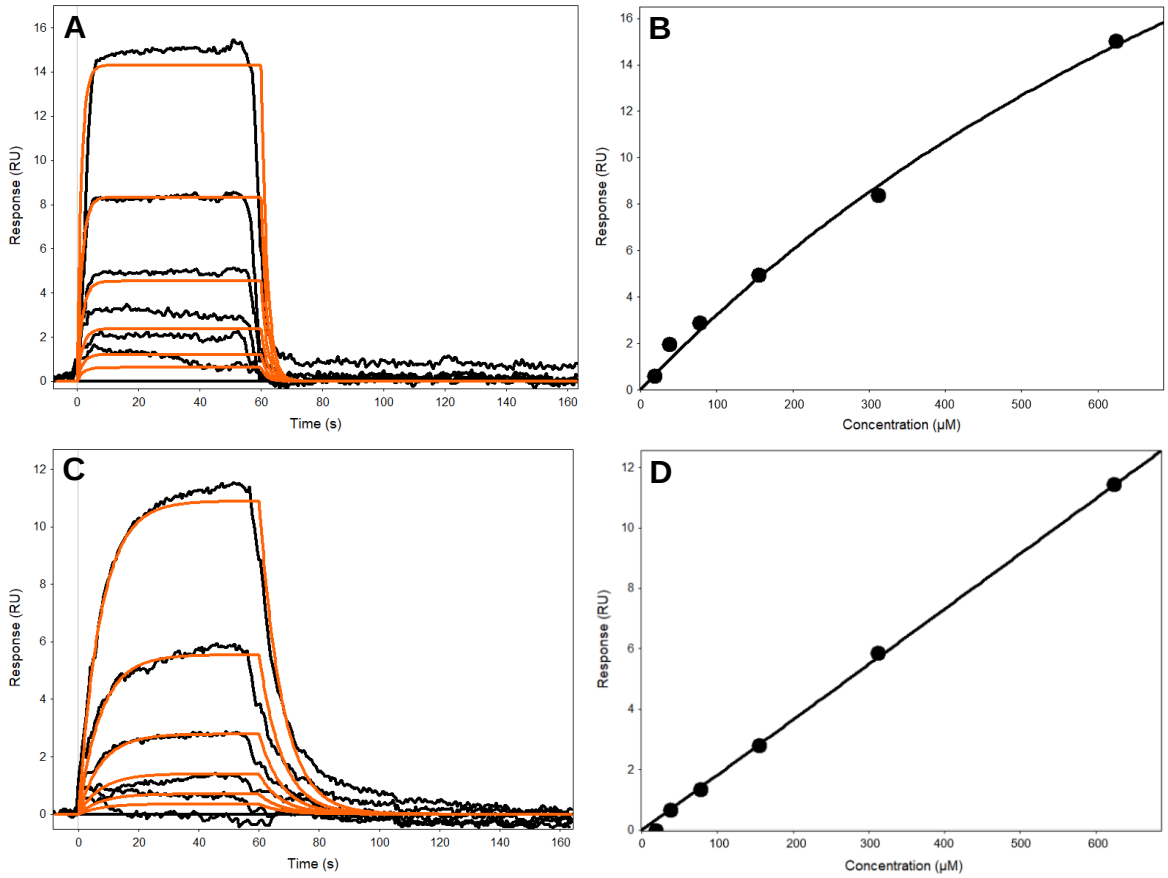

Figure S 42: Overlay of sensorgrams of fragment **14** injected at concentrations of 19.6−625.0 µM over immobilized **A**) Δ*Mt*DXPS and **C**) *Mt*DXPS. Fitting of responses at equilibrium according to 1:1 LANGMUIR binding model (orange lines). RU at equilibrium from 46−50 s plotted against fragment concentration in µM **B**) Δ*Mt*DXPS and **D**) *Mt*DXPS.

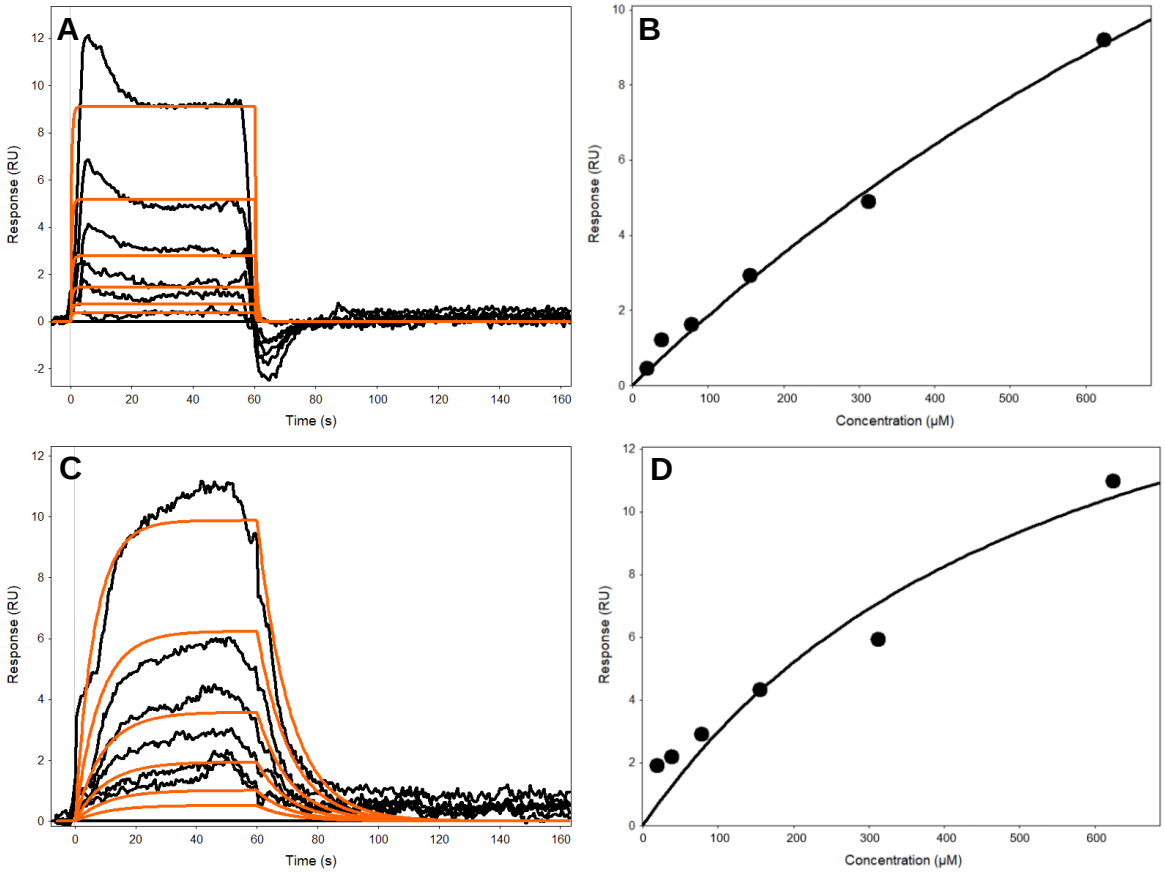

Figure S 43: Overlay of sensorgrams of fragment **15** injected at concentrations of 19.6−625.0 µM over immobilized **A**) Δ*Mt*DXPS and **C**) *Mt*DXPS. Fitting of responses at equilibrium according to 1:1 LANGMUIR binding model (orange lines). RU at equilibrium from 46−50 s plotted against fragment concentration in µM **B**) Δ*Mt*DXPS and **D**) *Mt*DXPS.

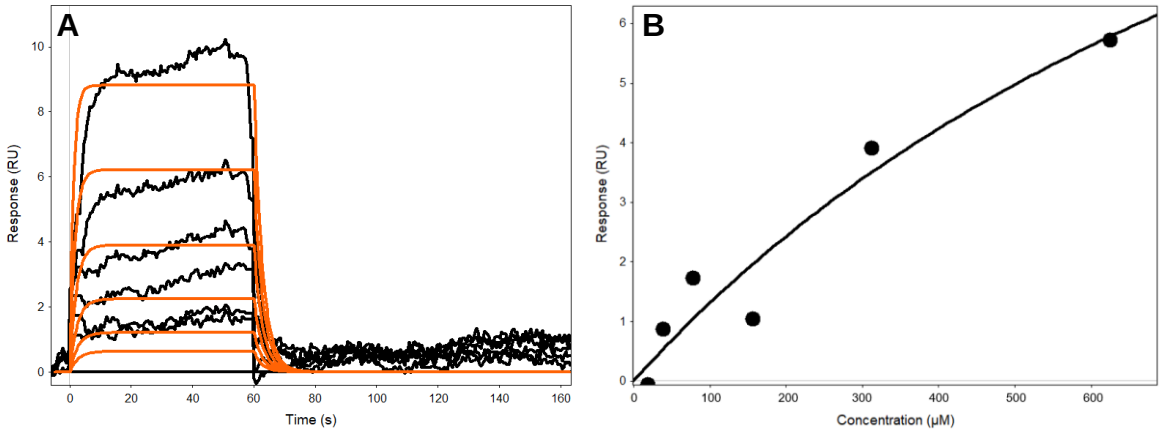

Figure S 44: Overlay of sensorgrams of fragment **125** injected at concentrations of 19.6−625.0 µM over immobilized **A**) Δ*Mt*DXPS. Fitting of responses at equilibrium according to 1:1 LANGMUIR binding model (orange lines). RU at equilibrium from 46−50 s plotted against fragment concentration in µM **B**) Δ*Mt*DXPS.

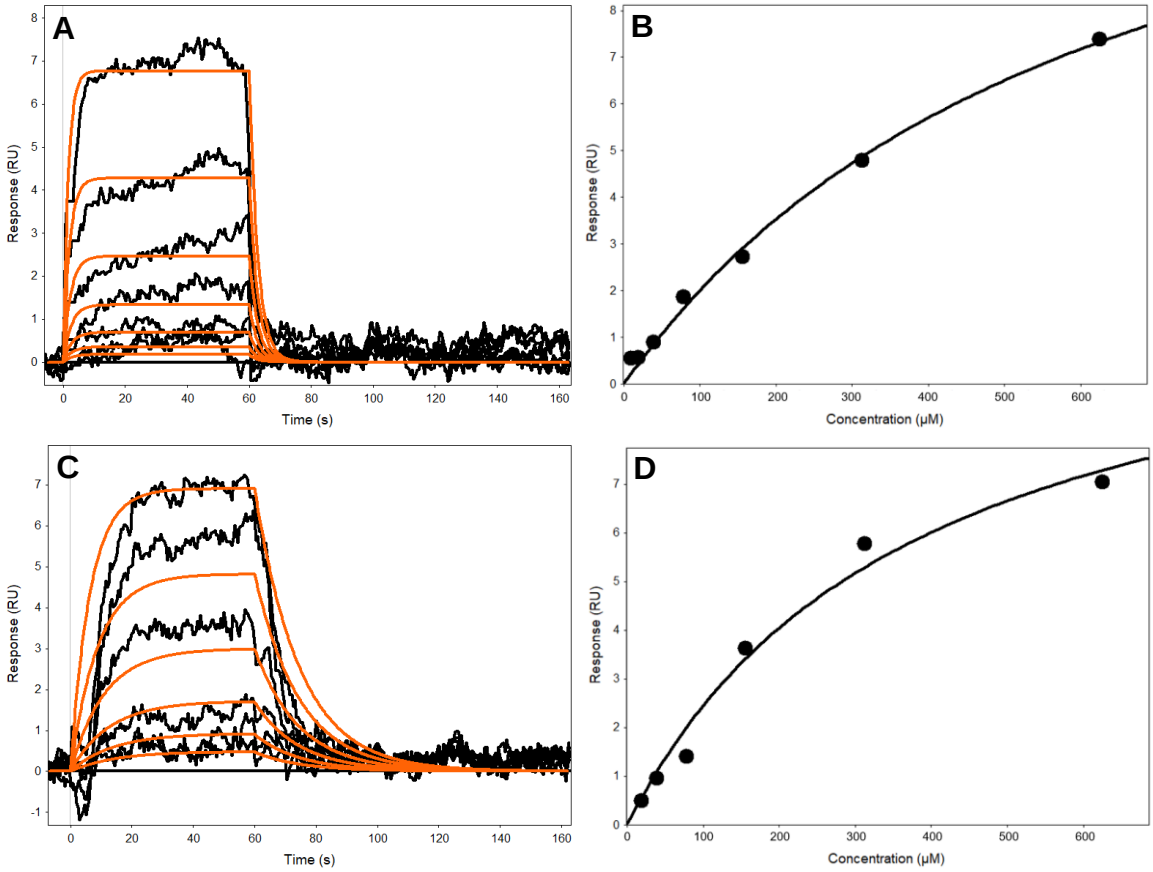

Figure S 45: Overlay of sensorgrams of fragment **126** injected at concentrations of 19.6−625.0 µM over immobilized **A**) Δ*Mt*DXPS and **C**) *Mt*DXPS. Fitting of responses at equilibrium according to 1:1 LANGMUIR binding model (orange lines). RU at equilibrium from 46−50 s plotted against fragment concentration in µM **B**) Δ*Mt*DXPS and **D**) *Mt*DXPS.

5.1.10 SPR sensorgrams of fragment-optimization compounds

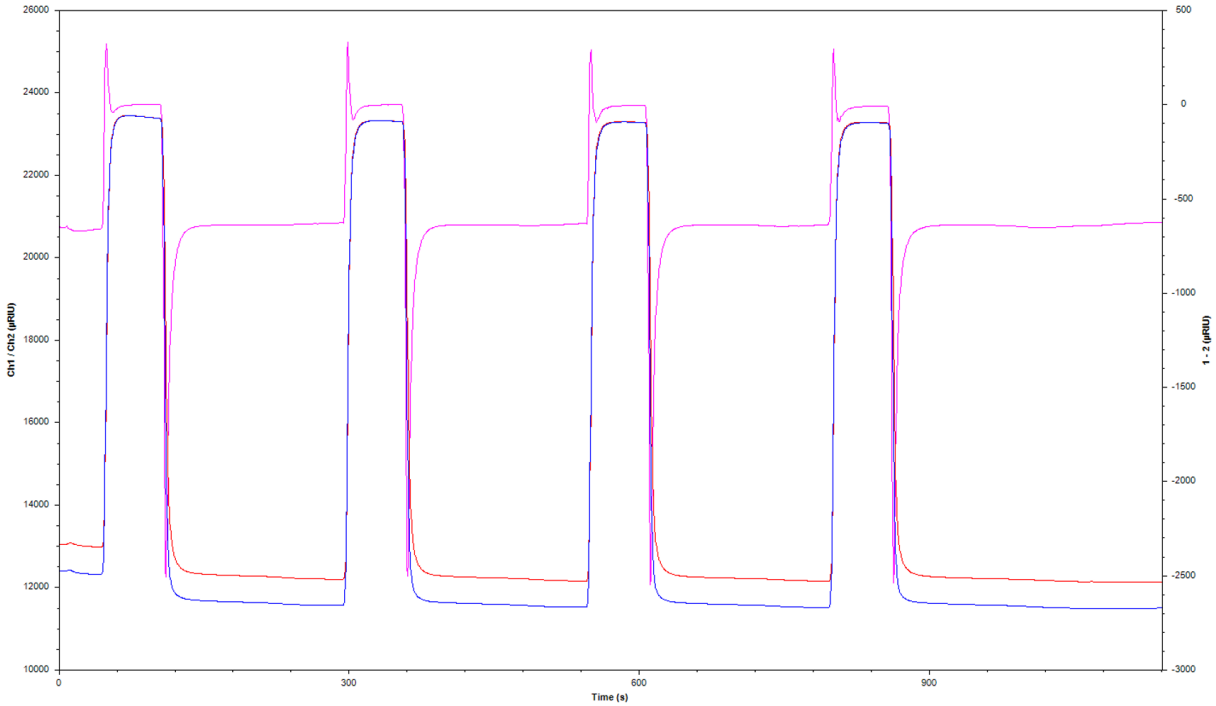

Figure S 46: Sensorgram of four injections of cleaning solution over CMD500M sensor chip before the immobilization of Δ*Mt*DXPS. The blue, red, and magenta curves represent the left (active) channel, right (reference) channel, and the difference, respectively.

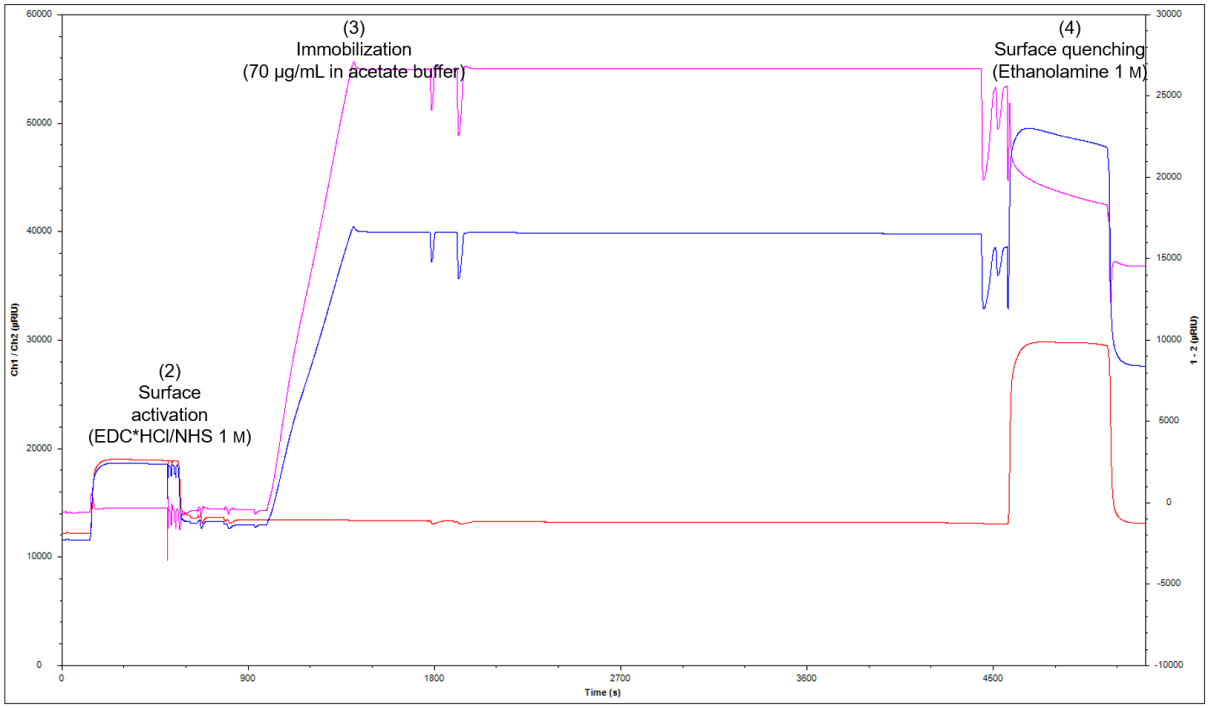

Figure S 47: Sensorgram of the immobilization procedure for Δ*Mt*DXPS on CMD500M sensor chip: (2) activation solution, (3) Δ*Mt*DXPS, and (4) quenching solution. The blue, red, and magenta curves represent the left (active) channel, right (reference) channel, and the difference, respectively.

Table S 5: Kinetics and binding affinities of all second-round fragments against Δ*Mt*DXPS by SPR. RU after immobilization = 14,905.

Cpd.	R_{max} (RU)[a]	k_{on} ($M^{-1}s^{-1}$)[b]	k_{off} (s^{-1})[c]	K_D (μM)[d]	RU at 625 μM
10	77 ± 1	67 ± 2	0.0115 ± 0.0002	172 ± 6	60
11	22.6 ± 0.3	3900 ± 100	0.094 ± 0.002	245 ± 6	16
61	19.7 ± 3	232 ± 6	0.087 ± 0.001	370 ± 10	13
66	60 ± 5	53 ± 4	0.169 ± 0.3	3200 ± 300	10
127	58.8 ± 0.8	209 ± 4	0.122 ± 0.001	590 ± 10	31
128	51 ± 1	190 ± 7	0.263 ± 0.004	1380 ± 50	16
131	42.4 ± 0.6	4300 ± 100	0.207 ± 0.004	480 ± 20	23
135	69 ± 2	78 ± 4	0.063 ± 0.001	810 ± 40	31
136	41 ± 3	1600 ± 200	0.121 ± 0.006	770 ± 80	19
137	20.2 ± 0.3	6600 ± 200	0.228 ± 0.006	350 ± 10	13
139	41.2 ± 0.8	169 ± 5	0.090 ± 0.002	530 ± 20	23
140	13.1 ± 0.2	152 ± 5	0.0524 ± 0.0009	340 ± 10	9

[a] maximum analyte binding capacity; [b] association constant rate; [c] dissociation constant rate; [d] equilibrium dissociation constant.

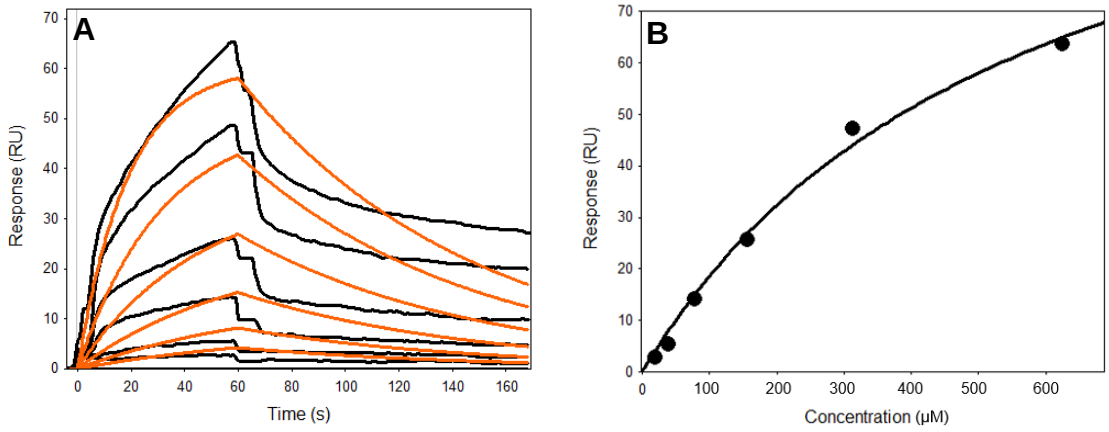

Figure S 48: Overlay of sensorgrams of fragment **10** injected at concentrations of 19.6−625.0 μM over immobilized **A**) Δ*Mt*DXPS. Fitting of responses at equilibrium according to 1:1 LANGMUIR binding model (orange lines). RU at equilibrium from 46−50 s plotted against fragment concentration in μM **B**) Δ*Mt*DXPS.

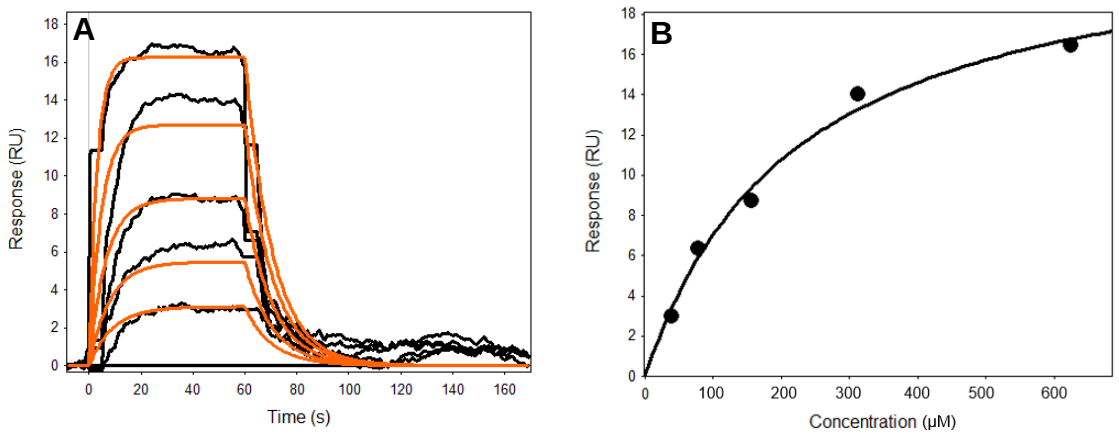

Figure S 49: Overlay of sensorgrams of fragment **11** injected at concentrations of 19.6−625.0 µM over immobilized **A**) Δ*Mt*DXPS. Fitting of responses at equilibrium according to 1:1 LANGMUIR binding model (orange lines). RU at equilibrium from 46−50 s plotted against fragment concentration in µM **B**) Δ*Mt*DXPS.

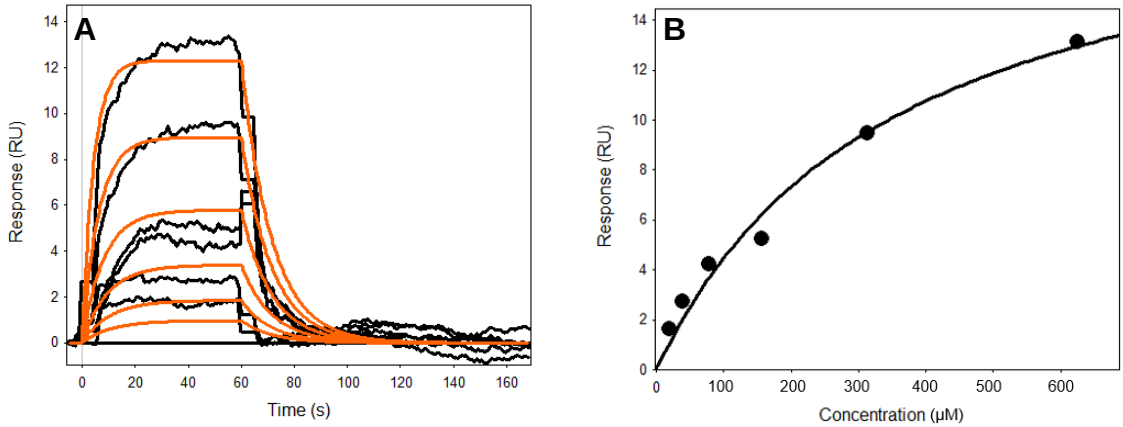

Figure S 50: Overlay of sensorgrams of fragment **61** injected at concentrations of 19.6−625.0 µM over immobilized **A**) Δ*Mt*DXPS. Fitting of responses at equilibrium according to 1:1 LANGMUIR binding model (orange lines). RU at equilibrium from 46−50 s plotted against fragment concentration in µM **B**) Δ*Mt*DXPS.

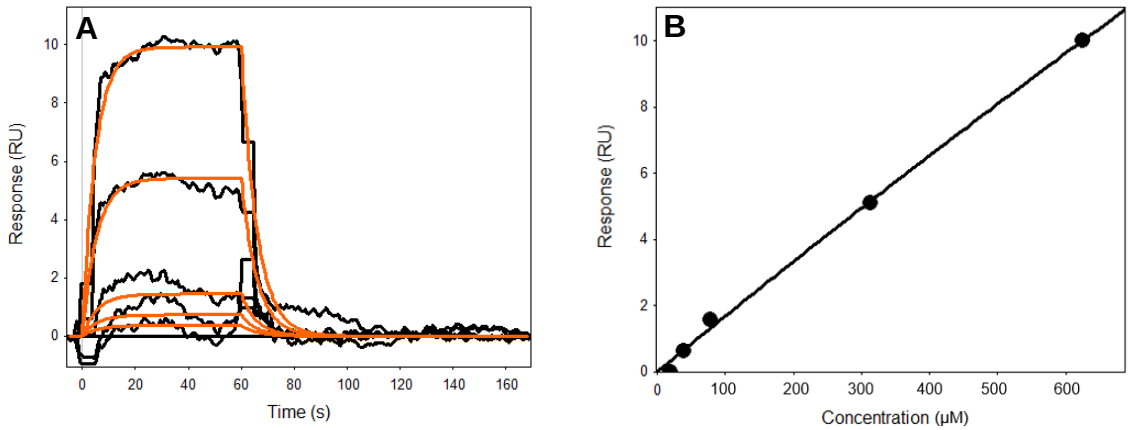

Figure S 51: Overlay of sensorgrams of fragment **66** injected at concentrations of 19.6−625.0 µM over immobilized **A**) Δ*Mt*DXPS. Fitting of responses at equilibrium according to 1:1 LANGMUIR binding model (orange lines). RU at equilibrium from 46−50 s plotted against fragment concentration in µM **B**) Δ*Mt*DXPS.

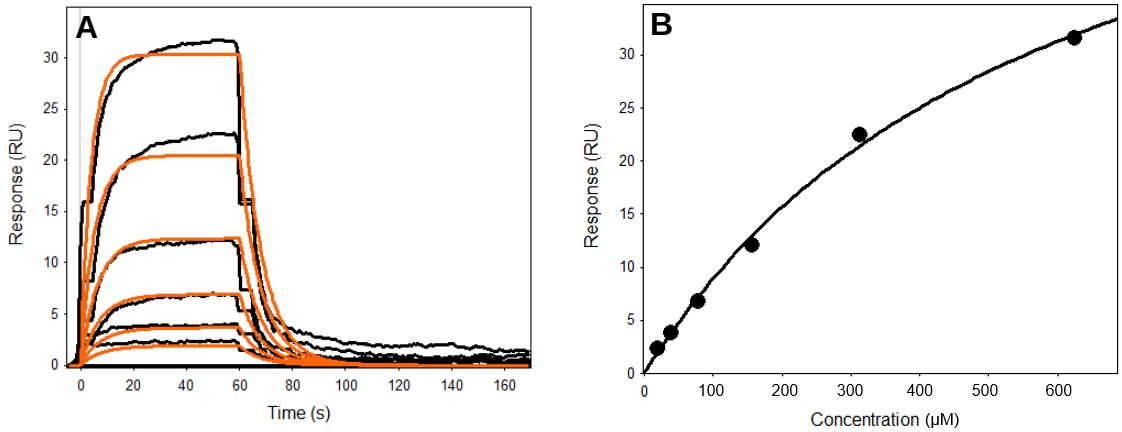

Figure S 52: Overlay of sensorgrams of fragment **127** injected at concentrations of 19.6−625.0 µM over immobilized **A**) Δ*Mt*DXPS. Fitting of responses at equilibrium according to 1:1 LANGMUIR binding model (orange lines). RU at equilibrium from 46−50 s plotted against fragment concentration in µM **B**) Δ*Mt*DXPS.

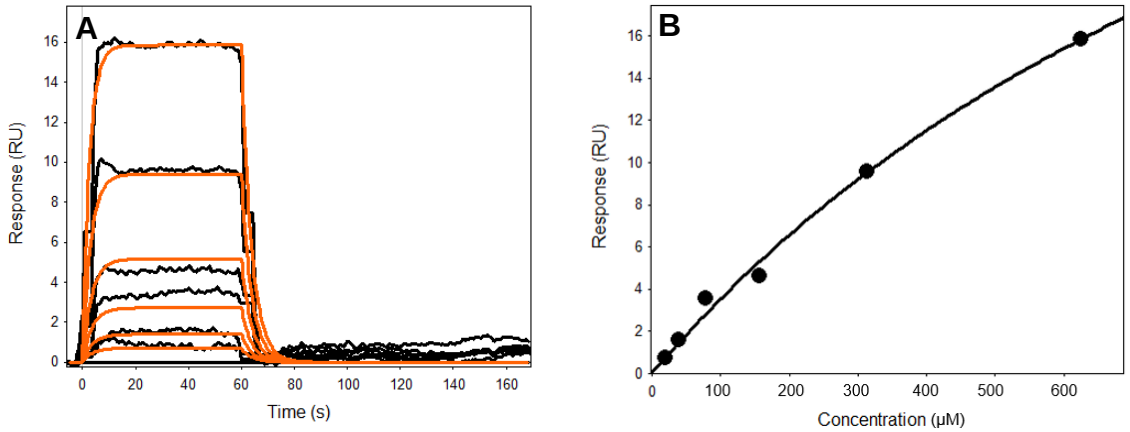

Figure S 53: Overlay of sensorgrams of fragment **128** injected at concentrations of 19.6−625.0 µM over immobilized **A**) Δ*Mt*DXPS. Fitting of responses at equilibrium according to 1:1 LANGMUIR binding model (orange lines). RU at equilibrium from 46−50 s plotted against fragment concentration in µM **B**) Δ*Mt*DXPS.

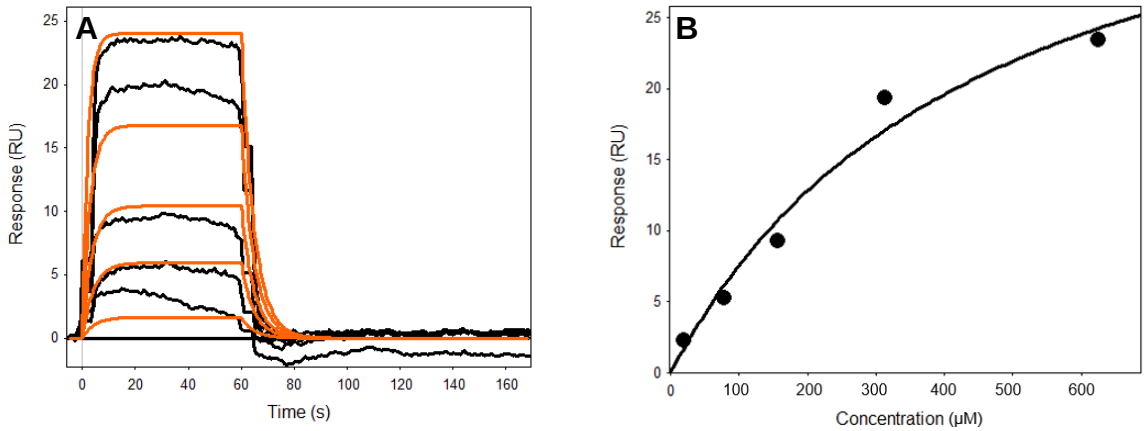

Figure S 54: Overlay of sensorgrams of fragment **131** injected at concentrations of 19.6−625.0 µM over immobilized **A**) Δ*Mt*DXPS. Fitting of responses at equilibrium according to 1:1 LANGMUIR binding model (orange lines). RU at equilibrium from 46−50 s plotted against fragment concentration in µM **B**) Δ*Mt*DXPS.

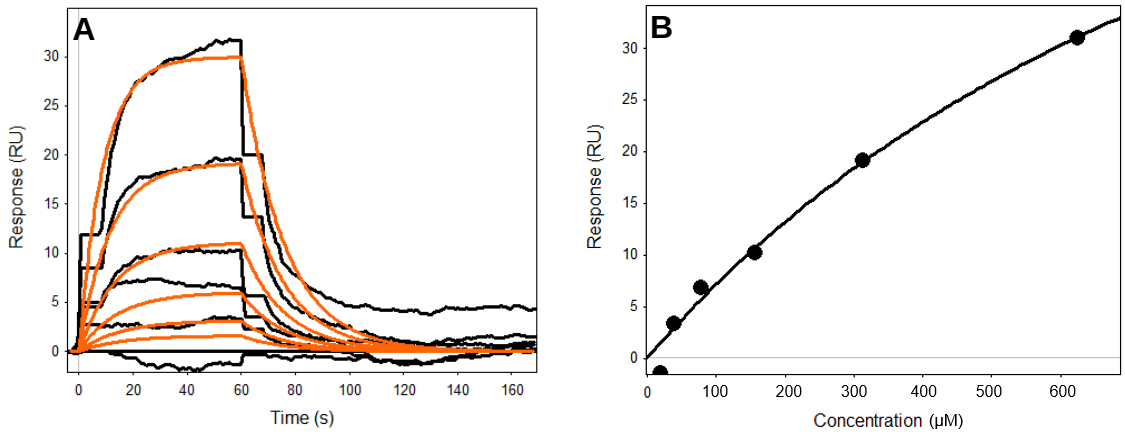

Figure S 55: Overlay of sensorgrams of fragment **135** injected at concentrations of 19.6−625.0 µM over immobilized **A**) Δ*Mt*DXPS. Fitting of responses at equilibrium according to 1:1 LANGMUIR binding model (orange lines). RU at equilibrium from 46−50 s plotted against fragment concentration in µM **B**) Δ*Mt*DXPS.

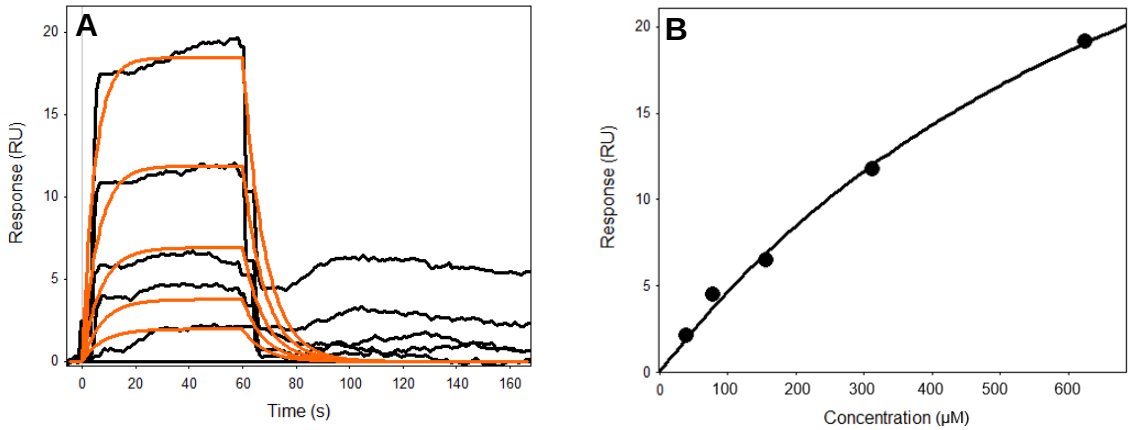

Figure S 56: Overlay of sensorgrams of fragment **136** injected at concentrations of 19.6−625.0 µM over immobilized **A**) Δ*Mt*DXPS. Fitting of responses at equilibrium according to 1:1 LANGMUIR binding model (orange lines). RU at equilibrium from 46−50 s plotted against fragment concentration in µM **B**) Δ*Mt*DXPS.

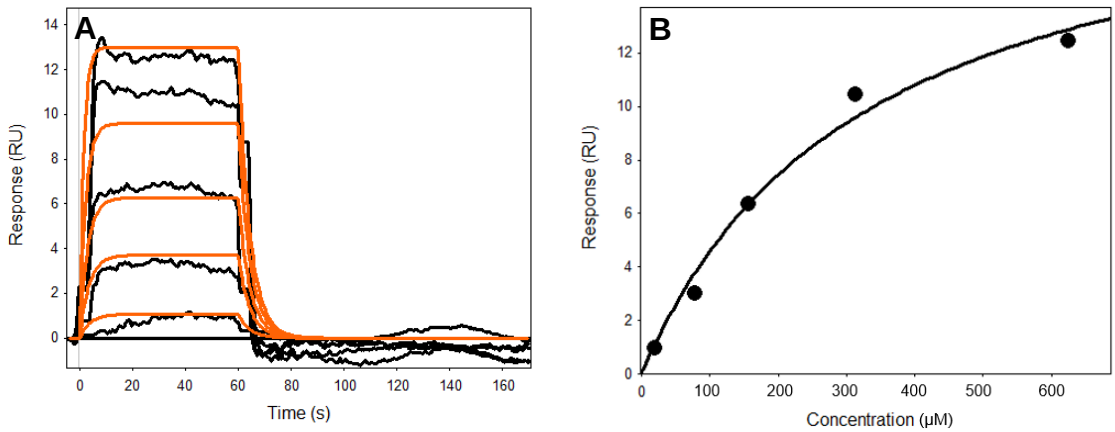

Figure S 57: Overlay of sensorgrams of fragment **137** injected at concentrations of 19.6−625.0 µM over immobilized **A**) Δ*Mt*DXPS. Fitting of responses at equilibrium according to 1:1 LANGMUIR binding model (orange lines). RU at equilibrium from 46−50 s plotted against fragment concentration in µM **B**) Δ*Mt*DXPS.

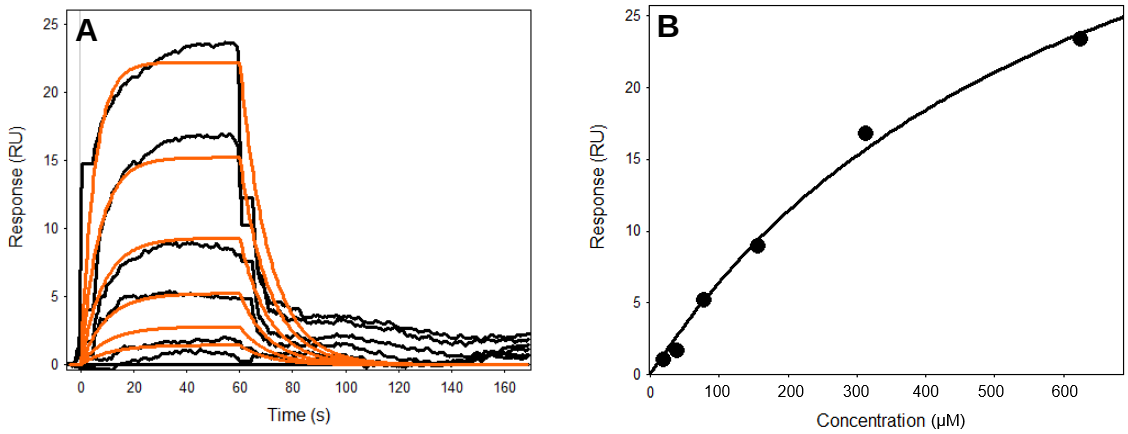

Figure S 58: Overlay of sensorgrams of fragment **139** injected at concentrations of 19.6−625.0 µM over immobilized **A**) Δ*Mt*DXPS. Fitting of responses at equilibrium according to 1:1 LANGMUIR binding model (orange lines). RU at equilibrium from 46−50 s plotted against fragment concentration in µM **B**) Δ*Mt*DXPS.

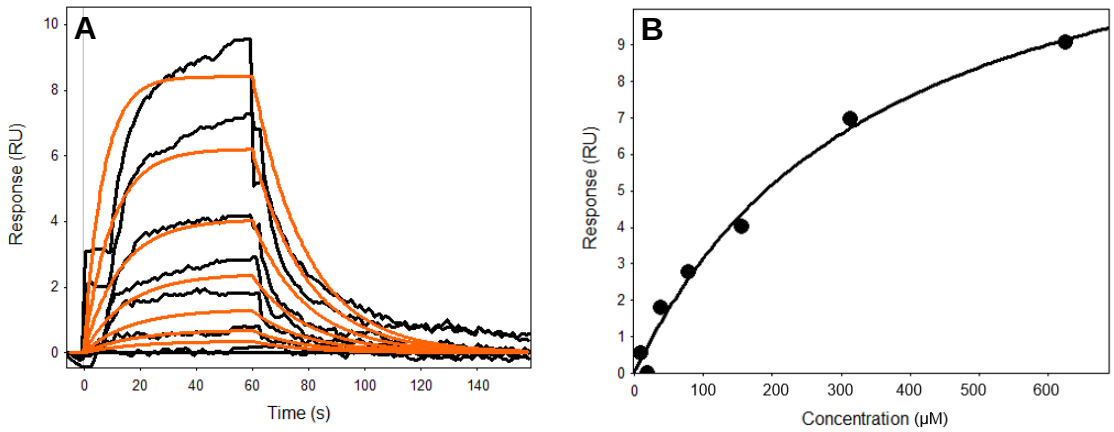

Figure S 59: Overlay of sensorgrams of fragment **140** injected at concentrations of 19.6−625.0 µM over immobilized **A**) Δ*Mt*DXPS. Fitting of responses at equilibrium according to 1:1 LANGMUIR binding model (orange lines). RU at equilibrium from 46−50 s plotted against fragment concentration in µM **B**) Δ*Mt*DXPS.

5.1.11 Tested compounds with poor data quality

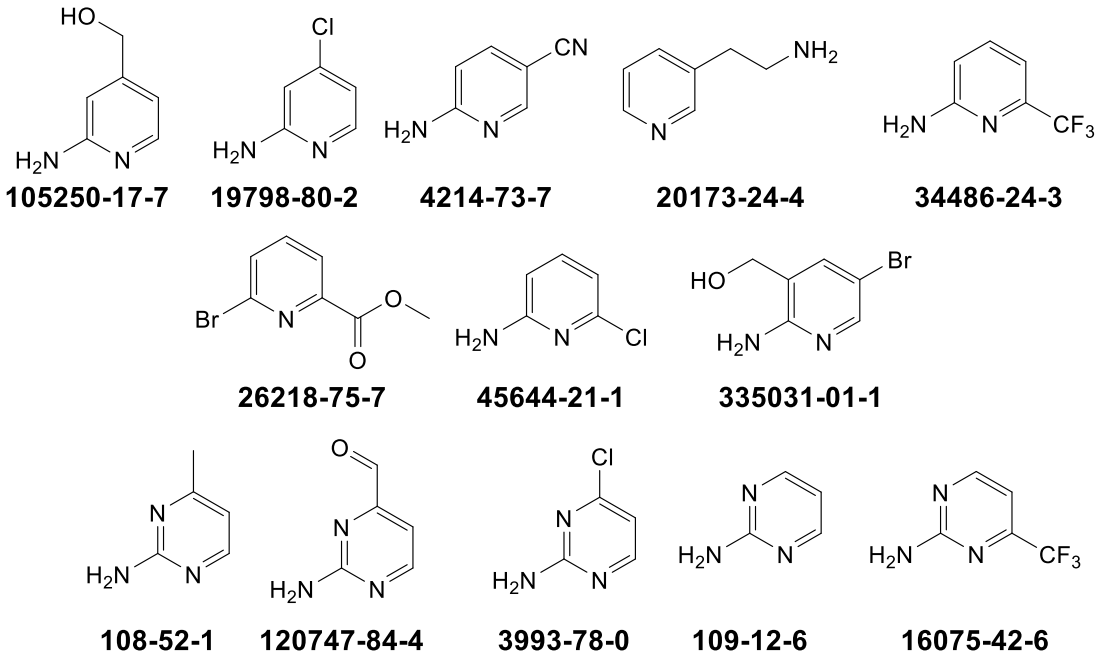

Figure S 60: Tested compound derivatives and corresponding Chemical Abstract Service (CAS) numbers with poor data quality that were not taken into consideration for fragment-optimization analysis.

5.2 Supplementary information Chapter 3.3

5.2.1 Assay for K_M determination

Determination of the kinetic properties of the different DXPS homologues followed a previously pulished procedure.[60] The assay is described in Chapter 5.3.4.1. Concentrations of pyruvate were varied 2 mM–0.98 µM and for D/L-GAP between 1 mM–0.49 µM.

Table S 6: K_M of pyruvate and D/L-GAP for DXPS homologues to determine optimal substrate concentrations for the HPLC-MS/MS activity assay. K_M for Δ*Dr*DXPS was assumed to be similar to *Dr*DXPS.

	$K_M^{pyruvate}$ [µM]	$K_M^{D/L\text{-}GAP}$ [µM]
*Dr*DXPS	94 ± 16	204 ± 62
Δ*Mt*DXPS	229 ± 180	1401 ± 583
Δ*Kp*DXPS	173 ± 14	241 ± 57
Δ*Pa*DXPS	377 ± 144	185 ± 24
Δ*Dr*DXPS	n.d.	n.d

n.d. = not determined.

5.2.2 Assay preparation

Two buffer solutions are prepared (Buffer A: 100 mM 2-amino-2-(hydroxymethyl)propane-1,3-diol (Tris)-HCl pH 7.6, 8 µM ThDP, 200 µM $MgCl_2$, 1 µM *Dr*DXPS or 20 µM Δ*Mt*DXPS. Buffer B *Dr*DXPS: 100 mM Tris-HCl pH 7.6, 800 µM D/L-GAP, 400 µM pyruvate. Buffer B Δ*Mt*DXPS: 100 mM Tris-HCl pH 7.6, 2 mM D/L-GAP, 500 µM pyruvate). Either single concentrations or dilution series of compounds were prepared on a 96-well plate in DMSO. Columns 1 and 2, 11 and 12 were DMSO only for blank and positive control, respectively. On a second 96-well plate 100 µL Tris-HCl buffer were filled in well 1 and 2 of every row and 100 µL of buffer A in wells 3–12. Then, 10 µL of each well from the compound plate were pipetted to this new plate, and the mixture incubated at 25 °C for 10 min. To start the reaction, 100 µL of buffer B were added to each well simultaneously and the plate was incubated at 37 °C for 25 min. During that time, a 2 mM solution of DMB in 1 M HCl (including 3 mM $NaHSO_4$ and 0.1 M β-mercaptoethanol) was prepared, and 50 µL of this solution was transferred into each well of a new plate. The assay plate was heated to 95 °C for 5 min, centrifuged at 10 °C for 3 min and 4000 rpm. Then, 50 µL of the supernatant were added to the DMB plate. This plate was incubated at 95 °C for 1 h. A forth plate was prepared with 198 µL of acetonitrile and 2 µL of the DMB solution were added.

Table S 7: Raw data for determination of *Dr*DXPS concentration in HPLC-MS/MS-assay. Blanks were performed in duplicate, all other measurements in quadruplicate, but with higher enzyme concentrations the peak area could not always be determined. Measurement was performed with 100 µM of pyruvate. Results for other homologues can be found in Zahra Adeli's Master's thesis.[99]

*Dr*DXPS [µM]	Peak area	%pyruvate
0	1300566[a]	100
0.5	262934[b]	20
0.75	78711[b]	6
1.0	39822[c]	3
1.25	51001[d]	4
1.5	61939[d]	5

[a] mean of two measurements, [b] mean of four measurements, [c] one measurement, [d] mean of three measurements.

5.2.3 HPLC-MS/MS measurement

HPLC conditions were as follows: column: NUCLEODUR C18 Pyramid, 3 µm, 150*2 mm, Macherey-Nagel; temperature: 40 °C; injection volume: 3 µL; flow rate: 600 µL min^{-1}; solvent A: water + 0.1% formic acid; solvent B: acetonitrile + 0.1% formic acid; gradient: 90% A at 0 min, 90%–5% A from 0.4 min to 1.10 min, 5% A until 3.70 min, 5%–90% A from 3.70 to 4.50 min. Mass spectrometric conditions were as follows: TSQ Quantum Access Max (Thermo Fisher Scientific, Waltham, MA, USA) instrument parameters: Spray voltage 3500 V, vaporizer temperature 370 °C, sheath gas pressure 60 psi, aux gas pressure 20 psi, capillary temperature 270 °C, collision pressure 1.5 mTorr, positive ionization mode, scan type: MRM. For AQ analyte reaction-monitoring parameters see **Table S 8**. Data acquisition and quantification were performed using Xcalibur software.

Table S 8: LC-ESI-MS/MS reaction monitoring parameters of AQ analytes in positive ionization mode.

	precursor ion m/z	product ion m/z	collision energy (V)	tube lens offset (V)	retention time (min)
DMB-py	205.013	90.110 187.000	31 22	88 88	1.9

5.2.4 Data analysis

Percent inhibition (%inhi.) was calculated using the blank peak area as the upper limit (no pyruvate consumption corresponding to full inhibition) and the control peak area as the lower limit (no inhibition and maximum pyruvate consumption).

$$\%\text{inhi.} = \frac{\text{area (sample} - \text{control)}}{\text{area (blank} - \text{control)}} * 100$$

Single point determinations were performed at least three times and only compounds with an average inhibition of >50% were used for IC_{50} experiments. IC_{50} calculations were performed in OriginPro 2020b using nonlinear sigmoidal growth fitting while fixing 100% inhibition as the upper limit. The average of the three independent IC_{50} determinations was calculated to determine the IC_{50}.

5.3 Supplementary information for Chapter 3.4

Numbering of compounds in this chapter follows the numbering in Chapter 3.4.

5.3.1 Gene expression and protein purification of DXPS and IspC

Gene expression and protein purification of *D. radiodurans*, native and truncated *M. tuberculosis* DXPS and *E. coli* IspC followed previously reported protocols.[55,60,195]

5.3.2 Binding affinity determination by SPR

The SPR binding studies were performed using a Reichert SR7500DC surface plasmon resonance spectrometer (Reichert Technologies, Depew, NY, USA), and medium density carboxymethyl dextran hydrogel CMD500M sensor chips (XanTec Bioanalytics, Düsseldorf, Germany). Milli-Q water was used as the running buffer for immobilization. Truncated *M. tuberculosis* DXPS (Δ*Mt*DXPS, 66.61 kDa) and native *Mt*DXPS (67.88 kDa) were immobilized in one of the two flow cells according to reported amine-coupling protocols.[194] The other flow cell was left blank to serve as a reference. The system was initially primed with borate buffer 100 mM (pH 9.0), then the carboxymethyldextran matrix was activated by a 1:1 mixture of EDC*HCl 100 mM and NHS 100 mM at a flow rate of 10 µL min^{-1} for 7 min. The Δ*Mt*DXPS or *Mt*DXPS was diluted to a final concentration of 1.1 µM and 1.4 µM, respectively, in 10 mM sodium acetate buffer (pH 4.5), and was injected at a flow rate of 5 µL min^{-1} for 10 min. Non-reacted surface was quenched by 1 M ethanolamine hydrochloride (pH 8.5) at a flow rate of 25 µL min^{-1} for 3 min. A series of 10 buffer injections was run initially on both reference and active surfaces to equilibrate the system resulting in a stable immobilization level of approximately 5,000 (9,000 for *Mt*DXPS) µRIU (**Figure S 61**, **Figure S 31**),), respectively. HEPES buffer (50 mM HEPES, 150 mM NaCl, 0.05% v/v Tween 20, 1 mM $MgCl_2$, pH 8.0) containing 5% v/v DMSO was used as the running buffer for binding studies. The running buffer was filtered and degassed prior to use. Binding experiments were performed at 20 °C. Compounds dissolved in DMSO were diluted with the running buffer (final DMSO concentration of 5% v/v) and were injected at a flow rate of 30 µL min^{-1}. The association time was set to 60 s, and the dissociation phase was recorded for 120 s. Ethylene glycol 80% in the running buffer was used for regeneration of the gold-chip surface. Differences in the bulk refractive index due to DMSO were corrected by a calibration curve (nine concentrations: 3–7% v/v DMSO in the running buffer). Data processing and analysis were performed by Scrubber software (Version 2.0c, 2008, BioLogic Software). Sensorgrams were calculated by

sequential subtractions of the corresponding curves obtained from the reference flow cell and the running buffer (blank). SPR responses are expressed in RU.

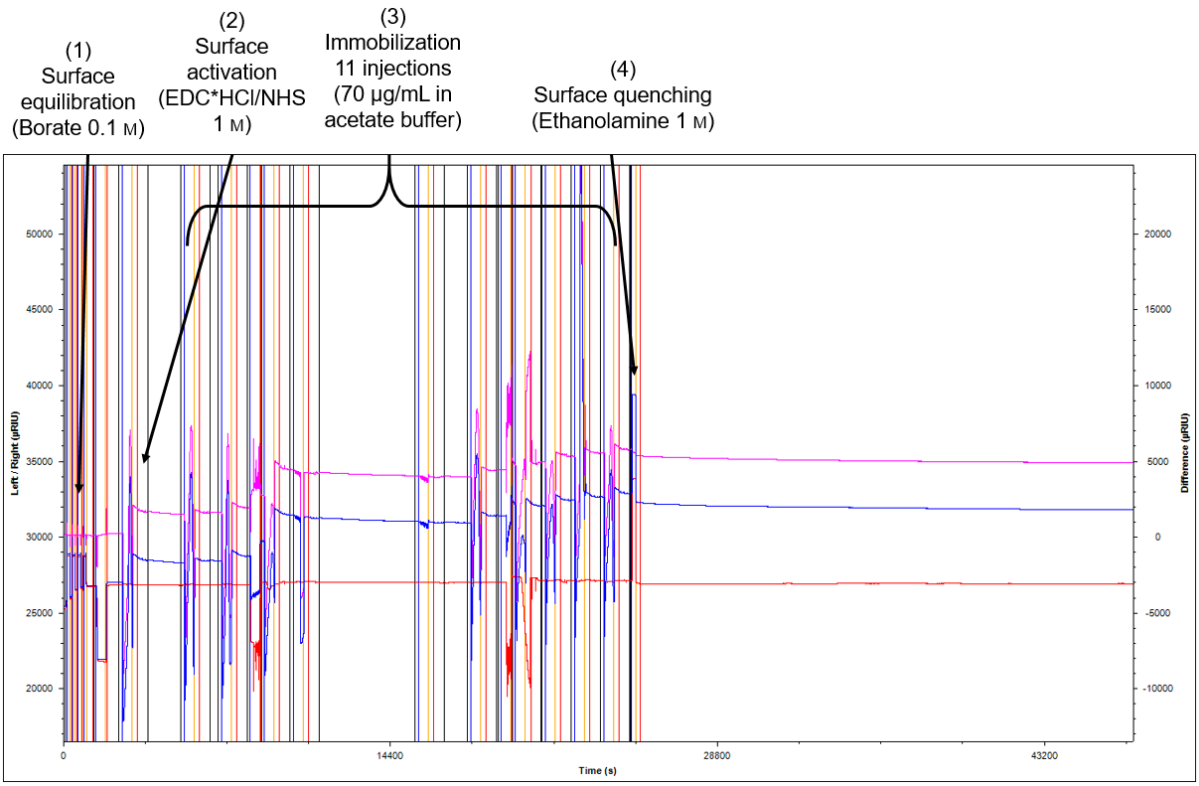

Figure S 61: Sensorgram of the immobilization procedure for Δ*Mt*DXPS on CMD500M sensor chip: (1) Five injections of cleaning solution, (2) activation solution, (3) Δ*Mt*DXPS, and (4) quenching solution. The blue, red, and magenta curves represent the left (active) channel, right (reference) channel, and the difference, respectively.

Table S 9: Structure and binding data for hits from the first round of VS. Compound were tested at 100 µM with 5% DMSO.

ID	Structure	Δ*Mt*DXPS RU 1	Δ*Mt*DXPS RU 2	RU *Mt*DXPS
1	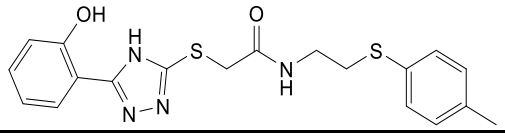	41	61	47
2	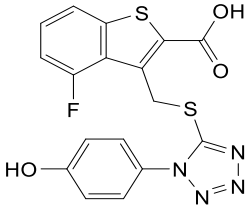	55	45	-

ID	Structure	Δ*Mt*DXPS RU 1	Δ*Mt*DXPS RU 2	RU *Mt*DXPS
3	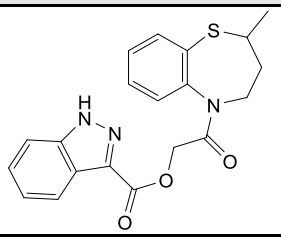	47	38	44
4	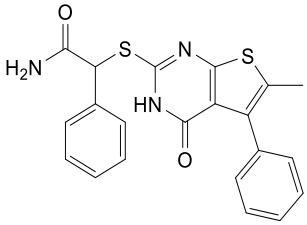	39	33	28
5	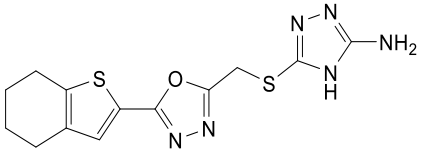	29	19	46
6	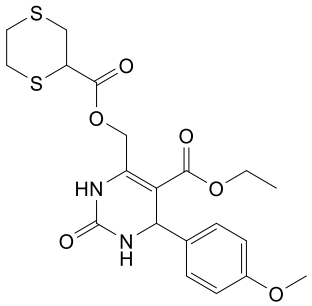	23	15	40
7	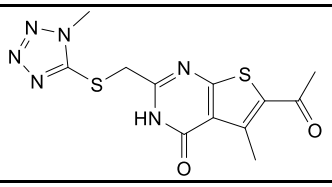	-	9	9
8	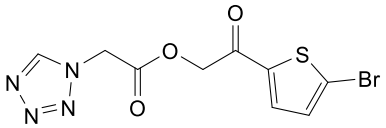	11	6	5
9	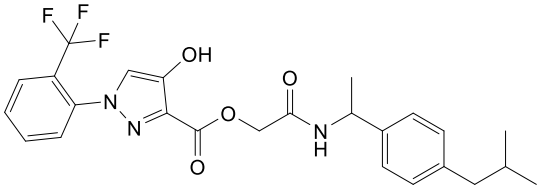	7	4	4
10	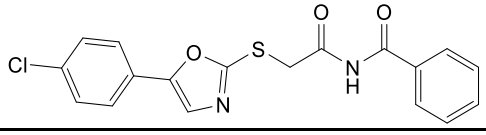	9	4	3
11	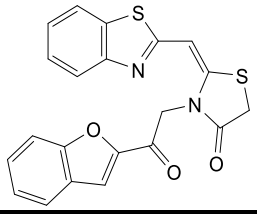	11	2	0

ID	Structure	Δ*Mt*DXPS RU 1	Δ*Mt*DXPS RU 2	RU *Mt*DXPS
12	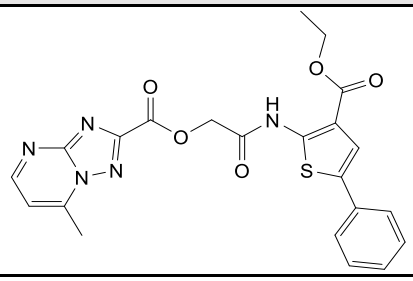	7	3	-
39	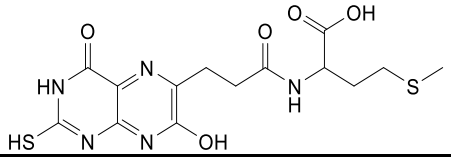	–3	–10	–6
40	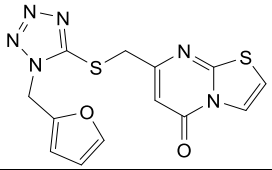	3	7	4
41	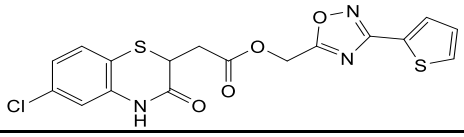	-	-	-
50	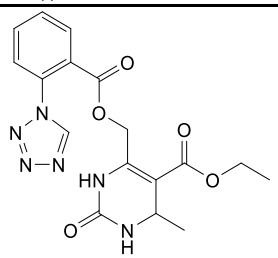	-	–5	–11
51	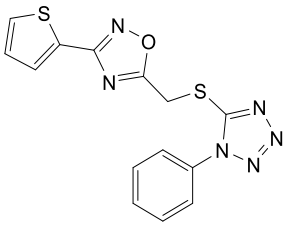	-	17	21
52	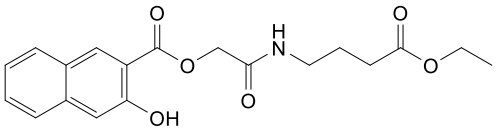	11	11	25
53	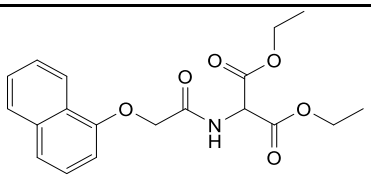	10	6	15
54	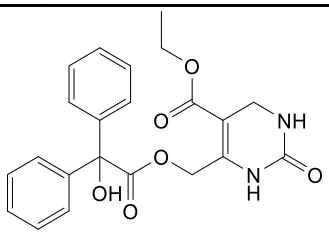	11	21	22

ID	Structure	ΔMtDXPS RU 1	ΔMtDXPS RU 2	RU MtDXPS
55	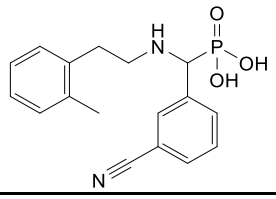	-	-	4
56	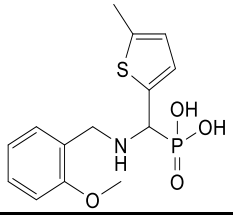	-	-	–17
57	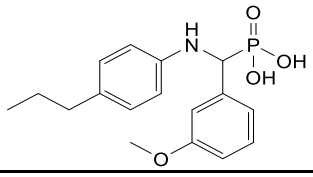	19	11	9
58	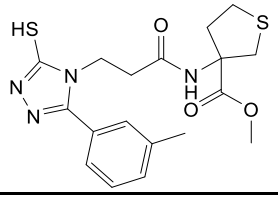	8	6	28
59	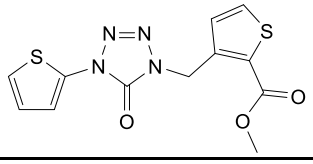	15	13	22
60	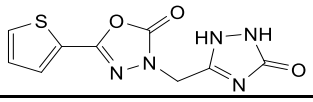	–2	5	8
61	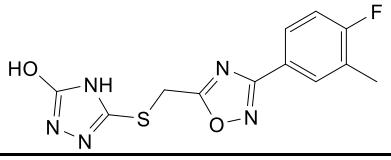	20	12	-
62	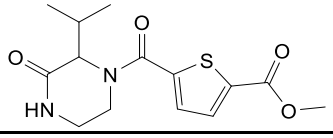	11	–1	0
63	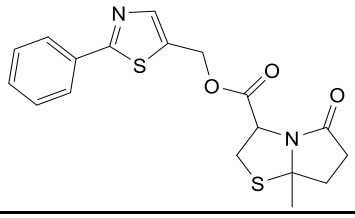	10	10	2
64	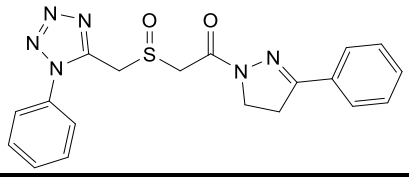	15	14	18

ID	Structure	ΔMtDXPS RU 1	ΔMtDXPS RU 2	RU MtDXPS
65	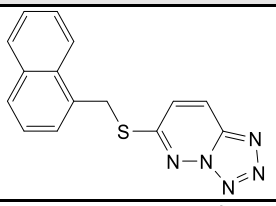	-	-	24
66	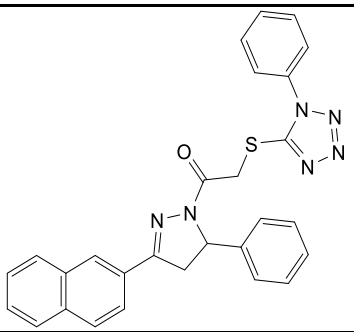	-	-	6
67	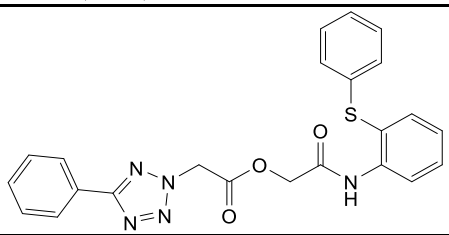	9	24	15
68	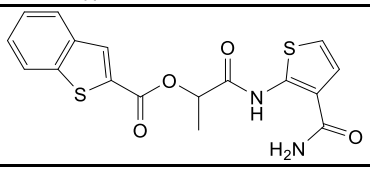	15	6	-
69	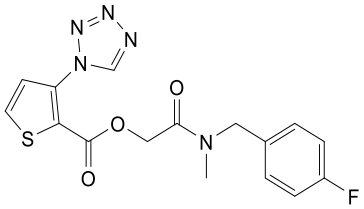	4	3	–4
70	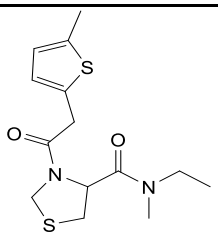	–7	7	7
71	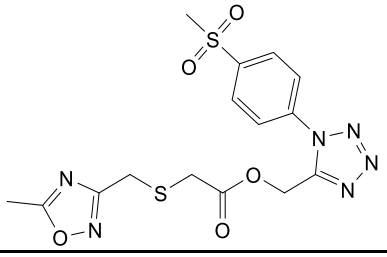	6	–4	8
72	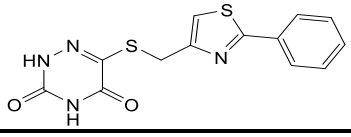	33	28	37

ID	Structure	ΔMtDXPS RU 1	ΔMtDXPS RU 2	RU MtDXPS
73	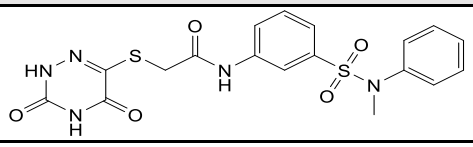	22	17	21
74	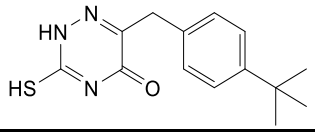	-	31	26
75	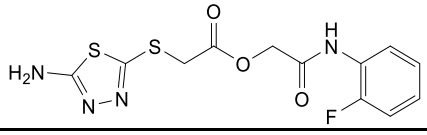	8	1	7
76	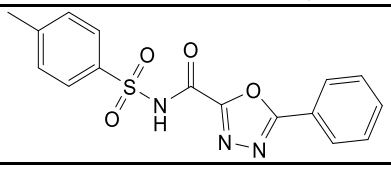	3	1	0
77	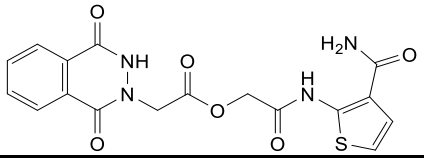	-	14	15
78	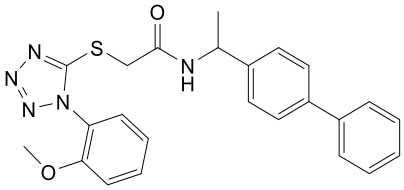	13	16	3
79	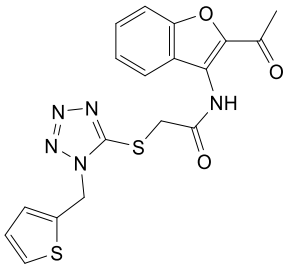	6	15	9
80	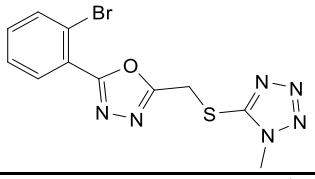	14	7	2
81	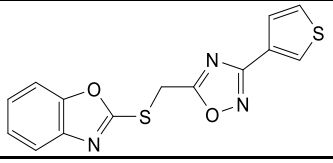	11	18	11
82	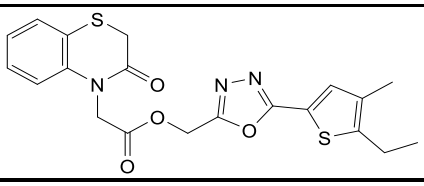	18	15	9

ID	Structure	ΔMtDXPS RU 1	ΔMtDXPS RU 2	RU MtDXPS
83	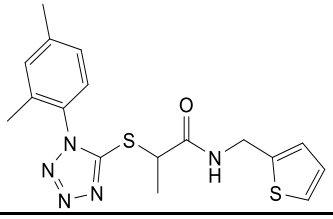	21	18	22
84	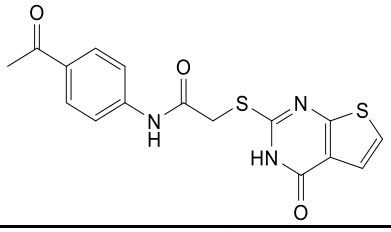	4	–5	15
85	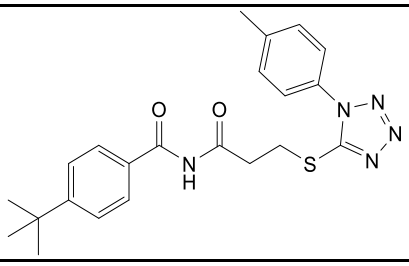	7	6	17
86	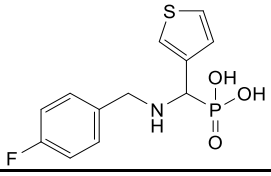	-	-	0
87	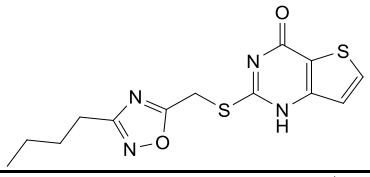	6	4	–1
88	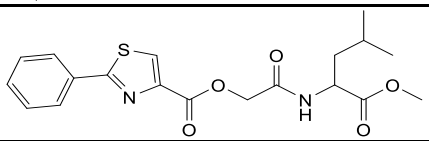	18	11	7
89	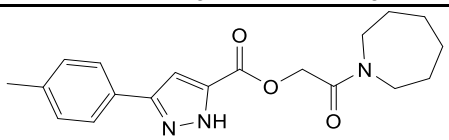	5	0	–11
90	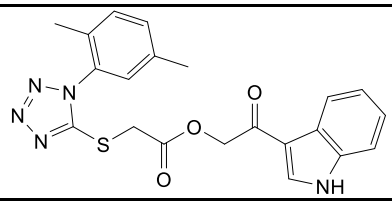	0	7	2
91	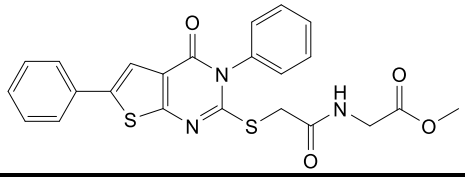	-	-	-

ID	Structure	Δ*Mt*DXPS RU 1	Δ*Mt*DXPS RU 2	RU *Mt*DXPS
92	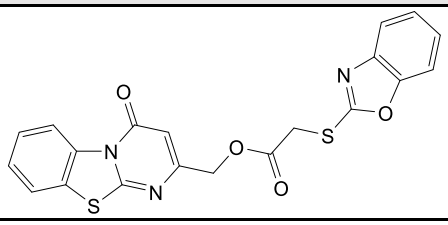	14	-	no dissoziation: 25
93	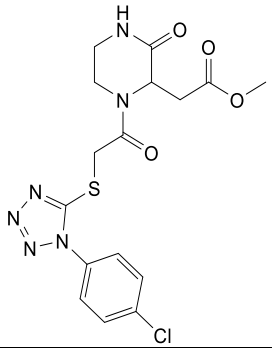	5	1	4
94	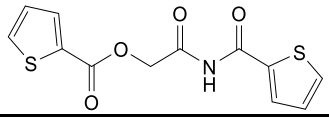	10	3	10
95	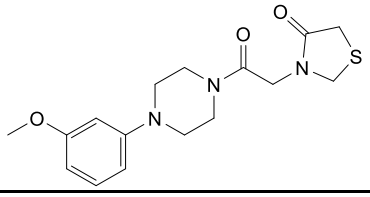	2	8	–1
96	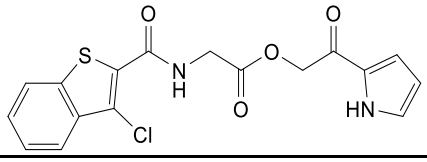	-	10	–7
97	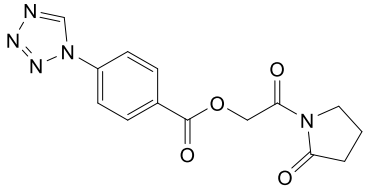	5	–5	–4
98	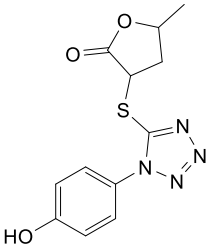	–2	–3	5
99	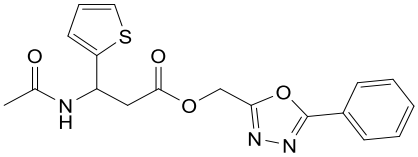	3	–4	-
100	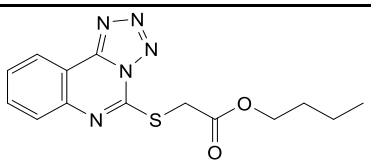	19	11	20

ID	Structure	ΔMtDXPS RU 1	ΔMtDXPS RU 2	RU MtDXPS
101	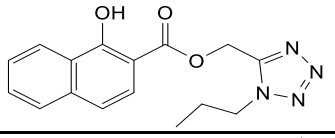	20	18	37
102	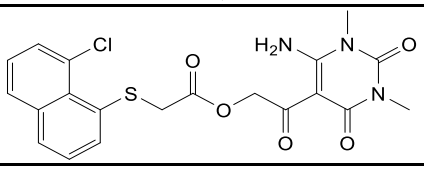	-	-	no dissoziation: 47
103	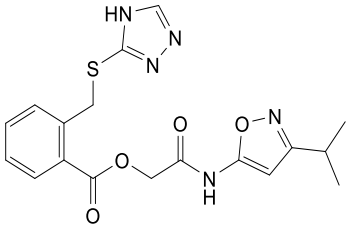	29	30	27
104	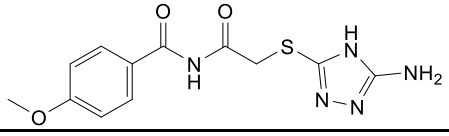	15	–3	–1
105	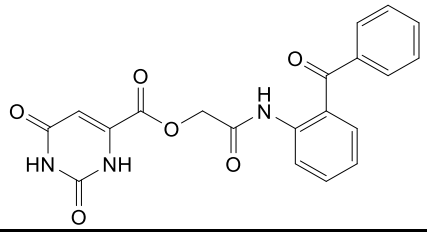	3	–2	15
106	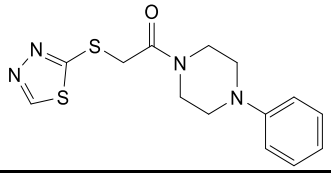	14	7	9
107	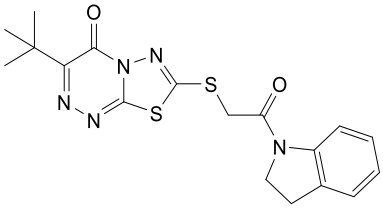	8	5	8
108	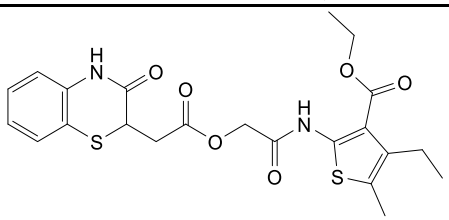	6	4	–2
109	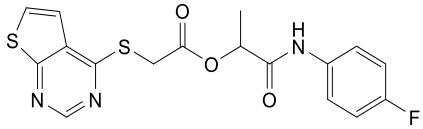	7	3	0
110	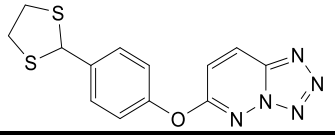	18	20	16

ID	Structure	Δ*Mt*DXPS RU 1	Δ*Mt*DXPS RU 2	RU *Mt*DXPS
111	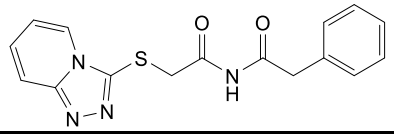	3	–4	7
112	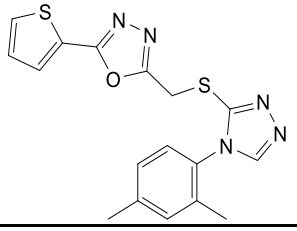	8	16	23
113	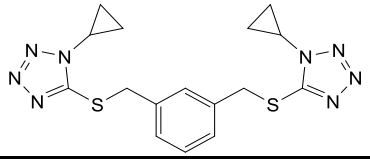	20	25	20
114	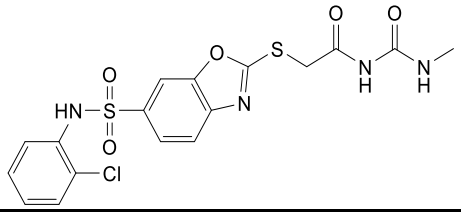	24	16	26
115	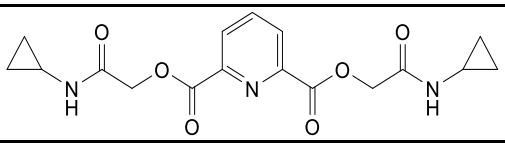	-3	3	6
116	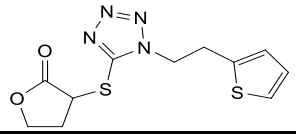	5	1	9
117	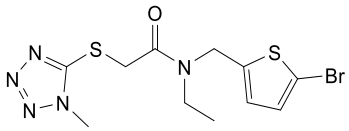	3	0	6
118	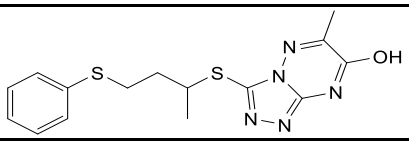	9	18	11
119	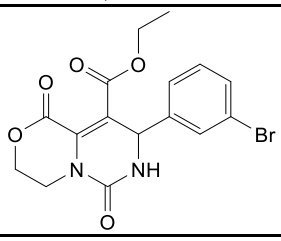	10	4	–12
120	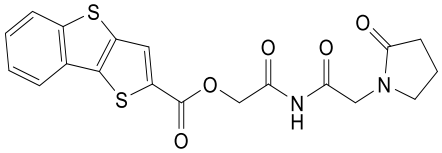	-	-	6

ID	Structure	ΔMtDXPS RU 1	ΔMtDXPS RU 2	RU MtDXPS
121	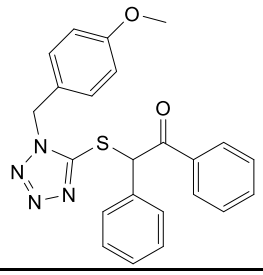	12	8	12
122	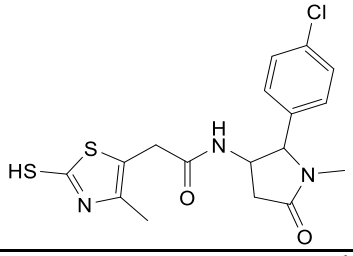	12	22	23
123	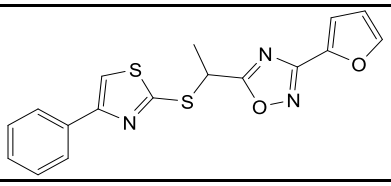	20	15	25
124	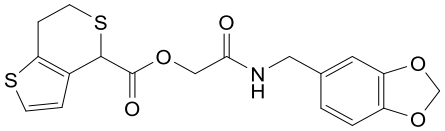	17	18	37
125	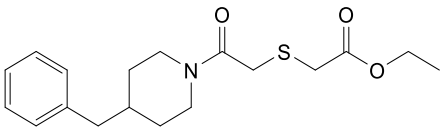	3	–2	2
126	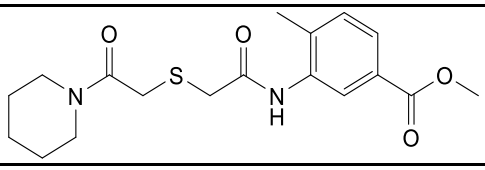	–2	–2	–4
127	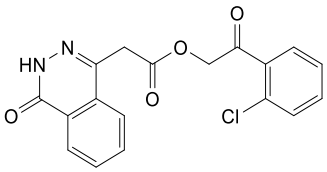	12	9	1
128	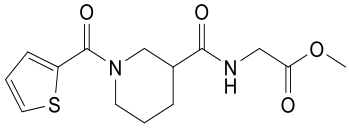	10	0	–12
	DMSO	6	–2	1
	DMSO	1	4	–1

RU = response units.

5.3.3 Kinetic-solubility determination

Procedure see 5.1.3, (but phosphate-buffered saline (PBS) instead of HEPES).

Table S 10: Solubility limit of derivatives of **1** and selected library compounds at 1% and 5% DMSO in PBS buffer.

Cpd.	Solubility at 1% DMSO [µM]	Solubility at 5% DMSO [µM]
1	51 ± 1	99 ± 30
2	n.d.	n.d.
3	44 ± 3	56 ± 2
4	52 ± 1	107 ± 14
5	>100	>250
6	>100	144 ± 5
7	>100	>250
8	n.d.	n.d.
9	36 ± 9	56 ± 2
10	>100	>250
11	24 ± 1	21 ± 11
12	n.d.	n.d.
17	>200	n.d.
22a	104 ± 1	151 ± 4
22b	73 ± 20	>250
22c	104 ± 3	>250
22d	111 ± 1	>200
22c	104 ± 3	>250
22e	45 ± 1	58 ± 1
22f	>200	>250
22g	102 ± 3	134 ± 1
22h	43 ± 1	59 ± 1
22i	34 ± 4	56 ± 1
22j	106 ± 3	>250
22k	83 ± 30	196 ± 12
22l	32 ± 3	72 ± 42
28a	>200	n.d.
28d	>200	n.d.
28e	>200	n.d.
28f	>200	n.d.
29a	24 ± 2	59 ± 2
29b	48 ± 1	89 ± 26
29c	101 ± 1	147 ± 4
29d	43 ± 1	60 ± 1
29e	133 ± 15	>250
29f	>200	n.d.
29g	152 ± 19	181 ± 9
38a	>200	n.d.
38b	>160	>250
38c	>200	n.d.
38d	>200	n.d.
38e	>200	n.d.
39	>100	>250
40	>100	>250
41	25 ± 3	29 ± 9

n.d. = not determined.

5.3.4 Determination of inhibition of DXPS activity

5.3.4.1 DXPS-IspC coupled assay

The experiments to determine the inhibitory activity of compounds in the DXPS-IspC-coupled assay have been carried out as reported previously with minor adjustments.[60] The assay was conducted in transparent, round bottom 96 well-plates (Greiner BioOne) and the absorbance was measured using a microplate reader (PHERAstar, BMG Labtech). The assay mixture contained 100 mM HEPES with a pH of 7.0, 2 mM β-mercaptoethanol (BME), 100 mM NaCl, 0.5 mM ThDP, 1.0 mM $MgCl_2$, 0.05 mM NADPH, 1.0 mM pyruvate, 1.0 mM D/L glyceraldehyde 3-phosphate (GAP) and 1.0 µM IspC (*E. coli*, expressed and purified see Chapter 5.3.1). The amount of DXPS used in the assays was determined experimentally by a dilution series of the enzyme. The concentration, which showed a reaction velocity in the range of −0.1 to −0.2 OD over a time range of 10 minutes was chosen for further experiments.

The assay was prepared using two buffers, buffer A containing HEPES, NaCl, BME and all components of the reaction (except substrates) in 2x the final concentration and buffer B, consisting of only HEPES, NaCl, BME and the substrates, 2.0 mM pyruvate and 2.0 mM D/L-GAP. After the addition of 60 µL of buffer A to the plate with a pre-made inhibitor dilution series in 6 µL DMSO the reaction was started by the addition of 60 µL buffer B. The plate was centrifuged for 1 min at 2000 rpm and 25 °C to remove possible air bubbles. The plate was then immediately supplied to the microplate reader and the absorbance measured at 340 nm using the mode slow kinetics with a cycle time of 30 seconds and 60 cycles at 25 °C. Blank correction and linear fitting of the raw data was performed using the program Origin2021. The obtained initial velocities were converted to percent inhibition and plotted against the inhibitor concentration. The IC_{50} values were determined by nonlinear curve fitting using Origin2021.

5.3.4.2 IspC assay

The assay was conducted in transparent, round bottom 96 well-plates (Greiner BioOne) and the absorbance was measured using a microplate reader (PHERAstar, BMG Labtech). Buffer A contained 100 mM HEPES with a pH of 7.0, 2 mM β-mercaptoethanol (BME), 100 mM NaCl, 500 nM ThDP, 1.0 mM $MgCl_2$, 1.0 mM pyruvate, 1.0 mM D/L glyceraldehyde 3-phosphate (GAP) and 1.2 µM *Dr*DXPS. Buffer B contained 0.05 mM NADPH and 10 nM *Ec*IspC. After mixing, buffer A is incubated for 2 h and then heated to 80 °C for 5 min. After cooling it down on ice for 10 min, 30 µL

were added to a plate and 3 µL of the inhibitor in DMSO was added. The reaction was started by adding 30 µL of buffer B. The plate was centrifuged for 1 min at 2000 rpm and 25 °C to remove possible air bubbles. The plate was then immediately supplied to the microplate reader and the absorbance measured at 340 nm using the mode slow kinetics with a cycle time of 30 seconds and 60 cycles at 25 °C. Blank correction and linear fitting of the raw data was performed using the program Origin2021. The obtained initial velocities were converted to percent inhibition and plotted against the inhibitor concentration. The IC_{50} values were determined by nonlinear curve fitting using Origin2021.

5.3.4.3 HPLC-MS/MS-based assay

See Chapter 5.2.

5.3.4.4 MOI assay to investigate GAP influence

Four buffer solutions are prepared (Buffer A: 100 mM Tris-HCl pH 7.6, 8 µM ThDP, 200 µM $MgCl_2$, 2 µM *Dr*DXPS. Buffer B: 100 mM Tris-HCl pH 7.6, 800 µM pyruvate. Buffer C: 100 mM Tris-HCl pH 7.6, 4 mM D-GAP). Buffers D1–6 were prepared by dilution series of buffer C with 100 mM Tris-HCl buffer followed by 1:2 dilution with buffer B (D1=0 µM, D2 =1 mM, D3=500 µM, D4=250 µM, D5=125 µM, D6=62.5 µM D-GAP). A dilution series of compound **4** was prepared on a 96-well plate in DMSO. Columns 1 and 2, 11 and 12 were DMSO only for blank and positive control, respectively. On a second 96-well plate 60 µL Tris-HCl buffer were filled in well 1 and 2 and 60 µL of buffer A in wells 3–12 of rows 1–6. Then, 6 µL of each well from the compound plate were pipetted to this new plate in rows 1–6, and the mixture incubated at 25 °C for 10 min. To start the reaction, 60 µL of buffer D1–6 (each row had its own buffer D and the final D-GAP concentration were then half of buffer D) were added to each well simultaneously and the plate was incubated at 37 °C for 25 min. During that time, a 2 mM solution of DMB in 1 M HCl (including 3 mM $NaHSO_4$ and 0.1 M β-mercaptoethanol) was prepared, and 50 µL of this solution was transferred into each well of a new plate. The assay plate was heated to 95 °C for 5 min, centrifuged at 10 °C for 3 min and 4000 rpm. Then, 50 µL of the supernatant were added to the DMB plate. This plate was incubated at 95 °C for 1 h. A forth plate was prepared with 198 µL of acetonitrile and 2 µL of the DMB solution were added.

5.3.4.5 Activity of compounds in DXPS-IspC-coupled and HPLC-MS/MS-based assay

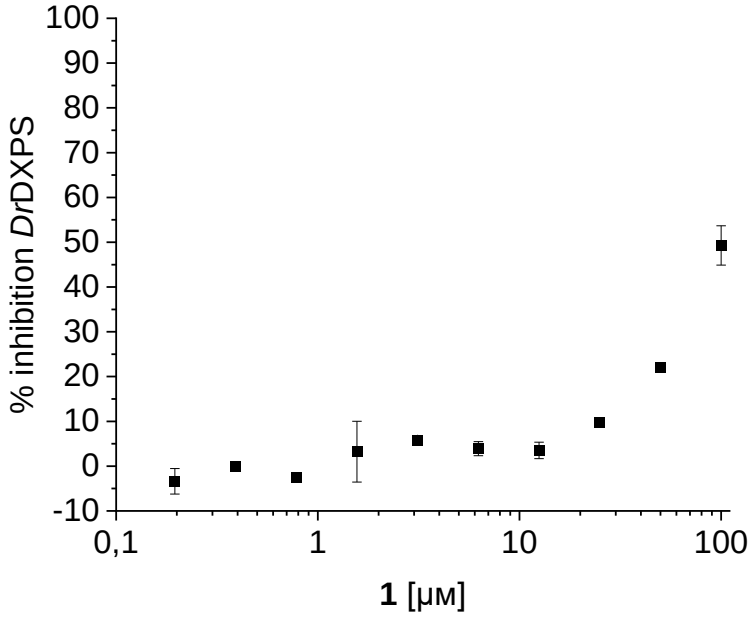

Figure S 62: IC_{50} determination of resynthesized hit **1** in DXPS-IspC coupled assay.

Table S 11: Activity of first round VS hits. Inhibition has been calculated from three independent measurements.

Cpd.	DXPS-IspC %inhi.[a]	HPLC-MS/MS %inhi. [b]	Cpd.	DXPS-IspC %inhi. [a]	HPLC-MS/MS %inhi. [b]
1	39 ± 16	14 ± 10	**83**	7 ± 8	18 ± 35
2	8 ± 10	23 ± 13	**84**	12 ± 2	29 ± 8
3	13 ± 2	9 ± 9	**85**	15 ± 4	8 ± 7
4	13 ± 8	89 ± 20	**86**	15 ± 6	–5 ± 15
5	8 ± 10	1 ± 10	**87**	5 ± 5	5 ± 4
6	7 ± 2	–2 ± 10	**88**	3 ± 1	20 ± 21
7	28 ± 25	27 ± 4	**89**	8 ± 0	17 ± 15
8	29 ± 18	17 ± 3	**90**	29 ± 8	41 ± 13
9	36 ± 9	5 ± 6	**91**	23 ± 7	15 ± 4
10	31 ± 12	27 ± 11	**92**	29 ± 1	7 ± 9
11	35 ± 16	1 ± 20	**93**	10 ± 2	–4 ± 14
12	23 ± 19	5 ± 16	**94**	22 ± 7	32 ± 5
39	18 ± 2	77 ± 8	**95**	12 ± 5	1 ± 9
40	17 ± 8	56 ± 9	**96**	5 ± 10	20 ± 26
41	23 ± 9	49 ± 13	**97**	0 ± 1	12 ± 13
50	1 ± 2	–4 ± 31	**98**	1 ± 6	1 ± 3
51	22 ± 16	26 ± 11	**99**	8 ± 7	–9 ± 14
52	9 ± 6	24 ± 7	**100**	–1 ± 4	–1 ± 11
53	7 ± 7	–6 ± 3	**101**	2 ± 2	13 ± 10
54	9 ± 6	–5 ± 13	**102**	2 ± 11	34 ± 21
55	7 ± 1	–2 ± 21	**103**	10 ± 4	11 ± 23
56	4 ± 2	0 ± 13	**104**	6 ± 3	17 ± 10

Cpd.	DXPS-IspC %inhi.[a]	HPLC-MS/MS %inhi. [b]	Cpd.	DXPS-IspC %inhi. [a]	HPLC-MS/MS %inhi. [b]
57	9 ± 12	5 ± 9	**105**	4 ± 6	23 ± 14
58	5 ± 0	35 ± 12	**106**	4 ± 6	12 ± 25
59	–9 ± 17	–23 ± 6	**107**	6 ± 10	–4 ± 12
60	1 ± 15	–4 ± 18	**108**	26 ± 3	18 ± 1
61	11 ± 4	14 ± 6	**109**	0 ± 4	26 ± 26
62	1 ± 3	1 ± 9	**110**	8 ± 1	4 ± 11
63	–1 ± 6	5 ± 9	**111**	5 ± 3	–4 ± 11
64	4 ± 2	16 ± 9	**112**	5 ± 3	–5 ± 18
65	–5 ± 11	–5 ± 18	**113**	–8 ± 8	–7 ± 22
66	17 ± 2	12 ± 12	**114**	9 ± 8	16 ± 7
67	–20 ± 21	8 ± 5	**115**	0 ± 3	18 ± 22
68	22 ± 10	40 ± 21	**116**	5 ± 5	2 ± 4
69	2 ± 0	1 ± 11	**117**	0 ± 8	–6 ± 3
70	4 ± 1	17 ± 10	**118**	3 ± 6	–1 ± 7
71	4 ± 5	–1 ± 7	**119**	4 ± 1	–1 ± 8
72	7 ± 4	–3 ± 20	**120**	22 ± 1	36 ± 22
73	16 ± 3	–7 ± 11	**121**	–9 ± 10	23 ± 3
74	27 ± 8	12 ± 6	**122**	24 ± 12	64 ± 28
75	4 ± 1	0 ± 19	**123**	10 ± 2	30 ± 13
76	–1 ± 1	0 ± 3	**124**	16 ± 0	11 ± 12
77	11 ± 2	36 ± 18	**125**	–18 ± 2	–13 ± 9
78	8 ± 5	5 ± 21	**126**	6 ± 3	–4 ± 10
79	–5 ± 13	10 ± 9	**127**	4 ± 3	–4 ± 12
80	16 ± 1	–11 ± 16	**128**	9 ± 3	29 ± 26
81	3 ± 13	11 ± 26	**DMSO**	3 ± 4	–2 ± 7
82	1 ± 15	11 ± 24	**DMSO**	–1 ± 6	35 ± 15

Measured [a] at 120 µM, [b] at 95 µM.

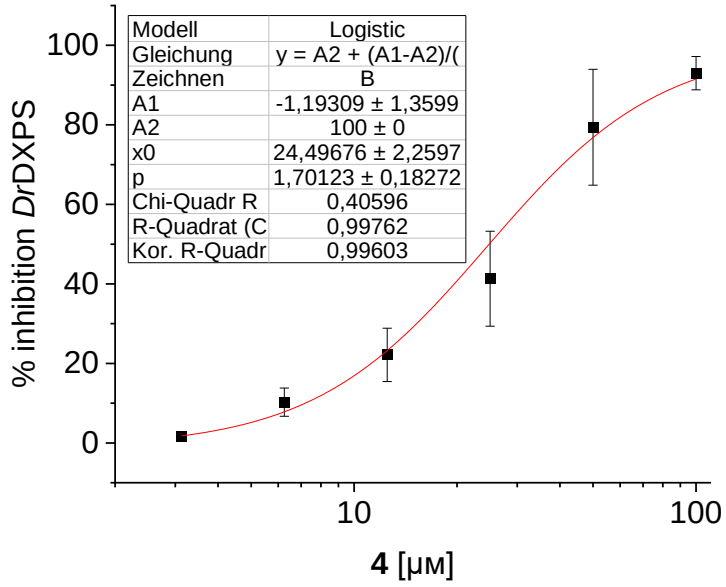

Figure S 63: IC_{50} determination of hit **4** in the HPLC-MS/MS-based assay. The IC_{50} value was calculated from a mean of three measurements.

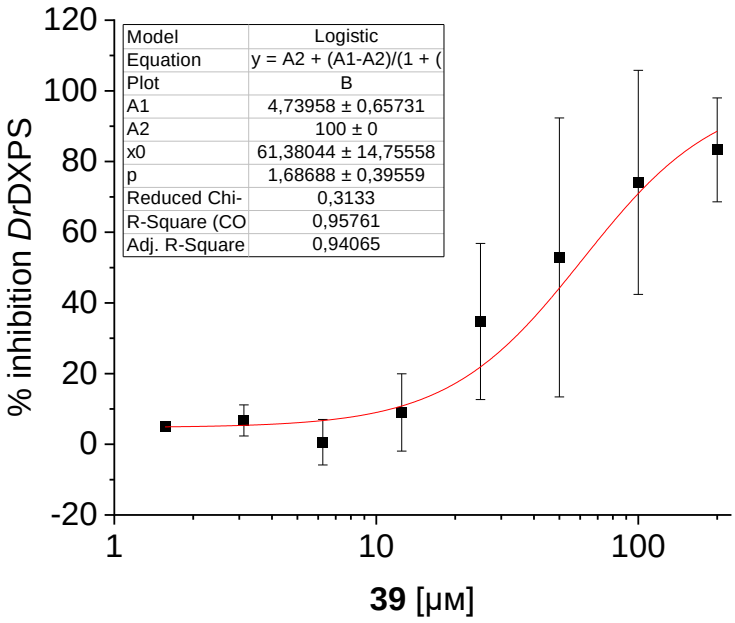

Figure S 64: IC_{50} determination of hit **39** in the HPLC-MS/MS-based assay. The IC_{50} was calculated from a mean of four measurements.

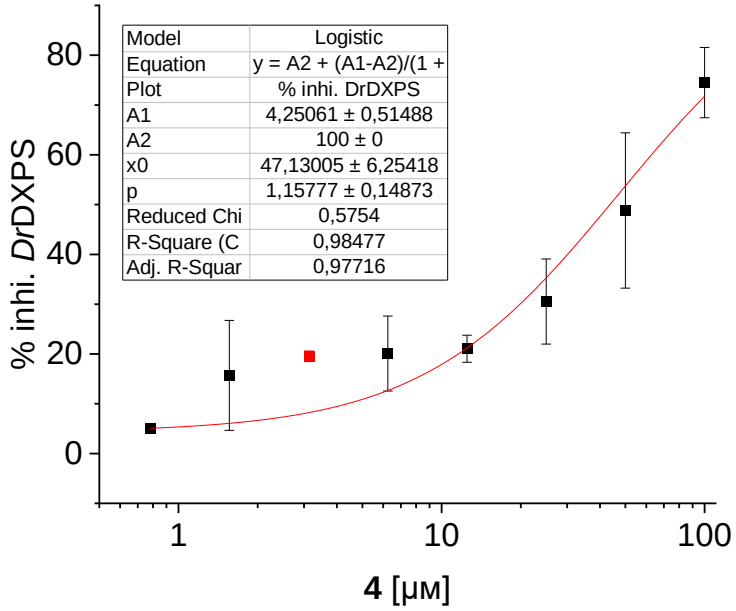

Figure S 65: IC_{50} determination of re-ordered and purified hit **4** in the HPLC-MS/MS-based assay. The IC_{50} value was calculated from a mean of two measurements.

Table S 12: Structures and activities of hits from second round VS derivatives at 95 µM. Mean of two measurements.

Cpd.	Parent	Structure	HPLC-MS/MS %inhi.
1		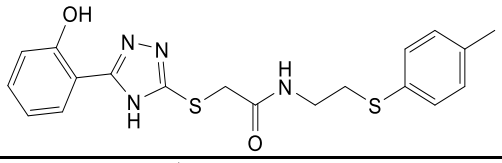	17 ± 6
7		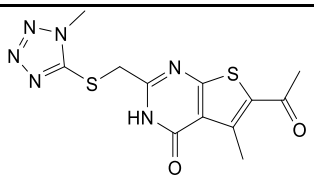	2 ± 4
8		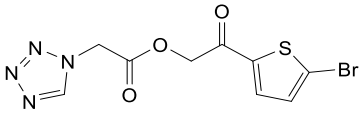	12 ± 11
9		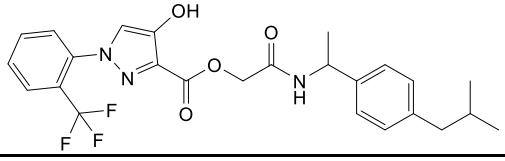	0 ± 7
12		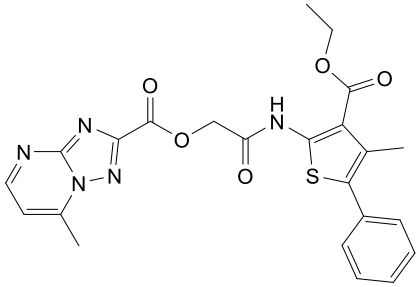	32 ± 10

Cpd.	Parent	Structure	HPLC-MS/MS %inhi.
47	**7**	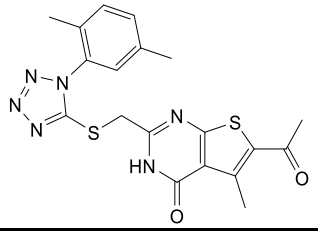	16 ± 13
48	**7**	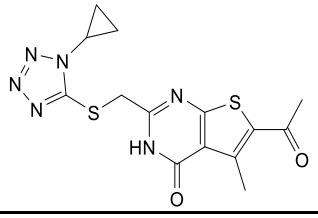	18 ± 12
49	**7**	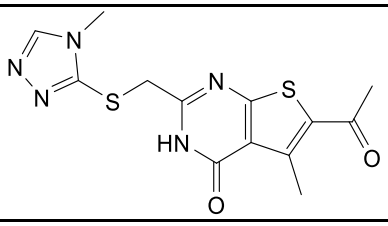	11 ± 8
129	**8**	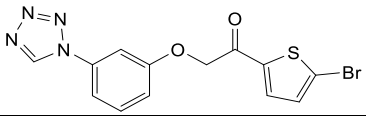	13 ± 5
130	**8**	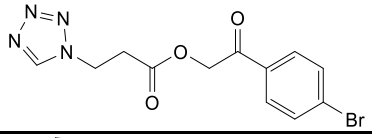	7 ± 3
131	**12**	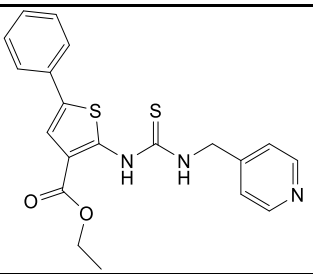	14 ± 8
132	**1**	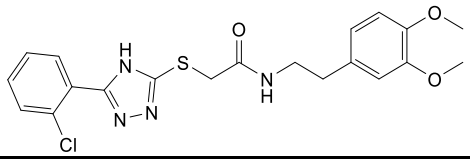	12 ± 3
133	**1**	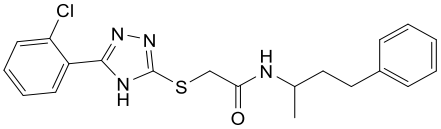	17 ± 8
134	**1**	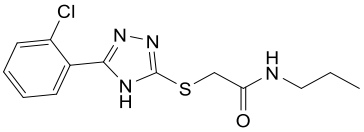	10 ± 1
135	**1**	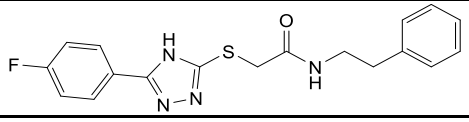	14 ± 6

Cpd.	Parent	Structure	HPLC-MS/MS %inhi.
136	**9**	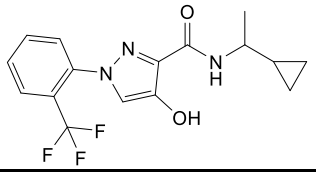	15 ± 8
137	**7**	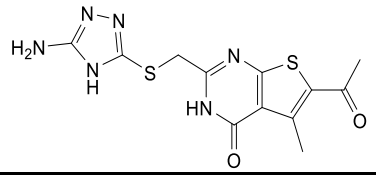	3 ± 5
138	**9**	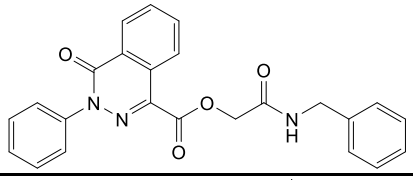	2 ± 5
139	**12**	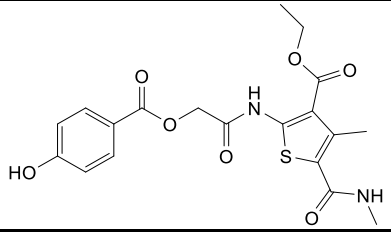	1 ± 8
140	**9**	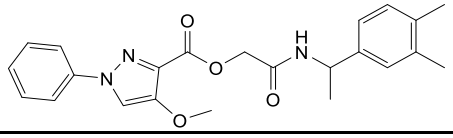	5 ± 7
141	**12**	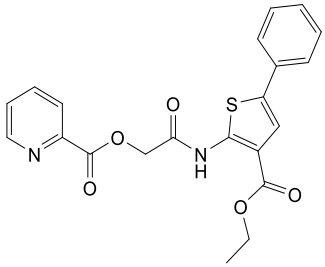	0 ± 10
142	**12**	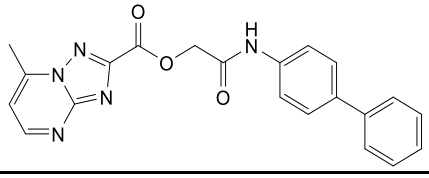	2 ± 6
143	**1**	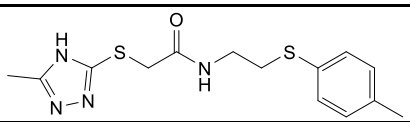	1 ± 5
144	**9**	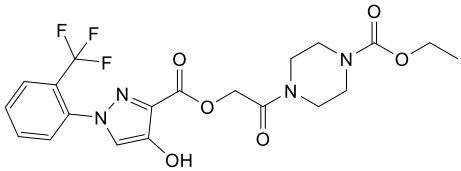	10 ± 15
145	**8**	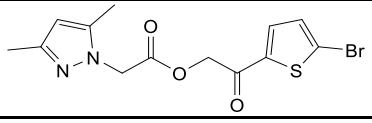	5 ± 0

Cpd.	Parent	Structure	HPLC-MS/MS %inhi.
146	**8**	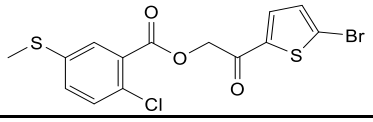	–7 ± 5
147	**1**	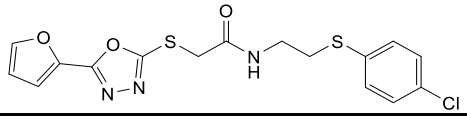	4 ± 4
148	**7**	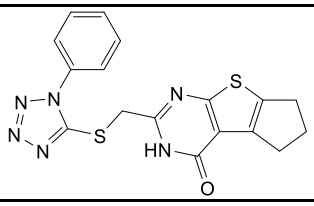	–1 ± 10
149	**9**	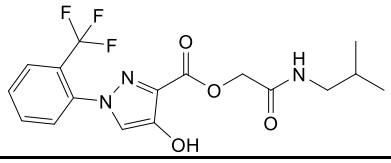	–15 ± 4
150	**8**	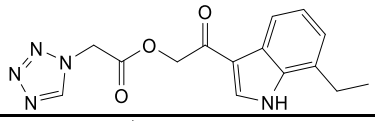	3 ± 0
151	**7**	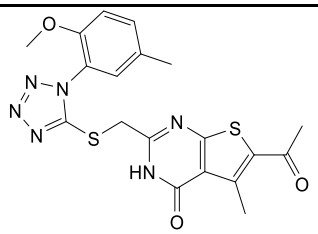	86 ± 45
152	**7**	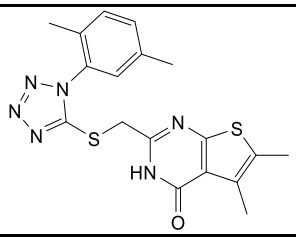	12 ± 13
153	**7**	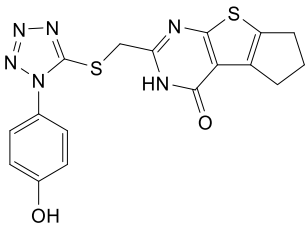	4 ± 17
154	**12**	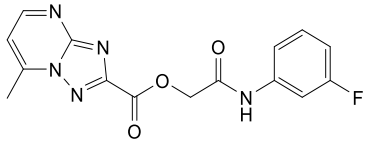	–3 ± 11
155	**8**	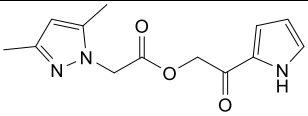	–3 ± 7

Cpd.	Parent	Structure	HPLC-MS/MS %inhi.
156	**7**	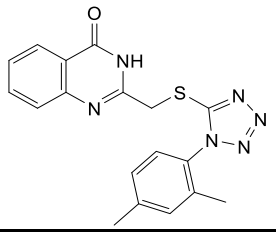	12 ± 12
157	**8**	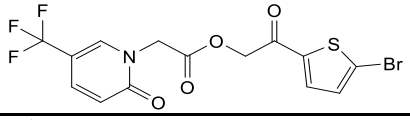	–3 ± 1
158	**1**	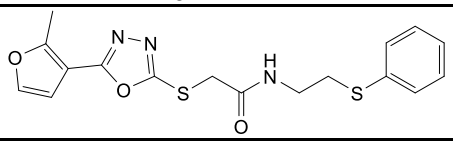	–2 ± 6
159	**1**	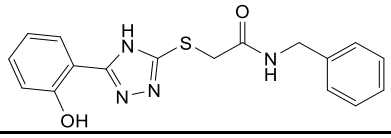	2 ± 11
160	**9**	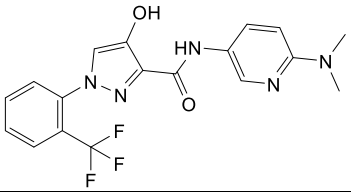	1 ± 5
161	**1**	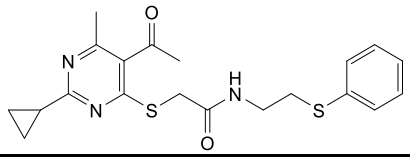	–1 ± 5
162	**8**	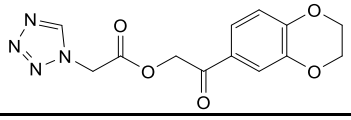	12 ± 11
163	**1**	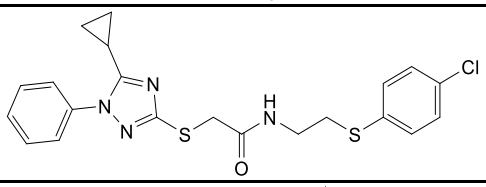	19 ± 7
164	**9**	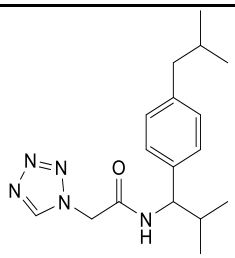	–19 ± 5
165	**9**	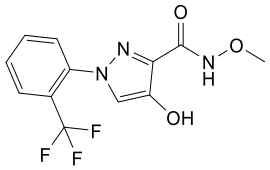	1 ± 4

Cpd.	Parent	Structure	HPLC-MS/MS %inhi.
166	**9**	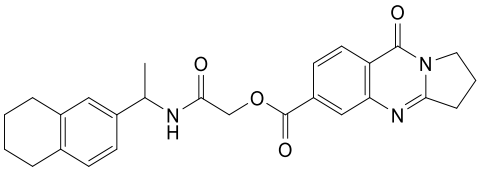	5 ± 12
167	**1**	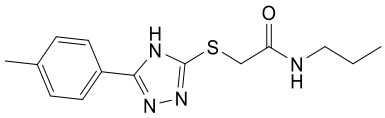	–8 ± 13
168	**7**	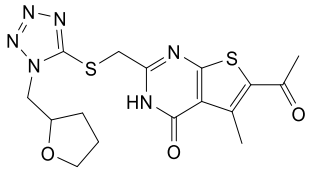	52 ± 24
169	**1**	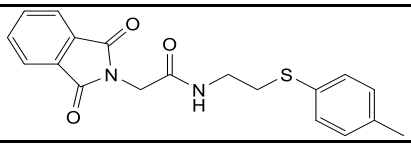	3 ± 10
170	**1**	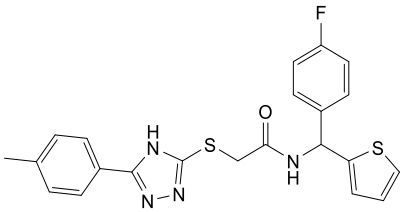	28 ± 11
171	**9**	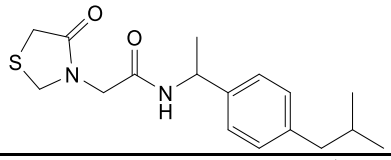	–9 ± 9
172	**9**	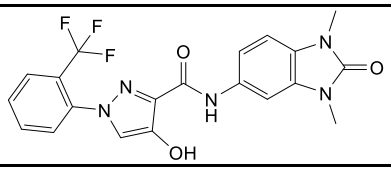	32 ± 13
173	**9**	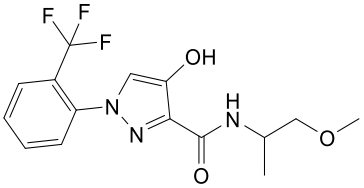	–2 ± 10
174	**1**	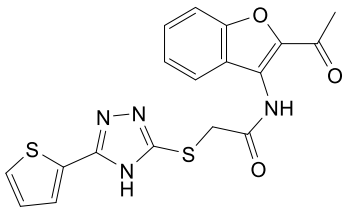	3 ± 9
175	**9**	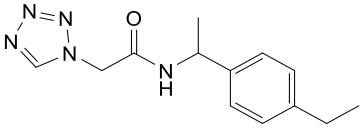	–4 ± 6

Cpd.	Parent	Structure	HPLC-MS/MS %inhi.
176	**1**	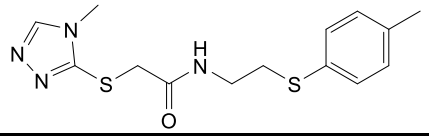	11 ± 2
177	**7**	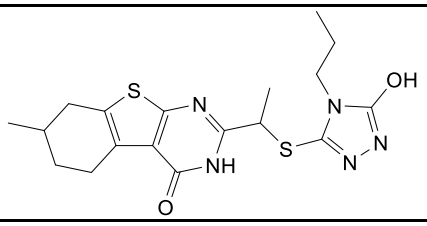	32 ± 6
178	**8**	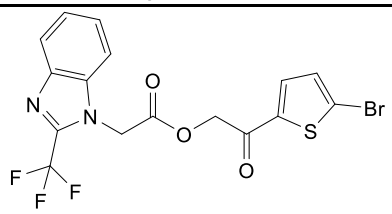	7 ± 7
179	**8**	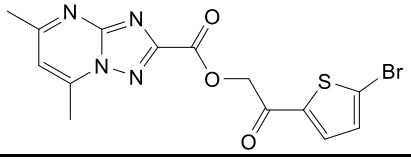	29 ± 4
180	**9**	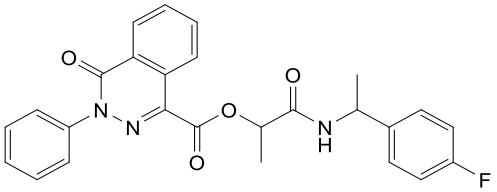	13 ± 1
181	**7**	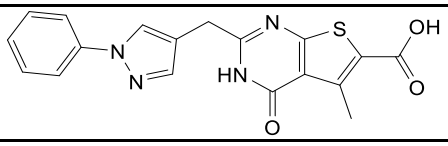	–3 ± 13
182	**9**	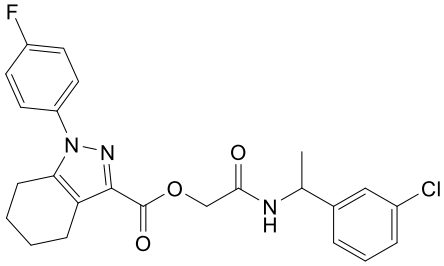	15 ± 1
183	**7**	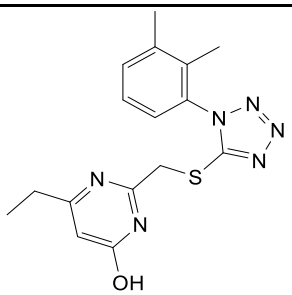	17 ± 0
184	**8**	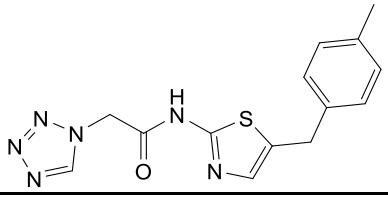	5 ± 0

Cpd.	Parent	Structure	HPLC-MS/MS %inhi.
185	**7**	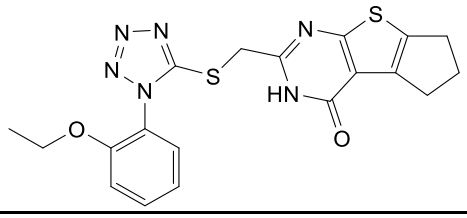	28 ± 8
186	**12**	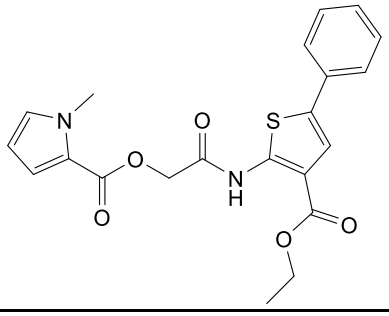	28 ± 22
187	**8**	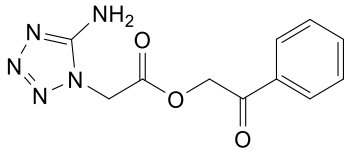	18 ± 16
188	**1**	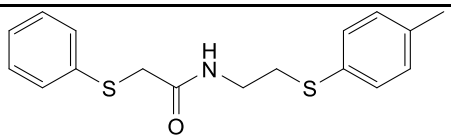	–3 ± 4
189	**1**	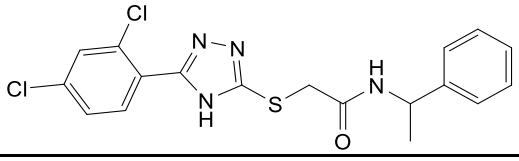	8 ± 7
190	**1**	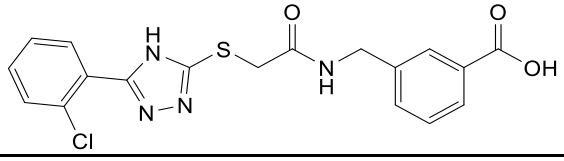	7 ± 3
191	**9**	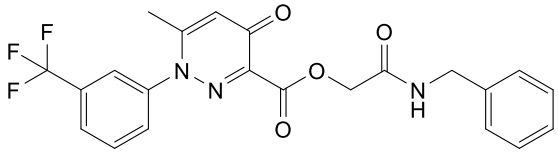	11 ± 10
192	**9**	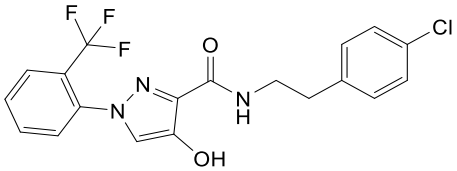	11 ± 11
193	**12**	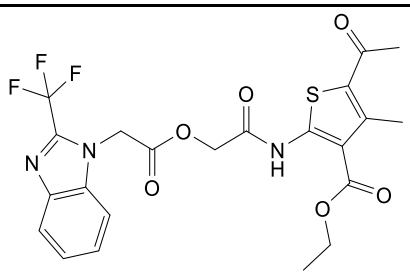	16 ± 17

Cpd.	Parent	Structure	HPLC-MS/MS %inhi.
194	**12**	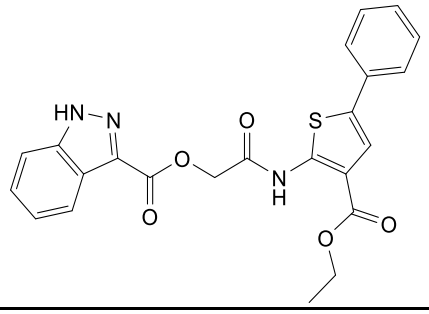	36 ± 19
195	**8**	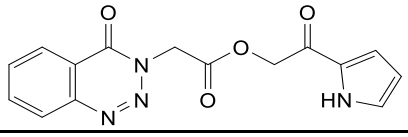	12 ± 12
196	**8**	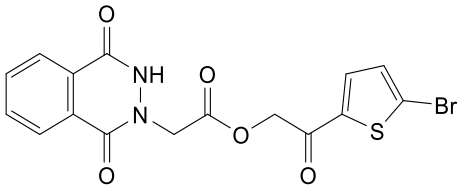	29 ± 18
197	**9**	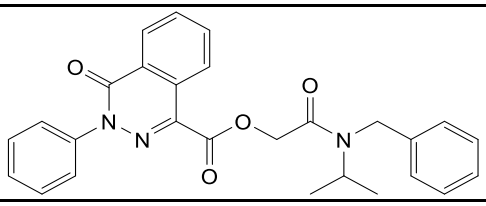	16 ± 14
198	**8**	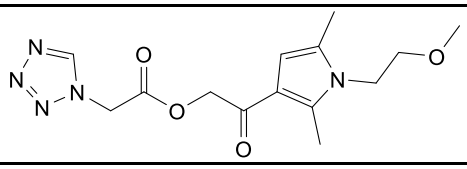	–7 ± 2
199	**1**	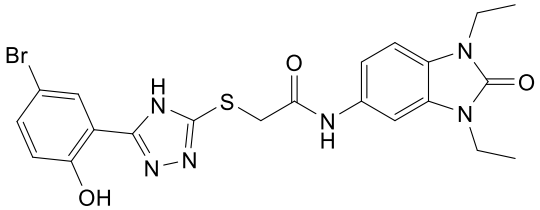	7 ± 7
200	**12**	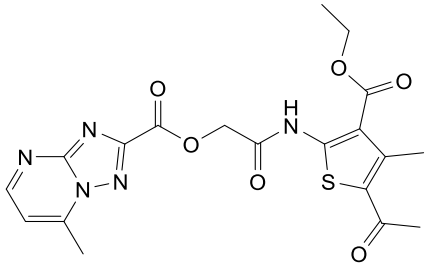	-2 ± 1
201	**12**	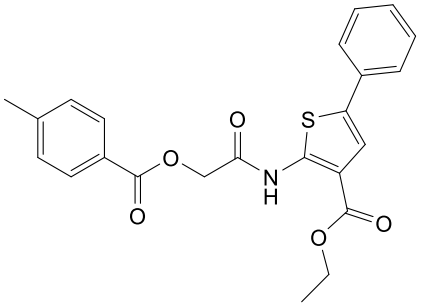	41 ± 12

Cpd.	Parent	Structure	HPLC-MS/MS %inhi.
202	**12**	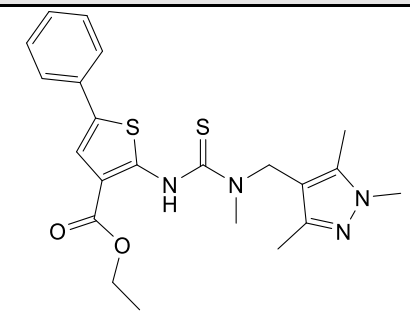	7 ± 15
203	**12**	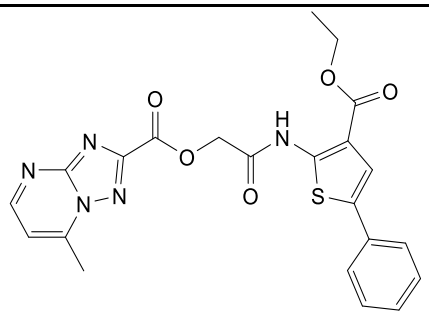	21 ± 3
204	**7**	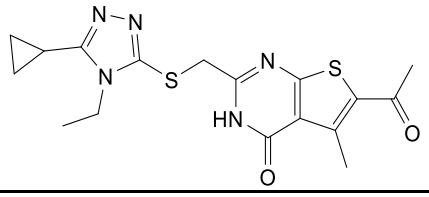	56 ± 39
205	**12**	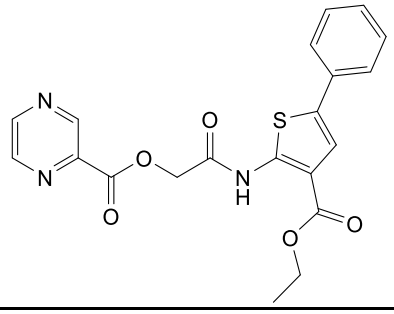	2 ± 2
206	**12**	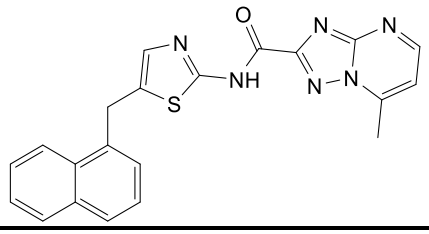	36 ± 7

%inhi. = percent inhibition.

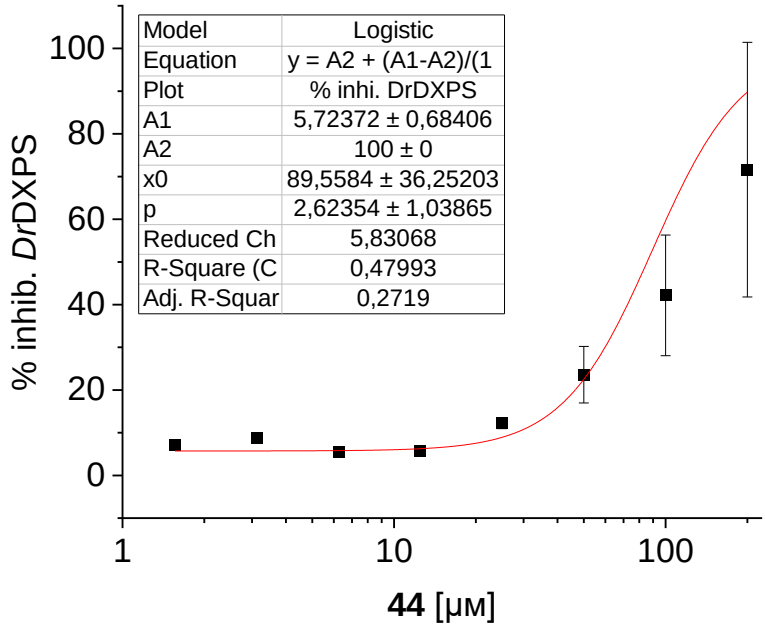

Figure S 66: IC_{50} determination of hit **44** in HPLC-MS/MS-based assay. The IC_{50} was calculated from a mean of two measurements.

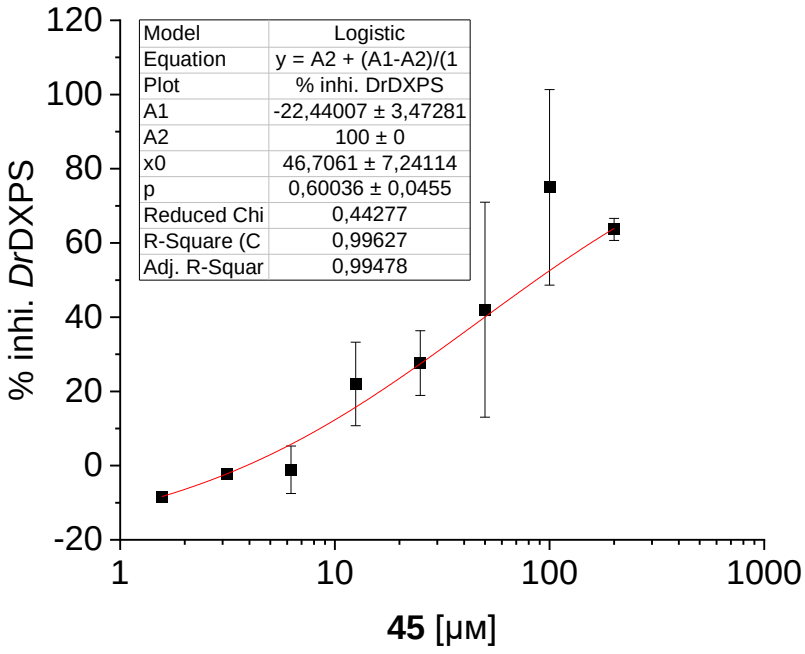

Figure S 67: IC_{50} determination of hit **45** in the HPLC-MS/MS-based assay. The IC_{50} was calculated from a mean of two measurements.

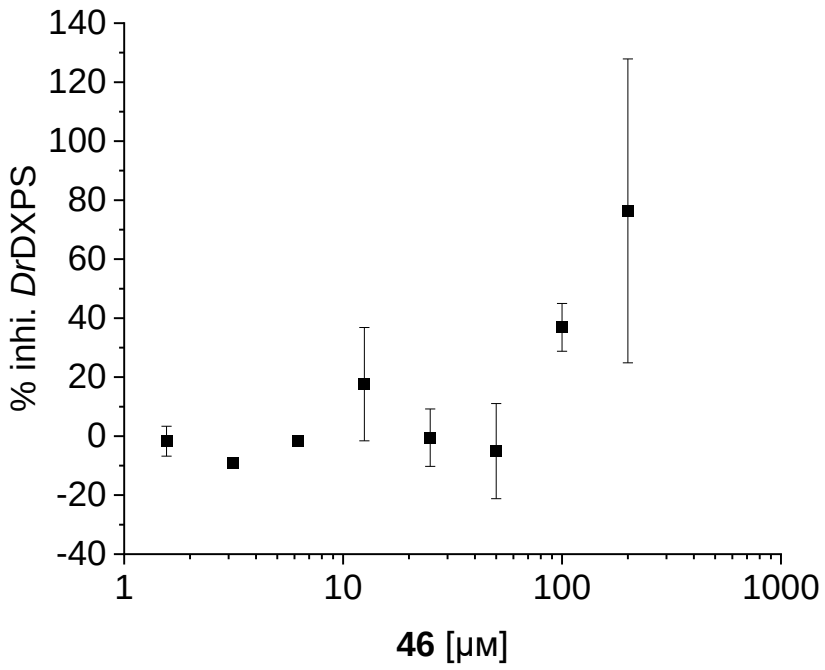

Figure S 68: IC_{50} determination of hit **46** in the HPLC-MS/MS-based assay. The IC_{50} was calculated from a mean of two measurements.

5.3.5 Antibacterial activity against *E. coli* K12 and ΔTolC

Experiments to determine the MIC have been carried out as described recently.[196,197] Briefly, our studies were performed with the efflux-pump deficient *E. coli* knockout strain ΔTolC in comparison to *E. coli* K12. In case MIC values could not be measured for activity reasons, the percentage (%) inhibition was determined at 100 µM (or lower, depending on the solubility of the compounds).

5.3.6 Toxicity in Hep G2

See Chapter 3.5.5.

5.4 Supplementary information for Chapter 3.5

Numbering of compounds in this chapter follows the numbering in Chapter 3.5.

5.4.1 Solubility test of oximes

Table S 13: Solubility in PBS buffer and 2% DMSO of new oxime derivatives in comparison to the original hit **2**.

Compound	Max. solubility [µM]
2	114.2 ± 6.7
4	202.6 ± 1.6
5	193.6 ± 95.7
6	119.4 ± 27.4

5.4.2 Comparison of actives sites of *Mt*DXPS and *Pf*DXPS

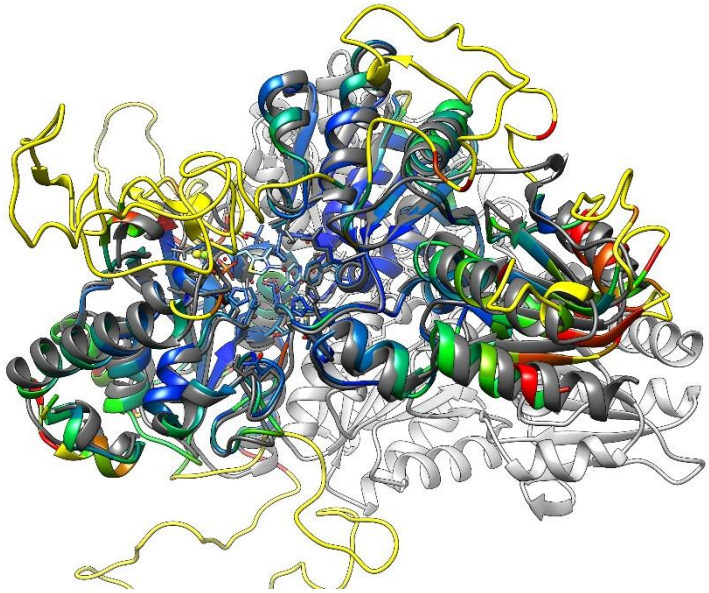

Figure S 69: Superposition of *Mt*DXPS crystal structure (grey, PDB: 6a9h) with the *Pf*DXPS homology model based on *dr*DXPS structure 2o1x. The core of the enzyme shows a high similarity with the *Mt*DXPS structure. *Pf*DXPS is coloured by Cα-RMSD to the *Mt*DXPS structure, from blue = low RMSD via green to red = high RMSD; yellow: no corresponding amino acids in *Mt*DXPS structure. Typical for *P. falciparum*, its structure shows many additional loops on the surface of the protein.

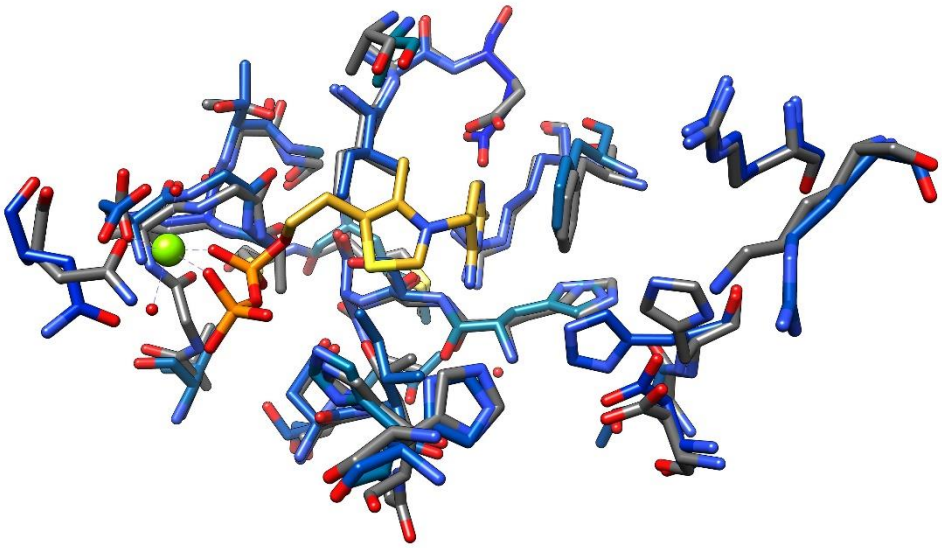

Figure S 70: Superposition of the active site of *Mt*DXPS and *Pf*DXPS. The *Pf*DXPS amino acids are coloured by Cα-RMSD to the *Mt*DXPS structure, from blue = low RMSD via green to red = high RMSD; the carbon atoms of the ThDP ligand are shown in gold; heteroatoms are coloured in red for oxygen, blue for nitrogen and yellow for sulphur atoms; the green sphere represents a Mg^{2+}-ion. Most amino acids are found in identical arrangements, except His941 (corresponding to His416 of *Mt*DXPS) at the bottom right, which is predicted to be in a different rotameric state.

5.4.3 Results IDP rescue assay against *P. falciparum* 3D7

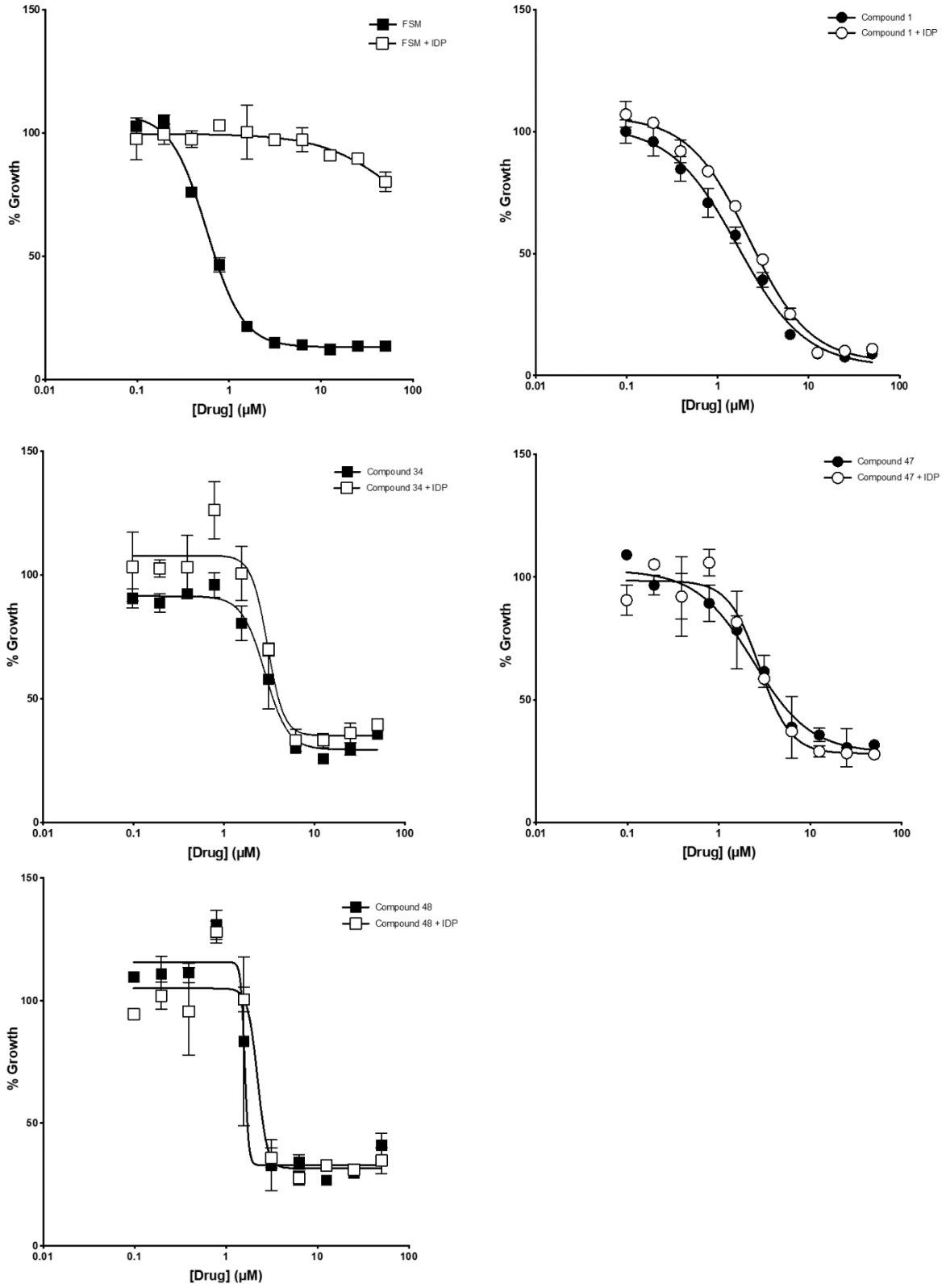

Figure S 71: IDP rescue assay: Representative graphs of growth inhibition of *P. falciparum* 3D7 of compounds **1**, **34**, **47**, **48** and fosmidomycin (FSM) as positive control.

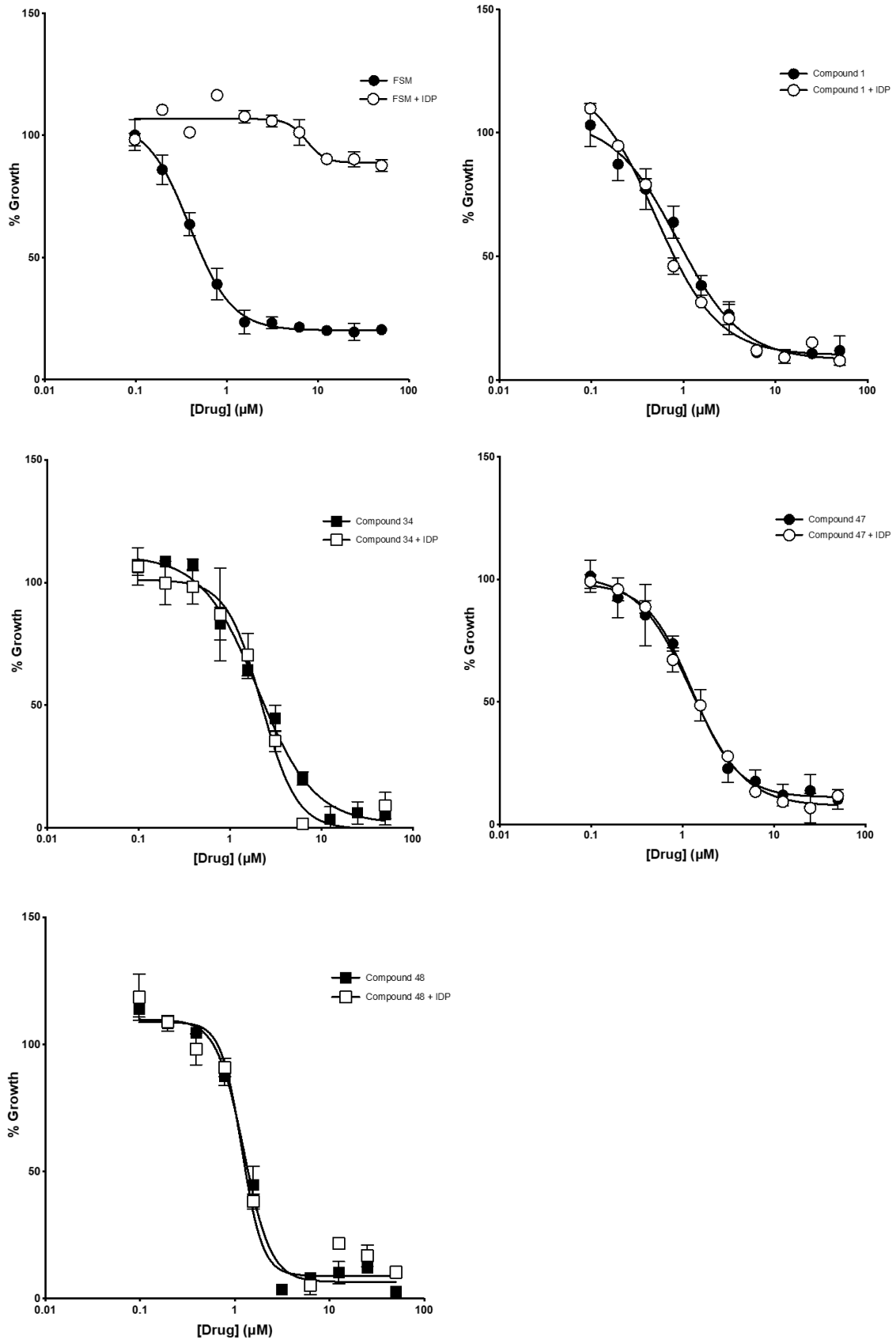

Figure S 72: IDP rescue assay: Representative graphs of growth inhibition of *P. falciparum* NF54 of compounds **1**, **34**, **47**, **48** and fosmidomycin (FSM) as positive control.

Table S 14: IDP rescue assay: IC_{50} values with and without IDP against *P. falciparum* 3D7 and NF54. SD is displayed as error measure when more than one experiment was performed. a = mean of triplicates, b = mean of duplicates.

Cmpd	**IC_{50} 3D7 [µM]**	**IC_{50} NF54 [µM]**
FSM	0.9 ± 0.4[a]	0.9 ± 0.5[b]
FSM + IDP	37.4 ± 18.2[a]	7.8 ± 0.3[b]
1	1.9 ± 0.2[b]	0.8 ± 0.1
1 + IDP	2.4 ± 0.2[b]	0.5
34	2.7 ± 0.3	2.4 ± 0.6
34 + IDP	3.1	2.2
47	2.3 ± 0.4	2.1 ± 0.8
47 + IDP	2.8	1.2
48	2.0 ± 0.7	1.6 ± 0.3
48 + IDP	2.2	1.2

5.4.4 Results LC-MS assay

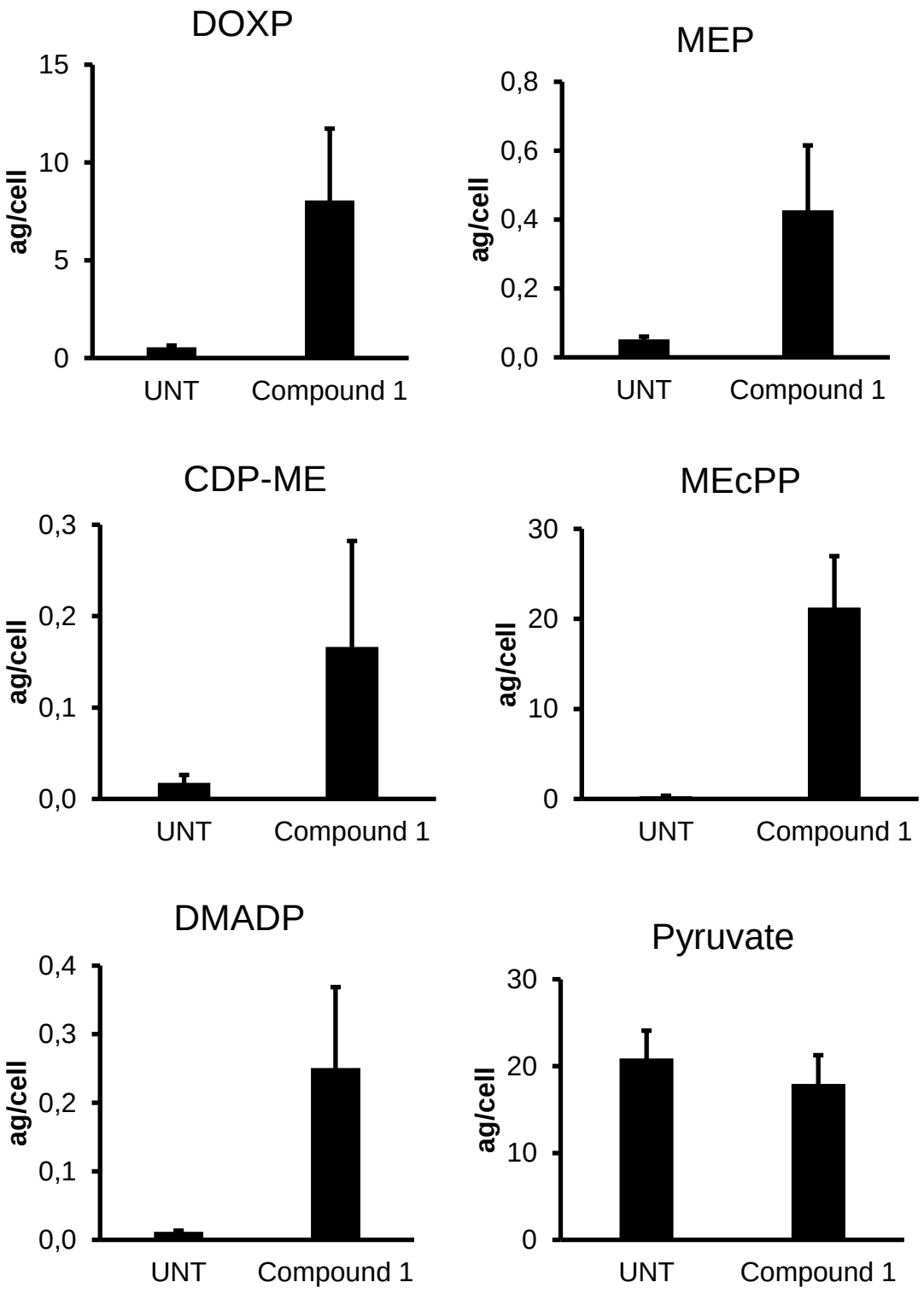

Figure S 73: LC-MS data of MEP pathway metabolites in *E. coli* after treatment with compound **1** at ten times the IC_{50}. Pyr = pyruvate, DOXP = 1-deoxy-D-xylulose-5-phosphate, MEP = methylerythritol phosphate, CDP-ME = 4-diphosphocytidyl-2-C-methyl-D-erythritol, MEcDP = methylerythritol cyclodiphosphate, DMADP = dimethylallyl diphosphate, UNT = untreated.

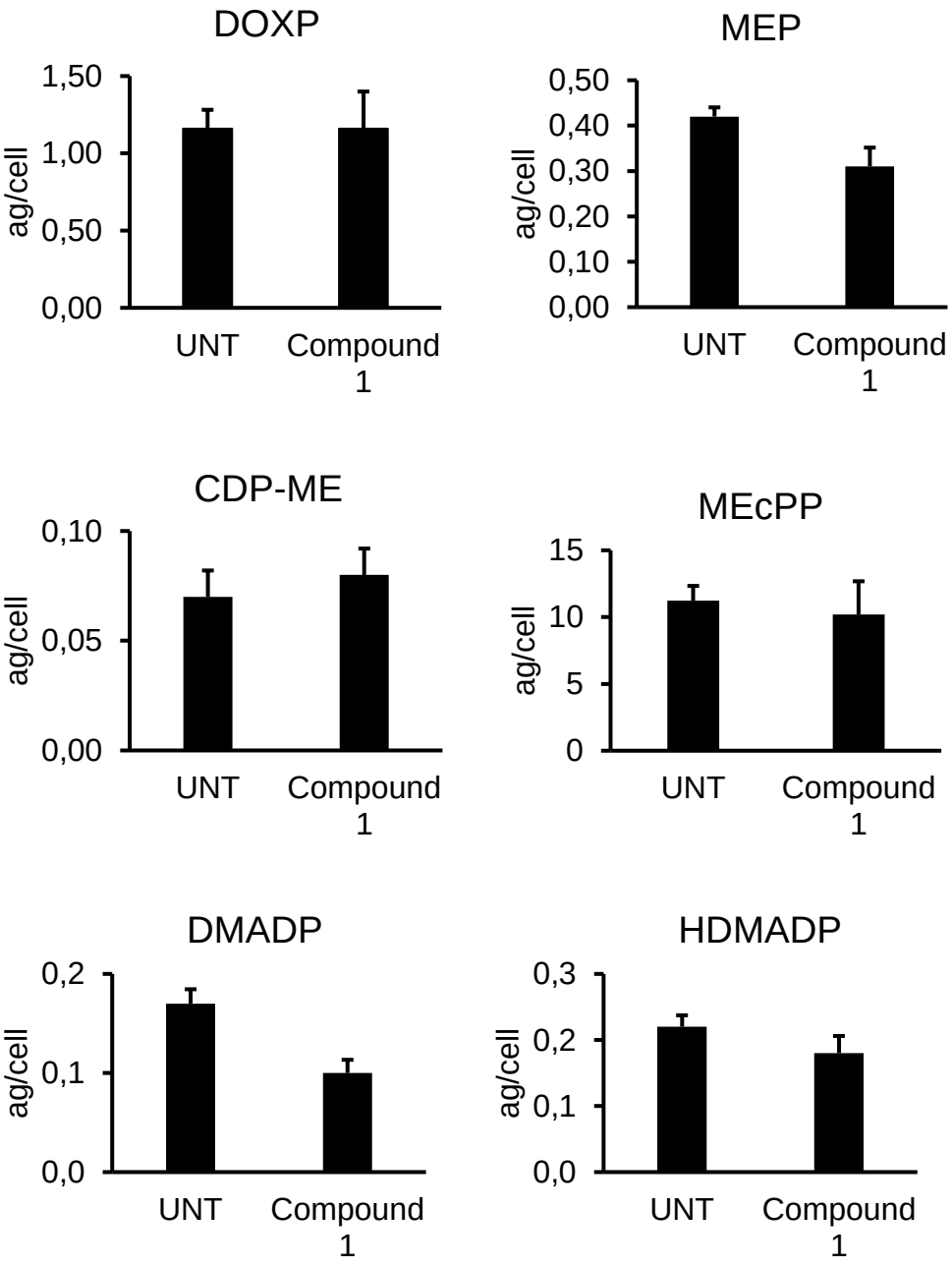

Figure S 74: LC-MS data of MEP pathway metabolites in *P. falciparum* with and without treatment with compound **1** at five times the IC_{50}. Pyr = pyruvate, DOXP = 1-deoxy-D-xylulose-5-phosphate, MEP = methylerythritol phosphate, CDP-ME = 4-diphosphocytidyl-2-C-methyl-D-erythritol, MEcDP = methylerythritol cyclodiphosphate, DMADP = dimethylallyl diphosphate, HDMADP = 1-hydroxy-2-methyl-2-buten-4-yl 4-diphosphate, UNT = untreated.

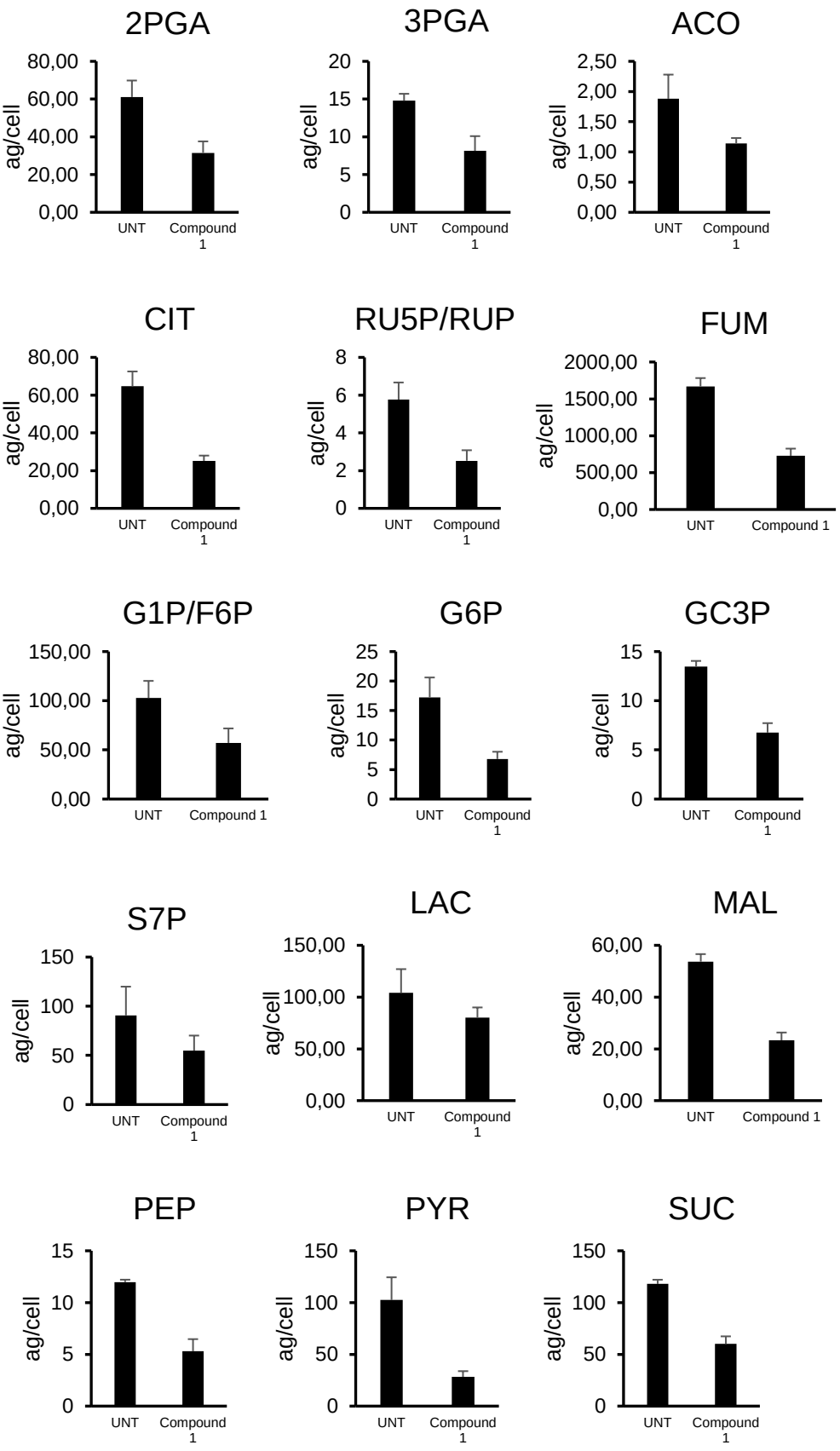

Figure S 75: LC-MS analysis of TCA cycle, glycolytic and pentose phosphate pathway metabolites in *P. falciparum* with and without treatment of compound **1**. 2PGA = 2-phospho glyceric acid, 3PGA = 3-phospho glyceric acid, G1P = glucose-1-phosphate,

F6P = fructose-6-phosphate, G6P = glucose-6-phosphate, R5P = ribose-5-phosphate, Ru5P = ribulose-5-phosphate, PEP = phosphoenolpyruvate, GC3P = glycerol-3-phosphate, S7P = sedoheptulose-7-phosphate, ACO = aconitate, LAC = lactate, SUC = succinate, FUM = fumarate, MAL = malate, CIT = citrate, PYR = pyruvate, UNT = untreated.

Table S 15: T-test analysis of LC-MS data for MEP pathway and TCA cycle metabolites. UNT = untreated, DOXP = 1-deoxy-D-xylulose-5-phosphate, MEP = methylerythritol phosphate, CDP-ME = 4-diphosphocytidyl-2-C-methyl-D-erythritol, MEcDP = methylerythritol cyclodiphosphate, DMADP = dimethylallyl diphosphate, HDMADP = 1-hydroxy-2-methyl-2-buten-4-yl 4-diphosphate, 2PGA = 2-phospho glyceric acid, 3PGA = 3-phospho glyceric acid, ACO = aconitate, CIT = citrate, FUM = fumarate, G1P = glucose-1-phosphate, F6P = fructose-6-phosphate, G6P = glucose-6-phosphate, GC3P = glycerol-3-phosphate, LAC = lactate, MAL = malate, PEP = phosphoenolpyruvate, PYR = pyruvate, R5P = ribose-5-phosphate, Ru5P = ribulose-5-phosphate, S7P = Sedoheptulose-7-phosphate, SUC = succinate.

Cmpd	Discovery? P value	Mean of UNT	Mean of + 1	Diff.	SE of diff.
DOXP	No >0,99999	1,163	1,163	0,000	0,2689
MEP	No 0,070645	0,4233	0,3100	0,1133	0,04631
CDP-ME	No 0,587914	0,06667	0,07667	-0,010	0,01700
MEcDP	No 0,720090	11,24	10,20	1,043	2,713
DMADP	No 0,032540	0,1667	0,1033	0,0633	0,01972
HDMADP	No 0,306022	0,2200	0,1833	0,0367	0,03127
2PGA	No 0,050194	61,07	31,49	29,58	10,67
3PGA	No 0,037010	14,78	8,127	6,657	2,163
ACO	No 0,144422	1,877	1,140	0,7367	0,4068
CIT	No 0,008553	64,80	25,15	39,65	8,234
FUM	No 0,003295	1668	727,7	940,6	149,9
G1P/F6P	No 0,112890	103,0	57,13	45,85	22,64
G6P	No 0,044056	17,23	6,793	10,43	3,596
GC3P	No 0,003896	13,48	6,757	6,720	1,121
LAC	No 0,388380	104,2	80,23	23,97	24,80
MAL	No 0,001940	53,67	23,30	30,37	4,200
PEP	No 0,005029	11,98	5,297	6,687	1,196
PYR	No 0,030535	102,5	28,19	74,26	22,65
RU5P/RUP	No 0,038874	5,757	2,520	3,237	1,069
S7P	No 0,340281	90,64	54,93	35,71	33,01
SUC	No 0,002161	118,0	60,23	57,74	8,218

5.4.5 Results of IC_{50} determination against *Pf*DXPS and *Pf*TPK overexpressing *P. falciparum* 3D7

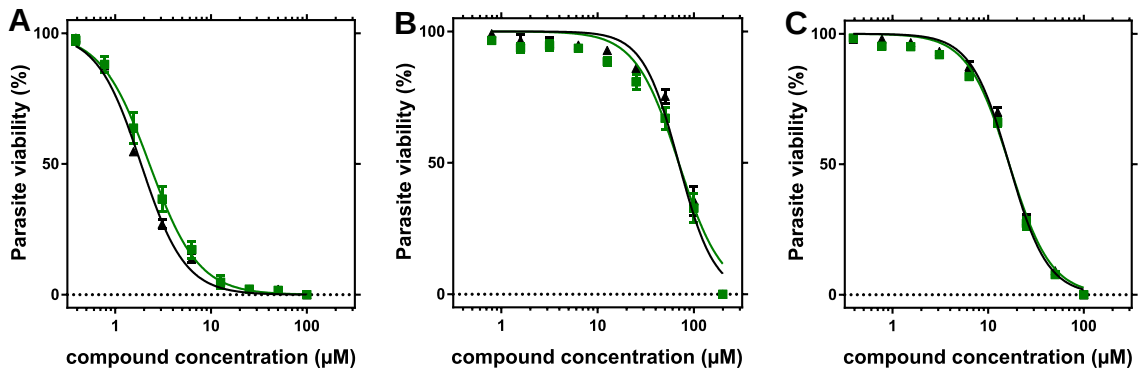

Figure S 76: **Target verification using *Pf*DXPS overexpressing parasites (3D7-DXPS$^+$).** Antiplasmodial activity of compounds (**A**: compound **1**, **B**: compound **2**, **C**: compound **3**) against 3D7-DXPS$^+$ overexpressing parasites (green squares) in comparison to the MOCK cell line (black triangles). All data were averaged from three independent experiments conducted in triplicate and is shown including SEM (error bars). For IC_{50} determination, data was analyzed using nonlinear regression of the log-concentration-response curves and interpolated from the sigmoidal curve.

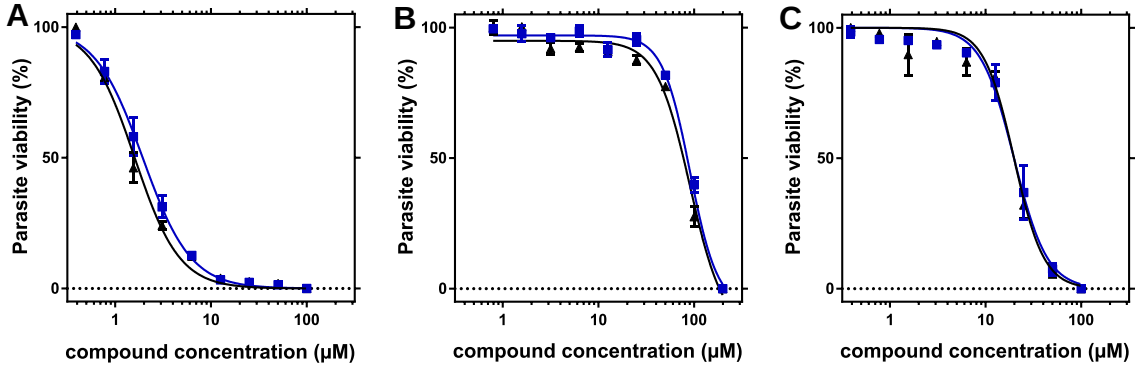

Figure S 77: **Target verification using *Pf*TPK overexpressing parasites (3D7-DXPS$^+$).** Antiplasmodial activity of compounds (**A**: compound **1**, **B**: compound **2**, **C**: compound **3**) against *Pf*TPK overexpressing parasites (blue squares) in comparison to the MOCK cell line (black triangles). Data represent the result from one experiment with technical triplicates (error bars indicate SEM). For IC_{50} determination, data was analyzed using nonlinear regression of the log-concentration-response curves and interpolated from the sigmoidal curve.

Table S 16: Compound evaluation against *P. falciparum* 3D7-TPK$^+$ and *P. falciparum* 3D7-DXPS$^+$ in comparison to MOCK cell line. The table displays the IC_{50} values from antiplasmodial screens using *P. falciparum* 3D7-*Pf*TPK$^+$ (3D7-TPK$^+$) and *P. falciparum* 3D7-*Pf*DXPS (3D7-DXPS$^+$) overexpression cell lines, as interpolated from nonlinear regression curves. 95% CI is displayed as error measure. Percentages indicate statistical probability of the simpler model "LogIC_{50} same for all data sets" being correct.

Cmpd	*Pf*DXPS IC_{50} (µM)	MOCK IC_{50} (µM)	Difference (yes/no)	*Pf*TPK[a] IC_{50} (µM)	MOCK[a] IC_{50} (µM)	Difference (yes/no)
2	109.9 (89.7–167.6)	109.9 (89.7–167.6)	78.49%	90.4 (78.6–116.9)	90.4 (78.6–116.9)	No 91.69%
3	17.9 (17.1–18.8)	17.9 (17.1–18.8)	77.18%	21.1 (19.4–23.1)	23.8	No 83.76%
1	2.08 (1.66–2.48)	1.61 (1.45–1.76)	Yes 15.25%	1.76 (1.36–2.1)	1.18 (0.87–1.41)	Yes 7.50%

[a]Single measurement.

5.4.6 Inhibition data for all compounds

Table S 17: Summary of determined IC_{50} values of all compounds. The numbers I-III are indicating the used method.

ID	Structure	IC_{50} 3D7-III [µM]	IC_{50} Dd2-III [µM]	IC_{50} 3D7-II [µM]	IC_{50} NF54-II [µM]	IC_{50} 3D7-I [µM]
2	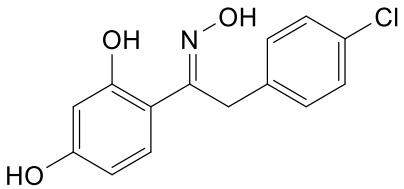	93.8 ± 8.0	89.4 ± 30.6	42.4 ± 4.4	41.4 ± 9.7	81.2 ± 3.3
4	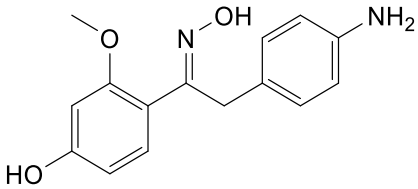	>111	93.6 ± 16.1			
5	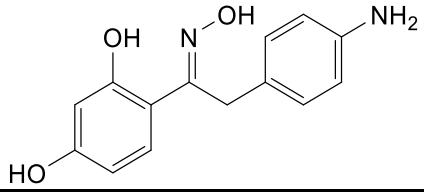	>111	>111			

ID	Structure	IC_{50} 3D7-III [µM]	IC_{50} Dd2-III [µM]	IC_{50} 3D7-II [µM]	IC_{50} NF54-II [µM]	IC_{50} 3D7-I [µM]
6	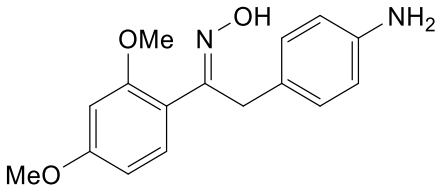	>111	>111			
7Z	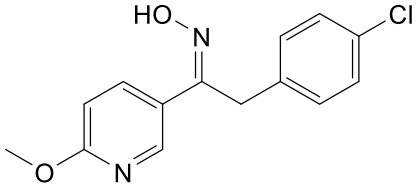	>111	>111			
8E	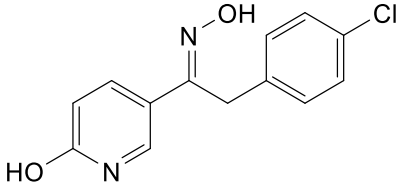	>111	>111			
8Z	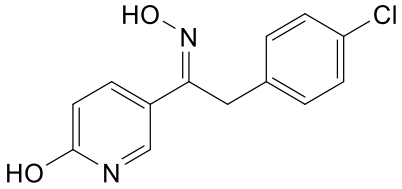	>28	>28			
9	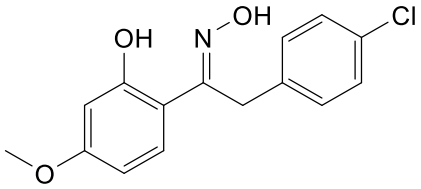	46.8 ± 15.0	24.1 ± 5.5			
7E	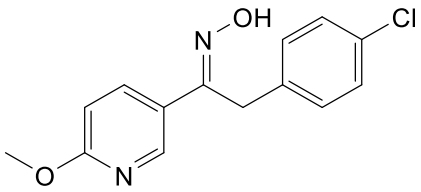	43.6 ± 9.5	>55			
10	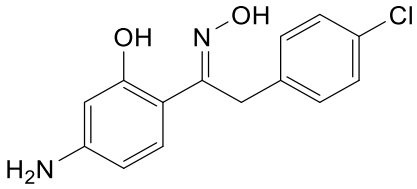	38.2 ± 11.2	24.3 ± 3.6			
11	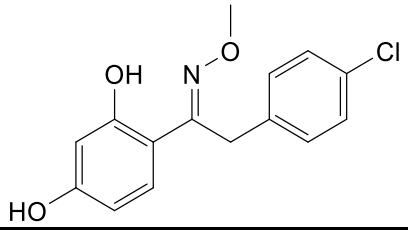	28.0 ± 8.8	19.1 ± 3.4			

ID	Structure	IC_{50} 3D7-III [µM]	IC_{50} Dd2-III [µM]	IC_{50} 3D7-II [µM]	IC_{50} NF54-II [µM]	IC_{50} 3D7-I [µM]
12	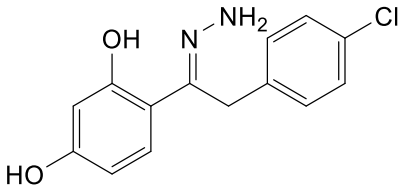	16.0 ± 0.2	14.4 ± 5.0	45.7 ± 3.2	45.0 ± 7.0	
13	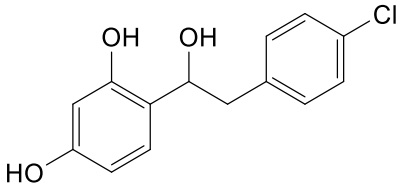	9.9 ± 1.7	27.9 ± 12.5			
3	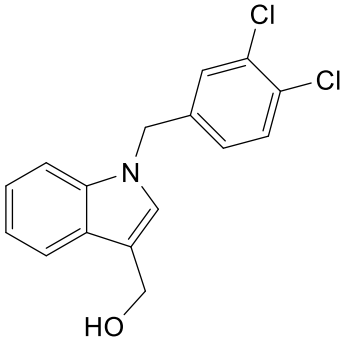	23.6 ± 6.4	12.8 ± 9.2	16.5 ± 2.3	14.8 ± 2.2	24.8 ± 2.9
14	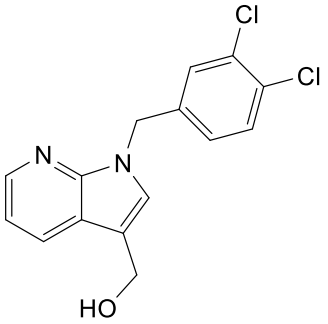	> 111	91.1 ± 18.1			
15	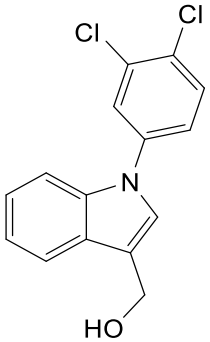	> 55.5	54.3 ± 5.8			
16	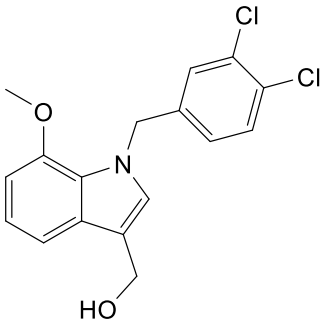	> 55.5	47.5 ± 12.5			

ID	Structure	IC_{50} 3D7-III [µM]	IC_{50} Dd2-III [µM]	IC_{50} 3D7-II [µM]	IC_{50} NF54-II [µM]	IC_{50} 3D7-I [µM]
17	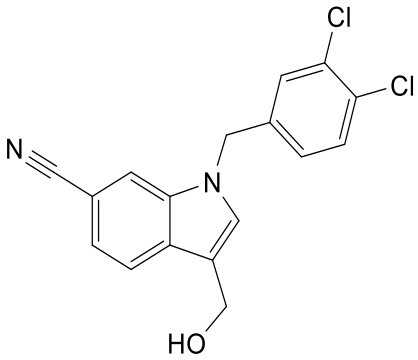	43.8 ± 19.2	44.4 ± 8.7			
18	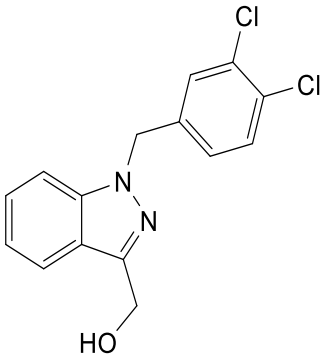	33.9 ± 0.2	69.2 ± 21.1			
19	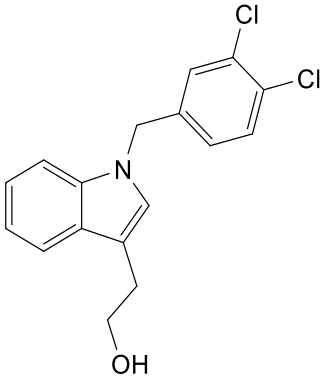	28.9 ± 1.2	12.2 ± 2.9			
20	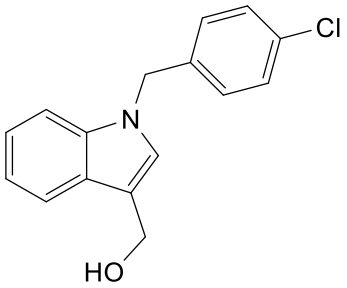	27.7 ± 13.6	21.5 ± 4.8			
21	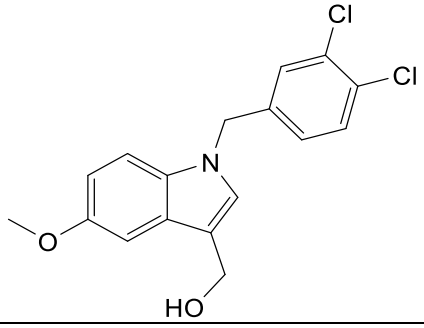	18.5 ± 1.1	53.7 ± 6.3			

ID	Structure	IC_{50} 3D7-III [µM]	IC_{50} Dd2-III [µM]	IC_{50} 3D7-II [µM]	IC_{50} NF54-II [µM]	IC_{50} 3D7-I [µM]
22	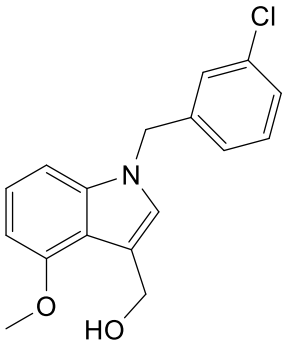	15.6 ± 3.3	13.5 ± 3.5			
23	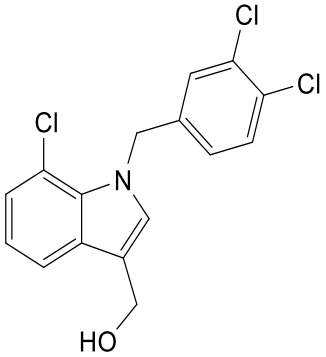	13.8 ± 0.9	35.5 ± 16.1			
24	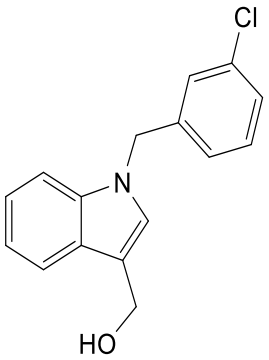	12.2 ± 2.8	8.4 ± 1.2			
25	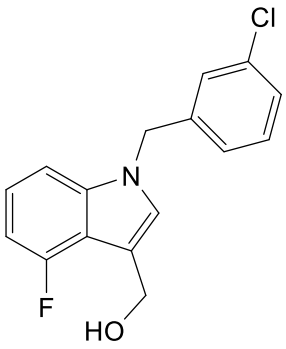	12.0 ± 1.0	9.9 ± 0.9			
26	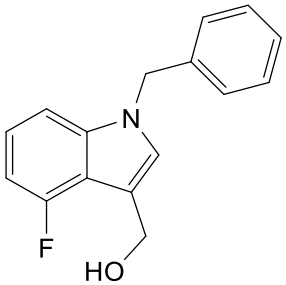	11.9 ± 1.5	9.2 ± 0.4			

ID	Structure	IC_{50} 3D7-III [µM]	IC_{50} Dd2-III [µM]	IC_{50} 3D7-II [µM]	IC_{50} NF54-II [µM]	IC_{50} 3D7-I [µM]
27	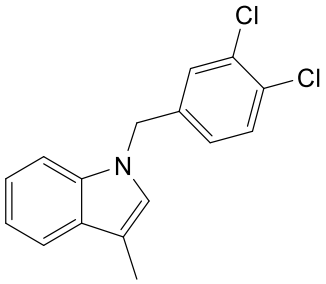	10.2 ± 3.4	11.1 ± 5.1			
28	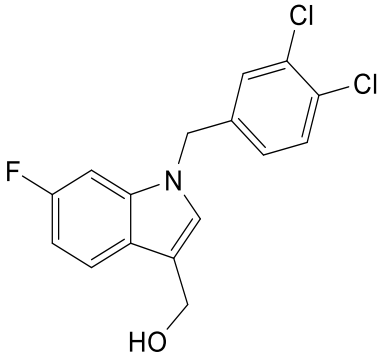	8.9 ± 2.4	10.4 ± 4.7			
29	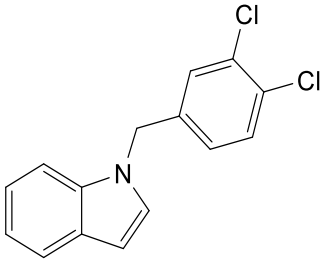	8.1 ± 0.1	17.8 ± 6.8			
30	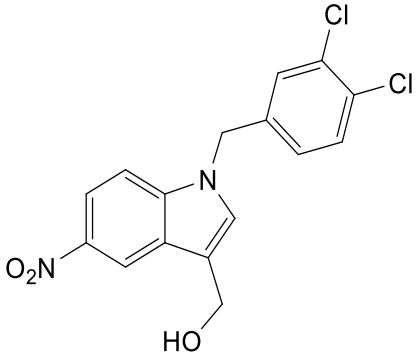	7.2 ± 0.1	4.2 ± 0.7			
31	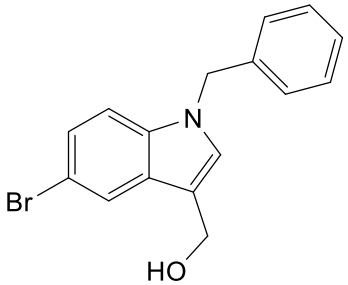	6.1 ± 1.3	5.3 ± 3.3			

ID	Structure	IC_{50} 3D7-III [µM]	IC_{50} Dd2-III [µM]	IC_{50} 3D7-II [µM]	IC_{50} NF54-II [µM]	IC_{50} 3D7-I [µM]
32	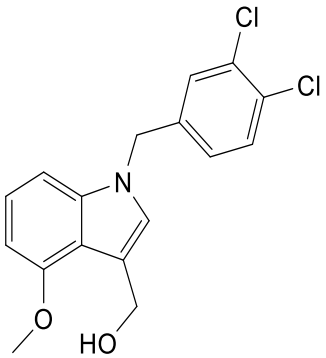	5.5 ± 1.5	4.9 ± 2.4			
33	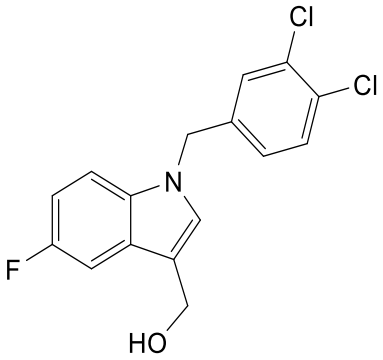	5.3 ± 1.3	7.5 ± 2.2			
34	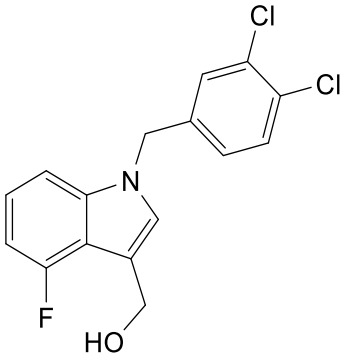	2.4 ± 0.2	2.8 ± 0.1	2.7 ± 0.3	2.4 ± 0.6	
35	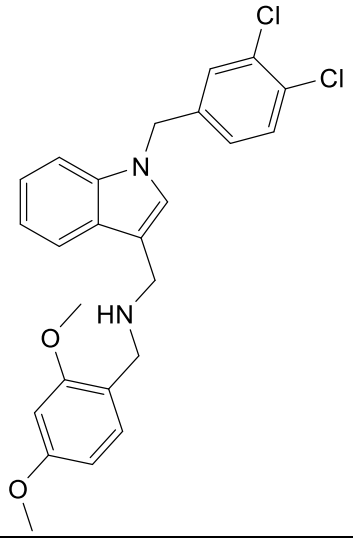	46.8 ± 15.0	21.1 ± 5.5			

ID	Structure	IC_{50} 3D7-III [µM]	IC_{50} Dd2-III [µM]	IC_{50} 3D7-II [µM]	IC_{50} NF54-II [µM]	IC_{50} 3D7-I [µM]
1	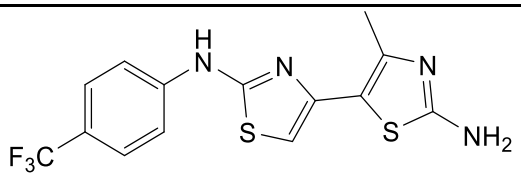	0.6 ± 0.2	0.8 ± 0.4	1.7 ± 0.6	0.8 ± 0.1	1.57 ± 0.6
36	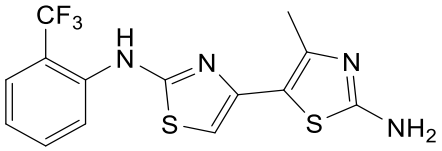	43.0 ± 2.4	47.5 ± 12.3			
37	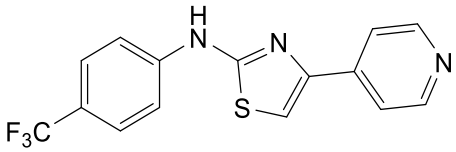	34.2 ± 1.8	24.5 ± 2.1			
38	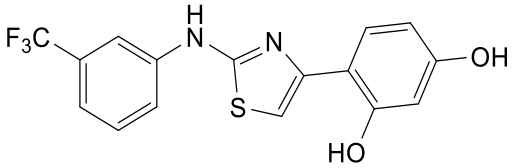	23.0 ± 0.7	19.4 ± 2.3			
39	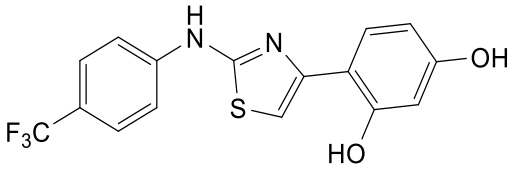	22.1 ± 5.6	24.8 ± 5.0			
40	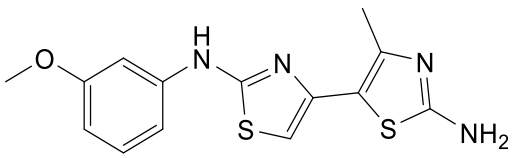	17.9 ± 0.4	43.0 ± 23.6			
41	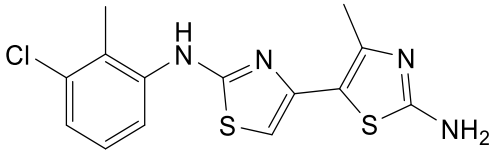	15.9 ± 1.8	17.1 ± 10.1			
42	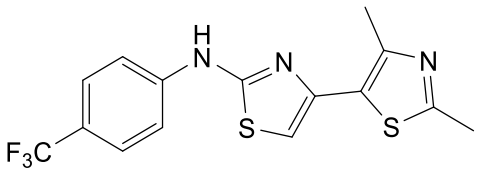	9.5 ± 1.1	5.4 ± 0.3			
43	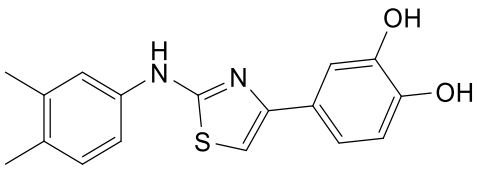	4.4 ± 1.0	6.8 ± 0.5			
44	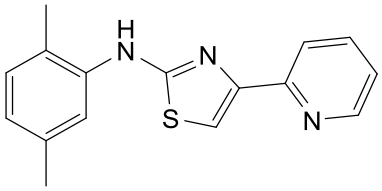	3.7 ± 1.6	5.0 ± 1.3			

ID	Structure	IC_{50} 3D7-III [µM]	IC_{50} Dd2-III [µM]	IC_{50} 3D7-II [µM]	IC_{50} NF54-II [µM]	IC_{50} 3D7-I [µM]
45	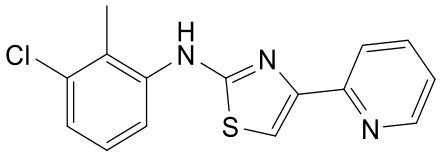	2.8 ± 0.1	1.7 ± 0.7			
46	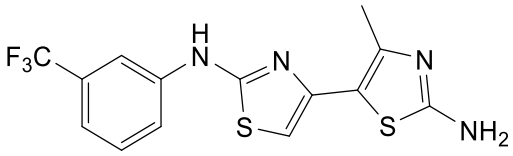	2.5 ± 0.1	4.6 ± 0.3			
47	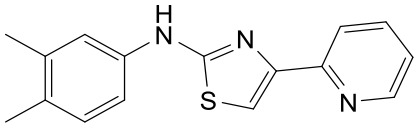	1.5 ± 0.8	1.7 ± 0.4	2.3 ± 0.4	2.1 ± 0.8	
48	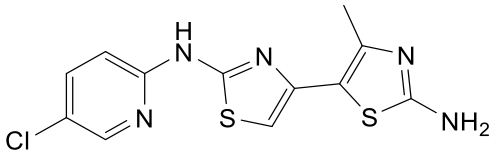	1.0 ± 0.1	1.6 ± 0.2	2.0 ± 0.7	1.6 ± 0.3	

5.4.7 Docking and scoring

The computer program SeeSAR, version 10.2 from BioSolveIT was used to dock compounds and calculate binding affinities. The program uses the FlexX docking function for the placement of ligands.[198] The affinities are estimated using the HYDE scoring function, which calculates the binding affinities based on the hydration differences between the bound and unbound state of the molecule.[199,200] The binding site was chosen based on co-crystal structures with a ligand or substrate. In the case of more than one binding site in a protein structure, the binding site with the highest calculated affinity to the ligand was selected. Analysis and visualisation of the results was done using the program StarDrop, version 6.6.7.25378 from Optibrium.

Table S 18: Results of the docking of the indole-class and benzimidazole CHEMBL_1945694 to the FabI protein crystal structure from *F. tularensis* with the PDB-code **3uic**.

ID	SMILES	HYDE_LOWER [nM]	HYDE_UPPER [nM]
16	COc1cccc2c1n(cc2CO)Cc3ccc(c(c3)Cl)Cl	0.2834	28.15
CHEMBL_194			
5694	Cc1cc2c(cc1C)n(cn2)Cc3ccc(c(c3)Cl)Cl	0.3163	31.43
23	c1cc2c(cn(c2c(c1)Cl)Cc3ccc(c(c3)Cl)Cl)CO	0.3265	32.44
22	COc1ccc2c(c1)c(cn2Cc3ccc(c(c3)Cl)Cl)CO	0.5139	51.05
34	c1cc2c(c(c1)F)c(cn2Cc3ccc(c(c3)Cl)Cl)CO	0.6834	67.9
33	c1cc(c(cc1Cn2cc(c3c2ccc(c3)F)CO)Cl)Cl	0.7494	74.45
19	c1ccc2c(c1)c(cn2Cc3ccc(c(c3)Cl)Cl)CCO	0.8641	85.85
27	Cc1cn(c2c1cccc2)Cc3ccc(c(c3)Cl)Cl	1.011	100.5
3	c1ccc2c(c1)c(cn2Cc3ccc(c(c3)Cl)Cl)CO	1.022	101.6
24	c1ccc2c(c1)c(cn2Cc3cccc(c3)Cl)CO	1.397	138.8
32	COc1cccc2c1c(cn2Cc3ccc(c(c3)Cl)Cl)CO	1.732	172.1
25	c1cc(cc(c1)Cl)Cn2cc(c3c2ccc(c3)F)CO	2.157	214.3
29	c1ccc2c(c1)ccn2Cc3ccc(c(c3)Cl)Cl	3.489	346.7
14	c1cc2c(cn(c2nc1)Cc3ccc(c(c3)Cl)Cl)CO	4.207	418
26	c1ccc(cc1)Cn2cc(c3c2ccc(c3)F)CO	6.774	673
17	c1cc(c(cc1Cn2cc(c3c2cc(cc3)C#N)CO)Cl)Cl	7.01	696.5
35	COc1ccc(c(c1)OC)CNCc2cn(c3c2cccc3)Cc4ccc(c(c4)Cl)Cl	7.292	724.5
20	c1ccc2c(c1)c(cn2Cc3ccc(cc3)Cl)CO	9.881	981.7
15	c1ccc2c(c1)c(cn2c3ccc(c(c3)Cl)Cl)CO	10.88	1081
28	c1cc(c(cc1Cn2cc(c3c2cc(cc3)F)CO)Cl)Cl	12.14	1206
31	c1ccc(cc1)Cn2cc(c3c2ccc(c3)Br)CO	13.57	1348

ID	SMILES	HYDE_LOWER [nM]	HYDE_UPPER [nM]
18	c1ccc2c(c1)c(nn2Cc3ccc(c(c3)Cl)Cl)CO	29.95	2975
30	c1cc(c(cc1Cn2cc(c3c2ccc(c3)N(=O)=O)CO)Cl)Cl	30.33	3014

Table S 19: Results of the docking of the indole-class and benzimidazole CHEMBL_1945694 to the FabI protein crystal structure from *P. falciparum* with the PDB-code **2op1**.

ID	SMILES	HYDE_LOWER [nM]	HYDE_UPPER [nM]
CHEMBL1945694	Cc1cc2c(cc1C)n(cn2)Cc3ccc(c(c3)Cl)Cl	0.3163	31.43
23	c1cc2c(cn(c2c(c1)Cl)Cc3ccc(c(c3)Cl)Cl)CO	0.3623	36
22	COc1ccc2c(c1)c(cn2Cc3ccc(c(c3)Cl)Cl)CO	0.5139	51.05
33	c1cc(c(cc1Cn2cc(c3c2ccc(c3)F)CO)Cl)Cl	0.7494	74.45
34	c1cc2c(c(c1)F)c(cn2Cc3ccc(c(c3)Cl)Cl)CO	0.805	79.98
16	COc1cccc2c1n(cc2CO)Cc3ccc(c(c3)Cl)Cl	0.8209	81.56
19	c1ccc2c(c1)c(cn2Cc3ccc(c(c3)Cl)Cl)CCO	0.8641	85.85
3	c1ccc2c(c1)c(cn2Cc3ccc(c(c3)Cl)Cl)CO	1.022	101.6
24	c1ccc2c(c1)c(cn2Cc3cccc(c3)Cl)CO	1.397	138.8
32	COc1cccc2c1c(cn2Cc3ccc(c(c3)Cl)Cl)CO	1.732	172.1
25	c1cc(cc(c1)Cl)Cn2cc(c3c2ccc(c3)F)CO	2.277	226.3
27	Cc1cn(c2c1cccc2)Cc3ccc(c(c3)Cl)Cl	2.718	270.1
29	c1ccc2c(c1)ccn2Cc3ccc(c(c3)Cl)Cl	3.489	346.7
14	c1cc2c(cn(c2nc1)Cc3ccc(c(c3)Cl)Cl)CO	4.207	418
17	c1cc(c(cc1Cn2cc(c3c2cc(cc3)C#N)CO)Cl)Cl	7.01	696.5
20	c1ccc2c(c1)c(cn2Cc3ccc(cc3)Cl)CO	10.1	1003
26	c1ccc(cc1)Cn2cc(c3c2ccc(c3)F)CO	11.96	1188
28	c1cc(c(cc1Cn2cc(c3c2cc(cc3)F)CO)Cl)Cl	12.14	1206
31	c1ccc(cc1)Cn2cc(c3c2ccc(c3)Br)CO	14.66	1456
15	c1ccc2c(c1)c(cn2c3ccc(c(c3)Cl)Cl)CO	17.17	1706
18	c1ccc2c(c1)c(nn2Cc3ccc(c(c3)Cl)Cl)CO	29.95	2975
30	c1cc(c(cc1Cn2cc(c3c2ccc(c3)N(=O)=O)CO)Cl)Cl	30.33	3014
35	COc1ccc(c(c1)OC)CNCc2cn(c3c2cccc3)Cc4ccc(c(c4)Cl)Cl	36.14	3591

Table S 20: Docking to of the oxime class to the FabI protein crystal structure from *F. tularensis* with the PDB-code **3uic**.

ID	SMILES	HYDE_LOWER [nM]	HYDE_UPPER [nM]
CHEMBL_194			
5694_1_009	Cc1cc2c(cc1C)n(cn2)Cc3ccc(c(c3)Cl)Cl	0.3193	31.73
11	CON=C(Cc1ccc(cc1)Cl)c2ccc(cc2O)O	157.9	1.569e+04
13	c1cc(ccc1CC(c2ccc(cc2O)O)O)Cl	204.5	2.031e+04
4	COc1cc(ccc1C(=NO)Cc2ccc(cc2)N)O	247.3	2.457e+04
10	c1cc(ccc1CC(=NO)c2ccc(cc2O)N)Cl	398.2	3.957e+04
5	c1cc(ccc1CC(=NO)c2ccc(cc2O)O)N	777.4	7.724e+04
2	c1cc(ccc1CC(=NO)c2ccc(cc2O)O)Cl	1082	1.075e+05
12	c1cc(ccc1CC(=NN)c2ccc(cc2O)O)Cl	3304	3.282e+05
9	COc1ccc(c(c1)O)C(=NO)Cc2ccc(cc2)Cl	6711	6.668e+05
7E	COc1ccc(cn1)C(=NO)Cc2ccc(cc2)Cl	1.09e+04	1.083e+06

Table S 21: Docking to of the aminothiazole class to the FabI protein crystal structure from *F. tularensis* with the PDB-code **3uic**.

ID	SMILES	HYDE_LOWER [nM]	HYDE_UPPER [nM]
CHEMBL_194			
5694_1_009	Cc1cc2c(cc1C)n(cn2)Cc3ccc(c(c3)Cl)Cl	0.3193	31.73
39	c1cc(ccc1C(F)(F)F)Nc2nc(cs2)c3ccc(cc3O)O	26.75	2657
1	Cc1c(sc(n1)N)c2csc(n2)Nc3ccc(cc3)C(F)(F)F	55.32	5496
45	Cc1c(cccc1Cl)Nc2nc(cs2)c3ccccn3	57.78	5741
46	Cc1c(sc(n1)N)c2csc(n2)Nc3cccc(c3)C(F)(F)F	62.49	6209
40	Cc1c(sc(n1)N)c2csc(n2)Nc3cccc(c3)OC	66.37	6595
41	Cc1c(cccc1Cl)Nc2nc(cs2)c3c(nc(s3)N)C	77.89	7739
36	Cc1c(sc(n1)N)c2csc(n2)Nc3ccccc3C(F)(F)F	132.8	1.319e+04
38	c1cc(cc(c1)Nc2nc(cs2)c3ccc(cc3O)O)C(F)(F)F	350.1	3.479e+04
43	Cc1ccc(cc1C)Nc2nc(cs2)c3ccc(c(c3)O)O	499.9	4.967e+04
37	c1cc(ccc1C(F)(F)F)Nc2nc(cs2)c3ccncc3	633.6	6.295e+04
47	Cc1ccc(cc1C)Nc2nc(cs2)c3ccccn3	1811	1.799e+05
48	Cc1c(sc(n1)N)c2csc(n2)Nc3ccc(cn3)Cl	2766	2.748e+05
44	c1ccc(cc1)Nc2nc(cs2)c3ccccn3	2979	2.959e+05
42	Cc1c(sc(n1)C)c2csc(n2)Nc3ccc(cc3)C(F)(F)F	2.082e+04	2.069e+06

Table S 22: Docking to of the oxime class to the FabI protein crystal structure from *P. falciparum* with the PDB-code **2op1**.

ID	SMILES	HYDE_LOWER [nM]	HYDE_UPPER [nM]
CHEMBL_19			
45694	Cc1cc2c(cc1C)n(cn2)Cc3ccc(c(c3)Cl)Cl	0.3193	31.73
11	CON=C(Cc1ccc(cc1)Cl)c2ccc(cc2O)O	157.9	1.569e+04
13	c1cc(ccc1CC(c2ccc(cc2O)O)O)Cl	204.5	2.031e+04
4	COc1cc(ccc1C(=NO)Cc2ccc(cc2)N)O	247.3	2.457e+04
10	c1cc(ccc1CC(=NO)c2ccc(cc2O)N)Cl	398.2	3.957e+04
5	c1cc(ccc1CC(=NO)c2ccc(cc2O)O)N	777.4	7.724e+04
2	c1cc(ccc1CC(=NO)c2ccc(cc2O)O)Cl	1082	1.075e+05
12	c1cc(ccc1CC(=NN)c2ccc(cc2O)O)Cl	3304	3.282e+05
9	COc1ccc(c(c1)O)C(=NO)Cc2ccc(cc2)Cl	6711	6.668e+05
7E	COc1ccc(cn1)C(=NO)Cc2ccc(cc2)Cl	1.09e+04	1.083e+06

Table S 23: Docking to of the aminothiazole class to the FabI protein crystal structure from *P. falciparum* with the PDB-code **2op1**.

ID	SMILES	HYDE_LOWER [nM]	HYDE_UPPER [nM]
09T_I_26			
2_1_009	Cc1cc2c(cc1C)n(cn2)Cc3ccc(c(c3)Cl)Cl	0.3193	31.73
39	c1cc(ccc1C(F)(F)F)Nc2nc(cs2)c3ccc(cc3O)O	26.75	2657
1	Cc1c(sc(n1)N)c2csc(n2)Nc3ccc(cc3)C(F)(F)F	55.32	5496
45	Cc1c(cccc1Cl)Nc2nc(cs2)c3ccccn3	57.78	5741
46	Cc1c(sc(n1)N)c2csc(n2)Nc3cccc(c3)C(F)(F)F	62.49	6209
40	Cc1c(sc(n1)N)c2csc(n2)Nc3cccc(c3)OC	66.37	6595
41	Cc1c(cccc1Cl)Nc2nc(cs2)c3c(nc(s3)N)C	77.89	7739
36	Cc1c(sc(n1)N)c2csc(n2)Nc3ccccc3C(F)(F)F	132.8	1.319e+04
38	c1cc(cc(c1)Nc2nc(cs2)c3ccc(cc3O)O)C(F)(F)F	350.1	3.479e+04
43	Cc1ccc(cc1C)Nc2nc(cs2)c3ccc(c(c3)O)O	499.9	4.967e+04
37	c1cc(ccc1C(F)(F)F)Nc2nc(cs2)c3ccncc3	633.6	6.295e+04
47	Cc1ccc(cc1C)Nc2nc(cs2)c3ccccn3	1811	1.799e+05
48	Cc1c(sc(n1)N)c2csc(n2)Nc3ccc(cn3)Cl	2766	2.748e+05
44	c1ccc(cc1)Nc2nc(cs2)c3ccccn3	2979	2.959e+05
42	Cc1c(sc(n1)C)c2csc(n2)Nc3ccc(cc3)C(F)(F)F	2.082e+04	2.069e+06

Table S 24: Docking of the aminothiazole class, the co-crystallized inhibitor TLM and compounds CHEMBL3344230 and CHEMBL546826 to the KasA protein crystal structure from *M. tuberculosis* with the PDB-code **2wgd**.

ID	SMILES	HYDE_LOWER [nM]	HYDE_UPPER [nM]
42	Cc1c(sc(n1)C)c2csc(n2)Nc3ccc(cc3)C(F)(F)F	37.1	3686
39	c1cc(ccc1C(F)(F)F)Nc2nc(cs2)c3ccc(cc3O)O	48.11	4780
46	Cc1c(sc(n1)N)c2csc(n2)Nc3cccc(c3)C(F)(F)F	51.6	5126
Ligand TLM	CC1=C(C(SC1=O)(C)C=C(C)C=C)O	319.1	3.171e+04
36	Cc1c(sc(n1)N)c2csc(n2)Nc3ccccc3C(F)(F)F	383.7	3.812e+04
CHEMBL33442			
30	c1cc(ccc1Nc2nc(cs2)c3ccncc3)Br	498	4.948e+04
43	Cc1ccc(cc1C)Nc2nc(cs2)c3ccc(c(c3)O)O	593.5	5.897e+04
CHEMBL54682			
6	c1ccnc(c1)c2csc(n2)Nc3ccc(cn3)Cl	869.3	8.637e+04
45	Cc1c(cccc1Cl)Nc2nc(cs2)c3ccccn3	923.9	9.18e+04
38	c1cc(cc(c1)Nc2nc(cs2)c3ccc(cc3O)O)C(F)(F)F	1517	1.507e+05
37	c1cc(ccc1C(F)(F)F)Nc2nc(cs2)c3ccncc3	1558	1.548e+05
47	Cc1ccc(cc1C)Nc2nc(cs2)c3ccccn3	5896	5.858e+05
44	c1ccc(cc1)Nc2nc(cs2)c3ccccn3	7891	7.841e+05
1	Cc1c(sc(n1)N)c2csc(n2)Nc3ccc(cc3)C(F)(F)F	8079	8.027e+05
41	Cc1c(cccc1Cl)Nc2nc(cs2)c3c(nc(s3)N)C	2.626e+04	2.609e+06
40	Cc1c(sc(n1)N)c2csc(n2)Nc3cccc(c3)OC	2.89e+04	2.871e+06
48	Cc1c(sc(n1)N)c2csc(n2)Nc3ccc(cn3)Cl	4.236e+05	4.208e+07

5.4.8 Human off-traget enzymes

Table S 25: Summary of possible human off-target enzymes encountered during the search for bacterial targets. The molecule drawn in “search hit” is reported in the cited source to be targeting the enzyme or pathway given in “target enzyme”. Only one hit molecule is shown, the cited source often reports many more derivatives. No ranking and in-depth analysis of likelihood to be a target was performed.

Search molecule	Search hit	Target enzyme(s)	Reference
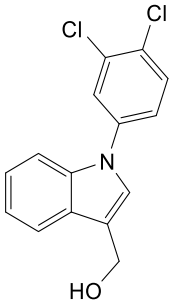	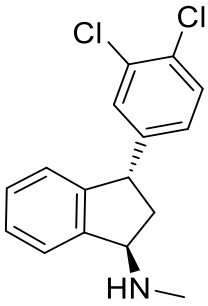 Indatraline	non-selective monoamine transporter inhibitor	[201,202]
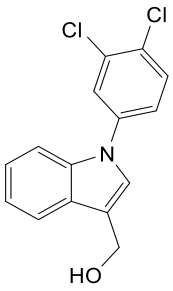	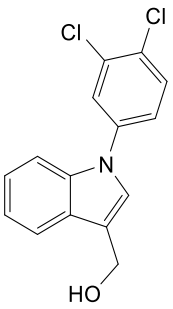 Oncrasin-1	RNA polymerase II	[137,162]
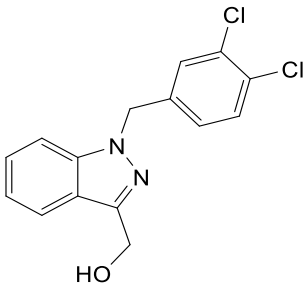	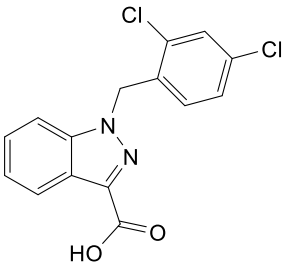 Lonidamine	Inhibitor of aerobic glycoloysis in cancer cells, in particular hexokinase	[203,204]
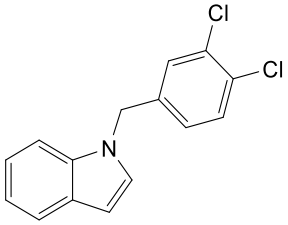	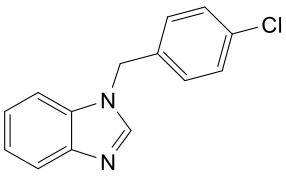	cortisol biosynthesis, CYP11B1	[205]
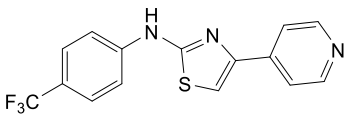	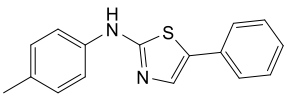	KDR kinase	[160]

Search molecule	Search hit	Target enzyme(s)	Reference
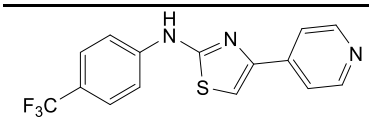	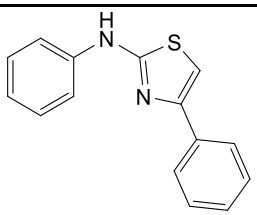	Eicosanoid metabolism	161
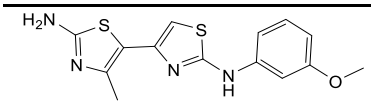	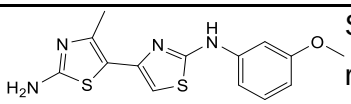	Several human targets reported	206
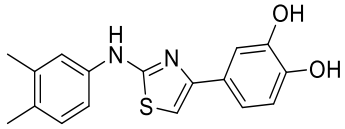	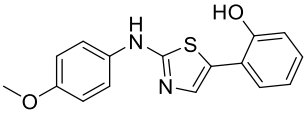	α-amylase	207

5.4.9 Table of compounds as SMILES with biological activity and PAINS count.

Structure	ID	MW	IC_{50} [µM]	IC_{50} [µM] StdDev	PAINS count*
c1ccc2c(c1)c(cn2Cc3ccc(c(c3)Cl)Cl)CO	**3**	306.2	23.6	6.4	0
c1ccc2c(c1)c(cn2Cc3cccc(c3)Cl)CO	**24**	271.7	12.2	2.8	0
c1ccc2c(c1)c(cn2Cc3ccc(cc3)Cl)CO	**20**	271.7	27.2	13.6	0
c1cc2c(cn(c2c(c1)Cl)Cc3ccc(c(c3)Cl)Cl)CO	**23**	340.6	13.8	0.9	0
COc1cccc2c1n(cc2CO)Cc3ccc(c(c3)Cl)Cl	**16**	336.2	55.5	0	0
c1ccc2c(c1)ccn2Cc3ccc(c(c3)Cl)Cl	**29**	276.2	8.1	0.1	0
COc1cccc2c1c(cn2Cc3ccc(c(c3)Cl)Cl)CO	**32**	336.2	5.5	1.5	0
Cc1cn(c2c1cccc2)Cc3ccc(c(c3)Cl)Cl	**27**	290.2	10.2	3.4	0
c1cc(c(cc1Cn2cc(c3c2cc(cc3)F)CO)Cl)Cl	**28**	324.2	8.9	2.4	0
c1ccc2c(c1)c(cn2Cc3ccc(c(c3)Cl)Cl)CCO	**19**	320.2	28.9	1.2	0
c1cc(c(cc1Cn2cc(c3c2cc(cc3)C#N)CO)Cl)Cl	**17**	331.2	43.8	19.2	0
c1cc(c(cc1Cn2cc(c3c2ccc(c3)N(=O)=O)CO)Cl)Cl	**30**	351.2	7.2	0.1	0
c1cc(c(cc1Cn2cc(c3c2ccc(c3)F)CO)Cl)Cl	**33**	324.2	5.3	1.3	0
COc1ccc2c(c1)c(cn2Cc3ccc(c(c3)Cl)Cl)CO	**21**	336.2	18.5	1.1	0
c1cc2c(cn(c2nc1)Cc3ccc(c(c3)Cl)Cl)CO	**14**	307.2	>111	0	0
c1ccc(cc1)Cn2cc(c3c2ccc(c3)Br)CO	**31**	316.2	6.1	1.3	0
c1ccc2c(c1)c(cn2c3ccc(c(c3)Cl)Cl)CO	**15**	292.2	55.5	0	0
COc1ccc(c(c1)OC)CNCc2cn(c3c2cccc3)Cc4ccc(c(c4)Cl)Cl	**35**	455.4	0.8	0.2	0
c1cc2c(c(c1)F)c(cn2Cc3ccc(c(c3)Cl)Cl)CO	**34**	324.2	2.4	0.2	0
c1ccc2c(c1)c(nn2Cc3ccc(c(c3)Cl)Cl)CO	**18**	307.2	33.9	0.2	0
c1cc(cc(c1)Cl)Cn2cc(c3c2ccc(c3)F)CO	**25**	289.7	12	0.1	0
COc1ccc2c(c1)c(cn2Cc3ccc(c(c3)Cl)Cl)CO	**22**	336.2	15.6	3.3	0

Structure	ID	MW	IC_{50} [µM]	IC_{50} [µM] StdDev	PAINS count*
c1ccc(cc1)Cn2cc(c3c2ccc(c3)F)CO	**26**	255.3	11.9	1.5	0
c1cc(ccc1CC(=NO)c2ccc(cc2O)O)N	**5**	258.3	>111	0	0
COc1ccc(c(c1)OC)/C(=N/O)/Cc2ccc(cc2)N	**6**	286.3	>111	0	0
COc1cc(ccc1C(=NO)Cc2ccc(cc2)N)O	**4**	272.3	>111	0	0
c1cc(ccc1CC(c2ccc(cc2O)O)O)Cl	**13**	264.7	9.9	1.7	0
c1cc(ccc1CC(=NN)c2ccc(cc2O)O)Cl	**12**	276.7	16	0.2	0
CON=C(Cc1ccc(cc1)Cl)c2ccc(cc2O)O	**11**	291.7	28	8.8	0
c1cc(ccc1CC(=NO)c2ccc(cc2O)N)Cl	**10**	276.7	38.2	11.2	0
COc1ccc(c(c1)O)C(=NO)Cc2ccc(cc2)Cl	**9**	291.7	46.8	1.5	0
c1cc(ccc1CC(=NO)c2ccc(cc2O)O)Cl	**2**	277.7	93.8	0.8	0
c1cc(ccc1C/C(=N\O)/c2ccc(nc2)O)Cl	**8Z**	262.7	>28	0	0
c1cc(ccc1C/C(=N\O)/c2ccc(nc2)O)Cl	**8E**	262.7	>111	0	0
COc1ccc(cn1)C(=NO)Cc2ccc(cc2)Cl	**7Z**	276.7	>111	0	0
COc1ccc(cn1)C(=NO)Cc2ccc(cc2)Cl	**7E**	276.7	43.6	9.5	0
Cc1c(cccc1Cl)Nc2nc(cs2)c3ccccn3	**45**	301.8	2.8	0.1	0
Cc1c(sc(n1)C)c2csc(n2)Nc3ccc(cc3)C(F)(F)F	**42**	355.4	9.5	1.1	0
Cc1c(sc(n1)N)c2csc(n2)Nc3ccccc3C(F)(F)F	**36**	356.4	43	2.4	0
c1cc(ccc1C(F)(F)F)Nc2nc(cs2)c3ccncc3	**37**	321.3	34.2	1.8	0
c1cc(ccc1C(F)(F)F)Nc2nc(cs2)c3ccc(cc3O)O	**39**	352.3	22.1	5.6	0
c1cc(cc(c1)Nc2nc(cs2)c3ccc(cc3O)O)C(F)(F)F	**38**	352.3	23	0.7	0
Cc1c(sc(n1)N)c2csc(n2)Nc3cccc(c3)OC	**40**	318.4	17.9	0.4	0
Cc1c(cccc1Cl)Nc2nc(cs2)c3c(nc(s3)N)C	**41**	336.9	15.9	1.8	0
Cc1ccc(cc1C)Nc2nc(cs2)c3ccc(c(c3)O)O	**43**	312.4	4.4	0.1	0
c1ccc(cc1)Nc2nc(cs2)c3ccccn3	**44**	253.3	3.7	1.6	0
Cc1c(sc(n1)N)c2csc(n2)Nc3cccc(c3)C(F)(F)F	**46**	356.4	2.5	0.1	0
Cc1ccc(cc1C)Nc2nc(cs2)c3ccccn3	**47**	281.4	1.5	0.8	0
Cc1c(sc(n1)N)c2csc(n2)Nc3ccc(cn3)Cl	**48**	323.8	1	0.1	0
Cc1c(sc(n1)N)c2csc(n2)Nc3ccc(cc3)C(F)(F)F	**1**	356.4	0.6	0.2	0

*****Compounds were checked for PAINS motives using the PAINS filter of the software StarDrop, which searches for functional groups defined in the publication by J.Baell and G. Holloway.[208]

5.5 Chemical synthesis

NMR experiments were run on a Bruker Avance Neo 500 MHz (^{1}H at 500.0 MHz; ^{13}C at 126.0 MHz; ^{19}F NMR at 470 MHz), equipped with a Prodigy Cryo-probe. Spectra were acquired at 298 K, using deuterated DMSO (^{1}H: 2.50 ppm, ^{13}C: 39.52 ppm), deuterated methanol (^{1}H: 3.31 ppm, ^{13}C: 49.00 ppm) or deuterated chloroform (^{1}H: 7.26 ppm, ^{13}C: 77.16 ppm) as solvent. Chemical shifts for ^{1}H and ^{13}C spectra were recorded in ppm using the residual non-deuterated solvent as the internal standard. Coupling constants (*J*) are given in Hertz (Hz). Data are reported as follows: Chemical shift, multiplicity (s = singlet, d = doublet, t = triplet, q = quartet, m = multiplet, br = broad and combinations of these) coupling constants and integration. Mass spectrometry was performed on a Dionex UltiMate 300 LCMS system (Thermo Fisher Scientific AG, Dreieich, Germany). Purification of products was either performed using semi-preparative HPLC (Dionex UltiMate 3000, Thermo Fisher Scientific AG, Dreieich, Germany) on a reversed-phase column (Nucleodur C18 column, 250 mm x 10 mm, 5 µm, Macherey-Nagel, Germany) or flash chromatography using the automated flash chromatography system CombiFlash Rf+ (Teledyne Isco, Lincoln, NE, USA) equipped with RediSepRf silica columns (Axel Semrau, Sprockhövel Germany) or by manual flash column chromatography using 0.04–0.063 mm or 0.063–0.2 mm silica (Macherey-Nagel) and solvents as indicated. High-resolution mass of final products was determined by LCMS/MS using Thermo Scientific Q Exactive Focus Orbitrap LC-MS/MS system equipped with an EC 150/2 Nucleodur C18 Pyramid (3 µm particle size) analytical column (Macherey-Nagel, Germany). The mobile phase consisted of solvent A (acetonitrile containing 0.1% formic acid) and solvent B (water containing 0.1% formic acid) with a flow rate of 0.25 mL/min. The purity of the final compounds was determined using Dionex Ultimate 3000-ISQ HPLC system (Thermo Fisher Scientific AG, Dreieich, Germany) equipped with a Hypersil Gold column (100 mm x 2.1 mm, 3 µm, Thermo Fisher Scientific AG, Dreieich, Germany). All final compounds had a purity >95%. Yields refer to analytically pure compounds and have not been optimized. All chemicals were purchased at SigmaAldrich or comparable commercial suppliers and used without further purification.

5.5.1 Synthesis of DMB-py

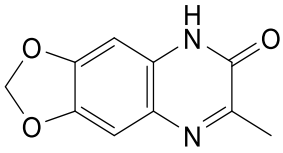

DMB-py was synthesized using a literature procedure and analytical data were in accordance with the reported values.[96]

5.5.2 Synthesis of fragment derivatives

Numbering of compounds in this chapter follows the numbering in Chapter 3.2.

Methyl 2-amino-5-bromonicotinate (**127**)

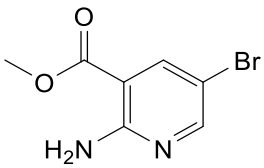

Compound **127** was synthesized using a literature procedure and analysis data were in accordance with the reported values.[209]

5-Bromo-2-(methylamino)nicotinic acid (**128**)

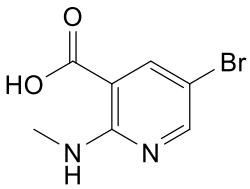

To a solution of methyl-5-bromo-2-(methylamino)nicotinate (0.41 mmol, 100 mg) in tetrahydrofuran (4 mL), sodium hydroxide (1.63 mmol, 65 mg, 4.0 equiv.) was added at 0 °C. The reaction was stirred for 24 h, the solution was acidified with hydrochloric acid (1 M, 2 mL) and extracted with ethyl acetate (3 x, 10 mL). The organic layer was dried over Na_2SO_4, filtered and concentrated under reduced pressure. Flash column chromatography (petroleum benzine/ethyl acetate 3:2) afforded the product as a white solid (18 mg, 19%).

^{1}H-NMR (500 MHz, $(CD_3)_2SO$): δ (ppm) = 13.37 (s, 1H), 8.35 (d, *J* = 2.57 Hz, 1H), 8.09 (d, *J* = 2.58 Hz, 1H), 8.04 (s, 1H), 2.92 (s, 3H). ^{13}C-NMR (126 MHz, $(CD_3)_2OS$): δ (ppm) = 167.7, 157.3, 153.4, 141.3, 107.9, 103.4, 27.8. HR-ESI-MS: calculated for

$C_7H_8BrN_2O_2$ $[M+H]^+$ 230.9764 (^{79}Br), 232.9743 (^{81}Br), found 230.9763 (100%), 232.9741 (96%). Purity: 97%.

5.5.3 Synthesis of virtual-screening hit derivatives

Numbering of compounds in this chapter follows the numbering in Chapter 3.4.

Compounds **20**, **14**, **21b**, **21c**, **21e**, **37a** are known and were synthesized following literature procedures.[105,108,110] However, one or more of the following experiments (^1H or ^{13}C NMR spectra in $(CD_3)_2SO$, HRMS) have not been reported before and therefore, full characterization of the respective compounds are reported below.

5.5.3.1 General procedure I

Amines **20** and **21a**–**l** were synthesized following a literature procedure.[108] Oxazolidin-2-one (**18**) (1.0 equiv.) was dissolved in ethanol or 2-propanol. Sodium ethanolate (2.0 equiv.) and the respective benzenethiol (3.0 equiv.) were added, and the mixture was stirred at 85 °C for 18–24 h. After cooling down, the mixture was diluted with ethyl acetate and washed with a saturated, aqueous NH_4Cl solution (1 x). The aqueous layer was extracted with ethyl acetate (1 x). The combined organic layers were dried over Na_2SO_4, filtered and concentrated *in vacuo*. The oil was purified by flash column chromatography as described below.

5.5.3.2 General procedure II

Triazoles **15** and **27a**–**g** were synthesized following a literature procedure.[105] A solution of the respective hydrazide (1.0 equiv.) and ammonium thiocyanate (3.0 equiv.) in ethanol and hydrochloric acid (37% or 1 M) was stirred at 90 °C for 24–48 h. After cooling down, the mixture was poured on ice and stirred until the ice was completely melted. The precipitated white solid was filtered and dried under reduced pressure. The resulting carbothioamide (1.0 equiv.) was dissolved in 10% sodium hydroxide solution and the mixture was stirred at 105 °C for 2 h. After cooling down, the mixture was filtered and the resulting white solid was evaporated under reduced pressure to remove residual water. The product was used without further purification.

5.5.3.3 General procedure III

Esters **16** and **209**–**211** were synthesized following a literature procedure.[106] Ethyl-2-bromoacetate (1.2 equiv.) was added to a stirred solution of the respective triazole (1.0 equiv.) and sodium bicarbonate (1.0 equiv.) in ethanol. After 24 h of stirring at room temperature, the mixture was acidified with hydrochloric acid (1 M) and ethanol

was evaporated under reduced pressure. Afterwards the residue was extracted with ethyl acetate (3 x), and the organic layer was dried over Na_2SO_4, filtered and evaporated under reduced pressure. The solid was purified by flash column chromatography (hexane/ethyl acetate 2:1) unless indicated otherwise.

5.5.3.4 General procedure IV

Acids **17**, **28a** and **28d**–**f** were synthesized following a literature procedure.[107] In contrast to that procedure, the ester was dissolved in tetrahydrofuran and/ or water. Then, sodium hydroxide (2.0 equiv. or 4.0 equiv.) was added at 0 °C, and the mixture stirred at 25 °C for 24 h. The tetrahydrofuran was removed under reduced pressure, and the remaining aqueous layer was acidified with hydrochloric acid (1 M). The precipitate was filtered off, washed with water and dried under reduced pressure. The resulting acids were used without further purification.

5.5.3.5 General procedure V

Final compounds **1**, **22a**–**l**, **29a**, **29d**–**f**, **31**, **36** and **38a**–**e** were synthesized following a literature procedure.[109] To a mixture of the respective carboxylic acid (1.0 equiv.), EDC*HCl (1.1 equiv.), HOBt (1.0 equiv.) and NMM (2.0 equiv.) in DMF, the respective amine (1.1 equiv.) was added (at 0 °C when using more than 100 mg starting material). After stirring for 16–72 h, the mixture was acidified with hydrochloric acid (1 M) and extracted with ethyl acetate (3 x). The organic layer was washed with brine (1 x), dried over anhydrous sodium sulfate, filtered and reduced *in vacuo*. The resulting material was purified by flash column chromatography (hexane/ethyl acetate 3:7) over 0.04–0.063 mm silica unless indicated otherwise. After purification, these products had to be suspended in a methanol-water mixture and freeze-dried to remove residual solvents.

Alternatively/ additionally, compounds were purified by preparative HPLC (H_2O/CH_3CN + 0.1% formic acid, gradient from 5% to 90% CH_3CN).

5.5.3.6 General procedure VI

Triazoles **27b**, **27c** and **27g** (1.0 equiv.) and compound **31** (1.2 equiv.) were dissolved in ethanol, potassium hydroxide (1.0 equiv.) was added, and the reaction stirred for 24 h. Water was added and the aqueous layer was extracted with ethyl acetate. The combined organic layers were dried over Na_2SO_4, and the solvent was removed under reduced pressure. The resulting material was purified by preparative HPLC (H_2O/ CH_3CN + 0.1% formic acid, gradient from 5% to 90% CH_3CN).

5.5.3.7 General notes

For amines **21d** and **21h**, the two protons of the amino group could not be identified in ^{1}H NMR. For compounds **22a**, **22b**, **22d**, and **22k** the quaternary carbon around 112 ppm cannot be seen in the ^{13}C NMR spectrum, but can be confirmed by heteronuclear multiple bond correlation (HMBC)-NMR. For ester **209**, acid **17** and all final compounds except for **22l**, **29a** and **36** both carbons of the triazole ring are not visible in the ^{13}C NMR spectrum. For acids **28a** and **28f** and final compound **38a** the proton of the triazole ring is not visible in the ^{1}H NMR spectrum.

2-(*p*-Tolylthio)ethan-1-amine (20)

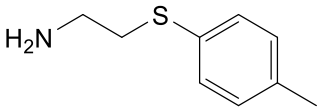

Following general procedure I, 2-oxazolidone (**18**) (1.00 g, 11.5 mmol, 1.0 equiv.) was dissolved in ethanol (10 mL). Sodium ethanolate (1.56 g, 23.0 mmol, 2.0 equiv.) and 4-methylbenzenethiol (4.28 g, 34.5 mmol, 3.0 equiv.) were added. The mixture was stirred at 85 °C for 24 h. After work up, the resulting orange liquid was purified by flash column chromatography (CH_2Cl_2/CH_3OH 9:1 + 0.5% NEt_3), affording the pure product (1.7 g, 89%) as an orange oil.

^{1}H NMR (500 MHz, $(CD_3)_2SO$): δ (ppm) = 7.23 (d, *J* = 8.0 Hz, 2H), 7.12 (d, *J* = 8.0 Hz, 2H), 2.90 (t, *J* = 6.1 Hz, 2H), 2.66 (t, *J* = 6.1 Hz, 2H), 2.26 (s, 3H), 1.67 (s, 2H). ^{13}C NMR (126 MHz, $(CD_3)_2SO$): δ (ppm) = 135.2, 132.3, 129.7, 128.9, 41.2, 36.7, 20.5. HR-ESI-MS: calculated for $C_9H_{11}S$ [*M*-NH_2]$^{\bullet}$ 151.0581, found 151.0576. Purity: >98%.

2-(*o*-Tolylthio)ethan-1-amine (21a)

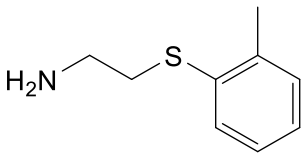

Following general procedure I, 2-oxazolidone (**18**) (500 mg, 5.7 mmol, 1.0 equiv.) was dissolved in ethanol (5 mL). Sodium ethanolate (780 mg, 11.5 mmol, 2.0 equiv.) and 2-methylbenzenethiol (2.14 g, 17.2 mmol, 3.0 equiv.) were added. The mixture was stirred at 85 °C for 24 h. After work up, the resulting orange liquid was purified by flash column chromatography (CH_2Cl_2/CH_3OH 9:1 + 0.5% NEt_3), affording the pure product (886 mg, 92%) as an orange oil.

^{1}H NMR (500 MHz, $(CD_3)_2SO$): δ (ppm) = 7.31 (d, *J* = 7.8 Hz, 1H), 7.22–7.14 (m, 2H), 7.08 (t, *J* = 7.3 Hz, 1H), 2.94 (t, *J* = 6.7 Hz, 2H), 2.71 (t, *J* = 6.7 Hz, 2H), 2.27 (s, 3H), 1.62 (s, 2H). ^{13}C NMR (126 MHz, $(CD_3)_2SO$): δ (ppm) = 136.1, 135.5, 129.9, 126.7, 126.5, 125.1, 41.1, 35.4, 19.9. HR-ESI-MS: calculated for $C_9H_{11}S$ [*M*-NH_2]$^{\bullet}$ 151.0581, found 151.0576. Purity: >98%.

2-(*m*-Tolylthio)ethan-1-amine (21b)

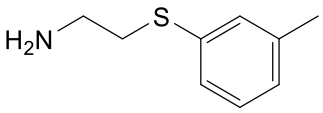

Following general procedure I, 2-oxazolidone (**18**) (500 mg, 5.7 mmol, 1.0 equiv.) was dissolved in ethanol (5 mL). Sodium ethanolate (780 mg, 11.5 mmol, 2.0 equiv.) and 3-methylbenzenethiol (2.14 g, 17.2 mmol, 3.0 equiv.) were added. The mixture was stirred at 85 °C for 24 h. After work up, the resulting orange liquid was purified by flash column chromatography (CH_2Cl_2/CH_3OH 9:1 + 0.5% NEt_3), affording the pure product (888 mg, 92%) as a yellow oil.

^{1}H NMR (500 MHz, $(CD_3)_2SO$): δ (ppm) = 7.19 (t, *J* = 7.5 Hz, 1H), 7.14 (s, 1H), 7.11 (m, 1H), 6.98 (m, 1H), 2.94 (t, *J* = 7.5 Hz, 2H), 2.69 (t, *J* = 7.4 Hz, 2H), 2.27 (s, 3H), 1.61 (s, 2H). ^{13}C NMR (126 MHz, $(CD_3)_2SO$): δ (ppm) = 138.3, 136.0, 128.8, 128.5, 126.3, 125.1, 41.3, 36.0, 20.9. HR-ESI-MS: calculated for $C_9H_{11}S$ [*M*-NH_2]$^{\bullet}$ 151.0581, found 151.0576. Purity: >98%.

2-(Phenylthio)ethan-1-amine (21c)

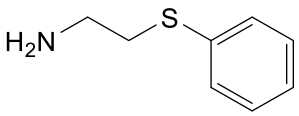

Following general procedure I, 2-oxazolidone (**18**) (100 mg, 1.2 mmol, 1.0 equiv.) was dissolved in 2-propanol (2 mL). Sodium ethanolate (157 mg, 2.3 mmol, 2.0 equiv.) and 4-benzenethiol (316 mg, 2.9 mmol, 2.5 equiv.) were added. The mixture was stirred at 85 °C for 24 h. After work up, the resulting orange liquid was purified by flash column chromatography (CH_2Cl_2/CH_3OH 95:5 + 0.5% NEt_3), affording the product (99 mg, 56%) as a yellow oil.

^{1}H NMR (500 MHz, $(CD_3)_2SO$): δ (ppm) = 7.32 (m, 4H), 7.17 (m, 1H), 2.97 (t, *J* = 7.0 Hz, 2H), 2.70 (t, *J* = 7.0 Hz, 2H), 2.10 (s, 2H). ^{13}C NMR (126 MHz, $(CD_3)_2SO$):

δ (ppm) = 136.2, 129.1, 128.0, 125.6, 41.2, 35.6. HR-ESI-MS: calculated for C_8H_9S [*M*-NH_2]$^{\bullet}$ 137.0425, found 137.0419 (100%). Purity: 62%.

2-((4-Methoxyphenyl)thio)ethan-1-amine (21d)

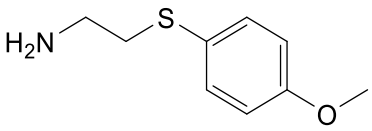

Amine **21d** has been synthesized following general procedure I and analytical data were in accordance with literature values.[210]

2-((4-Chlorophenyl)thio)ethan-1-amine (21e)

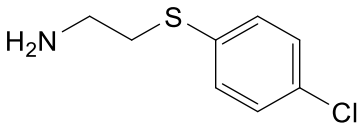

Following general procedure I, 2-oxazolidone (**18**) (100 mg, 1.2 mmol, 1.0 equiv.) was dissolved in 2-propanol (2 mL). Sodium ethanolate (157 mg, 2.3 mmol, 2.0 equiv.) and 4-chlorobenzenethiol (415 mg, 2.9 mmol, 2.5 equiv.) were added. The mixture was stirred at 85 °C for 24 h. After work up, the resulting orange liquid was purified by flash column chromatography (CH_2Cl_2/CH_3OH 96:4 + 0.2% NEt_3), affording the pure product (141 mg, 65%) as a yellow oil.

^{1}H NMR (500 MHz, $(CD_3)_2SO$): δ (ppm) = 7.35 (m, 4H), 2.97 (t, *J* = 6.9 Hz, 2H), 2.70 (t, *J* = 6.9 Hz, 2H), 1.89 (s, 2H). ^{13}C NMR (126 MHz, $(CD_3)_2SO$): δ (ppm) = 135.5, 130.0, 129.6, 128.9, 41.1, 36.0. HR-ESI-MS: calculated for C_8H_8ClS [*M*-NH_2]$^{\bullet}$ 171.0035 (^{35}Cl), 173.0006 (^{37}Cl), found 171.0030 (100%), 172.9999 (40%). Purity: 95%.

2-((4-Fluorophenyl)thio)ethan-1-amine (21f)

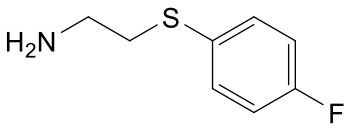

Following general procedure I, 2-oxazolidone (**18**) (100 mg, 1.2 mmol, 1.0 equiv.) was dissolved in 2-propanol (2 mL). Sodium ethanolate (157 mg, 2.3 mmol, 2.0 equiv.) and 4-fluorobenzenethiol (368 mg, 2.9 mmol, 2.5 equiv.) were added. The mixture was stirred at 85 °C for 18 h. After work up, the resulting orange liquid was purified by flash

column chromatography (CH_2Cl_2/CH_3OH 95:5 + 0.2% NEt_3), affording the product (161 mg, 82%) as a yellow oil.

^{1}H NMR (500 MHz, $(CD_3)_2SO$): δ (ppm) = 7.40 (m, 2H), 7.16 (m, 2H), 2.93 (t, *J* = 6.8 Hz, 2H), 2.67 (t, *J* = 6.8 Hz, 2H), 1.83 (s, 2H). ^{13}C NMR (126 MHz, $(CD_3)_2SO$): δ (ppm) = 160.7 (d, *J* = 243.01 Hz) 131.5 (d, *J* = 2.93 Hz), 131.1 (d, *J* = 8.14 Hz), 116.0 (d, *J* = 21.82 Hz), 41.1, 37.1. ^{19}F NMR (470 MHz, $(CD_3)_2SO$): δ (ppm) = –116.7. HR-ESI-MS: calculated for C_8H_8FS [*M*-NH_2]$^•$ 155.0331, found 155.0324. Purity: 60%.

2-((4-Nitrophenyl)thio)ethan-1-amine (21g)

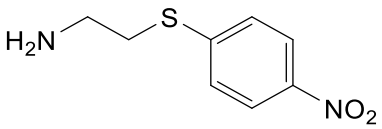

In contrast to the original procedure, where the synthesis of this compound failed, the reaction worked for us.

Following general procedure I, 2-oxazolidone (**18**) (100 mg, 1.2 mmol, 1.0 equiv.) was dissolved in 2-propanol (2 mL). Sodium ethanolate (157 mg, 2.3 mmol, 2.0 equiv.) and 4-nitrobenzenethiol (445 mg, 2.9 mmol, 2.5 equiv.) were added. The mixture was stirred at 85 °C for 18 h. After work up, the resulting orange liquid was purified by flash column chromatography (CH_2Cl_2/CH_3OH 95:5 + 0.2% NEt_3), affording the product (40 mg, 18%) as a red oil.

^{1}H NMR (500 MHz, $(CD_3)_2SO$): δ (ppm) = 8.12 (d, *J* = 8.9 Hz, 2H), 7.52 (d, *J* = 8.9 Hz, 2H), 3.13 (t, *J* = 6.9 Hz, 2H), 2.80 (t, *J* = 6.9 Hz, 2H), 2.12 (s, 2H). ^{13}C NMR (126 MHz, $(CD_3)_2SO$): δ (ppm) = 147.7, 144.3, 126.2, 123.9, 40.7, 34.2. HR-ESI-MS: calculated for $C_8H_8NO_2S$ [*M*-NH_2]$^•$ 182.0276, found 182.0269. Purity: 59%.

2-((4-(Trifluoromethyl)phenyl)thio)ethan-1-amine (21h)

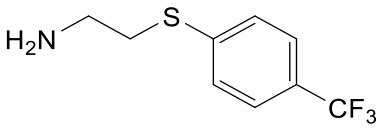

Following general procedure I, 2-oxazolidone (**18**) (163 mg, 1.9 mmol, 1.0 equiv.) was dissolved in 2-propanol (19 mL). Sodium ethanolate (250 mg, 3.7 mmol, 2.0 equiv.) and 4-(trifluoromethyl)thiophenol (1.0 g, 5.7 mmol, 3.0 equiv.) were added. The mixture was stirred at 85 °C for 24 h. After work up, the resulting orange liquid was

purified by flash column chromatography (CH_2Cl_2/CH_3OH 95:5), affording the product (48 mg, 12%) as a clear oil.

^{1}H NMR (500 MHz, $(CD_3)_2SO$): δ (ppm) = 7.67–7.60 (m, 2H), 7.50 (d, *J* = 8.4 Hz, 2H), 3.14–3.04 (m, 2H), 2.77 (t, *J* = 6.9 Hz, 2H). ^{13}C NMR (126 MHz, $(CD_3)_2SO$): δ (ppm) = 142.9, 126.9, 126.5 (q, *J* = 93.1 Hz), 125.7 (q, *J* = 3.9 Hz), 124.3 (q, *J* = 240.6 Hz), 40.9, 34.5. ^{19}F NMR (470 MHz, $(CD_3)_2SO$): δ (ppm) = –60.7. HR-ESI-MS: calculated for $C_9H_{11}F_3NS$ $[M+H]^+$ 222.0559, found 222.0553 (10%), $C_9H_8F_3S$ $[M-NH_2]^\bullet$ 205.0299, found 205.0289 (100%). Purity: >99%.

2-((4-Ethylphenyl)thio)ethan-1-amine (21i)

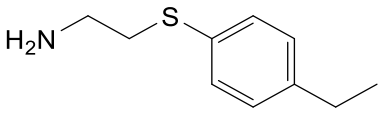

Following general procedure I, 2-oxazolidone (**18**) (200 mg, 2.4 mmol, 1.0 equiv.) was dissolved in 2-propanol (20 mL). Sodium ethanolate (330 mg, 4.8 mmol, 2.0 equiv.) and 4-ethylthiophenol (1.0 g, 7.2 mmol, 3.0 equiv.) were added. The mixture was stirred at 90 °C for 24 h. After work up, the resulting orange liquid was purified by flash column chromatography (CH_2Cl_2/CH_3OH 95:5), affording the product (107 mg, 25%) as a brown oil.

^{1}H NMR (500 MHz, $(CD_3)_2SO$): δ (ppm) = 7.30–7.23 (m, 2H), 7.19–7.12 (m, 2H), 2.91 (t, *J* = 7.5 Hz, 2H), 2.67 (t, *J* = 7.5 Hz, 2H), 2.56 (q, *J* = 7.6 Hz, 2H), 1.15 (t, *J* = 7.6 Hz, 3H), 2.22 (s, 2H). ^{13}C NMR (126 MHz, $(CD_3)_2SO$): δ (ppm) = 141.5, 132.6, 128.9, 128.5, 41.2, 36.6, 27.6, 15.5. HR-ESI-MS: calculated for $C_{10}H_{13}S$ $[M-NH_2]^\bullet$ 165.0738, found 165.0730. Purity: 98%.

***tert*-Butyl (2-((4-chlorophenyl)thio)ethyl)carbamate (23)**

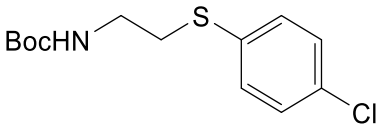

Compound **21e** (718 mg, 3.8 mmol, 1.0 equiv.) was dissolved in chloroform (38 mL) and the solution was cooled to 0 °C. Di-*tert*-butyl dicarbonate (835 mg, 3.8 mmol, 1.0 equiv.) was added and the reaction stirred for 16 h. The organic layer was washed with water (20 mL) and saturated, aqueous NH_4Cl solution (20 mL). Purification by

flash column chromatography (petroleum benzine/ethyl acetate, gradient up to 30% ethyl acetate) afforded the product (1.15 g, 67%) as a yellow oil.

^{1}H NMR (500 MHz, $(CD_3)_2SO$): δ (ppm) = 7.37 (s, 4H), 7.01 (t, *J* = 5.8 Hz, 1H), 3.13–3.10 (m, 2H), 3.02–2.95 (m, 2H), 1.37 (s, 9H). ^{13}C NMR (126 MHz, $(CD_3)_2SO$): δ (ppm) = 155.5, 135.0, 130.4, 129.8, 129.0, 77.8, 39.4, 32.0, 28.2. HR-ESI-MS: calculated for $C_{13}H_{19}ClON_2S$ [*M*-NH_2]$^{\bullet}$ 171.0035, (^{35}Cl), 173.0006 (^{37}Cl), found 171.0024 (100%), 172.9994 (30%). Purity: 50%. Impurity: di-*tert*-butyl dicarbonate.

tert-Butyl (2-((4-morpholinophenyl)thio)ethyl)carbamate (24)

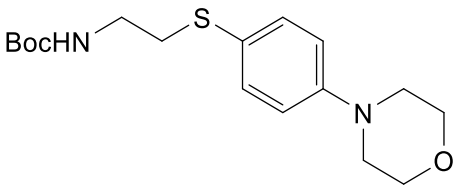

Compound **23** (100 mg, 0.35 mmol, 1.0 equiv.), morpholine (30 mg, 0.35 mmol, 1.0 equiv.) and sodium *tert*-butoxide (50 mg, 0.52 mmol, 1.5 equiv.) were dissolved in dioxane (3 mL), and argon was bubbled through the mixture for five minutes. Then, *t*BuXPhos Pd G3 (27 mg, 0.04 mmol, 0.1 equiv.) was added, and argon was bubbled through again for five minutes. The mixture was placed in a pre-heated heating block at 80 °C for two hours. After full conversion of the starting material (no product mass could be found), saturated, aqueous NH_4Cl solution (3 mL) was added and was extracted with ethyl acetate (3 x 6 mL). Purification by preparative HPLC (H_2O/CH_3CN + 0.1% formic acid, gradient from 5% to 90% CH_3CN) afforded the product (11 mg, 6%) as a yellow oil.

^{1}H NMR (500 MHz, $(CD_3)_2SO$): δ (ppm) = 7.31–7.25 (m, 2H), 6.98 (t, *J* = 5.8 Hz, 1H), 6.94–6.87 (m, 2H), 3.74–3.69 (m, 4H), 3.20–3.07 (m, 4H), 3.03 (dt, *J* = 8.2, 6.0 Hz, 2H), 2.79 (dd, J = 8.2, 6.0 Hz, 2H), 1.36 (s, 9H). ^{13}C NMR (126 MHz, $(CD_3)_2SO$): δ (ppm) = 155.5, 150.2, 132.4, 123.2, 115.6, 77.8, 66.1, 48.1, 39.2, 34.3, 28.3. Purity: 99%.

Note: Correct mass could not be found in HR-ESI-MS.

2-((4-Morpholinophenyl)thio)ethan-1-amine (21j)

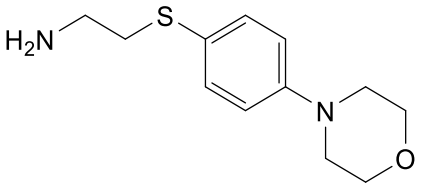

Compound **24** (11 mg, 0.03 mmol, 1.0 equiv.) was dissolved in dry dichloromethane (0.1 mL) and cooled to 0 °C.[211] Hydrochloric acid in dioxane (4 M, 0.1 mL) was added and the reaction was stirred at 25 °C for 6 h. The solvents were removed under reduced pressure and the product was used without further purification.

2-((Aminoethyl)thio)-5-chloroaniline (21k)

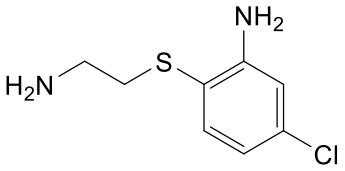

Following general procedure I, 2-oxazolidone (**18**) (100 mg, 1.2 mmol, 1.0 equiv.) was dissolved in 2-propanol (2 mL). Sodium ethanolate (157 mg, 2.3 mmol, 2.0 equiv.) and 2-amino-chlorobenzenethiol (458 mg, 2.9 mmol, 2.5 equiv.) were added. The mixture was stirred at 85 °C for 18 h. After work up, the resulting orange liquid was purified by flash column chromatography (CH_2Cl_2/CH_3OH 95:5 + 0.2% NEt_3), affording the product (97 mg, 42%) as a yellow oil.

^{1}H NMR (500 MHz, $(CD_3)_2SO$): δ (ppm) = 7.23 (d, *J* = 8.2 Hz, 1H), 6.74 (d, *J* = 2.3 Hz, 1H), 6.50 (dd, *J* = 8.2, 2.3 Hz, 1H), 5.66 (s, 2H), 2.71 (t, *J* = 6.7 Hz, 2H), 2.59 (t, *J* = 6.7 Hz, 2H), 2.31 (s, 2H). ^{13}C NMR (126 MHz, $(CD_3)_2SO$): δ (ppm) = 150.9, 136.4, 133.6, 115.7, 114.4, 113.1, 40.9, 37.2. HR-ESI-MS: calculated for $C_8H_{12}ClN_2S$ $[M+H]^+$ 203.0404 (^{35}Cl), 205.0375 (^{37}Cl), found 203.0403 (100%), 205.0372 (30%). Purity: 69%.

2-((3,5-Bis(trifluoromethyl)phenyl)thio)ethan-1-amine (21l)

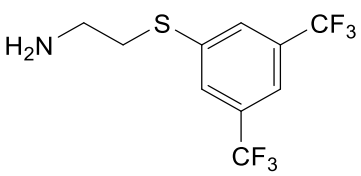

Following general procedure I, 2-oxazolidone (**18**) (100 mg, 1.2 mmol, 1.0 equiv.) was dissolved in 2-propanol (2 mL). Sodium ethanolate (157 mg, 2.3 mmol, 2.0 equiv.) and 3,5-bis(trifluoromethyl)benzenethiol (707 mg, 2.9 mmol, 2.5 equiv.) were added. The mixture was stirred at 85 °C for 18 h. After work up, the resulting orange liquid was purified by flash column chromatography (CH_2Cl_2/CH_3OH 95:5 + 0.2% NEt_3), affording the product (63 mg, 19%) as a brown oil.

^{1}H NMR (500 MHz, $(CD_3)_2SO$): δ (ppm) = 7.95 (s, 2H), 7.83 (s, 1H), 3.17 (t, *J* = 6.7 Hz, 2H), 2.77 (t, *J* = 6.7 Hz, 2H), 1.80 (s, 2H). ^{13}C NMR (126 MHz, $(CD_3)_2SO$): δ (ppm) = 141.6, 130.8 (q, *J* = 32.9 Hz), 127.2 (d, *J* = 2.6 Hz), 123.1 (q, *J* = 273.1 Hz), 118.4, 40.7, 35.1. ^{19}F NMR (470 MHz, $(CD_3)_2SO$): δ (ppm) = –61.4. HR-ESI-MS: calculated for $C_{10}H_{10}F_6NS$ $[M+H]^+$ 290.0433, found 290.0428 (60%), $C_{10}H_8F_6S$ $[M-NH_2]^\bullet$ 273.0173, found 273.0163 (100%). Purity: >99%.

N^1-(*p*-Tolyl)ethane-1,2-diamine (37a)

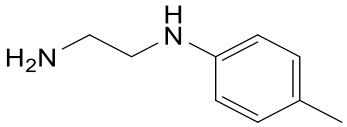

Compound **37a** was synthesized following a literature procedure.[110] In short, *p*-toluidine (1.0 g, 9.3 mmol, 3.0 equiv.) and 2-bromoethylamine hydrobromide (637 mg, 3.1 mmol, 1.0 equiv.) were dissolved in toluene (20 mL) and heated to 90 °C for 24 h. After work up, the product was obtained by reverse flash column chromatography (H_2O/CH_3CN + 0.1% formic acid, gradient from 5% to 100% CH_3CN) as a brown solid (329 mg, 24%).

^{1}H NMR (500 MHz, $(CD_3)_2SO$): δ (ppm) = 8.47 (formic acid, s, 1H), 7.74 (s, 2H), 6.90 (d, *J* = 8.3 Hz, 2H), 6.50 (d, *J* = 8.3 Hz, 2H), 5.81 (s, 1H), 3.20 (t, *J* = 6.3 Hz, 2H), 2.90 (t, *J* = 6.3 Hz, 2H), 2.14 (s, 3H). ^{13}C NMR (126 MHz, $(CD_3)_2SO$): δ (ppm) = 166.4 (formic acid), 146.1, 129.4, 124.5, 112.3, 41.6, 38.2, 20.1. HR-ESI-MS: calculated for $C_9H_{15}N_2$ $[M+H]^+$ 151.1230, found 151.1230 (60%), $C_9H_{12}S$ $[M-NH_2]^\bullet$ 134.0970, found 134.0964 (100%). Purity: 99%.

2-(5-Mercapto-4*H*-1,2,4-triazol-3-yl)phenol (15)

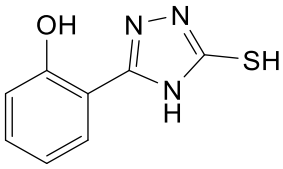

Following general procedure II, a solution of 2-hydroxybenzohydrazide (10 g, 66.0 mmol, 1.0 equiv.) and ammonium thiocyanate (14.9 g, 198.0 mmol, 3.0 equiv.) in ethanol (150 mL) and hydrochloric acid (37%, 24 mL) was stirred at 90 °C for 48 h. The precipitated carbothioamide was washed with water and used without further purification. It (9.6 g, 45.5 mmol, 1.0 equiv.) was dissolved in 10% sodium hydroxide solution and the mixture was stirred at 105 °C for 2 h. After work up, the product was obtained as a white solid (8.7 g, 68% over two steps (o2s)). Analytical data were in accordance with published values.[105]

5-(2-Methoxyphenyl)-4*H*-1,2,4-triazole-3-thiol (27a)

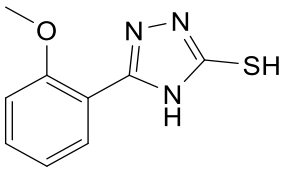

Following general procedure II, a solution of 2-methoxybenzohydrazide (1.0 g, 6.0 mmol, 1.0 equiv.) and ammonium thiocyanate (920 mg, 12.0 mmol, 2.0 equiv.) in hydrochloric acid (1 M, 3 mL) was stirred at 90 °C for 48 h. The precipitated carbothioamide **26a** was washed with water and used without further purification. It (1.0 g, 4.4 mmol, 1.0 equiv.) was dissolved in 10% sodium hydroxide solution (60 mL) and the mixture was stirred at 105 °C for 3 h. After work up, the product was obtained as a white solid (910 mg, 73% o2s). Analytical data were in accordance with published values.[212]

Note: Using hydrochloric acid (37%) instead of the diluted solution led to decomposition of the hydrazide.

5-(4-Methoxyphenyl)-4*H*-1,2,4-triazole-3-thiol (27b)

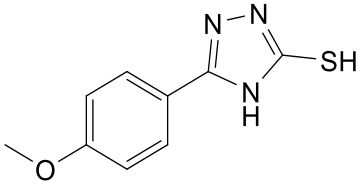

4-Hydroxybenzoic acid was methylated to form methyl 4-methoxybenzoate (**207**) that was subsequently used to form 4-methoxybenzohydrazide (**208**) following literature procedures.[213,214] Following general procedure II, a solution of 4-methoxybenzohydrazide (684 mg, 4.11 mmol, 1.0 equiv.) and ammonium thiocyanate (927 mg, 12.3 mmol, 3.0 equiv.) in hydrochloric acid (1 M, 2 mL) was stirred at 90 °C for 48 h. The resulting carbothioamide **26b** (740 mg, 3.3 mmol, 1.0 equiv.) was dissolved in 10% sodium hydroxide solution,n and the mixture was stirred at 105 °C for 3 h. After work up, the product was obtained as a white solid (286 mg, 34% o2s). All analytical data were in accordance with published values.[215]

5-(2-Nitrophenyl)-4*H*-1,2,4-triazole-3-thiol (27c)

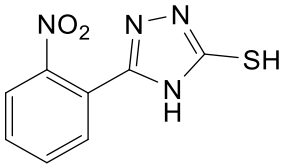

Following general procedure II, a solution of 2-nitrobenzoic hydrazide (2.0 mg, 11.0 mmol, 1.0 equiv.) and ammonium thiocyanate (1.7 mg, 22.0 mmol, 2.0 equiv.) in hydrochloric acid (1 M, 3 mL) was stirred at 90 °C for 48 h. Instead of the expected carbothioamide, the cyclized product **27c** was obtained directly after work up as a yellow solid (136 mg, 6%). Analytical data were in accordance with published values.[212]

5-(2-Chlorophenyl)-4*H*-1,2,4-triazole-3-thiol (27d)

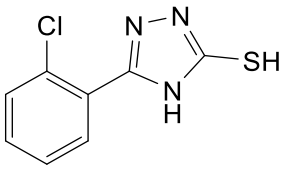

Following general procedure II, a solution of 2-chlorobenzoic hydrazide (1.0 g, 5.9 mmol, 1.0 equiv.) and ammonium thiocyanate (890 mg, 11.7 mmol, 2.0 equiv.) in hydrochloric acid (1 M, 3 mL) was stirred at 90 °C for 48 h. Instead of the expected carbothioamide, the cyclized product **27d** was obtained directly after work up as a white solid (619 mg, 49%). Analytical data were in accordance with published values.[212]

5-(Pyridin-2-yl)-4*H*-1,2,4-triazole-3-thiol (27e)

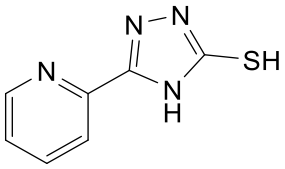

Following general procedure II, a solution of 2-pyridinecarboxylic acid hydrazide (1.0 g, 7.3 mmol, 1.0 equiv.) and ammonium thiocyanate (1.1 g, 14.6 mmol, 2.0 equiv.) in hydrochloric acid (1 M, 3 mL) was stirred at 90 °C for 48 h. Instead of the expected carbothioamide, the cyclized product **27e** was obtained directly after work up as a white solid (212 mg, 16%).

^{1}H NMR (500 MHz, $(CD_3)_2SO$): δ (ppm) = 13.93 (s, 1H), 13.76 (s, 1H), 8.69 (dt, *J* = 4.8, 1.4 Hz, 1H), 8.01–7.94 (m, 2H), 7.53 (td, *J* = 5.1, 3.3 Hz, 1H). ^{13}C NMR (126 MHz, $(CD_3)_2SO$): δ (ppm) = 168.0, 150.8, 150.1, 145.0, 138.2, 125.8, 121.4. HR-ESI-MS: calculated for $C_7H_7N_4S$ $[M+H]^+$ 179.0386, found 179.0383. Purity: 99%.

5-(Pyridin-3-yl)-4*H*-1,2,4-triazole-3-thiol (27f)

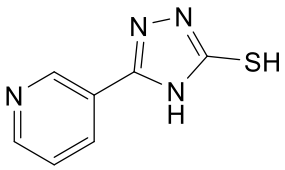

Following general procedure II, a solution of nicotinic acid hydrazide (1.0 g, 7.3 mmol, 1.0 equiv.) and ammonium thiocyanate (1.1 mg, 14.6 mmol, 2.0 equiv.) in hydrochloric acid (1 M, 3 mL) was stirred at 90 °C for 48 h. Instead of the expected carbothioamide, the cyclized product **27f** was obtained directly after work up as a white solid (445 mg, 31%). Analytical data were in accordance with published values.[216]

5-(Pyridin-4-yl)-4*H*-1,2,4-triazole-3-thiol (27g)

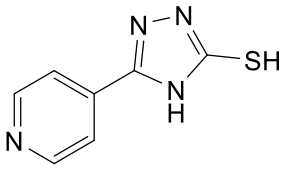

Following general procedure II, a solution of 4-pyridinecarboxylic acid hydrazide (1.0 g, 7.3 mmol, 1.0 equiv.) and ammonium thiocyanate (1.1 g, 14.6 mmol, 2.0 equiv.) in hydrochloric acid (1 M, 3 mL) was stirred at 90 °C for 48 h. Instead of the expected

carbothioamide, the cyclized product **27g** was obtained directly after work up as a white solid (468 mg, 36%). Analytical data were in accordance with published values.[212]

Ethyl 2-((5-(2-hydroxyphenyl)-4*H*-1,2,4-triazol-3-yl)thio)acetate (16)

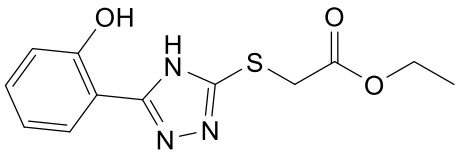

Following general procedure III, ethyl-2-bromoacetate (3.4 mL, 5.2 g, 31.0 mmol, 1.2 equiv.) was added to a stirred solution of **15** (4.9 g, 25.8 mmol, 1.0 equiv.) and sodium bicarbonate (2.2 g, 25.8 mmol, 1.0 equiv.) in ethanol (260 mL). After work up and purification, the product was obtained as a white solid (5.3 g, 74%).

^{1}H NMR (500 MHz, $(CD_3)_2SO$): δ (ppm) = 14.11 (s, 1H), 10.95 (s, 1H), 7.88 (d, *J* = 8.1 Hz, 1H), 7.34 (t, *J* = 7.7 Hz, 1H), 7.01 (d, *J* = 8.1 Hz, 1H), 6.95 (t, *J* = 7.7 Hz, 1H), 4.12 (q, *J* = 7.1 Hz, 2H), 4.04 (s, 2H), 1.18 (t, *J* = 7.1 Hz, 3H). ^{13}C NMR (126 MHz, $(CD_3)_2SO$): δ (ppm) = 168.9, 157.3, 155.6, 153.6, 131.8, 127.5, 119.5, 116.7, 112.0, 61.1, 33.4, 14.0. HR-ESI-MS: calculated for $C_{12}H_{14}N_3O_3S$ m/z: $[M+H]^+$ calculated: 280.0750, found 280.0747. Purity: >99%.

Ethyl 2-((5-(pyridin-3-yl)-4*H*-1,2,4-triazol-3-yl)thio)acetate (209)

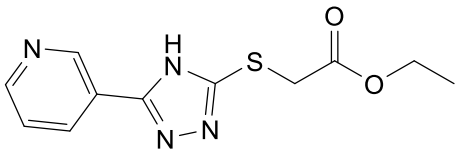

Following general procedure III, ethyl-2-bromoacetate (298 µL, 2.7 mmol, 1.2 equiv.) was added to a stirred solution of **27f** (400 mg, 2.3 mmol, 1.0 equiv.) and sodium bicarbonate (190 mg, 2.3 mmol, 1.0 equiv.) in ethanol (20 mL). After work up, the product was obtained without further purification as a yellow solid (374 mg, 63%).

^{1}H NMR (500 MHz, $(CD_3)_2SO$): δ (ppm) = 14.55 (s, 1H), 9.13–9.09 (m, 1H), 8.65 (dd, *J* = 4.9, 1.7 Hz, 2H), 8.26 (dt, *J* = 8.0, 2.0 Hz, 1H), 7.57–7.51 (m, 1H), 4.12 (q, *J* = 7.1 Hz, 2H), 1.18 (t, *J* = 7.1 Hz, 3H). ^{13}C NMR (126 MHz, $(CD_3)_2SO$): δ (ppm) = 170.3, 168.6, 150.7, 146.9, 133.3, 124.1, 61.1, 33.7, 14.0. HR-ESI-MS: calculated for $C_{11}H_{13}N_4O_2S$ $[M+H]^+$ 265.0754, found 265.0746. Purity: 98%.

Ethyl 2-((5-(2-methoxyphenyl)-4*H*-1,2,4-triazol-3-yl)thio)acetate (210)

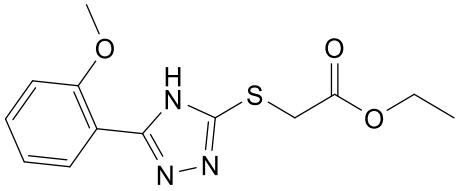

Following general procedure III, ethyl-2-bromoacetate (630 µL, 5.2 mmol, 1.2 equiv.) was added to a stirred solution of **27a** (600 mg, 4.3 mmol, 1.0 equiv.) and sodium bicarbonate (400 mg, 4.3 mmol, 1.0 equiv.) in ethanol (45 mL). After work up, the product was obtained without further purification as a yellow solid (810 mg, 64%).

^{1}H NMR (500 MHz, $(CD_3)_2SO$): δ (ppm) = 13.75 (s, 1H), 8.01 (dd, *J* = 7.6, 1.8 Hz, 1H), 7.47 (ddd, *J* = 8.5, 7.6, 1.8 Hz, 1H), 7.19 (d, *J* = 8.5 Hz, 1H), 7.08 (td, *J* = 7.6, 1.8 Hz, 1H), 4.11 (q, *J* = 7.1 Hz, 2H), 4.03 (s, 2H), 3.94 (s, 3H), 1.18 (t, *J* = 7.1 Hz, 3H). ^{13}C NMR (126 MHz, $(CD_3)_2SO$): δ (ppm) = 169.4, 158.2, 157.0, 152.9, 132.2, 129.4, 121.2, 115.4, 112.3, 61.4, 56.0, 33.8, 14.5. HR-ESI-MS: calculated for $C_{13}H_{16}N_3O_3S$ $[M+H]^+$ 294.0907, found 294.0898. Purity: 97%.

Ethyl 2-((5-(2-chlorophenyl)-4*H*-1,2,4-triazol-3-yl)thio)acetate (211)

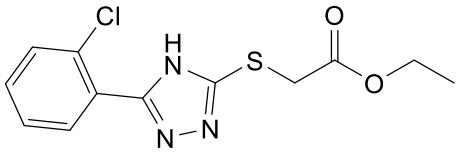

Following general procedure III, ethyl-2-bromoacetate (380 µL, 3.4 mmol, 1.2 equiv.) was added to a stirred solution of **27d** (600 mg, 2.8 mmol, 1.0 equiv.) and sodium bicarbonate (240 mg, 2.8 mmol, 1.0 equiv.) in ethanol (30 mL). After work up, the product was obtained without further purification as an off-white solid (748 mg, 90%).

^{1}H NMR (500 MHz, $(CD_3)_2SO$): δ (ppm) = 14.35 (s, 1H), 7.75 (s, 1H), 7.61 (s, 1H), 7.57–7.38 (m, 2H), 4.11 (q, *J* = 7.1 Hz, 2H), 4.05 (s, 2H), 1.17 (t, *J* = 7.1 Hz, 3H). ^{13}C NMR (126 MHz, $(CD_3)_2SO$): δ (ppm) = 168.8, 158.6, 152.9, 131.9, 131.5, 131.4, 130.4, 127.6, 126.5, 61.0, 33.3, 14.0. HR-ESI-MS: calculated for $C_{12}H_{13}ClN_3O_2S$ $[M+H]^+$ 298.0412 (^{35}Cl), 300.0382(^{37}Cl), found 298.0403 (100%), 300.0371 (30%). Purity: 90%.

2-((5-(2-Hydroxyphenyl)-4*H*-1,2,4-triazol-3-yl)thio)acetic acid (17)

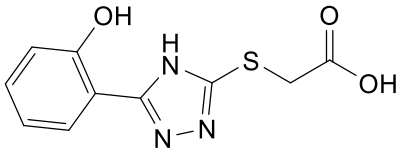

Following general procedure IV, sodium hydroxide (1.4 g, 35.8 mmol, 4.0 equiv.) was added under cooling to a stirred solution of compound **16** (2.5 g, 8.9 mmol, 1.0 equiv.) in THF (90 mL), and the mixture was stirred at 25 °C for 16 h. In contrast to the general procedure, the solution was acidified with hydrochloric acid (1 M) and extracted with ethyl acetate (3 x, 100 mL). The organic layer was washed with brine (150 mL), then dried over anhydrous sodium sulfate, filtered and evaporated under reduced pressure. The resulting white solid (2.3 g, 100%) was used without further purification.

^{1}H NMR (500 MHz, $(CD_3)_2SO$): δ (ppm) = 14.09 (s, 1H), 12.87 (s, 1H), 10.93 (s, 1H), 7.89 (dd, *J* = 7.9, 1.9 Hz, 1H), 7.33 (ddd, *J* = 8.7, 7.4, 1.9 Hz, 1H), 7.00 (d, *J* = 7.9 Hz, 1H), 6.98–6.92 (m, 1H), 4.00 (s, 2H). ^{13}C NMR (126 MHz, $(CD_3)_2SO$): δ (ppm) = 170.1, 155.6, 131.7, 127.4, 119.5, 116.7 112.3, 33.7. HR-ESI-MS: calculated for $C_{10}H_{10}N_3O_3S$ $[M+H]^+$ 252.0437 found: 252.0433. Purity: >99%.

2-((5-(2-Methoxyphenyl)-4*H*-1,2,4-triazol-3-yl)thio)acetic acid (28a)

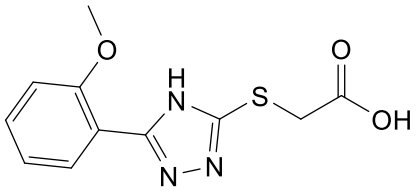

Following general procedure IV, ester **210** (700 mg, 2.4 mmol, 1.0 equiv.) was dissolved in THF (25 mL) and water (5 mL). Sodium hydroxide (190 mg, 4.8 mmol, 2.0 equiv.) was added under cooling, and the mixture was stirred at 25 °C for 24 h. After work up, the resulting off-white solid (610 mg, 96%) was used without further purification.

^{1}H NMR (500 MHz, $(CD_3)_2SO$): δ (ppm) = 13.74 (s, 1H), 8.02 (dd, *J* = 7.6, 1.8 Hz, 1H), 7.47 (ddd, *J* = 8.4, 7.6, 1.8 Hz, 1H), 7.18 (d, *J* = 8.4 Hz, 1H), 7.08 (t, *J* = 7.6 Hz, 1H), 3.97 (s, 2H), 3.94 (s, 3H). ^{13}C NMR (126 MHz, $(CD_3)_2SO$): δ (ppm) = 170.2, 157.9, 156.5, 152.6, 131.8, 129.1, 120.8, 115.1, 111.9, 55.6, 33.6. HR-ESI-MS: calculated for $C_{11}H_{12}N_3O_3S$ $[M+H]^+$ 266.0594, found 266.0586. Purity: 97%.

2-((5-(2-Chlorophenyl)-4*H*-1,2,4-triazol-3-yl)thio)acetic acid (28d)

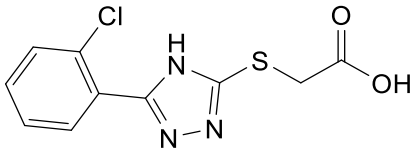

Following general procedure IV, ester **211** (100 mg, 0.3 mmol, 1.0 equiv.) was dissolved in tetrahydrofuran (4 mL) and water (1 mL). Sodium hydroxide (27 mg, 0.7 mmol, 2.0 equiv.) was added under cooling, and the mixture was stirred at 25 °C for 24 h. After work up, the resulting white solid (80 mg, 87%) was used without further purification.

^{1}H NMR (500 MHz, $(CD_3)_2SO$, one drop of D_2O): δ (ppm) = 14.33 (s, 1H), 12.83 (s, 1H), 7.79–7.74 (m, 1H), 7.62–7.61 (m, 1H), 7.55–7.44 (m, 2H), 4.00 (s, 2H). ^{13}C NMR (126 MHz, $(CD_3)_2SO$): δ (ppm) = 171.1, 158.4, 155.9, 131.5, 131.4, 130.8, 130.5, 130.0, 127.2, 38.9. HR-ESI-MS: calculated for $C_{10}H_9ClN_3O_2S$ $[M+H]^+$ 270.0099 (^{35}Cl), 272.0069 (^{37}Cl), found 270.0092 (100%), 272.0060 (30%). Purity: >98%.

2-((5-(Pyridin-2-yl)-4*H*-1,2,4-triazol-3-yl)thio)acetic acid (28e)

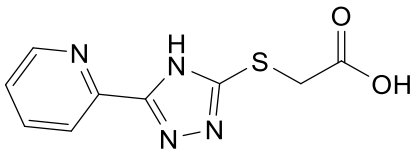

Following general procedure III, ethyl-2-bromoacetate (300 µL, 2.7 mmol, 1.2 equiv.) was added to a stirred solution of 5-(pyridin-2-yl)-1*H*-1,2,4-triazole-3-thiol (400 mg, 2.2 mmol, 1.0 equiv.) and sodium bicarbonate (180 mg, 2.2 mmol, 1.0 equiv.) in ethanol (25 mL), and the mixture was stirred at 25°C for 24 h. Full conversion was confirmed by LCMS, and the solvent was evaporated. Following general procedure IV, the remaining solid was dissolved in THF and a few drops of water. Sodium hydroxide (180 mg, 4.4 mmol, 2.0 equiv.) was added under cooling, and the mixture was stirred at 25 °C for 16 h. After work up, the resulting white solid (463 mg, 88%) was used without further purification.

^{1}H NMR (500 MHz, $(CD_3)_2SO$): δ (ppm) = 14.79 (s, 1H), 12.80 (s, 1H), 8.69 (d, *J* = 5.2 Hz, 1H), 8.01 (m, 2H), 7.77–7.24 (m, 1H), 3.99 (s, 2H). ^{13}C NMR (126 MHz, $(CD_3)_2SO$): δ (ppm) = 170.5, 163.5, 150.1, 146.2, 138.34, 127.5, 125.7, 121.8, 34.1. HR-ESI-MS: calculated for $C_9H_9N_4O_2S$ $[M+H]^+$ 237.0441, found 237.0435. Purity: 83%.

2-((5-(Pyridin-3-yl)-4*H*-1,2,4-triazol-3-yl)thio)acetic acid (28f)

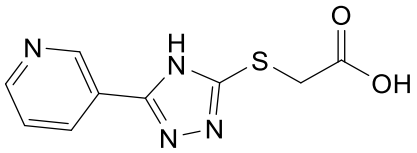

Following general procedure IV, ester **209** (300 mg, 1.1 mmol, 1.0 equiv.) was dissolved in THF (15 mL) and water (5 mL). Sodium hydroxide (90 mg, 2.3 mmol, 2.0 equiv.) was added under cooling and the mixture was stirred at 25 °C for 24 h. After work up and purification by preparative HPLC (H_2O/CH_3CN + 0.1% formic acid, gradient from 5% to 90% CH_3CN), the product (209 mg, 80%) was afforded as a white solid.

^{1}H NMR (500 MHz, $(CD_3)_2SO$, one drop of D_2O): δ (ppm) = 9.06 (d, *J* = 2.2 Hz, 1H), 8.56 (dd, *J* = 4.9, 1.7 Hz, 1H), 8.36 (formic acid, s, 1H), 8.27 (dt, *J* = 8.0, 2.2 Hz, 1H), 7.50 (dd, *J* = 8.0, 4.9 Hz, 1H), 3.76 (s, 2H). ^{13}C NMR (126 MHz, $(CD_3)_2SO$): δ (ppm) = 171.5, 168.0 (formic acid), 157.8, 156.5, 150.5, 147.0, 134.1, 126.2, 124.7, 38.5. HR-ESI-MS: calculated for $C_9H_9N_4O_2S$ $[M+H]^+$ 237.0441, found 237.0435. Purity: 99%.

Note: The acid proton is not visible in ^{1}H NMR.

2-((5-(2-Hydroxyphenyl)-4*H*-1,2,4-triazol-3-yl)thio)-*N*-(2-(*p*-tolylthio)ethyl)-acetamide (1)

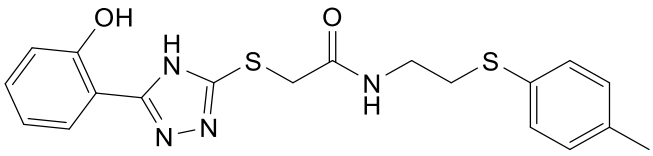

Following general procedure V, compound **20** (366 mg, 2.2 mmol, 1.1 equiv.) was added to a mixture of compound **17** (500 mg, 2.0 mmol, 1.0 equiv.), EDC*HCl (420 mg, 2.2 mmol, 1.1 equiv.), HOBt (269 mg, 2.0 mmol, 1.0 equiv.) and NMM (407.6 mg, 3.98 mmol, 2.0 equiv.) in DMF (3 mL), and stirred for 72 h. After work up and purification by flash column chromatorgraphy, the pure product (660 mg, 83%) was obtained as a white solid.

^{1}H NMR (500 MHz, $(CD_3)_2SO$): δ (ppm) = 14.15 (s, 1H), 10.95 (s, 1H), 8.41 (t, *J* = 6.0 Hz, 1H), 7.90 (dd, *J* = 7.9, 1.8 Hz, 1H), 7.33 (ddd, *J* = 8.7, 7.3, 1.8 Hz, 1H), 7.24 (d, *J* = 8.2 Hz, 2H), 7.11 (d, *J* = 8.1 Hz, 2H), 7.00 (d, *J* = 8.1 Hz, 1H), 6.98–6.92 (m, 1H), 3.87 (s, 2H), 3.24 (dt, *J* = 8.0, 6.0 Hz, 2H), 2.94 (dd, *J* = 8.0, 6.0 Hz, 2H), 2.25 (s,

3H). ^{13}C NMR (126 MHz, $(CD_3)_2SO$): δ (ppm) = 167.4, 155.7, 135.5, 131.8, 131.7, 129.7, 129.0, 127.3, 119.5, 116.7, 112.4, 38.7, 35.1, 32.0, 20.5. HR-ESI-MS $C_{19}H_{21}N_4O_2S_2$ m/z: $[M+H]^+$ calculated: 401.1106 found: 401.1095. Purity: >99%.

2-((5-(2-Hydroxyphenyl)-4*H*-1,2,4-triazol-3-yl)thio)-*N*-(2-(*o*-tolythio)ethyl)acetamide (22a)

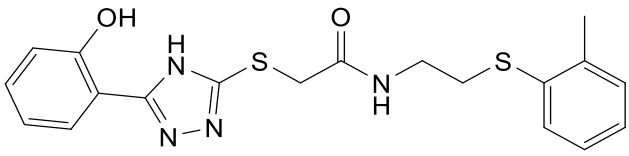

Following general procedure V, compound **21a** (18 mg, 0.11 mmol, 1.1 equiv.) was added to a mixture of compound **17** (25 mg, 0.1 mmol, 1.0 equiv.), EDC*HCl (21 mg, 0.11 mmol, 1.1 equiv.), HOBt (13 mg, 0.1 mmol, 1.0 equiv.) and NMM (20 mg, 0.2 mmol, 2.0 equiv.) in DMF (3 mL), and stirred for 36 h. After work up and purification by flash column chromatography, the pure product (27 mg, 68%) was obtained as a clear oil.

^{1}H NMR (500 MHz, $(CD_3)_2SO$): δ (ppm) = 14.14 (s, 1H). 10.95 (s, 1H), 8.46 (s, 1H), 7.90 (dd, *J* = 1.47, 7.96 Hz, 1H), 7.33 (m, 2H), 7.17 (m, 2H), 7.08 (m, 1H), 6.99 (d, *J* = 8.20 Hz, 1H), 6.95 (t, *J* = 7.52 Hz, 1H), 3.88 (s, 2H), 3.28 (q, *J* = 6.79 Hz, 2H), 2.98 (t, *J* = 6.79 Hz, 2H), 2.24 (s, 3H). ^{13}C NMR (126 MHz, $(CD_3)_2SO$): δ (ppm) = 167.4, 155.7, 136.2, 134.8, 131.7, 130.0, 127.3, 126.7, 126.6, 125.4, 119.5, 116.7,112.3, 38.5, 35.1, 30.5, 19.8. HR-ESI-MS: calculated for $C_{19}H_{21}N_4O_2S_2$ $[M+H]^+$ 401.1100, found 401.1097. Purity: 99%.

2-((5-(2-Hydroxyphenyl)-4*H*-1,2,4-triazol-3-yl)thio)-*N*-(2-(*m*-tolythio)ethyl)acetamide (22b)

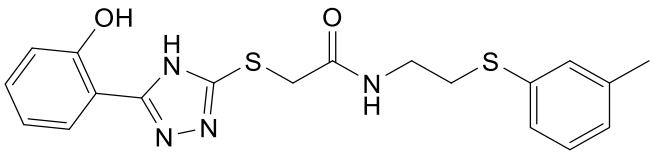

Following general procedure V, compound **21b** (18 mg, 0.11 mmol, 1.1 equiv.) was added to a mixture of compound **17** (25 mg, 0.1 mmol, 1.0 equiv.), EDC*HCl (21 mg, 0.11 mmol, 1.1 equiv.), HOBt (13 mg, 0.1 mmol, 1.0 equiv.) and NMM (20 mg, 0.2 mmol, 2.0 equiv.) in DMF (3 mL), and stirred for 36 h. After work up and purification

by flash column chromatography, the pure product (35 mg, 88%) was obtained as a clear oil.

^{1}H NMR (500 MHz, $(CD_3)_2SO$): δ (ppm) = 14.14 (s, 1H), 10.95 (s, 1H), 8.43 (t, *J* = 5.9 Hz, 1H), 7.90 (dd, *J* = 7.9, 1.8 Hz, 1H), 7.37–7.29 (m, 1H), 7.18 (t, *J* = 7.6 Hz, 1H), 7.15 (s, 1H), 7.12 (d, *J* = 7.9 Hz, 1H), 6.99 (t, *J* = 6.6 Hz, 2H), 6.95 (t, *J* = 7.6 Hz, 1H), 3.87 (s, 2H), 3.31–3.23 (m, 2H), 2.98 (dd, *J* = 8.2, 6.3 Hz, 2H), 2.26 (s, 3H). ^{13}C NMR (126 MHz, $(CD_3)_2SO$): δ (ppm) = 167.5, 155.7, 138.5, 135.3, 131.7, 129.0, 128.5, 127.4, 126.5, 125.0, 119.5, 116.7, 112.4, 38.7, 35.1, 31.1, 20.9. HR-ESI-MS: calculated for $C_{19}H_{21}N_4O_2S_2$ $[M+H]^+$ 401.1100, found 401.1096. Purity: >99%.

2-((5-(2-Hydroxyphenyl)-4*H*-1,2,4-triazol-3-yl)thio)-(2-(phenylthiol)ethyl)acetamide (22c)

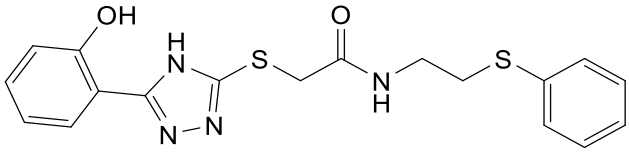

Following general procedure V, compound **21c** (17 mg, 0.11 mmol, 1.1 equiv.) was added to a mixture of compound **17** (25 mg, 0.1 mmol, 1.0 equiv.), EDC*HCl (21 mg, 0.11 mmol, 1.1 equiv.), HOBt (13 mg, 0.1 mmol, 1.0 equiv.) and NMM (20 mg, 0.2 mmol, 2.0 equiv.) in DMF (3 mL), and stirred for 72 h. After work up and purification by flash column chromatography (in contrast to the general procedure, hexane/ethyl acetate 2:3 was used), the pure product (15 mg, 39%) was obtained as a white solid.

^{1}H NMR (500 MHz, $(CD_3)_2SO$): δ (ppm) = 14.14 (s, 1H), 10.98 (s, 1H), 8.47 (t, *J* = 5.8 Hz, 1H), 7.90 (dd, *J* = 7.9, 1.8 Hz, 1H), 7.31 (m, 5H), 7.17 (t, *J* = 7.10 Hz, 1H), 7.00 (d, *J* = 8.2 Hz, 1H), 6.95 (t, *J* = 7.5 Hz, 1H), 3.87 (s, 2H), 3.27 (q, *J* = 6.9 Hz, 2H), 3.00 (t, *J* = 6.9 Hz, 2H). ^{13}C NMR (126 MHz, $(CD_3)_2SO$): δ (ppm) = 167.4, 155.7, 135.6, 131.7, 129.1, 128.0, 127.3, 125.7, 119.5, 116.7, 112.4, 38.7, 35.1, 31.2. HR-ESI-MS: calculated for $C_{18}H_{19}N_4O_2S_2$ $[M+H]^+$ 387.0944, found 387.0937. Purity: >99%.

2-((5-(2-Hydroxyphenyl)-4*H*-1,2,4-triazol-3-yl)-*N*-(2-((4-methoxyphenyl)thio)ethyl)acetamide (22d)

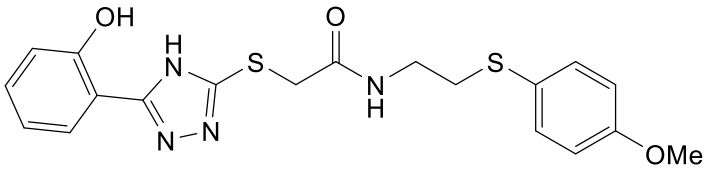

Following general procedure V, compound **21d** (22 mg, 0.11 mmol, 1.1 equiv.) was added to a mixture of compound **17** (25 mg, 0.1 mmol, 1.0 equiv.), EDC*HCl (21 mg, 0.11 mmol, 1.1 equiv.), HOBt (13 mg, 0.1 mmol, 1.0 equiv.) and NMM (20 mg, 0.2 mmol, 2.0 equiv.) in DMF (3 mL) and stirred for 36 h. After work up and purification by flash column chromatography, the pure product (16 mg, 39%) was obtained as a white solid.

^{1}H NMR (500 MHz, $(CD_3)_2SO$): δ (ppm) = 14.15 (s, 1H), 10.96 (s, 1H), 8.40 (s, 1H), 7.91 (dd, *J* = 7.9, 1.8 Hz, 1H), 7.32 (m, 3H), 7.00 (d, *J* = 8.2 Hz, 1H), 6.95 (t, *J* = 7.6 Hz, 1H), 6.88 (d, *J* = 8.7 Hz, 2H), 3.86 (s, 2H), 3.72 (s, 3H), 3.20 (q, *J* = 6.9 Hz, 2H), 2.86 (t, *J* = 6.9 Hz, 2H). ^{13}C NMR (126 MHz, $(CD_3)_2SO$): δ (ppm) = 167.8, 158.9, 156.1, 132.8, 132.1, 127.8, 125.5, 120.0, 117.2, 115.2, 112.9, 55.6, 39.9, 39.1, 35.5. HR-ESI-MS: calculated for $C_{19}H_{21}N_4O_3S_2$ $[M+H]^+$ 417.1050, found 417.1045. Purity: >99%.

N-(2-((4-Chlorophenyl)thio)ethyl)-2-((5-(2-hydroxyphenyl)-4*H*-1,2,4-triazol-3-yl)thio)acetamide (22e)

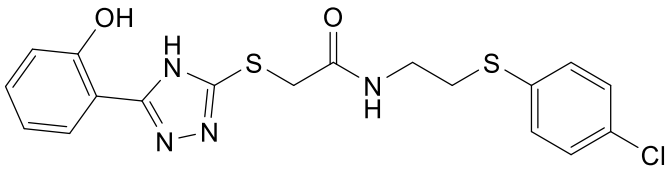

Following general procedure V, compound **21e** (20 mg, 0.11 mmol, 1.1 equiv.) was added to a mixture of compound **17** (25 mg, 0.1 mmol, 1.0 equiv.), EDC*HCl (21 mg, 0.11 mmol, 1.1 equiv.), HOBt (13 mg, 0.1 mmol, 1.0 equiv.) and NMM (20 mg, 0.2 mmol, 2.0 equiv.) in DMF (3 mL) and stirred for 72 h. After work up and purification by flash column chromatography (in contrast to the general procedure, hexane/ethyl acetate 1:1 was used), the pure product (29 mg, 69%) was obtained as a white solid.

^{1}H NMR (500 MHz, $(CD_3)_2SO$): δ (ppm) = 14.06 (s, 1H), 11.02 (s, 1H), 8.44 (t, *J* = 5.8 Hz, 1H), 7.90 (dd, *J* = 7.7, 1.8 Hz, 1H), 7.34 (m, 5H), 7.00 (d, *J* = 8.2 Hz, 1H), 6.95 (t, *J* = 7.7 Hz, 1H), 3.87 (s, 2H), 3.27 (q, *J* = 7.0 Hz, 2H), 3.01 (t, *J* = 7.0 Hz, 2H). ^{13}C NMR (126 MHz, $(CD_3)_2SO$): δ (ppm) = 167.5, 155.6, 134.8, 131.7, 130.4, 129.7, 129.0, 127.3, 119.5, 116.7, 112.4, 38.5, 35.1, 31.4. HR-ESI-MS: calculated for $C_{18}H_{18}ClN_4O_2S_2$ $[M+H]^+$ 421.0554 (^{35}Cl), 423.0525 (^{37}Cl), found 421.0549 (100%), 423.0512 (40%). Purity: 97%.

_N_-(2-((4-Fluorophenyl)thio)ethyl)-2-((5-(2-hydroxyphenyl)-4_H_-1,2,4-triazol-3-yl)thio)acetamide (22f)

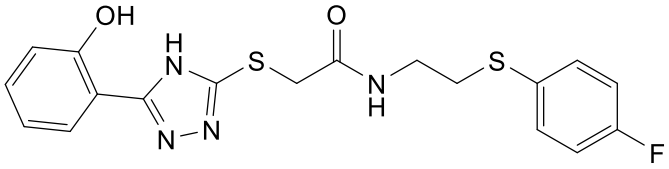

Following general procedure V, compound **21f** (19 mg, 0.11 mmol, 1.1 equiv.) was added to a mixture of compound **17** (25 mg, 0.1 mmol, 1.0 equiv.), EDC*HCl (21 mg, 0.11 mmol, 1.1 equiv.), HOBt (13 mg, 0.1 mmol, 1.0 equiv.) and NMM (20 mg, 0.2 mmol, 2.0 equiv.) in DMF (3 mL), and stirred for 72 h. After work up and purification by flash column chromatography (in contrast to the general procedure, hexane/ethyl acetate 1:1 was used), the pure product (6 mg, 15%) was obtained as a white solid.

^{1}H NMR (500 MHz, $(CD_3)_2SO$): δ (ppm) = 14.13 (s, 1H), 11.01 (s, 1H), 8.43 (t, *J* = 5.3 Hz, 1H), 7.89 (dd, *J* = 7.9, 1.8 Hz, 1H), 7.44–7.37 (m, 2H), 7.40–7.29 (m, 1H), 7.20–7.11 (m, 2H), 6.98 (d, *J* = 1.2 Hz, 1H), 6.95 (t, *J* = 7.6 Hz, 1H), 3.86 (s, 2H), 3.29–3.21 (m, 2H), 2.96 (dd, *J* = 8.1, 6.3 Hz, 2H). ^{13}C NMR (126 MHz, $(CD_3)_2SO$): δ (ppm) = 167.4, 161.9, 159.9, 155.7, 131.6, 131.2 (d, *J* = 7.8 Hz), 130.8 (d, *J* = 3.2 Hz), 127.2, 119.7, 116.7, 116.1 (d, *J* = 22.1 Hz), 38.6, 35.1, 32.4. ^{19}F NMR (470 MHz, $(CD_3)_2SO$): δ (ppm) = –116.3. HR-ESI-MS: calculated for $C_{18}H_{18}FN_4O_2S_2$ $[M+H]^+$ 405.0850, found 405.0844. Purity: 95%.

2-((5-(2-Hydroxyphenyl)-4_H_-1,2,4-triazol-3-yl)thio)-_N_-(2-((4-nitrophenyl)thio)ethyl)acetamide (22g)

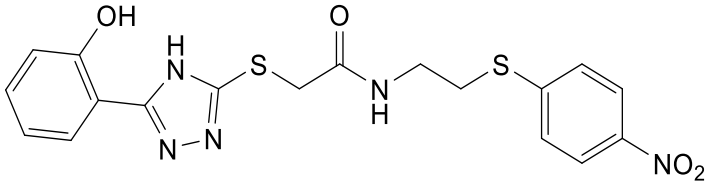

Following general procedure V, compound **21g** (22 mg, 0.11 mmol, 1.1 equiv.) was added to a mixture of compound **17** (25 mg, 0.1 mmol, 1.0 equiv.), EDC*HCl (21 mg, 0.11 mmol, 1.1 equiv.), HOBt (13 mg, 0.1 mmol, 1.0 equiv.) and NMM (20 mg, 0.2 mmol, 2.0 equiv.) in DMF (3 mL), and stirred for 72 h. After work up and purification (first flash chromatography, then preparative HPLC), the pure product (14 mg, 33%) was obtained as a white solid.

^{1}H NMR (500 MHz, $(CD_3)_2SO$): δ (ppm) = 14.13 (s, 1H), 10.97 (s, 1H), 8.54 (t, *J* = 5.8 Hz, 1H), 8.12–8.06 (m, 2H), 7.88 (dd, *J* = 7.8, 1.8 Hz, 1H), 7.53–7.46 (m, 2H), 7.32 (ddd, *J* = 8.6, 7.2, 1.8 Hz, 1H), 6.98 (d, *J* = 8.2 Hz, 1H), 6.94 (t, *J* = 7.6 Hz, 1H), 3.89 (s, 2H), 3.40–3.32 (m, 2H), 3.17 (t, *J* = 6.2 Hz, 2H). ^{13}C NMR (126 MHz, $(CD_3)_2SO$): δ (ppm) = 167.8, 155.7, 147.1, 144.5, 131.7, 127.4, 126.2, 124.0, 119.6, 116.7, 112.4, 38.1, 35.1, 30.1. HR-ESI-MS: calculated for $C_{18}H_{18}N_5O_4S_2$ $[M+H]^+$ 432.0795, found 432.0790. Purity: >99%.

2-((5-(2-Hydroxyphenyl)-4*H*-1,2,4-triazol-3-yl)thio)-*N*-(2-((4-(trifluoromethyl)phenyl)thio)ethyl)acetamide (22h)

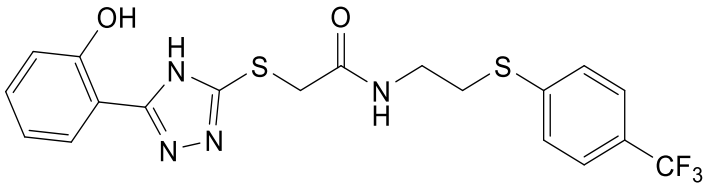

Following general procedure V, compound **21h** (24 mg, 0.11 mmol, 1.1 equiv.) was added to a mixture of compound **17** (25 mg, 0.1 mmol, 1.0 equiv.), EDC*HCl (21 mg, 0.11 mmol, 1.1 equiv.), HOBt (13 mg, 0.1 mmol, 1.0 equiv.) and NMM (20 mg, 0.2 mmol, 2.0 equiv.) in DMF (3 mL), and stirred for 72 h. After work up and purification by preparative HPLC, the pure product (7 mg, 15%) was obtained as a white solid.

^{1}H NMR (500 MHz, $(CD_3)_2SO$): δ (ppm) = 13.81 (s, 1H), 11.14 (s, 1H), 8.50 (t, *J* = 6.0 Hz, 1H), 7.89 (dd, *J* = 7.9, 1.7 Hz, 1H), 7.61 (d, *J* = 8.3 Hz, 2H), 7.49 (d, *J* = 8.4 Hz, 2H), 7.32 (ddd, *J* = 8.4, 7.1, 1.7 Hz, 1H), 6.99 (dd, *J* = 8.3, 1.0 Hz, 1H), 6.94 (t, *J* = 7.9 Hz, 1H), 3.88 (s, 2H), 3.32 (m, 2H), 3.11 (t, *J* = 6.0 Hz, 2H). ^{13}C NMR (126 MHz, $(CD_3)_2SO$): δ (ppm) = 168.1, 156.1, 142.7, 132.0, 126.8 (q, *J* = 237.0 Hz), 126.2, 126.1 (q, *J* = 3.9 Hz), 125.8 (q, *J* = 93.2 Hz), 123.7, 119.9, 117.1, 112.9, 38.7, 35.5, 30.6. ^{19}F NMR (470 MHz, $(CD_3)_2SO$): δ (ppm) = –60.8. HR-ESI-MS: calculated for $C_{19}H_{16}F_3N_4O_2S_2$ $[M-H]^-$ 453.0672, found 453.0675. Purity: >99%.

***N*-(2-((4-Ethylphenyl)thio)ethyl)-2-((5-(2-hydroxyphenyl)-4*H*-1,2,4-triazol-3-yl)thio)acetamide (22i)**

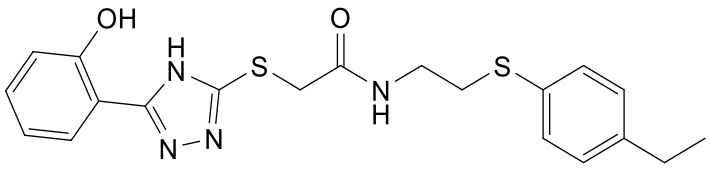

Following general procedure V, compound **21i** (20 mg, 0.11 mmol, 1.1 equiv.) was added to a mixture of compound **17** (25 mg, 0.1 mmol, 1.0 equiv.), EDC*HCl (21 mg, 0.11 mmol, 1.1 equiv.), HOBt (13 mg, 0.1 mmol, 1.0 equiv.) and NMM (20 mg, 0.2 mmol, 2.0 equiv.) in DMF (3 mL), and stirred for 72 h. After work up and purification by preparative HPLC, the pure product (22 mg, 52%) was obtained as a white solid.

^{1}H NMR (500 MHz, $(CD_3)_2SO$): δ (ppm) = 13.71 (s, 1H), 11.19 (s, 1H), 8.41 (t, *J* = 5.7 Hz, 1H), 7.90 (dd, *J* = 7.8, 1.7 Hz, 1H), 7.33 (ddd, *J* = 8.5, 7.2, 1.7 Hz, 1H), 7.28–7.23 (m, 2H), 7.17–7.11 (m, 2H), 6.99 (d, *J* = 8.5 Hz, 1H), 6.95 (t, *J* = 7.8 Hz, 1H), 3.86 (s, 2H), 3.30–3.21 (m, 2H), 2.95 (t, *J* = 7.2 Hz, 2H), 2.55 (q, *J* = 7.6 Hz, 2H), 1.14 (t, *J* = 7.6 Hz, 3H). ^{13}C NMR (126 MHz, $(CD_3)_2SO$): δ (ppm) = 167.4, 155.7, 141.8, 132.0, 131.6, 128.9, 128.6, 127.3, 119.5, 116.7, 112.5, 38.8, 35.1, 31.9, 27.6, 15.5. HR-ESI-MS: calculated for $C_{20}H_{23}N_4O_2S_2$ $[M+H]^+$ 415.1257, found 415.1248. Purity: >99%.

2-((5-(2-Chlorophenyl)-4*H*-1,2,4-triazol-3-yl)thio)-*N*-(2-((4-morpholinophenyl)thio)ethyl)acetamide (22j)

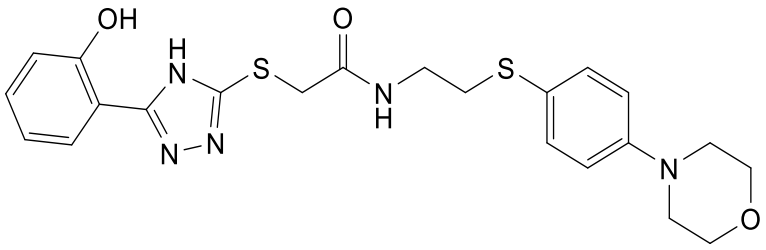

Following general procedure V, **21j** (11 mg, 0.05 mmol, 1.1 equiv.) was added to a mixture of compound **17** (11 mg, 0.04 mmol, 1.0 equiv.), EDC*HCl (9 mg, 0.5 mmol, 1.1 equiv.), HOBt (6 mg, 0.04 mmol, 1.0 equiv.) and NMM (9 mg, 0.08 mmol, 2.0 equiv.) in DMF (1 mL), and stirred for 72 h. After work up and purification by preparative HPLC, the pure product (4 mg, 20%) was obtained as a white solid.

^{1}H NMR (500 MHz, $(CD_3)_2SO$): δ (ppm) = 13.93 (s, 1H), 11.08 (s, 1H), 8.35 (t, *J* = 5.8 Hz, 1H), 7.90 (d, *J* = 7.7 Hz, 1H), 7.33 (tt, *J* = 8.6, 1.6 Hz, 1H), 7.25 (d, *J* = 8.9 Hz, 2H), 7.00 (d, *J* = 8.6 Hz, 1H), 6.95 (t, *J* = 7.7 Hz, 1H), 6.87 (d, *J* = 8.9 Hz, 2H), 3.85 (s, 2H), 3.73–3.68 (m, 4H), 3.19 (q, *J* = 6.2 Hz, 2H), 3.10–3.04 (m, 4H), 2.83 (t, *J* = 7.1 Hz, 2H). ^{13}C NMR (126 MHz, $(CD_3)_2SO$): δ (ppm) = 167.3, 155.7, 150.1, 132.3, 131.6, 127.2, 122.9, 119.5, 116.7, 115.6, 112.4, 66.0, 48.0, 38.8, 35.1, 33.7. HR-ESI-MS: calculated for $C_{22}H_{24}N_5O_3S_2$ $[M-H]^-$ 470.1321, found 470.1323. Purity: >99%.

_N_-(2-((2-Amino-4-chlorophenyl)thio)ethyl)-2-((5-(2-hydroxyphenyl)-4_H_-1,2,4-triazol-3-yl)thio)acetamide (22k)

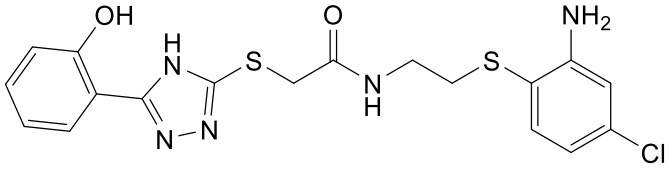

Following general procedure V, compound **21k** (22 mg, 0.11 mmol, 1.1 equiv.) was added to a mixture of compound **17** (25 mg, 0.1 mmol, 1.0 equiv.), EDC*HCl (21 mg, 0.11 mmol, 1.1 equiv.), HOBt (13 mg, 0.1 mmol, 1.0 equiv.) and NMM (20 mg, 0.2 mmol, 2.0 equiv.) in DMF (3 mL), and stirred for 72 h. After work up and purification (two flash purifications were needed), the pure product (10 mg, 23%) was obtained as a white solid.

^{1}H NMR (500 MHz, $(CD_3)_2SO$): δ (ppm) = 14.13 (s, 1H), 10.97 (s, 1H), 8.37 (s, 1H), 7.89 (dd, *J* = 7.8, 1.7 Hz, 1H), 7.33–7.22 (m, 1H), 7.23 (d, *J* = 8.2 Hz, 1H), 6.99 (d, *J* = 8.2 Hz, 1H), 6.98–6.89 (m, 1H), 6.73 (d, *J* = 2.3 Hz, 1H), 6.49 (dd, *J* = 8.2, 2.3 Hz, 1H), 5.66 (s, 2H), 3.86 (s, 2H), 3.16 (q, *J* = 6.2 Hz, 2H), 2.72 (t, *J* = 6.2 Hz, 2H). ^{13}C NMR (126 MHz, $(CD_3)_2SO$): δ (ppm) = 167.3, 155.6, 150.9, 136.8, 133.9, 131.7, 127.4, 119.5, 116.7, 115.8, 113.8, 113.3, 112.4, 38.8, 35.2, 33.0. HR-ESI-MS: calculated for $C_{18}H_{19}ClN_5O_2S_2$ $[M+H]^+$ 436.0663 (^{35}Cl), 438.0634 (^{37}Cl), found 436.0658 (100%), 438.0623 (40%). Purity: 97%.

_N_-(2-((3,5-Bis(trifluoromethyl)phenyl)thio)ethyl)-2-((5-(2-hydroxyphenyl)-4_H_-1,2,4-triazol-3-yl)thio)acetamide (22l)

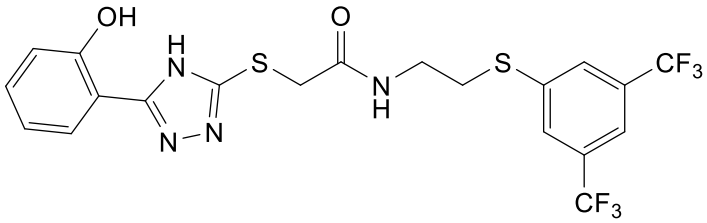

Following general procedure V, compound **21l** (32 mg, 0.11 mmol, 1.1 equiv.) was added to a mixture of compound **17** (25 mg, 0.1 mmol, 1.0 equiv.), EDC*HCl (21 mg, 0.11 mmol, 1.1 equiv.), HOBt (13 mg, 0.1 mmol, 1.0 equiv.) and NMM (20 mg, 0.2 mmol, 2.0 equiv.) in DMF (3 mL), and stirred for 72 h. After work up and purification (first flash chromatography, then preparative HPLC), the pure product (20 mg, 38%) was obtained as a white solid.

^{1}H NMR (500 MHz, $(CD_3)_2SO$): δ (ppm) = 14.11 (s, 1H), 10.98 (s, 1H), 8.50 (s, 1H), 7.96 (s, 2H), 7.89 (dd, *J* = 7.8, 1.7 Hz, 1H), 7.83 (s, 1H), 7.32 (t, *J* = 7.8 Hz, 1H), 6.98 (d, *J* = 8.1 Hz, 1H), 6.93 (t, *J* = 7.6 Hz, 1H), 3.86 (s, 2H), 3.86 (m, 2H), 3.21 (t, *J* = 6.1 Hz, 2H). ^{13}C NMR (126 MHz, $(CD_3)_2SO$): δ (ppm) = 167.7, 157.6, 155.6, 153.6, 140.9, 131.8, 130.9 (q, *J* = 33.1 Hz), 127.4, 127.3 (d, *J* = 4.1 Hz), 123.1 (q, *J* = 273.0 Hz), 119.5, 118.7 (q, *J* = 3.9 Hz), 116.7, 112.0, 38.1, 35.0, 30.6. ^{19}F NMR (470 MHz, $(CD_3)_2SO$): δ (ppm) = –61.4. HR-ESI-MS: calculated for $C_{20}H_{17}F_6N_4O_2S_2$ $[M+H]^+$ 523.0692, found 523.0688. Purity: 95%.

2-((5-(2-Methoxyphenyl)-4*H*-1,2,4-triazol-3-yl)thio)-*N*-(2-(*p*-tolylthio)ethyl)acetamide (29a)

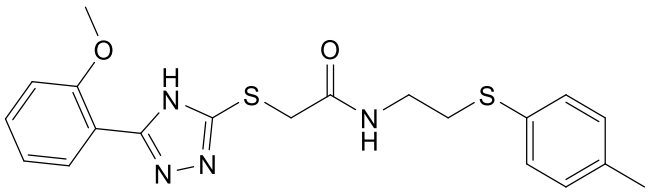

Following general procedure V, compound **20** (17 mg, 0.11 mmol, 1.1 equiv.) was added to a mixture of compound **28a** (25 mg, 0.1 mmol, 1.0 equiv.), EDC*HCl (21 mg, 0.11 mmol, 1.1 equiv.), HOBt (13 mg, 0.1 mmol, 1.0 equiv.) and NMM (20 mg, 0.2 mmol, 2.0 equiv.) in DMF (3 mL), and stirred for 24 h. After work up and purification by preparative HPLC, the pure product (16 mg, 40%) was obtained as a white solid.

^{1}H NMR (500 MHz, $(CD_3)_2SO$): δ (ppm) = 13.73 (s, 1H), 8.35 (t, *J* = 6.0 Hz, 1H), 8.03 (d, *J* = 7.9 Hz, 1H), 7.48 (ddd, *J* = 8.7, 7.4, 1.9 Hz, 1H), 7.23 (d, *J* = 8.3 Hz, 2H), 7.19 (d, *J* = 8.3 Hz, 1H), 7.11 (d, *J* = 8.2 Hz, 2H), 7.07 (t, *J* = 7.4 Hz, 1H), 3.94 (s, 3H), 3.84 (s, 2H), 3.23 (q, *J* = 6.0 Hz, 2H), 2.93 (t, *J* = 6.0 Hz, 2H), 2.25 (s, 3H). ^{13}C NMR (126 MHz, $(CD_3)_2SO$): δ (ppm) = 167.6, 158.0, 156.5, 152.4, 135.5, 131.8, 131.7, 129.7, 129.1, 129.0, 120.8, 115.0, 111.8, 55.6, 38.7, 35.0, 32.0, 20.5. HR-ESI-MS: calculated for $C_{20}H_{23}N_4O_2S_2$ $[M+H]^+$ 415.1257, found 415.1247. Purity: >99%.

2-((5-(2-Chlorophenyl)-4*H*-1,2,4-triazol-3-yl)thio)-*N*-(2-(*p*-tolylthio)ethyl)acetamide (29d)

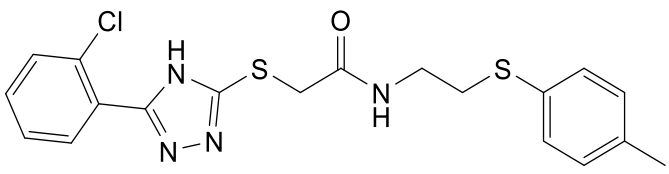

Following general procedure V, compound **20** (17 mg, 0.11 mmol, 1.1 equiv.) was added to a mixture of compound **28d** (25 mg, 0.1 mmol, 1.0 equiv.), EDC*HCl (21 mg, 0.11 mmol, 1.1 equiv.), HOBt (13 mg, 0.1 mmol, 1.0 equiv.) and NMM (20 mg, 0.2 mmol, 2.0 equiv.) in DMF (3 mL), and stirred for 24 h. After work up and purification by preparative HPLC, the pure product (17 mg, 40%) was obtained as a white solid.

^{1}H NMR (500 MHz, $(CD_3)_2SO$): δ (ppm) = 14.28 (s, 1H), 8.39 (t, *J* = 5.8 Hz, 1H), 7.77 (d, *J* = 7.6 Hz, 1H), 7.61 (d, *J* = 7.9 Hz, 1H), 7.51 (t, *J* = 7.6 Hz, 1H), 7.46 (t, *J* = 7.6 Hz, 1H), 7.24 (d, *J* = 8.2 Hz, 2H), 7.12 (d, *J* = 8.2 Hz, 2H), 3.87 (s, 2H), 3.27–3.20 (m, 2H), 2.93 (t, *J* = 7.2 Hz, 2H), 2.26 (s, 3H). ^{13}C NMR (126 MHz, $(CD_3)_2SO$): δ (ppm) = 167.3, 135.5, 131.7, 131.5, 131.4, 131.4, 130.4, 129.7, 129.0, 127.4, 116.6, 38.7, 35.3, 32.0, 20.5. HR-ESI-MS: calculated for $C_{19}H_{20}N_4OS_2$ $[M+H]^+$ 419.0762 (^{35}Cl), 421.0732 (^{37}Cl), found 419.0751 (100%), 421.0716 (40%). Purity: >98%.

2-((5-(Pyridin-2-yl)-4*H*-1,2,4-triazol-3-yl)thio)-*N*-(2-(*p*-tolylthio)ethyl)acetamide (29e)

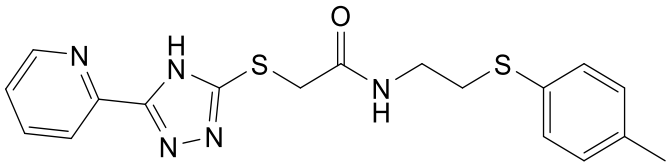

Following general procedure V, compound **20** (19 mg, 0.11 mmol, 1.1 equiv.) was added to a mixture of compound **28e** (25 mg, 0.1 mmol, 1.0 equiv.), EDC*HCl (21 mg, 0.11 mmol, 1.1 equiv.), HOBt (13 mg, 0.1 mmol, 1.0 equiv.) and NMM (20 mg, 0.2 mmol, 2.0 equiv.) in DMF (3 mL), and stirred for 24 h. After work up and purification by preparative HPLC, the pure product (18 mg, 46%) was obtained as a white solid.

^{1}H NMR (500 MHz, $(CD_3)_2SO$): δ (ppm) = 14.74 (s, 1H), 8.69 (d, *J* = 4.7 Hz, 1H), 8.37 (t, *J* = 5.7 Hz, 1H), 8.07–8.01 (m, 1H), 7.98 (td, *J* = 7.6, 1.6 Hz, 1H), 7.52 (ddd, *J* = 7.6, 4.7, 1.6 Hz, 1H), 7.24 (d, *J* = 8.2 Hz, 2H), 7.11 (d, *J* = 8.2 Hz, 2H), 3.86 (s, 2H), 3.27–3.20 (m, 2H), 2.94 (t, *J* = 6.3 Hz, 2H), 2.25 (s, 3H). ^{13}C NMR (126 MHz, $(CD_3)_2SO$): δ (ppm) = 167.5, 149.7, 145.9, 137.8, 135.5, 131.7, 129.7, 129.0, 125.2, 121.4, 38.7, 35.1, 32.0, 20.5. HR-ESI-MS: calculated for $C_{18}H_{20}N_5OS_2$ $[M+H]^+$ 386.1104, found 386.1093. Purity: >99%.

2-((5-(Pyridin-3-yl)-4*H*-1,2,4-triazol-3-yl)thio)-*N*-(2-(*p*-tolylthio)ethyl)acetamide (29f)

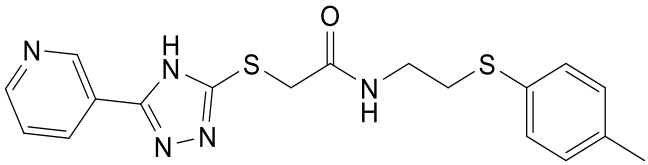

Following general procedure V, compound **20** (20 mg, 0.11 mmol, 1.1 equiv.) was added to a mixture of compound **28f** (25 mg, 0.1 mmol, 1.0 equiv.), EDC*HCl (21 mg, 0.11 mmol, 1.1 equiv.), HOBt (13 mg, 0.1 mmol, 1.0 equiv.) and NMM (20 mg, 0.2 mmol, 2.0 equiv.) in DMF (3 mL), and stirred for 24 h. After work up and purification by preparative HPLC, the pure product (22 mg, 57%) was obtained as a white solid.

^{1}H NMR (500 MHz, $(CD_3)_2SO$): δ (ppm) = 14.48 (s, 1H), 9.14 (d, *J* = 2.7 Hz, 1H), 8.65 (dd, *J* = 4.8, 1.9 Hz, 1H), 8.41 (t, *J* = 5.9 Hz, 1H), 8.28 (dt, *J* = 7.9, 1.9 Hz, 1H), 7.53 (dd, *J* = 7.9, 4.8 Hz, 1H), 7.23 (d, *J* = 8.2 Hz, 2H), 7.11 (d, *J* = 8.2 Hz, 2H), 3.90 (s, 2H), 3.24 (q, *J* = 7.9 Hz, 2H), 2.93 (t, *J* = 7.9 Hz, 2H), 2.25 (s, 3H). ^{13}C NMR (126 MHz, $(CD_3)_2SO$): δ (ppm) = 167.3, 150.6, 146.9, 135.5, 133.3, 131.6, 129.7, 129.0, 126.7, 124.0, 38.7, 35.4, 32.0, 20.5. HR-ESI-MS: calculated for $C_{18}H_{20}N_5OS_2$ $[M+H]^+$ 386.1104, found 386.1094. Purity: 98%.

2-Chloro-*N*-(2-(*p*-tolylthio)ethyl)acetamide (31)

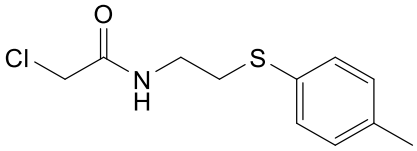

Following general procedure V, compound **20** (285 mg, 3.0 mmol, 1.1 equiv.) was added to a mixture of compound chloroacetic acid (257 mg, 2.7 mmol, 1.0 equiv.), EDC*HCl (572 mg, 3.0 mmol, 1.1 equiv.), HOBt (368 mg, 2.7 mmol, 1.0 equiv.) and NMM (549 mg, 5.4 mmol, 2.0 equiv.) in DMF (27 mL), and stirred for 24 h. After work up and purification by flash column chromatography (dichloromethane), the pure product (148 mg, 29%) was obtained as an off-white solid.

^{1}H NMR (500 MHz, $(CD_3)_2SO$): δ (ppm) = 8.41 (t, *J* = 5.7 Hz, 1H), 7.31–7.25 (m, 2H), 7.18–7.11 (m, 2H), 4.05 (s, 2H), 3.26 (dt, *J* = 7.8, 6.1 Hz, 2H), 2.98 (dd, *J* = 7.8, 6.1 Hz, 2H), 2.27 (s, 3H). ^{13}C NMR (126 MHz, $(CD_3)_2SO$): δ (ppm) = 165.1, 134.6, 130.7, 128.8, 128.0, 41.6, 37.7, 30.9, 19.5. HR-ESI-MS: calculated for $C_{11}H_{15}ClNOS$ $[M+H]^+$

244.0557 (^{35}Cl), 246.0528 (^{37}Cl), found 244.0548 (100%), 246.0517 (40%). Purity: 99%.

2-((5-(4-Methoxyphenyl)-4*H*-1,2,4-triazol-3-yl)thio)-*N*-(2-(*p*-tolylthio)ethyl)acetamide (29b)

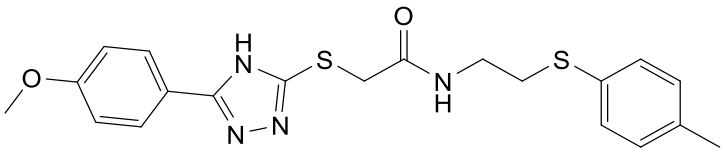

Following general procedure VI, compound **31** (50 mg, 0.21 mmol, 1.2 equiv.) and compound **27b** (35 mg, 0.17 mmol, 1.0 equiv.) were dissolved in ethanol (1.7 mL), potassium hydroxide (10 mg, 0.17 mmol, 1.0 equiv.) was added, and the reaction stirred for 24 h. After work up and purification the product (17 mg, 24%) was afforded as a white solid.

^{1}H NMR (500 MHz, $(CD_3)_2SO$): δ (ppm) = 14.22 (s, 1H), 8.37 (s, 1H), 7.89 (d, *J* = 8.7 Hz, 2H), 7.24 (d, *J* = 8.2 Hz, 2H), 7.11 (d, *J* = 8.2 Hz, 2H), 7.06 (d, *J* = 8.7 Hz, 2H), 3.84 (s, 2H), 3.81 (s, 3H), 3.24 (q, *J* = 7.1 Hz, 2H), 2.93 (t, *J* = 7.1 Hz, 2H), 2.25 (s, 3H). ^{13}C NMR (126 MHz, $(CD_3)_2SO$): δ (ppm) = 167.5, 160.8, 155.3, 135.5, 131.7, 129.7, 129.0, 127.6, 114.4, 55.3, 38.7, 35.1, 32.0, 20.5. HR-ESI-MS: calculated for $C_{20}H_{23}N_4O_2S_2$ $[M+H]^+$ 415.1257, found 415.1246. Purity: 99%.

2-((5-(2-Nitrophenyl)-4*H*-1,2,4-triazol-3-yl)thio)-*N*-(2-(*p*-tolylthio)ethyl)acetamide (29c)

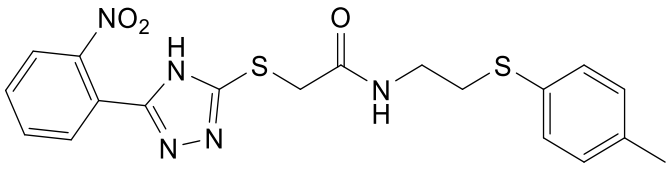

Following general procedure VI, compound **31** (40 mg, 0.16 mmol, 1.0 equiv.) and compound **27c** (73 mg, 0.32 mmol, 2.0 equiv.) were dissolved in ethanol (1.6 mL), aqueous, saturated sodium bicarbonate solution (1 mL) was added, and the reaction stirred for 24 h. After work up and purification the product (17 mg, 24%) was afforded as a white solid.

^{1}H NMR (500 MHz, $(CD_3)_2SO$): δ (ppm) = 14.41 (s, 1H), 8.37 (s, 1H), 7.92 (s, 2H), 7.81–7.51 (m, 2H), 7.24 (d, *J* = 8.1 Hz, 2H), 7.12 (d, *J* = 8.1 Hz, 2H), 3.87 (s, 2H), 3.24 (m, 2H), 2.97–2.91 (m, 2H), 2.26 (s, 3H). ^{13}C NMR (126 MHz, $(CD_3)_2SO$): δ (ppm) =

166.9, 148.6, 146.9, 135.5, 132.5, 131.7, 130.2, 129.7, 129.1, 129.0, 123.6, 38.7, 35.5, 32.0, 20.5. HR-ESI-MS: calculated for $C_{19}H_{18}N_5O_3S_2$ [*M*-H]$^-$ 428.0851, found 428.0861. Purity: >99%.

2-((5-(Pyridin-4-yl)-4*H*-1,2,4-triazol-3-yl)thio)-*N*-(2-(*p*-tolylthio)ethyl)acetamide (29g)

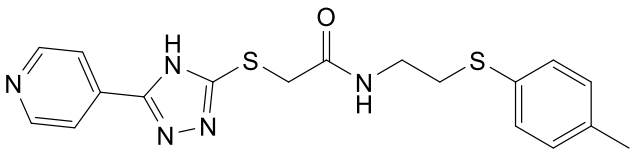

Following general procedure VI, compound **31** (73 mg, 0.3 mmol, 1.2 equiv.) and compound **27g** (44 mg, 0.25 mmol, 1.0 equiv.) were dissolved in ethanol (1.6 mL), sodium bicarbonate (21 mg, 0.25 mmol, 1.0 equiv.) was added, and the reaction stirred for 24 h. After work up and purification the product (51 mg, 53%) was afforded as a white solid.

^{1}H NMR (500 MHz, $(CD_3)_2SO$): δ (ppm) = 14.60 (s, 1H), 8.69 (dd, *J* = 4.4, 1.8 Hz, 2H), 8.45 (t, *J* = 5.7 Hz, 1H), 7.88 (dd, *J* = 4.4, 1.8 Hz, 2H), 7.23 (d, *J* = 8.2 Hz, 2H), 7.11 (d, *J* = 8.2 Hz, 2H), 3.92 (s, 2H), 3.23 (m, 2H), 2.93 (t, *J* = 7.1 Hz, 2H), 2.25 (s, 3H). ^{13}C NMR (126 MHz, $(CD_3)_2SO$): δ (ppm) = 167.2, 150.6, 136.9, 135.6, 131.7, 129.8, 129.0, 120.0, 38.7, 35.5, 32.0, 20.6. HR-ESI-MS: calculated for $C_{18}H_{18}N_5OS_2$ [*M*-H]$^-$ 384.0953, found 384.0962. Purity: 95%.

2-((5-(2-Hydroxyphenyl)-4*H*-1,2,4-triazol-3-yl)thio)-*N*-(2-(*p*-tolylamino)ethyl)acetamide (38a)

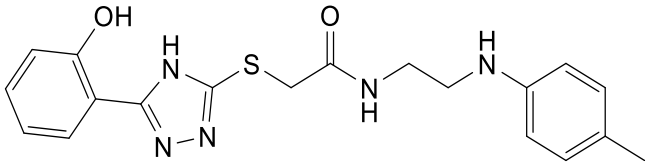

Following general procedure V, compound **37a** (16.5 mg, 0.11 mmol, 1.1 equiv.) was added to a mixture of compound **17** (25 mg, 0.1 mmol, 1.0 equiv.), EDC*HCl (21 mg, 0.11 mmol, 1.1 equiv.), HOBt (13 mg, 0.1 mmol, 1.0 equiv.) and NMM (20 mg, 0.2 mmol, 2.0 equiv.) in DMF (3 mL), and stirred for 72 h. After work up and purification by preparative HPLC (H_2O/MeCN + 0.1% formic acid, gradient from 5% to 90% MeCN), the pure product (8 mg, 20%) was obtained as a white solid.

^{1}H NMR (500 MHz, $(CD_3)_2SO$): δ (ppm) = 11.61 (s, 1H), 8.31 (t, *J* = 5.8 Hz, 1H), 8.14 (s, 0.7H, formic acid), 7.90 (dd, *J* = 7.8, 1.8 Hz, 1H), 7.33 (ddd, *J* = 8.5, 7.2, 1.8 Hz, 2H), 7.00 (d, *J* = 8.5 Hz, 1H), 6.95 (t, J = 7.5 Hz, 1H), 6.86 (d, *J* = 8.4 Hz, 2H), 6.45 (d, *J* = 8.4 Hz, 2H), 3.89 (s, 2H), 3.24 (q, *J* = 6.9 Hz, 2H), 3.03 (t, *J* = 6.9 Hz, 2H), 2.12 (s, 3H). ^{13}C NMR (126 MHz, $(CD_3)_2SO$): δ (ppm) = 167.5, 163.1 (formic acid), 155.7, 146.3, 131.7, 129.4, 127.3, 124.1, 119.5, 116.7, 112.4, 112.2, 42.6, 38.6, 35.3, 20.1. HR-ESI-MS: calculated for $C_{19}H_{22}N_5O_2S$ $[M+H]^+$ 384.1489, found 384.1481. Purity: >99%.

2-((5-(2-Hydroxyphenyl)-4*H*-1,2,4-triazol-3-yl)thio)-*N*-(*p*-tolyl)acetamide (38b)

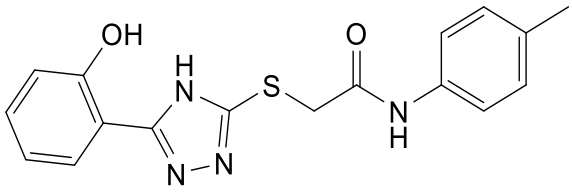

Following general procedure V, *p*-toluidine (12 mg, 0.11 mmol, 1.1 equiv.) was added to a mixture of compound **17** (25 mg, 0.1 mmol, 1.0 equiv.), EDC*HCl (21 mg, 0.11 mmol, 1.1 equiv.), HOBt (13 mg, 0.1 mmol, 1.0 equiv.) and NMM (20 mg, 0.2 mmol, 2.0 equiv.) in DMF (1 mL), and stirred for 72 h. After work up and purification by preparative HPLC, the pure product (4 mg, 10%) was obtained as a white solid.

^{1}H NMR (500 MHz, $(CD_3)_2SO$): δ (ppm) = 14.11 (s, 1H), 10.96 (s, 1H), 10.21 (s, 1H), 7.90 (dd, *J* = 7.9, 1.8 Hz, 1H), 7.46 (d, *J* = 8.5 Hz, 2H), 7.38–7.29 (m, 1H), 7.11 (d, *J* = 8.5 Hz, 2H), 6.99 (d, *J* = 8.1 Hz, 1H), 6.94 (td, *J* = 7.6, 1.3 Hz, 1H), 4.10 (s, 2H), 2.24 (s, 3H). ^{13}C NMR (126 MHz, $(CD_3)_2SO$): δ (ppm) = 165.9, 155.6, 136.4, 132.4, 131.7, 129.1, 127.5, 119.5, 119.1, 116.7, 111.3, 36.3, 20.4. HR-ESI-MS: calculated for $C_{17}H_{15}N_4O_2S$ $[M-H]^-$ 339.0916, found 339.0925. Purity: >99%.

2-((5-(2-Hydroxyphenyl)-4*H*-1,2,4-triazol-3-yl)thio)-*N*-methylacetamide (38c)

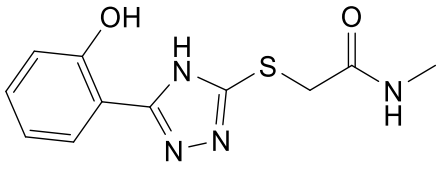

Following general procedure V, methylamine HCl (15 mg, 0.22 mmol, 1.1 equiv.) was added to a mixture of compound **17** (50 mg, 0.2 mmol, 1.0 equiv.), EDC*HCl (42 mg, 0.22 mmol, 1.1 equiv.), HOBt (27 mg, 0.2 mmol, 1.0 equiv.) and NMM (40 mg,

0.4 mmol, 2.0 equiv.) in DMF (1 mL), and stirred for 72 h. After work up and purification (first flash chromatography, then preparative HPLC), the pure product (16 mg, 31%) was obtained as a white solid.

^{1}H NMR (500 MHz, $(CD_3)_2SO$): δ (ppm) = 14.11 (s, 1H), 10.99 (s, 1H), 8.20–8.06 (m, 1H), 7.89 (dd, *J* = 7.9, 1.8 Hz, 1H), 7.33 (ddd, *J* = 8.5, 7.2, 1.8 Hz, 1H), 7.00 (dd, *J* = 8.3, 1.1 Hz, 1H), 6.99–6.92 (m, 1H), 3.86 (s, 2H), 2.61 (d, *J* = 4.6 Hz, 3H). ^{13}C NMR (126 MHz, $(CD_3)_2SO$): δ (ppm) = 167.6, 155.7, 131.7, 127.3, 119.51, 116.7, 112.4, 35.1, 26.0. HR-ESI-MS: calculated for $C_{11}H_{13}N_4O_2S$ $[M+H]^+$ 265.0754, found 265.0749. Purity: >99%.

tert-Butyl (2-(2-((5-(2-hydroxyphenyl)-4*H*-1,2,4-triazol-3-yl)thio)acetamido)ethyl) carbamate (38d)

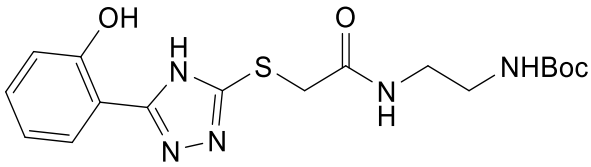

Following general procedure V, *N*-boc-ethylenediamine (35 mg, 0.22 mmol, 1.1 equiv.) was added to a mixture of compound **17** (50 mg, 0.2 mmol, 1.0 equiv.), EDC*HCl (42 mg, 0.22 mmol, 1.1 equiv.), HOBt (26 mg, 0.2 mmol, 1.0 equiv.) and NMM (40 mg, 0.4 mmol, 2.0 equiv.) in DMF (1 mL), and stirred for 72 h. After work up and purification by preparative HPLC, the pure product (27 mg, 31%) was obtained as a white solid.

^{1}H NMR (500 MHz, $(CD_3)_2SO$): δ (ppm) = 13.40 (s, 1H), 11.65 (s, 1H), 8.25 (t, *J* = 5.6 Hz, 1H), 7.89 (dd, *J* = 7.9, 1.8 Hz, 1H), 7.36–7.29 (m, 1H), 6.99 (dd, *J* = 8.3, 1.2 Hz, 1H), 6.95 (td, *J* = 7.6, 1.2 Hz, 1H), 6.79 (t, *J* = 5.8 Hz, 1H), 3.87 (s, 2H), 3.10 (q, *J* = 6.4 Hz, 2H), 2.98 (q, *J* = 6.4 Hz, 2H), 1.36 (s, 9H). ^{13}C NMR (126 MHz, $(CD_3)_2SO$): δ (ppm) = 167.4, 155.7, 155.6, 131.5, 127.2, 119.4, 116.7, 112.5, 77.7, 48.6, 39.9, 35.3, 28.2. HR-ESI-MS: calculated for $C_{17}H_{22}N_5O_4S$ $[M-H]^-$ 392.1392, found 392.1404. Purity: >99%.

_N_-(2-Aminoethyl)-2-((5-(2-hydroxyphenyl)-4*H*-1,2,4-triazol-3-yl)thio)acetamide (38e)

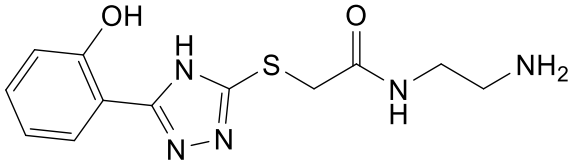

Compound **38d** (90 mg, 0.23 mmol, 1.0 equiv.) was dissolved in dry dichloromethane (2 mL) and cooled to 0 °C.[211] Hydrochloric acid in dioxane (4 M, 0.6 mL) was added and the reaction was stirred at 25 °C for 16 h. The solvents were removed under reduced pressure and purification (preparative HPLC H_2O/MeCN + 0.1% formic acid, gradient from 5% to 90% MeCN) afforded the product (46 mg, 69%) as a white solid.

^{1}H NMR (500 MHz, $(CD_3)_2SO$): δ (ppm) = 8.53 (t, *J* = 5.8 Hz, 1H), 8.25 (s, 1H), 7.88 (dd, *J* = 7.8, 1.8 Hz, 1H), 7.27–7.21 (m, 1H), 6.94 (d, *J* = 8.2 Hz, 1H), 6.93–6.86 (m, 1H), 3.77 (s, 2H), 3.34 (q, *J* = 6.0 Hz, 2H), 2.88 (t, *J* = 6.0 Hz, 2H). ^{13}C NMR (126 MHz, $(CD_3)_2SO$): δ (ppm) = 168.9, 164.4, 157.1, 155.9, 155.5, 130.5, 126.8, 116.5, 114.2, 38.8, 36.9, 35.8. HR-ESI-MS: calculated for $C_{12}H_{14}N_5O_2S$ [*M*-H]$^-$ 292.0868, found 292.0877. Purity: >99%.

2-Azidophenol (33)

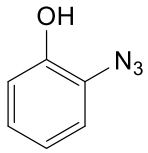

Compound **33** was synthesized following a literature procedure and was used for the next step without further purification.[217]

3-(1-(2-Hydroxyphenyl)-1*H*-1,2,3-triazol-4-yl)propanoic acid (35)

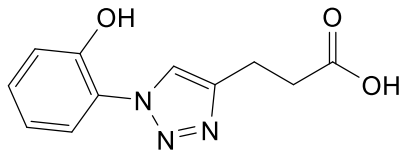

Compound **33** (500 mg, 3.7 mmol, 1.0 equiv.) was dissolved in acetonitrile (15 mL) under nitrogen atmosphere.[218] Then, sodium ascorbate (2.9 g, 14.8 mmol, 4.0 equiv.), copper sulfate pentahydrate (925 mg, 3.7 mmol, 1.0 equiv.) and pent-4-ynoic acid (**34**) (400 mg, 4.1 mmol, 1.1 equiv.) were added to the stirred solution, and the mixture was stirred for 72 h at room temperature.[219] Then, the mixture was acidified with hydrochloric acid (1 M, 10 mL) and extracted with dichloromethane (3 x, 20 mL). The organic layer was dried over Na_2SO_4, filtered and concentrated under reduced pressure to obtain a brown solid, which was used without further purification.

^{1}H NMR (500 MHz, $(CD_3)_2SO$): δ (ppm) = 12.19 (s, 1H), 10.47 (s, 1H), 8.22 (s, 1H), 7.57 (d, *J* = 7.9 Hz, 1H), 7.32 (t, *J* = 7.8 Hz, 1H), 7.10 (d, *J* = 8.3 Hz, 1H), 6.97 (t, *J* =

7.6 Hz, 1H), 2.94 (t, *J* = 7.2 Hz, 2H), 2.65 (s, 2H). ^{13}C NMR (126 MHz, $(CD_3)_2SO$): δ (ppm) = 174.1, 149.9, 130.4, 125.5, 125.2, 124.1, 120.0, 117.5, 38.0, 33.6, 21.2. HR-ESI-MS: calculated for $C_{11}H_{12}N_3O_3$ $[M+H]^+$ 234.0873, found 234.0870. Purity: >99%.

3-(1-(2-Hydroxyphenyl)-1*H*-1,2,3-triazol-4-yl)-*N*-(2-(*p*-tolylthio)ethyl)-propanamide (36)

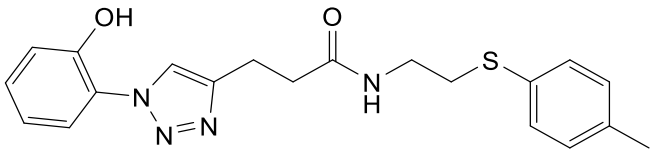

Following general procedure V, compound **20** (39 mg, 0.24 mmol, 1.1 equiv.) was added to a mixture of compound **35** (50 mg, 0.21 mmol, 1.0 equiv.), EDC*HCl (45 mg, 0.24 mmol, 1.1 equiv.), HOBt (29 mg, 0.21 mmol, 1.0 equiv.) and NMM (43 mg, 0.43 mmol, 2.0 equiv.) in DMF (2.5 mL), and stirred for 72 h. After work up and purification by preparative HPLC, the pure product (28 mg, 34%) was obtained as a white solid.

^{1}H NMR (500 MHz, $(CD_3)_2SO$): δ (ppm) = 10.48 (s, 1H), 8.18 (s, 1H), 8.12 (t, *J* = 5.7 Hz, 1H), 7.56 (dd, *J* = 8.1, 1.5 Hz, 1H), 7.40–7.28 (m, 1H), 7.24 (d, *J* = 8.2 Hz, 2H), 7.12 (d, *J* = 8.2 Hz, 2H), 7.10 (dd, *J* = 8.1, 1.4 Hz, 1H), 6.96 (td, *J* = 7.6, 1.5 Hz, 1H), 3.19–3.23 (m, 2H), 2.96–2.88 (m, 4H), 2.50–2.43 (m, 2H), 2.26 (s, 3H). ^{13}C NMR (126 MHz, $(CD_3)_2SO$): δ (ppm) = 171.3, 149.5, 145.7, 135.4, 131.9, 129.8, 129.7, 128.9, 125.0, 124.7, 123.5, 119.5, 117.0, 38.3, 34.7, 32.2, 21.2, 20.5. HR-ESI-MS: calculated for $C_{20}H_{23}N_4O_2S$ $[M+H]^+$ 383.1536 found 383.1531. Purity: 96%.

6 Appendix

6.1 Discovery of novel drug-like antitubercular hits targeting the MEP pathway enzyme DXPS by strategic application of ligand-based virtual screening

This manuscript has been published in *Chemical Science* **2022**, *13*, 10686–10698. Supplementary Information can be accessed *via* doi: 10.1039/D2SC02371G.

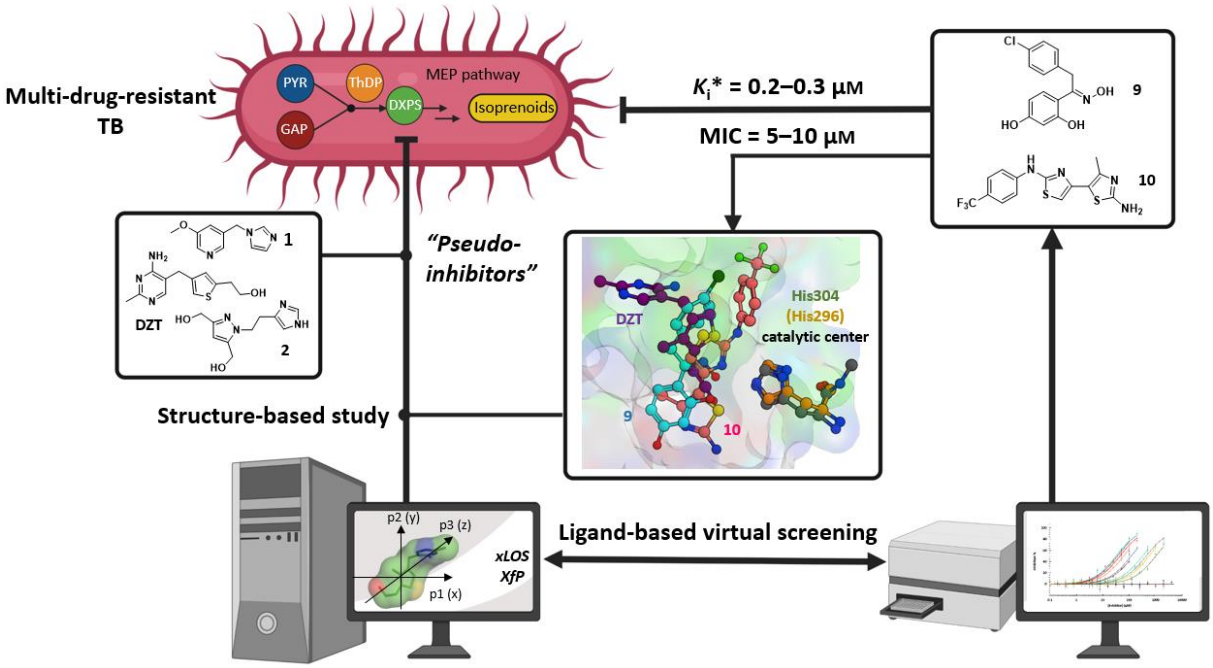

Antibiotic drug discovery is challenging and most conventional drug-development tools, including computer-aided drug design, often give disappointing results for antibiotic targets. In this paper, we present the successful discovery of drug-like antitubercular hits against the particularly difficult target 1-deoxy-D-xylulose-5-phosphate synthase by strategically employing ligand-based virtual screening.

6.1.1 Contributions

Di Zhu conceived and wrote the manuscript. She performed the DXPS activity assay and MOI studies. In addition, she wrote the experimental procedures for all biological experiments. Sandra Johannsen measured and analyzed all previously synthesized final compounds by ^{1}H NMR, ^{13}C NMR, HRMS and ^{19}F NMR, if applicable. She re-synthesized **9**, **10**, and **25** either for NMR analysis or for further tests such as activity against *M. tuberculosis* or metabolic stability. She also performed docking experiments and wrote the experimental section for synthesized compounds with the corresponding experimental procedures as well as the general chemistry part. In the final stages of writing the manuscript, she was responsible for proof-reading and correcting the main text. Tiziana Masini and Céline Simonin performed the LBVS together with Mahendra Awale, and the DXPS activity assay together with Boris Illarionov. Jörg Haupenthal coordinated and interpreted the *E. coli* MIC and target validation assays. The zebra fish experiments were performed by Anastasia Andreas. Robin M. Gierse performed the site-directed mutagenesis and was involved in the expression and purification of proteins. Alicia DeColli performed the selectivity assay, while Tridia van der Laan was responsible for the *M. tuberculosis* MIC assay of compounds tested at RIVN. Norbert Reiling tested compounds **17** and **25** against *M. tuberculosis*. Rita Nasti, Mael Poizat and Ramon van der Vlag synthesized derivatives for the SAR analysis. Eric Buhler performed the dynamic light scattering experiments. Rolf Müller, Markus Fischer, Caren L. Freel Meyers supervised the experiments in their respective laboratories. Jean-Loia Reymond and Anna K. H. Hirsch supervised, conceptualized and coordinated the project. All authors contributed to reviewing and editing.

Chemical Science

ROYAL SOCIETY OF CHEMISTRY

EDGE ARTICLE

View Article Online
View Journal | View Issue

Cite this: *Chem. Sci.*, 2022, **13**, 10686

All publication charges for this article have been paid for by the Royal Society of Chemistry

Discovery of novel drug-like antitubercular hits targeting the MEP pathway enzyme DXPS by strategic application of ligand-based virtual screening†

Di Zhu,‡[abc] Sandra Johannsen,‡[ab] Tiziana Masini,‡[c] Céline Simonin,‡[d] Jörg Haupenthal,[a] Boris Illarionov,[e] Anastasia Andreas,[ab] Mahendra Awale,[d] Robin M. Gierse,[abc] Tridia van der Laan,[f] Ramon van der Vlag,[c] Rita Nasti,[c] Mael Poizat,[g] Eric Buhler,[h] Norbert Reiling,[ij] Rolf Müller,[abk] Markus Fischer,[e] Jean-Louis Reymond*[d] and Anna K. H. Hirsch*[abck]

In the present manuscript, we describe how we successfully used ligand-based virtual screening (LBVS) to identify two small-molecule, drug-like hit classes with excellent ADMET profiles against the difficult to address microbial enzyme 1-deoxy-D-xylulose-5-phosphate synthase (DXPS). In the fight against antimicrobial resistance (AMR), it has become increasingly important to address novel targets such as DXPS, the first enzyme of the 2-*C*-methyl-D-erythritol-4-phosphate (MEP) pathway, which affords the universal isoprenoid precursors. This pathway is absent in humans but essential for pathogens such as *Mycobacterium tuberculosis*, making it a rich source of drug targets for the development of novel anti-infectives. Standard computer-aided drug-design tools, frequently applied in other areas of drug development, often fail for targets with large, hydrophilic binding sites such as DXPS. Therefore, we introduce the concept of pseudo-inhibitors, combining the benefits of pseudo-ligands (defining a pharmacophore) and pseudo-receptors (defining anchor points in the binding site), for providing the basis to perform a LBVS against *M. tuberculosis* DXPS. Starting from a diverse set of reference ligands showing weak inhibition of the orthologue from *Deinococcus radiodurans* DXPS, we identified three structurally unrelated classes with promising *in vitro* (against *M. tuberculosis* DXPS) and whole-cell activity including extensively drug-resistant strains of *M. tuberculosis*. The hits were validated to be specific inhibitors of DXPS and to have a unique mechanism of inhibition. Furthermore, two of the hits have a balanced profile in terms of metabolic and plasma stability and display a low frequency of resistance development, making them ideal starting points for hit-to-lead optimization of antibiotics with an unprecedented mode of action.

Received 27th April 2022
Accepted 7th August 2022

DOI: 10.1039/d2sc02371g

rsc.li/chemical-science

[a]*Helmholtz Institute for Pharmaceutical Research Saarland (HIPS) – Helmholtz Centre for Infection Research (HZI), Campus Building E8.1, 66123 Saarbrücken, Germany. E-mail: anna.hirsch@helmholtz-hips.de*

[b]*Department of Pharmacy, Saarland University, Campus Building E8.1, 66123 Saarbrücken, Germany*

[c]*Stratingh Institute for Chemistry, University of Groningen, Nijenborgh 7, 9747 AG Groningen, The Netherlands*

[d]*Department of Chemistry, Biochemistry and Pharmaceutical Sciences, University of Bern, Freiestrasse 3, 3012 Bern, Switzerland. E-mail: jean-louis.reymond@unibe.ch*

[e]*Hamburg School of Food Science, Institute of Food Chemistry, Grindelallee 117, 20146 Hamburg, Germany*

[f]*Department of Mycobacteria, National Institute of Public Health and the Environment (RIVM), Diagnostics and Laboratory Surveillance (IDS), Infectious Diseases Research, Antonie van Leeuwenhoeklaan 9, 3721 MA Bilthoven, The Netherlands*

[g]*Symeres, Kadijk 3, 9747 AT Groningen, The Netherlands*

[h]*Laboratoire Matière et Systèmes Complexes (MSC), UMR CNRS 7057, Université Paris Cité, Bâtiment Condorcet, 75205 Paris Cedex 13, France*

[i]*RG Microbial Interface Biology, Research Center Borstel, Leibniz Lung Center, Borstel, Germany*

[j]*German Center for Infection Research (DZIF), Partner Site Hamburg-Lübeck-Borstel-Riems, Borstel, Germany*

[k]*Helmholtz International Lab for Anti-infectives, Campus Building E8.1, 66123 Saarbrücken, Germany*

† Electronic supplementary information (ESI) available. See https://doi.org/10.1039/d2sc02371g

‡ D. Zhu, S. Johannsen, T. Masini and C. Simonin contributed equally to this work.

Introduction

The discovery of novel antibiotics with unprecedented mode of action is increasingly important due to the fast development of antimicrobial resistance (AMR), but it has been notoriously difficult to expand the pool of targets and active compounds in the past decades.[1] Conventional methods such as screening of natural-product libraries and their optimization have resulted in most of the antibiotics on the market today, but to keep up with AMR, new techniques need to be employed.[2,3] Standard tools for oral drug discovery against eukaryotic targets, like computer-aided drug design (CADD) and screening of combinatorial libraries, are mostly ineffective for the development of anti-infective drugs.[4,5] Compound libraries often follow Lipinski's "rule-of-5" (Ro5) but since antibiotic targets tend to have large, hydrophilic binding sites, these libraries rarely result in new hits.[6,7] Although great efforts have been made to expand the limits of the Ro5, a lot still needs to be done to improve and adjust known tools to facilitate fast and effective discovery and development of drug-like antibiotics.[8–12]

The 2-*C*-methyl-D-erythritol-4-phosphate (MEP) pathway is essential for the biosynthesis of the universal isoprenoid precursors isopentenyl diphosphate (IDP) and dimethylallyl diphosphate (DMADP) in many important pathogens, including *Plasmodium falciparum*, *Haemophilus influenzae*, *Mycobacterium tuberculosis* and *Escherichia coli* but its absence in humans makes it a source of validated anti-infective targets.[13–16] The pathway is composed of seven enzymes, with most of the substrates and cofactors being phosphorylated and involved in metal interactions. This makes all MEP enzymes challenging drug targets due to a lack of hydrophobic anchor points (APs) in these pockets.[17] Hydrophobic inhibitors being in compliance with the Ro5 are less likely to gain sufficient binding affinity to outcompete the tight-binding, natural binders while retaining their drug-like properties. In consequence, it is not surprising that up to date, though there is an increasing number of (co) crystal structures of MEP pathway enzymes, only a few promising inhibitor scaffolds were found with *in vitro* and cell-based anti-infective activity against MEP pathway-utilizing pathogens (Fig. 1A).[14,16] Butylacetylphosphonate (BAP), ketoclomazone and fosmidomycin are hydrophilic small molecules beyond the Ro5 that mimic the tight-binding nature of substrates or cofactors.[18–26] 1*R*,3*S*-MMV008138, BITZ and TZLP are drug-like molecules based on their physicochemical properties.[15,27–29] BITZ (possibly also TZLP) does not function through typical lock–key interaction, but covalently inhibits the target enzyme by reaction with a cysteine in the active site. Most of the inhibitors are in hit or early lead stage development except fosmidomycin, which is in phase II clinical trials to treat uncomplicated malaria.[30] These outcomes are not meeting the high expectations that were raised upon the discovery of the MEP pathway in the 1990s. Here, antibiotic development appears to be trapped in a limited system, where the discovery of novel hits/leads depends too heavily on direct screening, while rational methods, such as computational approaches are underrepresented. Although the MEP pathway enzymes are considered encouraging targets to obtain novel anti-infectives to fight against drug-resistant tuberculosis, no hits/leads have been verified against *M. tuberculosis* yet.[16,31] Therefore, our main goal is to develop novel antitubercular agents targeting the MEP pathway, *via* virtual screening (VS) guided by rational drug-design principles and demonstrate that it is possible to use these methods successfully in antibiotic research.[32]

The first enzyme in the MEP pathway is 1-deoxy-D-xylulose-5-phosphate synthase (DXPS), which catalyzes the thiamine diphosphate (ThDP)-dependent decarboxylation of pyruvate (PYR) and addition of D-glyceraldehyde 3-phosphate (D-GAP) to afford 1-deoxy-D-xylulose-5-phosphate (DXP).[33,34] Unlike other ThDP-dependent enzymes, DXPS catalyzes a random sequential mechanism, requiring ternary complex formation *en route* to DXP. This mechanism has been investigated thoroughly for *Deinococcus radiodurans* (*Dr*)DXPS and *E. coli* (*Ec*)DXPS and inhibition of *M. tuberculosis* (*Mt*)DXPS by BAP, targeting the large active site of DXPS, suggests that *Mt*DXPS shares these mechanistic characteristics.[24,33,34] The tight-binding nature of ThDP, the highly hydrophilic metal ion-containing binding sites, the complex mechanism and the uncertainty of substrate binding throughout the reaction mechanism are challenging features and reasons why the standard structure-based VS (SBVS) algorithms have been less reliable on DXPS.[35–38]

The prerequisite for a conventional ligand-based virtual screening (LBVS) campaign is to have at least one bioactive reference against the target, but since no known hydrophobic, small-molecule inhibitors against *Mt*DXPS were available to directly initialize the LBVS, we chose a few weak drug-like inhibitors against the structurally similar *Dr*DXPS instead.[37,39]

For the first time in literature, we took advantage of structure-based modeling and ligand-based alignment by combining the concepts of pseudo-receptor and pseudo-ligands, and defined the new term "pseudo-inhibitor" (Fig. 1B).[40–42] A pseudo-receptor is built based on true inhibitors against the target enzyme, where the APs come from homology modeling or 3D-quantitative structure–activity relationships (QSARs) and the real receptor structure is not known. In contrast, pseudo-ligands are virtual inhibitors that have never been tested as inhibitors of a target, and are adducts of pharmacophores proposed based on the (co)crystal structure of the target enzyme. In both cases, knowledge gaps are overcome by computational analyses of the known entities, either active ligands or known crystal structures. For both pseudo-receptor- and pseudo-ligand-based methods, pharmacophore mapping and validation are necessary to assure the accuracy. Our proposed concept of pseudo-inhibitors is combining both methods. As a starting point, compounds that are not active on the target, but are true inhibitors of a structurally close homologue or orthologue of the target, are used to identify the key APs and pharmacophores. Then, if the APs are conserved between the homologue and the target of interest, we assume the pseudo-inhibitors bear the same interaction on both proteins and work as a guideline for LBVS to help us find true inhibitors against the target with the proposed interaction. We propose that this method is especially powerful, if the pseudo-inhibitors have a unique mode of inhibition (MOI), like

A

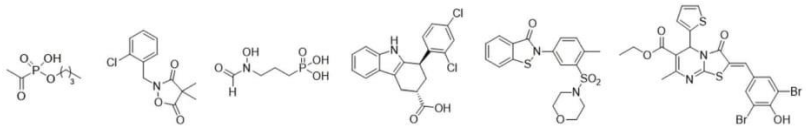

Name/ abbrev.	BAP	Ketoclomazone	Fosmidomycin	1*R*,3*S*-MMV008138	BITZ	TZLP
Target pathogen	*E. coli*	*H. influenzae*	*P. falciparum*	*P. falciparum*	*P. falciparum*	*P. falciparum*
Activity on target pathogen	MIC = 5 μM	MIC = 49 μM	EC_{50} = 0.98 μM	EC_{50} = 110 nM	EC_{50} = 4.3 μM	EC_{50} = 1.5 μM
Target enzyme	DXPS	DXPS	IspC	IspD	IspD	IspF
Activity on target enzyme	K_i = 5.6 μM	IC_{50} = 1.0 μM	IC_{50} = 350 nM	IC_{50} = 7 nM	IC_{50} = 0.45 μM	IC_{50} = 9.6 μM
Binding site	PYR	D-GAP	NADPH	unknown	CTP	unknown
MW [g/mol]	108.14	253.68	183.10	360.23	390.47	584.30
cLogP*	−1.85	−1.02**	−4.52	1.69	2.59	3.85
Origin	substrate mimic	screening natural products	screening natural products	screening „Malaria Box" library	HTS	HTS

*Calculated at pH = 7.4.
**Calculated as active hydrolyzed form.

B

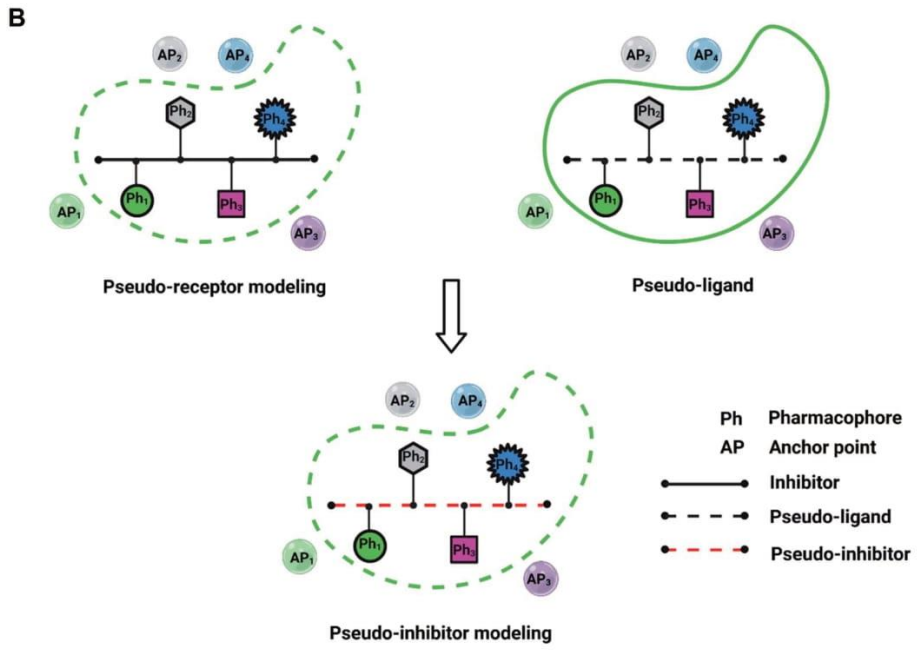

Fig. 1 (A) Representative inhibitors of the 2-*C*-methyl-D-erythritol-4-phosphate pathway showing promising on-target and cell-based activity against certain relevant pathogens. MIC = minimum inhibitory concentration, EC_{50} = half maximal effective concentration, NADPH = nicotinamide adenine dinucleotide phosphate, CTP = cytidine triphosphate, HTS = high-throughput screening. (B) The concept of pseudo-inhibitors, *i.e.*, the combination of pseudo-receptor modeling and pseudo-ligands. Created with https://BioRender.com.

targeting the catalytic or allosteric center that is conserved among homologues.

Results and discussion

Selection of pseudo-inhibitors

We defined three structurally diverse pseudo-inhibitors: deazathiamine (DZT) and fragments **1** and **2**. DZT (Fig. 2A) was derived from ThDP by removing the ylide functionality and the diphosphate group. It is a weak inhibitor of *Dr*DXPS, but is not active against the target enzyme *Mt*DXPS.[37] Despite the high structural similarity compared to ThDP, DZT shows a unique MOI on *Dr*DXPS by being competitive with ThDP, PYR and D-GAP (Fig. 2B). Docking studies suggest that while the aminopyrimidine and thiophene rings are likely to occupy the same pocket as ThDP (Fig. 2C), the hydroxyl group of DZT, whose linker is too short to reach the diphosphate anchors of ThDP, is free to move. In the top-ranked docking poses of DZT, the hydroxyl group forms a hydrogen bond with His304 (Fig. 2A). It has been reported that His304 is essential in substrate

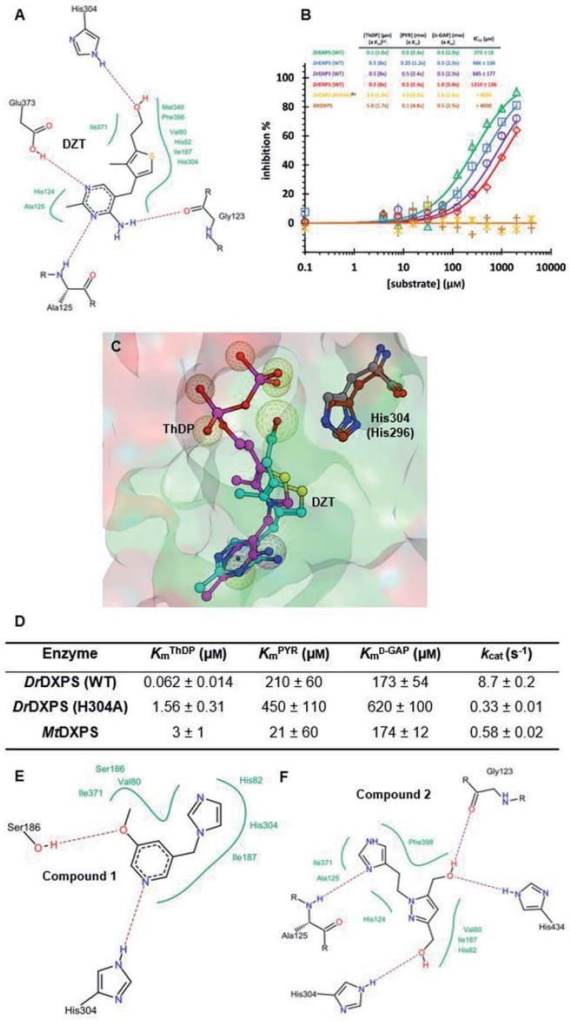

D

Enzyme	K_m^{ThDP} (μM)	K_m^{PYR} (μM)	$K_m^{D\text{-}GAP}$ (μM)	k_{cat} (s^{-1})
***Dr*DXPS (WT)**	0.062 ± 0.014	210 ± 60	173 ± 54	8.7 ± 0.2
***Dr*DXPS (H304A)**	1.56 ± 0.31	450 ± 110	620 ± 100	0.33 ± 0.01
***Mt*DXPS**	3 ± 1	21 ± 60	174 ± 12	0.58 ± 0.02

Fig. 2 (A) Top-ranked docking pose of deazathiamine (DZT) with crystal structure of *Dr*DXPS (PDBID: 2O1X).[38] *ApoDr*DXPS was prepared by directly removing the cocrystalized ThDP, and docking was performed in presence of Mg^{2+} (same for the other docking operations in this paper). (B) Mode-of-inhibition study of DZT against *Dr*DXPS and dose–response curves of DZT against *Mt*DXPS and H304A mutant. [a] To make the comparison more convenient, we also present the value of $[S]/K_m$, as (x K_m). [b] The assay condition of *Dr*DXPS (H304A) are the lowest working concentrations of ThDP, PYR and D-GAP for the mutant, to maximize the chance of observing inhibition of the inhibitors. Color code: reference condition: purple; varying [ThDP]: green; varying [PYR]: blue; varying [D-GAP]: red. (C) Pharmacophore view of ThDP and DZT. Color code: C-skeleton: DZT: light blue; ThDP: magenta; His304 (*Dr*DXPS): gray; His296 (*Mt*DXPS): brown. Surface: hydrophobic site: green; hydrophilic site: red. (D) Kinetic characterization of *Dr*DXPS (WT), *Dr*DXPS (H304A) and *Mt*DXPS (see curves in Fig. S1†). (E) Top-ranked docking pose of compound **1** with *Dr*DXPS with His304 interaction. (F) Top-ranked docking pose of compound **2** with *Dr*DXPS with H304 interaction. All the docking studies in this paper were performed with the software LeadIT;[44] Fig. 2C was generated with MOE;[45] Fig. 2A, E and F were generated with Poseview.[46]

recognition, so we performed site-directed mutagenesis (SDM) to confirm the AP of DZT by mutation of His304 to alanine.[43] The H304A mutant of *Dr*DXPS shows significant attenuation of Michaelis–Menten constants (K_m) of ThDP, PYR and D-GAP, indicating that His304 plays a vital role in both cofactor binding and substrate recognition (Fig. 2D and S1†). When tested against the H304A mutant, DZT completely lost its activity (Fig. 2B), suggesting the interaction with H304 is necessary to correctly orient the aromatic pharmacophores into the hydrophobic pocket. Therefore, by directly targeting His304, DZT was validated as a promising prototype of a drug-like inhibitor against DXPS. Superimposing *Dr*DXPS (PDB code: 2O1X) with the validated homology model of *Mt*DXPS, reveals His296 as the analogous residue to His304 on *Dr*DXPS, supporting the structural basis and confirming the feasibility of the pseudo-inhibitor model (Fig. 2C).[36,38] To enhance the structural diversity of our initial ligands for LBVS, we also included pseudo-inhibitors **1** and **2** as ligands, which are weak inhibitors against *Dr*DXPS developed by *de novo* fragment-based drug design (FBDD) and are predicted to bind to His304 in docking experiments (Fig. 2E and F).[37]

LBVS

Starting from the pseudo-inhibitors DZT, **1** and **2**, we performed three rounds of LBVS against *Mt*DXPS (Fig. 3A and B). First, the 3D structures of the reference ligands were generated with CORINA.[47] To focus on drug-like molecules and to save computer power, we restricted our search to ~800 000 compounds from the Princeton catalogue. To calculate the structure similarity of the screening compounds, two LBVS algorithms were used. The atom-category extended Ligand Overlap Score (xLOS) is a 3D-shape and -pharmacophore matching algorithm, which is uniquely suited for scaffold hopping and has been successfully employed in hit discovery.[48–50] xLOS was extensively used in the first round of LBVS, to search for inhibitors against *Mt*DXPS "from scratch". As soon as the reference inhibitor showed a moderate potency against *Mt*DXPS in the second and third round of LBVS, we implemented a topological shape and pharmacophore fingerprint algorithm called extended atom pair FingerPrint (XfP).[47] This method was developed to overcome the computational demand associated with precise 3D-shape screening of large databases and it was shown to correlate well with various representations of molecular shape extracted from 3D structures. Of note, the combination of xLOS and XfP in the second round of LBVS led to the highest hit rate.

Then, we carefully analyzed the virtual ligands on the basis of clustering, visual inspection, modeling and docking. We considered scaffold diversity as the most important factor during the first round of LBVS, as the pseudo-inhibitors are not active against *Mt*DXPS. To boost the chance of hitting the target, we wanted to cover as many scaffolds as possible (Table S1†). Later, when we performed the second and third round of LBVS from true inhibitors against *Mt*DXPS using the XfP algorithm, the resulting virtual ligands were less structurally diverse (Tables S2 and S3†). Although the His304 interaction was not

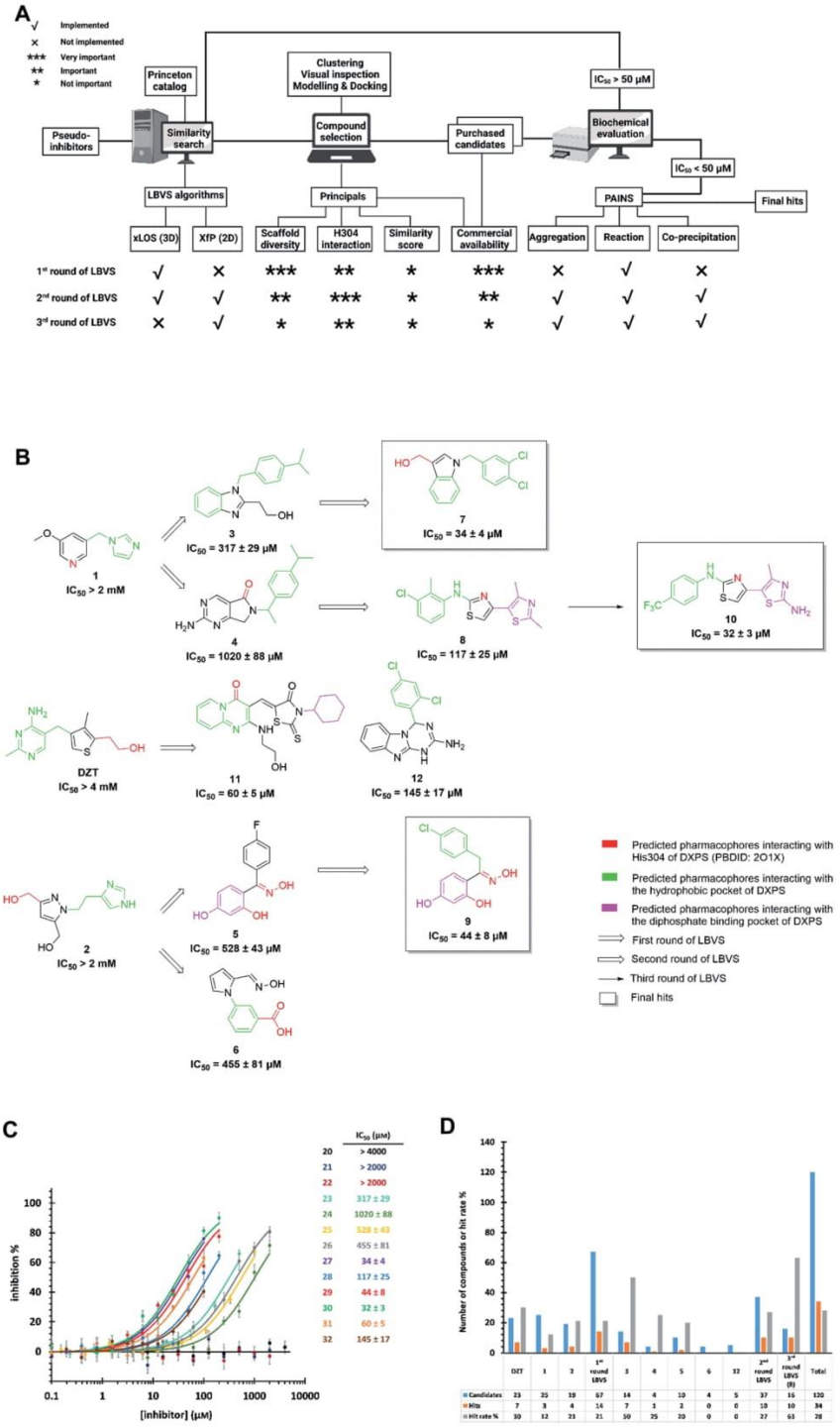

Fig. 3 (A) Flow-chart of ligand-based virtual screening (LBVS) created with https://BioRender.com. (B) Schematic presentation of LBVS with most active hits of each round. (C) Dose–response curves of deazathiamine (DZT) and compounds **1–10** against *Mt*DXPS. Assay conditions: [ThDP] = 15 µM, [pyruvate] = 0.5 mM, [D-GAP] = 0.5 mM, [DXPS] = 1.25 µM. (D) Statistics of purchased candidates and hits.

mandatory in any of the LBVS rounds, all key candidates showed it in the top-ranked docking pose, indicating hits with such MOI were "enriched" *via* LBVS (Fig. 3B; see PoseView in Fig. S2†). Commercial availability was a crucial factor for the first round of LBVS to get rapid feedback without any synthetic work. In subsequent iterations of LBVS, commercial availability was no longer a limitation as we initiated the synthesis of derivatives of the hits.

After purchasing and chemical characterization, the candidates were submitted for biochemical evaluation using a coupled spectrophotometric enzyme activity assay in duplicate (Fig. 3C).[37] When the IC_{50} values of the hits were greater than 50 μM, they would become the starting points for the next round of LBVS. For IC_{50} values smaller than 50 μM, they were first tested to exclude Pan-Assay Interference Compounds (PAINS).[51]

We purchased 67, 37 and 16 compounds for the first, second and third LBVS rounds, respectively, adding up to a total number of 120, with a hit rate of 28% well above the average hit rate of 13% for conventional VS campaigns (Fig. 3D).[52] Even for the first round of LBVS, starting from pseudo-ligands, the hit rate was 21%, demonstrating the power of the xLOS algorithm in identifying novel hit scaffolds. In addition, most of the LBVS candidates were small, hydrophobic and drug-like molecules, with a mean value of 286 Da overall and 304 Da for hits (Fig. S3A†), and a cLogP of 2.78 overall and 3.23 for hits (Fig. S3B†), demonstrating the feasibility and efficiency of standard CADD tools in antibiotic drug discovery.

The best hits of each LBVS round are presented in Fig. 3B. The first round of LBVS led to moderate inhibitors of *Mt*DXPS (hits **3–6**, **11** and **12**). All six hits served as a reference for the second round of LBVS providing hits **7–9**. As there was a rich source of derivatives of **8** available, we performed the third round of LBVS starting from **8** and achieved hit **10**. We did not further screen based on **7** and **9** because they already have promising activity. Compounds **6** and **12** were discontinued because they could not be improved in the next round of screening and compound **11** is a reactive false positive as it also inhibits several other related or unrelated enzymes. Its inhibition could be significantly attenuated by increasing the dithiothreitol (DTT) concentration (Fig. S4A and S4B†).[53] In summary, DZT failed to afford validated hits, indicating the importance of including diverse reference structures at the beginning. The most promising hits **7**, **9** and **10**, derived from compounds **1** and **2**, were evaluated with dynamic light scattering (DLS), DTT dependency and in centrifugation experiments to exclude the possibilities of aggregation, reactive false positives and co-precipitation, respectively (Fig. S5A–C†).[53,54] In summary, our iterative LBVS campaign afforded indole **7**, oxime **9** and aminothiazole **10** as final hits, representing three structurally diverse, drug-like scaffolds, with promising *in vitro* activity against *Mt*DXPS.

Characterization of compounds 7, 9 and 10 against *Mt*DXPS

The time-dependent progress curves indicate that the final hits **7**, **9** and **10** inhibit *Mt*DXPS in a slow-binding manner, with an equilibration time of ~100 s (Fig. 4A). Increasing DXPS concentration leads to a drop of inhibitory potency of **7**, **9** and **10**, which points to a tight-binding pattern (Fig. 4B). In addition, MOI studies show that compound **7** is competitive with ThDP and D-GAP, but non-competitive with PYR (Fig. 4C); while compounds **9** and **10** were competitive with ThDP and both substrates (Fig. 4D and E). As the conventional Cheng–Prusoff model is not suitable to characterize slow, tight-binding inhibitors, we implemented a tight-binding Morrison model based on the random sequential mechanism of DXPS.[55,56] Slow, tight-binding inhibition is most commonly attributed to one of two binding models: (1) one-step binding: $E + I = E \cdot I$ or (2) two-step binding: $E + I = E \cdot I = E^* \cdot I$. The hyperbolic plot of the apparent catalytic constant k_{obs} against the inhibitor concentrations suggests the two-step Morrison model is appropriate (Fig. S6†). By fitting the dose-dependent curves into the Morrison model with the software Dynafit as done in the past, we determined the Morrison constants (K_i^*) of **7**, **9** and **10** to be 1.29 μM, 0.271 μM and 0.212 μM, respectively.[57–59] Direct measurement of dissociation constants (K_D) with microscale thermophoresis (MST) further validated the accuracy of the Morrison model, with K_D for **7**, **9** and **10** to be 1.370 μM, 0.221 μM and 0.206 μM, respectively (Fig. 4F and S7†). Inspiringly, compounds **9** and **10** were the first drug-like inhibitors with sub-micromolar inhibition potency against any DXPS homologue. In contrast, other potent DXPS inhibitors are not cell-permeable and need a prodrug approach to enter cells.[60] The final hits also revealed promising selectivity by being inactive against the ThDP-dependent mammalian pyruvate dehydrogenase (PDH) (Fig. S8†).

Pharmacophore validation on *Dr*DXPS

As *Mt*DXPS was 15-fold less active (Fig. 2E) and more unstable than *Dr*DXPS, performing an SDM study directly on *Mt*DXPS was challenging. However, the success of pseudo-inhibitor-based LBVS and the weak activity against *Dr*DXPS suggest that *Dr*DXPS is a suitable model for *Mt*DXPS for the pharmacophore validation on *Dr*DXPS.

For this, we used our previously created His304 mutant, in which His304 is replaced by an alanine. Based on the docking results (Fig. 5A–D), all compounds interact with His304 and should therefore, not be able to inhibit the mutant. This hypothesis was confirmed for compounds **9** and **10** that are both inactive (Fig. 5F and G), but compound **7** (Fig. 5E) retained some activity. A closer look at the docking pose of compound **7** explains this phenomenon as the hydroxyl group of **7** also interacts with His82, which has been shown to be involved in catalysis in the wild type and without His304 present, might take over this role in the mutant.[43]

Pharmacophore validation on *Mt*DXPS

Pharmacophore validation on *Mt*DXPS was mainly based on the analysis of structure–activity relationships (SARs). We designed and synthesized a series of derivatives of compounds **7** and **9** according to docking results and the Topliss scheme, as there were no commercially available derivatives of the two hits.[61] For

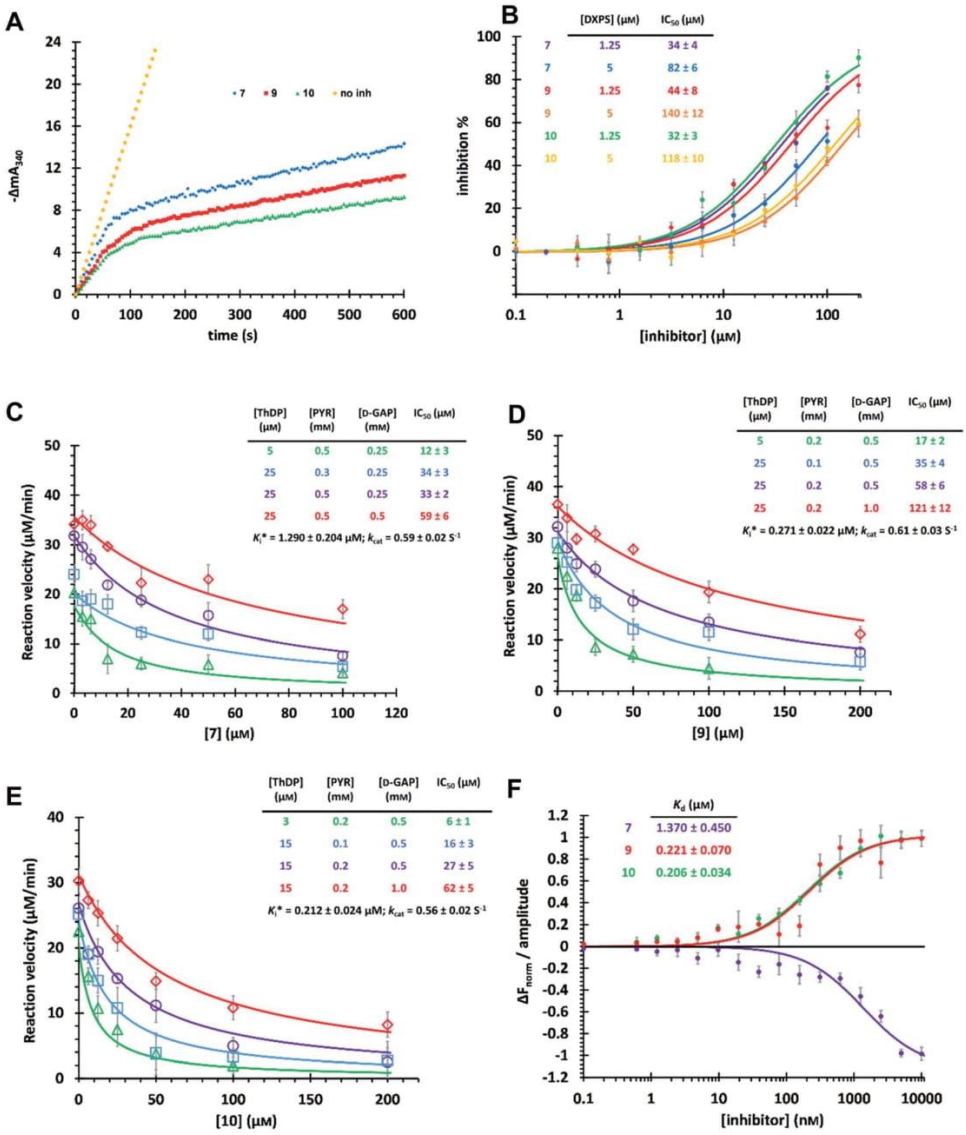

Fig. 4 (A) Time-dependent progress curves of the final hits. Conditions can be found in ESI Methods 3.2.7.† (B) Dose–response curves of the final hits by varying *Mt*DXPS concentration. (C), (D) and (E) Mode-of-inhibition study and determination of K_i* of compounds **7**, **9** and **10**, respectively. Color code: reference condition: purple; varying [ThDP]: green; varying [PYR]: blue; varying [D-GAP]: red. (B)–(E) The reaction velocity was measured after 200 s, when the slow-onset phase was considered complete. (F) Determination of K_D of the final hits with microscale thermophoresis (MST) (binding curves). Curve shape is dependent on molecular movement during measurement and has no influence on K_D determination.

compound **10**, SARs were derived from the third round of LBVS. Their inhibitory activities were calculated as K_i* against *Mt*DXPS (Table 1A–C and S9A–C†). We focused on three moieties: R^0, the key pharmacophore that interacts with His304 (His296 in *Mt*DXPS) and positions the inhibitor in the right orientation, *i.e.* the hydroxyl group of compound **7**, the oxime group of compound **9**, and the nitrogen atom of the thiazolyl ring of compound **10**; ring 1, the methylene- or imino-linked aromatic groups that grow into the hydrophobic pocket lined by phenylalanine and histidine residues, possibly contributing to π–π or halogen–π interactions; ring 2, the aromatic rings that flip towards the opening of the diphosphate binding pocket (Fig. 5D). The results indicate that R^0 is an essential anchor for all derivatives, but inhibition can be lost if ring 1 is not electron-deficient. Compounds **15**, **16** and **22** still contain a hydroxyl or oxime group, but R^1 is not sufficiently electron-withdrawing and activity is lost. If R^0 is replaced with a different group, as in derivatives **13**, **14** and **20**, activity is lost as well, but the oxime hydroxyl group can be replaced with an amino group (compound **21**) and activity is partially retained. Modifications

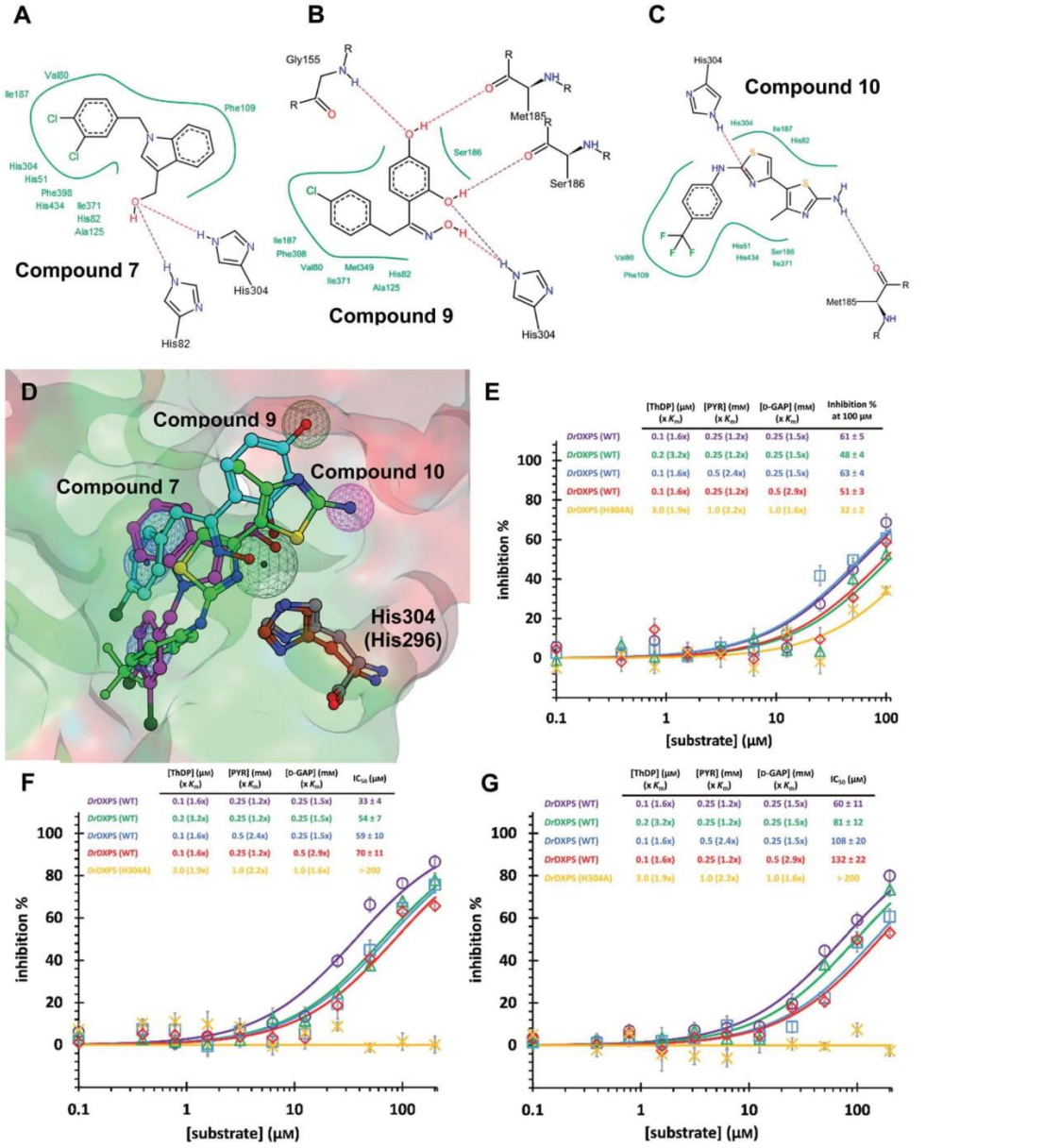

Fig. 5 (A) (B) (C) Poseview of compounds **7**, **9** and **10**. (D) Superimposed docked pose of the final hits into *Dr*DXPS with pharmacophore view. Color code: C skeleton: **7**: magenta; **9**: light blue; **10**: green; His304 (*Dr*DXPS): gray; His296 (*Mt*DXPS): brown. Surface: hydrophobic site: green; hydrophilic site: red. (E), (F) and (G) Mode-of-inhibition and site-directed mutagenesis studies of the final hits against *Dr*DXPS. Fig. 5D was generated with MOE;[45] Fig. 5A–C were generated with Poseview.[46]

on ring 2 lead to a moderate increase or decrease of activity. Compounds **17** and **25** are more active than their parent molecules **7** and **9** due to different substituents on ring 2. Derivatives of compound **10** showed the same trends. Ring 1 has to be electron-deficient, otherwise activity is lost (compound **26**), while different R^2 groups are tolerated in most cases. For the aminothiazole class, no improved hit could be found, but the parent compound **10** is a potent inhibitor already. We could demonstrate that R^0 is essential for binding to *Mt*DXPS as predicted and that strategic planning can reduce the synthetic effort significantly while still giving important insights into the SAR.

Intracellular target validation, cell-based antitubercular activity and ADMET study

The high biosafety level and slow growth of *M. tuberculosis* strains complicate target-validation studies. Therefore, we used

Table 1 (A), (B) and (C) K_i* and structures of the derivatives of the final hits

A

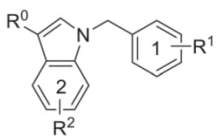

Cmpd no.	R^0	R^1 *meta*	R^1 *para*	R^2	K_i* (μM)
7	$-CH_2OH$	–Cl	–Cl	—	1.3 ± 0.2
13	–CHO	–Cl	–Cl	—	>10
14	$-CH_2OCH_3$	–Cl	–Cl	—	>5
15	$-CH_2OH$	–Cl	–H	—	>10
16	$-CH_2OH$	–H	–Cl	—	5.5 ± 0.6
17	$-CH_2OH$	–Cl	–Cl	5-F	0.4 ± 0.06
18	$-CH_2OH$	–Cl	–Cl	6-CN	1.7 ± 0.3
19	$-CH_2OH$	–Cl	–Cl	7-OCH_3	1.4 ± 0.3

B

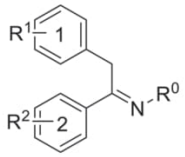

Cmpd no.	R^0	R^1	R^2 *ortho*	R^2 *para*	K_i* (μM)
9	–OH	4-Cl	–OH	–OH	0.3 ± 0.02
20	$-OCH_3$	4-Cl	–OH	–OH	>10
21	$-NH_2$	4-Cl	–OH	–OH	0.4 ± 0.05
22	–OH	4-OCH_3	–OH	–OH	>10
23	–OH	4-Cl	–H	–H	1.1 ± 0.2
24	–OH	4-Cl	–OH	$-OCH_3$	0.5 ± 0.1
25	–OH	4-Cl	–OH	$-NH_2$	0.1 ± 0.03

C

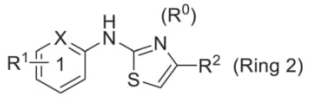

Cmpd no.	X	R^1	R^2	K_i* (μM)
10	–CH	4-CF_3	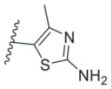	0.2 ± 0.02
26	–CH	–H	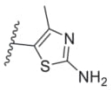	>10
27	–CH	2-CF_3	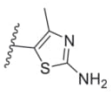	0.3 ± 0.02

Table 1 (*Contd.*)

C

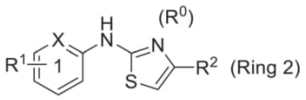

Cmpd no.	X	R^1	R^2	K_i* (μM)
28	–CH	3-CF_3	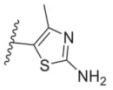	0.4 ± 0.06
29	–CH	3-CF_3	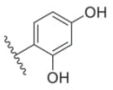	0.5 ± 0.04
30	–N	4-Cl	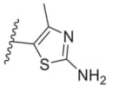	0.3 ± 0.1
31	–N	4-Cl	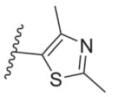	>10

E. coli (BL21(DE3)) as a model strain for target validation, as our hits are also active on *E. coli* (*Ec*)DXPS (Fig. S10†). To check if *E. coli* is suitable for target validation by overexpression of MEP pathway enzymes, we used the nanomolar inhibitor of *Ec*IspC fosmidomycin in an *E. coli* strain carrying an IspC-expressing plasmid. We observed attenuation of inhibition by fosmidomycin by adding isopropyl β-D-1-thiogalactopyranoside (IPTG) to trigger the IspC overexpression, while our hits showed unchanged MIC values, making *E. coli* a suitable model for target validation (Fig. 6A). In turn, for the *E. coli* strain carrying *Mt*DXPS-expressing plasmids, adding IPTG leads to a significant increase of MIC values for compounds **9** and **10**, but shows little effect on compound **7** and fosmidomycin (Fig. 6B). The results suggest *Mt*DXPS could be the intracellular target of **9** and **10**, but not the main target of compound **7**.

Our LBVS hits show promising antitubercular activities (5–10 μM) against multiple strains of *M. tuberculosis*, including drug-resistant (DR), multidrug-resistant (MDR) and extensively-drug-resistant (XDR) strains (Fig. 6C). The improved indole derivative **17**, however, shows no activity against *M. tuberculosis* strains and oxime **25** retains some activity, which can have different reasons such as additional targets or a different uptake behavior in *M. tuberculosis* and has to be investigated further.

An *in vitro* ADMET study indicated toxicity against human cell lines and a short half-life of **7**, but compounds **9** and **10** display promising ADMET properties of lead quality. Compared with sub-micromolar activities on the target DXPS and low micromolar MIC values against *M. tuberculosis* strains, hits **9** and **10** have a relatively wide safety window in human cell lines and zebrafish larvae embryos (Fig. 6C and Table S4†). Furthermore, their metabolic half-lives are acceptable (Fig. 6C and

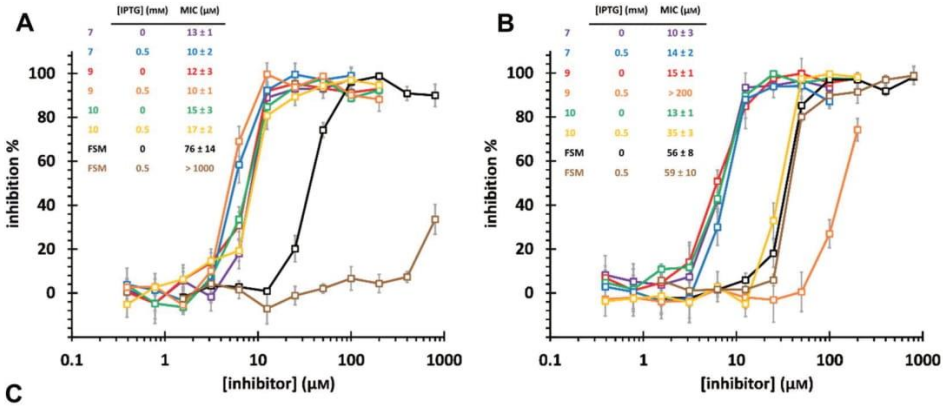

C

Cmpd. No.	Antitubercular activity						Toxicity				Metabolic stability[d]
	Strain[a] & MIC (μM)						Human cell lines [c] EC_{50} (μM)			Zebrafish larvae Non-lethal concentration (μM)	$t_{1/2}$ (min)
	A	B	C	D	E	F	HepG2	HEK293	A549		
7	10	10	5	5–10	5–10	5–10	0.8 ± 0.2	16 ± 7	~50	-	6 ± 2
9	10	10	10	10	10	5–10	>50	>50	>50	30	20 ± 0
10	>10	5	5	10	5–10	5–10	>50	25–50	>50	10	>60
17	not active at 64 μM[b]						>50	>50	>50	-	27 ± 10
25	66% inhibition at 64 μM[b]						0.73 ± 0.12	18.0 ± 5.5	~50	-	56 ± 0.4

[a]: Tested at RIVM. Strain A: 1010900234, all-susceptible; strain B (drug-resistant, DR): 1011000848, resistant to isoniazid; strain C (multidrug-resistant, MDR): 1011200189, resistant to isoniazid, rifampicin, ethambutol, streptomycin, pyrazinamide; strain D (MDR): 1011200345, same as strain C plus resistant to ciprofloxacin and clarithromycin; strain E (extensively-drug-resistant, XDR): 1010900268, same as strain C plus resistant to kanamycin and capreomycin; strain F (XDR): 1010901542, resistant to isoniazid, rifampicin, ethambutol, streptomycin, kanamycin. [b]: Due to a limited number of tested compounds in the agreement, compounds 17 and 25 were not tested at RIVM. The results were obtained at the Leibniz Lung Center, against wildtype TB. [c] HepG2: human liver hepatocellular cells; HEK293: human embryonic kidney cells; A549: human lung epithelial cells. [d]: Metabolic stability was determined in human liver S9 fraction.

Fig. 6 (A) Minimum inhibitory concentration (MIC) determination on *E. coli* strain BL21 (DE3) pQEYAEM. The overexpression of *E. coli* IspC triggered by isopropyl-β-D-thiogalactopyranosid (IPTG) leads to a significant increase in MIC of fosmidomycin, but has little effect on hits **7**, **9** and **10**. (B) MIC determination on *E. coli* strain BL21 (DE3) pET22b-H6TEVEKMTDXS. The overexpression of *Mt*DXPS triggered by IPTG leads to significant attenuation of inhibitory activity of compounds **9** and **10**, but has little effect on compound **7** and fosmidomycin. (C) Cell-based antitubercular activity of compounds **7**, **9**, **10**, **17** and **25**, and their ADMET study results.

S11†). In addition, compound **10** displays a lower frequency-of-resistance development than clinically used antibiotics (Tables S5 and S6†). With these encouraging properties, the hit scaffolds **9** and **10** could be selected as early drug leads to develop antitubercular agents with a novel MOI, fighting against AMR.

Conclusions

In the midst of the current AMR crisis where current research efforts are struggling to fill the antibiotic pipeline, we show that a thorough study of the challenges and risks paired with strategic steps, makes the use of computational tools on difficult antibiotic targets as smooth as on conventional targets as exemplified by DXPS. We found that: (i) targeting the catalytic center under careful consideration of known parameters is essential. For antimicrobial targets with large, hydrophilic binding sites, tight natural binders and complex catalytic mechanisms, locating and focusing on the key amino acids involved in key interactions boosts the efficacy of hit identification. (ii) Pseudo-inhibitors are effective starting points to initiate LBVS. Introducing the concept of pseudo-inhibitors has helped us work with a target with few known inhibitors. The selection of versatile structures ensured successful LBVS rounds. (iii) Structure-based methods successfully support LBVS. Pharmacophore validation of the initial ligands (here pseudo-inhibitors) provided guidance for LBVS and

implementing modeling and docking to pre-order candidates helped to "enrich" the hits with the desired inhibition pattern. In addition, we confirmed that *in vitro* inhibitory potency of inhibitors should be evaluated correctly. For the antibiotic agents interfering with the behavior of multiple reaction components of the target, IC_{50} values may not truly reflect their inhibition activity. Inhibition or dissociation constants are preferred.

By strategic application of LBVS on the challenging target DXPS, we achieved small-molecule, drug-like antibiotic agents **9** and **10** as slow-, tight-binding inhibitors competitive with both cofactor and substrates, with submicromolar activity ($K_i^* = 0.2$–0.3 μM, $K_D = 0.2$ μM) against *Mt*DXPS, which are the most potent drug-like inhibitors against any DXPS homologue to date. Compounds **9** and **10** are selective over mammalian ThDP-dependent enzymes. SDM and SAR studies indicate that the H-bonding with His304 (His296) and hydrophobic interactions in the histidine-rich pocket are essential for the inhibitory activities. Meanwhile, compounds **9** and **10** display promising cell-based antitubercular activity (MIC 5–10 μM) against multiple susceptible and resistant strains. We confirmed DXPS as the intracellular target in *E. coli* and hope to do the same in *M. tuberculosis* in the future. The promising antitubercular activity and ADMET profile are encouraging for hit-to-lead optimization. They are the first antitubercular, drug-like agents targeting the MEP pathway discovered by CADD. Our approach should find application to other challenging targets.

Data availability

The datasets supporting this article have been uploaded as part of the ESI† material.

Author contributions

D. Z.: conceptualization, methodology, validation, formal analysis, investigation, writing, visualization. S. J.: methodology, validation, formal analysis, investigation, writing, visualization. T. M., C. S.: conceptualization, methodology, software, formal analysis, investigation. J. H., B. I., A. A., R. M. G., T. v. d. L., E. B., N. R.: formal analysis, investigation. M. A.: software, formal analysis. R. v. d. V., R. N., M. P.: investigation. R. M., M. F.: resources, supervision. J.-L. R., A. K. H. H.: resources, supervision, project administration, funding acquisition. All authors: writing – review & editing.

Conflicts of interest

The authors declare no competing financial interest.

Acknowledgements

The authors thank Alicia DeColli and Caren L. Freel Meyers for performing the PDH control experiments to confirm target specificity and their thorough feedback on the manuscript. D. Z. acknowledges support from the CSC Fellowship. Jörg Haupenthal and Andreas M. Kany are acknowledged for coordinating the *in vitro* ADMET profiling and Jeannine Jung and Tabea Wittmann for carrying out the corresponding *in vitro* assays. This work has been supported by The Netherlands Organisation for Scientific Research (LIFT grant: 731.015.414, A. K. H. H. and R. M. G.), the European Research Council (ERC Starting grant: 757913, A. K. H. H. and S. J.) and the Helmholtz Association's Initiative and Networking fund.

References

1 K. Lewis, The Science of Antibiotic Discovery, *Cell*, 2020, **181**(1), 29–45.
2 C. Agoni, M. E. Soliman, *et al.*, Druggability and drug-likeness concepts in drug design: are biomodelling and predictive tools having their say?, *J. Mol. Model.*, 2020, **26**(6), 120.
3 M. Miethke, R. Müller, *et al.*, Towards the sustainable discovery and development of new antibiotics, *Nat. Rev. Chem.*, 2021, **5**(10), 726–749.
4 S. Frantz, Better antibiotics through chemistry, *Nat. Rev. Drug Discovery*, 2004, **3**(11), 900–901.
5 K. Lewis, Platforms for antibiotic discovery, *Nat. Rev. Drug Discovery*, 2013, **12**(5), 371–387.
6 D. G. Brown, R. Tommasi, *et al.*, Trends and exceptions of physical properties on antibacterial activity for Gram-positive and Gram-negative pathogens, *J. Med. Chem.*, 2014, **57**(23), 10144–10161.
7 G. Mugumbate and J. P. Overington, The relationship between target-class and the physicochemical properties of antibacterial drugs, *Bioorg. Med. Chem.*, 2015, **23**(16), 5218–5224.
8 D. G. Brown and H. J. Wobst, A Decade of FDA-Approved Drugs (2010-2019): Trends and Future Directions, *J. Med. Chem.*, 2021, **64**(5), 2312–2338.
9 M. D. Shultz, Two Decades under the Influence of the Rule of Five and the Changing Properties of Approved Oral Drugs, *J. Med. Chem.*, 2019, **62**(4), 1701–1714.
10 S. B. Singh, K. Young and L. L. Silver, What is an "ideal" antibiotic? Discovery challenges and path forward, *Biochem. Pharmacol.*, 2017, **133**, 63–73.
11 R. Tommasi, A. A. Miller, *et al.*, ESKAPEing the labyrinth of antibacterial discovery, *Nat. Rev. Drug Discovery*, 2015, **14**(8), 529–542.
12 W. Yu and A. D. MacKerell, Computer-Aided Drug Design Methods, *Methods Mol. Biol.*, 2017, **1520**, 85–106.
13 A. Frank and M. Groll, The Methylerythritol Phosphate Pathway to Isoprenoids, *Chem. Rev.*, 2017, **117**(8), 5675–5703.
14 T. Masini and A. K. H. Hirsch, Development of inhibitors of the 2*C*-methyl-D-erythritol 4-phosphate (MEP) pathway enzymes as potential anti-infective agents, *J. Med. Chem.*, 2014, **57**(23), 9740–9763.
15 K. E. Price, A. R. O. John, *et al.*, Molecular Mechanism of Action of Antimalarial Benzoisothiazolones: Species-Selective Inhibitors of the Plasmodium spp. MEP Pathway enzyme, IspD, *Sci. Rep.*, 2016, **6**, 36777.

16 X. Wang and C. S. Dowd, The Methylerythritol Phosphate Pathway: Promising Drug Targets in the Fight against Tuberculosis, *ACS Infect. Dis.*, 2018, **4**(3), 278–290.
17 T. Masini, B. S. Kroezen and A. K. H. Hirsch, Druggability of the enzymes of the non-mevalonate-pathway, *Drug Discovery Today*, 2013, **18**(23–24), 1256–1262.
18 D. Bartee and C. L. Freel Meyers, Toward Understanding the Chemistry and Biology of 1-Deoxy-D-xylulose 5-Phosphate (DXP) Synthase: A Unique Antimicrobial Target at the Heart of Bacterial Metabolism, *Acc. Chem. Res.*, 2018, **51**(10), 2546–2555.
19 D. Hayashi, J. Ohkanda, *et al.*, Antimicrobial *N*-(2-chlorobenzyl)-substituted hydroxamate is an inhibitor of 1-deoxy-D-xylulose 5-phosphate synthase, *Chem. Commun.*, 2013, **49**(49), 5535–5537.
20 Y. Matsue, T. Kuzuyama, *et al.*, The herbicide ketoclomazone inhibits 1-deoxy-D-xylulose 5-phosphate synthase in the 2-*C*-methyl-D-erythritol 4-phosphate pathway and shows antibacterial activity against Haemophilus influenzae, *J. Antibiot.*, 2010, **63**(10), 583–588.
21 C. Mueller, H. K. Lichtenthaler, *et al.*, Properties and inhibition of the first two enzymes of the non-mevalonate pathway of isoprenoid biosynthesis, *Biochem. Soc. Trans.*, 2000, **28**(6), 792–793.
22 M. Okuhara, H. Imanaka, *et al.*, Studies on new phosphonic acid antibiotics. I. FR-900098, isolation and characterization, *J. Antibiot.*, 1980, **33**(1), 13–17.
23 S. Sanders, C. L. Freel Meyers, *et al.*, Growth medium-dependent antimicrobial activity of early stage MEP pathway inhibitors, *PLoS One*, 2018, **13**(5), e0197638.
24 J. M. Smith, C. L. Freel Meyers, *et al.*, Targeting DXP synthase in human pathogens: enzyme inhibition and antimicrobial activity of butylacetylphosphonate, *J. Antibiot.*, 2014, **67**, 77–83.
25 T. Umeda, K. T. Nakamura, *et al.*, Molecular basis of fosmidomycin's action on the human malaria parasite Plasmodium falciparum, *Sci. Rep.*, 2011, **1**, 9.
26 E. Yeh and J. L. DeRisi, Chemical rescue of malaria parasites lacking an apicoplast defines organelle function in blood-stage Plasmodium falciparum, *PLoS Biol.*, 2011, **9**(8), e1001138.
27 J. G. Geist, F. Diederich, *et al.*, Thiazolopyrimidine inhibitors of 2-methylerythritol 2,4-cyclodiphosphate synthase (IspF) from Mycobacterium tuberculosis and Plasmodium falciparum, *ChemMedChem*, 2010, **5**(7), 1092–1101.
28 L. S. Imlay, A. R. Odom, *et al.*, Plasmodium IspD (2-*C*-Methyl-D-erythritol 4-Phosphate Cytidylytransferase), an Essential and Druggable Antimalarial Target, *ACS Infect. Dis.*, 2015, **1**(4), 157–167.
29 W. Wu, E. Yeh, *et al.*, A chemical rescue screen identifies a Plasmodium falciparum apicoplast inhibitor targeting MEP isoprenoid precursor biosynthesis, *Antimicrob. Agents Chemother.*, 2015, **59**(1), 356–364.
30 G. Mombo-Ngoma, P. G. Kremsner, *et al.*, Efficacy and Safety of Fosmidomycin-Piperaquine as Non artemisinin-Based Combination Therapy for Uncomplicated Falciparum Malaria: A Single-Arm, Age De-escalation Proof-of-Concept Study in Gabon, *Clin. Infect. Dis.*, 2018, **66**(12), 1823–1830.
31 World Health Organisation. *Global tuberculosis report*, 2020.
32 A. Gimeno, S. Garcia-Vallvé, *et al.*, The Light and Dark Sides of Virtual Screening: What Is There to Know?, *Int. J. Mol. Sci.*, 2019, **20**(6), 1375–1399.
33 L. A. B. Basta, C. L. F. Meyers, *et al.*, Defining critical residues for substrate binding to 1-deoxy-D-xylulose 5-phosphate synthase – active site substitutions stabilize the predecarboxylation intermediate C2α-lactylthiamin diphosphate, *FEBS J.*, 2014, **281**(12), 2820–2837.
34 L. A. Brammer, C. F. Meyers, *et al.*, 1-Deoxy-D-xylulose 5-phosphate synthase catalyzes a novel random sequential mechanism, *J. Biol. Chem.*, 2011, **286**(42), 36522–36531.
35 A. Y. Chen, S. M. Cohen, *et al.*, Targeting Metalloenzymes for Therapeutic Intervention, *Chem. Rev.*, 2019, **119**(2), 1323–1455.
36 T. Masini, A. K. H. Hirsch, *et al.*, Validation of a homology model of Mycobacterium tuberculosis DXS: rationalization of observed activities of thiamine derivatives as potent inhibitors of two orthologues of DXS, *Org. Biomol. Chem.*, 2015, **13**(46), 11263–11277.
37 T. Masini, A. K. H. Hirsch, *et al.*, De novo fragment-based design of inhibitors of DXS guided by spin-diffusion-based NMR spectroscopy, *Chem. Sci.*, 2014, **5**(9), 3543–3551.
38 S. Xiang, L. Tong, *et al.*, Crystal structure of 1-deoxy-D-xylulose 5-phosphate synthase, a crucial enzyme for isoprenoids biosynthesis, *J. Biol. Chem.*, 2007, **282**(4), 2676–2682.
39 F. Berenger, O. Vu and J. Meiler, Consensus queries in ligand-based virtual screening experiments, *J. Cheminf.*, 2017, **9**(1), 60.
40 A. Schüller, G. Schneider, *et al.*, A pseudo-ligand approach to virtual screening, *Comb. Chem. High Throughput Screening*, 2006, **9**(5), 359–364.
41 Y. Tanrikulu and G. Schneider, Pseudoreceptor models in drug design: bridging ligand- and receptor-based virtual screening, *Nat. Rev. Drug Discovery*, 2008, **7**(8), 667–677.
42 G. Wolber and W. Sippl, Pharmacophore Identification and Pseudo-Receptor Modeling. in *The Practice of Medicinal Chemistry*, ed. Wermuth, C. G., Elsevier Science & Technology, 4th edn, 2015; pp. 489–510. DOI: **10.1016/B978-0-12-417205-0.00021-3**.
43 J. K. White, H. L. Woodcock, *et al.*, Thiamin Diphosphate Activation in 1-Deoxy- d -xylulose 5-Phosphate Synthase: Insights into the Mechanism and Underlying Intermolecular Interactions, *J. Phys. Chem. B*, 2016, **120**(37), 9922–9934.
44 S. Augustin, *LeadIT version 2.3.2*. BioSolveIT GmbH:An der Ziegelei, 2021, vol. 79, p. 53757.
45 09 Chemical Computing Group, ULC:1010 Sherbrooke St. West, Suite #910, *Molecular Operating Environment. 2020*, Montreal, OC, Canada, H3A 2R7, 2022.
46 K. Stierand, P. C. Maass and M. Rarey, Molecular complexes at a glance: automated generation of two-dimensional complex diagrams, *Bioinformatics*, 2006, **22**(14), 1710–1716.

47 M. Awale and J.-L. Reymond, Atom pair 2D-fingerprints perceive 3D-molecular shape and pharmacophores for very fast virtual screening of ZINC and GDB-17, *J. Chem. Inf. Model.*, 2014, **54**(7), 1892–1907.
48 F. Kilchmann, J.-L. Reymond, *et al.*, Discovery of a Selective Aurora A Kinase Inhibitor by Virtual Screening, *J. Med. Chem.*, 2016, **59**(15), 7188–7211.
49 L. C. Ozhathil, H. Abriel, *et al.*, Identification of potent and selective small molecule inhibitors of the cation channel TRPM4, *Br. J. Pharmacol.*, 2018, **175**(12), 2504–2519.
50 C. Simonin, J.-L. Reymond, *et al.*, Optimization of TRPV6 Calcium Channel Inhibitors Using a 3D Ligand-Based Virtual Screening Method, *Angew. Chem., Int. Ed.*, 2015, **54**(49), 14748–14752.
51 J. B. Baell and G. A. Holloway, New substructure filters for removal of pan assay interference compounds (PAINS) from screening libraries and for their exclusion in bioassays, *J. Med. Chem.*, 2010, **53**(7), 2719–2740.
52 T. Zhu, K. E. Hevener, *et al.*, Hit identification and optimization in virtual screening: practical recommendations based on a critical literature analysis, *J. Med. Chem.*, 2013, **56**(17), 6560–6572.
53 J. R. Huth, P. J. Hajduk, *et al.*, ALARM NMR: a rapid and robust experimental method to detect reactive false positives in biochemical screens, *J. Am. Chem. Soc.*, 2005, **127**(1), 217–224.
54 B. K. Shoichet, Screening in a spirit haunted world, *Drug Discovery Today*, 2006, **11**(13–14), 607–615.
55 D. Bartee and C. L. Freel Meyers, Targeting the Unique Mechanism of Bacterial 1-Deoxy-d-xylulose-5-phosphate Synthase, *Biochem*, 2018, **57**(29), 4349–4356.
56 C. Yung-Chi and W. H. Prusoff, Relationship between the inhibition constant (KI) and the concentration of inhibitor which causes 50 per cent inhibition (I50) of an enzymatic reaction, *Biochem. Pharmacol.*, 1973, **22**(23), 3099–3108.
57 R. P. Jumde, A. K. H. Hirsch, *et al.*, Hit-optimization using target-directed dynamic combinatorial chemistry: development of inhibitors of the anti-infective target 1-deoxy-d-xylulose-5-phosphate synthase, *Chem. Sci.*, 2021, **12**(22), 7775–7785.
58 P. Kuzmic, Program DYNAFIT for the analysis of enzyme kinetic data: application to HIV proteinase, *Anal. Biochem.*, 1996, **237**(2), 260–273.
59 A. Marcozzi, A. K. H. Hirsch, *et al.*, Phage Display on the Anti-infective Target 1-Deoxy-d-xylulose-5-phosphate Synthase Leads to an Acceptor-Substrate Competitive Peptidic Inhibitor, *ChemBioChem*, 2018, **19**(1), 58–65.
60 D. Bartee, C. L. Freel Meyers, *et al.*, Enamide Prodrugs of Acetyl Phosphonate Deoxy-d-xylulose-5-phosphate Synthase Inhibitors as Potent Antibacterial Agents, *ACS Infect. Dis.*, 2019, **5**(3), 406–417.
61 J. G. Topliss, Utilization of operational schemes for analog synthesis in drug design, *J. Med. Chem.*, 1972, **15**(10), 1006–1011.

6.2 Further work on the LBVS hit classes

We found strong evidence that *Mt*DXPS is a target of aminothiazole **1** in *M. tuberculosis*, but the low micromolar activity against the pathogen suggests additional targets. In *P. falciparum*, we could not identify the target with the employed methods. For both pathogens we continued with different strategies to validate and to identify the target of aminothiazole **1**.

6.2.1 Contributions

Sandra Johannsen has synthesized compounds **1** and **2** and has organized shipment of all compounds to Cornell. Furthermore, she has written this summary and coordinated the proceeding of the experiments. Curtis Engelhart has performed all experiments described below.

6.2.2 Target validation in *M. tuberculosis*

Aminothiazole hit **1** (number corresponds to the manuscript in Chapter 3.5; in Chapter 6.1 the compound number is **10**) was sent to the lab of Dirk Schnappinger at Weill Cornell Medicine Graduate School of Medical Sciences for target validation by using a *dxs1* Clustered Regularly Interspaced Short Palindromic Repeats Interference (CRISPRi) TetOFF mutant and for frequency of resistance studies. In preliminary activity assays, they could not reproduce the MIC of 5–10 µM for aminothiazole **1**.[126] In their growth assays, the compound was approximately ten-fold less active (**Figure S 78**).

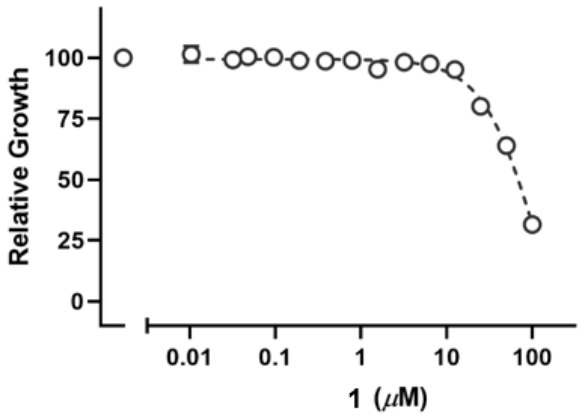

Figure S 78: Relative growth of *M. tuberculosis* H37Rv with different concentrations of aminothiazole **1**.

Nevertheless, aminothiazole **1** was tested against the *dxs1* CRISPRi TetOFF mutant (**Figure S 79**). The experiment was performed by adding anhydrotetracycline (Atc) in

different concentrations to the cells.[220] This induces suppression of DXPS expression, which results in less protein in the cell. If an inhibitor of DXPS is present, its MIC should be decreased, as less compound is needed to inhibit growth. In an initial experiment, the MIC of **1**, was decreased with increasing concentrations of Atc (**Figure S 79A**). Repeating the assay resulted in a much weaker effect and it cannot be confirmed that DXPS is a target of aminothiazole **1** (**Figure S 79B**).

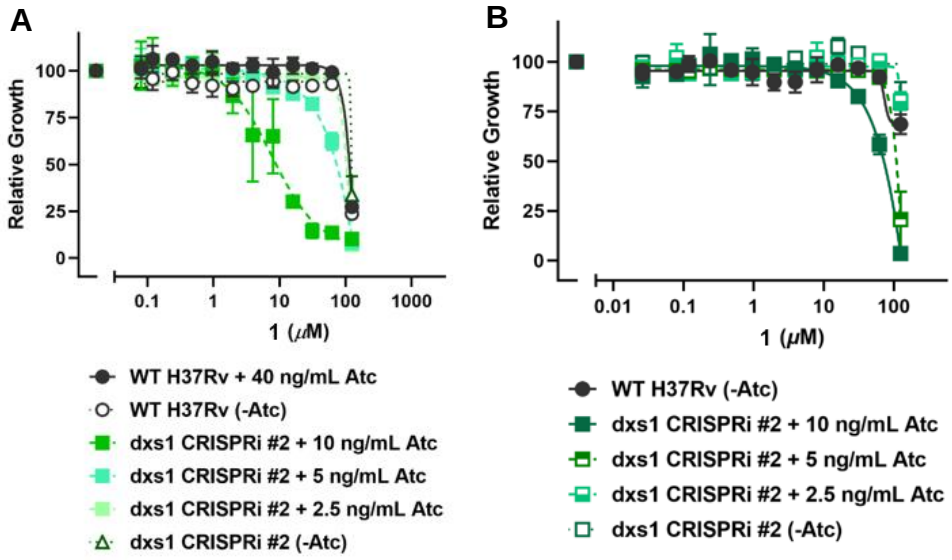

Figure S 79: MIC of compound **1** against *M. tuberculosis* H37Rv and *dxs1* CRISPRi TetOFF mutant at different Atc concentrations to reduce DXPS expression. (**A**) Initial experiment, (**B**) follow-up experiment.

As can be seen in **Figure S 79**, the compound was only tested up to its solubility limit of 100 µM, which corresponds to the MIC value and especially in the second experiment, this was not enough to stop bacterial growth. To get more reliable results, we looked for a better inhibitor among the already synthesized aminothiazole derivatives. For that, we re-synthesized **2**, since this compound has a MIC of 1.25–2.5 µM against multiple strains of *M. tuberculosis*, including multi- and extensively drug-resistant strains in previous studies.[221] As for aminothiazole **1**, it was not possible to reproduce these values. Instead, three alternative compounds with promising MIC values of around 10 µM were identified (**Table S 26**). They all contain a pyridine instead of the aminothiazole ring (**3**, **4**, **5**) and the left-hand ring carries either two methyl groups or a chloro- and a methyl-substituent.

Table S 26: Comparison of IC_{50} against *Mt*DXPS and MIC values of aminothiazole derivatives. MIC determined against *M. tuberculosis* H37Rv.

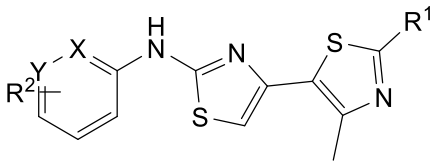

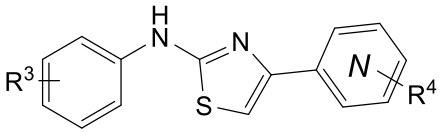

Cpd.	R^1	X	Y	R^2	R^3	R^4	N	IC_{50} [µM][221]	MIC [µM]
1	NH_2	CH	CH	4-CF_3	-	-	-	45 ± 9	>100
2	CH_3	CH	CH	2-Me, 3-Cl	-	-	-	37 ± 5	59
3	-	-	-	-	3,4-Me	-	2-N	55 ± 5	17
4	-	-	-	-	2,5-Me	-	2-N	25 ± 6	15
5	-	-	-	-	2-Me, 4-Cl	-	2-N	n.d.	25
6	-	-	-	-	4-CF_3	-	4-N	n.d.	>250
7	NH_2	CH	CH	2-CF_3	-	-	-	56 ± 4	>250
8	NH_2	CH	CH	3-CF_3	-	-	-	36 ± 9	230
9	NH_2	N	CH	4-Cl	-	-	-	56 ± 4	58
10	NH_2	CH	CH	3-OMe	-	-	-	n.d.	>250
11	CH_3	CH	CH	4-CF_3	-	-	-	n.d.	30
12	-	-	-	-	3,4-Me	3,4-OH	-	42 ± 7	>250
13	-	-	-	-	3-CF_3	2,4-OH	-	48 ± 9	>250
14	-	-	-	-	4-CF_3	2,4-OH	-	n.d.	>250

n.d. = not determined.

A variety of similar aminothiazoles have been identified by the group of Tanya Parish as good inhibitors of *M. tuberculosis* growth with a MIC of 2–11 µM (**Table S 27**).[222] The only difference of compounds **15**–**18** is the substitution pattern of the phenyl ring. However, they found that inserting a carbonyl group in between the aminothiazole and the phenyl ring (compound **19**) boosts activity to 300 nM. In this initial publication, they also tried to elucidate whether iron chelation between the three nitrogen atoms was responsible for the good activity, but this was not the case.

Table S 27: Activity of aminothiazoles against *M. tuberculosis* H37Rv identified by Parish and co-workers.

Cpd.	Structure	MIC [µM]
15	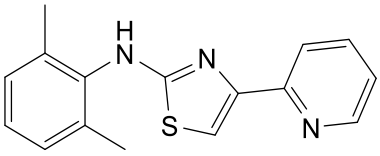	4.5
16	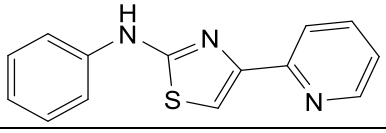	3.7

Cpd.	Structure	MIC [µM]
17	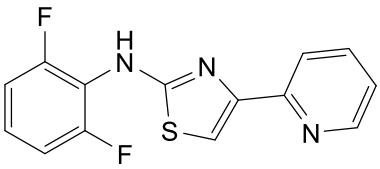	2.1
18	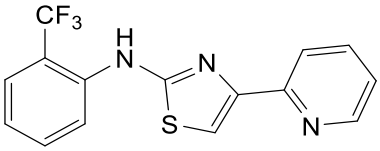	11
19	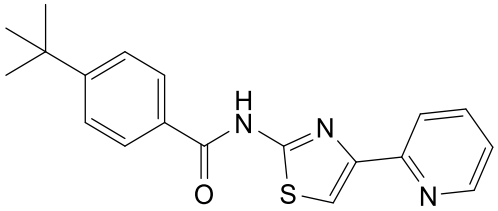	0.3

In a follow-up publication, enolase was first confirmed as a target of **19** in a pull down assay in *M. smegmatis*, and later in enolase over- and underexpressing strains in *M. tuberculosis*.[223] Enolase is part of the essential glycolysis/gluconeogenesis pathway and therefore, a probable target. However, purification of *M. tuberculosis* enolase was not possible and so, human enolase with a sequence similarity of 49.6% was chosen to confirm on-target activity. By confirming inhibition of human enolase activity with a selection of aminothiazoles between 35% and 90%, they also confirmed potential side effects on human cells, which pose a challenge for further development of the class. Although, enolase is highly conserved across organisms, they argue that selectivity can be achieved by careful synthetic modifications.

It was decided to test aminothiazole **1** against an *eno* CRISPRi TetOFF mutant. It works like the *dxs1* CRISPRi TetOFF mutant described above. In the initial and in the follow-up experiment, the MIC of **1** was decreased when more Atc was added (**Figure S 80**). This suggests that enolase is a target of aminothiazole **1** in *M. tuberculosis*.

To continue this investigation, additional experiments are planned. First, we will test if compound **3** as a representative of the pyridine-containing class also inhibits enolase and/or DXPS. Additionally, frequency of resistance studies are ongoing, but have not given any results yet.

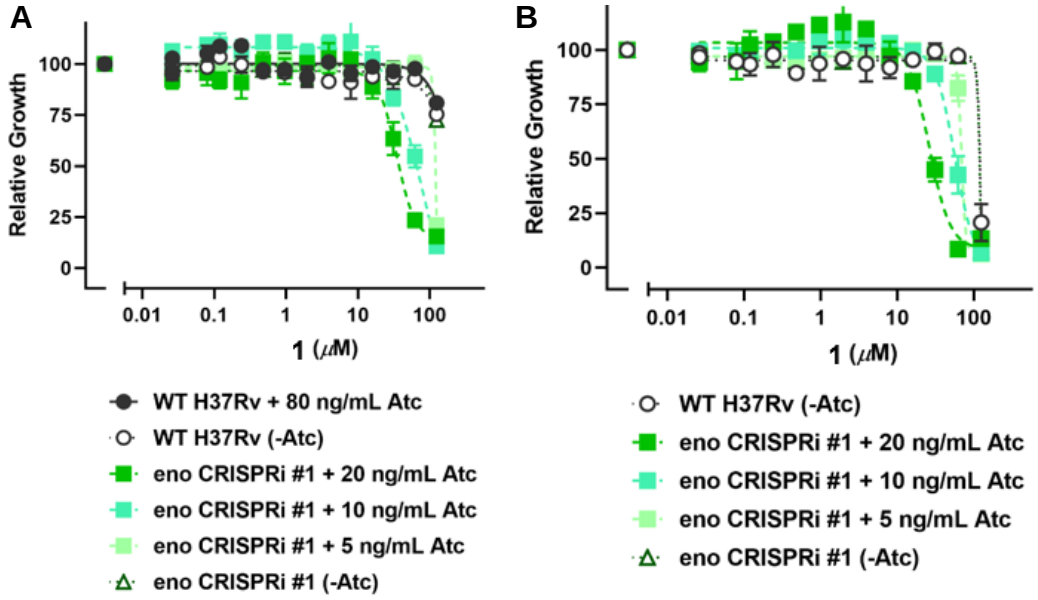

Figure S 80: MIC of compound **1** against *M. tuberculosis* H37Rv and *eno* CRISPRi TetOFF mutant at different Atc concentration to reduce enolase expression. (**A**) Initial experiment, (**B**) follow-up experiment.

6.2.3 Synthesis of a chemical probe for target validation in *P. falciparum*

Our previous investigations presented in Chapter 3.5 did not result in validation of DXPS as target of aminothiazole **1**. Therefore, we decided to synthesize a chemical probe to perform target fishing from cell lysate. A chemical probe is a derivative of a hit compound that retains activity, but carries functional groups that enable covalent binding to proteins. There are several methods available that will not be discussed here in detail.[224] After extensive SAR studies, compound **1** was the most active against *P. falciparum* that we identified so the probe design was based on its structure. We chose a diazirine on one side of the molecule and an alkyne on the other.[225] If the probe is incubated with cell lysate from *P. falciparum* and binds to a protein, the diazirine can be activated to form a carbene, which covalently binds to this protein. The alkyne can then be functionalized with biotin and fished from the lysate. Mass analysis of the complex mass identifies the target.

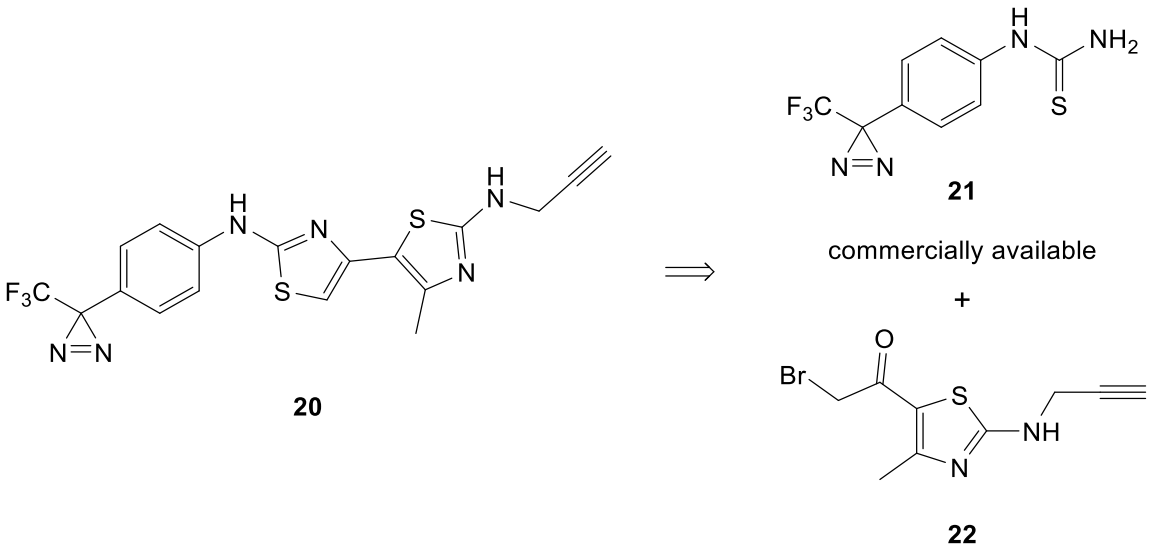

Scheme S 1: Retrosynthetic approach for compound **20**.

The synthesis of compound **20** was planned according to synthetic and commercial availability (**Scheme S 1**). Some SAR knowledge was also taken into account. The *para*-position on the phenyl-ring was the easiest to modify with a diazirine, since building block **21** is commercially available. The final reaction step to form the thiazole ring in the middle is also mild enough to keep the diazirine intact. The synthesis of building block **22** was started from propagylamine (**23**) and KSCN to form thioaurea **24** in quantitative yield (**Scheme S 2**). The following reaction converted only for 20% and then stopped. Heating and addition of base did not increase the conversion after several days. In the end, the reaction was stopped and 15% of the product **25** could be isolated after purification.

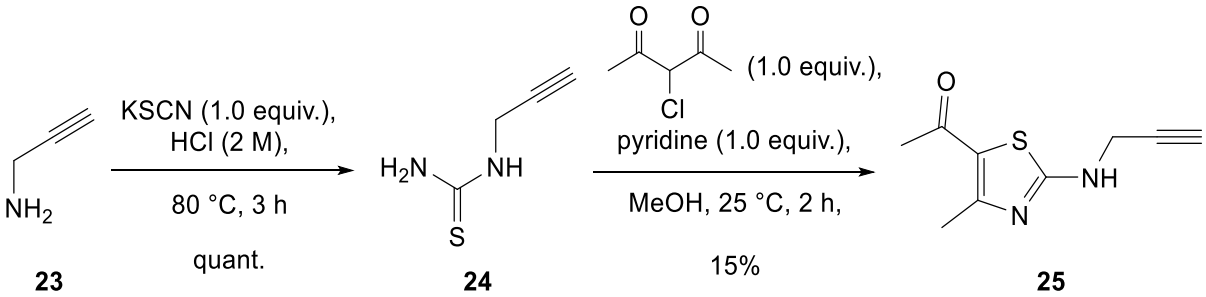

Scheme S 2: Initial reactions to synthesize building block **22**.

To improve the conversion of the reaction, it was repeated in dry EtOH and in pyridine as the solvent. In both cases, heating did not result in a higher conversion. On a small scale, compound **25** was brominated by the addition of bromine in chloroform, in hope that a mixture of the single bromination product and the double or triple brominated compound forms that could be purified. However, the bromination occurred only on the

double bond. There are two options to continue with this synthesis: Either the triple bond has to be protected for the bromination (a first trial with trimethylsilyl chloride failed) or selective bromination conditions have to be found that keep the alkyne intact.

6.2.4 Synthesis of LBVS hit derivatives

_N_-(3-Chloro-2-methylphenyl)-2',4'-dimethyl-[4,5'-bithiazol]-2-amine (2)

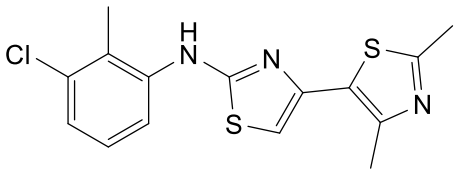

Compound **2** was synthesized following a literature procedure.[126]

^{1}H NMR (500 MHz, $(CD_3)_2SO$) δ (ppm) = 9.63 (s, 1H), 7.86 (dd, *J* = 7.3, 2.0 Hz, 1H), 7.58–7.08 (m, 2H), 6.93 (s, 1H), 2.57 (s, 3H), 2.49 (s, 3H), 2.32 (s, 3H). ^{13}C NMR (126 MHz, $(CD_3)_2SO$) δ (ppm) = 164.9, 162.1, 147.07, 142.1, 140.8, 134.0, 127.4, 127.3, 126.6, 124.4, 120.4, 104.1, 18.6, 16.9, 15.0. HR-ESI-MS: calculated for $C_{15}H_{15}ClN_3S_2$ $[M+H]^+$ 336.0390, found 336.0390.

6.2.5 Growth inhibition of aminothiazoles against *M. tuberculosis*

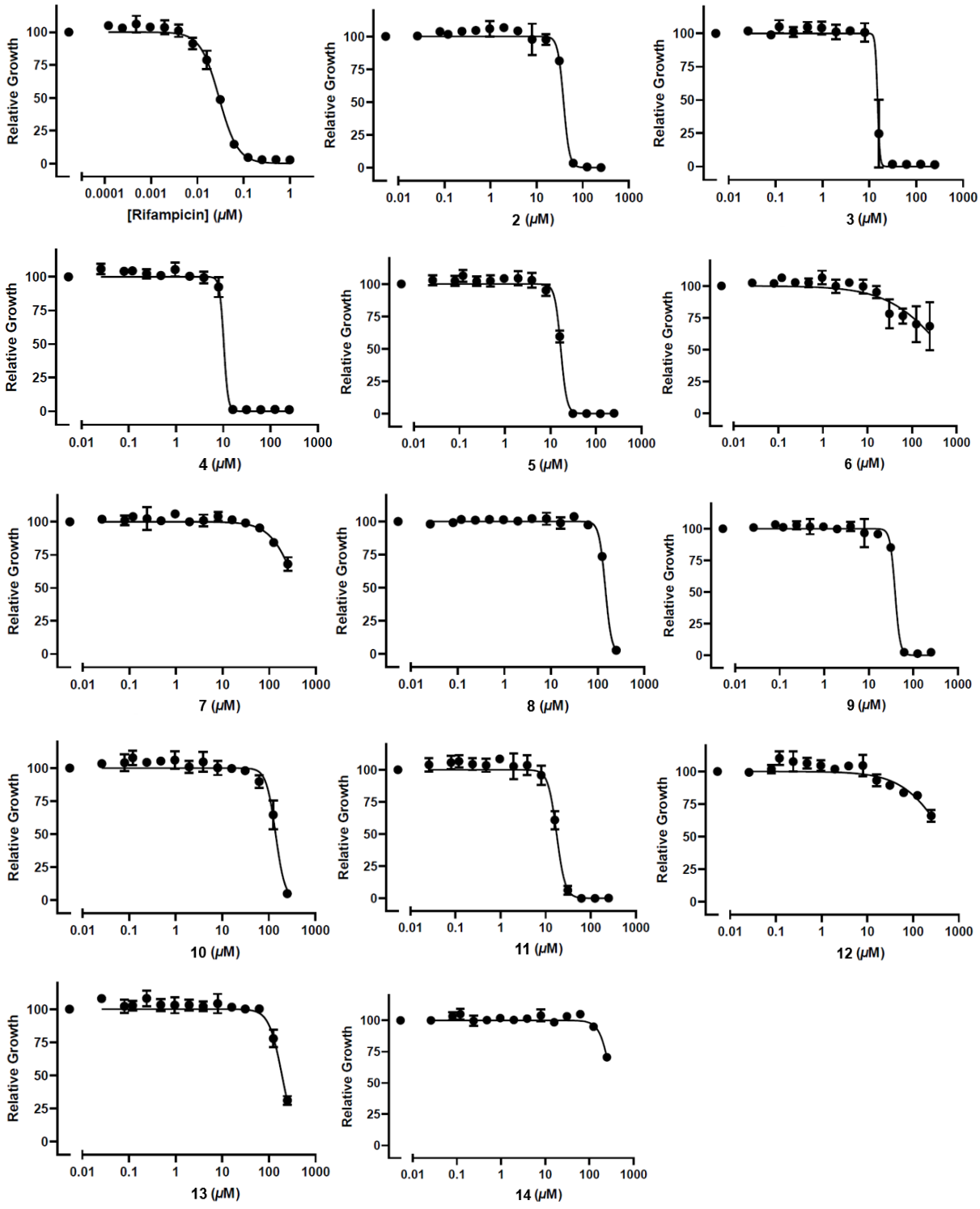

Figure S 81: MIC determination of different aminothiazoles against *M. tuberculosis* H37Rv.

6.2.6 Synthesis of probe for target validation

1-(Prop-2-yn-1)thiourea (24)

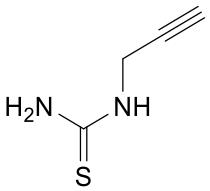

Compound **24** was synthesized following a literature procedure.[226]

1-(4-Methyl-2-(prop-1-yn-1-ylamino)thiazol-5-yl)ethan-1-one (25)

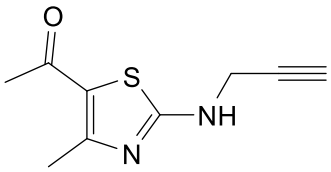

Compound **25** was synthesized following a literature procedure.[227] Compound **24** (3.5 mmol, 400 mg), 3-chloro-2,4-pentanedione (3.5 mmol, 400 µL, 1.0 equiv.) and pyridine (3.5 mmol, 280 µL, 1.0 equiv.) were dissolved in methanol (35 mL) and stirred at 25 °C for 2 h. Water (10 mL) and ethyl acetate (30 mL) were added, and the layers were separated. The organic layer was dried over Na_2SO_4, filtered and concentrated *in vacuo*. Purification by flash column chromatography (CH_2Cl_2/MeOH, gradient up to 10% MeOH) did not result in a clean product. After preparative HPLC the final product (0.5 mmol, 100 mg, 15%) was obtained as a white solid.

^{1}H NMR (500 MHz, CD_3OD): δ (ppm) = 4.13 (d, *J* = 2.5 Hz, 2H), 2.69 (t, *J* = 2.5 Hz, 1H), 2.53 (s, 3H), 2.42 (s, 3H). ^{13}C NMR (126 MHz, CD_3OD) δ (ppm) = 191.78, 172.0, 159.9, 123.1, 79.8, 73.2, 34.4, 29.7, 18.6. HR-ESI-MS: calculated for $C_9H_{11}N_2OS$ $[M+H]^+$ 195.0587, found 195.0581. Purity: >99%.

References

(1) Oliveira, D. M. P. de; Forde, B. M.; Kidd, T. J.; Harris, P. N. A.; Schembri, M. A.; Beatson, S. A.; Paterson, D. L.; Walker, M. J. Antimicrobial Resistance in ESKAPE Pathogens. *Clin. Microbiol. Rev.* **2020**, *33* (3), e00181-19.

(2) Mahoney, A. R.; Safaee, M. M.; Wuest, W. M.; Furst, A. L. The silent pandemic: Emergent antibiotic resistances following the global response to SARS-CoV-2. *iScience* **2021**, *24* (4), 102304.

(3) World Health Organisation. Prioritization of pathogens to guide discovery, research and development of new antibiotics for drug-resistant bacterial infections, including tuberculosis, **2017**.

(4) World Health Organisation. Global tuberculosis report, **2020**.

(5) Singh, R.; Dwivedi, S. P.; Gaharwar, U. S.; Meena, R.; Rajamani, P.; Prasad, T. Recent updates on drug resistance in Mycobacterium tuberculosis. *J. Appl. Microbiol.* **2020**, *128* (6), 1547–1567.

(6) World Health Organisation. World malaria report 2020: 20 years of global progress and challenges, **2020**.

(7) World Health Organisation. Artemisinin resistance and artemisinin-based combination therapy efficacy:*Status Report*, **2018**.

(8) Ashley, E. A.; Dhorda, M.; Fairhurst, R. M.; Amaratunga, C.; Lim, P.; Suon, S.; Sreng, S.; Anderson, J. M.; Mao, S.; Sam, B.; Sopha, C.; Chuor, C. M.; Nguon, C.; Sovannaroth, S.; Pukrittayakamee, S.; Jittamala, P.; Chotivanich, K.; Chutasmit, K.; Suchatsoonthorn, C.; Runcharoen, R.; Hien, T. T.; Thuy-Nhien, N. T.; Thanh, N. V.; Phu, N. H.; Htut, Y.; Han, K.-T.; Aye, K. H.; Mokuolu, O. A.; Olaosebikan, R. R.; Folaranmi, O. O.; Mayxay, M.; Khanthavong, M.; Hongvanthong, B.; Newton, P. N.; Onyamboko, M. A.; Fanello, C. I.; Tshefu, A. K.; Mishra, N.; Valecha, N.; Phyo, A. P.; Nosten, F.; Yi, P.; Tripura, R.; Borrmann, S.; Bashraheil, M.; Peshu, J.; Faiz, M. A.; Ghose, A.; Hossain, M. A.; Samad, R.; Rahman, M. R.; Hasan, M. M.; Islam, A.; Miotto, O.; Amato, R.; MacInnis, B.; Stalker, J.; Kwiatkowski, D. P.; Bozdech, Z.; Jeeyapant, A.; Cheah, P. Y.; Sakulthaew, T.; Chalk, J.; Intharabut, B.; Silamut, K.; Lee, S. J.; Vihokhern, B.; Kunasol, C.; Imwong, M.; Tarning, J.; Taylor, W. J.; Yeung, S.; Woodrow, C. J.; Flegg, J. A.; Das, D.; Smith, J.; Venkatesan, M.; Plowe, C. V.; Stepniewska, K.; Guerin, P. J.; Dondorp, A. M.; Day, N. P.; White, N. J. Spread of artemisinin resistance in Plasmodium falciparum malaria. *N. Engl. J. Med.* **2014**, *371* (5), 411–423.

(9) Reygaert, W. C. An overview of the antimicrobial resistance mechanisms of bacteria. *AIMS Microbiol.* **2018**, *4* (3), 482–501.

(10) Martinez, J. L. General principles of antibiotic resistance in bacteria. *Drug Discov. Today Technol.* **2014**, *11*, 33–39.

(11) Christaki, E.; Marcou, M.; Tofarides, A. Antimicrobial Resistance in Bacteria: Mechanisms, Evolution, and Persistence. *J. Mol. Evol.* **2020**, *88* (1), 26–40.

(12) Heuston, S.; Begley, M.; Gahan, C. G. M.; Hill, C. Isoprenoid biosynthesis in bacterial pathogens. *Microbiology* **2012**, *158* (6), 1389–1401.

(13) Bailey, A. M.; Mahapatra, S.; Brennan, P. J.; Crick, D. C. Identification, cloning, purification, and enzymatic characterization of Mycobacterium tuberculosis 1-deoxy-D-xylulose 5-phosphate synthase. *Glycobiology* **2002**, *12* (12), 813–820.

(14) Tillery, L. M.; Barrett, K. F.; Dranow, D. M.; Craig, J.; Shek, R.; Chun, I.; Barrett, L. K.; Phan, I. Q.; Subramanian, S.; Abendroth, J.; Lorimer, D. D.; Edwards, T. E.; van Voorhis, W. C. Toward a structome of Acinetobacter baumannii drug targets. *Protein Sci.* **2020**, *29* (3), 789–802.

(15) Putra, S. R.; Disch, A.; Bravo, J. M.; Rohmer, M. Distribution of mevalonate and glyceraldehyde 3-phosphate/pyruvate routes for isoprenoid biosynthesis in some gram-negative bacteria and mycobacteria. *FEMS Microbiol. Lett.* **1998**, *164* (1), 169–175.

(16) Ramos, P. I. P.; Fernández Do Porto, D.; Lanzarotti, E.; Sosa, E. J.; Burguener, G.; Pardo, A. M.; Klein, C. C.; Sagot, M.-F.; Vasconcelos, A. T. R. de; Gales, A. C.; Marti, M.; Turjanski, A. G.; Nicolás, M. F. An integrative, multi-omics approach towards the prioritization of Klebsiella pneumoniae drug targets. *Sci. Rep.* **2018**, *8* (1), 10755.

(17) Rohmer, M.; Knani, M.; Simonin, P.; Sutter, B.; Sahm, H. Isoprenoid biosynthesis in bacteria: a novel pathway for the early steps leading to isopentenyl diphosphate. *Biochem.* **1993**, *295* (2), 517–524.

(18) van Cuon, D. Enhanced β-Carotene Biosynthesis in Recombinant Escherichia Coli Harboring the Bottom Portion of Mevalonate Pathway of Enterococcus Faecium VTCC-B-935 Isolated in Vietnam. *J. appl. biotechnol.* **2017**, *3* (4), 374–379.

(19) Hammond, R. K.; White, D. C. Carotenoid formation by Staphylococcus aureus. *J. Bacteriol. Res.* **1970**, *103* (1), 191–198.

(20) Pérez-Gil, J.; Bergua, M.; Boronat, A.; Imperial, S. Cloning and functional characterization of an enzyme from Helicobacter pylori that catalyzes two steps of the methylerythritol phosphate pathway for isoprenoid biosynthesis. *Biochim. Biophys. Acta* **2010**, *1800* (9), 919–928.

(21) Eberl, M.; Hintz, M.; Reichenberg, A.; Kollas, A.-K.; Wiesner, J.; Jomaa, H. Microbial isoprenoid biosynthesis and human γδ T cell activation. *FEBS Lett.* **2003**, *544* (1-3), 4–10.

(22) Wilding, E. I.; Brown, J. R.; Bryant, A. P.; Chalker, A. F.; Holmes, D. J.; Ingraham, K. A.; Iordanescu, S.; So, C. Y.; Rosenberg, M.; Gwynn, M. N. Identification, evolution, and essentiality of the mevalonate pathway for isopentenyl diphosphate biosynthesis in gram-positive cocci. *J. Bacteriol. Res.* **2000**, *182* (15), 4319–4327.

(23) Boucher, Y.; Doolittle, W. F. The role of lateral gene transfer in the evolution of isoprenoid biosynthesis pathways. *Mol. Microbiol.* **2000**, *37* (4), 703–716.

(24) Jomaa, H.; Wiesner, J.; Sanderbrand, S.; Altincicek, B.; Weidemeyer, C.; Hintz, M.; Türbachova, I.; Eberl, M.; Zeidler, J.; Lichtenthaler, H. K.; Soldati, D.; Beck, E. Inhibitors of the nonmevalonate pathway of isoprenoid biosynthesis as antimalarial drugs. *Science* **1999**, *285* (5433), 1573–1576.

(25) Brown, A. C.; Eberl, M.; Crick, D. C.; Jomaa, H.; Parish, T. The nonmevalonate pathway of isoprenoid biosynthesis in Mycobacterium tuberculosis is essential and transcriptionally regulated by Dxs. *J. Bacteriol. Res.* **2010**, *192* (9), 2424–2433.

(26) Brown, A. C.; Parish, T. Dxr is essential in Mycobacterium tuberculosis and fosmidomycin resistance is due to a lack of uptake. *BMC Microbiol.* **2008**, *8*, 78.

(27) Cornish, R. M.; Roth, J. R.; Poulter, C. D. Lethal mutations in the isoprenoid pathway of Salmonella enterica. *J. Bacteriol. Res.* **2006**, *188* (4), 1444–1450.

(28) Kuzuyama, T.; Takahashi, S.; Seto, H. Construction and characterization of Escherichia coli disruptants defective in the yaeM gene. *Biosci. Biotechnol. Biochem.* **1999**, *63* (4), 776–778.

(29) Rodríguez-Concepción, M.; Boronat, A. Elucidation of the methylerythritol phosphate pathway for isoprenoid biosynthesis in bacteria and plastids. A metabolic milestone achieved through genomics. *Plant Physiol.* **2002**, *130* (3), 1079–1089.

(30) Lichtenthaler, H. K. Non-mevalonate isoprenoid biosynthesis: enzymes, genes and inhibitors. *Biochem. Soc. Trans.* **2000**, *28* (6), 785–789.

(31) Masini, T.; Hirsch, A. K. H. Development of inhibitors of the 2C-methyl-D-erythritol 4-phosphate (MEP) pathway enzymes as potential anti-infective agents. *J. Med. Chem.* **2014**, *57* (23), 9740–9763.

(32) Hill, R. E.; Himmeldirk, K.; Kennedy, I. A.; Pauloski, R. M.; Sayer, B. G.; Wolf, E.; Spenser, I. D. The Biogenetic Anatomy of Vitamin B 6. *J. Biol. Chem.* **1996**, *271* (48), 30426–30435.

(33) Du, Q.; Wang, H.; Xie, J. Thiamin (vitamin B1) biosynthesis and regulation: a rich source of antimicrobial drug targets? *Int. J. Biol. Sci.* **2011**, *7* (1), 41–52.

(34) Moreno-Sánchez, R.; Saavedra, E.; Rodríguez-Enríquez, S.; Olín-Sandoval, V. Metabolic control analysis: a tool for designing strategies to manipulate metabolic pathways. *J. Biomed. Biotechnol.* **2008**, *2008*, 1–30.

(35) Volke, D. C.; Rohwer, J.; Fischer, R.; Jennewein, S. Investigation of the methylerythritol 4-phosphate pathway for microbial terpenoid production through metabolic control analysis. *Microb. Cell Fact.* **2019**, *18* (1), 192.

(36) Xiang, S.; Usunow, G.; Lange, G.; Busch, M.; Tong, L. Crystal structure of 1-deoxy-D-xylulose 5-phosphate synthase, a crucial enzyme for isoprenoids biosynthesis. *J. Biol. Chem.* **2007**, *282* (4), 2676–2682.

(37) Morris, F.; Vierling, R.; Boucher, L.; Bosch, J.; Freel Meyers, C. L. DXP synthase-catalyzed C-N bond formation: nitroso substrate specificity studies guide selective inhibitor design. *ChemBioChem* **2013**, *14* (11), 1309–1315.

(38) Battistini, M. R.; Shoji, C.; Handa, S.; Breydo, L.; Merkler, D. J. Mechanistic binding insights for 1-deoxy-D-Xylulose-5-Phosphate synthase, the enzyme catalyzing the first reaction of isoprenoid biosynthesis in the malaria-causing protists, Plasmodium falciparum and Plasmodium vivax. *Protein Expr. Purif.* **2016**, *120*, 16–27.

(39) Eubanks, L. M.; Poulter, C. D. Rhodobacter capsulatus 1-deoxy-D-xylulose 5-phosphate synthase: steady-state kinetics and substrate binding. *Biochemistry* **2003**, *42* (4), 1140–1149.

(40) Brammer, L. A.; Smith, J. M.; Wade, H.; Meyers, C. F. 1-Deoxy-D-xylulose 5-phosphate synthase catalyzes a novel random sequential mechanism. *J. Biol. Chem.* **2011**, *286* (42), 36522–36531.

(41) Patel, H.; Nemeria, N. S.; Brammer, L. A.; Freel Meyers, C. L.; Jordan, F. Observation of thiamin-bound intermediates and microscopic rate constants for their interconversion on 1-deoxy-D-xylulose 5-phosphate synthase: 600-fold rate acceleration of pyruvate decarboxylation by D-glyceraldehyde-3-phosphate. *J. Am. Chem. Soc.* **2012**, *134* (44), 18374–18379.

(42) Basta, L. A. B.; Patel, H.; Kakalis, L.; Jordan, F.; Meyers, C. L. F. Defining critical residues for substrate binding to 1-deoxy-D-xylulose 5-phosphate synthase--active site

substitutions stabilize the predecarboxylation intermediate C2α-lactylthiamin diphosphate. *FEBS J.* **2014**, *281* (12), 2820–2837.

(43) DeColli, A. A.; Nemeria, N. S.; Majumdar, A.; Gerfen, G. J.; Jordan, F.; Freel Meyers, C. L. Oxidative decarboxylation of pyruvate by 1-deoxy-d-xyulose 5-phosphate synthase, a central metabolic enzyme in bacteria. *J. Biol. Chem.* **2018**, *293* (28), 10857–10869.

(44) Brammer, L. A.; Meyers, C. F. Revealing substrate promiscuity of 1-deoxy-D-xylulose 5-phosphate synthase. *Org. Lett.* **2009**, *11* (20), 4748–4751.

(45) DeColli, A. A.; Zhang, X.; Heflin, K. L.; Jordan, F.; Freel Meyers, C. L. Active Site Histidines Link Conformational Dynamics with Catalysis on Anti-Infective Target 1-Deoxy-d-xylulose 5-Phosphate Synthase. *Biochemistry* **2019**, *58* (49), 4970–4982.

(46) Zhou, J.; Yang, L.; DeColli, A.; Freel Meyers, C.; Nemeria, N. S.; Jordan, F. Conformational dynamics of 1-deoxy-d-xylulose 5-phosphate synthase on ligand binding revealed by H/D exchange MS. *PNAS* **2017**, *114* (35), 9355–9360.

(47) Chen, P. Y.-T.; DeColli, A. A.; Freel Meyers, C. L.; Drennan, C. L. X-ray crystallography-based structural elucidation of enzyme-bound intermediates along the 1-deoxy-d-xylulose 5-phosphate synthase reaction coordinate. *J. Biol. Chem.* **2019**, *294* (33), 12405–12414.

(48) Masini, T.; Kroezen, B. S.; Hirsch, A. K. H. Druggability of the enzymes of the non-mevalonate-pathway. *Drug Discov. Today* **2013**, *18* (23-24), 1256–1262.

(49) Volkamer, A.; Kuhn, D.; Grombacher, T.; Rippmann, F.; Rarey, M. Combining global and local measures for structure-based druggability predictions. *J. Chem. Inf. Model.* **2012**, *52* (2), 360–372.

(50) Matsue, Y.; Mizuno, H.; Tomita, T.; Asami, T.; Nishiyama, M.; Kuzuyama, T. The herbicide ketoclomazone inhibits 1-deoxy-D-xylulose 5-phosphate synthase in the 2-C-methyl-D-erythritol 4-phosphate pathway and shows antibacterial activity against Haemophilus influenzae. *J. Antibiot.* **2010**, *63* (10), 583–588.

(51) Gierse, R. M.; Redeem, E.; Diamanti, E.; Wrenger, C.; Groves, M. R.; Hirsch, A. K. DXS as a target for structure-based drug design. *Future Med. Chem.* **2017**, *9* (11), 1277–1294.

(52) Masini, T.; Lacy, B.; Monjas, L.; Hawksley, D.; Voogd, A. R. de; Illarionov, B.; Iqbal, A.; Leeper, F. J.; Fischer, M.; Kontoyianni, M.; Hirsch, A. K. H. Validation of a homology model of Mycobacterium tuberculosis DXS: rationalization of observed activities of thiamine derivatives as potent inhibitors of two orthologues of DXS. *Org. Biomol. Chem.* **2015**, *13* (46), 11263–11277.

(53) Gierse, R. M.; Reddem, E. R.; Alhayek, A.; Baitinger, D.; Hamid, Z.; Jakobi, H.; Laber, B.; Lange, G.; Hirsch, A. K. H.; Groves, M. R. Identification of a 1-deoxy-D-xylulose-5-phosphate synthase (DXS) mutant with improved crystallographic properties. *Biochem. Biophys. Res. Commun.* **2021**, *539*, 42–47.

(54) Hamid, R.; Adam, S.; Lacour, A.; Gomez, L. M.; Hirsch, A. K. H. Structural analysis of 1-deoxy-D-xylulose 5-phosphate synthase from Pseudomonas aeruginosa and Klebsiella pneumoniae reveals conformational changes upon cofactor binding. *bioRxiv* **2022**.

(55) Gierse, R. M.; Oerlemans, R.; Reddem, E. R.; Gawriljuk, V. O.; Alhayek, A.; Baitinger, D.; Jakobi, H.; Laber, B.; Lange, G.; Hirsch, A. K. H.; Groves, M. R. First crystal structures of 1-deoxy-d-xylulose 5-phosphate synthase (DXPS) from

Mycobacterium tuberculosis indicate a distinct mechanism of intermediate stabilization. *Sci. Rep.* **2022**, *12* (1).

(56) Altincicek, B.; Hintz, M.; Sanderbrand, S.; Wiesner, J.; Beck, E.; Jomaa, H. Tools for discovery of inhibitors of the 1-deoxy-D-xylulose 5-phosphate (DXP) synthase and DXP reductoisomerase: an approach with enzymes from the pathogenic bacterium Pseudomonas aeruginosa. *FEMS Microbiol. Lett.* **2000**, *190* (2), 329–333.

(57) Mueller, C.; Schwender, J.; Zeidler, J.; Lichtenthaler, H. K. Properties and inhibition of the first two enzymes of the non-mevalonate pathway of isoprenoid biosynthesis. *Biochem. Soc. Trans.* **2000**, *28* (6), 792–793.

(58) Marcozzi, A.; Masini, T.; Di Zhu; Pesce, D.; Illarionov, B.; Fischer, M.; Herrmann, A.; Hirsch, A. K. H. Phage Display on the Anti-infective Target 1-Deoxy-d-xylulose-5-phosphate Synthase Leads to an Acceptor-Substrate Competitive Peptidic Inhibitor. *ChemBioChem* **2018**, *19* (1), 58–65.

(59) Mao, J.; Eoh, H.; He, R.; Wang, Y.; Wan, B.; Franzblau, S. G.; Crick, D. C.; Kozikowski, A. P. Structure-activity relationships of compounds targeting mycobacterium tuberculosis 1-deoxy-D-xylulose 5-phosphate synthase. *Bioorg. Med. Chem. Lett.* **2008**, *18* (19), 5320–5323.

(60) Masini, T.; Pilger, J.; Kroezen, B. S.; Illarionov, B.; Lottmann, P.; Fischer, M.; Griesinger, C.; Hirsch, A. K. H. De novo fragment-based design of inhibitors of DXS guided by spin-diffusion-based NMR spectroscopy. *Chem. Sci.* **2014**, *5* (9), 3543–3551.

(61) Bartee, D.; Morris, F.; Al-Khouja, A.; Freel Meyers, C. L. Hydroxybenzaldoximes Are D-GAP-Competitive Inhibitors of E. coli 1-Deoxy-D-Xylulose-5-Phosphate Synthase. *ChemBioChem* **2015**, *16* (12), 1771–1781.

(62) Smith, J. M.; Vierling, R. J.; Meyers, C. F. Selective inhibition of E. coli 1-deoxy-D-xylulose-5-phosphate synthase by acetylphosphonates. *Med. Chem. Commun.* **2012**, *3*, 65–67.

(63) Smith, J. M.; Warrington, N. V.; Vierling, R. J.; Kuhn, M. L.; Anderson, W. F.; Koppisch, A. T.; Freel Meyers, C. L. Targeting DXP synthase in human pathogens: enzyme inhibition and antimicrobial activity of butylacetylphosphonate. *J. Antibiot.* **2014**, *67*, 77-83.

(64) Bartee, D.; Freel Meyers, C. L. Targeting the Unique Mechanism of Bacterial 1-Deoxy-d-xylulose-5-phosphate Synthase. *Biochem.* **2018**, *57* (29), 4349–4356.

(65) Jumde, R. P.; Guardigni, M.; Gierse, R. M.; Alhayek, A.; Di Zhu; Hamid, Z.; Johannsen, S.; Elgaher, W. A. M.; Neusens, P. J.; Nehls, C.; Haupenthal, J.; Reiling, N.; Hirsch, A. K. H. Hit-optimization using target-directed dynamic combinatorial chemistry: development of inhibitors of the anti-infective target 1-deoxy-d-xylulose-5-phosphate synthase. *Chem. Sci.* **2021**, *12* (22), 7775–7785.

(66) Flournoy, D. S.; Frey, P. A. Inactivation of the pyruvate dehydrogenase complex of Escherichia coli by fluoropyruvate. *Biochemistry* **1989**, *28* (25), 9594–9602.

(67) Ferhatoglu, Y.; Barrett, M. Studies of clomazone mode of action. *Pestic. Biochem. Physiol.* **2006**, *85* (1), 7–14.

(68) Oh, S.; Libardo, M. D. J.; Azeeza, S.; Pauly, G. T.; Roma, J. S. O.; Sajid, A.; Tateishi, Y.; Duncombe, C.; Goodwin, M.; Ioerger, T. R.; Wyatt, P. G.; Ray, P. C.; Gray, D. W.; Boshoff, H. I. M.; Barry, C. E. Structure-Activity Relationships of Pyrazolo1,5-

apyrimidin-7(4H)-ones as Antitubercular Agents. *ACS Infect. Dis.* **2021**, *7* (2), 479–492.

(69) Arjunan, P.; Sax, M.; Brunskill, A.; Chandrasekhar, K.; Nemeria, N.; Zhang, S.; Jordan, F.; Furey, W. A thiamin-bound, pre-decarboxylation reaction intermediate analogue in the pyruvate dehydrogenase E1 subunit induces large scale disorder-to-order transformations in the enzyme and reveals novel structural features in the covalently bound adduct. *J. Biol. Chem.* **2006**, *281* (22), 15296–15303.

(70) Bartee, D.; Sanders, S.; Phillips, P. D.; Harrison, M. J.; Koppisch, A. T.; Freel Meyers, C. L. Enamide Prodrugs of Acetyl Phosphonate Deoxy-d-xylulose-5-phosphate Synthase Inhibitors as Potent Antibacterial Agents. *ACS Infect. Dis.* **2019**, *5* (3), 406–417.

(71) Swinney, D. C.; Lee, J. A. Recent advances in phenotypic drug discovery. *F1000Research* **2020**, *9*.

(72) Croston, G. E. The utility of target-based discovery. *Expert Opin. Drug Discov.* **2017**, *12* (5), 427–429.

(73) Vázquez, J.; López, M.; Gibert, E.; Herrero, E.; Luque, F. J. Merging Ligand-Based and Structure-Based Methods in Drug Discovery: An Overview of Combined Virtual Screening Approaches. *Molecules* **2020**, *25* (20).

(74) Kirsch, P.; Hartman, A. M.; Hirsch, A. K. H.; Empting, M. Concepts and Core Principles of Fragment-Based Drug Design. *Molecules* **2019**, *24* (23).

(75) Murray, C. W.; Newell, D. R.; Angibaud, P. A successful collaboration between academia, biotech and pharma led to discovery of erdafitinib, a selective FGFR inhibitor recently approved by the FDA. *Med. Chem. Commun.* **2019**, *10* (9), 1509–1511.

(76) Tap, W. D.; Wainberg, Z. A.; Anthony, S. P.; Ibrahim, P. N.; Zhang, C.; Healey, J. H.; Chmielowski, B.; Staddon, A. P.; Cohn, A. L.; Shapiro, G. I.; Keedy, V. L.; Singh, A. S.; Puzanov, I.; Kwak, E. L.; Wagner, A. J.; Hoff, D. D. von; Weiss, G. J.; Ramanathan, R. K.; Zhang, J.; Habets, G.; Zhang, Y.; Burton, E. A.; Visor, G.; Sanftner, L.; Severson, P.; Nguyen, H.; Kim, M. J.; Marimuthu, A.; Tsang, G.; Shellooe, R.; Gee, C.; West, B. L.; Hirth, P.; Nolop, K.; van de Rijn, M.; Hsu, H. H.; Peterfy, C.; Lin, P. S.; Tong-Starksen, S.; Bollag, G. Structure-Guided Blockade of CSF1R Kinase in Tenosynovial Giant-Cell Tumor. *N. Engl. J. Med.* **2015**, *373* (5), 428–437.

(77) Bollag, G.; Hirth, P.; Tsai, J.; Zhang, J.; Ibrahim, P. N.; Cho, H.; Spevak, W.; Zhang, C.; Zhang, Y.; Habets, G.; Burton, E. A.; Wong, B.; Tsang, G.; West, B. L.; Powell, B.; Shellooe, R.; Marimuthu, A.; Nguyen, H.; Zhang, K. Y. J.; Artis, D. R.; Schlessinger, J.; Su, F.; Higgins, B.; Iyer, R.; D'Andrea, K.; Koehler, A.; Stumm, M.; Lin, P. S.; Lee, R. J.; Grippo, J.; Puzanov, I.; Kim, K. B.; Ribas, A.; McArthur, G. A.; Sosman, J. A.; Chapman, P. B.; Flaherty, K. T.; Xu, X.; Nathanson, K. L.; Nolop, K. Clinical efficacy of a RAF inhibitor needs broad target blockade in BRAF-mutant melanoma. *Nature* **2010**, *467* (7315), 596–599.

(78) Itchaki, G.; Brown, J. R. The potential of venetoclax (ABT-199) in chronic lymphocytic leukemia. *Therapeutic advances in hematology* **2016**, *7* (5), 270–287.

(79) Ostrem, J. M.; Peters, U.; Sos, M. L.; Wells, J. A.; Shokat, K. M. K-Ras(G12C) inhibitors allosterically control GTP affinity and effector interactions. *Nature* **2013**, *503* (7477), 548–551.

(80) Schoepfer, J.; Jahnke, W.; Berellini, G.; Buonamici, S.; Cotesta, S.; Cowan-Jacob, S. W.; Dodd, S.; Drueckes, P.; Fabbro, D.; Gabriel, T.; Groell, J.-M.; Grotzfeld, R. M.; Hassan, A. Q.; Henry, C.; Iyer, V.; Jones, D.; Lombardo, F.; Loo, A.; Manley, P. W.; Pellé, X.; Rummel, G.; Salem, B.; Warmuth, M.; Wylie, A. A.; Zoller, T.; Marzinzik, A. L.; Furet, P. Discovery of Asciminib (ABL001), an Allosteric Inhibitor of the Tyrosine Kinase Activity of BCR-ABL1. *J. Med. Chem.* **2018**, *61* (18), 8120–8135.

(81) Atta-ur-Rahman; Choudhary, M. I. Frontiers in Anti-Infective Drug Discovery: Volume 8; Bentham Science Publishers, **2020**.

(82) Rees, D. C.; Congreve, M.; Murray, C. W.; Carr, R. Fragment-based lead discovery. *Nat. Rev. Drug Discovery* **2004**, *3* (8), 660–672.

(83) Coyle, J.; Walser, R. Applied Biophysical Methods in Fragment-Based Drug Discovery. *SLAS Discov.* **2020**, *25* (5), 471–490.

(84) Renaud, J.-P.; Chung, C.-W.; Danielson, U. H.; Egner, U.; Hennig, M.; Hubbard, R. E.; Nar, H. Biophysics in drug discovery: impact, challenges and opportunities. *Nat. Rev. Drug Discov.* **2016**, *15* (10), 679–698.

(85) Viegas, A.; Manso, J.; Nobrega, F. L.; Cabrita, E. J. Saturation-Transfer Difference (STD) NMR: A Simple and Fast Method for Ligand Screening and Characterization of Protein Binding. *J. Chem. Educ.* **2011**, *88* (7), 990–994.

(86) Singh, M.; Tam, B.; Akabayov, B. NMR-Fragment Based Virtual Screening: A Brief Overview. *Molecules* **2018**, *23* (2), 233.

(87) Cala, O.; Krimm, I. Ligand-Orientation Based Fragment Selection in STD NMR Screening. *J. Med. Chem.* **2015**, *58* (21), 8739–8742.

(88) Giannetti, A. M. From experimental design to validated hits a comprehensive walk-through of fragment lead identification using surface plasmon resonance **2011**, *493*, 169–218.

(89) Seidel, S. A. I.; Dijkman, P. M.; Lea, W. A.; van den Bogaart, G.; Jerabek-Willemsen, M.; Lazic, A.; Joseph, J. S.; Srinivasan, P.; Baaske, P.; Simeonov, A.; Katritch, I.; Melo, F. A.; Ladbury, J. E.; Schreiber, G.; Watts, A.; Braun, D.; Duhr, S. Microscale thermophoresis quantifies biomolecular interactions under previously challenging conditions. *Methods* **2013**, *59* (3), 301–315.

(90) Wilcken, R.; Liu, X.; Zimmermann, M. O.; Rutherford, T. J.; Fersht, A. R.; Joerger, A. C.; Boeckler, F. M. Halogen-enriched fragment libraries as leads for drug rescue of mutant p53. *J. Am. Chem. Soc.* **2012**, *134* (15), 6810–6818.

(91) Wilcken, R.; Zimmermann, M. O.; Lange, A.; Joerger, A. C.; Boeckler, F. M. Principles and applications of halogen bonding in medicinal chemistry and chemical biology. *J. Med. Chem.* **2013**, *56* (4), 1363–1388.

(92) Zimmermann, M. O.; Lange, A.; Wilcken, R.; Cieslik, M. B.; Exner, T. E.; Joerger, A. C.; Koch, P.; Boeckler, F. M. Halogen-enriched fragment libraries as chemical probes for harnessing halogen bonding in fragment-based lead discovery. *Future Med. Chem.* **2014**, *6* (6), 617–639.

(93) Buskes, M. J.; Blanco, M.-J. Impact of Cross-Coupling Reactions in Drug Discovery and Development. *Molecules* **2020**, *25* (15), 3493.

(94) Scrubber 2.0c; BioLogic Software Pty Ltd., **2008**.

(95) Liang, Y.-F.; Liu, H.; Li, H.; Gao, W.-Y. Determination of the Activity of 1-Deoxy-D-Xylulose 5-Phosphate Synthase by Pre-column Derivatization-HPLC Using 1,2-

Diamino-4,5-Methylenedioxybenzene as a Derivatizing Reagent. *Protein J.* **2019**, *38* (2), 160–166.

(96) Nakamura, M.; Hara, S.; Yamaguchi, M.; Takemori, Y.; Ohkura, Y. 1,2-Diamino-4,5-methylenedioxybenzene as a highly sensitive fluorogenic reagent for alpha-keto acids. *Chem. Pharm. Bull.* **1987**, *35* (2), 687–692.

(97) Bisswanger, H. Enzyme assays. *Perspect. Sci.* **2014**, *1* (1-6), 41–55.

(98) Zhang; Chung; Oldenburg. A Simple Statistical Parameter for Use in Evaluation and Validation of High Throughput Screening Assays. *J. Biomol. Screening* **1999**, *4* (2), 67–73.

(99) Adeli, Z. Screening, identification, and co-crystallization of inhibitors of the anti-infective target 1-deoxy-D-xylulose 5-phosphate (DXP) synthase enzyme. Masterthesis, Saarland University, **2022**.

(100) Origin(Pro) 2020b; OriginLab Corporation Northampton, MA, USA.

(101) Wallach, I.; Dzamba, M.; Heifets, A. AtomNet: A Deep Convolutional Neural Network for Bioactivity Prediction in Structure-based Drug Discovery. https://arxiv.org/pdf/1510.02855.

(102) Hsieh, C.-H.; Li, L.; Vanhauwaert, R.; Nguyen, K. T.; Davis, M. D.; Bu, G.; Wszolek, Z. K.; Wang, X. Miro1 Marks Parkinson's Disease Subset and Miro1 Reducer Rescues Neuron Loss in Parkinson's Models. *Cell Metab.* **2019**, *30* (6), 1131-1140.e7.

(103) Huang, C.; Bernard, D.; Zhu, J.; Dash, R. C.; Chu, A.; Knupp, A.; Hakey, A.; Hadden, M. K.; Garmendia, A.; Tang, Y. Small molecules block the interaction between porcine reproductive and respiratory syndrome virus and CD163 receptor and the infection of pig cells. *Virol. J.* **2020**, *17* (1), 116.

(104) Stecula, A.; Hussain, M. S.; Viola, R. E. Discovery of Novel Inhibitors of a Critical Brain Enzyme Using a Homology Model and a Deep Convolutional Neural Network. *J. Med. Chem.* **2020**, *63* (16), 8867–8875.

(105) Sarshira, E. M.; Hamada, N. M.; Moghazi, Y. M.; Abdelrahman, M. M. Synthesis and Biological Evaluation of Some Heterocyclic Compounds from Salicylic Acid Hydrazide. *J. Heterocycl. Chem.* **2016**, *53* (6), 1970–1982.

(106) Cristina, A.; Leonte, D.; Laurian, V.; Bencze, L. C.; Imre, S.; Zaharia, V. Heterocycles 42. Synthesis and characterization of new thiazolo [3, 2-b][1, 2, 4] triazole derivatives with anti-inflammatory potential. *Farmacia* **2018**, *66* (1), 88–96.

(107) Sung, K.; Lee, A.-R. Synthesis of [(4,5-disubstituted-4 H -1,2,4-triazol-3-yl)thio]alkanoic acids and their analogues as possible antiinflammatory agents. *J. Heterocycl. Chem.* **1992**, *29* (5), 1101–1109.

(108) Ishibashi, H.; Uegaki, M.; Sakai, M. A Simple Synthesis of β-Amino Sulfides. *Synlett* **1997**, *1997* (8), 915–916.

(109) Steinman, D. H.; Curtin, M. L.; Garland, R. B.; Davidsen, S. K.; Heyman, H.; Holms, J. H.; Albert, D. H.; Magoc, T. J.; Nagy, I. B.; Marcotte, P. A.; Li, J.; Morgan, D. W.; Hutchins, C.; Summers, J. B. The design, synthesis, and structure-activity relationships of a series of macrocyclic MMP inhibitors. *Bioorg. Med. Chem. Lett.* **1998**, *8* (16), 2087–2092.

(110) Poindexter, G. S.; Owens, D. A.; Dolan, P. L.; Woo, E. The use of 2-oxazolidinones as latent aziridine equivalents. 2. Aminoethylation of aromatic amines, phenols, and thiophenols. *J. Org. Chem.* **1992**, *57* (23), 6257–6265.

(111) Koronakis, V.; Eswaran, J.; Hughes, C. Structure and function of TolC: the bacterial exit duct for proteins and drugs. *Annu. Rev. Biochem.* **2004**, *73*, 467–489.

(112) Richter, M. F.; Drown, B. S.; Riley, A. P.; Garcia, A.; Shirai, T.; Svec, R. L.; Hergenrother, P. J. Predictive compound accumulation rules yield a broad-spectrum antibiotic. *Nature* **2017**, *545* (7654), 299–304.

(113) Le Zhai; Zhang, Y.-L.; Kang, J. S.; Oelschlaeger, P.; Xiao, L.; Nie, S.-S.; Yang, K.-W. Triazolylthioacetamide: A Valid Scaffold for the Development of New Delhi Metallo-β-Lactmase-1 (NDM-1) Inhibitors. *ACS Med. Chem. Lett.* **2016**, *7* (4), 413–417.

(114) Sahi, S.; Sodhi, R. K.; Jamwal, B.; Paul, S. Synthesis and in vitro Biological Evaluation of Some Novel Triazole-Based Heterocycles as Potential Antimicrobial Agents. *J. Heterocycl. Chem.* **2018**, *55* (7), 1596–1603.

(115) World Health Organization. World Malaria Report 2021, **2021**.

(116) World Health Organization. Status report on artemisinin resistance and ACT, **2018**.

(117) Yeh, E.; DeRisi, J. L. Chemical rescue of malaria parasites lacking an apicoplast defines organelle function in blood-stage Plasmodium falciparum. *PLoS biology* **2011**, *9* (8), e1001138.

(118) Frank, A.; Groll, M. The methylerythritol phosphate pathway to isoprenoids. *Chem. Rev.* **2017**, *117* (8), 5675–5703.

(119) Gierse, R. M.; Redeem, E.; Diamanti, E.; Wrenger, C.; Groves, M. R.; Hirsch, A. K. DXS as a target for structure-based drug design. *Future Med. Chem.* **2017**, *9* (11), 1277–1294.

(120) Hale, I.; O'Neill, P. M.; Berry, N. G.; Odom, A.; Sharma, R. The MEP pathway and the development of inhibitors as potential anti-infective agents. *Med. Chem. Commun.* **2012**, *3* (4), 418.

(121) Fernandes, J. F.; Lell, B.; Agnandji, S. T.; Obiang, R. M.; Bassat, Q.; Kremsner, P. G.; Mordmüller, B.; Grobusch, M. P. Fosmidomycin as an antimalarial drug: a meta-analysis of clinical trials. *Future Microbiol.* **2015**, *10* (8), 1375–1390.

(122) Umeda, T.; Tanaka, N.; Kusakabe, Y.; Nakanishi, M.; Kitade, Y.; Nakamura, K. T. Molecular basis of fosmidomycin's action on the human malaria parasite Plasmodium falciparum. *Sci. Rep.* **2011**, *1*, 9.

(123) Du, Q.; Wang, H.; Xie, J. Thiamin (vitamin B1) biosynthesis and regulation: a rich source of antimicrobial drug targets? *Int. J. Biol. Sci.* **2011**, *7* (1), 41–52.

(124) Hill, R. E.; Himmeldirk, K.; Kennedy, I. A.; Pauloski, R. M.; Sayer, B. G.; Wolf, E.; Spenser, I. D. The biogenetic anatomy of vitamin B6. A 13C NMR investigation of the biosynthesis of pyridoxol in Escherichia coli. *J. Biol. Chem.* **1996**, *271* (48), 30426–30435.

(125) Müller, I. B.; Hyde, J. E.; Wrenger, C. Vitamin B metabolism in Plasmodium falciparum as a source of drug targets. *Trends. Mol. Med.* **2010**, *26* (1), 35–43.

(126) Di, Z.; Johannsen, S.; Masini, T.; Simonin, C.; Haupenthal, J.; Andreas, A.; Awale, M.; Gierse, R. M.; van der Laan, T.; van der Vlag, R.; Nasti, R.; Poizat, M.; Buhler, E.; Reiling, N.; Müller, R.; Fischer, M.; Reymond, J.-L.; Hirsch, A. K. H. Discovery of novel drug-like antitubercular hits targeting the MEP pathway enzyme DXPS by strategic application of ligand-based virtual screening. *Chem. Sci.* **2022**.

(127) Goswami, A. M. Computational analysis, structural modeling and ligand binding site prediction of Plasmodium falciparum 1-deoxy-d-xylulose-5-phosphate synthase. *Comput. Biol. Chem* **2017**, *66*, 1–10.

(128) Masini, T.; Lacy, B.; Monjas, L.; Hawksley, D.; Voogd, A. R. de; Illarionov, B.; Iqbal, A.; Leeper, F. J.; Fischer, M.; Kontoyianni, M.; Hirsch, A. K. H. Validation of a homology model of Mycobacterium tuberculosis DXS: rationalization of observed activities of thiamine derivatives as potent inhibitors of two orthologues of DXS. *Org. Biomol. Chem.* **2015**, *13* (46), 11263–11277.

(129) Bajorath, J. Selected concepts and investigations in compound classification, molecular descriptor analysis, and virtual screening. *J. Chem. Inf. Model.* **2001**, *41* (2), 233–245.

(130) Masini, T.; Pilger, J.; Kroezen, B. S.; Illarionov, B.; Lottmann, P.; Fischer, M.; Griesinger, C.; Hirsch, A. K. H. De novo fragment-based design of inhibitors of DXS guided by spin-diffusion-based NMR spectroscopy. *Chem. Sci.* **2014**, *5* (9), 3543–3551.

(131) Princeton Biomolecular Research. Express Collection. http:// www.princetonbio.com/products/diverse_targeted_screening_compounds (accessed 2015).

(132) Awale, M.; Reymond, J.-L. The polypharmacology browser: a web-based multi-fingerprint target prediction tool using ChEMBL bioactivity data. *J. Cheminformatics* **2017**, *9* (1), 11.

(133) Awale, M.; Reymond, J.-L. The Polypharmacology Browser PPB2: Target Prediction Combining Nearest Neighbors with Machine Learning, **2018**.

(134) Mendez, D.; Gaulton, A.; Bento, A. P.; Chambers, J.; Veij, M. de; Félix, E.; Magariños, M. P.; Mosquera, J. F.; Mutowo, P.; Nowotka, M.; Gordillo-Marañón, M.; Hunter, F.; Junco, L.; Mugumbate, G.; Rodriguez-Lopez, M.; Atkinson, F.; Bosc, N.; Radoux, C. J.; Segura-Cabrera, A.; Hersey, A.; Leach, A. R. ChEMBL: towards direct deposition of bioassay data. *Nucleic Acids Res.* **2019**, *47* (D1), D930-D940.

(135) Plouffe, D.; Brinker, A.; McNamara, C.; Henson, K.; Kato, N.; Kuhen, K.; Nagle, A.; Adrián, F.; Matzen, J. T.; Anderson, P.; Nam, T.-G.; Gray, N. S.; Chatterjee, A.; Janes, J.; Yan, S. F.; Trager, R.; Caldwell, J. S.; Schultz, P. G.; Zhou, Y.; Winzeler, E. A. In silico activity profiling reveals the mechanism of action of antimalarials discovered in a high-throughput screen. *PNAS* **2008**, *105* (26), 9059–9064.

(136) Wilkinson, C.; McPhillie, M. J.; Zhou, Y.; Woods, S.; Afanador, G. A.; Rawson, S.; Khaliq, F.; Prigge, S. T.; Roberts, C. W.; Rice, D. W.; McLeod, R.; Fishwick, C. W.; Muench, S. P. The benzimidazole based drugs show good activity against T. gondii but poor activity against its proposed enoyl reductase enzyme target. *Bioorg. Med. Chem. Lett.* **2014**, *24* (3), 911–916.

(137) Mehboob, S.; Hevener, K. E.; Truong, K.; Boci, T.; Santarsiero, B. D.; Johnson, M. E. Structural and enzymatic analyses reveal the binding mode of a novel series of Francisella tularensis enoyl reductase (FabI) inhibitors. *J. Med. Chem.* **2012**, *55* (12), 5933–5941.

(138) Ren, J.; Mistry, T. L.; Su, P.-C.; Mehboob, S.; Demissie, R.; Fung, L. W.-M.; Ghosh, A. K.; Johnson, M. E. Determination of absolute configuration and binding efficacy of benzimidazole-based FabI inhibitors through the support of electronic

circular dichroism and MM-GBSA techniques. *Bioorg. Med. Chem. Lett.* **2018**, *28* (11), 2074–2079.

(139) Mehboob, S.; Song, J.; Hevener, K. E.; Su, P.-C.; Boci, T.; Brubaker, L.; Truong, L.; Mistry, T.; Deng, J.; Cook, J. L.; Santarsiero, B. D.; Ghosh, A. K.; Johnson, M. E. Structural and biological evaluation of a novel series of benzimidazole inhibitors of Francisella tularensis enoyl-ACP reductase (FabI). *Bioorg. Med. Chem. Lett.* **2015**, *25* (6), 1292–1296.

(140) Freundlich, J. S.; Wang, F.; Tsai, H.-C.; Kuo, M.; Shieh, H.-M.; Anderson, J. W.; Nkrumah, L. J.; Valderramos, J.-C.; Yu, M.; Kumar, T. R. S.; Valderramos, S. G.; Jacobs, W. R.; Schiehser, G. A.; Jacobus, D. P.; Fidock, D. A.; Sacchettini, J. C. X-ray structural analysis of Plasmodium falciparum enoyl acyl carrier protein reductase as a pathway toward the optimization of triclosan antimalarial efficacy. *J. Biol. Chem.* **2007**, *282* (35), 25436–25444.

(141) Hevener, K. E.; Mehboob, S.; Su, P.-C.; Truong, K.; Boci, T.; Deng, J.; Ghassemi, M.; Cook, J. L.; Johnson, M. E. Discovery of a novel and potent class of F. tularensis enoyl-reductase (FabI) inhibitors by molecular shape and electrostatic matching. *J. Med. Chem.* **2012**, *55* (1), 268–279.

(142) Rana, P.; Ghouse, S. M.; Akunuri, R.; Madhavi, Y. V.; Chopra, S.; Nanduri, S. FabI (enoyl acyl carrier protein reductase) - A potential broad spectrum therapeutic target and its inhibitors. *Eur. J. Med. Chem.* **2020**, *208*, 112757.

(143) Wickramasinghe, S. R.; Inglis, K. A.; Urch, J. E.; Müller, S.; van Aalten, D. M. F.; Fairlamb, A. H. Kinetic, inhibition and structural studies on 3-oxoacyl-ACP reductase from Plasmodium falciparum, a key enzyme in fatty acid biosynthesis. *Biochem.* **2006**, *393* (2), 447–457.

(144) Fernández de Luco, J.; Recio-Balsells, A. I.; Ghiano, D. G.; Bortolotti, A.; Belardinelli, J. M.; Liu, N.; Hoffmann, P.; Lherbet, C.; Tonge, P. J.; Tekwani, B.; Morbidoni, H. R.; Labadie, G. R. Exploring the chemical space of 1,2,3-triazolyl triclosan analogs for discovery of new antileishmanial chemotherapeutic agents. *RSC Med. Chem.* **2021**, *12* (1), 120–128.

(145) Lu, X.; Huang, K.; You, Q. Enoyl acyl carrier protein reductase inhibitors: a patent review (2006 - 2010). *Expert Opin. Ther. Pat.* **2011**, *21* (7), 1007–1022.

(146) Marreddy, R. K. R.; Wu, X.; Sapkota, M.; Prior, A. M.; Jones, J. A.; Sun, D.; Hevener, K. E.; Hurdle, J. G. The fatty acid synthesis protein enoyl-ACP reductase II (FabK) is a target for narrow-spectrum antibacterials for Clostridium difficile infection. *ACS Infect. Dis.* **2019**, *5* (2), 208–217.

(147) Zitko, J.; Doležal, M. Enoyl acyl carrier protein reductase inhibitors: an updated patent review (2011 - 2015). *Expert Opin. Ther. Pat.* **2016**, *26* (9), 1079–1094.

(148) Shears, M. J.; Botté, C. Y.; McFadden, G. I. Fatty acid metabolism in the Plasmodium apicoplast: Drugs, doubts and knockouts. *Mol. Biochem. Parasitol.* **2015**, *199* (1-2), 34–50.

(149) van Schaijk, B. C. L.; Kumar, T. R. S.; Vos, M. W.; Richman, A.; van Gemert, G.-J.; Li, T.; Eappen, A. G.; Williamson, K. C.; Morahan, B. J.; Fishbaugher, M.; Kennedy, M.; Camargo, N.; Khan, S. M.; Janse, C. J.; Sim, K. L.; Hoffman, S. L.; Kappe, S. H. I.; Sauerwein, R. W.; Fidock, D. A.; Vaughan, A. M. Type II fatty acid biosynthesis is essential for Plasmodium falciparum sporozoite development in the midgut of Anopheles mosquitoes. *Eukaryot. Cell* **2014**, *13* (5), 550–559.

(150) Vaughan, A. M.; O'Neill, M. T.; Tarun, A. S.; Camargo, N.; Phuong, T. M.; Aly, A. S. I.; Cowman, A. F.; Kappe, S. H. I. Type II fatty acid synthesis is essential only for malaria parasite late liver stage development. *Cell. Microbiol.* **2009**, *11* (3), 506–520.

(151) Meissner, A.; Boshoff, H. I.; Vasan, M.; Duckworth, B. P.; Barry, C. E.; Aldrich, C. C. Structure-activity relationships of 2-aminothiazoles effective against Mycobacterium tuberculosis. *Bioorg. Med. Chem.* **2013**, *21* (21), 6385–6397.

(152) Makam, P.; Kannan, T. 2-Aminothiazole derivatives as antimycobacterial agents: Synthesis, characterization, in vitro and in silico studies. *Eur. J. Med. Chem.* **2014**, *87*, 643–656.

(153) Al-Balas, Q.; Anthony, N. G.; Al-Jaidi, B.; Alnimr, A.; Abbott, G.; Brown, A. K.; Taylor, R. C.; Besra, G. S.; McHugh, T. D.; Gillespie, S. H.; Johnston, B. F.; Mackay, S. P.; Coxon, G. D. Identification of 2-aminothiazole-4-carboxylate derivatives active against Mycobacterium tuberculosis H37Rv and the beta-ketoacyl-ACP synthase mtFabH. *PloS one* **2009**, *4* (5), e5617.

(154) Waters, N. Functional characterization of the acyl carrier protein (PfACP) and beta-ketoacyl ACP synthase III (PfKASIII) from Plasmodium falciparum. *Mol. Biochem. Parasitol.* **2002**, *123* (2), 85–94.

(155) Bhuniya, D.; Mukkavilli, R.; Shivahare, R.; Launay, D.; Dere, R. T.; Deshpande, A.; Verma, A.; Vishwakarma, P.; Moger, M.; Pradhan, A.; Pati, H.; Gopinath, V. S.; Gupta, S.; Puri, S. K.; Martin, D. Aminothiazoles: Hit to lead development to identify antileishmanial agents. *Eur. J. Med. Chem.* **2015**, *102*, 582–593.

(156) Bursavich, M. G.; Parker, D. P.; Willardsen, J. A.; Gao, Z.-H.; Davis, T.; Ostanin, K.; Robinson, R.; Peterson, A.; Cimbora, D. M.; Zhu, J.-F.; Richards, B. 2-Anilino-4-aryl-1,3-thiazole inhibitors of valosin-containing protein (VCP or p97). *Bioorg. Med. Chem. Lett.* **2010**, *20* (5), 1677–1679.

(157) Harbut, M. B.; Patel, B. A.; Yeung, B. K. S.; McNamara, C. W.; Bright, A. T.; Ballard, J.; Supek, F.; Golde, T. E.; Winzeler, E. A.; Diagana, T. T.; Greenbaum, D. C. Targeting the ERAD pathway via inhibition of signal peptide peptidase for antiparasitic therapeutic design. *PNAS* **2012**, *109* (52), 21486–21491.

(158) Chung, D.-W. D.; Ponts, N.; Prudhomme, J.; Rodrigues, E. M.; Le Roch, K. G. Characterization of the ubiquitylating components of the human malaria parasite's protein degradation pathway. *PloS one* **2012**, *7* (8), e43477.

(159) Chou, T.-F.; Brown, S. J.; Minond, D.; Nordin, B. E.; Li, K.; Jones, A. C.; Chase, P.; Porubsky, P. R.; Stoltz, B. M.; Schoenen, F. J.; Patricelli, M. P.; Hodder, P.; Rosen, H.; Deshaies, R. J. Reversible inhibitor of p97, DBeQ, impairs both ubiquitin-dependent and autophagic protein clearance pathways. *PNAS* **2011**, *108* (12), 4834–4839.

(160) Bilodeau, M. T.; Rodman, L. D.; McGaughey, G. B.; Coll, K. E.; Koester, T. J.; Hoffman, W. F.; Hungate, R. W.; Kendall, R. L.; McFall, R. C.; Rickert, K. W.; Rutledge, R. Z.; Thomas, K. A. The discovery of N-(1,3-thiazol-2-yl)pyridin-2-amines as potent inhibitors of KDR kinase. *Bioorg. Med. Chem. Lett.* **2004**, *14* (11), 2941–2945.

(161) Rödl, C. B.; Vogt, D.; Kretschmer, S. B. M.; Ihlefeld, K.; Barzen, S.; Brüggerhoff, A.; Achenbach, J.; Proschak, E.; Steinhilber, D.; Stark, H.; Hofmann, B. Multi-dimensional target profiling of N,4-diaryl-1,3-thiazole-2-amines as potent inhibitors of eicosanoid metabolism. *Eur. J. Med. Chem.* **2014**, *84*, 302–311.

(162) Wu, S.; Wang, L.; Guo, W.; Liu, X.; Liu, J.; Wei, X.; Fang, B. Analogues and derivatives of oncrasin-1, a novel inhibitor of the C-terminal domain of RNA polymerase II and their antitumor activities. *J. Med. Chem.* **2011**, *54* (8), 2668–2679.

(163) Bridgford, J. L.; Xie, S. C.; Cobbold, S. A.; Pasaje, C. F. A.; Herrmann, S.; Yang, T.; Gillett, D. L.; Dick, L. R.; Ralph, S. A.; Dogovski, C.; Spillman, N. J.; Tilley, L. Artemisinin kills malaria parasites by damaging proteins and inhibiting the proteasome. *Nat. Commun.* **2018**, *9* (1), 3801.

(164) Shibeshi, M. A.; Kifle, Z. D.; Atnafie, S. A. Antimalarial drug resistance and novel targets for antimalarial drug discovery. *Infect. Drug. Resist.* **2020**, *13*, 4047–4060.

(165) Urgin, K.; Jida, M.; Ehrhardt, K.; Müller, T.; Lanzer, M.; Maes, L.; Elhabiri, M.; Davioud-Charvet, E. Pharmacomodulation of the antimalarial plasmodione: synthesis of biaryl- and N-arylalkylamine analogues, antimalarial activities and physicochemical properties. *Molecules* **2017**, *22* (1), 161.

(166) Wu, G.; Yin, W.; Shen, H. C.; Huang, Y. One-pot synthesis of useful heterocycles in medicinal chemistry using a cascade strategy. *Green Chem.* **2012**, *14* (3), 580.

(167) Snyder, S. A.; Zografos, A. L.; Lin, Y. Total synthesis of resveratrol-based natural products: a chemoselective solution. *Angew. Chem. Int. Ed Engl.* **2007**, *46* (43), 8186–8191.

(168) To, T. A.; Vo, Y. H.; Nguyen, A. T.; Phan, A. N. Q.; Truong, T.; Phan, N. T. S. A new route to substituted furocoumarins via copper-catalyzed cyclization between 4-hydroxycoumarins and ketoximes. *Org. Biomol. Chem.* **2018**, *16* (28), 5086–5089.

(169) Ivanov, I.; Nikolova, S.; Statkova-Abeghe, S. Efficient one-pot Friedel–Crafts Acylation of benzene and its derivatives with unprotected aminocarboxylic acids in polyphosphoric acid. *Synth. Commun.* **2006**, *36* (10), 1405–1411.

(170) Wang, S.; Shen, Y.-B.; Li, L.-F.; Qiu, B.; Yu, L.; Liu, Q.; Xiao, J. N-Alkylation-initiated redox-neutral 5 + 2 annulation of 3-alkylindoles with o-aminobenzaldehydes: access to indole-1,2-fused 1,4-benzodiazepines. *Org. Lett.* **2019**, *21* (22), 8904–8908.

(171) Giraud, F.; Loge, C.; Pagniez, F.; Crepin, D.; Barres, S.; Picot, C.; Le Pape, P.; Le Borgne, M. Design, synthesis and evaluation of 3-(imidazol- 1-ylmethyl)indoles as antileishmanial agents. Part II. *J. Enzyme Inhib. Med. Chem.* **2009**, *24* (5), 1067–1075.

(172) Somei, M.; Yamada, F.; Kobayashi, K.; Shimizu, A.; Aoki, N. A synthesis method of indole-3-methanamine and/or gramine from indole-3-carboxaldehyde, and its application for the synthese of brassinin, its 4-substituted analogus, and 1,3,4,5-tetrahydropyrrolo[4,3,2-de]quinoline. *Heterocycles* **1993**, *36* (12), 2783.

(173) Kulkarni, A.; Soni, I.; Kelkar, D. S.; Dharmaraja, A. T.; Sankar, R. K.; Beniwal, G.; Rajendran, A.; Tamhankar, S.; Chopra, S.; Kamat, S. S.; Chakrapani, H. Chemoproteomics of an indole-based quinone epoxide identifies druggable vulnerabilities in vancomycin-resistant Staphylococcus aureus. *J. Med. Chem.* **2019**, *62* (14), 6785–6795.

(174) Caracciolo Torchiarolo, G.; Iacoangeli, T.; Furlotti, G.; (None). Process for the preparation of 1-benzyl-3-hydroxymethyl-1H-indazole and its derivatives and required magnesium intermediates. WO2010EP60937 20100728.

(175) Matsumoto, K.; Arai, S.; Nishida, A. Formal synthesis of (±) —quebrachamine through regio- and stereoselective hydrocyanation of arylallene. *Tetrahedron* **2018**, *74* (23), 2865–2870.

(176) Kesicki, E. A.; Bailey, M. A.; Ovechkina, Y.; Early, J. V.; Alling, T.; Bowman, J.; Zuniga, E. S.; Dalai, S.; Kumar, N.; Masquelin, T.; Hipskind, P. A.; Odingo, J. O.; Parish, T. Synthesis and evaluation of the 2-aminothiazoles as anti-tubercular agents. *PloS one* **2016**, *11* (5), e0155209.

(177) Collins, W. E.; Moss, D.; Chin, W. The Continuous Cultivation of Plasmodium Fragile by the Method of Trager-Jensen. *Am. J. Trop. Med. Hyg.* **1979**, *28* (3), 591–592.

(178) Das Gupta, R.; Krause-Ihle, T.; Bergmann, B.; Müller, I. B.; Khomutov, A. R.; Müller, S.; Walter, R. D.; Lüersen, K. 3-Aminooxy-1-aminopropane and derivatives have an antiproliferative effect on cultured Plasmodium falciparum by decreasing intracellular polyamine concentrations. *Antimicrob. Agents Chemother.* **2005**, *49* (7), 2857–2864.

(179) Smilkstein, M.; Sriwilaijaroen, N.; Kelly, J. X.; Wilairat, P.; Riscoe, M. Simple and inexpensive fluorescence-based technique for high-throughput antimalarial drug screening. *Antimicrob. Agents Chemother.* **2004**, *48* (5), 1803–1806.

(180) Meissner, K. A.; Kronenberger, T.; Maltarollo, V. G.; Trossini, G. H. G.; Wrenger, C. Targeting the Plasmodium falciparum plasmepsin V by ligand-based virtual screening. *Chem. Biol. Drug Des.* **2019**, *93* (3), 300–312.

(181) Trager, W.; Jensen, J. B. Human malaria parasites in continuous culture. *Science (New York, N.Y.)* **1976**, *193* (4254), 673–675.

(182) Zhang, B.; Watts, K. M.; Hodge, D.; Kemp, L. M.; Hunstad, D. A.; Hicks, L. M.; Odom, A. R. A second target of the antimalarial and antibacterial agent fosmidomycin revealed by cellular metabolic profiling. *Biochemistry* **2011**, *50* (17), 3570–3577.

(183) Coley, P. D.; Corbett, Y.; Cubilla, L.; Ortega-Barria, E.; Herrera, L.; Capson, T. L.; Gonzalez, J.; Kursar, T. A.; Romero, L. I. A Novel DNA-Based Microfluorimetric Method to Evaluate Antimalarial Drug Activity. *Am. J. Trop. Med. Hyg.* **2004**, *70* (2), 119–124.

(184) Noedl, H.; Bronnert, J.; Yingyuen, K.; Attlmayr, B.; Kollaritsch, H.; Fukuda, M. Simple histidine-rich protein 2 double-site sandwich enzyme-linked immunosorbent assay for use in malaria drug sensitivity testing. *Antimicrob. Agents Chemother.* **2005**, *49* (8), 3575–3577.

(185) Carvalho, L. P. de; Sandri, T. L.; José Tenório de Melo, E.; Fendel, R.; Kremsner, P. G.; Mordmüller, B.; Held, J. Ivermectin Impairs the Development of Sexual and Asexual Stages of Plasmodium falciparum In Vitro. *Antimicrob. Agents Chemother.* **2019**, *63* (8).

(186) Vienna Austria R Foundation for Statical Computing. A language and environment for statistical computing, Vol. 1, **2008**.

(187) Haupenthal, J.; Baehr, C.; Zeuzem, S.; Piiper, A. RNAse A-like enzymes in serum inhibit the anti-neoplastic activity of siRNA targeting polo-like kinase 1. *Int. J. Cancer* **2007**, *121* (1), 206–210.

(188) Müller, I. B.; Knöckel, J.; Eschbach, M.-L.; Bergmann, B.; Walter, R. D.; Wrenger, C. Secretion of an acid phosphatase provides a possible mechanism to acquire host nutrients by Plasmodium falciparum. *Cell. Microbiol.* **2010**, *12* (5), 677–691.

(189) Chan, X. W. A.; Wrenger, C.; Stahl, K.; Bergmann, B.; Winterberg, M.; Müller, I. B.; Saliba, K. J. Chemical and genetic validation of thiamine utilization as an antimalarial drug target. *Nat. Commun.* **2013**, *4* (1), 2060.

(190) Schmittgen, T. D.; Livak, K. J. Analyzing real-time PCR data by the comparative CT method. Nature Protocols, 3(6), 1101-1108. *Nat. Protoc.* **2008**, *3* (6), 1101–1108.

(191) Waterhouse, A.; Bertoni, M.; Bienert, S.; Studer, G.; Tauriello, G.; Gumienny, R.; Heer, F. T.; Beer, T. A. P. de; Rempfer, C.; Bordoli, L.; Lepore, R.; Schwede, T. SWISS-MODEL: homology modelling of protein structures and complexes. *Nucleic Acids Res.* **2018**, *46* (W1), 296-303.

(192) Benkert, P.; Biasini, M.; Schwede, T. Toward the estimation of the absolute quality of individual protein structure models. *Bioinformatics* **2011**, *27* (3), 343–350.

(193) Xiao, Z.; Huang, S.; Wang, X.; Yang, P.; Xiangy, Y. Phenyl benzyl propionyl-N-methyloxyxamic urease inhibitor and synthesis and use thereof. CN201210590545A·2012-12-29.

(194) Schasfoort, R. B. M. Handbook of surface plasmon resonance, 2nd edition; Royal Society of Chemistry, **2017**.

(195) Hecht, S.; Wungsintaweekul, J.; Rohdich, F.; Kis, K.; Radykewicz, T.; Schuhr, C. A.; Eisenreich, W.; Richter, G.; Bacher, A. Biosynthesis of terpenoids: efficient multistep biotransformation procedures affording isotope-labeled 2C-methyl-D-erythritol 4-phosphate using recombinant 2C-methyl-D-erythritol 4-phosphate synthase. *J. Org. Chem.* **2001**, *66* (23), 7770–7775.

(196) Elgaher, W. A. M.; Fruth, M.; Groh, M.; Haupenthal, J.; Hartmann, R. W. Expanding the scaffold for bacterial RNA polymerase inhibitors: design, synthesis and structure–activity relationships of ureido-heterocyclic-carboxylic acids. *RSC Adv* **2014**, *4* (5), 2177–2194.

(197) Sahner, J. H.; Groh, M.; Negri, M.; Haupenthal, J.; Hartmann, R. W. Novel small molecule inhibitors targeting the "switch region" of bacterial RNAP: structure-based optimization of a virtual screening hit. *Eur. J. Med. Chem.* **2013**, *65*, 223–231.

(198) Rarey, M.; Kramer, B.; Lengauer, T.; Klebe, G. A fast flexible docking method using an incremental construction algorithm. *J. Mol. Biol.* **1996**, *261* (3), 470–489.

(199) Schneider, N.; Lange, G.; Hindle, S.; Klein, R.; Rarey, M. A consistent description of HYdrogen bond and DEhydration energies in protein-ligand complexes: methods behind the HYDE scoring function. *J. Comput. Aided Mol. Des.* **2013**, *27* (1), 15–29.

(200) Reulecke, I.; Lange, G.; Albrecht, J.; Klein, R.; Rarey, M. Towards an integrated description of hydrogen bonding and dehydration: decreasing false positives in virtual screening with the HYDE scoring function. *ChemMedChem* **2008**, *3* (6), 885–897.

(201) Bøgesø, K. P.; Christensen, A. V.; Hyttel, J.; Liljefors, T. 3-Phenyl-1-indanamines. Potential antidepressant activity and potent inhibition of dopamine, norepinephrine, and serotonin uptake. *J. Med. Chem.* **1985**, *28* (12), 1817–1828.

(202) EMBL-EBI. CHEMBL296602, **accessed 2021**. https://www.ebi.ac.uk/chembl/compound_report_card/CHEMBL296602/.

(203) EMBL-EBI. CHEMBL1257030, **accessed 2021**. https://www.ebi.ac.uk/chembl/compound_report_card/CHEMBL1257030/.

(204) Floridi, A.; Paggi, M. G.; Marcante, M. L.; Silvestrini, B.; Caputo, A.; Martino, C. de. Lonidamine, a selective Iinhibitor of aerobic glycolysis of murine tumor cells. *J. Natl. Cancer Inst.* **1981**.

(205) Hille, U. E.; Zimmer, C.; Vock, C. A.; Hartmann, R. W. First selective CYP11B1 inhibitors for the treatment of cortisol-dependent diseases. *ACS Med. Chem. Lett.* **2011**, *2* (1), 2–6.

(206) EMBL-EBI. CHEMBL1384007, **accessed 2021**. https://www.ebi.ac.uk/chembl/compound_report_card/CHEMBL1384007/.

(207) Al-Asri, J.; Fazekas, E.; Lehoczki, G.; Perdih, A.; Görick, C.; Melzig, M. F.; Gyémánt, G.; Wolber, G.; Mortier, J. From carbohydrates to drug-like fragments: Rational development of novel α-amylase inhibitors. *Bioorg. Med. Chem.* **2015**, *23* (20), 6725–6732.

(208) Baell, J. B.; Holloway, G. A. New substructure filters for removal of pan assay interference compounds (PAINS) from screening libraries and for their exclusion in bioassays. *J. Med. Chem.* **2010**, *53* (7), 2719–2740.

(209) Zhou, Q.; Reekie, T. A.; Abbassi, R. H.; Indurthi Venkata, D.; Font, J. S.; Ryan, R. M.; Munoz, L.; Kassiou, M. Synthesis and in vitro evaluation of diverse heterocyclic diphenolic compounds as inhibitors of DYRK1A. *Bioorg. Med. Chem.* **2018**, *26* (22), 5852–5869.

(210) Deng, S.; Cheng, Z.; Ingalls, C.; Kontes, F.; Yan, J.; Belvedere, S. Synthesis of 2,3,4,5-Tetrahydrobenzo[1,4]thiazepines via N -Acyliminium Cyclization. *Org. Process Res. Dev.* **2017**, *21* (11), 1801–1805.

(211) Conroy, T.; Manohar, M.; Gong, Y.; Wilkinson, S. M.; Webster, M.; Lieberman, B. P.; Banister, S. D.; Reekie, T. A.; Mach, R. H.; Rendina, L. M.; Kassiou, M. A systematic exploration of the effects of flexibility and basicity on sigma (σ) receptor binding in a series of substituted diamines. *Org. Biomol. Chem.* **2016**, *14* (39), 9388–9405.

(212) Guda, D. R.; Wang, T.; Cho, H. M.; Lee, M. E. Trimethylsilyl isothiocyanate (TMSNCS): an efficient reagent for the one-pot synthesis of mercapto-1,2,4-triazoles. *Tetrahedron Lett.* **2012**, *53* (39), 5238–5242.

(213) Andrews, P. C.; Beck, T.; Fraser, B. H.; Junk, P. C.; Massi, M.; Moubaraki, B.; Murray, K. S.; Silberstein, M. Functionalised β-diketonate polynuclear lanthanoid hydroxo clusters: Synthesis, characterisation, and magnetic properties. *Polyhedron* **2009**, *28* (11), 2123–2130.

(214) Yuan, C.; Yan, J.; Song, C.; Yang, F.; Li, C.; Wang, C.; Su, H.; Chen, W.; Wang, L.; Wang, Z.; Qian, S.; Yang, L. Discovery of 1,2,4Triazole Derivatives as New Metallo-β-Lactamase Inhibitors. *Molecules* **2019**, *25* (1), 56.

(215) Chaudhary, P. M.; Chavan, S. R.; Kavitha, M.; Maybhate, S. P.; Deshpande, S. R.; Likhite, A. P.; Rajamohanan, P. R. Structural elucidation of propargylated products of 3-substituted-1,2,4-triazole-5-thiols by NMR techniques. *Magn. Reson. Chem.* **2008**, *46* (12), 1168–1174.

(216) Katkevica, S.; Salun, P.; Jirgensons, A. Synthesis of 5-substituted 3-mercapto-1,2,4-triazoles via Suzuki–Miyaura reaction. *Tetrahedron Lett.* **2013**, *54* (34), 4524–4525.

(217) Kaushik, C. P.; Luxmi, R. Synthesis, antibacterial, and antioxidant activities of naphthyl-linked disubstituted 1,2,3-triazoles. *J. Heterocycl. Chem.* **2020**, *57* (6), 2400–2409.

(218) Li, S.; Li, X.; Zhang, T.; Kamara, M. O.; Liang, J.; Zhu, J.; Meng, F. Design, synthesis and biological evaluation of homoerythrina alkaloid derivatives bearing a triazole moiety as PARP-1 inhibitors and as potential antitumor drugs. *Bioorg. Chem.* **2020**, *94*, 103385.

(219) Landge, S. M.; Lazare, D. Y.; Freeman, C.; Bunn, J.; Cruz, J. I.; Winder, D.; Padgett, C.; Aiken, K. S.; Ghosh, D. Rationally designed phenanthrene derivatized triazole as a dual chemosensor for fluoride and copper recognition. *Spectrochim. Acta A Mol. Biomol.* **2020**, *228*, 117758.

(220) Evans, J. C.; Mizrahi, V. The application of tetracyclineregulated gene expression systems in the validation of novel drug targets in Mycobacterium tuberculosis. *Front. Microbiol.* **2015**, *6*, 812.

(221) Tiziana Masini. The enzyme DXS as an anti-infective target:Exploiting multiple hit-identification strategies. PhD thesis, University of Groningen, **2015**.

(222) Kesicki, E. A.; Bailey, M. A.; Ovechkina, Y.; Early, J. V.; Alling, T.; Bowman, J.; Zuniga, E. S.; Dalai, S.; Kumar, N.; Masquelin, T.; Hipskind, P. A.; Odingo, J. O.; Parish, T. Synthesis and Evaluation of the 2-Aminothiazoles as Anti-Tubercular Agents. *PLoS One* **2016**, *11* (5), e0155209.

(223) Wescott, H. H.; Zuniga, E. S.; Bajpai, A.; Trujillo, C.; Ehrt, S.; Schnappinger, D.; Roberts, D. M.; Parish, T. Identification of Enolase as the Target of 2-Aminothiazoles in Mycobacterium tuberculosis. *Front. Microbiol.* **2018**, *9*, 2542.

(224) Chen, X.; Wang, Y.; Ma, N.; Tian, J.; Shao, Y.; Zhu, B.; Wong, Y. K.; Liang, Z.; Zou, C.; Wang, J. Target identification of natural medicine with chemical proteomics approach: probe synthesis, target fishing and protein identification. *Signal Transduct. Target. Ther.* **2020**, *5* (1), 72.

(225) Hill, J. R.; Robertson, A. A. B. Fishing for Drug Targets: A Focus on Diazirine Photoaffinity Probe Synthesis. *J. Med. Chem.* **2018**, *61* (16), 6945–6963.

(226) Diab, S.; Abdelaziz, A. M.; Li, P.; Teo, T.; Basnet, S. K. C.; Noll, B.; Rahaman, M. H.; Lu, J.; Hou, J.; Yu, M.; Le, B. T.; Albrecht, H.; Milne, R. W.; Wang, S. Dual Inhibition of Mnk2 and FLT3 for potential treatment of acute myeloid leukaemia. *Eur. J. Med. Chem.* **2017**, *139*, 762–772.

(227) Yura, Y. Studies on Acetylenic Compounds. XXV.Ring Closure.(5). New Synthetic Method of Heterocyclic Compounds from α-Amino-and α-N-substitued Aminoacetylenic Compounds. *Chem. Pharm. Bull.* **1962**, *10* (11), 1087–1093.